Dusty plasma physics: Nanoparticle growth and complex plasma crystals

Lénaïc Couëdel

November 7, 2022

Contents

1 Introduction **5**

2 Career Overview **7**
2.1 Overview of research activities . . . 7
2.1.1 Research funds . . . 10
2.1.2 Collaborations avec des partenaires académiques . . . 10
2.2 Reception and impact of my research . . . 11
2.2.1 Consequence of the COVID-19 pandemic on my research program . . . 12
2.3 Supervisory and teaching activities . . . 12
2.3.1 Supervisory activities . . . 13
2.3.2 Teaching activities . . . 14
2.4 Professional and administrative services . . . 15
2.4.1 Research facilitation . . . 15
2.4.2 Professional services . . . 15
2.4.3 Administrative services . . . 16

3 Summary of main research results **17**
3.1 Introduction to laboratory dusty plasma physics . . . 17
3.1.1 Charge of dust particles . . . 18
3.1.2 Force acting on dust particles . . . 21
3.1.3 Growth of nanoparticles in low pressure plasmas . . . 24
3.1.4 Sheath profile in a capacitively-coupled radio-frequency discharge . . . 26
3.1.5 Microparticle levitation in the rf sheath . . . 31
3.1.6 Two-dimensional complex plasma crystals . . . 32
3.2 Nanoparticle growth . . . 40
3.2.1 General motivations . . . 40
3.2.2 Nanoparticle growth in direct-current glow discharge . . . 41
3.2.3 Characterisation of a direct-current planar magnetron discharge used for nanoparticle growth . . . 48
3.2.4 Nanoparticle growth in magnetised capacitivelly-coupled radio-frequency discharge . . . 56
3.2.5 Main publications . . . 63
3.3 Two-dimensional plasma crystals . . . 93
3.3.1 Experimental set-up . . . 93
3.3.2 Measurement of in-plane and out-of-plane waves . . . 94
3.3.3 Hybrid modes in two-dimensional complex plasma crystals . . . 96
3.3.4 Threshold of the mode-coupling instability . . . 99
3.3.5 Early stage of the Mode-coupling instability: particle motion synchronisation . . . 101
3.3.6 Mode-coupling induced melting . . . 103

3.3.7 Main publications . . . 114

4 Current and future research projects **135**
4.1 Context . . . 135
4.2 Main research themes . . . 135
4.2.1 Theme 1: Sheath studies, plasma-surface surface interactions . . . 136
4.2.2 Theme 2: Dynamics and transport of micro- and nano-particles in laboratory plasmas . . . 136
4.2.3 Theme 3: Dynamics, transport and lifetime of dusts in tokamaks . . . 137
4.2.4 Theme 4: Theoretical and numerical studies . . . 138
4.3 Collaboration with industry . . . 138

A Curriculum Vitae
B Complete list of publications and presentations **147**
B.1 Articles in refereed journals . . . 147
B.1.1 Submitted articles . . . 151
B.2 Invited Presentations . . . 151
B.3 Peer-reviewed conference proceedings . . . 152
B.4 Contributed Oral Presentations . . . 152
B.5 Posters presentations . . . 154
B.6 Seminars and workshops . . . 156
B.7 Science outreach . . . 157

Chapter 1

Introduction

This manuscript is aimed at demonstrating that my qualifications meet the standard requirement to be warded the "Habilitation à diriger des recherches" degree at the Université Paul Sabatier. This manuscript is not a PhD style manuscript and focusses more on my abilities to define a research strategy, derive innovative approach and lead a coherent research program over time and my abilities to educate the next generation of researchers.
In the next chapters, I detail my research activities and my career achievements. The document is therefore structured as followed:

- In Chap. 2, I give an overview of my research activities and their impact. I give details and my supervisory and teaching activities. Finally, I give an overview of my professional and administrative services. This chapter aims at quickly demonstrating that I meet all the necessary criteria to be awarded the Habilitation degrees without overflowing the reader with too much details.
- In Chap. 3, I present an extended summary of two of my principal research activities in the field of complex (dusty) plasma physics. After an introduction to the essential concepts of complex plasmas physics used in my research activities (Section 3.1), I summarize the most important results obtained since I defended my PhD. In addition to the discussion of the most relevant scientific results, I also acknowledge the main collaborators (especially the graduate students and postdoctoral fellows). In Sec. 3.2, I present the main results of the studies on nanoparticle growth in unmagnetised and magnetised plasmas. In Sec. 3.3, I present the main results on the studies of waves and instabilities in two-dimensional (2D) complex plasma crystals. Secs. 3.2 and 3.3 each end with a copy of the five main publication of the considered research activities.
- In Chap. 4, I detailed my current and future research project for 5 years to come. The research projects are designed to be achievable at both the Plasma Physics Laboratory at the University of Saskatchewan, Canada (where I am currently on secondment on a Professor position in the department of Physics and Engineering Physics) and the PIIM laboratory at Aix-Marseille Université where I wish to be reaffected at the end of my secondment (July 2024).
- In App. A, I provide a detailed copy of my CV containing a list of my 10 most important publications since 2009.
- In App. B, I provide a list of all my publications in peer-reviewed scientific journals since the beginning of my research career. I also list all the presentations (invited, oral and posters) me or the students I supervise(d) gave at national and international conferences and workshops. I also provide a list of invited seminar I gave at Canadian and US universities

This manuscript hopefully shows that, since my recruitment at CNRS in 2011, I have proven my abilities in all the key areas of research, student supervision, teaching, administration and

public services in different academic and professional bodies and that I meet the standards to be granted the "Habilitation à diriger des recherches" degree. My performances were acknowledged by CNRS in different annual evaluations and by the University of Saskatchewan that promoted me to the rank of Full Professor.

Chapter 2

Career Overview

In this chapter, I provide an overview of my research activities, my research funds and my collaborations. Then I follow with on discussion on the reception and impact of my research. Then, I detail my supervisory and teaching activities. I conclude with an overview of my professional and administrative services.

2.1 Overview of research activities

In this section I give a short review of my five current research axis. The two first axis are the core of my research activities and the associated main results are detailed in Chap. 3.

1. Dust particle growth and dynamics in plasmas:

   I have investigated with my collaborators (including several graduate students) at Aix-Marseille université (AMU), France, at Auburn University, Alabama, USA, and more recently at the University of Toulouse, France, the growth and the dynamics of nanoparticles (NP) in low pressure gas discharges [direct-current (dc) glow discharges, dc magnetron discharges, moderately magnetized microwave discharges, and highly magnetised capacitivelly-coupled radio-frequency (cc-rf) discharges).

   The growth of a tungsten (W) NP cloud by cathode sputtering in a low pressure argon dc glow discharge was investigated [Publications 32, 35, 40, 41, 18 in App. B.1]. Through interactions with the ambient plasma, NP acquire a net (usually negative) charge resulting in their dynamics being linked to the evolution of the discharge parameters. Tungsten NP growth by successive agglomerations was evidenced and connected to the evolution of discharge voltage, electron density, and optical emission intensities of the different species present in the discharge. Real-time analyses of the dust particle size and number concentration were performed in-situ by light extinction spectrometry [Publications 32, 35 in App. B.1]: the studies revealed the complex dynamics of the growing NP cloud and clearly evidenced the agglomeration phase followed by the appearance of new generation of NP.

   More recently, with my collaborator at AMU (including a graduate student), metal NP growth in a dc magnetron discharge was investigated [Publications 3, 8, 16 in App. B.1]. This dc magnetron discharge assembly resembles a classic dc glow discharge assembly with the addition of permanent magnet behind the cathode to increase the plasma density and the sputtering rate. We found that tungsten NP are of core-shell type with a monocrystal mainly in the metastable beta-tungsten phase, and tungsten-oxide shell [Publications 16 in App. B.1]. Grown NP in the magnetron discharge were much smaller than the NP grown in a dc glow discharge due to the significant influence of the sputtered tungsten atoms on

the plasma parameters (lower electron temperature, enhanced plasma density; see peer-reviewed conference publication 3 in App. B.3). Additional studies using an aluminium cathode have confirmed the influence of sputtered metal atoms on the magnetron plasma properties [Publications 8 in App. B.1].

With my collaborators at Auburn University (USA), we performed experiments on NP growth and dynamics in highly magnetised (up to 2.5 T) cc-rf discharges using the MDPX facility. In a dedicated cc-rf discharge that I designed and built, we have shown that the NP size and structure are strongly affected by the magnetic field intensity. These results open the door a new approach for controllable NP synthesis [Publications 15, 19 in App. B.1]. Complementary experimental and theoretical studies have shown that the magnetic field intensity also as a strong influence on the discharge conditions that can be directly associated with a change of the NP growth conditions (weakening of the confining electric fields, plasma filamentation, modifications of the electron temperature) [Publications 11, 15 in App. B.1].

This research activity is detailed in Section 3.2.

2. Wave and instabilities in complex plasma crystals:

In laboratory a cc-rf discharge, it is possible to create a monolayer of calibrated micron-sized microparticles levitating in the sheath above the electrode where the electric force can balance gravity. By tuning the discharge conditions, the monolayer can crystallise and create a so-called 2D complex plasma crystal. Because microparticles are easily imaged, 2D complex plasma crystals are natural model systems for studies of fundamental processes occurring in classical 2D solids at the "atomic" level (wave propagation, dislocation, phase transition, see Ref. [1] and references therein). As the microparticles levitate in the sheath, they are also subject to an intense ion flow coming from the bulk plasma. The trajectories of the ions are modified by the negatively charged microparticles and an ion wake field is formed downstream of each particle. These ion wake fields render the microparticle-microparticle interactions non-reciprocal leading to some plasma-specific phenomena.

With my collaborators (including several graduate students) at Max-Planck Institute for extraterrestrial physics and DLR (Germany) and Bauman Moscow State Technical University (Russia), we have demonstrated theoretically and experimentally that the ion wakes are at the origin of the plasma-specific mode-coupling instability (MCI) in 2D complex plasma crystals [Publications 5, 20, 21, 23, 28, 31, 37, 38, 42–44, 51, 55, 59 in App. B.1]. In 2D complex plasma crystals, there are three wave modes, two in-plane modes (compression and shear) and an out-of-plane (OoP) mode with an optical dispersion relation due to the finite strength of the vertical confinement. When the OoP mode crosses the compression in-plane mode, a resonant coupling occurs due to the non-reciprocal particle-wake interactions leading to the formation of an unstable hybrid mode that triggers a synchronisation of the microparticles' oscillations at the hybrid mode frequency. Due to MCI, energy is transferred from the ion flow to the crystal and the kinetic energy of the microparticles rapidly increases, leading to the melting of the crystal [Publications 20, 21, 23, 28, 44, 51, 55 in App. B.1]. Note that propagation of the melting front occurs because MCI also exist when the monolayer is in the fluid state [2]. We have shown that the kinetics of MCI-induced melting is similar to flame propagation in ordinary reactive matter [Publications 23, 28 in App. B.1] and is therefore a useful model system to study thermoacoustic instability at the kinetic (particle) level [Publications 21 in App. B.1]. Since a fluid monolayer is always experiencing MCI, there exists experimental parameters for which both stable crystalline and fluid monolayer can

exist [Publications 5 in App. B.1]. In an experiment in collaboration with DLR, we clearly demonstrated its is possible to trigger an "explosive" melting of the 2D complex plasma crystal as observed in ordinary reactive matter [Publications 23 in App. B.1].

This research activity is detailed in Section 3.3.

3. Thermodynamics of strongly coupled systems:

With my collaborators at DLR, Germany and IHED, Russia, we have studied the thermodynamics properties of strongly coupled systems (Yukawa and repulsive Inverse power law (IPL) systems) [Publications 10, 24, 29, 33, 36 in App. B.1]. The thermodynamics of Yukawa fluids at different coupling strength in 2D and 3D was explored. We have shown that the thermal component of the excess internal energy at weak coupling exhibits a scaling pertinent to the corresponding one-component-plasma limit providing a simple and accurate practical tool to estimate thermodynamic properties of weakly screened Yukawa fluids [Publications 36 in App. B.1]. At strong coupling the quasi-localized charge approximations (QLCA) method (also called quasi-crystalline approximation (QCA)) can be used to calculate the dispersion relations in strongly coupled Yukawa fluids [Publications 33 in App. B.1]. In classical fluid systems of particles with repulsive IPL interactions near the fluid-solid coexistence and IPL exponent varied from $n = 10$ to $n = 100$ (transition from moderately soft to hard-sphere-like interactions) we found that QCA becomes grossly inaccurate for $n \geq 20$ [Publications 29 in App. B.1]. Additionally, we found that conventional expressions for high-frequency (instantaneous) elastic moduli which divergence as n increases, are meaningless in this regime. We also compared different theoretical approaches to describe the dispersion of collective modes in Yukawa fluids at relatively weak coupling (kinetic and potential contributions to the dispersion relation compete with each other) [Publications 10 in App. B.1]. A thorough comparison with molecular dynamics simulation showed that in this regime, the best description is provided by the sum of the generalized excess bulk modulus and the Bohm-Gross kinetic term.

4. Experimental investigation of plasma enhanced ion implantation system:

Since I started my secondment at the University of Saskatchewan (USask), I have started a research activity on the diagnostics of plasma enhanced ion implantation (PIII) system. For this project, I have recruited a PhD student (defence scheduled early 2023) and a MSc student (thesis defended in December 2019) to work on Langmuir probe diagnostics and laser induced fluorescence diagnostics of the USask PIII system. We have investigated the nature of the perturbations induced by a high-voltage pulse applied to a target immersed in an argon plasma on the plasma parameters and their link to operating conditions (mainly power and pressure) of the inductively coupled radio frequency argon discharge [Publications 6 in App. B.1]. We have observed fluctuations in electron density , temperature , and plasma potential that propagate deep in the plasma and well after the end of the high voltage pulse. We showed that perturbations are significantly dampened at high rf power and close to the RF coil. Perturbation amplitudes are also higher for target materials with large secondary electron yield. Laser induced fluorescence measurement are currently on the way to complement the Langmuir probe studies.

5. Dust in fusion devices:

This research area was originally the motivation behind NP growth studies in plasma. In fusion devices, plasma-wall interactions lead to the creation and mobilization of dust

that will be a major issue for future fusion devices [Publications 30 in App. B.1]. Indeed, because of interactions with the plasma, dust undergoes erosion and releases impurities that can reduce fusion reactor performances, stability and safety. Thus with my collaborator at CEA, France (including one graduate student), and at AMU, we have study the influence of magnetic fields on dust charge in fusion relevant conditions [Publications 26 in App. B.1]. We have also investigated the Space-Charge Limited (SCL) regime on the collection of charged species by dust, especially the formation of a virtual cathode [Publications 22 in App. B.1]. Since I started my secondment at the University of Saskatchewan, I am interested in studying dust transport in the STOR-M tokamak operating at USask. For that purpose, a graduate student (MSc thesis defended in 2020, registered as a PhD student since 2021) has been recruited to build and characterized a calibrated tungsten dust dispenser [Publications 4 in App. B.1]. Dust injection experiments in the STOR-M tokamak will start soon. In addition, this student is also participating to the analysis of the plasma facing components exposed to the plasma of the WEST tokamak (collaboration with IRFM, CEA, Cadarache and AMU)

2.1.1 Research funds

My research program at the University of Saskatchewan is currently supported by a NSERC Discovery Grant entitled "*Sheath and dust particle transport in plasmas* (C$34,000/year for the period 2019-2024. This grant allows me to support a couple of graduate students as well as looking after the current experimental devices.

A MITACS Accelerate grant (co-applicants: Profs. Bradley, Smolyakov and Xiao from the Plasma Physics Laboratory at the University of Saskatchewan) currently supports a research project in collaboration with the private company Fuse Energy Technologies Inc.,Napierville, Quebec. The awarded amount of C$533k for three years (2021/09 -2024/08) aims at financing the stipends of seven graduate students, two of them whom I directly supervise.

As a new faculty member, I was awarded a grant from the New Faculty Graduate Student Support Program to fund one graduate student. The grant is used to fund the PhD scholarship of Mr Nathan Nelson currently on dust transport in the STOR-M tokamak (total amoun awarded C$ 20k).

When I started my secondment at USask in 2018, I was awarded C$ 135k from the Faculty, Recruitment and Retention Program of the University of Saskatchewan as well as an extra C$ 7,200.00 from the University President's NSERC Fund. This starting have allowed my to recruit immediately a few graduate students and buy the necessary equipment to build a laser induced fluorescence system and a new cc-rf discharge dedicated to the study of 2D complex plasma crystals.

In 2013-2014, I was awarded PHC PROCOPE grant for the Project 28444XH, "2D complex plasmas: Mode coupling and interparticle interactions" (funding agencies: Ministère de l'Europe et des Affaires étrangères/Ministère de l'Enseignement supérieur, de la Recherche et de l'Innovation (MESRI)/Deutscher Akademischer Austausch Dienst). The co-applicant was Dr. A. Ivlev from Max Planck Institute for extraterrestrial Physics, Garching b. München (Allemagne). We were awarded € 5,4k to support visit in the respective co-applicants institutions.

2.1.2 Collaborations avec des partenaires académiques

My collaborations are all listed in my CV (see App. A). I list here the collaborations the most relevant to my current research projects.:

— Dr R. Clergereaux (LAPLACE laboratory, UMR CNRS/Université Paul Sabatier) on nanoparticles growth in magnetized microwave plasmas.

— IRFM/CEA Cadarache (Dr C. Grisolia and Dr E. Bernard) on dust and plasma wall interactions in the WEST tokamak. This collaboration has led to a six months visit of PhD student, N. Nelson, (shared visit to PIIM laboratory, see below) to work on the characterisation of plasma facing components exposed to the WEST tokamak plasmas.

— Collaborations with Prof. A. Smolyakov (University of Saskatchewan, Canada) on numerical studies of instabilities in magnetised and unmagnetised plasmas. This collaboration is particularly helpful for the research project of PhD student J. H. Mun (international Cotutelle, USask/Aix-Marseille Université)

— Collaboration with PIIM laboratory (UMR 7345, CNRS/Aix-Marseille Université (France)) on impurity transport in plasmas and dusty plasmas (Dr C. Arnas, Prof. O. Agulo, Prof. M. Muraglia) and on plasma-surface interactions (Prof. C. Martin and Prof. G. Cartry). I currently co-supervise a PhD student (J.H. Mun) enrolled in a cotutelle program at AMU and USask. This collaboration is also useful to PhD student N. Nelson who works with Prof. Martin on the characterisation of the WET plasma facing components.

— Collaborations with Prof. E. Thomas Jr. (Auburn University, Alabama, USA) on nanoparticle growth in highly magnetized chemically active plasmas. Prof. Thomas is the principal investigator at the MDPX facility at Auburn University. This collaboration is extremely important to my still relatively new research axis: nanoparticle growth in magnetised plasmas.

— My research activities on complex plasma crystals and strongly coupled systems have lead to many collaboration: Prof. S. Yurchenko (Bauman Moscow State Technical University, Russia), V. Nosenko, S. Zhdanov, S. Khrapak and H. Thomas (DLR (German Space Agency), Oberpfaffenhoffen, Allemagne), A. Ivlev (Max-Planck-Institute for extraterrestrial physics, Garching b. Muenchen, Germany) , E. Thomas Jr. (Auburn University, Alabama, USA), J. Williams (Wittenberg University, Springfield, Ohio, USA) and L. Matthews (Baylor University, Texas, USA). I regularly visit these institutions for short visit for experimental campaigns and/or work on articles. These collaborations have also given me the opportunity to interact with many graduate students.

2.2 Reception and impact of my research

My research results are regularly cited. According to ISI Web of Science in November 2022, my articles published in peer-reviewed journals have been cited more than 940 times (Excluding auto-citations) with an average of ∼14 citations per published article. My most cited article, published in Physical Review Letters, has been cited more than 115 times (more than 150 times according to Google Scholar).

My research activities on waves and instabilities in two-dimensional complex plasma crystals are recognised at an international level. My results on the mode-coupling instability and the melting of 2D complex plasma crystals have been noticed by my peers and the have allowed my to be invited to give a few invited oral presentation at International Conferences such as the European Physical Society conference on Plasma Physics in 2022, the International Conference on Phenomena in Ionized Gases in 2017 and the International Congress on the Physics of Plasmas in 2016. In August 2018, I have been invited to give an oral presentation at the 1st Asia-Pacific Conference on Plasma and Terahertz Science for which I won the prize for the best oral presentation. In 2011, my invited presentation 6th International Conference on the Physics of Dusty Plasmas won young scientist best oral presentation. A list of my invited oral

presentation can be found in my CV (see App. A). I have been also invited to give numerous invited seminars on this topic at different universities across Canada and the USA (University of Alberta, University of Winipeg, University of Manitoba, University of Montreal, University of Illinois at Urbana-Champain). My expertise in this domain also allowed me to join an international project lead by Prof. Gregor Morfill and Prof. Stanislav Yurchenko at Bauman Moscow State University, Russia between in 2015 and 2016.

My expertises in plasma diagnostics, simulation (molecular dynamics and particle in cell) and on nanoparticle growth and transport in plasmas is equally well received and I regularly published results in peer-reviewed journals on these subjects with international collaborators. In 2017, I spent six months as an invited research scholar in the group of Prof. Edward Thomas at Auburn University, Alabama, USA. During my visit at Auburn University, I built a new device dedicated to the study of nanoparticle growth in highly magnetised plasma (steady magnetic fields up to 2.5 T). Since then, I have visited Prof. Thomas's group on a regular basis to perform experiments and to work with graduate students and postdocs on this subject. This collaboration has lead to a few publications and have earned me an invitation to give an oral presentation at the MagnetUS workshop in June 2022. In addition, I have been awarded in 2020 a Mourou-Strickland scholarship to spend a month as an invited researcher at the Laplace laboratory at the University Paul Sabatier, Toulouse, France in the group of Dr Richard Clergereaux. The scholarship was awarded to do research on nanoparticle growth in moderately magnetised microwave plasmas. Dr Clergereaux are currently looking for a graduate student to take over these research.

In June 2019, I was elected Chair of the Division of Plasma Physics (DPP) of the Canadian Association of Physicists. My term finished in June 2021. This election shows the Canadian plasm physics community considers me as an active researcher able to assume a leadership position.

Finally, many funding agencies [NSERC (Canada), FRQNT (Québec), ANR (France), DFG (Allemagne)] recognise my expertise in the field of plasma physics and ask me regularly to evaluate the merit of grant proposals.

2.2.1 Consequence of the COVID-19 pandemic on my research program

From March 2020 to July 2020, the access to the University of Saskatchewan campus was forbidden. It was then strongly restricted from August 2020 to July 2021. Consequently the construction of my new experimental device as well as many experimental campaigns have been delayed. The laser-induce fluorescence experiments and the new plasma source dedicated to the study of complex plasma crystals have been impacted the most. This unavoidable delays have had a significant impact on the progress of the projects of my graduate students.

Moreover, a cotutelle PhD student co-supervised by Prof. Gilles Cartry and Porf. Céline Martin at Aix-Marseille Université has resigned from the PhD program to the stress induced by the strict lock-down in France. This has virtually paused the collaboration on the interaction of tungsten surfaces with hydrogen plasmas.

2.3 Supervisory and teaching activities

Since March 2018, I am on secondment at the University of Saskatchewan (Associate Professor from March 2018 to June 2022 and promoted to Professor in July 2022). I am affiliated to the Department of Physics and Engineering Physics and I am one of the four professors of the Plasma Physics Laboratory.

In this context, I had the opportunity to lead my own research group and teach physics at all levels. Since March 2018, my research activities and my teaching activities represent each $\sim 40\%$ of my working time.The remaining $\sim 20\%$ are devoted to administrative tasks at the departmental, college and university levels.

In the next sub-sections, I summarise the different supervisory and teaching activities I had since I was recruited at CNRS in February 2011. The activities that have occurred since my secondment at USask are marked with an asterisk. My administrative activities will be described in a following section.

2.3.1 Supervisory activities

PhD thesis supervision

- *2022/01–present:Marilyn Jimenez, subject:"Spectro-tomography of Z-pinch systems", University of Saskatchewan, Main supervisor. Collaboration with the startup company Fuse Energy Inc., Napierville, Quebec, Canada.
- *2021/01–present: Nathan Nelson, subject: "Dust transport in the STOR-M tokamak", University of Saskatchewan, Co-supervisor. This thesis is linked to one of my main research axis (Dust transport in tokamaks). The thesis is co-supervised by Prof. X. Xiao, PI of the STOR-M tokamak. The thesis has triggered a collaboration with IRFM, CEA Cadarache (Dr. Elodie Bernard) and the PIIM laboratory (Dr Martin et Dr Arnas) on the characterisation of plasma facing components exposed to the WEST tokamak plasma.
- *2019/09–present:Jung Hern Mun, subjet: "Modelling of a magnetron discharge", International Cotutelle, Aix-Marseille Université (France) and University of Saskatchewan (Canada), Main supervisor (University of Saskatchewan). Supervisors at Aix-Marseille Université: Prof. O. Agullo, Dr C. Arnas et Prof. M. Muraglia
- *2018/09–present: Joel Moreno, subject: "Characterisation of an inductively-coupled plasma immersion ion implantation system", University of Saskatchewan (Canada), Main supervisor. Joel has worked on the Langmuir probe characterisation of a PIII system at USask. Joel is also in charge of the installation of a laser-induced fluorescence diagnostics to measure the ion velocity distribution function in front of biased target immersed in a inductively-coupled radio-frequency argon plasma. Mr Moreno is co-supervised by Prof. M. Bradley, leader of the ion implantation group. Mr Moreno has published two articles in peer-reviewed journals since the beginning of his PhD [Publications 6 and 8 in App. B.1]. Mr Moreno will defend his PhD in early 2023.

Master thesis/internship supervision

- *Since March 2018, 5 MSc thesis supervised at the University of Saskatchewan: A. Khodaee (2018-2019, "RF-compensated Langmuir Probe Diagnostics of Pulsed Plasma Ion Implantation System", co-supervisor); A. Chang (2018-2020, "ICP Enhanced HIPIMS System Design and Characterisation", co-supervisor); N. Nelson (2019-2020, "Design and Characterization of a Dust Injector for Future Studies of Tungsten Dust in the STOR-M Plasma", co-supervisor); J. Vanegas (2021–present, "Probe characterisation of a plasma gun", collaboration with Fuse Enrgey Inc.); and N. Smith (2021–present, "Experimental investigation of complex plasma crystals".
- Between 2013 and 2017, I have supervised two Master 2 internship at Aix-Marseille Université: C. Hu (2013, Agglomeration of nanoparticles in plasmas") and L. Terraz (2016, "Thermalization of sputtered atoms in a magnetron discharge"). I have co-supervised two other Master 2 internship: A. Gaith (2015, "Nanoparticle formation in magnetron discharges") and A. Chami (2017, "Nanoparticle formation in magnetron discharges").

Undergraduate internship supervision

In this section, the student projects are not detailed and I only list the supervised and co-supervised students. More details can be found in my CV (see App. A).

— * Since March 2018, I have supervised five undergraduate (Bachelor of Engineering in Engineering Physics or equivalent) student internship: The students are W. Kozicki (USask), D. Okerstrom (USask), G. Elder (USask), M. D. Au (USask) and J. Pascal (U. Paul Sabatier). I have co-supervised one undergraduate student internship (1^{st} intership of W. Kozicki).

— In 2016, I have supervised an internship from the I UT Mesure Physique at Aix-Marseille Université (Z. Samahna).

2.3.2 Teaching activities

Since March 2018, being on secondment at the University of Saskatchewan, teaching activities have been a regular part of my assignment of duties. From March 208 to February 2020, it represented ∼20% of my working time (∼ 20% teaching release for new faculty members). Since March 2020, teaching activities make up ∼40% of my working time (preparation, lectures and exam marking).

In this section, I list all the classes I have taught since I started at CNRS in February 2011. More details on my past teaching activities (including before 2011) can be found on my CV (see App. A).

— * Winters 2022 and 2023: Undergraduate lectures (equivalent L1), "Electromagnetism and waves for engineers (PHYS 156)", Physics and Engineering Physics department, University of Saskatchewan, 4.5h/week (lecture) over 7 weeks. PHYS 156 is a mandatory class for all starting engineering students at the University of Saskatchewan (it has replaced PHYS 155 since January 2022). ∼ 400 students divided in 12 sections are taking the class each year. I was the course coodinator in Winter 2022. I teach the magnetism part to all sections and coordinated the two other parts.

— *Fall 2021, Graduate "Reading course" (doctorate), "Plasma wall interactions in fusion reactors (PHYS 898)" at the University of Saskatchwan, 1h/week over 12 weeks. The class consist at evaluating a student presentation/week on a sub-topic of the class on weekly assigned reading material.

— *Winter 2019, 2020 et 2021 Undergraduate lectures (equivalent L1), "Introduction to Electricity and Magnetism (PHYS 155)". Physics and Engineering Physics department, University of Saskatchewan, 3h/week (lecture) over 12 weeks. PHYS 155 was a mandatory class for all starting engineering students at the University of Saskatchewan until 2021. ∼ 400 students divided in three sections were taking the class each year. In 2020 and 2021, I was also course coordinator: I taught directly one section and coordinated the two others.

— *Falls 2020 and 2022, Graduate lectures (Master and doctorate), "Statistical Physics (PHYS 873)", Physics and Engineering Physics department, University of Saskatchewan, 3h/week (lecture) over 12 weeks. The graduate statistical physics course is one of the care course of the physics graduate program at USask (along Electrodynamics and Quantum mechanics) and must be followed by most graduate students. The course is offered every second year.

— *Winter 2021,Graduate "Reading course" (doctorate), "Plasma transport and Plasma diagnostics (PHYS 865)" at the University of Saskatchewan, 1h/week over 12 weeks. The

class consist at evaluating a student presentation/week on a sub-topic of the class on weekly assigned reading material.

— 2015-2016: laboratories and seminar for graduate students on experimental studies of complex plasmas at Bauman Moscow State Technical University (BMSTU), Moscow, Russia (∼40h over two years in the framework of an international project on the physics of complex plasma lead by Prof. G Morfill (Max Planck Institute for Extraterrestrial Physics) and Prof. S. Yurchenko (BMSTU) (see my CV in App. A) for complementary details).

— 2013-2016: Graduate(Master 2) lectures and laboratories, "Introduction to dusty plasmas and plasma diagnostics", Aix-Marseille Université, France, 9h/year. The class was coordinated by Prof. G. Cartry and was a part of the Mater program: Plasma and fusion.

2.4 Professional and administrative services

2.4.1 Research facilitation

— *__Chair, Dvision of Plasma Physics (DPP), Canadian association of Physicists__, elected for 2 years (non-renewable) in June 2019. My role was to ensure communication among the different plasma physics research group across Canada and help at the organisation of the annual congress of the Canadian Association of Physicists, in particular the annual symposium day of the DPP and parallel sessions devoted to plasma physics. My DPP chair duty took 2–3h/month in average with a more intense activity during the few weeks leading to the annual conference.

— * Co-organiser, Division of Plasma Physics virtual Symposium day, Online Annual Congress of the Canadian Association of Physicists, Juin 2021.

— * Co-organiser, Division of Plasma Physics virtual Symposium day, Annual Congress of the Canadian Association of Physicists, Juin 2020. Due to the COVID-19 pandemic, the symposium day had to be reorganised urgently into an online meeting. It had lead to ∼20h of extra work compared to the normal involvement of the DPP chair.

— * Since December 2020, member of Science Definition Team (SDT) of the COMPACT project (COMplex PlAsma faCiliTy). It is a project supported by DLR, NASA, ESA, NSF and ROSCOSMOS (until February 2022) to install a new experiment on board the International Space Station dedicated to the study of complex plasmas under microgravity conditions (successor of the PK4 experiment). SDT membership takes about 2 hours of my time every month. The detailed of the proposed project have been recently published [see publication 1 in App. B.1].

— Member of the international scientific committee of the International Congress on Plasma Physics, International Union of Pure and Applied Physics, June 2018. ∼5h for the selection of invited presentation.

— Co-chair (local organising committee, co-chair: Prof. G. Cartry, PIIM, Aix-Marseille Université) of the workshop "Frontier in Low Temperature Plasma Diagnostics", May 2015, Porquerolles, France. It took ∼30 hours of my time before the conference to help at the organisation of the conference.

2.4.2 Professional services

— *Academic reviewer of grant proposals submitted to German Research Foundation (2020), the National Scientific and Engineering Research Council of Canada (2020, 2021, 2022),

ANR, France (2019) and the Fonds de Recherche Nature et Technologies, Gouvernement of Québec (2020, 2021). Each project evaluations takes 3–4 hours.

— External examiner for PhD thesis for the University of Sydney, Australia (5 theses), the University of Montreal, Canada (2 theses) and the University of Alberta (1 thesis)

— *Since 2018, members of numerous graduate advisory committees in the Physics and Engineering Physics department at the University of Saskatchewan. This activity takes ∼15h of my time per term

— Since 2009, reviewer for numerous peer-reviewed academic journals including Physical Review Letters, Physical Review E, Physics of Plasmas, Plasma Sources, Science and Technology, Journal of Physics D: Applied Physics, IEEE Transactions on Plasma Science, etc.

2.4.3 Administrative services

My assignment of duties at the University of Saskatchewan comprises 20% of administrative tasks. Accordingly, I am a member of many committees for the department of Physics and Engineering Physics, the College of Arts and Science, the College of Graduate and Postdoctoral Studies and the University as a whole. .

— Since July 2019, I am member of the executive committee of the University of Saskatchewan Faculty Association (faculty union). In this context, I belong to many other sub-committees, including the External relation committee, which I chair since 2020, in charge of the relations with the students' unions and other workers' unions at the university. From July 2020 to June 2022, I was also a member of the Joint Committee on the Management of the Collective Agreement (JCMA). This committee is in charge of the discussions with university upper administration to enforce the provision of the collective agreement. Since July 2021, I am also the treasurer of the faculty association. My faculty association duties take 6 to 8 hours per week.

— From July 2019 to June 2021, I was a member of the Equity and Internationalisation Committee of the University of Saskatchewan's College of Graduate and Postdoctoral Studies (committee I chaired from July 2019 to June 2020). The role of this committee was to ensure that the regulation governing master's and PhD programs were not discriminatory. This duty took 1 hour/month in average.

— From June 2019 to April 2020, I was a member of the Indigenous recruitment committee of the College of Arts and Science at USask.

— From January 2019 to April 2020, I was a member of the Nomination Committee of the the College of Arts and Science at USask.

— Since 2018, I am a member of the Graduate Affairs Committee of the Department of Physics and Engineering Physics. I chair this committee since July 2021. The committee is in charge of defining and enforcing the regulation of the graduate physics program as well as annually distributing scholarships and other stipends to the enrolled graduate students. As the chair I work 3–3 hours per month for this committee.

Chapter 3

Summary of main research results

3.1 Introduction to laboratory dusty plasma physics

Complex or dusty plasmas are partially ionised gases containing charged solid nano- or micro-particles (often referred to as dusts). They can be found everywhere from astrophysical environment (stars, interstellar medium) to industrial applications (plasma etching, ion implantation, semiconductor manufacturing). Some example are planetary rings [3], industrial plasmas [4, 5], fusion devices plasmas [6–8], laboratory gas discharges [9–13], etc. In laboratory experiments, dust particles can be either injected or grown directly in the plasma. Injected dust particles are usually micron-size particles (microparticles). Dense clouds of submicron particles are usually formed of particles grown directly in the plasmas and can be obtained using reactive gases such as silane [14–16], acetylene [17–19] (see Sec. 3.1.3) or using a target sputtered with ions coming from the plasma [20–22].

Due to their interactions with the surrounding electrons and ions of the plasma, dust particles acquire a net electric charge (see Sec. 3.1.1) that can significantly change the plasma charge equilibrium (especially at high dust number density [see Sec. 3.1.1]) [1, 23, 24]. Dusty plasmas can be thus seen as three component plasmas. In complex plasmas, the dust electric charge is obviously a key parameter. In laboratory low temperature plasmas, the dust grains are usually negatively charged due to the higher mobility of the plasma electrons [1, 13, 23–26]. Other processes can also significantly influence dust electric charges depending on the ambient plasma conditions. For example, photoemission induced by ultraviolet radiation can lead to positively charged particles [27–29]. Positively charged particles can also be observed when thermionic or secondary emission of electrons are important effects as it is the case in fusion plasmas [30–32]. The dust charge determines the interactions of the dust particles with the background ions and electrons as well as the dust-dust interactions It is also a fundamental parameter in many processes such as the ion drag force [33, 34], electric charge shielding [35], etc. The knowledge of the charge is therefore essential to the understanding of the basic properties of a complex plasma, the dust dynamics, as well as developing method for grain manipulations [36].

In addition, complex plasmas are often used as models to study self-organised strongly coupled systems [13]. Indeed, since microparticles can easily be imaged (using laser light scattering and fast cameras for example), the microparticles' trajectories can be easily determined and information about the crystal at the kinetic ("particle") level can be obtained. Generic phenomena such as wave propagation [37, 38], shocks [39, 40] and phase transitions [41–44] have been studied using complex plasmas.

In laboratory experiments, due to their mass, injected microparticles are usually confined in the sheath region near the electrode where the electric force can balance gravity (microparticle clouds filling the bulk plasma can be obtained in experiments performed under microgravity [45–47] or when a thermophoresis force (see Sec. 3.1.2) is applied by imposing a temperature gradient

[48, 49]). In ground-based laboratory discharges, two-dimensional (2D) dust monolayers can be created by injecting calibrated microspheres into the plasma. Thus, microparticles are all levitating at the same height in the sheath above the electrode. By tuning the experimental conditions, it is possible to crystallise the monolayer and create so-called two-dimensional (2D) complex plasma crystal in which the dust particles form a hexagonal lattice. These structure can support waves and instabilities (see Sec. 3.1.6).

On the contrary, dust particles grown directly in the plasma are generally light enough to be trapped in the bulk plasma and form dense clouds. The nanoparticle charges have a fundamental role during the growth process and for nanoparticle transport [50, 51]. In discharges containing (very) dense three dimensional (3D) cloud of dust particles, the net electric charge carried by the dust component is a significant part of the total plasma charge. Local fluctuations in the dust density can therefore disturb the plasma. For example, in direct-current (dc) discharges, nanoparticle (NP) growth and discharge parameters are strongly interdependent [52–57] (see Sec. 3.2). In capacitively-coupled (cc) radio-frequency (rf) discharges in which a dense cloud of dust particles is trapped between the parallel electrodes (e.g., in rf sputtering discharges [20, 58], or experiments under microgravity conditions [59]), the dust cloud exhibits in its centre a self-organised region free of dust particles called the "void" [20, 58–61]. Voids arise from an equilibrium between the inward confining electric force on the dust particles and the outward ion drag force due to ions flowing out of the void region where the ionisation is enhanced. This is due to the absence of plasma species losses on dust particle surfaces in the void region. Under specific conditions, voids exhibit regular oscillations of their sizes (heartbeat instability) [59–61] thought to be due to the transition from an ambipolar electric field at the void boundary to a sheath-like structure with an intense outward electric field due to the high losses of plasma species on dust particles at the void boundary which acts then as a floating wall [61].

In this section, the main concepts of dusty plasma physics are reviewed in order to facilitate the reading of the extended summary of two main research axes: (i) nanoparticle growth in plasmas (Sec. 3.2), and (ii) waves and instabilities in 2D plasma crystals (Sec. 3.3). For that purpose, Sec. 3.1.1 is devoted to the dust charging process. In Sec. 3.1.2 the different forces acting on the dust particles are discussed. In Sec. 3.1.3, an overview of the dust growth dynamics in plasma is given. In Sec. 3.1.3. In Sec. 3.1.4, a simple model of the sheath in cc-rf discharge is presented followed by a discussion on microparticle levitation in cc-rf discharges (Sec. 3.1.5). Finally a short introduction to 2D plasma crystals will be given (Sec. 3.1.6).

3.1.1 Charge of dust particles

When a dust particle is immersed in a plasma, it collects or emits different current (electrons, ions, thermoionic emission, UV-induced secondary emission, etc.) and acquires a net electric charge on a dust particle arises from the it collects or emits. Since the dust particle is not connected to any power source, it will eventually reach a potential (floating potential) at which the contributions of all currents to the particle surface vanishes [1, 23, 24]:

$$\frac{\mathrm{d}Q_\mathrm{d}}{\mathrm{d}t} = \sum_k I_k = 0, \tag{3.1}$$

where I_k corresponds to the current induced by process k when the dust particle is at floating potential and Q_d is the dust particle charge. In laboratory discharges, the main processes are the currents due to the flow of plasma electrons and ions to the dust particles. In the following, these are the only processes that are discussed.

OML theory

Consider that the background plasma is made of Maxwellian ions and electrons with densities n_i and n_e, respectively and temperature T_i and T_e, respectively. The ion and electrons current on the dust particle can be obtained using the Orbital Motion Limited (OML) model [62–64]. This model assume that the electrons and the ions are moving without collisions from infinity on orbits around the dust particle (assumed spherical with a radius r_d) that are only due to electrostatic interactions. Due to the higher mobility of the plasma electrons, the dust potential Φ_d, is usually negative with respect to the plasma potential and the corresponding dust particle charge is negative. The derivation of OML currents is textbook material and can be found for example in Refs. [1, 24, 65]. For Maxwellian plasmas, the OML ions and electron charging currents on a spherical dust particle of radius r_d are:

$$I_\mathrm{i} = \pi r_\mathrm{d}^2 n_\mathrm{i} e v_{\mathrm{th_i}} \left(1 - \frac{e\Phi_\mathrm{d}}{k_\mathrm{B} T_\mathrm{i}}\right) , \tag{3.2}$$

$$I_\mathrm{e} = -\pi r_\mathrm{d}^2 n_\mathrm{e} v_{\mathrm{th_e}} \exp\left(\frac{e\Phi_\mathrm{d}}{k_\mathrm{B} T_\mathrm{e}}\right) , \tag{3.3}$$

where k_B is the Boltzmann constant, and $v_{\mathrm{th_e}} = \sqrt{8k_\mathrm{B}T_\mathrm{e}/\pi m_\mathrm{e}}$ and $v_{\mathrm{th_i}} = \sqrt{8k_\mathrm{B}T_\mathrm{i}/\pi m_\mathrm{i}}$ are the electron and ion thermal velocities respectively.

In equilibrium, the net current on the dust particle surface is equal to zero (i.e. $I_\mathrm{i} + I_\mathrm{e} = 0$) and the dust surface potential is equal to the floating potential Φ_f. From Eqs. 3.2, Φ_f can be deduced from the following equation:

$$1 - \frac{e\Phi_\mathrm{f}}{k_\mathrm{B} T_\mathrm{i}} = \sqrt{\frac{m_\mathrm{i} T_\mathrm{e}}{m_\mathrm{e} T_\mathrm{i}}} \frac{n_\mathrm{e}}{n_\mathrm{i}} \exp\left(\frac{e\Phi_\mathrm{f}}{k_\mathrm{B} T_\mathrm{e}}\right) . \tag{3.4}$$

In a typical laboratory argon discharge in which $T_\mathrm{e}/T_\mathrm{i} \simeq 100$, the floating potential for an isolated dust grain is $\Phi_\mathrm{d} = \Phi_\mathrm{f} = -2.41 k_\mathrm{B} T_\mathrm{e}$ [66].

The charge on the dust particle can then be calculated by considering that the microparticle is a small spherical capacitor of capacitance $C = 4\pi\varepsilon_0 r_\mathrm{d}$ (assuming $r_\mathrm{d} \ll \lambda_\mathrm{D}$) which leads to the dust charge:

$$Q_\mathrm{d} = Z_d e = C \cdot \Phi_\mathrm{f}. \tag{3.5}$$

In Figure 3.1, the dust particle charge number $|Z_\mathrm{d}|$ as a function the electron temperature T_e is shown for different dust radii. For an isolated particles (or very low dust number density n_d), the electron density is equal to the ion density and the charge is a quasi-linear function of T_e and r_d. In an argon plasma, the charge of an isolated spherical dust particle is given by [66]:

$$|Z_\mathrm{d}| \simeq 1675 \cdot r_{\mathrm{d},\mu\mathrm{m}} \cdot T_\mathrm{e}(\mathrm{eV}). \tag{3.6}$$

Influence of a large dust density

When the dust particle number density n_d is very large, a significant fraction of the plasma electrons is attached to the dust particles and the density of free electron in the plasma is significantly reduced compared to the dust-free plasma. This electron depletion results in a modification of the dust charging process. The influence of large dust particle number density can be taken into account using the quasi-neutrality condition:

$$n_\mathrm{i} e - n_\mathrm{e} e - n_\mathrm{d} Z_\mathrm{d} e = 0 \tag{3.7}$$

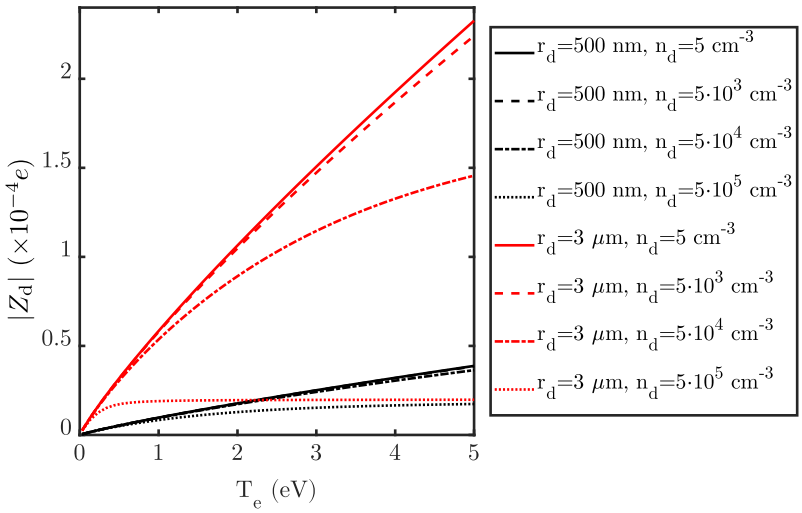

Figure 3.1 – Calculated particle charge number $|Z_\mathrm{d}|$ as a function of electron temperature T_e for two different dust radii r_d and different dust number densities n_d. A argon plasma with $n_\mathrm{i} = 1 \cdot 10^9$ cm^{-3} and $T_\mathrm{i} = 0.03$ eV is considered.

Assuming Boltzmann electrons, the dust charge is obtained by solving simultaneously the following equations [1, 67]:

$$\exp\left(\tilde{\psi}\right) - 1 - \underbrace{\frac{4\pi\epsilon_0 r_\mathrm{d}}{e}\frac{k_\mathrm{B}T_\mathrm{e}}{e}\frac{n_\mathrm{d}}{n_\mathrm{i}}}_{P}\left(\tilde{\Phi}_f - \tilde{\psi}\right) = 0 \ , \tag{3.8}$$

$$\left(1 - \frac{T_\mathrm{e}}{T_\mathrm{i}}\left(\tilde{\Phi}_f - \tilde{\psi}\right)\right) - \sqrt{\frac{T_\mathrm{e} m_\mathrm{i}}{T_\mathrm{i} m_\mathrm{e}}}\exp\left(\tilde{\Phi}_f\right) = 0 \ , \tag{3.9}$$

where $\tilde{\Phi}_f = e\Phi_f/k_\mathrm{B}T_\mathrm{e}$ is the normalised floating potential and $\tilde{\psi} = e\psi/k_\mathrm{B}T_\mathrm{e}$ is the normalised plasma potential in the dust particle cloud with respect to the outer dust-free plasma. The Havnes parameter [1, 68] is defined as:

$$P = \frac{4\pi\epsilon_0 r_\mathrm{d}}{e}\frac{k_\mathrm{B}T_\mathrm{e}}{e}\frac{n_\mathrm{d}}{n_\mathrm{i}} = 695 T_{\mathrm{e,eV}} r_{\mathrm{d},\mu\mathrm{m}}\frac{n_\mathrm{d}}{n_\mathrm{i}} \approx \frac{Z_\mathrm{d} n_\mathrm{d}}{n_\mathrm{i}} \ . \tag{3.10}$$

When $P \sim 0$, dust particles can be considered as isolated and the plasma is largely unperturbed by their presence. On the contrary, when $P \gg 1$, the presence of dust particles induces a significant electron depletion and in the limiting case, the dust particle charge number is $Z_\mathrm{d} \sim n_\mathrm{i}/n_\mathrm{d}$. The effect of increasing dust particle number density is illustrated in Figure 3.1. In experiments in which nanoparticles are growing, the dust particle number density can reach very large values and induce a measurable electron density depletion.

Influence of collisions

The presence of ion-neutral collisions can considerably change the ion current on the dust particle surface. Indeed, because of collisions with neutral atoms, especially charge-exchange collisions, ions that would normally be too energetic to be collected by the dust particle, loose most of their energies and are trapped on orbits around the dust particle or even fall on the dust surface and thus increasing the ion current with respect to OML theory. In the presence

of ion-neutral collisions, the electron and ion charging currents are modified as follows [33, 69]:

$$I_\mathrm{e} = (-e) \cdot \sqrt{8\pi} r_\mathrm{d}^2 n_\mathrm{e} v_{T_\mathrm{e}} \exp(-\tilde{\varphi}), \tag{3.11}$$

$$I_\mathrm{i} = (e) \cdot \sqrt{8\pi} r_\mathrm{d}^2 n_\mathrm{e} v_{T_\mathrm{i}} \left(1+\tilde{\varphi}\right) \times \left[1 + \frac{\tilde{\varphi}\left(\frac{T_\mathrm{e}}{T_\mathrm{i}}\frac{r_\mathrm{d}}{\lambda_\mathrm{i}}\right)}{0.07 + 2\left(\frac{r_\mathrm{d}}{\lambda}\right) + 2.5\left(\frac{r_\mathrm{d}}{\lambda_\mathrm{i}}\right) + \left[0.27\left(\frac{r_\mathrm{d}}{\lambda}\right)^{1.5} + 0.8\left(\frac{r_\mathrm{d}^2}{\lambda_\mathrm{i}\lambda}\right)\right]\frac{T_\mathrm{e}}{T_\mathrm{i}}\tilde{\varphi} + \frac{0.4\left(\frac{r_\mathrm{d}}{\lambda_\mathrm{i}}\right)^2\left(\frac{T_\mathrm{e}}{T_\mathrm{i}}\right)\tilde{\varphi}}{1-0.4\left(\frac{r_\mathrm{d}}{\lambda_\mathrm{i}}\right)}}\right], \tag{3.12}$$

where $\tilde{\varphi} = e\Phi_\mathrm{d}/k_\mathrm{B}T_\mathrm{e}$ is the normalised microparticle floating potential, $\lambda = \lambda_{\mathrm{D_i}}/\sqrt{1+(\lambda_{\mathrm{D_i}}/\lambda_{\mathrm{D_e}})^2}$ is the linearised Debye length at the considered position in the sheath with $\lambda_{\mathrm{D_{i,e}}} = (\epsilon_0 T_\mathrm{i,e}/n_\mathrm{i,e}e)^{1/2}$, and λ_i is the ion-nutral mean free path.

Influence of streaming ions

In experiments, dust particles can be found in region where the ions have a drift velocity u_i much larger than their thermal velocities $v_{\mathrm{th_i}}$ (for example in the sheath). Under these conditions, the ion current has to be written as [1, 70]:

$$I_\mathrm{i} = \pi r_\mathrm{d}^2 n_\mathrm{i} v_{\mathrm{th_i}} f(u_\mathrm{i}) \ , \tag{3.13}$$

with

$$f(u_\mathrm{i}) = \sqrt{\frac{\pi}{4}} x \left[\left(1 + \frac{1}{2x^2} - \frac{e\Phi_d}{k_\mathrm{B}T_\mathrm{i}x^2}\right)\mathrm{erf}(x) + \frac{1}{\sqrt{\pi}x}\exp(-x^2)\right] \ , \tag{3.14}$$

where $x = u_\mathrm{i}/\sqrt{2k_\mathrm{B}T_\mathrm{i}/m_\mathrm{i}}$. When $u_\mathrm{i} \gg v_{\mathrm{th_i}}$, Eq. 3.13 reduces to:

$$I_\mathrm{i} = \pi r_\mathrm{d}^2 n_\mathrm{i} e u_\mathrm{i} \left(1 - \frac{2e\Phi_\mathrm{d}}{m_\mathrm{i}u_\mathrm{i}^2}\right) \ . \tag{3.15}$$

3.1.2 Force acting on dust particles

When dust particles are injected in a plasma, they will be subjected to different forces. The main ones are the gravity, the electric force, the neutral drag force, the thermophoresis and the ion drag force. Radiation pressure force can also play an important role when illuminating the dust particles with a focus laser light beam. In this section, the expressions for these main forces are given and their importance depending on the dust particle size is discussed

Gravity force

The gravity force is given by:

$$\mathbf{F}_\mathrm{g} = m_\mathrm{d}\mathbf{g} = \frac{4}{3}\pi r_\mathrm{d}^2 \rho_\mathrm{d}\mathbf{g} \ , \tag{3.16}$$

where $\mathbf{g}$ is the gravitational acceleration and ρ_d the mass density of the dust particles. Note that since $|\mathbf{F}_\mathrm{g}| \propto r_\mathrm{d}^3$, the gravity force is dominant for micrometre size particle (two-dimensional complex plasma crystal, see Section 3.1.6)) while its is negligible for nanometre size particles (particle growth experiments, see Sec. 3.2)

Electric force

As any charge particle, a charged dust particle is subjected to an electric force $\mathbf{F}_\mathrm{E}$ when immersed in an electric field $\mathbf{E}$. $\mathbf{F}_\mathrm{E}$ is given by:

$$\mathbf{F}_\mathrm{E} = Q_\mathrm{d}\mathbf{E} = 4\pi\epsilon_0 r_\mathrm{d}\Phi_\mathrm{d}\mathbf{E} \ . \tag{3.17}$$

Note that when applying the capacitor model (second term), $|\mathbf{F}_\mathrm{E}| \propto r_\mathrm{d}$. As it will be seen in Section 3.1.5, the electric force is strong enough in the sheath region to balance the gravity force and allow a microparticle to levitate. In the bulk plasma where quasi-neutrality holds, the existing electric fields (such as the ambipolar field) are too weak and only nanometre-size particles can be trapped in ground-based laboratory experiments (Under microgravity conditions, large particles can also be trapped in the bulk plasma).

Neutral drag force

The neutral drag force is due to neutral atom colliding with the dust particle. The neutral drag leads to the slowing down of dust particle and is particularly important for the formation of plasma crystals. For a dust particle moving with a velocity $\mathbf{v}_\mathrm{d}$ in the gas, the neutral drag force is given by [1]:

$$\mathbf{F}_\mathrm{nd} = -\delta\frac{4}{3}\pi r_\mathrm{d}^3 v_{\mathrm{th_n}} n_\mathrm{n}\mathbf{v}_\mathrm{d} \ , \tag{3.18}$$

where $v_{\mathrm{th_n}} = \sqrt{8k_\mathrm{B}T_\mathrm{g}/\pi m_\mathrm{n}}$ is the neutral atom thermal velocity with T_g the temperature of the gas and m_n the mass of the neutral atoms, n_n is the neutral atom number density, and δ is a parameter lying between 1 and 1.44 depending on how the neutral atom are reflected from the particle surface (specular reflection ($\delta = 1$), diffuse reflection ($\delta = 1.44$)). For plastic microparticles (for example melamine-formaldehyde microparticles), experimental results tend to favour $\delta = 1.44$ [71].

Thermophoretic force

The presence of a temperature gradient in the neutral gas lead to a thermophoretic force acting on the particle due to the differential bombardment of the dust particle surface by the neutral atoms. A simplify picture at the microscopic level is the following: the gas atoms or molecules moving from the hot side carry greater kinetic energy than those moving from the cold side, resulting in a net force on the particle from the hot side towards the cold side. In the free molecular regime, i.e. when the mean free path of the gas atoms/molecules is much larger than the dust particle radius (relevant to most laboratory dusty/complex plasma experiments), the thermophoretic force $\mathbf{F}_\mathrm{th}$ is given by [72]:

$$\mathbf{F}_\mathrm{th} = -\frac{32}{15}\frac{r_\mathrm{d}^2 k_\mathrm{n}}{v_{\mathrm{th_n}}}\nabla T_\mathrm{g} \ , \tag{3.19}$$

where k_n is the thermal conductivity of the gas and ∇T_g is the temperature gradient of the neutral gas.

The thermophoretic force is particularly important for sub-micron particles (nanoparticle growth experiments).The non-uniform heating of the gas by the plasma discharge can affect the transport of nanoparticles [73]. Sometimes a thermophoretic force is forced by differential heating or cooling of the discharge walls or electrode (with heater or Peltier element) in order to compensate for gravity and obtained three-dimensional structures of microparticles in ground based experiments [48, 49, 74].

Ion drag force

An ion moving towards a negatively charged dust particles can be, depending on its initial velocity v_0, collected or scattered by the dust particle. In both cases, it results in momentum being transferred from ions to the dust particles. The ion collection radius b_c is defined as [1, 66]:

$$b_\mathrm{c} = r_\mathrm{d}\sqrt{1 - \frac{2e\Phi_\mathrm{d}}{m_\mathrm{i}v_\mathrm{s}^2}} \ , \tag{3.20}$$

with $v_\mathrm{s} = \sqrt{u_\mathrm{i}^2 + v_\mathrm{th_i}^2}$. When the ion impact parameters is smaller than b_c, the ion is collected and contribute to the collection force $\mathbf{F}_\mathrm{coll}$. When the ion impact parameters is smaller than b_c, the ion is scattered and contribute to the Coulomb force $\mathbf{F}_\mathrm{Coul}$. The resulting ion drag force is the sum of the two components, i.e.:

$$\mathbf{F}_\mathrm{id} = \mathbf{F}_\mathrm{coll} + \mathbf{F}_\mathrm{Coul} \ , \tag{3.21}$$

In most experiments, the dust particles move much slower than the ions so that the relative dust-ion velocity can be approximated by the ion velocity. Considering that there are no interactions between the ions and the dust particle outside the Debye sphere and that the ion mean free path is larger than the Debye length (Barnes model), the collection force is [1, 66, 75]:

$$\mathbf{F}_\mathrm{coll} = \pi r_\mathrm{d}^2 m_\mathrm{i} n_\mathrm{i} v_\mathrm{s} \mathbf{u}_\mathrm{i} \left(1 - \frac{2e\Phi_\mathrm{d}}{m_i v_\mathrm{s}^2}\right) \ , \tag{3.22}$$

and the Coulomb force is ::

$$\mathbf{F}_\mathrm{Coul} = 4\pi b_{\pi/2}^2 m_\mathrm{i} n_\mathrm{i} v_\mathrm{s} \mathbf{u}_\mathrm{i} \ln\Lambda \ , \tag{3.23}$$

where the impact parameters for 90° deflection, $b_{\pi/2}$, is defined as (for small spherical particles so that the capacitor model can be used) [1]:

$$b_{\pi/2} = \frac{r_\mathrm{d} e\Phi_\mathrm{d}}{m_\mathrm{i}v_\mathrm{s}^2} \ . \tag{3.24}$$

and the Coulomb logarithm, $\ln\Lambda$, is defined as [1, 66, 75]:

$$\ln\Lambda = \frac{1}{2}\ln\left(\frac{\lambda_\mathrm{s}^2 + b_{\pi/2}^2}{b_\mathrm{c}^2 + b_{\pi/2}^2}\right) \ . \tag{3.25}$$

where the modified Debye shielding length is [66]:

$$\lambda_\mathrm{s} \approx \lambda_\mathrm{D_e}\left(1 + \frac{2k_\mathrm{B}T_\mathrm{e}}{2k_\mathrm{B}T_\mathrm{i} + m_\mathrm{i}u_i^2}\right)^{-1/2} \tag{3.26}$$

The ion drag force has been the subject of many experimental investigations (deflection of falling dust particle [76, 77]). It was found that significant discrepancies existed at low ion drift velocities. More accurate expression taking into account Coulomb collisions with ions outside of the Debye sphere and a corrected Debye length taking into account the different ion ion streaming velocities can be found in Refs. [78, 79]. Example of self-consistent calculations of the ion drag force taking into account charge-exchange collisions can be found in Ref. [80]

Laser forces

In complex plasmas, lasers can be used to manipulate microparticles (see Sec. 3.3.6). When a laser light beam is focussed on a dust particle, the beam interacts with it and pushes it in the direction of the beam. The force due to the laser light/dust particle interaction can have two origins: the radiation pressure and the photophoretic force.

The radiation pressure is due to momentum transfer of the photons hitting the dust particles and can be written as [1, 81]:

$$P_{\mathrm{rad}} = \frac{1}{A}\frac{\mathrm{d}N_{\mathrm{ph}}}{\mathrm{d}t}\frac{h}{\lambda_{\mathrm{l}}} = \frac{I_{\mathrm{l}}}{c} \ , \tag{3.27}$$

where N_{ph} is the number of photons hitting the particles , A is the focus cross section, λ_{l} is the laser light wave length, h is the Planck constant, c the speed of light and I_{l} is the intensity of the laser beam. The force exerted on the dust particle is then [1]:

$$F_{\mathrm{rad}} = \gamma\frac{I_{\mathrm{l}}}{c}\pi r_{\mathrm{d}}^2 \ , \tag{3.28}$$

where γ is a coefficient linked to the type of interaction the photons have with the dust particle (total reflection $\gamma = 2$, pure absorption $\gamma = 1$). Note that for partially transparent dust particle the radiation force can have a component perpendicular to the direction of propagation of the beam [1, 81].

The photophoretic force is due to the heating of the dust particle surface by the focussed laser light [82–84]. The side of the particle exposed to light can get significantly hotter that the side in the shadow. Similarly to thermophoresis (Sec. 3.1.2), the temperature differential induces a force that pushes the particle away from the hot side. For an opaque spherical microparticle, the photophoretic force is given by [83, 84]:

$$F_{\mathrm{ph}} = \frac{\pi}{6}\alpha\frac{p}{T_{\mathrm{n}}}\frac{r_{\mathrm{d}}^2}{k_{\mathrm{d}}}I_{\mathrm{r}} \ , \tag{3.29}$$

where I_{r} is the irradiance, p is the gas pressure, α is the thermal accommodation coefficient and k_{d} is the thermal conductivity of the particle.

3.1.3 Growth of nanoparticles in low pressure plasmas

The growth of nanoparticles in low-pressure chemically active plasmas has been the subject of active research since the discovery of nanoparticles in chemically active plasmas [85] and in plasma etching systems [5, 86]. Studies of the growth process have been mainly carried out in low pressure radio-frequency (Rf) plasma discharges using silane (SiH_4) mixture (see for example Refs. [85, 87–99] or hydrocarbon gases (such as acetylene (C_2H_2 or methane CH_4) mixture (see for example Refs. [100–103]).

The growth of nanoparticles in plasma-enhanced chemical vapour deposition reactors (usually capacitive radio-frequency reactors) is detailed in the review articles written by Watanabe [14] and Kortshagen et al. [105]. The growth process is roughly comprised of three phases. Despite the fact that in capacitive radio-frequency discharges, nanoparticles are usually trapped by electric fields and can grow to hundred of nanometres thanks to the continuous supply of chemical precursors, it is believed that nanoparticle growth in other king low-pressure gas discharges follows nearly the same general phases [105]. The specific of the growth process generally depends on the experimental conditions (pressure, power, gas mixture, temperature, etc.). Consequently, in the following, the different growth phases are described in all generality. For more details, the reader is invited to read the aforementioned reviews [14, 105].

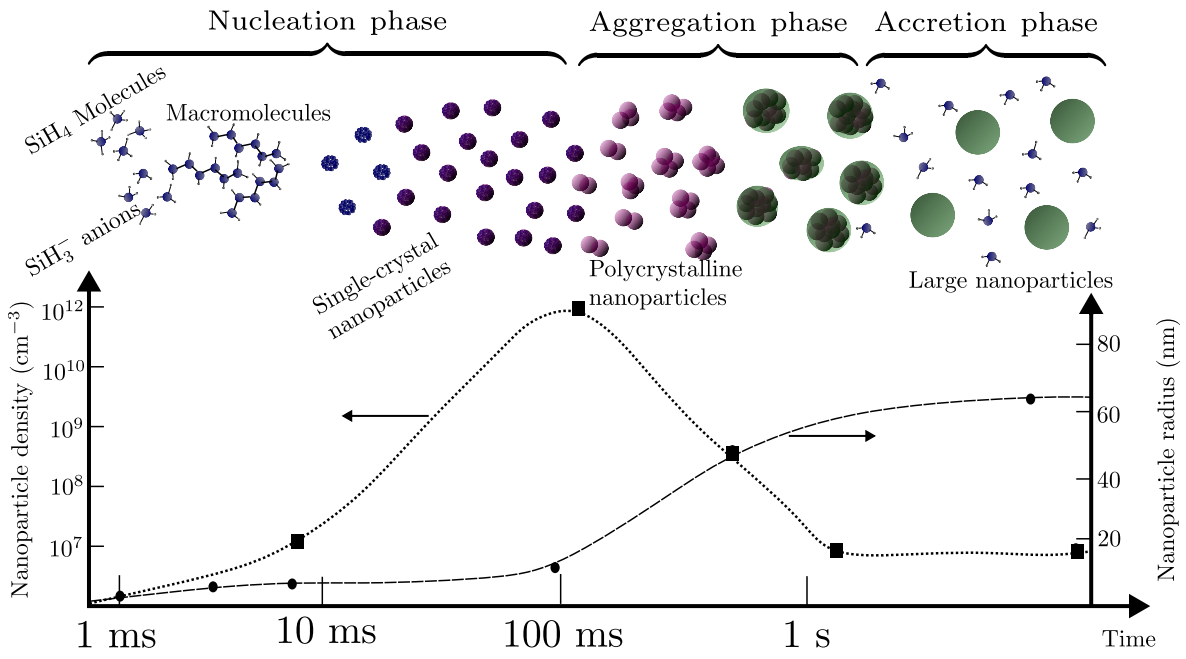

Figure 3.2 – Illustration of the evolution of nanoparticle size and number density as a function of time after discharge ignition if an Ar/SiH_4 discharge. After Ref. [104].

1. Nucleation phase (initial growth phase [14]): during this phase, plasma chemistry is responsible of the transformation of molecules into molecular clusters of a few nanometres in size (typically (∼2–3 nm). This phase is usually studied using mass spectroscopy of neutral, positively charged and negatively charged molelcules. This phase is sensitive to the discharge conditions (gas mixture, gas flow, power, temperature) [14]. The anion-neutral clustering is generally the most robust pathway [105]. This is partly due to the fact that ion-neutral reactions are generally faster than neutral-neutral reactions and partly due to the fact that anion are confined in the discharge by the ambipolar electric field while neutral species and cations diffuse out of the bulk plasma relatively quickly and might not spend enough time in the bulk plasma to significantly contribute to the nucleation process. This is thought to be also the case in the case of sputtering of single element target where the physical condensation of monomers dominates. Numerical studies of the nucleation phase in DC argon plasma in the absence of hydrogen have indeed confirmed that anion-neutral reactions are keys in cluster growth [106]. During this phase, the cluster number density reaches very high values and the clusters are either neutral or singly negatively charged. In the case of silicon nanoparticles growth in Ar/SiH_4 plasmas, it was shown that these initial nanometre-sized clusters are single crystal particles [98, 104, 107, 108].
2. Agglomeration phase (rapid growth phase [14]): At the end of the nucleation stage the density of nanoparticles is extremely high ($10^{11} - 10^{12}$ cm^{-3} [14, 104]). As a results, the nanoparticles are not uniformly negatively charged and larger particles grow quickly by initial agglomeration of the original clusters. The agglomeration of the smaller original clusters with the larger particles is favoured by charge fluctuations [50]. This phase continues until all particles are large enough (a few tens of nanometres) to be negatively charged and the repulsive electric force prevents further agglomeration. The nanoparticle number density drops drastically during this phase [104].
3. Accretion phase (growth saturation phase [14]): At the end of the agglomeration phase, the nanoparticles are large enough to all have acquired a quite large negative charge and their growth can continue only through surface reactions with the remaining precursors/molecules or with the continuously provided precursors/molecules (e.g. continuous

flow of precursor gas or target sputtering) [105]. The surface growth can be either through physical vapour deposition (for example a super saturated metal vapour due to the sputtering of a metal cathode) or through chemical vapour deposition (collisions of reactive molecules, radicals or ions at the particle surface that trigger chemical reactions). The growth rate during this phase is much slower than in the previous phases and the particle number density is nearly constant. While they are confined in the discharge, the nanoparticles will continue to grow. They can become quite large (hundreds of nanometres to micrometers)

In Figure 3.2, the nanoparticle growth process in an Ar/SiH_4 discharge is illustrated. Note that the growth process is known to happen in cycle: when the particles are getting too big, they are expelled from the plasma and a new generation of particle can start to grow [15, 52, 109–112].

3.1.4 Sheath profile in a capacitively-coupled radio-frequency discharge

Complex plasma crystal experiments are generally performed in capacitively-coupled radio-frequency (cc-rf) discharges [113, 114] where the microparticles are levitating in the sheath above the powered electrode. In these experiments, any modification of the discharge parameters (for example, the argon pressure p_{Ar} and/or the rf power P_{W}) has an effect on the gas discharge plasma and results in a modification of the sheath properties. It is obvious that, since microparticle monolayers levitates in the rf sheath above the powered electrode (see Section 3.1.6), the monolayer properties are also affected by any changes of the discharge parameters.

In this section, a simple model allowing the calculation of the sheath profile above the powered electrode in an asymmetric cc-rf discharge as a function of the discharge parameters is presented. The model was published in Ref.[115] (Publication 5 in App. B.1, a copy of which is found at the end of Sec. 3.3). It has been validated against available experimental data and was then used to obtain an estimate of the dependence of sheath parameters (sheath length, ion and electron densities, electric field) as a function of the discharge parameters (p_{Ar} and P_{W}).

Model description

In a cc-rf discharge, the rf frequency is generally much higher than the ion plasma frequency and much lower than the electron plasma frequency, i.e. $\omega_{\mathrm{pi}} \ll \omega_{\mathrm{rf}} \ll \omega_{\mathrm{pe}}$ where ω_{pi}, ω_{pe}, ω_{rf} are the ion plasma frequency, the electron plasma frequency and the rf angular frequency, respectively. Consequently, the ions respond only to the time-averaged sheath electric field while the electrons follow the rf field. Since in most of 2D complex plasma crystal experiments, the working pressure is around 1 Pa, ion collisions must be taken into account [116]. The model's main assumptions are based on earlier work by M. Lieberman [116]:

1. Collisional ion motion with a constant ion mean free path λ_i in the sheath,
2. Cold ions (ion temperature $T_{\mathrm{i}} \simeq 0$),
3. Inertia-less electrons that respond instantaneously to the electric field,
4. No secondary electrons emitted from the electrode,
5. No ionisation in the sheath.

In most experiments, the area of the powered electrode is much smaller than the area of the grounded surfaces (asymmetric cc-rf discharge). In addition, the matching circuit often contains a blocking capacitor preventing any direct current to flow in the external circuit.

Because of the difference in electrode area, the amount of ions and electrons collected during each rf cycle is different, resulting in the appearance of a negative self-bias voltage on the powered electrode [117, 118]. Ideally, it is necessary to consider the sheaths in front of both electrodes (powered and grounded) simultaneously [118]. However, the following assumptions can be made to simplify the problem:

1. The voltage on the rf electrode is of the form:

$$V_{\mathrm{rf}}(t) = -V_0 \cdot \cos(\omega_{\mathrm{rf}} t) - |V_{\mathrm{dc}}| \tag{3.30}$$

   The input values of V_0 and V_{dc} can be measured experimentally.

2. The plasma remains quasi neutral at all time. Therefore, the current flowing through the powered electrode sheath and the anode sheath are equal in intensity and of opposite signs. According to Song et al. [119], the time dependent plasma potential with respect to the grounded wall follows approximately:

$$V_{\mathrm{p}}(t) = T_{\mathrm{e}} \ln \left[\left(1 + \frac{A_{\mathrm{rf}}}{A_{\mathrm{g}}} \exp\left(\frac{V_{\mathrm{rf}}(t)}{T_{\mathrm{e}}} \right) \right) \cdot \left(1 + \frac{A_{\mathrm{rf}}}{A_{\mathrm{g}}} \right)^{-1} \right] + \frac{T_{\mathrm{e}}}{2} \ln \left(\frac{m_{\mathrm{i}}}{2.3 m_{\mathrm{e}}} \right), \tag{3.31}$$

   where the electron temperature T_{e} is given here in eV.

As it was the case for the microparticle charge derivation, the plasma potential is the reference potential in the following ($V_{\mathrm{p}} = 0$). Consequently, the potential of the rf electrode V_{c} with respect to the plasma as a function of time is:

$$V_{\mathrm{c}}(t) = V_{\mathrm{rf}}(t) - V_{\mathrm{p}}(t). \tag{3.32}$$

The time-dependant sheath potential profile $V(z,t)$ obeys the Poisson equation:

$$\nabla^2 V(z,t) = -\frac{e}{\epsilon_0} \Big(n_{\mathrm{i}}(z) - n_{\mathrm{e}}(z,t) \Big), \tag{3.33}$$

The boundary conditions are $V(0,t) = 0$ and $V(\ell_s, t = V_{\mathrm{c}}(t)$, where ℓ_s is the length of the ion sheath.

Ions react only to the time-averaged electric field $\bar{E} = -\mathrm{d}\bar{V}/\mathrm{d}z$ where $\bar{V}$ is the time-averaged powered electrode sheath electric potential. Therefore, in the sheath, the ions particle and momentum conservation equations are [120, 121]:

$$n_0 v_{\mathrm{s}} = n_{\mathrm{i}} v_{\mathrm{i}}, \tag{3.34}$$

$$M v_{\mathrm{i}} \frac{\mathrm{d}v_i}{\mathrm{d}z} + e \frac{\mathrm{d}\bar{V}}{\mathrm{d}z} + \frac{\pi M v_{\mathrm{i}}^2}{2\lambda_{\mathrm{i}}} = 0, \tag{3.35}$$

where n_0 is the plasma density at the plasma sheath boundary, v_{i} is the ion velocity at a given position z in the sheath and v_{s} is the velocity of the ions at the ion sheath boundary ($z = 0$). Due to collisions, v_{s} is the modified Bohm velocity [120, 121]:

$$v_{\mathrm{s}} = \left(\frac{e T_{\mathrm{e}}}{M} \right)^{1/2} \cdot \left(1 + \frac{\pi \lambda_{\mathrm{D_e}}}{2\lambda_{\mathrm{i}}} \right)^{-1/2}, \tag{3.36}$$

The sheath profile calculation requires a few approximations. The ion mean free path and the electron density in the bulk can be easily estimated from the discharge pressure, interferometry measurements and/or literature data. In experiments, the self-bias voltage and the amplitude of the rf voltage can also be easily measured as a function of the forward rf power

and argon pressure. The electron temperature can be directly measured (using Langmuir probe) or estimated using a uniform density discharge model [122]:

$$\frac{K_{iz}(T_\mathrm{e})}{u_\mathrm{B}(T_\mathrm{e})} = \frac{1}{n_\mathrm{g} d_{eff}}, \tag{3.37}$$

where $K_{iz}(T_\mathrm{e}) = 2.34{\cdot}10^{-14}{\cdot}T_\mathrm{e}^{0.59}{\cdot}\exp(-17.44/T_\mathrm{e})$ is the ionisation rate [122], $u_\mathrm{B}(T_\mathrm{e}) = \sqrt{eT_\mathrm{e}/M}$ is the Bohm velocity, n_g is the neutral gas number density and $d_{eff} = 0.5 \cdot Rl/(Rh_l + lh_r)$ is the effective plasma size for particle loss with l the height of the discharge chamber, R its radius, $h_r = 0.80 \cdot (4 + R/\lambda_{in})^{-1/2}$ and $h_l = 0.86 \cdot (3 + l/(2\lambda_{in}))^{-1/2}$ [122] and λ_{in} the ion mean free path in the plasma bulk.

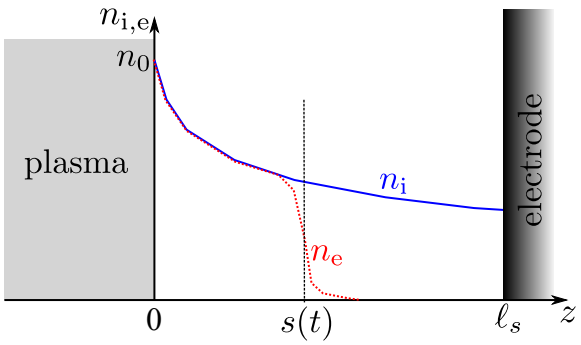

Figure 3.3 – (Reproduced from Ref. [115]) Schematic of a capacitive rf sheath at a time $0 < t < \pi/\omega_\mathrm{rf}$. The dotted vertical line shows the position of the electron sheath boundary $s(t)$. For $z < s(t)$, $n_\mathrm{e} \sim n_\mathrm{i}$ and for $z > s(t)$, $n_\mathrm{e} \sim 0$.

In addition, the solution to Eq. 3.33 requires the knowledge of the exact position of the time-varying (electron) sheath boundary $s(t)$ which depends on the voltage drop across the sheath and thus oscillates between the position of the (average) ion sheath boundary and a minimum distance to the electrode (see Fig. 3.3). However, the time-dependent sheath extension is rarely measured during experiments. Moreover, the current and voltage waveforms on the powered electrode are usually not monitored. Nevertheless, in cc-rf discharges, the electron temperature (in eV) is generally much smaller than the amplitude of the rf voltage, i.e. $V_0 \gg T_\mathrm{e}$ and $\lambda_{\mathrm{D_e}}$ is much smaller than the sheath width ℓ_s. On the plasma side ($z < s(t)$), quasi-neutrality holds ($n_\mathrm{e} \sim n_\mathrm{i}$) while on the sheath side ($z > s(t)$), the electron density falls quickly ($n_\mathrm{e} \sim 0$). Many studies dealing cc-rf sheath therefore use this approximation known as the step model [116, 118, 121, 123–127]. Here, the sheath profile is calculated using the following approximation for the time-dependent Poisson equation:

$$\nabla^2 V(z,t) \simeq -\frac{en_i(z)}{\epsilon_0}\Big(1 - \exp\frac{V(z,t)}{T_\mathrm{e}}\Big). \tag{3.38}$$

This approximation lies between the ion matrix sheath approximation ($n_i(z) = n_0$) and the step model. However it allows the calculation of an approximate solution of the Poisson equation at anytime if the voltage drop across the sheath is known. The mean electric field and ion density profiles can be then obtained in a recursive approach. Starting from the collision-less dc sheath profile with a potential drop equal to the maximum of $V_\mathrm{c}(t)$, a maximum sheath length and an

initial ion density profile can be calculated [122, 128]:

$$\ell_s = \frac{\sqrt{2}}{3}\lambda_{\mathrm{D_e}} \cdot \left(\frac{2 \cdot \max(|V_c(t)|)}{T_\mathrm{e}}\right)^{3/4}, \tag{3.39}$$

$$\bar{V}(z) = -\max(|V_c(t)|) \cdot \left(\frac{z}{\ell_s}\right)^{4/3}, \tag{3.40}$$

$$n_\mathrm{i}(z) = n_0 \cdot \left(1 - \frac{2\bar{V}(z)}{T_\mathrm{e}}\right)^{-1/2}. \tag{3.41}$$

Then the time-dependant potential profile over one rf period is calculated by solving Eq. (3.38) with MATLAB and using the following boundary conditions:

$$V(0,t) = 0, \tag{3.42}$$

$$V(\ell_s,t) = V_\mathrm{c}(t), \tag{3.43}$$

Afterwards, a new time-averaged potential (over one rf period) and a time-averaged electric field are calculated. If the time-averaged electric field on the plasma side ($z = 0$) is lower than $E_\mathrm{min} = (\pi/2) \cdot (T_\mathrm{e}/\lambda_i)$, (a value necessary to ensure monotonically decreasing ion density and increasing ion velocity in the sheath region) then the sheath boundary on the plasma side is moved towards the wall until the average electric field reaches E_min and the sheath length ℓ_s is adjusted. Using Eqs. (3.34) and (3.35) with the boundary conditions:

$$n_\mathrm{i}(0) = n_0, \tag{3.44}$$

$$v_\mathrm{i}(0) = v_\mathrm{s}, \tag{3.45}$$

a new ion density profile is then obtained and the time-dependant potential profile is calculated again. The procedure is repeated until convergence which typically occurs after 10 to 15 iterations.

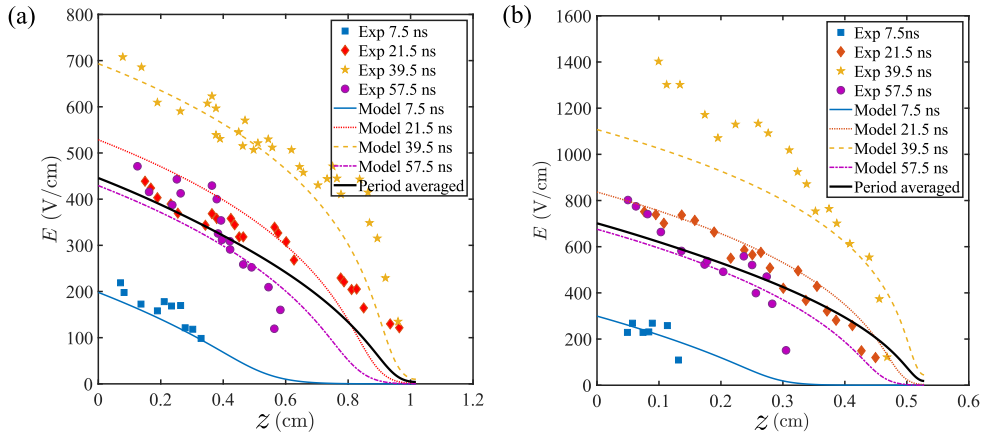

Figure 3.4 – (Reproduced from Ref. [115]) Experimental time-resolved electric field in krypton cc-rf discharge compared to the calculated electric field using the model decribed in this article. The experimental data are extracted from Ref. [129]. (a) $p_\mathrm{Kr} = 1$ Pa and $P_\mathrm{rf} = 8$ W, (b) $p_\mathrm{Kr} = 10$ Pa and $P_\mathrm{rf} = 8$ W. The time instants are given in the inset and in both plots the plain black line corresponds to the time-averaged electric field.

Model validation

In order to validate the above simple rf sheath model, it needs to be compared to available experimental data. Schulze et al. have reported experimental measurements of the time-dependant electric field in a cc-rf discharge in krypton at different pressures [129] which were

already used to validate other (more complex and more accurate) rf sheath model [127]. For the calculation, the grounded surface is assumed 100 times larger than the powered surface. The charge exchange cross section in krypton is $\sigma_{CX} = 40{\cdot}10^{-20}$ m^2 [130]. Two sets of measurements discharge were used to validate the model:

(a) $p_{\mathrm{Kr}} = 1$ Pa and $P_{\mathrm{rf}} = 8$ W, corresponding to $V_0 \simeq 250V$ and $V_{\mathrm{dc}} \simeq -250$ V (see Fig. 12 of Ref. [129]). As in Ref. [127], the electron temperature is fixed to $T_{\mathrm{e}} = 2.6$ eV and the plasma density at the sheath edge to $n_0 = 2.0 \cdot 10^{15}$ m^{-3}.

(b) $p_{\mathrm{Kr}} = 10$ Pa, and $P_{\mathrm{rf}} = 8$ W, corresponding to $V_0 \simeq 225V$ and $V_{\mathrm{dc}} \simeq -225$ V (see Fig. 5 of Ref. [129]). As in Ref. [127], the electron temperature is fixed to $T_{\mathrm{e}} = 1.1$ eV and the plasma density at the sheath edge to $n_0 = 7.3 \cdot 10^{15}$ m^{-3}.

In Fig. 3.4, the model results and the experimental data of Schulze et al. [129] are compared to each other. As can be seen, while not in perfect agreement, the simple model gives reasonable results. The sheath length is recovered within a few percent and the electric field values are in respectable agreement with the measured ones. Nevertheless, the model tends to slightly underestimate the electric field, especially at high pressure. The simple model described here is thus able to catch the main features of the collisional cc-rf sheath and can reasonably estimate the variation of the main sheath parameters as a function of position for the experimentally relevant range of discharge parameters.

Sheath profile in a cc-rf argon discharge

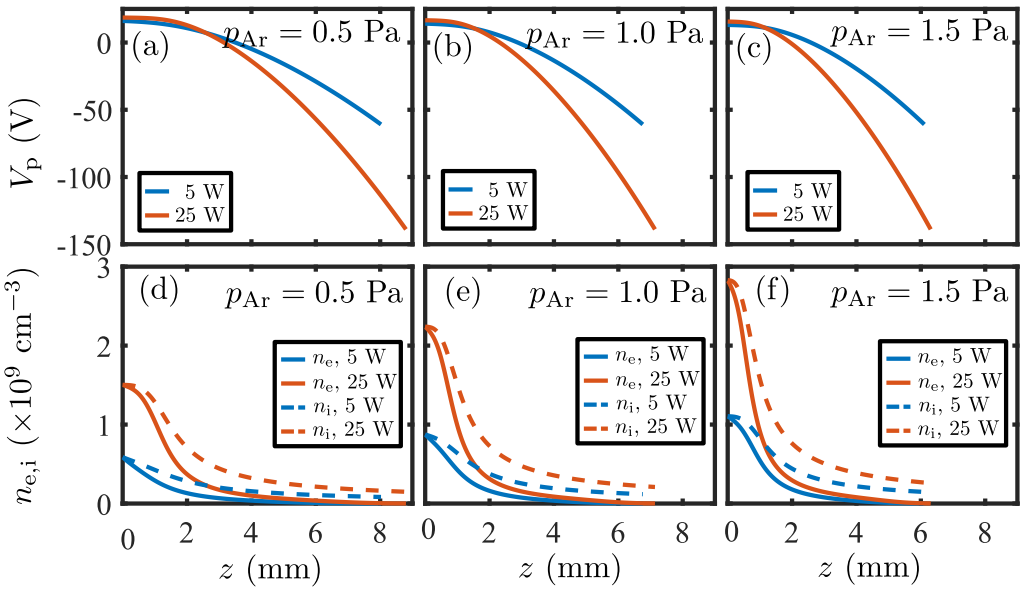

Figure 3.5 – (Reproduced from Ref. [115]) (a-c) Potential and (d-f) density profiles for different pressures and powers. Note that potentials are plotted with respect to ground (i.e. $V_{\mathrm{p}}(0) \neq 0$).

The model is used for discharge conditions relevant to two-dimensional complex plasma crystal experiments described in Ref. [115]. The argon pressure range is between 0.5 Pa and 2 Pa and the rf power range is between 5 W and 25 W by steps of 1 W. In Fig. 3.5 the sheath potential (Figs. 3.5(a-c)) and the electron and ion densities (Figs. 3.5(d-f)) are shown as a function of position for different pressures and rf powers.

As can be seen in the top row of Fig. 3.5, a pressure increase at constant rf power results in shorter sheath length for a similar potential drop (sheath length of $\sim 8-9$ mm at $p = 0.5$ Pa and $\sim 6-6.5$ mm at $p = 1.5$ Pa). Therefore, it results in weaker vertical electric field at lower pressures. An increase of the rf power at constant pressure results in a slight sheath length

increase but larger plasma potential drops due to increasing self-bias voltage ($\Delta V \sim 50$ V at $P_W = 5$ W and $\Delta V \sim 140$ V at $P_W = 25$ W) and therefore, a stronger vertical electric field.

Both P_{W} and p_{Ar} have an impact on plasma density. It was measured that at a given pressure, the plasma density is increasing almost linearly with the forward rf power (see Fig. 2 of Ref. [115]). Since the sheath length is weakly dependant on rf power (see previous paragraph), the gradients of ion and electron densities in the sheath increase with rf power as can be seen in the bottom row of Fig. 3.5. At high pressure, the plasma density is higher (due to collisions), the sheath length is shorter resulting in steep density gradients.

3.1.5 Microparticle levitation in the rf sheath

When injecting a calibrated spherical microparticle into a gas discharge plasma, the microparticle acquires a large negative charge and can be levitate in the sheath region where the gravity force is balanced by the electric force. At the equilibrium position, the total electric current on the microparticle surface $I_{\mathrm{i}} + I_{\mathrm{e}}$ is equal to zero. Since the sheath profile can be calculated, the normalised floating potential $\tilde{\varphi}$ and the microparticle charge number $Z_{\mathrm{d}} = Q_{\mathrm{d}}/e$ can be obtained for any position in the sheath (see Secs. 3.1.1 and 3.1.4) Since the microparticle radius r_{d} and therefore microparticle mass m_{d} of the microparticle are known, the equilibrium levitation height z_{lev} can be calculated using the calculated sheath electric field profile and the vertical resonance (confinement) frequency $f_{\mathrm{v}} = \omega_v/(2\pi)$ can be obtained using the following equations [131–134]:

$$Q_{\mathrm{d}} E(z_{\mathrm{lev}}) = -m_{\mathrm{d}} g, \tag{3.46}$$

$$\omega_v = \sqrt{\frac{|Q_{\mathrm{d}}|}{m_{\mathrm{d}}} \frac{\partial E(z)}{\partial z}}_{|z=z_{\mathrm{lev}}}. \tag{3.47}$$

In Fig. 3.6, the the calculated equilibrium levitation height, equilibrium particle charge at equilibrium levitation height and vertical resonance frequency as a function of rf power and background argon pressure are shown. The obtained equilibrium particle charges are between

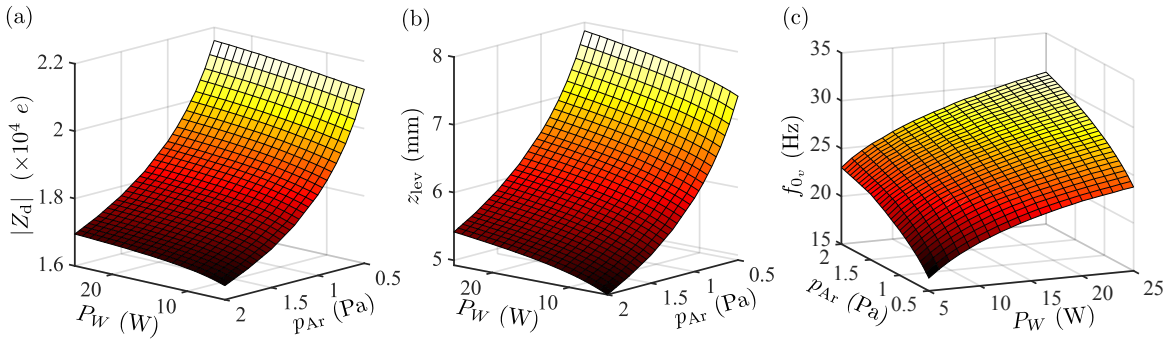

Figure 3.6 – (Reproduced from Ref. [115]) (a) Equilibrium particle charge. (b) Equilibrium levitation height. (c) Vertical resonance frequency. The microparticle has a diameter $d = 9.16$ μm and its mass density is $\rho_m = 1510$ kg $\cdot$ m^{-3}.

$-2.2{\cdot}10^4 e$ and $-1.6{\cdot}10^4 e$ (see Fig. 3.6(a)), which is in reasonable agreement with experimentally reported values (see Refs. [113, 115]).

One can see that at a given argon background pressure, Z_{d} and z_{lev} are weakly increasing function of the rf power. Moreover, the microparticles levitate quite high in the sheath near the sheath edge (for example at 1 Pa, the sheath length is around ~ 7 mm [see Fig. 3.5] and the levitation height is around ~ 6.5 mm [see Fig. 3.6(b)]). This is due to the fact that even though the ion and electron densities are increasing with rf power, the electron temperature

is mostly set by the background gas pressure. Since T_e has a greater influence than n_e on the magnitude of the electron current onto a microparticle and therefore the microparticle charge, the microparticle equilibrium charge depends weakly on rf power. Since at the equilibrium levitation height, the gravity force is compensated by the electric force and, as seen previously, and the sheath length being only weakly dependant on rf power, the particle levitation height is only slightly modified.

The calculated vertical resonance frequency varies in the range 15–30 Hz depending on discharge parameters and is very close to the vertical resonance frequency reported in similar setups [38, 114, 135–138]. The vertical resonance frequency is increasing significantly with both rf power and argon background pressure (see Fig. 3.6(c)). In both cases, this is due to steeper electric field when increasing rf power (resulting in larger self-bias) and when increasing the background argon pressure (resulting in shorter sheath).

Ion wakes

The sheath electric field and the ion flow in the sheath are tight together. It is indeed the electric field that accelerate the ions towards the electrode. Therefore, when a dust particle levitate in the sheath, the plasma screening is no longer spherically symmetric and become highly polarised. The microparticle generates a wake field potential due to the downstream ion focus. The ion wake field can be calculated via linear response theory [139–141], self-consistent kinetic theory [142], using particle-in-cell (PIC) simulations [143] or molecular dynamics simulations [144–146]. There are different level of refinement to calculate the ion wake potential which can include the presence of electric fields, ion-neutral collisions, and different shape of ion velocity distribution (see for example Ref. [142]).

In Fig. 3.7, the perturbations of the ion density and the electric potential due to the presence of a levitating microparticle in the sheath are presented [146]. The results were calculated using the DRIAD code [144–146]. The charge of the microparticle and the density and field perturbations were calculated by taking into account the ambient electric field and ion-neutral collisions. As can be seen, the ion wake is quite sensitive to the discharge parameters: high pressure and low power tends to increase the amplitude of the ion wake.

The presence of ion wake renders the interaction between microparticles highly anisotropic [139, 140, 147]: the excess ions downstream of each microparticle attracts other negatively-charge microparticles to stationary points. These interactions with the ion wakes make the microparticle-microparticle interactions non-reciprocal (the ion wake acts like a third body in the interaction and hence Newton third law is violated when considering only the microparticles) [148–152] and energy from the ion flow can be converted into microparticle kinetic energy. This effect can lead to two type of instabilities in complex plasmas [153]: (i) the Schweigert instability in multilayer systems [154–156] where a dust particle sitting further downstream in the ion flow feels the attraction from the ion wake of the upstream particles whereas the upstream particles are repelled from the downstream one leading to growing oscillations, (ii) the mode-coupling instability in monolayer of microparticles where the horizontal motion of the microparticles gets coupled to their vertical motions because of the wake-induced force asymmetry that can results in growing oscillations in both the horizontal and vertical directions [114, 148–150, 157]. The mode-coupling instability is detailed in Sections 3.1.6 and 3.3.

3.1.6 Two-dimensional complex plasma crystals

In experiments in which calibrated (monosized) spherical microparticles are injected, they generally all trapped at the same height in the sheath above the confining electrode (all the particles have the same mass and acquire the same charge) and form a monolayer of microparticles. Two-dimensional (2D) complex plasma monolayers are particularly convenient systems for the

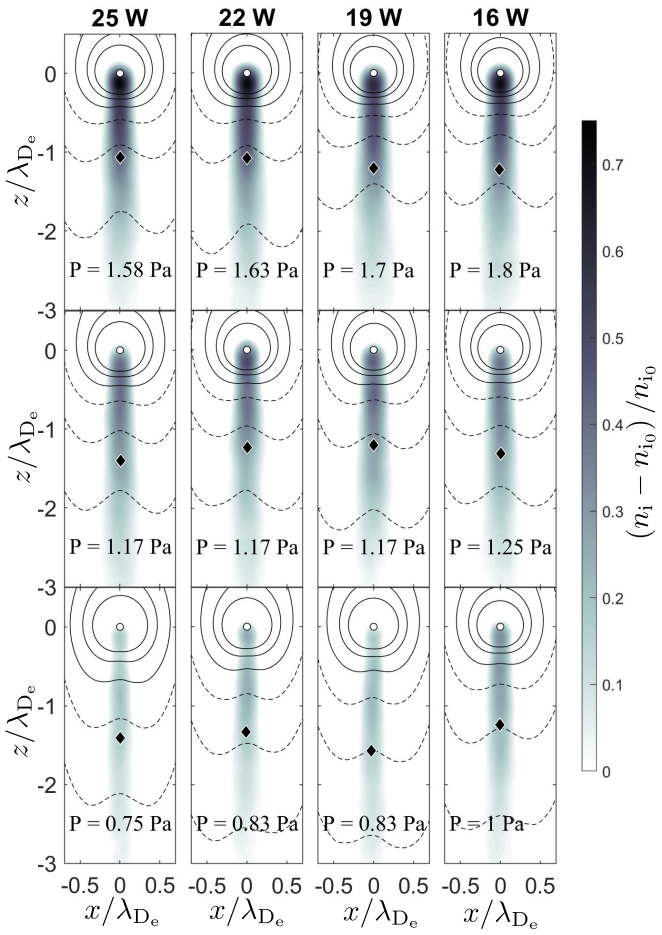

Figure 3.7 – (Reproduced from Ref.[146]) Ion density in the vicinity of a dust grain levitating in the sheath for different rf power and gas pressure. The grayscale image depicts the ion density perturbation region $(n_i - n_{i_0}/n_{i_0}) > 0$ (ion wake). The contour lines are equipotential lines from -0.1 V to 0.15 V in steps of 0.05 V. Dashed lines are positive potential line contours and solid lines indicate negative potential contours. The black diamond is the location of the ion-wake center of charge, and the white dot is the location of the microparticle (size not to scale).

detailed experimental studies of strongly coupled phenomena at the "atomic" (particle) level. The essential advantage of such systems is that the complete information about the state of the entire particle ensemble in phase space can be measured (fast camera imaging combined to particle tracking [158]). This is an invaluable advantage for the investigation of collective processes occurring in strongly coupled systems and generic phenomena such as wave propagation [37, 38], shocks [39, 40], phase transitions [41–44], etc.

2D complex plasma monolayers are usually studied in ground-based cc-rf discharges. Microparticles injected in such discharges levitate in the sheath region near the bottom electrode, where the electric field can balance gravity. Under specific conditions, the microparticle monolayer arrange itself into an ordered structure (hexagonal lattice) if the electrostatic coupling is strong enough – a 2D plasma crystals [37, 114, 158–160, 160–163]. Such a lattice is shown in Fig. 3.8.

Waves in complex plasma crystals

In 2D complex plasmas, as in any (strongly coupled) 2D system, two in-plane wave modes can be sustained. In crystals, both modes have an acoustic dispersion, one of them is longitudi-

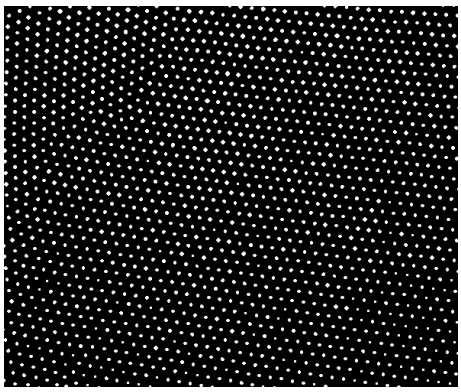

Figure 3.8 – Top view of a 2D complex plasma crystal. Note the hexagonal lattice.

nal (compression), the other is transverse (shear). Since the strength of the vertical confinement is finite, there is also a third fundamental wave mode associated with the out-of-plane oscillations. Propagation of dust-lattice (DL) waves in 2D lattices is often used as a diagnostic tool to determine parameters of the plasma crystal (charge Q_d of the microparticles, screening length λ and coupling parameter κ).

The DL mode can be derived following the method described in Ref. [150]. Consider an hexagonal microparticle monolayer located in the horizontal xy-plane as shown in Fig. 3.9. The interaction potential between two microparticles i and j in the 2D lattice are in a first approximation given by the screened-Coulomb (Yukawa) potential $\varphi(r_{ij})$:

$$\varphi(r_{ij}) = \frac{Z_d^2 e^2}{4\pi\varepsilon_0} \frac{\exp(-r_{ij}/\lambda_D)}{r_{ij}} \ , \tag{3.48}$$

where $r_{ij}^2 = (x_i - x_j)^2 + (y_i - y_j)^2 + (z_i - z_j)^2$. If the thermal agitation is neglected, then the motion of particle j with coordinate $\mathbf{r}_j$ is governed by:

$$m_\mathrm{d}\ddot{\mathbf{r}}_j + m_\mathrm{d}\nu\dot{\mathbf{r}}_j = \sum_{i\neq j} \mathbf{F}_{ij} + \mathbf{F}_\mathrm{conf}(\mathbf{r}_j) \ , \tag{3.49}$$

where ν is the damping rate due to neutral gas friction, $\mathbf{F}_{ij} = -\nabla\varphi(r_{ij})$ is the interaction force exerted by the i$^\mathrm{th}$ particle, and $\mathbf{F}_\mathrm{conf}$ is the force of external confinement. In this derivation, the lattice is considered infinite on the xy-plane and the finite strength of the vertical confinement in the sheath is reduced to a harmonic potential, i.e. $\mathbf{F}_\mathrm{conf} = -m_\mathrm{d}\Omega_\mathrm{conf}^2 z_j \hat{z}$ where z_j is the the vertical position of the j$^\mathrm{th}$ particle with respect to the plane of the crystal, Ω_conf is the eigenfrequency of vertical confinement and $\hat{z}$ the unit vector in the vertical direction. Then, small displacements of the form $\mathbf{r}_j \propto \exp\left(i(\mathbf{k}\cdot\mathbf{r}_j - \omega t)\right)$ (with a wave vector $\mathbf{k}$ and a angular frequency ω) are introduced into Eq. 3.49 which is subsequently linearised yielding to the equation:

$$\det\left[\mathbf{D}_k - \Omega^2\mathbb{1}\right] = 0, \tag{3.50}$$

where $\mathbb{1}$ is the unit matrix, $\mathbf{D}_k$ is the dynamical matrix with eigenvalues $\Omega^2 = \omega(\omega + i\nu)$. $\mathbf{D}_k$ can be written has [150]:

$$\mathbf{D}_k = \begin{pmatrix} \alpha_h - \beta & 2\gamma & 0 \\ 2\gamma & \alpha_h + \beta & 0 \\ 0 & 0 & \Omega_\mathrm{conf}^2 - 2\alpha_v \end{pmatrix} \ , \tag{3.51}$$

where the elements $\alpha_h(\mathbf{k})$, $\beta(\mathbf{k})$, and $\gamma(\mathbf{k})$ govern the dispersion of two horizontal in-plane modes, and $\alpha_v()$ govern the vertical out-of-plane mode. Let us define the the lattice screening

parameter $\kappa = \Delta/\lambda_{\rm D}$, and the dust lattice frequency $\Omega_{DL} = \sqrt{Q_{\rm d}^2/(4\pi\epsilon_0 m_{\rm d}\lambda_{\rm D}^3)}$. All frequencies are renormalised by Ω_{DL} and the wave vector is renormalized as $\mathbf{k}\Delta \to \mathbf{k}$. The matrix element of $\mathbf{D}_k$ can then be written as [150]:

$$\alpha_h = \sum_{m,n} e^{-K}(K^{-1} + K^{-2} + K^{-3}) \sin^2 \frac{1}{2}\mathbf{k}\cdot\mathbf{s}, \tag{3.52}$$

$$\alpha_v = \sum_{m,n} e^{-K}(K^{-2} + K^{-3}) \sin^2 \frac{1}{2}\mathbf{k}\cdot\mathbf{s},$$

$$\beta = \sum_{m,n} e^{-K}(K^{-1} + 3K^{-2} + 3K^{-3})[(s_y^2 - s_x^2)/s^2] \sin^2 \frac{1}{2}\mathbf{k}\cdot\mathbf{s},$$

$$\gamma = \sum_{m,n} e^{-K}(K^{-1} + 3K^{-2} + 3K^{-3})[s_x s_y/s^2] \sin^2 \frac{1}{2}\mathbf{k}\cdot\mathbf{s},$$

where $K = \kappa\sqrt{m^2 + n^2 + mn}$, m and n are integer numbers linked to the particle position (see Fig. 3.9). The vector $\mathbf{s}$ with components $s_x = (\sqrt{3}/2)m$ and $s_y = \frac{1}{2}m + n$ characterises the positions of all particles in the hexagonal lattice. Note that the sums exclude the central particle (0,0).

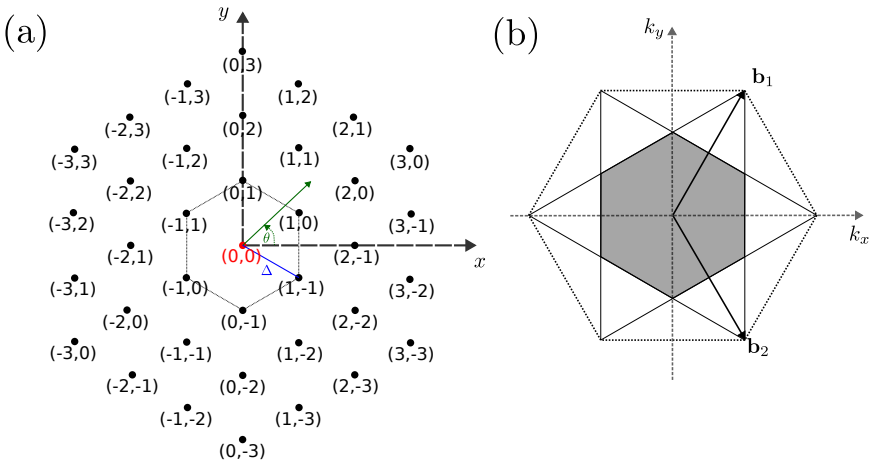

Figure 3.9 – (a) Illustration of an ideal hexagonal lattice. The elementary hexagonal lattice cell with the frame of reference, and the lattice constant Δ are shown at the center. The particles' positions are given by a set of two integer (m, n). For a given particle (m, n), the position is $x_{(m,n)} = \Delta \cdot m\sqrt{3}/2$ and $y_{(m,n)} = \Delta \cdot (m/2 + n)$. The central particle (0,0) is excluded from the sum in the definition of the dynamical matrix element, Eqs. 3.52. (b) Reciprocal lattice in k-space with the reciprocal basis vectors $|\mathbf{b}_1| = |\mathbf{b}_2| = \frac{4\pi}{\Delta\sqrt{3}}$. Due to the lattice symmetry, it is sufficient to consider wave vectors $\mathbf{k}$ with angle $0° \leq \theta \leq 30°$ and from within the first Brillouin zone (gray region), i.e. $\mathbf{k}\Delta \leq 2\pi/\sqrt{3}$ at $\theta = 0°$ and $\mathbf{k}\Delta \leq 4\pi/3$ at $\theta = 30°$

The dispersion relation of the DL modes can then be written in the form:

$$(\Omega^2 - \Omega_{h_+}^2)(\Omega^2 - \Omega_{h_-}^2)(\Omega^2 - \Omega_v^2) = 0\ , \tag{3.53}$$

where $\Omega_{h_\pm}(\mathbf{k}) = \sqrt{\alpha_h \pm \sqrt{\beta^2 + 4\gamma^2}}$ corresponds to the pair of in-plane wave mode (compression and shear, respectively) and $\Omega_v = \sqrt{\Omega_{\rm conf}^2 - 2\alpha_v}$ corresponds to the out-of-plane mode. The shape of the modes obviously depend on the direction of the propagation of the wave with respect to the main lattice axis (i.e. the angle θ that $\mathbf{k}$ makes with the x-axis (see Fig. 3.9). The wave modes for teh propagation angles $\theta = 0°$ and $\theta = 30°$ are plotted in Fig. 3.10.

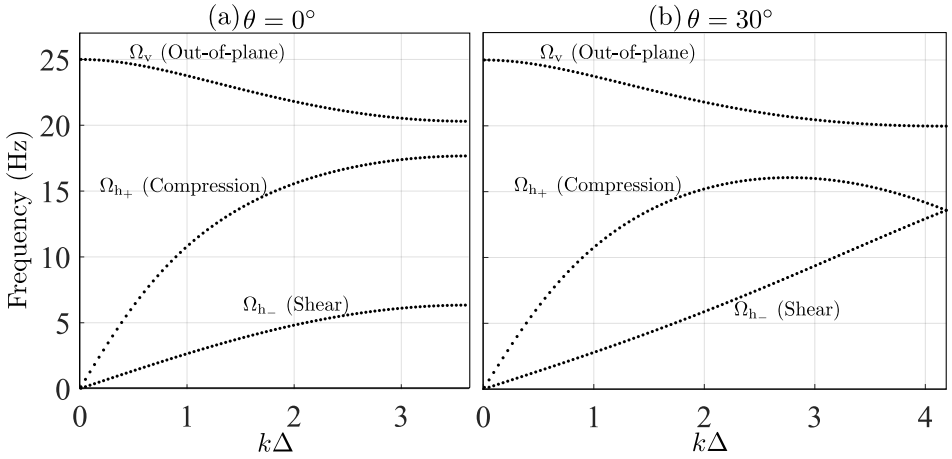

Figure 3.10 – Wave modes in a 2D complex plasma crystal assuming Yukawa interparticle interaction and a parabolic vertical confinement. (a) $\theta = 0°$, (b)$\theta = 30°$. The interparcle distance was $\Delta = 500$ μm, the microparticle charge was $Q_\mathrm{d} = -20000e$, and the vertical confinement frequency was $f_v = \Omega_\mathrm{conf}/2\pi = 25$ Hz.

Ion wakes-induced mode-coupling instability

2D plasma crystals are systems with many interacting species (dust, ions, electrons and neutral atoms). Although the exchange of momentum through electrostatic interactions between microspheres largely dominates interactions with other particles (especially neutral atoms) providing a "quasi-monoatomic" system for kinetic studies, some aspects specific to the presence to the presence of the ambient plasma cannot be neglected.

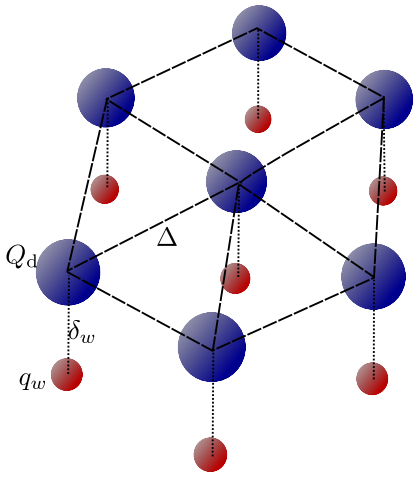

Figure 3.11 – Illustration of the point-like wake model for an hexagonal microparticle lattice. The positively charge ion wake (red spheres, charge q_w) are at a distance δ_w of the negatively charged microparticles (blue spheres, charge Q_d).

Indeed, as seen in Sec. 3.1.5, since the microparticles are levitating in the sheath, an ion wake forms down stream of each microparticles and renders the microparticle interactions non-reciprocal. The simplest way to model the ion wake is to consider them as fixed positive point-like charge q_w at a distance δ_w below each particle [148, 150, 157]. In that case, the

microparticle interaction potential can be written as follows:

$$\varphi_w(r_{ij}) = \underbrace{\frac{Z_d^2 e^2}{4\pi\varepsilon_0}\frac{\exp(-r_{ij}/\lambda_D)}{r_{ij}}}_{\text{Interaction with the microparticles}} \overbrace{- \frac{\tilde{q}_w Z_d^2 e^2}{4\pi\varepsilon_0}\frac{\exp(-r_{w_{ij}}/\lambda_D)}{r_{w_{ij}}}}^{\text{Interaction with the wakes}} , \tag{3.54}$$

where $r_{w_{ij}}^2 = (x_i - x_j)^2 + (y_i - y_j)^2 + (z_i - (z_j - \delta_w))^2$. Then, the dynamical matrix has to be rewritten as [150]:

$$\mathbf{D}_k = \begin{pmatrix} \alpha_\mathrm{h} - \beta & 2\gamma & i\sigma_y \\ 2\gamma & \alpha_\mathrm{h} + \beta & i\sigma_x \\ i\sigma_y & i\sigma_x & \Omega_\mathrm{conf}^2 - 2\alpha_\mathrm{v} \end{pmatrix} . \tag{3.55}$$

The elements $\sigma_{x,y}$ appear due to particle-wake interactions and describe the coupling between the out-of-plane and in-plane modes. They are given by:

$$\sigma_{x,y} = \tilde{q}_w \tilde{\delta}_w \sum_{m,n} e^{-K}(K^{-1} + 3K^{-2} + 3K^{-3})[s_{x,y}/s] \sin \mathbf{k}\cdot\mathbf{s} , \tag{3.56}$$

where $\tilde{q}_w = |q_w/Q_\mathrm{d}|$ and $\tilde{\delta}_w = \delta_w/\Delta$. Then, the dispersion relation of the DL modes becomes:

$$(\Omega^2 - \Omega_{h_+}^2)(\Omega^2 - \Omega_{h_-}^2)(\Omega^2 - \Omega_v^2) + \Omega_\mathrm{coup}^4 \left(\Omega^2 - \Omega_\mathrm{mix}^2\right) = 0 , \tag{3.57}$$

where the coupling frequency is $\Omega_\mathrm{coup}^2(\mathbf{k}) = \sqrt{\sigma_x^2(\mathrm{k}) + \sigma_y^2(\mathrm{k})}$ and the mixing frequency is:

$$\Omega_\mathrm{mix}^2(\mathrm{k}) = \alpha_h + \beta\frac{\sigma_x^2 - \sigma_y^2}{\sigma_x^2 + \sigma_y^2} - 4\gamma\frac{\sigma_x\sigma_y}{\sigma_x^2 + \sigma_y^2} . \tag{3.58}$$

Considering weakly damped waves (i.e. $\omega \gg \nu$ so that $\Omega = \omega + \frac{1}{2}i\nu$), it is enough to analyse the undamped dispersion relation ($\Omega = \omega$) and add $-\frac{1}{2}\nu$ to the imaginary part of ω [150].

In Fig. 3.12, the DL wave modes calculated with the point-wake model are presented. As can be seen, wake-mediated coupling between the longitudinal in-plane and out-of-plane modes occurs when the out-of-plane and in-plane compression modes intersect. This results in the appearance of a hybrid mode (red lines in Fig. 3.12) which has a positive imaginary part meaning. Therefore this hybrid mode is possibly unstable if the neutral gas damping is sufficiently low. Mode-coupling occurs first at $\theta = 0°$ (and equivalent directions) for "shallow" crossing of the modes and occurs at any θ for deeper crossing. The appearance of hybrid mode can lead to the mode coupling instability (MCI) which is extensively discussed in Sec. 3.3.

The distinct fingerprints at the mode-coupling instability onset are, in addition to the emergence of the hybrid mode (which depends critically on the angle of propagation), a mixed polarization and distinct thresholds. To illustrate mixed polarisation, results from molecular dynamics simulations of a 2D complex plasma crystal are presented in Fig. 3.13. The simulations was performed for a very shallow crossing so that the hybrid mode appears only at $\theta = 0°$ ($\theta = 30°$ in Fig. 3.13(b) since the reference cell was rotated by 30° in Ref.[157]). This illustrates the angular dependence of the of wake-mediated mode coupling. It can be further evidence by looking at wave spectrum in the $\mathbf{k}$-plane integrated over frequency around the hybrid frequency (Fig. 3.13(c)): a hot spot appears only in the direction at which the hybrid mode can form. In addition, when looking in the vicinity of the hybrid mode, one can see traces of mixed polarization for both intersecting mode branches (Fig. 3.13(d)): far from mode intersection (or when the modes do not cross at all), the out-of-plane mode is purely transverse and the in-plane modes are purely longitudinal or transverse. Near the hybrid mode, where the coupling

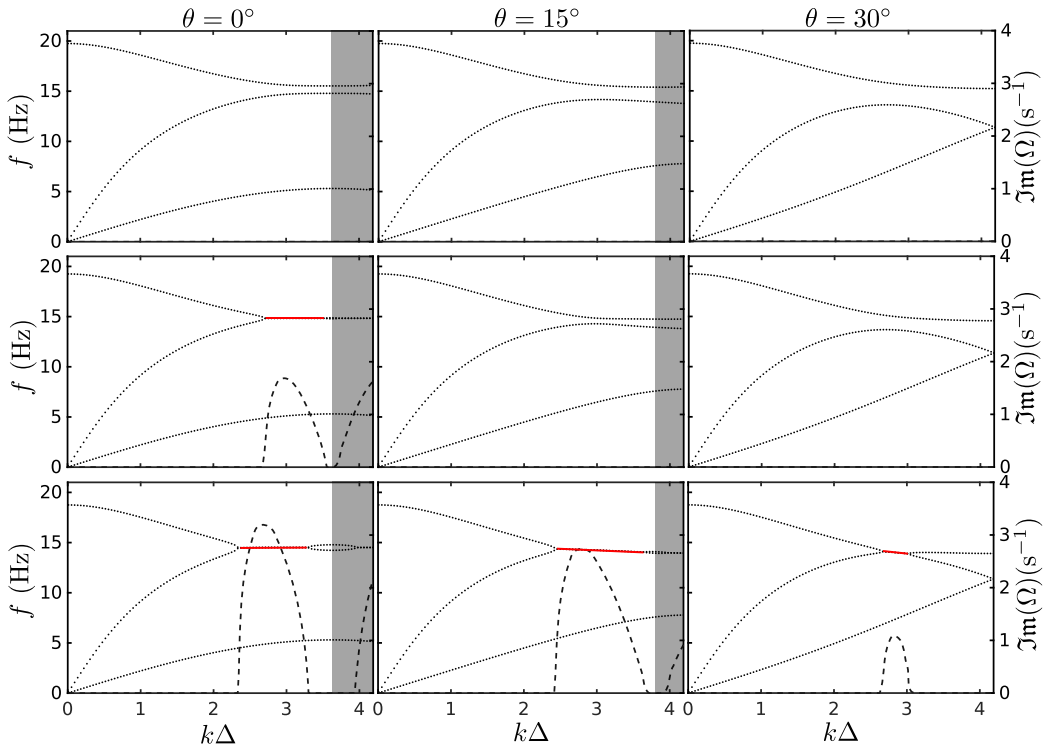

Figure 3.12 – Wave modes in a 2D complex plasma crystal assuming Yukawa interparticle interaction, point ion wakes and a parabolic vertical confinement. The interparcle distance was set to $\Delta = 500$ μm, the microparticle charge to $Q_\mathrm{d} = -20000e$, and the vertical confinement frequency is changed $f_v = 19.75$ Hz to $f_v = 18.75$ Hz by step of 0.5 Hz. The ion wake parameters are $\tilde{q}_w = 0.3$ and $\tilde{\delta}_w = 0.3$. The red lines show the hybrid mode. The dashed curves show the imaginary part of Ω. The region outside of the first Brillouin zone at $\theta = 0°$ and $\theta = 30°$ are greyed.

between the out-of-plane and in-plane compression modes is strong, their polarizations become oblique (i.e. in the plane formed by $\mathbf{k}$ and the vertical axis but with mutually orthogonal eigenvectors) and are therefore not purely out-of-plane nor in-plane any more. They can thus be seen in the in-plane and out-of-plane wave mode spectra simultaneously.

Finally, distinct thresholds are necessary to trigger the mode-coupling instability. Obviously, the mode needs to cross which leads to confinement and dust particle density thresholds [115, 157]. Secondly, the growth rate of the instability needs to be higher than neutral damping to lead to an instability and the mode coupling-induced melting. The detailed feature of the hybrid mode and the resulting mode-coupling instability are discussed in great details in Refs. [150, 157] and in Sec. 3.3. Note that mode-coupling instability also exist in 2D fluid complex plasma monolayer [2] but with the following specificities: no confinement and dust particle density thresholds and a higher growth rate for the instability leading to conditions for which both the crystalline and the fluid states are possible (no crossing of the modes in the crystal state and MCI growth rate high enough in the fluid state to prevent crystallization). This has implication for the stability of 2D complex plasma crystals (see Sec. 3.3 and Ref.[115]) and the melting dynamics of 2D complex plasma crystals (see Sec. 3.3 and Refs[164–166]).

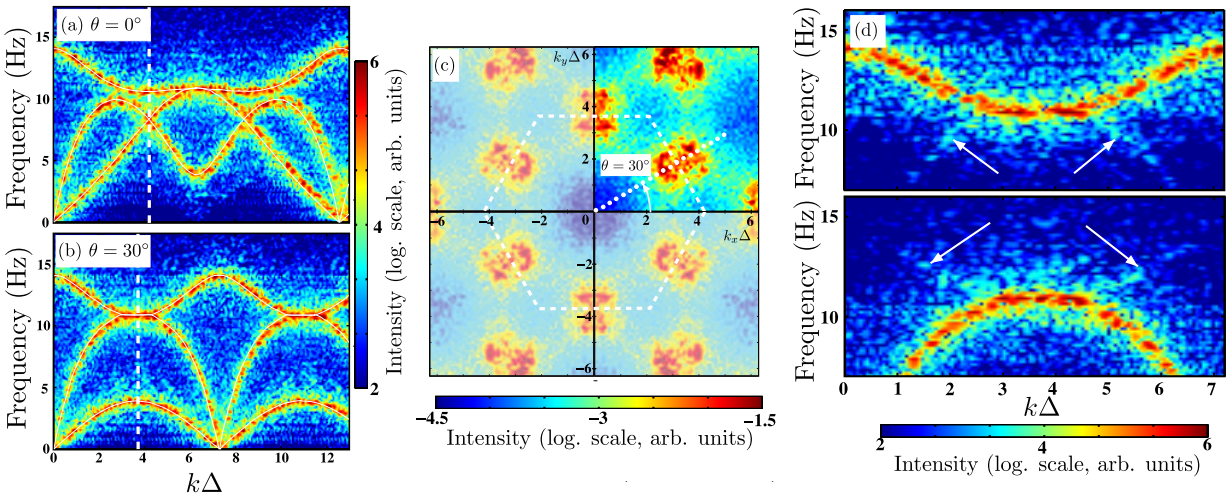

Figure 3.13 – (Reproduced from Ref. [157]). Current fluctuation spectra (wave mode spectra) for "shallow" mode intersection (molecular dynamics simulations). Shown are the DL modes (positive branches) for $\mathbf{k}$ at (a) $\theta = 0°$ and (b) $\theta = 30°$. (c) Spectrum in the $\mathbf{k}$-plane integrated over frequency (in the range between 10 Hz $\leq f \leq$ 14 Hz). Note that the elementary cell is rotated by 30° with respect to Fig. 3.9. Simulations are for $N = 16384$ particles of mass $m = 6.1 \times 10^{-13}$ kg and charge $Q = -18500\ e$, a screening length $\lambda = 600\ \mu$m, and a damping rate $\nu = 0.87\ \mathrm{s}^{-1}$. The horizontal and vertical confinements have eigenfrequencies $f_{\mathrm{conf}}^{(\mathrm{h})} = 0.11$ Hz and $f_{\mathrm{conf}}^{(\mathrm{v})} = 14.03$ Hz, respectively. The lattice constant in its center is $\Delta \simeq 612\ \mu$m ($\kappa = \Delta/\lambda \simeq 1.02$). The wake parameters are $q = -0.2Q$ and $\delta = 0.3\lambda$. The dashed lines show the border of the first Brillouin zones, solid lines in (a) and (b) are theoretical curves. In (c) the calculations for the upper right quadrant are mirrored in other three (shown in lighter colors). (d) Mixed polarization near the hybrid mode (simulations). Shown are the fluctuation spectra with the transverse out-of-plane (a) and longitudinal (b) polarization, for $\mathbf{k}$ at $\theta = 30°$ Arrows indicate traces of mixed polarization. Far from the hybrid mode (i e. the "hot spots") the modes become purely out-of-plane (top) and in-plane (bottom).

3.2 Nanoparticle growth

3.2.1 General motivations

Dust is observed in many industrial [5] or laboratory plasmas [1]. When dust particle are homogeneously formed in the plasma, they are generally spherical. Dust can also be created as a result of the flaking of thin layers deposited on reactor walls. They pose a contamination problem in PECVD plasmas [92], etching plasmas [167], etc. During thin film deposition using plasma processes, the highest deposition rates also lead to the formation of large amounts of dusts in the plasma [23, 168].

However, dust does not only form in laboratory plasmas but also in the cold plasma on board fusion reactors. [6, 7, 169–178] In tokamaks, they can be produced in large quantities. They result from the physical erosion (sputtering) of the walls by high flows of energetic particles . In addition, abnormal events such as disruptions, arcs and other instabilities can lead to the melting or the sublimation of parts of the reactor walls [178]. Some of the eroded material contributes to the formation of dust of various sizes and shapes. For sizes ranging from a few micrometres to a few millimetres or more, wall fragments, irregular grains from brittle redeposited layers, chips from thin layers and fibrous particles are observed [175, 179, 180]. For smaller dusts, primary spherical particle (PPs) are observed and grouped into macroscopic agglomerates in which nanotubes have also been observed . These PPs can aggregate to form chains of particles and dense spheres as also seen in plasmas used for materials processing (deposition, etching, etc.) [170, 171]. These PPs are either condensed from the sputtered materials or from multiple collisions between atoms and molecules released from the reactor walls. In particular, in tokamak with graphite walls, radicals from hydrocarbon gases can polymerise through specific chemical pathways to form macromolecular precursors to dusts.

Although not a serious issue on current tokamaks, dust will pose serious problems in the future International Thermonuclear Experimental Reactor (ITER) in which dust production will increase by several orders of magnitude[181]. A significant accumulation of dust can degrade the performance of ITER, increased tritium inventory on the walls (not available for core plasma reactions), lead to production of radioactive (mainly tungsten) and toxic (beryllium) dust, production of hydrogen by reaction with steam in case of loss of coolant event, explosive risk of dust after hydrogen production, contamination of the environment after accidental venting, contamination of core plasma, etc [182].

To limit wall erosion in ITER, two materials were chosen: beryllium for the main wall where particle fluxes are the lowest, tungsten for the divertor where particle fluxes are higher. Tungsten was chosen for its good thermomechanical properties and for its high sputtering threshold by D^+ ions ($\sim$220 eV). The choice of these elements is not without risks: the melting point of beryllium is low ($\sim$1200°C). The injection of tungsten into the core plasma can lead to the extinction of fusion reactions. Although strongly studied until the mid-200s, graphite was abandoned as a tokamak wall material because of its high tritium retention capacity due to its very high reactivity with hydrogen and its isotopes [183] (the physico-chemical erosion of graphite walls leads to co-deposited thin layers, i.e. containing deuterated and tritiated carbon, resulting in a loss of fuel for the core plasma as observed in the JET tokamak) . Dust can thus increase the inventory of (radioactive) tritium on the reactor walls up to the safety limit on hot surfaces in order to avoid the risk of explosion in case of a LOV in particular in the shaded areas (not exposed to the plasma) likely to be exposed to the air for element removal (ITER administrative limits: 11 kg Be and 77 kg W) [182].

The original objective of this research activity was thus to study the formation of tungsten nanoparticles in conditions simulating some aspects of divertor plasmas. These research was included in one of the research axis of the PIIM laboratory (CNRS/Aix-Marseille Université) with which I was affiliated from 2011 to 2018: fusion science and tokamak physics. These

studies rapidly evolved to more fundamental studies on nanoparticle growth dynamics and transport in different kind of laboratory discharges. In Sec. 3.2.2, I present the results on tungsten nanoparticle growth in direct-current (DC) argon discharge. In Sec. 3.2.3, I present the results on the characterisation of a DC magnetron discharge used for the growth of metal nanoparticles. Finally, in Sec. 3.2.4, I present the results on particle growth in highly magnetised radio-frequency discharges.

3.2.2 Nanoparticle growth in direct-current glow discharge

This work was performed in collaboration with Dr C. Arnas group (PIIM laboratory, CNRS, Aix-Marseille Université) in particular, Postoctoral fellow: Dr. Kishor Kumar K. The main objective was to study the synthesis of tungsten (W) nanoparticles by sputtering in a direct current argon glow discharge equipped with a tungsten cathode.

Experimental setup

The system consisted of two parallel electrodes separated by 10 cm and enclosed in two glass half-cylinders. The 10 cm diameter cathode was surrounded by a ceramic support so that only one side was exposed to the plasma. The cathode was facing a grounded stainless steel anode. To facilitate optical diagnostics, the glass half-cylinders were separated by 1 cm gap that faced the vacuum chamber optical ports. A hole in the centre of the anode allows the collection of nanoparticles produced on mirror polished stainless steel samples (see Figure 3.14).

We worked at a (relatively high) constant argon pressure of 60 Pa and a t a fixed current of 40 mA. The power supply adjusted automatically the discharge voltage. Under these conditions, an estimate of the fluxes of fast particles (ions and fast neutral atoms due to charge exchange) was calculated in order to evaluate the sputtering rate. The voltage at the cathode being about -600 V, the flux of particles reaching the cathode was $\Phi_t \sim 7 \cdot 10^{15}$ cm^{-2}/s and the sputtering rate was $\Upsilon \sim 3.8$ %. Thus the flux of W atoms was $\Phi_W \sim 3 \cdot 10^{14}$ cm^{-2}/s. At the cathode exit the average energy of the sputtered atoms was ∼12 eV and the sputtered atoms thermalised with the argon gas background in about ∼1 cm. These conditions were thus favourable to the formation of nanoparticles by homogeneous nucleation from the sputtered atoms.

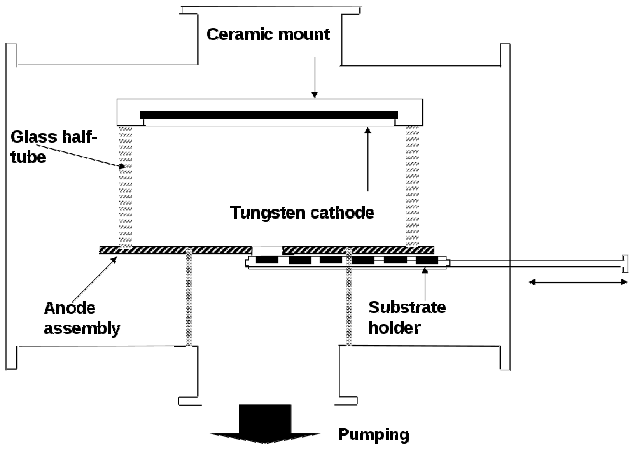

Figure 3.14 – (Reproduced from Ref. [53]) Schematic of the DC glow discharge set-up.

In order to study the evolution of the plasma parameters, optical emission spectroscopy (OES) was performed on different lines: ArI (763.5 nm and 800.6 nm coming from the 4P level), ArII (454.5 nm), WI (498.26 nm), WII (341.66 nm), H_α (646.28 nm). We used two monochromators (Jobin-Yvon HRS, 600 mm focal length and, Acton Spectra Pro 2500i, 500 mm focal length) coupled to photomultiplier tubes (Hamamatsu R3896). Convex lenses and optical

fibres collected the light emitted by the plasma ∼1 cm under the cathode at the start of the negative glow. The evolution of the electron density was measured by microwave interferometry (Miwitron MWI 2650) and the dust collected on the stainless steal sample were analysed by scanning electron microscopy (SEM) and transmission electron microscopy (TEM). More details on the experimental protocol are given in Refs. [53, 55].

Main results

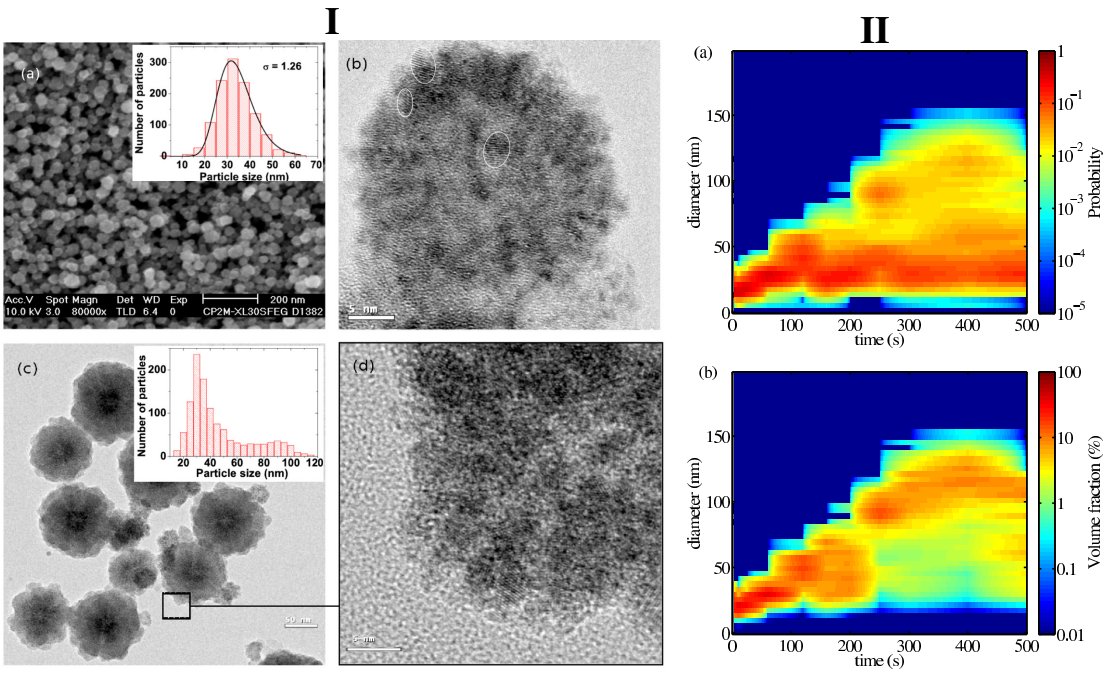

Figure 3.15 – (Reproduced from Ref. [53]) I-(a) Tungsten nanoparticles observed after a 120 s discharge (SEM). Inset: corresponding PSD f itted by a log-normal distribution. (b) HR-TEM image of a ∼30 nm PP obtained after a 60 s discharge: it is an agglomerate of nano-crystallites (2-4 nm) (identified by diffraction fringes, a few are circled). (c) TEM image of particles produced after a 300 s discharge. PPs and larger particles can be seen. The latter appear to be an agglomerate of PPs. The corresponding PSD is shown in the inset. (d) Zoom of the selected edge region of one of the big particles in (c), showing nanocrystallites.. II-(a) Probability of finding a particle of a given diameter at a given time. (b) Fraction of the total particle volume occupied by particles of a given diameter at a given time.

Representative electron microscopy images of nanoparticles produced in the discharge are shown in Fig. 3.15-I. Histograms showing the particle size distribution (PSD) of the collected nanoparticles for different discharge durations are shown on the inset of Figures 3.15-I-(a) and -(c) (for discharge duration of 120 s and 300 s). In Fig. 3.15-I-(b), the structure of a primary particle (PP) of ∼30 nm diameter can bee seen. These PPs are made of ∼2-4 nm nanocrystallites (evidenced by the diffraction fringes on the HR-TEM image). These nanocrystallites are the smallest structures formed but have never been observed individually. For long discharge duration, large particles appearing to be agglomerates of PPs are observed (Fig. 3.15-I-(c)). PSDs can be described accurately by log-normal distributions up to ∼200 s. For longer discharge durations, a second hump corresponding to larger particles appears in the distributions. In Fig. 3.15-II, the evolution of the PSD and o f the volume fraction of the nanoparticles are presented. It can be seen that PPs are present for all plasma durations and are always the most numerous although most of the tungsten (in volume) is found in the large particles for long discharge duration. The appearance of the second bump in the PSD can be related to

the formation of a second generation of nanoparticles in the plasma. More details are given in Ref. [53] (a copy of which can be found at the end of this Section).

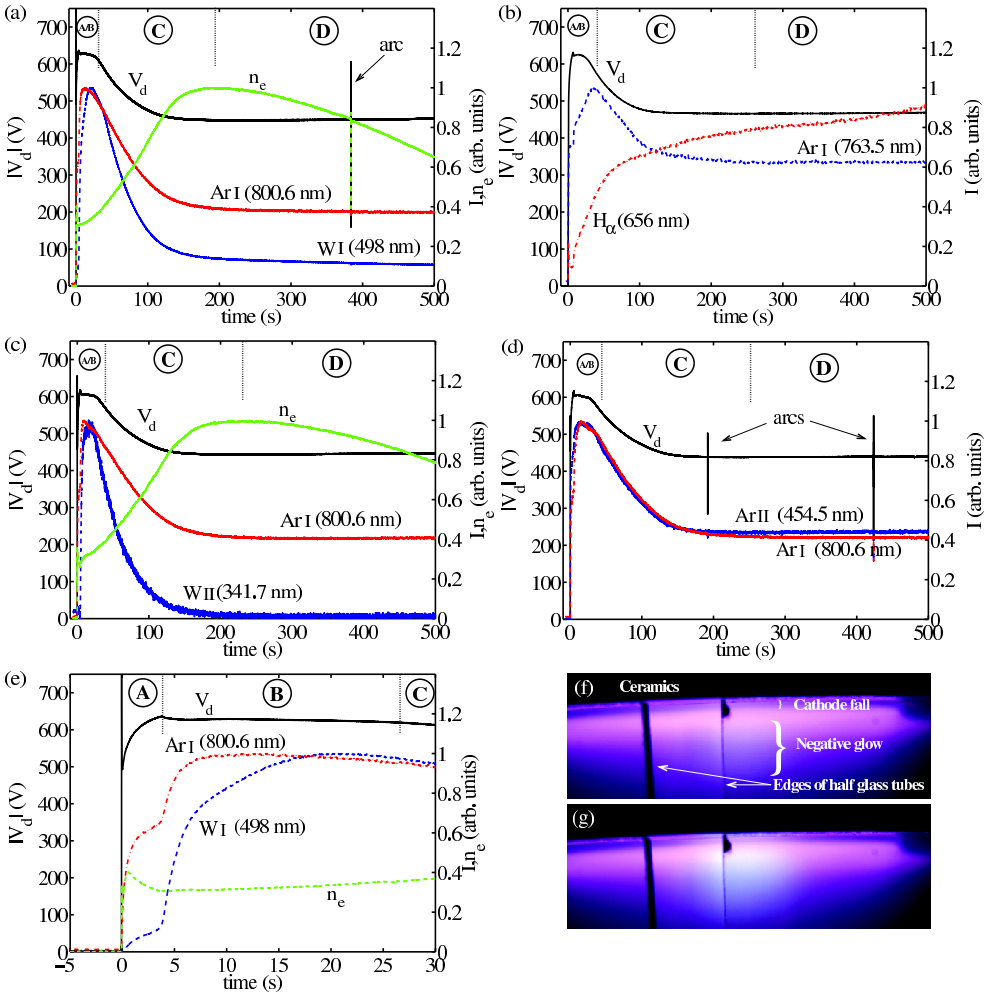

Figure 3.16 – (Reproduced from Ref. [53]) ((a)-(d) Evolution of the cathode voltage V_d and the intensity of emission lines (ArI, ArII, WI, WII, and H_α) as a function of time. V_d is given for reference in each case. The signals are divided into 4 phases: A, B, C, and D. (e) zoom of (a). (f) Photo of the cathode fall and the start of the negative glow at the end of phase A. (g) same as (f) at the beginning of phase (B).

During the formation of the nanoparticles, the discharge voltage, the electron density and the intensity of different emission lines change significantly (see Fig. 3.16). This evolution can be divided into 4 distinct phases:

— Phase A: It corresponds to the first seconds after the ignition of the discharge. With the naked eye, the luminosity under the cathode is uniform and decreases within a few centimetres when moving away from it (see Fig. 3.16(f)). After the breakdown, the absolute value of the discharge voltage $|V_d|$ decreases during ∼70 ms until $|V_d|$ ∼500 V then increases again for 3-4 s until $|V_d|$ ∼650 V. During this time, the intensities of all emission lines increase at different rates. The argon lines increase rapidly for a few hundred ms and at a slower pace thereafter. The W lines increase slowly during the entire duration of this phase. The electron density which is relatively high after breakdown decreases to its lowest measured value during this phase.

— Phase B: At the beginning of this phase, the discharge voltage decreases by ∼15 V in 0.5 s. Visually, this corresponds to the appearance of an intense blue glow at the center

of the cathode (Fig. 3.16 (g)). $|V_d|$ then remains constant for about 30 seconds. During this time the blue glow spreads slowly over the rest of the cathode surface. At the end of this phase, $|V_d|$ starts to decrease rapidly. OES shows that at the beginning of the phase, the intensities all emission lines are rapid growing (Fig. 3.16 (e)). This increase is the most important for WI lines. All line intensities reach a maximum during this phase. The electron density increases during the whole duration of this phase.

— Phase C: $|V_d|$ decreases continuously during 200-250 s (ΔV_d ∼150 V) until the end of phase C. At this moment, the blue glow has spread over the entire cathode surface. OES shows a decrease of the intensity of every lines. Argon lines reach their minimum at the end of this phase and WII lines are no longer detectable. Electron density continues to increase and reaches a maximum at the end of the phase.

— Phase D: V_d increases slowly as well as ArI and ArII lines. The intensity of WI continues to decrease. The electron density also decreases.

The results obtained with tungsten are very different from those obtained by C. Arnas on the production of nanoparticles by sputtering a graphite cathode [52, 53, 55]. The main differences are:

— In the case of a graphite cathode, the evolution of the discharge voltage and the intensity of the emission lines can be directly related to the growth kinetics of the nanoparticles and the effects of their electric charge (electrostatic coupling)). More details in the references [52, 55]

— Unlike carbon, the growth of the first generation of W nanoparticles does not saturate. More details in references [53, 55]

Some of the observed differences can be explained by the specificities of tungsten. Here is a summary of the detailed explanation given in Reference [53]:

— Tungsten oxide has a lower secondary electron emission coefficient than pure tungsten for ions striking the cathode with kinetic energies less than 100 eV [184, 185]. However, at a pressure of 60 Pa, the average energy of ions striking the cathode is 50-60 eV. Moreover, the sputtering rate of tungsten is higher than that of its oxide [186, 187]. The base vacuum of our vacuum chamber being around 10^{-6} mbar, an oxide layer is rapidly formed between two discharges. During phase A, this oxide layer is sputtered away and as soon as pure tungsten is exposed the secondary emission and sputtering rate increases explaining the $|V_d|$ drop and the increase of all other signals at the beginning of phase B.

— Tungsten has a lower ionisation energy than argon (7.86 eV and 15.76 eV, respectively). Tungsten ionization energy is in addition lower than the excitation energy of argon to metastable levels (11.56 eV and 13.15 eV). A part of the injected tungsten is thus ionised, explaining the increase of the WII lines intensities and the increase of the electron density.

— During phase C, the modifications of the surface state still play an important role but the presence of the nanoparticles increasingly influences the plasma, explaining the slower pace of evolution of all signals.

— In Phase D, nanoparticles have a major influence on the plasma and the discharge parameters evolve as expected (i.e. as in graphite cathode discharges). As the particles capture more and more electrons, $|V_d|$ increases to maintain ionisation, the electron density decreases and the intensity of the argon lines increases following $|V_d|$ and indicating a probable increase of the electron temperature.

The main assumption made so far when growing nanoparticles in a laboratory discharge is that they remain trapped in the discharge volume for the duration of the plasma until they are to big and fall due to gravity or their number density is too high so that repulsive forces

overcome confining forces (as it is observed in cc-rf discharges [15, 110, 112]). Consequently, the dynamics of the NP cloud in the DC discharge needed to be investigated in order to confirm or not this assumption. For this purpose, a 2 cm vertical laser sheet was installed on the experimental set-up. Its vertical position between the two electrodes could be adjusted. The scattered light was recorded at 90^{irc} with a CCD camera (Basler ACE acA1300-60gm) operating at 1 frame per second with an integration time of 0.5 s. This low frame rate and long integration time were necessary to detect the weak signal due to the laser light scattered by the nanoparticles. Moreover, in order to verify whether the nanoparticles remained trapped throughout the discharge, stainless steel samples positioned at the centre of the anode were now exposed to the plasma for selected period of times after plasma ignition and then analysed by electron microscopy.

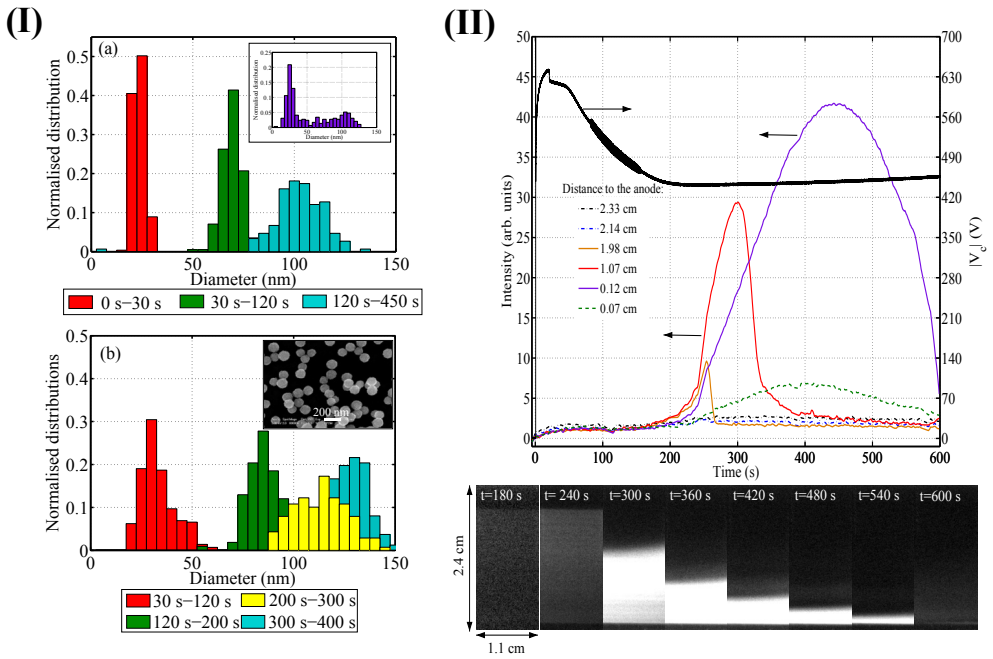

Figure 3.17 – (Reproduced from Ref. [54]) (I) Normalised size histograms of the nanoparticles collected on samples exposed to the plasma at different times after discharge ignition. (a) and (b) correspond to two different experiments. In the inset of (a), the normalized size distribution of particles collected at the end of a 500 s discharge is shown. In the inset of (b): SEM image of nanoparticles collected on a sample exposed to the plasma from 200 s to 300 s after ignition.(II) Top: Evolutions of cathode voltage V_{d} (right axis) and the scattered light intensity recorded by the camera at different distances from the anode (left axis). The two highest positions are outside the laser light sheet and serve as reference for the residual plasma light. The lowest position is the light recorded in the anode sheath. Bottom: Snapshots from the video (the laser light sheet was grazing the anode.

In Fig.3.17-I, the PSDs of the particles formed in two different experiments are presented. It can be seen that at all exposure times, nanoparticles were collected on the samples demonstrating that the nanoparticles are in fact not confined in the DC glow discharge: the later the sample were exposed after plasma ignition, the larger the collected nanoparticles were. Furthermore, an important difference with the previously discussed results is that the distributions were monomodal even for long times after plasma ignition. However, the PSD of the nanoparticles collected on samples exposed to the plasma when the power supply was turned off (in the inset of Figure 3.17-I-(a)) is similar to the results obtained in the previous studies with the observation of a PPs peak at ∼30nm [53].

In figure 3.17-II, the evolution of intensity of the scattered light recorded at different posi-

tions above the anode is presented. At the bottom of the figure are snapshots from the video. It can be seen that the NP cloud was detected after about 150 s. It is initially homogeneous and then compressed towards the anode. After a few hundred seconds, a new dim cloud of nanoparticles was visible above the main (original) cloud and must certainly correspond to the PPs collected on the sample when the discharge is turned off.

The deconfinement of the particles can be explained by the thermophoresis force and gravity which are only partially compensated by the ion drag force and the electrostatic forces at the anode sheath of the DC discharge. Indeed, due to a relatively low electron temperature (~ 0.1 eV) [188] and a weak electric field in the anode sheath (1–20 V/cm at the boundary between the negative glow and the anode sheath) [189], the electrostatic forces cannot compensate for the other forces for particles larger than a few tens of nanometres. The observation of a PPs peak at ~30nm can be explained by the constant nucleation and growth of nanoparticles in the upper parts of the discharge (on the cathode side at the beginning of the negative glow) where favourable conditions for nanoparticle formation prevail almost permanently. More details are can be found in Ref.[54] (a copy of which can be found at the end of this Section).

In order to obtain more information on the evolution of the size and density of nanoparticles in the plasma, a light extinction spectrometry (LES) diagnostics was added to the experimental set-up in addition to the light-light scattering. The experiments were perform in collaboration with Dr F. Onofri and Dr S. Barbosa from IUSTI laboratory (CNRS/Aix-Marseille Université).

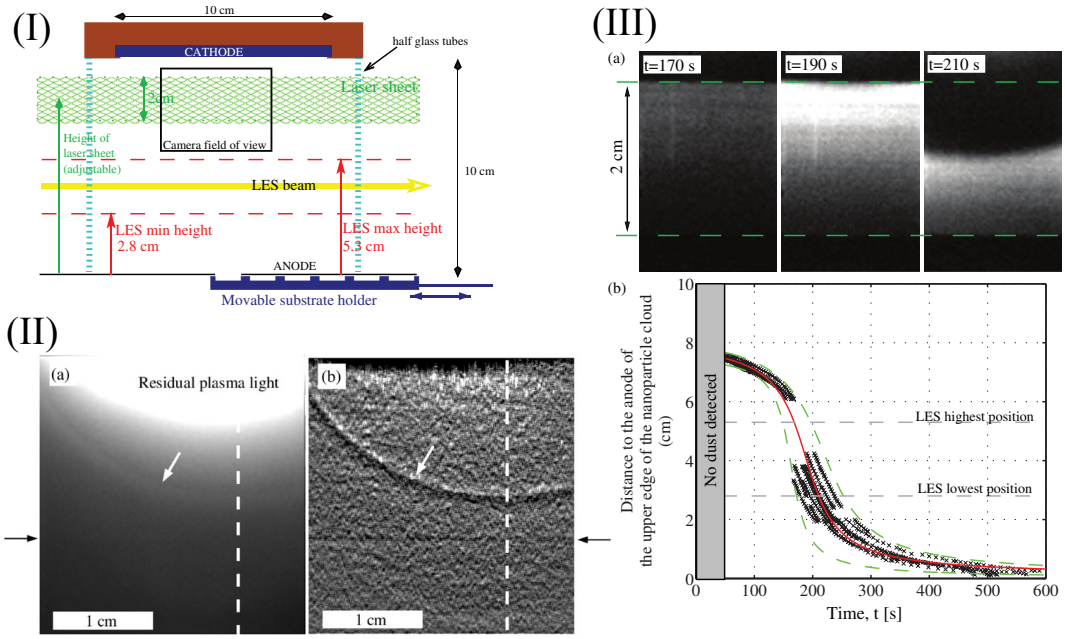

Figure 3.18 – (Reproduced from Ref. [56]) (I) Schematic of the modified experimental setup. (II) Typical snapshot of the scattered laser-light 45 s after plasma ignition: (a) raw image, (b) same as (a) with an edge detection filter applied to the image. The horizontal arrows show the position of the lower edge of the laser-light sheet positioned 2 cm below the cathode. The white oblique arrow shows the upper edge of the nanoparticle cloud. The vertical dotted line indicates the position of the central axis of the discharge. (III) (a) Snapshots of the scattered laser light at different times after plasma ignition. The dotted green lines show the positions of the lower and upper edges of the laser-light sheet positioned 3.4 cm above the anode. (b) Distance of the upper edge of the nanoparticle cloud (1st generation) to the anode on the central axis of the discharge as a function of time (data extracted from the laser light scattering results, accumulated over 21 experiments). The red line represents the mean position and the dotted green lines the error bar at 3σ.

LES consists in measuring the extinction at all wavelengths of a white light beam crossing the discharge from one side to the other (see diagram in figure reffig:scatteringLES-I). The transmitance T_{lambda} is a decreasing exponential function whose argument is the product of the length of the line of sight L (i.e. the width of the NP cloud) with the turbidity τ of the NP cloud. The latter is the product of the nanoparticle number concentration N with the average extinction cross section C_{ext} of the nanoparticles illuminated by the probe light beam. C_{ext} is an integral quantity that depends on the effective cross section of each nanoparticle (shape, size, refractive index, etc) and its statistical weight in the cloud. The transmission equation is often written in its discrete and linearized form:

$$\ln(T(\lambda_i)) = -NL \sum_{j=1}^{M_D} C_{ij} n_j \tag{3.59}$$

where C_{ij} is the extinction cross section weighted by the statistical weight of nanoparticles belonging to the size class j (with $j = 1, 2, \ldots M_D$ where M_D is the maximum size taken into account) and for wavelengths λ_i (with $i = 1, 2, \ldots K_i$, où K_i is the maximum number of wavelengths considered), n_j is the normalised number density associated with the nanoparticle size class centred on diameter D_j. In this study, compact tungsten were assumed for the inversion of the transmittance equation. The details of the method as well as the justification of our nanoparticle model (compact sphere) are discussed in Refs. [56, 57]. (a copy of Ref. [56] can be found at the end of this section).

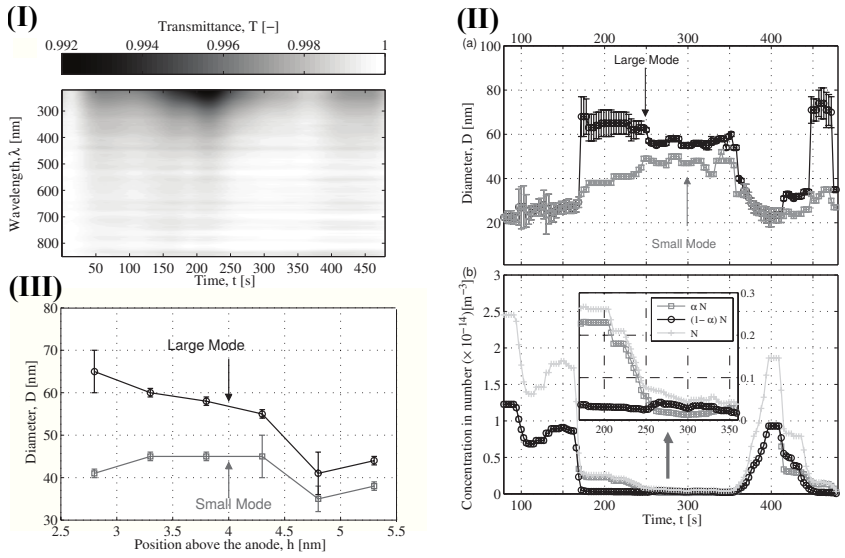

Figure 3.19 – (Reproduced from Ref. [56]) (I) Raw transmittance spectrum. (II) (a) Temporal evolution of mean diameters (represented by squares or by circles) and the associated standard-deviations (represented by bars) measured by LES at a height $h = 2.8$ cm from the anode. A bimodal PSD is detected, its large mode is represented by the circle line, while its small mode is represented by the square line. (b) Temporal evolution of N, as well as αN and $(1 - \alpha)N$ associated with the small and large modes of the PSD, respectively (α is the fraction of small particles). (III) Evolution of the particle size reached at the minima in transmittance.

Thanks to LES, a detailed time-resolved study of the tungsten nanoparticle cloud growing in a DC discharge was performed. Here is a summary of the main results:

— The shape and composition of the nanoparticles were studied ex-situ by electron microscopy (scanning, transmission, wide angle transmission dark field imaging, Raman spectroscopy). The previous results were confirmed: NPs are compact spheres of tung-

sten nanocrystallites. This allowed the use of the refractive index of pure tungsten and LES data w ere analysed assuming compact spheres.

— Laser light scattering from a vertical laser sheet positioned at different heights in the inter-electrode gap showed that the nanoparticle cloud is pushed towards the edges of the discharge and the anode (see figures 3.18-II and 3.18-III), the emptied area becoming favourable to the nucleation of new nanoparticles.

— The evolution of the PSD and the number density N were studied in situ by LES. A transmittance spectrum and associated inversion results are presented in Figures 3.19-I and 3.19-II. By combining the results of measurements at different positions in the inter-electrode space, LES revealed a phase of nanoparticle growth by agglomeration, followed by the appearance of a second NP generation. The agglomeration phase was identified by a sudden change of the PSD from monomodal to bi-modal (figure 3.19-II at $t \sim 180$ s) followed by a gradual disappearance of the smaller NPs. The results also confirmed that the second generation of nanoparticles appeared in the space freed by the first generation. At the transmittance minimum, while the PSD was bimodal at all the positions studied, the average size of NPs belonging to the large mode of the PSD increased when a pproaching the anode. On the contrary, the average size of the NPs belonging to the small mode remained approximately constant (see figure 3.19-III). These results suggest that agglomeration is triggered when the larger nanoparticles pass through a cloud of smaller nanoparticles. NP thus grow by agglomeration until they reach the anode. The largest particles are thus agglomerates of small particles of $\sim$35 nm. This result is compatible with our previous results obtained by electron microscopy measurements on particles collected at the centre of the anode [53–55] and discussed at the beginning of this section.

The LES diagnostics as well as the results obtained are discussed in great details in the References [56, 57].

In this subsection, I have summarised the main results from tungsten NP growth investigation in a dc argon glow discharge [53–57]. It was shown that the NP growth and transport is very specific to the cathode material and that the cloud of growing NP exhibits a very complex dynamics.

3.2.3 Characterisation of a direct-current planar magnetron discharge used for nanoparticle growth

Magnetron discharges have been used since many decades for thin film deposition [190]. In a planar magnetron discharge, permanent magnets positioned behind the cathode create permanent magnetic fields used to trap electrons near the cathode region. It allows plasma production at relatively low pressures [191, 192] and favours cathode sputtering by energetic ions accelerated in the cathode sheath[193]. In magnetron device, inert gases such as argon (Ar) or krypton (Kr) are usually used for the deposition of metallic coating (copper, aluminium, tungsten, etc) [190, 194–197].

Since the mid-1990's, (RF and DC) magnetron sputtering is used in gas aggregation sources (MS-GAS) in order to produce metal NP [198–206]. MS-GAS usually consists of a high-pressure chamber where the magnetron discharge is located connected to a low pressure expansion chamber where the beam of produced NP can be filtered and collected. NP are indeed formed in the high-pressure chamber from sputtered cathode atoms. However, even though the use of MS-GAS is relatively standard to produce NP of many different materials, very few studies are devoted to the correlation of the parameters of the magnetron discharge with NP growth dynamics [204, 207, 208]. The formation of NP in a DC planar magnetron discharge in argon

occurs at relatively high pressures (10s of Pa) [209, 210]. In particular, the formation and transport of tungsten NP in high pressure DC planar magnetron argon discharges have been the subject of recent studies performed by C. Arnas at Aix-Marseille University (in which I am an active collaborator) [22, 73, 211, 212].

The main goal of these studies was to complement our previous results in DC discharge in which we have shown that dusts can be easily created by the sputtering of tungsten cathode and that NP growth and dynamics is very sensitive to the discharge conditions (see Sec. 3.2.2). The use of DC magnetron discharge allows a considerable increase of the plasma density and the amount of sputtered material (conditions which are more relevant for tokamak edge plasmas). Tungsten and aluminium targets were used and it was found again that it is relatively easy to grow metal NPs [211]. Details studies on NP growth in a DC magnetron discharge using a tungsten cathode have shown that the produced tungsten NP are core-shell type (monocrystal core mainly in the metastable beta-tungsten phase surrounded by a tungsten oxide shell) [22]. The 2D mapping of the magnetic field, electron density, electron temperature and plasma potential have revealed the correlation between the magnetic field and the existence of a plasma potential well able to trap growing NP [212]. In a DC magneton discharge, NP transport is due to electric, thermophoretic and ion drag forces which depend on NP sizes and their localisation in the discharge which can explain the observed size segregation in the NP deposits on the device walls [73]. Nevertheless, the high pressure regime of DC magnetron plasmas used for NP production is still poorly understood.

In this Section, I will concentrate on the dependence of the plasma parameters on discharge conditions in a conventional DC magnetron. The section is therefore a summary of Ref.[213] (a copy of which can be found at the end of this section). Here, contrary to Refs. [22, 73, 212], an aluminium (Al) cathode was used. The background gas was again argon. The dependence of the plasma parameters on the argon pressure (p_{Ar}) and the discharge current (I_{d}) was studied. The current–voltage relations of the magnetron plasma were established and optical emission spectroscopy (OES) measurements on Ar I and Al I lines were made. Finally, the different plasma parameters (n_{e}, T_{e} and plasma potential V_p) were also measured using a cylindrical Langmuir probe. A collisional radiative model including self-absorption corrections was used to find the argon metastable atom density, aluminium atom density, electron temperature T_{e} and the electron density n_{e} and compared to probe measurements. Note that this studies was performed in collaboration with Dr Mitic (Justus-Liebig-University, Giessen, Germany) and as also involved PhD student, Mr J. Moreno.

Experimental setup

A planar unbalanced DC magnetron source (mcse-ROBEKO) was used for the experiments. An aluminium cathode with a diameter of 3 inches was used and was facing a grounded stainless-steel anode positioned 10 cm below. A grounded guard-ring of 2 cm width and 1 cm height and ∼7.4 cm inner diameter surrounded the cathode assembly [see Fig.3.20-(I)]. Two glass half-cylinders separated by a a 1 cm gap were used to confine the plasma (and the produced NPs). The gap was necessary to perform optical emission spectroscopy (OES) and Langmuir probe measurements. The discharge assembly was installed in the same stainless steel cylindrical vacuum chamber described in Sec.3.2.2. More details about the experimental set-up can be found in Refs. [22, 73, 212, 213].

An argon pressure between 10 Pa and 40 Pa (constant flow of 5 sccm) was set during the experiments. A current-regulated DC power supply (Glassman HV, 1 A–1 kV) was used to bias the cathode and maintain the discharge current at a constant value (from 100 mA to 500 mA). The cathode was actively cooled with a flow of $\sim$ 1 L/min of water at room temperature. Before each series of experiments, the cathode was cleaned by of low pressure ($\sim 10^{-1}$ Pa),

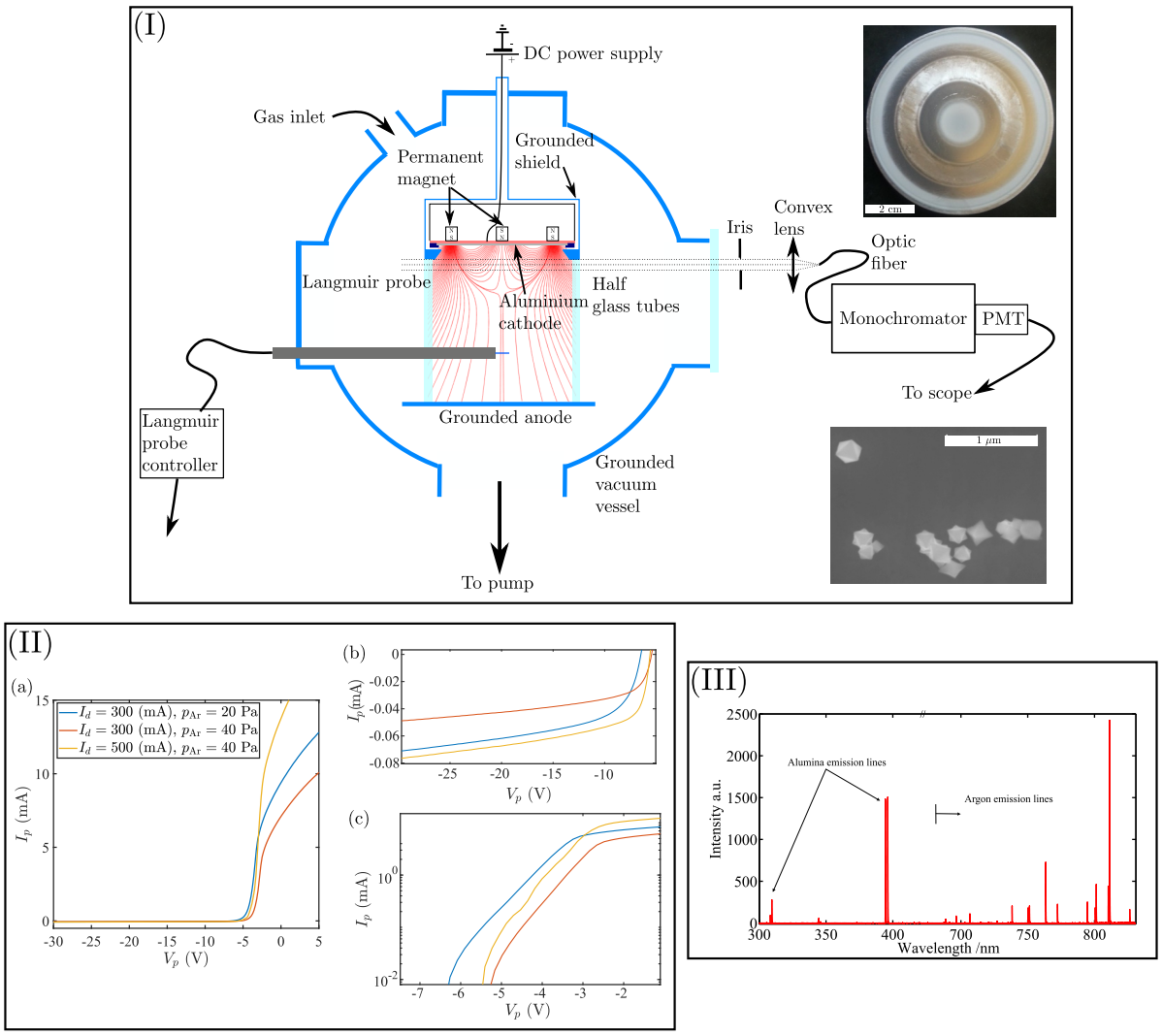

Figure 3.20 – (Reproduced from Ref. [213]) (I) Schematic of the experimental setup. The red lines depict the magnetic field lines. The top right inset shows the state of aluminium cathode after the experiments. Note the circular sputtering track. The bottom right inset shows a scanning electron microscope image of aluminium nanoparticle grown in a plasma with $I_{\mathrm{d}} = 300$ mA at $p_{\mathrm{Ar}} = 30$ Pa for a plasma duration of 60 s. (II) Langmuir probe IV curves (a) Raw curves for different discharge parameters. (b) Zoom on the ion part. (c) Zoom on the transition part in semi-log scale. (III) Example of measured optical emission spectrum

high current (>0.5 A) plasma pulses. Under the chosen operating conditions, the cathode was sputtered and aluminium nanoparticles could be grown [see bottom right inset of Fig.3.20-(I)]. Each experimental measurements were made after the discharge had reached a steady state (constant V_{c} and optical emission intensities) in order to minimize the effect of changing cathode surface conditions and the effect of growing nanoparticles in the plasma [53, 214–216].

A cylindrical Langmuir probe (tungsten filament, 300 μm in diameter, 11.28 mm long) was used to measured plasma parameters ∼3 cm above the anode on the discharge axis (see Fig. 3.27) (region where the magnetic field is sufficiently low to consider unmagnetised electrons and where the magnetic field lines are perpendicular to the probe axis, allowing us to use standard probe analysis). The quite large distance to the cathode (∼ 7 cm) allowed measurements in a region where the expected NP number density is low [208] (additional laser light scattering experiments seemed to indicate that there were indeed no trapped NP in the probed region) and where the aluminium coating of the probe assembly develops slowly enough to obtain

reproducible probe characteristics for the duration of the experiment (each measurement was repeated 3 times to check reproducibility and averaged out to obtain the $I_p - V_p$ curves). The probe current-voltage (IV) characteristics was obtained by ramping the probe voltage V_p from -35 V to +10 V by step of 0.33 V. Depending on the discharge parameters and probe bias, the probe current I_p varied from ~ -100 μA to $\sim +35$ mA. Raw IV characteristics are shown in Fig.3.20-(II).

OES studies of the discharge plasma were carried out using a monochromator (Acton Spectra Pro 2500i, 500 mm focal length) coupled to a photomultiplier tube (Hamamatsu R3896). Convex lenses and an optic fibre were used to collect the emitted plasma radiation, ~1.5 cm below the cathode where the line of sight crosses the high density plasma ring below the cathode (see Fig.3.20I). A study with a tungsten cathode showed that nanoparticles might be trapped on the edge of the last magnetic arch (~4 cm below the cathode) [212]. Consequently the line of sight used for OES measurements can be considered mostly free of large nanoparticles. However the presence of transiting small NP pushed by thermophoresis and the electric force is very likely according to the deposit seen on the different surface [73]. In order to the relative intensities of each spectral line, the OES spectra were calibrated in intensity using a spectral radiance calibrated SphereOptics SR-3A integration sphere placed in front of the light collection system (glass window, convex lenses, optic fibre, monochromator, and photomultiplier tube). An example spectrum is shown in Fig.3.20-(III).

Main results

The measured current-voltage relation of the planar magnetron discharge measured for 4 argon pressures and for currents varying between 100 mA and 600 mA is shown in Fig. 3.21. Being strongly dependant on the background gas pressure and the dynamics of the sputtered cathode atoms, it can provide indirect information about the sputtering rate in the magnetron [217]. However, magnetron current-voltage relationships also depend on the gas-target combination, the secondary electron emission rate due to ion impact, the design of the magnetron, the magnetic field strength, and other experimental parameters [218]. As can be seen, the

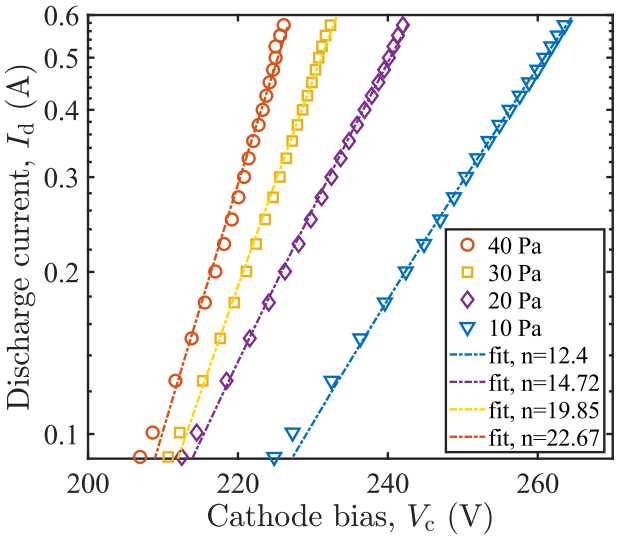

Figure 3.21 – (Reproduced from Ref. [213]) Discharge current I_d as a function of the cathode voltage V_c for different argon pressures. Each $I_d - V_c$ curve is fitted by a power law curve of the form $I_d = k \cdot V_c^n$. The value of n obtained for each pressure is given in the inset.

measured $I_d - V_c$ characteristics obey the relation:

$$I_d = k \cdot V_c^n \tag{3.60}$$

When increasing the argon pressure from 10 Pa to 40 Pa, the exponent n increases from $n \simeq 12$ to $n \simeq 23$. According to Ref. [191], it means that electron trapping in the plasma is more efficient at high pressures. Since collisions with the neutral background are more frequent at high pressures, the secondary electrons emitted by the cathode due to ion and fast neutral bombardment with a non-zero energy are less likely to be recaptured by the cathode due to gyration around the magnetic field lines [219, 220]

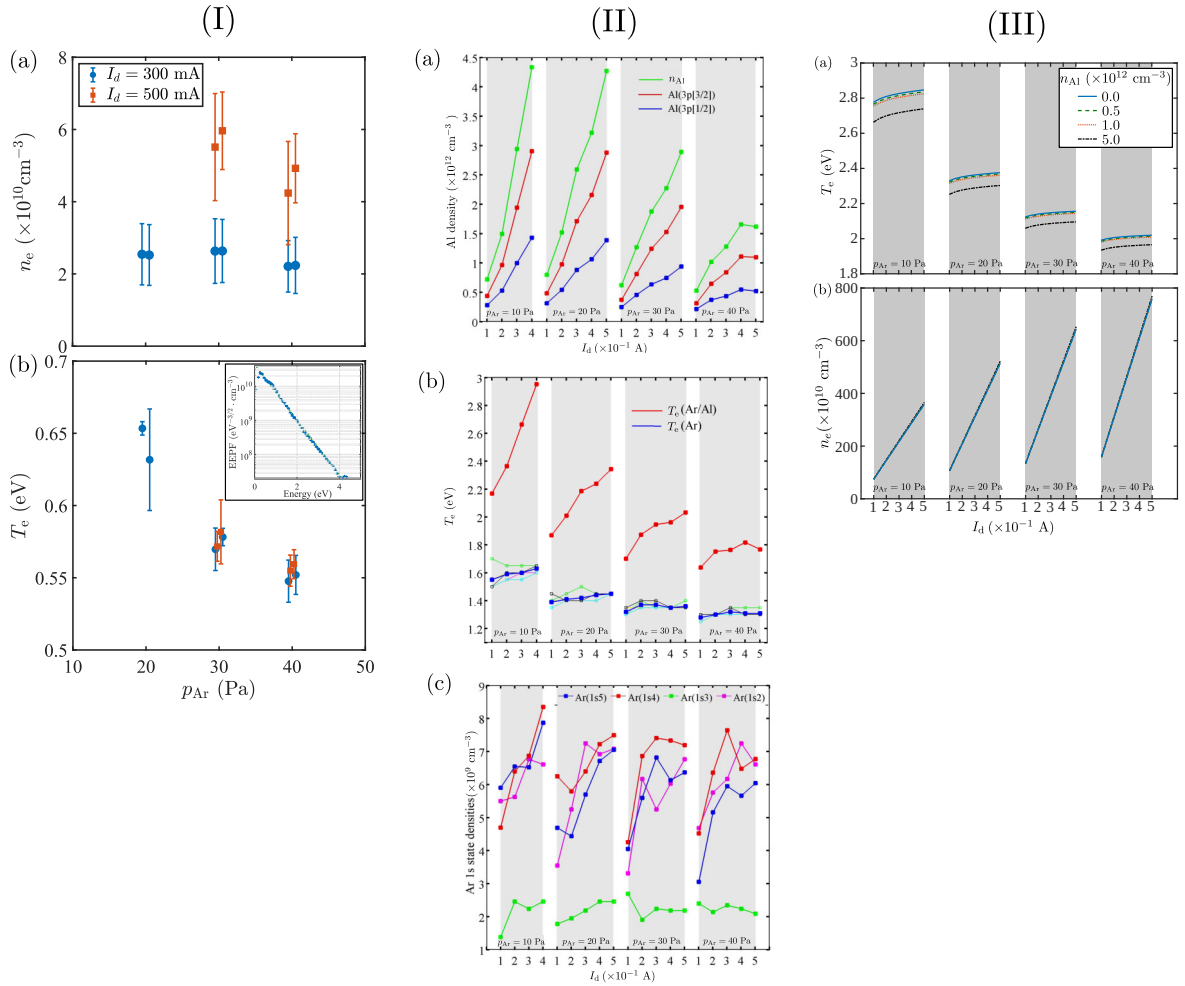

Figure 3.22 – (Reproduce from Ref. [213]) Evaluated densities of Ar 1s states

The plasma was also characterised by Langmuir probe measurements. However, due to the high sputtering rate of aluminium by argon which resulted in a fast coating of the probe making the measurements unreliable after only a few tens of seconds of exposure of the probe tip to the plasma, the measurements were therefore limited to a reduced set of currents and pressures ($I_\mathrm{d} = 300$ mA and $I_\mathrm{d} = 500$ mA for pressures between 20 Pa and 40 Pa).

In Fig. 3.20-(II), raw Langmuir probe IV characteristics are shown for different conditions. Analysis indicated quasi-Maxwellian electron energy distribution functions [see Fig. Fig. 3.20-(II-c) and inset of Fig. 3.22-(I-b)]. Using both the Langmuir analysis [221] and Druyvesteyn analysis [222], n_e and T_e were extracted. The two methods gave similar results and the average values of n_e and T_e are shown in Fig. 3.22-(I). Since the measurements were made far from where the electrons are confined by the magnetic field, the reported n_e values are at least one to two orders of magnitude lower than that in the magnetic arch above the cathode surface. In addition, the electrons are colder by about ∼1 eV [204, 212]. Consequently only the trends can be here analysed.

As expected, the highest plasma density are obtained for the highest currents (Fig. 3.22-(I-a)).

The values of electron density ($n_e \sim 2.5 \cdot 10^{10}$ cm^{-3} at $I_d = 300$ mA and $n_e \sim 5 \cdot 10^{10}$ cm^{-3} at $I_d = 500$ mA) are in agreement with those observed in experiments using a tungsten cathode [212] or using a titanium cathode [204] with similar discharge currents and background gas pressures. The plasma density is only weakly dependant on gas pressure (a small decrease is even observed when increasing the background gas pressure at constant discharge current). Increasing the pressure results in a decrease of the electron temperature [from 0.65 eV down to 0.55 eV, see Fig. 3.22-(I-b)]. On the contrary, electron temperature is almost independent of the discharge current. However, the measured electron temperatures are lower than those measured in the same setup using a tungsten cathode [22, 212] but close to the one measured under similar experimental conditions with a titanium cathode [204].

Optical emission spectra (from 300 to 830 nm) were also used to evaluate the plasma parameters as a function of the argon pressure and the discharge current. The spectra consist of a set of most prominent argon lines in the red and near infra-red range as well as a few strong Al transition lines close to the UV range. The spectra were analysed by Dr Mitic (Justus-Liebig-University, Giessen, Germany) using a collisional radiative (CR) model based on his previous work [223, 224]: the argon spectra were first analysed using the line branching method in order to estimate the argon 1s state densities by comparing measured intensities of lines originating from the same excited level, to the theoretically estimated ratios (ratios of the Einstein coefficients for spontaneous emission). Self-absorption mechanism could be included [225] depending on the densities of the lower state of the considered transitions (in this case two sets of lines transitioning to the same two lower levels (e.g. Ar(1s4) and Ar(1s5)) lead to the evaluation of the lower state densities). The evaluated Ar(1s) states densities were further used as an input parameter in the rate balance equations describing populations of Ar(2p) states. Then, steady state solutions of the rate balance equations, for different Ar(2p) levels, were further used to describe emitted radiation including the radiation trapping effects (self-absorption). The resulting modelled spectra could be calculated for different electron temperatures and compared with the measured spectra until the best fit was found. The line branching method was also used for the characterisation of the aluminium-containing plasma by comparing the intensities of emission lines terminating on the ground states (Al(3p[1/2]) and Al(3p[3/2]) multiplets) (hybrid Al/Ar CR model). It provided an estimation of the Al atom density in the plasma. While the structure and the energy of the argon levels and the associated CR relations are well know, only partial information is available for the Al energy levels and the associated radiative coupling. The results obtained from the Al/Ar CR model are therefore not as precise as the result obtained by the Ar CR model (strictly speaking only valid for pure Ar plasmas). All the details concerning the CR models and the associated data analysis can be found in Refs. [213, 223, 224].

The results obtained by OES and CR modelling analysis are shown in Fig. 3.22-(II). The overall trends are more or less similar to the Langmuir probe results (highest plasma density obtained for the highest currents and high background gas pressure results in low electron temperature). However, the results obtained by the different methods and techniques should be carefully discussed. Indeed, the strong spatial inhomogeneity of the DC planar magnetron discharge and the modification of the plasma glow due to changes of pressure and power must be taken into account. Thus, Langmuir probe measurements taken further away from the cathode provide values characteristic of the positive column of a DC magnetron discharge, while the OES measurements closer to the cathode characterise the more energetic high-density plasma ring confined by the magnetic arch. Below are the similarities and differences:

— At fixed current discharge current I_d, a background gas pressure p_{Ar} increase leads to an electron temperature decrease. No clear trend for the electron density is observed: a small decrease of the electron density is observed with Langmuir probe measurements when increasing the pressure while OES measurements analysed with the Ar CR model

favour a slight increase up to 30 Pa. Above 30 Pa, the trend depends on I_d. The OES analysis using the hybrid Ar/Al CRM tend to favour a steady electron density increase. Since Langmuir probe measurement were made relatively far away from the "active" plasma ring, they lead to much lower values of T_e than OES measurements ($T_e \sim 0.60 \pm 0.05$ eV compared to $T_e \sim 1.5 \pm 0.2$ eV for OES with Ar CRM). Similar experiments performed with a tungsten cathode reported a decrease of T_e on the discharge axis when moving away from the cathode [212], explaining the difference in the reported values. Nevertheless note that the reported T_e is slightly smaller than T_e measured at the same position when using a tungsten cathode ($T_e \sim 0.6$ eV for Al and $T_e \sim 1$ eV for W for $I_d = 300$ mA and $p_{Ar} = 30$ Pa [212]), and close to T_e measured in the plasma of the condensation chamber of a MS-GAS ($T_e \simeq 0.5$ eV using a titanium cathode, $I_d = 300$ mA and $p_{Ar} = 34.5$ Pa [204]). The measured n_e are in agreement with literature data [204, 212] and show only a slight dependence to the background gas pressure.
OES measurements were performed just below the cathode (line of sight going through the high density plasma ring) unsurprisingly lead to higher T_e but showed the same trend as the Langmuir probe measurements. Using the Ar CRM, T_e decreased from $T_e \simeq 1.6$ eV at $p_{Ar} = 10$ Pa to $T_e \simeq 1.3$ eV at $p_{Ar} = 40$ Pa In addition, T_e showed little sensitivity to I_d (only a small increase of T_e is observed). The reported T_e T_e is in agreement with literature data for the electron temperature in the plasma ring of the condensation chamber of a MS-GAS [207]. The simultaneous use of aluminium and argon lines (hybrid A/Ar CRM) lead to higher T_e. However the pressure trend did not change. Not that with the Ar/Ar CRM, the electron temperature reacts strongly to changes of the discharge current, especially at the lowest investigated pressure. Both CRM have drawbacks that could explain the observed T_e discrepancies. Due to the low density of Ar(1s) states, the excitation from Ar ground state by energetic electrons is the dominant process and secondary excitation are negligible. The method is thus impervious to low energy electrons [224, 226] which results in large T_e uncertainties. Relative changes of electron density were estimated using the evaluated electron temperatures in order to obtain the overall response of the discharge to variations of pressure and current.

— As expected, at fixed p_{Ar}, an increase of I_d leads to an increase of n_e while T_e is marginally affected. Langmuir probe measurements (on the discharge axis and way form the high density plasma confined near the cathode) showed density on the order of $n_e \sim 10^{10}$ cm^{-3} (comparable to literature data [204, 212]). The density of the dense plasma ring just below the cathode is one to two orders of magnitude higher [204, 212].
OES studies (using Ar CRM) show a linear increase of the relative plasma density with I_d. The hybrid Ar/Al CRM did not lead to a linear increase of n_e at low pressure. The differences in T_e and n_e obtained with the Ar CRM and the hybrid Al/Ar CRM can be explained by the fact that the hybrid Ar/Al CRM takes into account low energy electrons since the excitation of Al states is possible for electron energies as low as ~ 3 eV. However the knowledge of Al collisional-radiative coupling constants and the excitation processes cross-sections is quite limited and only a basic corona model was thus used for the modelling of the Al excited state. Consequently, in case of pure Ar CRM, changes of the discharge current is mostly reflected in electron density variations while in the hybrid Al/Ar CRM T_e is more sensitive to I_d. This discrepancy is most pronounced at low pressure.

— In addition to T_e and n_e, OES studies give access to the densities of the argon resonant states ($1s_2$, $1s_4$) and metastable states ($1s_3$, $1s_5$) . The $1s_3$ density is found to be almost insensitive to I_d and p_{Ar}. However, at low pressure (10 Pa and 20 Pa), an increase of I_d tends to increase the $1s_3$ density. The densities of all other states increase of with increasing current and slightly decrease when increasing pressure at fixed I_d (particularly

visible for the $1s_5$ metastable state). Overall Ar(1s) state densities are much lower than the neutral Ar density making excitation from ground state the dominant process. As previously stated, under such conditions the estimation of T_e based on the line ratio is not very accurate and predominantly accounts for high energy electrons [224]. Therefore T_e can be systematically over or under estimated due to experimental errors.
T_e estimated using the hybrid Al/Ar CRM is directly coupled to the aluminium atom density through excitation processes and self-absorption of Al emission lines (strong in our experimental conditions). The resulting aluminium atom densities were thus estimated $\sim 10^{11}-10^{12}$ cm^{-3}. This results is additionally justified considering that the line branching ratio of the Al(394)/Al(396) lines imposes a lower limit on the Al atom density of $\sim 5 \times 10^{10}$ cm^{-3}. The recovered Al densities reported in our experiment are slightly higher than the ones reported in Ref. [227] (experiments at much lower pressures) and close to the values reported for aluminium or titanium sputtering of under similar conditions [228, 229].

To understand the influence of discharge conditions and the presence of aluminium atoms on plasma parameters, a simple global particle and power balance model based on the methodology found in Refs. [222, 227] was developed. As in Ref. [227], the planar magnetron plasma is reduced to a homogeneous half torus located above the cathode racetrack. The model only takes into account the electron density n_e, the electron temperature T_e, the background neutral argon density n_{Ar} and the thermalised aluminium atom density n_{Al}. Direct impact ionisation of argon and aluminium atoms and Penning ionisation of aluminium through collisions with argon metastable atoms are considered. It is indeed known that Penning ionisation of sputtered metal atoms through collisions with argon metastable states is important in magnetron discharges and consistent with diffusive losses of argon metastables [230, 231]. The details of the model are given in Ref. [213].

The results of the calculation are shown in Fig. 3.22-(III). As expected and as in experiments, T_e decreases with increasing pressure. The calculated T_e values are close to the OES one. Nevertheless due to the model's numerous approximations, only qualitative comparison can be made. Due to the lower excitation and ionisation thresholds of aluminium (3.2 eV and 6 eV, respectively) with respect to argon (11.5 eV and 15.8 eV, respectively), the presence of a low density of aluminium atoms ($n_{Al} \simeq 5 \cdot 10^{12}$ cm^{-3} (less than 0.3% of n_{Ar} at $p_{Ar} = 10$ Pa)) is enough to cool the electron by a few percent and might partially explain the relatively low measured T_e. Higher discharge currents lead in a small increase of T_e and a linear increase of n_e. Note that the plasma density is almost insensitive to the presence of Al atoms. The model allows to calculate the fraction of ions f_t leaving the plasma towards the target (not shown). It changes from around $f_t \sim 0.6$ at $p_{Ar} = 10$ Pa to $f_t \sim 0.9$ at $p_{Ar} = 40$ Pa. However, our simple model does not include many relevant physical phenomena and cannot be used to obtain quantitative values. For instance, it is known that increasing pressure leads to lower sputtering rate due to the lower energy of the ion hitting the cathode. Moreover, the influence of power and pressure on the racetrack width is ignored, as is the thermalisation of sputtered atom and the heating of the background gas. Therefore, a high discharge current might not necessarily lead to more sputtering and a higher aluminium atom density in the plasma. For example, at the highest background gas pressure, collisions might results in smaller sputtering rate due to the lower energies of the ions colliding with the cathode and thus a reduced aluminium atom density [see Fig. 3.22-(IIa)].

For future studies, a more complete hybrid CRM will be developed. It will allow more precise derivation of plasma parameters from OES measurements. Direct measurement of the aluminium atom density through absorption spectroscopy is also planned. In addition, a careful modelling of the planar magnetron discharge should also be performed in order to study the influence of the sputtered aluminium atoms and their transport on plasma parameters.

3.2.4 Nanoparticle growth in magnetised capacitivelly-coupled radio-frequency discharge

In tokamaks, dust particles are formed by interaction of the plasma with the plasma facing components [6, 7, 169–171, 178, 232–234]. Since fusion devices generally operate at high magnetic field intensity, understanding dust particle growth and transport at high magnetic field intensity is of great importance.

Magnetic fields alter the transport of electrons and ions and thus the properties of a plasma are affected by the presence of a magnetic field. In a dusty plasma subjected to low or moderate magnetic fields (or equivalently for large enough dust particles) the effect of the magnetic field on dust particle is weak and indirect, due to their very small charge-to-mass ratio. However, even at low magnetic fields ($B < 1$ T), the fluxes of electrons and ions on the dust particle is modified thus changing the dust particle charges and the different forces acting on them. For example, the drag force resulting from the ion flow, of great importance for dust particles dynamics, is directly modified. In moderately magnetised conventional discharges, NP growth is easily achieved [22, 73, 210, 212, 235, 236]. In such discharges, the magnetic field trap electrons and thus the plasma density is higher due to the resulting increase of ionising collisions. For example, in planar magnetron discharges, metallic NPs can be grown and trap above the cathode [22, 73, 210, 212]. In magnetron discharges, dust rotation arising from the ion $\mathbf{E} \times \mathbf{B}$ drift is sometimes observed and can be used to enhance particle coating [196]. In electron cyclotron resonance (ECR) discharges, NP growth is observed in the discharge regions where the magnetic field is the highest [236, 237]. This results in the appearance of plasma potential wells able to confine negatively charged NPs where the electrons are trapped (Lorenz force must be considered for electrons dynamics and transport). NP growth can be monitored by measuring the floating potential of a probe immersed in the ECR plasma.

In this Section, I summarize results on measurements of the characteristics of a highly magnetised cc-rf discharge and the characterisation of nanometre-sized particles formed in highly magnetised chemically active plasmas published in Ref. [19] (a copy of which can be found at the end of this section). This work was done in collaboration with the research group of Prof. Ed. Thomas (Auburn University, Alabama, USA) and has involved many students and post-doctoral fellow. Experiments discussed here were performed in the Magnetized Dusty Plasma Experiment (MDPX) device using a modified ccc-rf plasma source. Plasmas were generated in pure argon (Ar) or in a gas mixture of argon and acetylene (C_2H_2). The magnetic field could be changed from 0 T to 2.5 T. In this section, the changes of discharge parameters such as the self-bias of the powered electrode due to the applied magnetic field in pristine argon discharge as well as the effect on NP growth in magnetised Ar/C_2H_2 discharges are discussed. The grown NPs were also characterised using electron microscopy.

Experimental set-up

The experiments were performed in the Magnetized Dusty Plasma Experiment (MDPX) device at Auburn University, Alabama, USA. It is multi-user, high magnetic field experimental platform consisting of two main components: the superconducting magnets (extensively described in Refs [238–240]) and a plasma chamber which can be changed according to the type of experiments. For the NP growth studies in magnetised chemically active plasmas, the MDPX device was operated in the vertical configuration ($\mathbf{B} \parallel \mathbf{g}$). The cc-rf discharged was install at the center of the experimental volume. In this region, a uniform magnetic field ($\Delta B/B < 1\%$) was created by the four MDPX superconducting coils energised at the same current.

The cc-rf plasma source consisted of parallel aluminium electrodes installed at the center of a 6-way cross vacuum chamber with 100 mm ISO ports (see Fig. 3.23). In order to ionise the gas, the powered electrode was connected through a matching to a 13.56 MHz rf generator.

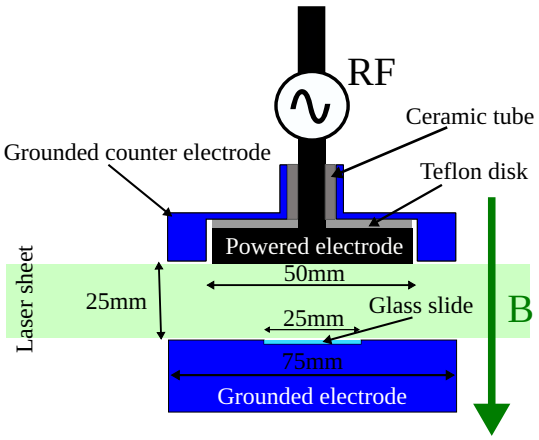

Figure 3.23 – (Reproduced from Ref. [19]) Schematic of the electrode assembly installed in the MDPX facility

The rf power was set between $5 < P_{\mathrm{rf}} < 30$ W. The top (powered) electrode had a diameter of 50.8 mm and is surrounded by a grounded guard ring. During operation, the powered electrode acquired a self-bias, V_{bias} which was monitored using a National Instrument data acquisition card. The grounded bottom electrode had a diameter of 76.2 mm. A ∼1 mm deep, 25 mm wide 75 mm long notch was cut in its center to install microscopy glass slides needed to collect the grown NPs.

Before each experiments, the vacuum chamber was pumped down to a base pressure of ∼ 1 mTorr. Then, an argon flow $5< \mathrm{Q_{Ar}} <10$ sccm and an acetylene flow $0< \mathrm{Q_{C_2H_2}} < 2$ sccm were injected. Before the plasma was switched on, the pumping port opening was adjusted to stabilise the pressure p inside the chamber to a value 200 mTorr $< p <$ 600 mTorr. A MKS Baratron capacitance manometer was used to monitor the pressure. The grown NP cloud was then illuminated with a 532 nm, 100 mW green laser light sheet (∼ 3 cm height, ∼ 200 μm width). The scattered light was recorded from the side port of the vacuum chamber at an angle of 90° using a USB3-based, 2048 by 2048 pixel, Ximea model xiQ camera (up to 90 frames per second (fps)). Most experiments used a frame rate of 30 fps.

Main results

Pristine plasma

Before studying the NP growth process in magnetised plasma, the pristine argon discharge behaviour as a function of the applied magnetic field intensity was first studied. For that purpose, the operating pressure was set at $p = 300$ mTorr ($\mathrm{Q_{Ar}} = 7$ sccm) and the forward rf power was set at $P_{\mathrm{rf}} = 20$ W. A clean glass slide was installed in the bottom grounded electrode notch to remain as close as possible to the NP growth conditions. Starting from a high initial value ($B = 2.5$ T), the magnetic field was slowly ramped down to $B = 0.0$ T. The plasma glow was continuously recorded by the camera at 1 fps and the powered electrode self-bias voltage of the was continuously monitored. In Fig. 3.24-(a), the evolution of the self bias voltage as a function of B is shown and in Fig. 3.24-(b), snapshots of the plasma glow for different magnetic field strengths are presented.

As can be seen in Fig. 3.24-(b), an increasing magnetic field intensity seems to induce a stronger light emission from the plasma glow. In addition, the glow appears more localised under the powered electrode at high magnetic field, indicating a strong confinement of the plasma. With magnetic fields $B > 0.25$ T, plasma filamentation occurred: filaments tended to be mostly localised at the edge of the powered electrode and the number of observed filaments

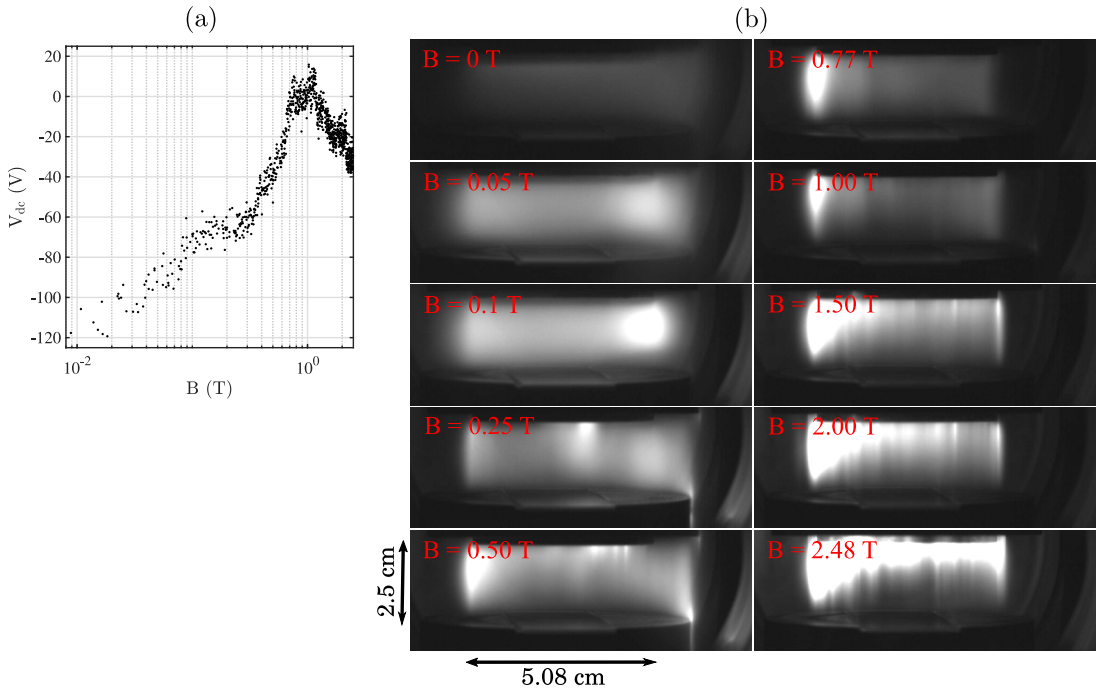

Figure 3.24 – (Reproduced from Ref. [19]) (a) Self-bias as a function of magnetic field strength. (b) Snaphots of the plasma glow at different magnetic fields for pure argon plasmas. The argon flow was $Q_{Ar} = 7$ sccm, the pressure was $p = 300$ mTorr and the rf power was $P_w = 20$ W.

increased with the intensity of the applied magnetic field. Note that filaments were not fixed and could move around the discharge. These filaments were also observed in the NP growth experiments and their role on NP growth and dynamics remains unclear.

In Fig. 3.24-(a), it can be seen that, as expected, the self-bias voltage is negative at low magnetic field because the surface area of the powered electrode is smaller than the surface area of the grounded areas [117, 122]. When the magnetic field increased, the absolute value of the self-bias voltage decreased and reached 0 V at B$\sim$1 T. At magnetic field $B \gtrsim 1$ T, the absolute value of the self-bias voltage started to increase again. Not that the ramping of the magnetic field did not induced a noticeable change in the settings of the matching network and therefore the impedance of the whole circuit (plasma + external circuit) seemed to remained quasi constant. It can be deduced that, at a given forward rf power, the variations of rf peak to peak voltage applied on the powered electrode remained limited and could thus not explain the large variation of the self-bias voltage.

The physical mechanism of the self-bias dependence on the magnetic field intensity are discussed in details in Ref. [19]. The main idea is the following: the presence of the magnetic field affects ambipolar diffusion, especially the diffusion perpendicular to the magnetic field. The increase of the magnetic field results in a better confinement of the plasma under the powered electrode leading to higher ionisation and reduced losses on the grounded surfaces naturally (symmetrisation of the discharge) leading to a decrease of the self-bias voltage (in absolute value). Complementary Particle-in-cell (PIC) simulations showed that the overall electric field distribution is also changed by the applied magnetic field intensity which as implication for NP confinement during the growth process.

Dusty plasma

The addition of acetylene (C_2H_2) to the gas enabled the growth of carbon NP. During experiments, a Ar/C_2H_2 gas mixture ($Q_{Ar} = 7$ sccm and $Q_{C_2H_2} = 1$ sccm) was injected in the vacuum vessel and the pressure was stabilised to $p = 300 \pm 2$ mTorr before the plasma was

ignited. As for pristine plasma experiments, the forward rf power was set to $P_{rf} = 20$ W. In order to obtain an accurate view of the growth process, the discharge was pulsed manually with a plasma duration $t_{on} = 60$ s followed by $t_{off} \simeq 60$ s off times.

In Fig. 3.25-(Ia), the evolution of the vessel pressure normalised to the maximum pressure during the plasma pulse is shown. As can be seen, the pressure slightly increased just after discharge ignition up to a maximum p_{max}. This can be attributed to heating of the gas by the gas discharge. Then, after roughly 1 s, the total gas pressure started to decrease. At the end of the plasma pulse, the pressure was ∼3-4% lower than the ignition pressure (well bellow the normal fluctuations induced by the gas flow regulation system). Since the C_2H_2 flow was constant, it indicates that C_2H_2 was partially dissociated. This behaviour was observed for all applied magnetic fields. Note however that high magnetic field resulted in faster and greater pressure decrease. At the end of every rf pulse, the pressure returned to its original (pre-ignition) value within ∼ 30 s.

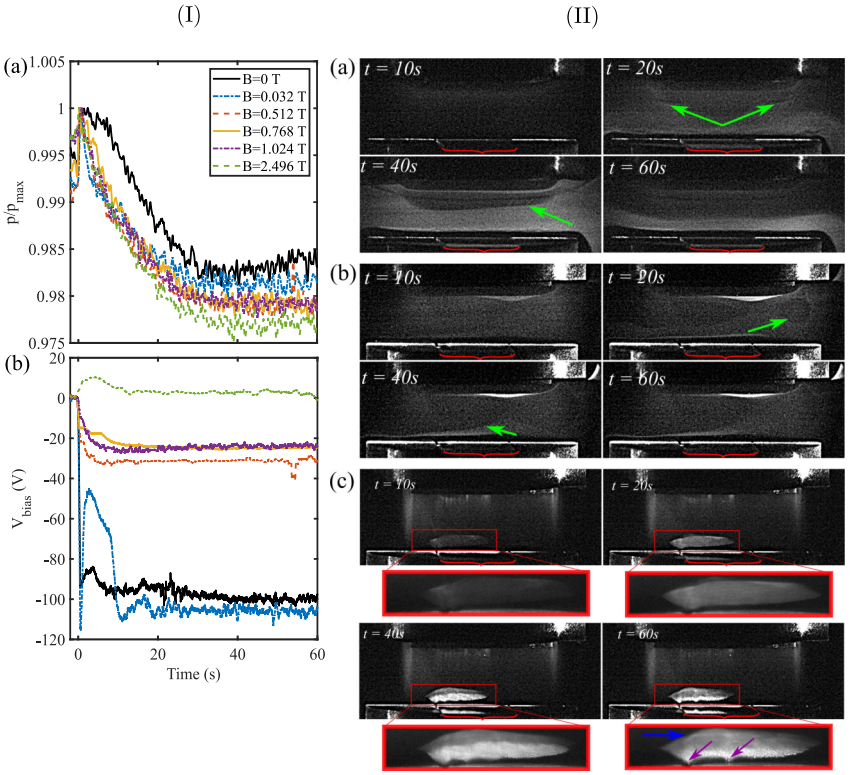

Figure 3.25 – (Reproduced from Ref. [19]) (I) Evolution of (a) normalised chamber pressure and (b) self-bias voltage as a function of time for different magnetic field strengths in Ar/C_2H_2 discharges. The argon flow was $Q_{Ar} = 7$ sccm, the acetylene flow was $Q_{C_2H_2} = 1$ sccm, the pressure before ignition was $p = 300$ mTorr and the rf power was $P_w = 20$ W. (II) Images of the scattered laser light at different instants after discharge ignition for: (a) B = 0.0 T, (b) B = 0.032 T and, (c) B = 1.024 T. The other discharge conditions are the same as in (I). The bright vertical and horizontal stripes visible on all images are reflections of the laser light on the electrode assembly. On all images, a red horizontal curly bracket indicates the position of the glass slide used to collect the dust particles. In (a) and (b), the oblique green arrows indicate the edge of the void in which a new generation of dust particles can grow. In (c), the horizontal blue arrow point to a dust density wave and the oblique purple arrows show dips in the dust cloud induced by plasma filamentation. On all images except the magnified ones, a sharpen filter has been applied to improve visibility of the different features.

The evolution of the powered electrode self-bias voltage of the V_{bias} was also monitored and is shown in Fig. 3.25-(Ib) for different magnetic field strengths. The general behaviour reported in

pristine argon plasma was again observed: the stronger the magnetic field, the lower (in absolute value) the self-bias voltage of the powered electrode. However, in contrast with pristine argon plasma, the self-bias voltage was not constant. It is known that plasma impedance is strongly affected by the presence of growing NP (see for examples Ref. [241]) and that working at fixed forward rf power leads to variations of the peak to peak rf voltage applied to the electrode and variations the self-bias voltage directly correlated to the NP growth dynamics. Large self-bias oscillations are linked to the growth of successive generation of NP [98, 242–245]. Thus, at low or zero magnetic field, within the first 20 seconds after plasma ignition strong V_{bias} oscillations could be seen. The strongest oscillations occurred at B =0.032 T (see Fig. 3.25-(Ib)). Note that pulse after pulse, the recorded V_{bias} signal shape was roughly reproducible (slight changes were observed due normal modifications of discharge conditions, i.e. coating of the electrode, gas purity, temperature of the electrode, etc.). Note that at the highest investigated magnetic field ($B = 2.496$ T), the powered electrode self-bias was surprisingly positive. In an electropositive plasma (such as a pristine argon plasma), the appearance of self-bias on the powered electrode connected to the rf generator through a blocking capacitor (matching network) is the irreversible electron losses to the electrodes leading to positive plasma potential (with respect to ground) [117]. Since the discharge is asymmetric (ie. grounded area are much larger than the powered electrode area), different amounts of charge goes to each electrodes leading to a difference in the dc electrode potentials (self-bias). In Ar/C_2H_2 discharges with growing NP, the complicated chemistry leads to the existence of many types of charged species (positive and negative ions such as Ar^+, $C_2H_2^+$, C_2H^-, $C_4H_2^+$, etc) [100, 101, 246, 247]. Moreover, the high density of growing NP reduces the electron density [248] (see also Sec. 3.1.1). The observed positive self bias is most probably caused by a modified charged balance at the electrodes due to the complicated chemistry of the Ar/C_2H_2 plasma and the presence of growing NP.

Fig. 3.25-(II) shows snapshots of the scattered laser light sheet by the growing NP cloud for different applied magnetic field intensities. Without applied magnetic field [Fig. 3.25-(IIa)] we observed the well-known cyclic growth behaviour [20, 58, 59, 109–111, 214, 249–253]: the dust cloud started to be visible on the camera ~ 15 s after plasma ignition, and occupied almost the entire interelectrode region. A "void" (a region without visible NP) started to open at $t \sim 20$ s in the discharge in the middle of the gap below the powered electrode edge (see Fig.3.25-(IIa) at $t = 20$ s). However, in our experiment, the void did not have the typical eye shape reported in the literature. This is most probably an effect of the geometry of our experiment which is significantly different from the discharge geometry used in other studies (size of the electrodes and/or interelectrode spacing). New NP were then growing inside the void while the first cloud was pushed towards the edges (see Fig.3.25-(IIa). With our chosen experimental parameters, the growth cycle (appearance of a new NP generation in the "void") was $\sim 40-60$ s, depending on the number of previous plasma pulses. Density waves were observed near the lower electrode as in similar experiments [254, 255]. These waves are known to favour the agglomeration of NP [254, 256].

At low applied magnetic field [$B = 0.032$ T, Fig.3.25-(IIb)] direct imaging of the NP cloud revealed a quicker NP growth. This matches with the faster gas pressure decrease during the plasma-on phases and the observed larger oscillations of the self-bias voltage. The duration of a NP growth cycle was then $\sim 15-20$ s. Interestingly, the void is not symmetric any more (see Fig.3.25-(IIb) at t =20 s.). Moreover, the intensity of the scattered light was stronger close to the top electrode sheath indicating a very dense NP cloud and/or the presence of large dust particles.

At high applied magnetic field intensities ($B \gtrsim 0.1$ T), no growth cycles were observed (i.e. growth cycle if they existed were longer than 60 s)). In Fig.3.25-(IIc), snapshots of the recorded laser light scattering at $B = 1.024$ T are presented but the observations were qualitatively similar for other high magnetic field intensities. In each cases, a NP cloud above

the grounded bottom electrode was rapidly detected [see Fig.3.25-(IIc)], in agreement with the fast gas pressure decrease observed after plasma ignition due to the dissociation/polymerisation of acetylene leading to NP formation. Note that the NP cloud did not cover the entire grounded electrode area but was instead locked near the edge of the glass slide (used for NP collection). Depending on the experiment, the NP cloud extension above the glass slide changed. Laser light scattering also revealed a quick agglomeration of the NP. Large individual particles levitating above the grounded electrode indeed appeared on camera only a few tens of seconds after plasma ignition (see Fig.3.25-(IIc) at t =40 s and t =60 s). NP also formed much closer to the electrode compared to the cases with no and low intensity applied magnetic fields.

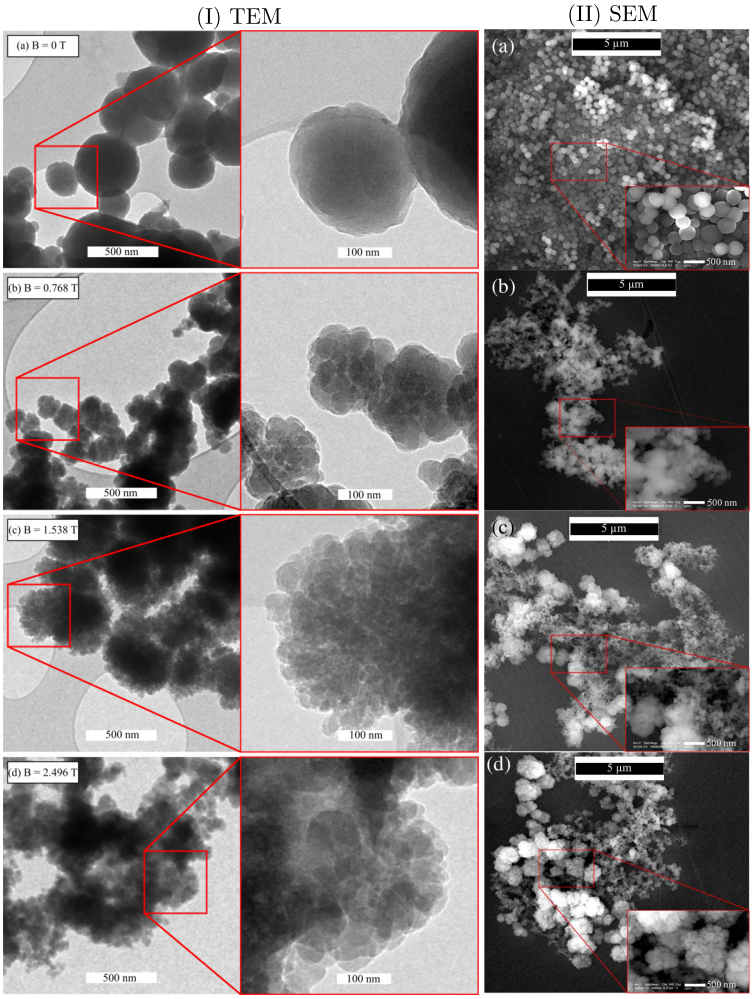

Figure 3.26 – (Reproduced from Ref. [19]) (I) TEM images of dust particles grown for different magnetic fields. (II) SEM images of dust particles grown for different magnetic fields. (a) 0 T, (b) 0.768 T, (c) 1.024 T and, (d) 2.496 T. The other discharge conditions are the same as in Fig.3.25.

In order to perform ex-situ characterisation of the grown NP under different values of the applied magnetic field, NP were collected for 15 consecutive 60 s plasma pulses separated by off period of 60 s (necessary for gas renewal). After each fifteen plasmas series, the electrode assembly was thoroughly cleaned and a new glass slide was positioned in the bottom electrode groove. The vacuum chamber was further cleaned with an argon oxygen plasma run ∼15 min at 20 W of forward rf power (any residual carbon coating was thus burnt away). Finally the chamber was pumped down to its base pressure for a minimum of 30 min before proceeding with the next plasmas series.

Fig. 3.26 shows scanning electron microscopy (SEM) images and transmission electron mi-

croscocopy (TEM) images of NP grown at different applied magnetic field strengths. As can be seen in Figs 3.26-(Ia) and 3.26-(IIa), the NP grown at B =0 T are almost spherical and compact as reported in similar experiments [102]. The observed NP have diameters ranging from $\sim$ 20 nm to $\sim$ 250 nm in agreement with the existence of a few growth cycles during the 60 s plasma pulses. In the zoom of 3.26-(Ia), the NP surface roughness indicate that NP are most probably agglomerate of smaller NP as reported in similar experiments [102, 257].

The applied magnetic field intensity has a great effect on the NP shape and size. At low applied magnetic field [see Fig. 3.26-(IIb)], the size distribution looks much broader than without magnetic field but NP still appear relatively compact. This observation coincides with the quicker NP growth cycle reported earlier. A further increase of the applied magnetic field resulted in the NP sample being a mixture of very small NP ($\sim$ 10 nm) with larger spherical "fluffy" porous NP (diameters up to a few hundreds of nanometres). These particles are clearly visible in Fig. 3.26-(IIc-d). As can be seen in the TEM images [Fig. 3.26-(Ib-d)] the porous NP clearly are agglomerates of smaller NP. Higher magnetic field results in fluffier agglomerates as both SEM and TEM images demonstrate. These agglomerates are probably the large NP levitating in the sheath above the grounded electrode revealed by laser light scattering at the end of the plasma pulse [Fig. .3.25-(IIc)]. Smaller NP most probably correspond to the observed dim cloud levitating above the larger NP.

Discussion and Perspectives

Experiments have clearly demonstrated that high magnetic field intensities have a major effect on the discharge characteristics (plasma glow distribution, self-bias voltage of the powered electrode). The modification of the ambipolar diffusion process (especially the reduction of diffusion perpendicular to the magnetic field) have a significant impact on the discharge. Basic modelling of the ambipolar diffusion process (detailed in Ref [19]) qualitatively explain the experimental observations (decrease of the self-bias voltage, confinement of the plasma below the powered electrode). PIC simulations have also shown that the electric fields are also affected by the magnetic field intensity [19] and thus NP confinement.

Experiments have also revealed that the magnetic field intensity also has a significant effect on the morphology of NP grown in Ar/C_2H_2 plasma. At low magnetic field intensities ($B < 0.1$ T), NP growth follows the well-known cyclic growth behaviour with the opening of a void region in the plasma bulk in which growns the next NP generation. At higher magnetic fields ($B > 0.1$ T), the growth cycles seem to disappear. However, a NP cloud above the grounded bottom electrode appears quicker than in the low magnetic field cases. Large agglomerates also forms above the grounded electrode in tens of seconds after plasma ignition. Electron microscopy have shown that they are porous spherical agglomerates of very small NP. The enhanced agglomeration, probably at the origin of the observed large porous spherical agglomerates, is probably due to the presence of dust acoustic waves and/or the plasma filamentation occurring at high magnetic fields.

In on-going studies made in collaboration with Prof. Ed Thomas group at Auburn University, different magnetic field and electrode configurations are investigated. Preliminary results indicate that plasma filamentation is affected by NP growth [258]. Plasma filaments also seem to favour the formation of porous agglomerate. Addition campaign of experiments in the MDPX device will concentrate on discharge with forces filamentation and with suppressed filamentation

3.2.5 Main publications

The following publications corresponding to the main results described in this section are attached to the manuscript.

1. Kishor Kumar K., L. Couëdel and C. Arnas, *Growth of tungsten nanoparticles in direct-current argon glow discharges*, Phys. Plasmas **20**, 043707 (2013)

   Abstract: The growth of nanoparticles from the sputtering of a tungsten cathode in DC argon glow discharges is reported. The study was performed at fixed argon pressure and constant discharge current. The growth by successive agglomerations is evidenced. First, tungsten nanocrystallites agglomerate into primary particles, the most probable size of which being $\sim$ 30 nm. Primary particles of this size are observed for all plasma durations and always remain the most numerous in the discharge. Primary particles quickly agglomerate to form particles with size up to $\sim$ 150 nm. For short plasma duration, log-normal functions describe accurately the dust particle size distributions. On the contrary, for long discharge durations, a second hump appears in the distributions toward large particle sizes. In the meantime, the discharge voltage, electron density, and emission line intensities strongly evolve. Their evolutions can be divided in four separate phases and exhibit unusual distinctive features compared to earlier observations in discharges in which particles were growing. The evolution of the different parameters is explained by a competition between the surface state of the tungsten cathode and the influence of the growing nanoparticles. The differences with sputtering glow discharges and chemically active plasmas suggest that the nanoparticle growth and its influence on discharge parameters is system and material dependent.

2. L. Couëdel, Kishor Kumar K. and C. Arnas, *Detrapping of tungsten nanoparticles in a direct-current argon glow discharge*, Phys. Plasmas **21**, 123703 (2014)

   Abstract: Nanoparticles are grown from the sputtering of a tungsten cathode in a direct current argon glow discharge. Laser light scattering of a vertical laser sheet going through the plasma reveals that the dust particle cloud is compressed and pushed towards the anode during the discharge. Scanning electron microscopy images of substrates exposed to the plasma for given durations show that dust particles are continuously falling down on the anode during the discharge. These observations are explained by the fact that the electrostatic force at the negative glow-anode sheath boundary cannot balance the ion drag, gravity, and thermophoresis forces for particles of more than a few tens of nanometres in diameter.

3. S. Barbosa, L. Couëdel, C. Arnas, Kishor Kumar K. et al., *In-situ characterisation of the dynamics of a growing dust particle cloud in a direct-current argon glow discharge*, J. Phys. D: Appl. Phys. **49**, 045203 (2016)

   Abstract: The growth and the dynamics of a tungsten nanoparticle cloud were investigated in a direct-current low pressure argon glow discharge. Real-time analyses of the dust particle size and number concentration were performed in-situ by light extinction spectrometry, while spatial dynamics of the cloud was investigated with the laser light-sheet scattering method. Additional off-line electron microscopy and Raman spectroscopy measurements were also performed for comparison purpose. This experimental work reveals the existence of an agglomeration phase followed by the appearance of a new dust particle generation. While growing, the dust cloud is pushed towards the anode and the discharge edge. Afterwards, a new dust particle generation can grow in the space freed by the first generation of nanoparticles. The continuous growth, below the light extinction spectrometry scanning positions, explains the apparent dissimilarities observed between the in-line optical and the off-line electron microscopy analyses.

4. S. Mitic, J. Moreno, C. Arnas and L. Couëdel, *Diagnostics of a high-pressure DC magnetron argon discharge with an aluminium cathode*, Eur. Phys. J. D **75**, 240 (2021)

   Abstract: In this article, the plasma parameters of a direct current magnetron discharge in argon at moderate pressure (10 to 40 Pa) using an aluminium cathode are explored. The density of argon excited states, the sputtered aluminium atom density and the electron temperature are estimated using a collisional-radiative model. The electron temperature obtained using optical emission spectroscopic data agrees well with measurements taken using a Langmuir probe. The influence of the discharge parameters, namely the background argon pressure and the discharge current, are discussed.

5. L. Couëdel, D. Artis, M.P. Khanal,C. Pardanaud, et al., *Influence of magnetic field strength on nanoparticle growth in a capacitively-coupled radio-frequency* Ar/C_2H_2 *discharge*, Plasma Research Express **1**, 015012 (2019)

   Abstract: The growth of nanoparticles in a magnetised chemically active discharge (Ar/C2H2) is investigated. The influence of the strength of the magnetic field on dust particle growth dynamics is explored. The structure of the grown nanoparticles is studied ex situ. It is revealed that the strength of the magnetic field (up to 2.5 T) has a major impact on discharge parameters (such as the self-bias of the powered electrode) as well as on the growth and morphology of the nanoparticles. At high magnetic field, the dust cloud is confined in the sheath above the grounded electrode while without magnetic field the dust cloud occupies most of the interelectrode space. Moreover, at high magnetic field, large porous spherical agglomerates were grown. The modification of the self-bias is explained by the influence of the magnetic field on the diffusion of charged species resulting in a confinement of the plasma under the powered electrode. Complementary particle-in-cell simulations confirm that the electric field and plasma distributions are strongly affected by the magnetic field explaining the experimentally observed dust cloud localisation. The large porous spherical agglomerates are most probably due to an enhanced agglomeration caused by the modified confinement owing to the magnetic field.

Growth of tungsten nanoparticles in direct-current argon glow discharges

Kishor Kumar K., L. Couëdel,[a] and C. Arnas
Laboratoire de Physique des Intéractions Ioniques et Moléculaires, CNRS-Aix-Marseille Université, 13397 Marseille, France

(Received 18 February 2013; accepted 5 April 2013; published online 25 April 2013)

The growth of nanoparticles from the sputtering of a tungsten cathode in DC argon glow discharges is reported. The study was performed at fixed argon pressure and constant discharge current. The growth by successive agglomerations is evidenced. First, tungsten nanocrystallites agglomerate into primary particles, the most probable size of which being ∼30 nm. Primary particles of this size are observed for all plasma durations and always remain the most numerous in the discharge. Primary particles quickly agglomerate to form particles with size up to ∼150 nm. For short plasma duration, log-normal functions describe accurately the dust particle size distributions. On the contrary, for long discharge durations, a second hump appears in the distributions toward large particle sizes. In the meantime, the discharge voltage, electron density, and emission line intensities strongly evolve. Their evolutions can be divided in four separate phases and exhibit unusual distinctive features compared to earlier observations in discharges in which particles were growing. The evolution of the different parameters is explained by a competition between the surface state of the tungsten cathode and the influence of the growing nanoparticles. The differences with sputtering glow discharges and chemically active plasmas suggest that the nanoparticle growth and its influence on discharge parameters is system and material dependent. © *2013 AIP Publishing LLC*. [http://dx.doi.org/10.1063/1.4802809]

I. INTRODUCTION

The synthesis of nanoparticles is of great interest for many applications. For example, due to their high surface to volume ratio, metal nanoparticles dispersed on an inert support are the key components of catalysis reactions.[1] Nanoparticles are also at the origin of innovative materials such as polymorphous silicon films for their photoluminescence properties or for energy production (photovoltaic).[2–4] They can be used as quantum dots for single electron devices,[5,6] as raw material for lithium battery electrodes,[7,8] for electron field emission[9] or as sensors to detect very small amounts of chemical vapors.[10,11] They also could provide barriers to gas (oxygen or moisture) in films[12] and, coated with biological molecules, they have promising applications in medicine.[13,14]

Low pressure, low temperature plasmas can generate particulates from specific complex chemical reactions.[15–19] In particular, a lot of studies have been devoted to the formation of silicon nanoparticles in silane-based plasmas.[20–23] The formation of carbonaceous particles has also been investigated either by sputtering of a graphite target[24–27] or by using reactive hydrocarbon gases.[28–32]

As discovered more recently, erosion of carbon-based plasma facing materials by plasma surface interactions is one of the processes leading to the production of very fine dust in fusion devices. It has motivated many studies dedicated to their formation in the coldest plasma regions near the walls.[33–36]

Nanoparticle formation can be analysed by *ex-situ* scanning electron microscopy (SEM) of collected deposits or by *in-situ* laser-light scattering, laser extinction and also, through strong modifications of the plasma and discharge parameters.[21,37–40] These modifications are the result of the particulate charging mechanism, which affect self-consistently the plasma electron density and temperature, and therefore the plasma resistivity and sustaining conditions.[41–43]

In this article, we report on the growth of tungsten nanoparticles from the sputtering of a tungsten cathode in a direct-current (DC) argon glow discharge. Indeed, very few studies were devoted to the formation of these particles in low-pressure, low temperature plasmas.[26] Tungsten or tungsten alloy nanoparticles are usually produced with methods using vapour precursors, such as chemical vapour synthesis in thermal plasmas,[44] laser assisted homogeneous gas-phase nucleation,[45] combustion synthesis,[46] and methods using solid precursors as in laser ablation[47] and arc discharges.[48]

A detailed study at a fixed argon pressure and discharge current was performed. We show that tungsten nanoparticles had morphological features resembling silicon and carbon nanoparticles grown in plasmas. It is also shown that these particles modified the discharge voltage and the emission line intensities of various plasma species, all of which exhibiting strong variations. However, these modifications were different from those reported in radio-frequency (RF) plasmas (for example, silane-based plasmas[21,38] or hydrocarbon-based plasmas[29]). They were also different from those we reported in similar DC discharges in which carbon nanoparticles were grown from the sputtering of a graphite cathode.[40] In this previous investigation, we provided evidence that the variations of the discharge and plasma parameters during particle growth were strongly dependent on the discharge system (RF or DC). In this article, we also show that the nature and the surface state of the cathode material play a major role.

[a]Electronic mail: lenaic.couedel@univ-amu.fr

 © 2013 AIP Publishing LLC

Downloaded 03 May 2013 to 147.94.187.189. This article is copyrighted as indicated in the abstract. Reuse of AIP content is subject to the terms at: http://pop.aip.org/about/rights_and_permissions

II. EXPERIMENTAL CONDITIONS

Fig. 1 is a schematic of the experimental set-up, showing the electrode assembly and the substrate holder. It is contained in a cylindrical vacuum chamber of 30 cm diameter and 40 cm length. An oil diffusion pump achieved a base pressure of $\leq 1 \cdot 10^{-6}$ mbar. A manually operated gate valve was used to isolate the chamber from the oil diffusion pump during the experiments. DC glow discharges in argon at a static pressure of 0.6 mbar (no gas flow) were initiated between two parallel electrodes: a tungsten cathode of 9.9 cm diameter and a grounded stainless steel anode. The tungsten cathode was mounted on an insulating ceramic disc, such as only one face was exposed to the plasma. The electrodes were separated by a distance of 10 cm by two half glass cylinders. In order to facilitate optical emission spectroscopy (OES) diagnostics, the half cylinders were positioned with a 1 cm gap facing the radial view ports of the chamber. The anode disc had a hole at the centre through which the tungsten nanoparticles produced during the discharge were collected. Stainless steel foils, mounted on a holder were used as substrates for collecting the dust. The substrate holder could be manipulated from one of the axial ports of the chamber, such that each of them could be positioned under the hole in the anode.

A regulated power supply (Sefelec HT15A, 1 kV, 300 mA) was used to bias the cathode. The discharge current density was kept at a constant value ($0.53\,\text{mA} \cdot \text{cm}^{-2}$, the current variation being less than 0.05%). The discharge voltage was the free parameter whose time evolution was acquired during the discharge.

Under the chosen operating conditions, it was possible to estimate the flux of fast particles (argon ions and charge exchange neutrals) to the cathode and also to calculate the expected sputtering yield.[49] The cathode voltage was $V_d \sim -600$ V. Consequently, the total flux of impinging particles was $\Phi_t \sim 7 \cdot 10^{15}\,\text{cm}^{-2}/\text{s}$, the sputtering yield was $\Upsilon \sim 3.8\%$ and the flux of sputtered tungsten atom (considering pure tungsten) was $\Phi_W \sim 3 \cdot 10^{14}\,\text{cm}^{-2}/\text{s}$. The sputtered atoms had a mean energy of ∼12 eV at the cathode surface and got thermalised at a distance of ∼1 cm from the cathode. The chosen discharge parameters were thus favourable to nanoparticle formation by homogeneous nucleation from the sputtered atoms.

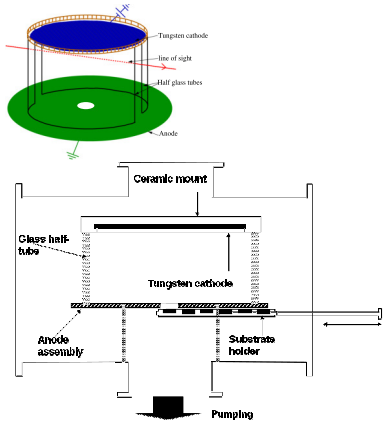

FIG. 1. Schematic of the experimental set-up. On top is a three-dimensional schematic of the electrode assembly.

OES study of the discharge plasma was carried out. The intensity of different emission lines—ArI (763.5 nm and 800.6 nm coming from the 4P level), ArII (454.5 nm), WI (498.26 nm), WII (341.66 nm), and H_α (646.28 nm)—were measured using two monochromators (Jobin-Yvon HRS, 600 mm focal length and, Acton Spectra Pro 2500i, 500 mm focal length) coupled to photomultiplier tubes (Hamamatsu R3896). Convex lenses and optic fibres were used to collect the emitted plasma radiation, ∼1 cm below the tungsten cathode in the negative glow (see on top of Fig. 1).

The time evolutions of the photomultiplier tube signals and the discharge voltage were acquired using a National Instruments data acquisition system, interfaced to a computer. The errors on the measured values were ∼0.5%. The evolution of the electron density was measured using a commercial Ka-band microwave interferometer operating at 26.5 GHz (Miwitron MWI 2650). The error on the relative value of the electron density was ∼2%, and the error on the absolute value was ∼20%. The size distributions of the collected dust particles were established using SEM (Philips XL30 SFEG STEM), and their structures were analysed by High Resolution-Transmission Electron Microscopy (HR-TEM) (JEOL 2010F).

For the present investigation, discharges of various durations (10 s–500 s) were produced.

III. RESULTS

A. Evolution of the dust particle size distribution

Representative SEM and TEM images of nanoparticles produced at different plasma durations are shown in Fig. 2(a) (t = 120 s) and Fig. 2(c) (t = 300 s). The nanoparticle size histograms are in the inset of Figs. 2(a) and 2(c). For $t = 120$ s, the best fit is given by a lognormal function with a multiplicative standard deviation, $\sigma^* \sim 1.26$. The smallest size measurement of 10 nm corresponds to the limit of the SEM resolution. The HR-TEM image of Fig. 2(b) shows the structure of a primary particle (PP) of ∼30 nm, produced after 60 s. This PP is made by agglomeration of tungsten crystallites or nanocrystallites of ∼2–4 nm, evidenced by parallel diffraction fringes (several of these units are circled with white ovals in Fig. 2(b)). These nanocrystallites are the smallest solid units, which are produced but could not be observed separately, in particular for shorter time. For longer discharge durations, the PPs agglomerate to form bigger nanoparticles (80–150 nm), looking like "raspberries" as shown by the TEM image of Fig. 2(c) (300 s). Examining the edges of such big particles with HR-TEM, PPs as well as the

Downloaded 03 May 2013 to 147.94.187.189. This article is copyrighted as indicated in the abstract. Reuse of AIP content is subject to the terms at: http://pop.aip.org/about/rights_and_permissions

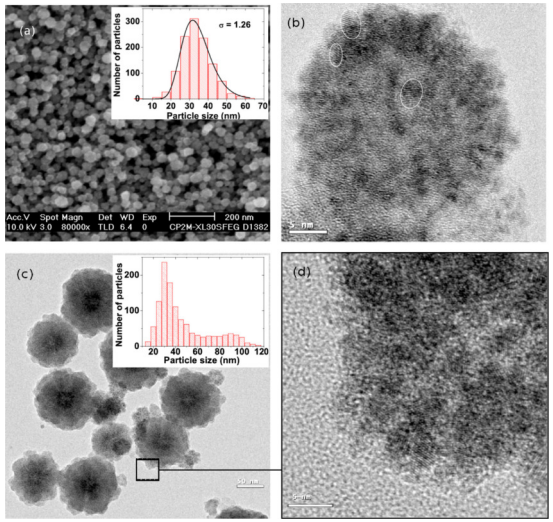

FIG. 2. (a) Dust particles of Tungsten observed after t = 120 s (SEM). Inset: corresponding size histogram fitted by a log-normal function. (b) HRTEM image of a ∼30 nm PP obtained after t = 60 s, which is an agglomerate of nanocrystallites (2–4 nm), identified by diffraction fringes (several of these units are circled). (c) TEM image of particles produced after t = 300 s. It shows PPs as well as bigger particles (80–120 nm), which appear to be agglomerates of PPs. Inset: the corresponding size histogram build from SEM images. (d) Zoom of the selected edge region of one of the big particles, showing nanocrystallites.

inner nanocrystallites can be observed. An example is given Fig. 2(d) were one can see the structure of the edge of a 110 nm particle localized at the bottom right corner of Fig. 2(c). Fig. 2(c) also shows the presence of separated PPs. The growth by successive agglomeration is general in dusty plasmas. It was already observed in silane-based[50] or hydrocarbon discharges[51] as well as in graphite sputtering discharges.[40,52] Due to a higher mobility of the electrons, dust particles acquire a negative charge except for very small particles (few nanometres) for which charge fluctuations can result in neutral and positively charged particles responsible of the nanocrystallites agglomeration.[53–55] For larger size, the influence of each dust particle on its neighbour can result in dipole-like interactions and/or image potential also favouring the agglomeration process.[54,56–58]

A complete evolution of the particle growth during 500 s was established from the size distribution measurements. Each distribution was normalized, and the data were interpolated between measurement points. Fig. 3(a) shows the probability (colour-coded) to find a particle of a given size at a given time. It can be seen that the maximum particle size was increasing up to $t \sim 320$ s and was ∼150 nm. The tail in the distribution toward the big diameter was growing with time. Consequently, the distribution could not be fitted with a log-normal function after 200 s (inset of Fig. 2(c). It is worth noting that the lowest measured size was almost the same for all the plasma durations. Moreover, up to ∼120 s, the most probable dust particle diameter was increasing almost linearly from ∼15 nm to ∼30 nm. Before ∼120 s, the dust particle size distribution could be reasonably fitted with a log-normal distribution. After ∼120 s, two interesting features can be seen: (i) ∼30 nm PPs remained the most probable and (ii) big particles were growing in the plasma resulting in the appearance of a second hump in the distribution function as shown in the inset of Fig. 2(c). One should note that the probability to find PPs was always higher than that to find particles with larger diameter.

Fig. 3(b) presents the evolution of the fraction of the total particle volume (volume fraction, colour-coded) occupied by particles of a given size at a given time. By comparing this figure to Fig. 3(a), it can be seen that for discharge duration ≤ 120 s, most of the matter was carried by the most probable particle (in size). For longer time, the matter volume of the big particle was steadily increasing and was more prominent than the volume carried by the smaller but more numerous particles. It could indicate that the PPs (∼30 nm) were continuously produced in the discharge through constant nucleation-agglomeration and were replacing the particles consumed by agglomeration to form the bigger ones.

The above results are significantly different from our earlier results in graphite sputtering discharge.[40] In these conditions, the width of the particle size distributions exhibited a constant multiplicative standard deviation, resulting from a global shift of the size histograms towards larger sizes. This showed that after a while, the nucleation probably stopped and the PPs, which were consumed during the agglomeration process, were not replaced. Meanwhile, the most probable size and the size of the biggest particles were increasing through agglomeration and latter by deposition. Hence, the number of big particles was significantly lower

Downloaded 03 May 2013 to 147.94.187.189. This article is copyrighted as indicated in the abstract. Reuse of AIP content is subject to the terms at: http://pop.aip.org/about/rights_and_permissions

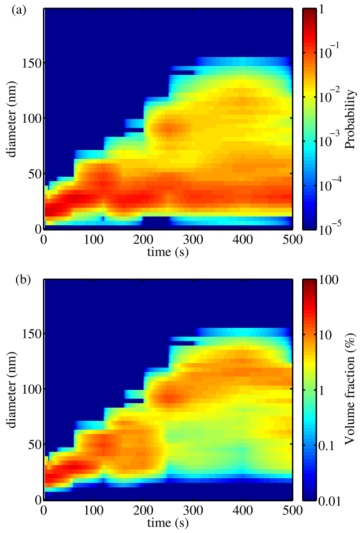

FIG. 3. (a) Probability to find a particle of given diameter at a given time. (b) Fraction of the total particle volume occupied by particles of a given diameter at a given time.

than in the case of tungsten particles and the observation of a second hump in the size distribution appeared only during the formation of a second nanoparticle generation.

B. Evolution of the discharge parameters

In Fig. 4, the evolution of the cathode voltage V_d, electron density n_e and line emission intensities (ArI, ArII, WI, and WII) as a function of time are presented. Each plot was obtained from different experiments. A few arcs were sometimes observed but did not have any significant effect on the overall evolution of the discharges. The recorded signals were similar from a plasma to another and could be divided into four phases named A, B, C, and D (Figs. 4(a)–4(e))

- Phase A: It corresponds to the first few seconds after the breakdown. During this phase, the glow appeared to have, with the naked eye, a uniform intensity under the cathode region, with an emission intensity decreasing within a few centimetres away from the cathode (see Fig. 4(f)). After the breakdown, the absolute value of the cathode voltage $|V_d|$ decreased in $\simeq$70 ms to $|V_d| \sim 500$ V and then increased up to $|V_d| \sim 650$ V in 3–4 s as shown in Fig. 4(e). Meanwhile, the emission intensity of the lines increased but at a different rate depending on the species (Fig. 4(e)). The argon line intensities (ArI and ArII) increased in hundreds of millisecond from zero and then had a slower growth rate until the end of phase A. Tungsten line intensities (WI and WII) started also from zero but exhibited a slow growth rate until the end of phase A. The electron density was relatively high just after the breakdown and fell to its lowest measured value towards the end of the phase.
- Phase B: At the beginning of this phase, the cathode voltage dropped by ∼15 V in a time less than 0.5 s. This drop was associated with the simultaneous appearance of a luminous "blue glow" at the center of the tungsten cathode (see Fig. 4(g)). Then, for the next ∼30 s, the cathode voltage remained nearly constant. During this time, the "blue glow" began to spread towards the edge of the cathode. Towards the end of the phase, V_d started to decrease quickly. OES showed that at the beginning of phase B, all the emission line intensities exhibited a sharp increase as shown in Fig. 4(e). The maximum increase was observed for the WI line and the minimum for the ArII line.[59] All the lines intensities reached a maximum and started to decrease before the end of the phase. Regarding the electron density, it was continuously increasing throughout this phase.
- Phase C: The cathode voltage decreased steadily ($\Delta V_d \sim 150$ V) to its lowest value in ∼200 − 250 s. By the end of phase C, the "blue glow" had spread over the cathode area and could not be distinguished with the naked eye. OES showed that line intensities of all species continued to decrease (see Figs. 4(a)–4(d)). Argon lines reached a minimum towards the end of phase C and the WII line decreased to noise level. Regarding the electron density, it increased at a faster rate than in phase B and, reached a maximum at the end of phase C.
- Phase D: The cathode voltage exhibited a slow increase. The emission lines of ArI and ArII followed the discharge voltage and exhibited a small increase. On the contrary, the intensity of the WI line continued to decrease slowly until the end of the discharge. The electron density also decreased during the whole phase (see Figs. 4(a)–4(d)).

The 656 nm H_α line intensity was also followed in order to monitor the impurity content of the plasma due to the outgasing of the cathode. The line appeared at breakdown and increased in intensity throughout the whole discharge duration (see Fig. 4(b)). Its general evolution indicates that the density of impurities increased during the discharge as expected in experiments without gas flow.

IV. DISCUSSION

As described in Sec. III, the behaviour of the line intensities and the cathode voltage was different from what was observed in similar conditions with a graphite cathode[40] and also from chemically active RF discharges.[29,60] In general, the dust particles in the plasma are getting negatively charged due to their interaction with ions and electrons. In RF discharges, the growth of dust particles and the resulting decreasing electron density induce a modification of the amplitude of the RF current harmonics and a decrease (in absolute value) of the self-bias voltage of the powered electrodes.[29,37,60] In a DC discharge with fixed current, when

Downloaded 03 May 2013 to 147.94.187.189. This article is copyrighted as indicated in the abstract. Reuse of AIP content is subject to the terms at: http://pop.aip.org/about/rights_and_permissions

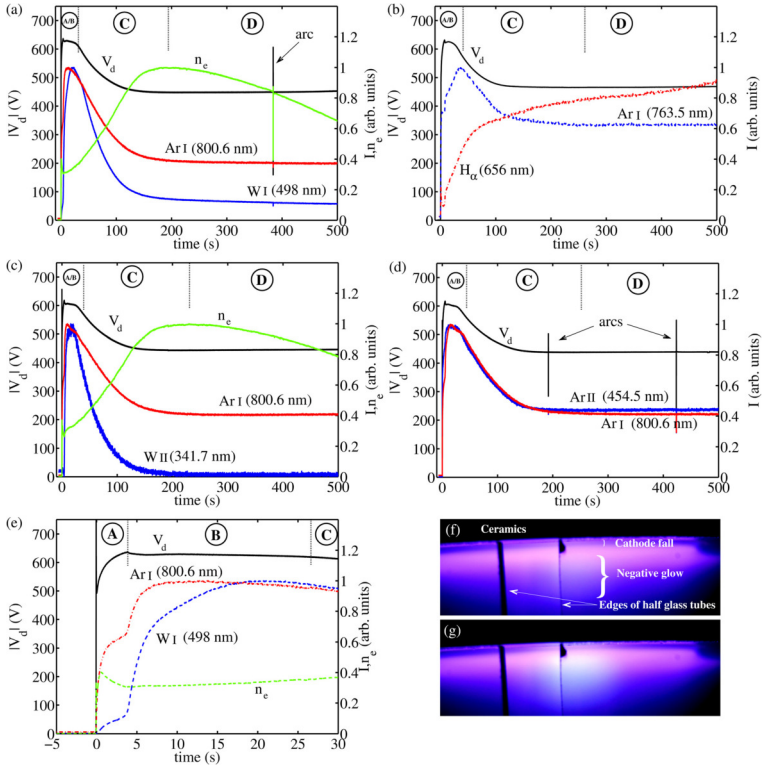

FIG. 4. ((a)–(d)) Evolutions of the cathode voltage V_d and line intensities (ArI, ArII, WI, WII, and H_α) as a function of time. V_d is the reference plot in each case. The signals are divided in four phases: A, B, C, and D. (e) Zoom of (a). (f) Picture of the cathode-fall region and the beginning of the negative glow at the end of phase A. (g) Same as (f) at the start of phase B. In (g) and (f), the contrast was increased for an improved visibility.

the dust particles are growing, the density of free electrons in the discharge is decreasing. Consequently, the cathode voltage should increase in order to maintain the ionisation necessary to sustain the imposed discharge current. This effect was clearly observed for carbon dust particles grown in our previous experiments similar to those discussed in this paper.[40] In the present experiments, this behaviour was not observed. Here are some possible explanations associated with the specificity of the tungsten cathode,

- As can be seen in Figs. 4(a) and 4(c), both neutral and ionised tungsten line intensities followed the same trend. They exhibited a strong increase after the sharp drop of the cathode voltage (beginning of phase B). One possible explanation is the increase of the tungsten atom density in the plasma. This might be surprising as one expect the sputtering yield to diminish when the cathode voltage decreases as the energy of the impinging ions and fast neutrals also decreases. However, it can be explained by comparing the physical properties of tungsten oxide and those of pure tungsten. When exposed to the residual oxygen in the chamber, a tungsten oxide layer is formed on the cathode surface. Typical time scales for the formation of a impurity monolayer are in the order of few seconds at a base pressure of $\sim 10^{-6}$ mbar.[61,62] For the chosen discharge parameters, the calculated mean energy of the ions and fast neutrals sputtering the cathode is 50–60 eV.[49] It is known that for low energy ion bombardment ($\lesssim 100$ eV), the secondary electron emission of tungsten oxide is lower than that of pure tungsten while the contribution of neutrals is negligible.[63,64] This oxide layer is sputtered away during the phase A. When non-oxidised tungsten is exposed to the plasma, the secondary electron emission becomes higher.[63,64] This leads to an increase of the ionisation in the negative glow. As a consequence, the electron density increases during phase B (see Fig. 4(e)). As the current is kept constant, the cathode voltage drops at the beginning of phase B. The strong increase of tungsten lines when the cathode voltage drops (beginning of phase B) account for the fact that the sputtering yield of tungsten is higher than the one of tungsten oxide.[65,66] A similar effect was observed by Penning *et al.* and was associated to the removal of an oxide layer from the cathode (see page 86 of Ref. 67).
- A strong increase of the WII line intensity was observed during phase B. This indicates that a part of the sputtered tungsten atoms were ionised in the discharge. In magnetron discharges, the sputtering of metal species in an argon plasma is known to decrease the electron temperature due to low ionisation potential of metals. It was put in evidence by a decrease of the intensity of argon optical emission in a discharge in which aluminium was present.[68,69] In our case, as the ionisation energy of tungsten atoms (7.56 eV) is lower than both the ionisation energy of argon (15.76 eV) and the excitation energy of argon metastables (11.56 eV and 13.15 eV), they can be ionised through electron impact ionisation and Penning ionisation. Thus, an effect similar to that in magnetron discharges can occur, which will result in a decrease of the electron temperature. Microwave interferometry showed that the electron density was increasing, while the intensity of argon emission was decreasing, supporting our hypothesis. The ionisation of tungsten could also partially explain the rise of the electron density. In phases A and B, the effect of the nanoparticle growth is thus overcome by the influence of the cathode material.
- In phase C, all signals were decreasing at a reduced rate except the electron density, which was still increasing. While the modification of the tungsten surface was still playing an important role, the dust particles were growing in the plasma and the charging phenomena became more and more important. At the end of phase C, dust particles counterbalanced the effect of the modification of the cathode surface.
- In Phase D, the dust particles, whose maximum size increased continuously due to agglomeration, played the main role in the discharge evolution. As also observed in graphite sputtering DC discharges,[40] the discharge parameters showed the expected behaviour: (i) V_d increased in order to maintain the ionisation necessary to sustain the imposed discharge current, (ii) the electron density decreased and, (iii) argon line intensities followed V_d likely indicating a rise of the electron temperature.

V. CONCLUSION

In this article, the growth of tungsten nanoparticles from the sputtering of a tungsten cathode in DC argon glow discharges was investigated. The study was performed at fixed argon pressure and constant discharge current.

We have shown that the nanoparticles are formed by successive agglomerations. First, tungsten nanocrystallites (∼2–4 nm) agglomerate into ∼30 nm primary particles. These primary particles further agglomerate to form particles with size up to ∼150 nm. The evolution of the dust particle size distribution revealed two important features: (i) 30 nm primary particles always remain the most probable (except for very short plasma durations) and (ii) for long discharge duration, big particles are growing in the plasma resulting in the appearance of a second hump in the distribution function. These results are significantly different from our earlier investigations in graphite sputtering DC glow discharge[40] in which the mean size evolved continuously up the appearance of a second nucleation. The evolution of the discharge voltage, electron density, and emission line intensities were also different from graphite sputtering DC glow discharge.[40] With a tungsten cathode, the signals were divided in four distinct phases exhibiting unusual distinctive features. We explain the evolution of the different parameters by a competition between the surface state of the tungsten cathode and the influence of the growing nanoparticles. The differences with a similar system[40] and chemically active plasmas[29,38] suggest that the nanoparticle growth and its influence on discharge parameters is system and material dependent. Future experiments will be devoted to full spectroscopic studies under identical conditions and the development of a collisional-radiative model in order to follow the evolution of the electron temperature.

ACKNOWLEDGMENTS

This work was supported by ANR Contract (No. ANR-09-BLAN-0070-01-CRWTH) and by Euratom/CEA association in the framework of FR-FCM and EFDA.

[1]M. Boutonnet, S. Lgdberg, and E. E. Svensson, Curr. Opin. Colloid Interface Sci. **13**, 270 (2008).
[2]H. Takagi, H. Ogawa, Y. Yamazaki, A. Ishizaki, and T. Nakagiri, Appl. Phys. Lett. **56**, 2379 (1990).
[3]P. R. i Cabarrocas, P. Gay, and A. Hadjadj, J. Vac. Sci. Technol. **14**, 655 (1996).
[4]F. Wang, R. Deng, J. Wang, Q. Wang, Y. Han, H. Zhu, X. Chen, and X. Liu, Nature Mater. **10**, 968 (2011).
[5]G. Gay, D. Belhachemi, J. P. Colonna, S. Minoret, P. Brianceau, D. Lafond, T. Baron, G. Molas, E. Jalaguier, A. Beaurain *et al.*, Appl. Phys. Lett. **97**, 152112 (2010).
[6]L. Qi, P. H. McMurry, D. J. Norris, and S. L. Girshick, Langmuir **27**, 12677 (2011).
[7]T. Kobayashi, Y. Imade, D. Shishihara, K. Homma, M. Nagao, R. Watanabe, T. Yokoi, A. Yamada, R. Kanno, and T. Tatsumi, J. Power Sources **182**, 621 (2008).
[8]M. Nagao, A. Hayashi, and M. Tatsumisago, J. Mater. Chem. **22**, 10015 (2012).
[9]J. Yu, E. G. Wang, and X. D. Bai, Appl. Phys. Lett. **78**, 2226 (2001).
[10]K. Zdansky, P. Kacerovsky, J. Zavadil, J. Lorincik, and A. Fojtik, Nanoscale Res. Lett. **2**, 450 (2007).
[11]N. Garg, A. Mohanty, N. Lazarus, L. Schultz, T. R. Rozzi, S. Santhanam, L. Weiss, J. L. Snyder, G. K. Fedder, and R. Jin, Nanotechnology **21**, 405501 (2010).
[12]J. Jin, J. J. Lee, B.-S. Bae, S. J. Park, S. Yoo, and K. Jung, Org. Electron. **13**, 53 (2012).
[13]O. Salata, J. Nanobiotechnol. **2**, 3 (2004).

Downloaded 03 May 2013 to 147.94.187.189. This article is copyrighted as indicated in the abstract. Reuse of AIP content is subject to the terms at: http://pop.aip.org/about/rights_and_permissions

Downloaded 03 May 2013 to 147.94.187.189. This article is copyrighted as indicated in the abstract. Reuse of AIP content is subject to the terms at: http://pop.aip.org/about/rights_and_permissions

[14]B. Samanta, H. Yan, N. O. Fischer, J. Shi, D. J. Jerry, and V. M. Rotello, J. Mater. Chem. **18**, 1204 (2008).
[15]C. Hollenstein, J. L. Dorier, J. Dutta, L. Sansonnens, and A. A. Howling, Plasma Sources Sci. Technol. **3**, 278 (1994); A. A. Howling, L. Sansonnens, J.-L. Dorier, and C. Hollenstein, J. Appl. Phys. **75**, 1340 (1994).
[16]A. A. Fridman, L. Boufendi, T. Hbid, B. V. Potapkin, and A. Bouchoule, J. Appl. Phys. **79**, 1303 (1996).
[17]S. Stoykov, C. Eggs, and U. Kortshagen, J. Phys. D: Appl. Phys. **34**, 2160 (2001).
[18]K. De Bleecker, A. Bogaerts, and W. Goedheer, Phys. Rev. E **73**, 026405 (2006).
[19]A. Michau, G. Lombardi, L. Colina Delacqua, M. Redolfi, C. Arnas, P. Jestin, X. Bonnin, and K. Hassouni, Plasma Chem. Plasma Process. **32**, 451 (2012); A. Michau, G. Lombardi, C. Arnas, L. C. Delacqua, M. Redolfi, X. Bonnin, and K. Hassouni, Plasma Sources Sci. Technol. **19**, 034023 (2010).
[20]K. G. Spears, T. J. Robinson, and R. M. Roth, IEEE Trans. Plasma Sci. **14**, 179 (1986).
[21]A. Bouchoule and L. Boufendi, Plasma Sources Sci. Technol. **2**, 204 (1993); L. Boufendi, J. Gaudin, S. Huet, G. Viera, and M. Dudemaine, Appl. Phys. Lett. **79**, 4301 (2001).
[22]E. Stoffels, W. W. Stoffels, G. M. W. Kroesen, and F. J. de Hoog, J. Vac. Sci. Technol. **14**, 556 (1996).
[23]P. R. i Cabarrocas, A. F. i Morral, S. Lebib, and Y. Poissant, Pure Appl. Chem. **74**, 359 (2002); P. R. i Cabarrocas, T. Nguyen-Tran, Y. Djeridane, A. Abramov, E. Johnson, and G. Patriarche, J. Phys. D: Appl. Phys. **40**, 2258 (2007).
[24]B. Ganguly, A. Garscadden, J. Williams, and P. Haaland, J. Vac. Sci. Technol. A **11**, 1119 (1993).
[25]G. Praburam and J. Goree, Astrophys. J. **441**, 830 (1995).
[26]D. Samsonov and J. Goree, J. Vac. Sci. Technol. A **17**, 2835 (1999).
[27]C. Arnas and A. A. Mouberi, J. Appl. Phys. **105**, 063301 (2009); C. Arnas, A. Mouberi, K. Hassouni, A. Michau, G. Lombardi, X. Bonnin, F. Bénédic, and B. Pégourié, J. Nucl. Mater. **390–391**, 140 (2009).
[28]C. Deschenaux, A. Affolter, D. Magni, C. Hollenstein, and P. Fayet, J. Phys. D: Appl. Phys. **32**, 1876 (1999).
[29]S. Hong, J. Berndt, and J. Winter, Surf. Coat. Technol. **174–175**, 754 (2003); Plasma Sources Sci. Technol. **12**, 46 (2003).
[30]E. Kovačević, I. Stefanović, J. Berndt, and J. Winter, J. Appl. Phys. **93**, 2924 (2003).
[31]M. Hundt, P. Sadler, I. Levchenko, M. Wolter, H. Kersten, and K. K. Ostrikov, J. Appl. Phys. **109**, 123305 (2011).
[32]S. Mitic, M. Y. Pustylnik, G. E. Morfill, and E. Kovačević, Opt. Lett. **36**, 3699 (2011).
[33]J. Winter, Phys. Plasmas **7**, 3862 (2000).
[34]J. Sharpe, D. Petti, and H.-W. Bartels, Fusion Eng. Design **63–64**, 153 (2002).
[35]C. Arnas, C. Pardanaud, C. Martin, P. Roubin, G. D. Temmerman, and G. Counsell, J. Nucl. Mater. **401**, 130 (2010); C. Arnas, C. Martin, P. Roubin, B. Pégourié, G. D. Temmerman, K. Hassouni, A. Michau, G. Lombardi, and X. Bonnin, Plasma Phys. Controlled Fusion **52**, 124007 (2010).
[36]R. Smirnov, S. Krasheninnikov, A. Pigarov, A. Roquemore, D. Mansfield, and J. Nichols, J. Nucl. Mater. **415**, S1067 (2011); A. Pigarov, R. Smirnov, S. Krasheninnikov, T. Rognlien, M. Rosenberg, and T. Soboleva, J. Nucl. Mater. **363–365**, 216 (2007).
[37]M. Mikikian, M. Cavarroc, L. Couëdel, and L. Boufendi, Phys. Plasmas **13**, 092103 (2006).
[38]M. Cavarroc, M. Mikikian, Y. Tessier, and L. Boufendi, Phys. Rev. Lett. **100**, 045001 (2008).
[39]I. Stefanović, N. Sadeghi, and J. Winter, J. Phys. D: Appl. Phys. **43**, 152003 (2010).
[40]C. Arnas, A. Michau, G. Lombardi, L. Couëdel, and K. K. Kumar, Phys. Plasmas **20**, 013705 (2013).
[41]M. J. McCaughey and M. J. Kushner, J. Appl. Phys. **69**, 6952 (1991).
[42]J. P. Boeuf and P. Belenguer, J. Appl. Phys. **71**, 4751 (1992).
[43]U. Kortshagen and U. Bhandarkar, Phys. Rev. E **60**, 887 (1999).
[44]T. Ryu, H. Sohn, K. S. Hwang, and Z. Z. Fang, Int. J. Refract. Met. Hard Mater. **27**, 149 (2009).
[45]O. Alm, L. Landstrm, M. Boman, C. Granqvist, and P. Heszler, Appl. Surf. Sci. **247**, 262 (2005).
[46]H. Nersisyan, J. Lee, and C. Won, Combust. Flame **142**, 241 (2005).
[47]L. Landström, Z. Márton, N. Arnold, H. Högberg, M. Boman, and P. Heszler, J. Appl. Phys. **94**, 2011 (2003).
[48]M. Kassaee, S. Soleimani-Amiri, and F. Buazar, J. Manufact. Process. **12**, 85 (2010).
[49]C. Dominique and C. Arnas, J. Appl. Phys. **101**, 123304 (2007).
[50]L. Boufendi, A. Plain, J. P. Blondeau, A. Bouchoule, C. Laure, and M. Toogood, Appl. Phys. Lett. **60**, 169 (1992).
[51]S. Dap, D. Lacroix, F. Patisson, R. Hugon, L. de Poucques, and J. Bougdira, New J. Phys. **12**, 093014 (2010).
[52]D. Samsonov and J. Goree, Phys. Rev. E **59**, 1047 (1999).
[53]T. Matsoukas, M. Russell, and M. Smith, J. Vac. Sci. Technol. A **14**, 624 (1996).
[54]L. Ravi and S. L. Girshick, Phys. Rev. E **79**, 026408 (2009).
[55]B. M. Annaratone, Y. Elskens, C. Arnas, T. Antonova, H. M. Thomas, and G. E. Morfill, New J. Phys. **11**, 103013 (2009).
[56]V. N. Tsytovich, Phys. Usp. **40**, 53 (1997).
[57]M. Lampe, G. Joyce, G. Ganguli, and V. Gavrishchaka, Phys. Plasmas **7**, 3851 (2000).
[58]Y. Mankelevich, M. Olevanov, A. Pal, T. Rakhimova, A. Ryabinkin, A. Serov, and A. Filippov, Plasma Phys. Rep. **35**, 191 (2009).
[59]It is worth noting that the tungsten line exhibited a much stronger increase.
[60]M. Cavarroc, M. C. Jouanny, K. Radouane, M. Mikikian, and L. Boufendi, J. Appl. Phys. **99**, 064301 (2006); M. Cavarroc, M. Mikikian, G. Perrier, and L. Boufendi, Appl. Phys. Lett. **89**, 013107 (2006).
[61]M. Ohring, *Materials Science and Thin Film*, 2nd ed. (Academic Press, London, 2001).
[62]J. A. Venables, *Introduction to Surface and Thin Film Processes* (Cambridge University Press, 2000).
[63]G. Vida, V. Josepovits, M. Gyor, and P. Deák, Microsc. Microanal. **9**, 337 (2003).
[64]A. V. Phelps and Z. L. Petrovic, Plasma Sources Sci. Technol. **8**, R21 (1999).
[65]R. Boulmani, M. Bendahan, C. Lambert-Mauriat, M. Gillet, and K. Aguir, Sens. Actuators B **125**, 622 (2007).
[66]J. Heller, Thin Solid Films **17**, 163 (1973).
[67]G. Francis, "The glow discharge at low pressure," in *Gas Discharges II* (Springer-Verlag, 1956), pp. 53–208.
[68]J. Hopwood and F. Quian, J. Appl. Phys. **78**, 758 (1995).
[69]M. Dickson, F. Quian, and J. Hopwood, J. Vac. Sci. Technol. A **15**, 340 (1997).

Downloaded 03 May 2013 to 147.94.187.189. This article is copyrighted as indicated in the abstract. Reuse of AIP content is subject to the terms at: http://pop.aip.org/about/rights_and_permissions

Detrapping of tungsten nanoparticles in a direct-current argon glow discharge

L. Couëdel,[a] Kishor Kumar K.,[b] and C. Arnas
Laboratoire de Physique des Interactions Ioniques et Moléculaires, CNRS, Aix-Marseille Université, 13397 Marseille, France

(Received 3 October 2014; accepted 20 November 2014; published online 11 December 2014)

Nanoparticles are grown from the sputtering of a tungsten cathode in a direct current argon glow discharge. Laser light scattering of a vertical laser sheet going through the plasma reveals that the dust particle cloud is compressed and pushed towards the anode during the discharge. Scanning electron microscopy images of substrates exposed to the plasma for given durations show that dust particles are continuously falling down on the anode during the discharge. These observations are explained by the fact that the electrostatic force at the negative glow-anode sheath boundary cannot balance the ion drag, gravity, and thermophoresis forces for particles of more than a few tens of nanometres in diameter. © *2014 AIP Publishing LLC*. [http://dx.doi.org/10.1063/1.4903465]

I. INTRODUCTION

Dusty or complex plasmas are partially ionised gas which contains solid dust particles.[1,2] These particles acquire an electric charge due to their interactions with the surrounding ions and electrons. In laboratory experiments, particles can be either injected or grown directly inside the plasma. For example, they can be produced in astrophysical plasmas,[3] in industrial plasma processing reactors,[4] in tokamaks from the physical and chemical erosions of the wall,[5] etc.

The production of nanoparticles in low pressure, low temperature plasmas has been extensively studied. It was shown that the particles can be generated following specific chemical reactions up to the formation of solid particles. In particular, the growth of nanoparticles in radio-frequency (rf) discharges using reactive gases[6–12] or by sputtering of a cathode[13] was carefully investigated. In such systems, it was shown that the dust particles are confined in the plasma and that their growth occurs in cycles.[11,12,14] In particular, the growth of new particles can occur when the previous dust cloud is expelled from the central region of the plasma so that the conditions are again favourable to nucleation and growth.[12,14] The dust cloud can be expelled towards the edges of the discharge when the dust density is too high and/or the particles are too big so that the repulsion forces become larger than the confining forces.[15–17] The particles can also fall on the electrode when they reach a critical size and their weight cannot be balanced by the confining forces. In rf discharges, this is normally the case when the particles reach a few tens of micrometers in diameter.[18]

The growth of nanoparticles by cathode sputtering in direct-current (dc) glow discharges has also been reported.[19–22] Using an aluminium cathode, it was shown that the spatial profile of the particle cloud was very sensitive to discharge parameters, especially the applied voltage.[19] Moreover, studies on the production of nanoparticles in dc discharges by sputtering of a graphite cathode have shown a strong coupling between plasma and discharge parameters and, the particle growth kinetics.[21] In a recent study in which we used a tungsten cathode in similar condition as in Ref. 21, we showed that the evolution of the dust particle size distribution (PSD) was quite unusual:[22,23]

- small particles were always observed indicating constant nucleation,
- growth by agglomeration did not seem to saturate as reported for carbon nanoparticles,
- there was a strong dispersion in the appearance time of the second dust particle generation.

Furthermore, the evolution of the discharge and plasma parameters was a competition between the influence of the cathode surface state (tungsten oxidation) and the influence of the charging process of the nanoparticles.[22] The latter was evident only after a few hundreds of seconds. However, the motion of the dust particle cloud was not investigated and it was supposed that the dust particles remained confined in the plasma until the discharge was switched off.

In this article, we investigated the behaviour of a nanoparticle cloud grown by sputtering of a tungsten cathode in a dc argon glow discharge with similar conditions to those of Refs. 21 and 22. The aim of these investigations was to link the previously reported evolution of the PSDs to the dust cloud motion. For this purpose, laser light scattering of a vertical laser sheet going through the plasma revealed that the dust particle cloud was compressed and pushed towards the anode during the discharge. By exposing substrates to the plasma on the anode side of the discharge, it was also found that dust particles were continuously falling down on the anode. This result is explained by the inhomogeneous nature of the dc glow discharge. Due to the low electron temperature and the weak electric field in the anode sheath, the confining electric force is too weak to balance the ion drag, gravity, and thermophoretic forces for particles of more than a few tens of nanometres in diameter.

[a]Electronic mail: lenaic.couedel@univ-amu.fr
[b]Present address: Center for Plasma-Materials Interactions, 216 Talbot Laboratory, 104 S Wright Street, University of Illinois at Urbana-Champaign, 61801 Illinois, USA.

 © 2014 AIP Publishing LLC

This article is copyrighted as indicated in the article. Reuse of AIP content is subject to the terms at: http://scitation.aip.org/termsconditions. Downloaded to IP: 147.94.187.189 On: Thu, 11 Dec 2014 14:58:22

II. EXPERIMENTAL SET-UP

A detailed description of the experimental set-up is given in Ref. 22. The tungsten nanoparticles were grown in a dc argon glow discharge initiated between a ∼10 cm diameter tungsten cathode and a stainless-steel grounded anode. The inter-electrode distance was 10 cm. The cathode was enclosed in an insulating ceramic holder so that only one side was exposed to the plasma. Two glass half-cylinders were used to confine the plasma. A 1 cm gap was kept between them for optical studies (see Fig. 1). A static argon pressure of 0.6 mbar (no gas flow) was set during the experiments. The electrode assembly was contained in a cylindrical vacuum chamber of 30 cm diameter and 40 cm length. An oil diffusion pump achieved a base pressure of $\lesssim 10^{-6}$ mbar. A manually operated gate valve was used to isolate the chamber from the oil diffusion pump during experiments.

A regulated power supply (Sefelec HT15A, 1 kV, 300 mA) was used to bias the cathode. The discharge current density was kept at a constant value (0.53 mA cm^{-2}). The current variations were less than 0.05%. The discharge parameters were such that the plasma mainly consisted of a negative glow. The discharge voltage was the free parameter whose time evolution was acquired during the discharge. Under the chosen operating conditions, the cathode was sputtered and tungsten nanoparticles were grown. More details about the evolution of discharge parameters during the nanoparticle growth are given in Ref. 22.

In order to image the dust particle cloud and to measure the evolution of the PSD during the discharge, two diagnostics have been used.

A. Laser light scattering

A 2 cm height vertical laser sheet (40 mW, wavelength $\lambda = 532$ nm) was passing through the electrode assembly in the gap between the half-cylinders (see Fig. 1). The scattered light by the dust particles was recorded at 90° by a CCD camera (BASLER ACE acA1300–60 gm). A low frame rate of 1 frame per second and a long exposure time of 0.5 s were used in order to detect the weak scattered light signal. The position of the laser sheet between the electrodes could be chosen at the time of the experiment. A bandpass filter centred on the laser wavelength was placed in front of the camera in order to minimise the recorded plasma light.

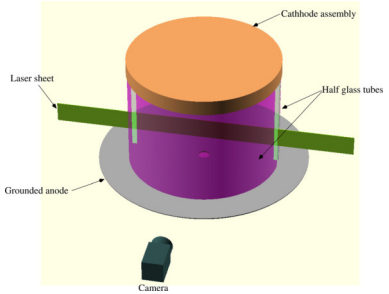

FIG. 1. Schematic of the cathode assembly.

B. Scanning electron microscopy (SEM)

The anode disc had a 1.6 cm diameter hole at the centre through which the tungsten nanoparticles produced during the discharge were collected. Stainless steel foils, mounted on a holder, were used as substrates for collecting the dust. The substrate holder could be manipulated from one of the axial ports of the chamber, such that each of them could be positioned under the hole in the anode. Dust particles were then analysed *ex-situ* using a scanning electron microscope.

Two methods of collection have been used:

(i) The substrate holder was moved under the anode so that successive substrates were exposed to the plasma only during a given time interval.
(ii) The substrate saw the end of the discharge. Note that in this case, the substrate could be or not exposed to the plasma during the whole discharge duration.

III. RESULTS

A. Laser light scattering

During the experiment, the vertical laser sheet was grazing the anode. In Fig. 2(a), snapshots of the video at different instants after the plasma ignition are presented. The time evolutions of the recorded light signal at different positions above the anode are also shown as well as the evolution of the cathode voltage V_c (Fig. 2(b)). The light recorded above the laser sheet (positions 2.33 cm and 2.14 cm) represents the residual plasma light. This allowed us to discriminate the scattered light from the plasma emission. During the first ∼150 s, no particles could be detected in the video images. However, it is known from the cathode voltage evolution (Fig. 2(b)) that dust particles were already present between the electrodes (for more details, see Ref. 22). It probably indicates that either the dust particles were not located above the anode or they were too small and/or their density was too low to be detectable through laser light scattering. From $t \sim 150$ s, scattered light could be detected at the top edge of the laser sheet. Note that this appearance time varied of ∼30 s from one experiment to the other as the dust particle growth kinetics is very sensitive to initial conditions. This behaviour was also reported in rf discharges in which particles were growing from the sputtering of a polymer layer.[24] At t ∼ 180 s, a dust cloud could be observed across the whole laser sheet except in the anode sheath (a ∼ 0.15 cm wide region above the anode). Up to t ∼ 250 s, the scattered light signal was increasing across the whole laser sheet. This indicated that the dust particle cloud was getting denser and/or the particles were getting bigger. In Fig. 2(a) (snapshot at $t = 240$ s), the dust cloud seems to be homogeneous. This is also supported by the recorded scattered light intensities at different height in the laser sheet which have almost the same values.

This article is copyrighted as indicated in the article. Reuse of AIP content is subject to the terms at: http://scitation.aip.org/termsconditions. Downloaded to IP: 147.94.187.189 On: Thu, 11 Dec 2014 14:58:22

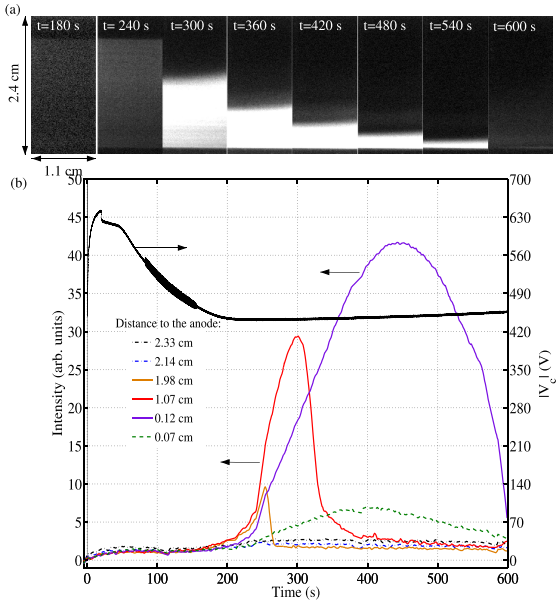

FIG. 2. (a) Snapshots of the video. The laser sheet was grazing the anode. At $t = 180$ s, luminosity and contrast were enhanced compared to the other images. (b) Evolution of the cathode voltage as a function of time (right vertical-axis, black plain line) and evolution of the recorded scattered light intensities at different distances from the anode (left vertical-axis). The two highest positions (2.33 cm and 2.14 cm) show intensities recorded outside the laser sheet and show only the residual plasma light. The lowest position (0.07 cm) shows the light intensity recorded in the anode sheath.

For $t \gtrsim 250$ s, the scattered light signal at the top of the laser sheet decreased strongly, while the signal in the middle and at the bottom of the laser sheet (except in the anode sheath) was still strongly growing. From the snapshots of Fig. 2(a), it is clear that the dust cloud was compressed towards the anode. After $t \gtrsim 300$ s, the dust cloud occupied only half of the laser sheet width and was shrinking continuously. It should however be noted that a faint scattered light signal revealed the presence of a second nanoparticle cloud above the main dust cloud (Fig. 2(a) snapshots at $t = 300$ s, $t = 360$ s, $t = 420$ s, $t = 480$ s, and $t = 540$ s). Both clouds were separated by a non-emissive layer. From $t \sim 580$ s, only the second dust cloud was visible above the anode. It should also be noted that from $t \sim 250$ s, the intensity recorded inside the anode sheath was systematically above the residual plasma light signals (see Fig. 2(b), curve at 0.07 cm). It is not clear that this was due to particle falling inside the sheath or due to an anode glow.

B. Scanning electron microscopy

In a previous study,[22] the dust particles were collected at the end of the discharge on substrates exposed to the plasma for the entire experiment duration. In the present study, the samples were exposed to the plasma during a given time interval. Consequently, only the particles which were expelled from the plasma (i.e., falling on the anode) during this time lapse were collected. In Fig. 3, PSDs of particles collected at different moments during two different discharges are shown. For example, in Fig. 3(a), it can be seen that dust particles were collected for all chosen time intervals. The SEM image in the inset of Fig. 3(a) shows particles which fell on the anode from $t = 200$ s to $t = 300$ s. Moreover, the later the substrate is exposed the bigger the particles. A striking difference with the previous study of Kishor Kumar *et al.*[22] was that even for long time, PSDs remained here mono-modal. It was indeed previously shown that for long discharge duration ($t \gtrsim 200$ s), the PSDs were bi-modal. However, in the present case, PSDs are bimodal only when the plasma was switched off (see Sec. II B, method (ii)). For example, the inset of Fig. 3(b) shows the bi-modal distribution obtained at the end of a 500 s plasma. These PSDs were similar to the distributions already reported in Ref. 22. Laser light scattering explains this result: the smallest particles were confined in the negative glow above the cloud of big particles (the dim cloud above the bright cloud) and they could be collected only after the discharge was switched off.

It should be noted that from one experiment to the other, the size and the number of the collected dust particles were not exactly the same. This observation could be explained by the fact that the particle growth kinetics is very sensitive to the initial condition as previously stated. However, it was possible to get a rough estimate of the flux of dust particle falling on the anode. Depending on the experiment, the number of particles collected on a substrate exposed to the plasma during 100 s was $N_p = 1$–$100\ \mu\text{m}^{-2}$ giving a flux of falling particles $\Gamma_p \sim 10^6$–$10^8\ \text{cm}^{-2}\ \text{s}^{-1}$.

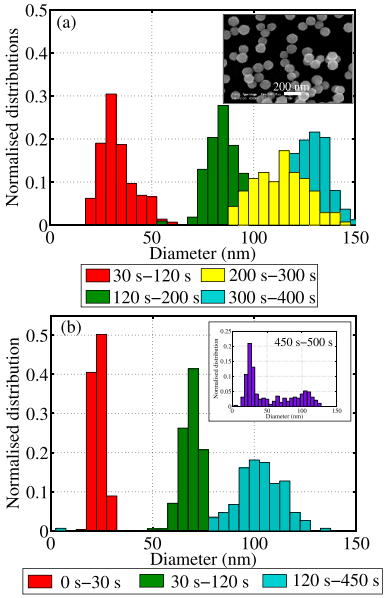

FIG. 3. Normalised PSDs of particles collected on substrates exposed to the plasma at different times after ignition. (a) and (b) are two different experiments with the same discharge parameters. Inset of (a): SEM image of particles collected on a substrate exposed to the plasma from 200 s to 300 s. Inset of (b): normalised PSD of particles collected after the discharge was switched off at $t = 500$ s.

IV. DISCUSSION

In Sec. III, it was shown that nanometre size particles were falling continuously on the anode at a rate $\Gamma_p \sim 10^6$–$10^8\ \text{cm}^{-2}\ \text{s}^{-1}$. This result might be surprising as it is believed that as in rf discharges, growing dust particles remain confined in the inter-electrode space until they are too large (usually a few tens of micrometers) or their density is too high for the confining forces to balance the repulsion forces.[11,15–18,25]

In order to understand why dust particles are constantly falling on the anode during their growth, the forces acting on them must be estimated. Let us first consider the force pushing the particles towards the anode. (a) The gravity force $F_g = (4/3)\pi r_d^3 \rho g$, where r_d is the radius of the dust particle, g the gravitational constant, and ρ the mass density. In our experimental conditions, considering pure tungsten particles, the gravity force was for $r_d = 15$ nm and $r_d = 50$ nm, $|F_g| = 2.5 \times 10^{-18}$ N, and $|F_g| = 9 \times 10^{-17}$ N, respectively. (b) During the discharge, the cathode was heated up to $\sim 100\,^\circ\text{C}$ while the anode stayed at room temperature.[21,26] The dust particle were then subject to a downward thermophoretic force[27–30]

$$F_t = -(32/15) r_d^2 k_{tr} / v_{Tn} \nabla T,$$

where $v_{Tn} = \sqrt{8 k_B T_n / (\pi m_n)}$ is the neutral thermal velocity with k_B the Boltzmann constant, T_n the neutral atom temperature and m_n their mass. ∇T is the temperature gradient, and the thermal conductivity $k_{tr} = (15 k_B/(4m_n)) \mu_{ref} (T/T_{ref})^{\nu}$ with $\mu_{ref} = 2.117 \times 10^{-5}$ Pa s for argon, $T_{ref} = 273$ K and $\nu = 0.81$.[31] In our discharge, considering a temperature gradient $\nabla T = 7$ K/cm, the thermophoretic forces were $|F_t| = 1.5 \times 10^{-17}$ N and $|F_t| = 1.7 \times 10^{-16}$ N for $r_d = 15$ nm and $r_d = 50$ nm, respectively. Note that during our experiments, the motion of the dust cloud and dust collection was performed close to the discharge axis far from the glass wall. Moreover, no convective motion of the dust particle cloud was observed on the video. Consequently, the gas creep effect induced by the thermal gradient was neglected in our force estimate. However, close to the edge of the discharge, this effect might be of great importance as it has been proven to be very efficient to induce strong convective dust motion.[32–34]

In order to estimate the magnitude of forces due to the plasma, it is necessary to have a good approximation of the potential, electric field, electron and ion densities at the boundary between the negative glow and the anode sheath. The structure of a dc glow discharge is stratified and the plasma parameters are inhomogeneous along the discharge axis:

- In the negative glow, the electron distribution function is composed of three electron populations:[35–37] the fast electrons (secondary electrons emitted by the cathode surface and accelerated in the cathode fall region), the intermediate electrons (which ensure the current continuity), and the cold electrons produced by ionisation (with a temperature $T_e \sim 0.1$ eV). The density of the cold electrons is orders of magnitude higher than the densities of intermediate and fast electrons. Modelling performed for our discharge geometry and similar discharge parameters showed that in the negative glow, the contribution of fast and intermediate electrons to the dust particle charging is limited.[36] Consequently, only cold electrons will be considered in the following. Langmuir probe measurements near the cathode[36] have shown that the plasma density in the negative glow is $n \sim 10^{10}\,\text{cm}^{-3}$. The plasma density quickly drops when getting closer to the anode.[38] A density $n \sim 10^9\,\text{cm}^{-3}$ is assumed at the anode sheath boundary.

This article is copyrighted as indicated in the article. Reuse of AIP content is subject to the terms at: http://scitation.aip.org/termsconditions. Downloaded to IP: 147.94.187.189 On: Thu, 11 Dec 2014 14:58:22
This article is copyrighted as indicated in the article. Reuse of AIP content is subject to the terms at: http://scitation.aip.org/termsconditions. Downloaded to IP: 147.94.187.189 On: Thu, 11 Dec 2014 14:58:22

- In the negative glow region, the electric field is weak.[39] Close to the sheath boundary, the plasma potential is positive with respect to the anode potential for high current density.[37] Consequently, the electric field tends to confine negatively charged particles in the inter-electrode space. However, the voltage drop in the anode sheath is around two order of magnitude lower that in the cathode sheath. Hybrid and PIC simulations have shown that the maximum electric field in the anode sheath is 10–20 V/cm and around 1 V/cm at the negative glow anode sheath boundary.[38]

The dust density n_d in the discharge is unknown but typical values for dust particles grown from the sputtering of an electrode in plasmas are in the range[13,40,41] 10^4–10^8 cm^{-3}. Using the orbital motion limited theory[42–44] and the quasi-neutrality condition $n_i = n_e + Z_d n_d$ where $n_{i(e)}$ is the ion (electron) density, one can calculate the dust particle charge number Z_d. Depending on the dust density, one obtains $Z_d = [-5, -4]$ and $Z_d = [-13, -7]$ for $r_d = 15$ nm and $r_d = 50$ nm, respectively. At the anode sheath boundary, two forces tend to push the particles: the ion drag which tends to push the particles on the anode and, the electric force which confines them in the plasma. The ion drag force is[45]

$$F_{di} = F_{di}^{coll} + F_{di}^{coul}$$
$$F_{di}^{coll} = \pi n_i m_i v_i v_s b_c^2$$
$$F_{di}^{coul} = 4\pi n_i m_i v_i v_s b_{\pi/2}^2 \Gamma_c,$$

where m_i is the ion mass, $v_i = \mu_i E$ the ion drift velocity. μ_i is the ion mobility, E the electric field, $v_s = \sqrt{v_{Ti}^2 + v_i^2}$ with the ion thermal velocity $v_{Ti} = v_{Tn}$. $b_c = r_d \cdot (1 - 2e^2 Z_d / (4\pi\epsilon_0 r_d m_i v_s^2))^{1/2}$ is the radius of closest approach, $b_{\pi/2} = e^2 Z_d / (4\pi\epsilon_0 m_i v_s^2)$, and the Coulomb logarithm: $\Gamma_c = 0.5 \cdot \ln((\lambda_{De}^2 + b_{\pi/2}^2)/(b_c^2 + b_{\pi/2}^2))$ where λ_{De} is the electron Debye length. Depending on the strength of the electric field, the ion drag force was in the range $F_{di} \sim 10^{-19}$ -10^{-18} N for 15 nm radius. For 50 nm radius, the ion drag force was in the range $F_{di} \sim 10^{-18}$–10^{-17} N. In both cases, it is negligible compared to the combined influence of the gravity and thermophoretic forces. However, the upward force due to the anode sheath electric field is $F_E \sim 5 \times 10^{-17}$–$5 \times 10^{-16}$ N for $r_d = 15$ nm and $F_E \sim 2 \times 10^{-16}$–$2 \times 10^{-15}$ N for $r_d = 50$ nm.

By balancing the different forces, one can see that the 50 nm radius dust particles can be pushed on the anode by the gravity and the thermophoretic force while the 15 nm radius ones can be confined in the negative glow. In our force estimate, the influence of photoemission[46] which charges the particle positively, i.e., decreases their negative charges, and the influence of a high dust density which can drastically affect the plasma parameters was neglected. However, it was observed experimentally from SEM images that growing dust particles were falling on the anode at all times. Nevertheless, laser light scattering showed that even if the dust cloud was compressed toward the anode, it took hundreds of seconds before it disappeared completely from the plasma. This indicates that the force pushing down the dust particles was of the same order of magnitude as the confining one, as our force estimate shows. Furthermore, small particles were always collected on the substrate at the end of a discharge as shown here and in our previous studies.[22] On the contrary, they were only collected at the beginning of the discharge for substrates exposed to the plasma at the beginning of the experiments (see Sec. II B, method (i)). These results indicate that small dust particles were always produced in the plasma and located above the big particles (first generation), these last ones being expelled little by little. As the big particles are evacuated, favourable conditions for a constant formation occur in the upper part of the negative glow.

V. CONCLUSION

In this article, it was shown that in dc argon glow discharges, dust nanoparticles were pushed towards the anode located at the bottom of the discharge set-up and could be detrapped and fell on it. Due to a low electron temperature and weak electric field in the anode sheath, the electric force cannot balance the ion drag, thermophoretic, and the gravity forces as soon as the particle size reaches a few tens of nanometres. The previous observation of $r_d \sim 15$ nm particles when the discharge was operated with different durations[22] can be explained by the constant nucleation and growth of particles in the upper part of the discharge (cathode side). Indeed, as the big particles are evacuated, favourable condition for nucleation and growth might occur at all time at the top of the negative glow.

ACKNOWLEDGMENTS

This work was supported by ANR contract (No. ANR-09-BLAN-0070-01-CRWTH) and by Euratom/CEA association in the framework of FR-FCM and EFDA.

[1]A. Bouchoule, *Dusty Plasmas: Physics, Chemistry and Technological impacts in Plasma Processing* (Wiley, New York, 1999).
[2]G. E. Morfill and A. V. Ivlev, Rev. Mod. Phys. **81**, 1353 (2009).
[3]C. K. Goertz and G. Morfill, Icarus **53**, 219 (1983); C. J. Mitchell, M. Horanyi, O. Havnes, and C. C. Porco, Science **311**, 1587 (2006).
[4]G. S. Selwyn, J. Singh, and R. S. Bennett, J. Vac. Sci. Technol. A **7**, 2758 (1989); L. Boufendi, J. Gaudin, S. Huet, G. Viera, and M. Dudemaine, Appl. Phys. Lett. **79**, 4301 (2001); D. Vollath, J. Nanopart. Res. **10**, 39 (2008).
[5]J. Winter, Plasma Phys. Controlled Fusion **40**, 1201 (1998); J. Sharpe, D. Petti, and H.-W. Bartels, Fusion Eng. Des. **63–64**, 153 (2002); C. Arnas, C. Pardanaud, C. Martin, P. Roubin, G. D. Temmerman, and G. Counsell, J. Nucl. Mater. **401**, 130 (2010).
[6]A. Bouchoule and L. Boufendi, Plasma Sources Sci. Technol. **2**, 204 (1993).
[7]C. Hollenstein, Plasma Phys. Controlled Fusion **42**, R93 (2000).
[8]C. Hollenstein, J. L. Dorier, J. Dutta, L. Sansonnens, and A. A. Howling, Plasma Sources Sci. Technol. **3**, 278 (1994),.
[9]Y. Watanabe, J. Phys. D: Appl. Phys. **39**, R329 (2006).
[10]C. Deschenaux, A. Affolter, D. Magni, C. Hollenstein, and P. Fayet, J. Phys. D: Appl. Phys. **32**, 1876 (1999).
[11]S. Hong, J. Berndt, and J. Winter, Plasma Sources Sci. Technol. **12**, 46 (2003).
[12]M. Hundt, P. Sadler, I. Levchenko, M. Wolter, H. Kersten, and K. K. Ostrikov, J. Appl. Phys. **109**, 123305 (2011).
[13]D. Samsonov and J. Goree, J. Vac. Sci. Technol. A **17**, 2835 (1999).
[14]M. Cavarroc, M. Mikikian, Y. Tessier, and L. Boufendi, Phys. Rev. Lett. **100**, 045001 (2008).
[15]A. A. Howling, C. Hollenstein, and P. Paris, Appl. Phys. Lett. **59**, 1409 (1991).

This article is copyrighted as indicated in the article. Reuse of AIP content is subject to the terms at: http://scitation.aip.org/termsconditions. Downloaded to IP: 147.94.187.189 On: Thu, 11 Dec 2014 14:58:22

[16]P. R. i Cabarrocas, P. Gay, and A. Hadjadj, J. Vac. Sci. Technol. A **14**, 655 (1996).
[17]F. Greiner, J. Carstensen, N. Khler, I. Pilch, H. Ketelsen, S. Knist, and A. Piel, Plasma Sources Sci. Technol. **21**, 065005 (2012),.
[18]T. Nitter, Plasma Sources Sci. Technol. **5**, 93 (1996).
[19]G. M. Jellum and D. B. Graves, J. Appl. Phys. **67**, 6490 (1990).
[20]C. Arnas, A. Mouberi, K. Hassouni, A. Michau, G. Lombardi, X. Bonnin, F. Bénédic, and B. Pégourié, J. Nucl. Mater. **390–391**, 140 (2009).
[21]C. Arnas, A. Michau, G. Lombardi, L. Couëdel, and Kishor Kumar K., Phys. Plasmas **20**, 013705 (2013).
[22]Kishor Kumar K., L. Couëdel, and C. Arnas, Phys. Plasmas **20**, 043707 (2013).
[23]Kishor Kumar K., L. Couëdel, and C. Arnas, J. Plasma Phys. **80**, 849 (2014).
[24]M. Mikikian, M. Cavarroc, L. Couëdel, and L. Boufendi, Phys. Plasmas **13**, 092103 (2006).
[25]J. H. Chu, J.-B. Du, and I. Lin, J. Phys. D: Appl. Phys. **27**, 296 (1994).
[26]C. Arnas and A. A. Mouberi, J. Appl. Phys. **105**, 063301 (2009).
[27]Z. Li and H. Wang, Phys. Rev. E **70**, 021205 (2004).
[28]L. Waldmann, Z. Naturforsch. **14a**, 589 (1959).
[29]H. Rothermel, T. Hagl, G. E. Morfill, M. H. Thoma, and H. Thomas, Phys. Rev. Lett. **89**, 175001 (2002).
[30]The thermophoretic force expression used by Rothermel *et al.*[29] is almost the same as the original expression derived by Waldmann,[28] the difference being in the multiplicative coefficient, and gives the same result within experimental errorbars (∼30%).
[31]M. A. Gallis, D. J. Rader, and J. R. Torczynski, Aerosol Sci. Technol. **36**, 1099 (2002).
[32]S. Mitic, R. Sütterlin, A. V. I. H. Höfner, M. H. Thoma, S. Zhdanov, and G. E. Morfill, Phys. Rev. Lett. **101**, 235001 (2008).
[33]M. Schwabe, M. Rubin-Zuzic, S. Zhdanov, A. V. Ivlev, H. M. Thomas, and G. E. Morfill, Phys. Rev. Lett. **102**, 255005 (2009).
[34]M. Schwabe, L.-J. Hou, S. Zhdanov, A. V. Ivlev, H. M. Thomas, and G. E. Morfill, New J. Phys. **13**, 083034 (2011).
[35]V. I. Kolobov and L. D. Tsendin, Phys. Rev. A **46**, 7837 (1992).
[36]A. Michau, G. Lombardi, L. Colina Delacqua, M. Redolfi, C. Arnas, P. Jestin, X. Bonnin, and K. Hassouni, Plasma Chem. Plasma Process. **32**, 451 (2012).
[37]L. D. Tsendin, Plasma Sources Sci. Technol. **20**, 055011 (2011).
[38]Z. Donkó, P. Hartmann, and K. Kutasi, Plasma Sources Sci. Technol. **15**, 178 (2006).
[39]J. D. Cobine, *Gaseous Conductors: Theory and Engineering Applications* (Dover Publications, New York, 1958).
[40]G. M. Jellum and D. B. Graves, Appl. Phys. Lett. **57**, 2077 (1990).
[41]A. Zeinert, C. Arnas, C. Dominique, and A. Mouberi, J. Vac. Sci. Technol. A **26**, 1450 (2008).
[42]J. E. Allen, Phys. Scr. **45**, 497 (1992).
[43]C. Cui and J. Goree, IEEE Trans. Plasma Sci. **22**, 151 (1994).
[44]T. Matsoukas and M. Russell, Phys. Rev. E **55**, 991 (1997).
[45]M. S. Barnes, J. H. Keller, J. C. Forster, J. A. O'Neill, and D. K. Coultas, Phys. Rev. Lett. **68**, 313 (1992).
[46]P. K. Shukla and A. A. Mamun, *Introduction to Dusty Plasma* (IOP Publishing, Bristol, 2002).

This article is copyrighted as indicated in the article. Reuse of AIP content is subject to the terms at: http://scitation.aip.org/termsconditions. Downloaded to IP: 147.94.187.189 On: Thu, 11 Dec 2014 14:58:22

IOP Publishing Journal of Physics D: Applied Physics
J. Phys. D: Appl. Phys. **49** (2016) 045203 (12pp) doi:10.1088/0022-3727/49/4/045203

In-situ characterisation of the dynamics of a growing dust particle cloud in a direct-current argon glow discharge

S Barbosa[1], L Couëdel[2], C Arnas[2], K Kishor Kumar,[2,3], C Pardanaud[2] and F R A Onofri[1]

[1] Aix-Marseille Université, CNRS, IUSTI, UMR 7343, 13453 Marseille cedex 13, France
[2] CNRS, Aix-Marseille Université, Laboratoire de Physique des Interactions Ioniques et Moléculaires UMR 7345, 13397 Marseille cedex 20, France

E-mail: lenaic.couedel@univ-amu.fr

Received 4 September 2015, revised 26 November 2015
Accepted for publication 3 December 2015
Published 29 December 2015

Abstract

The growth and the dynamics of a tungsten nanoparticle cloud were investigated in a direct-current low pressure argon glow discharge. Real-time analyses of the dust particle size and number concentration were performed *in-situ* by light extinction spectrometry, while spatial dynamics of the cloud was investigated with the laser light-sheet scattering method. Additional off-line electron microscopy and Raman spectroscopy measurements were also performed for comparison purpose. This experimental work reveals the existence of an agglomeration phase followed by the appearance of a new dust particle generation. While growing, the dust cloud is pushed towards the anode and the discharge edge. Afterwards, a new dust particle generation can grow in the space freed by the first generation of nanoparticles. The continuous growth, below the light extinction spectrometry scanning positions, explains the apparent dissimilarities observed between the in-line optical and the off-line electron microscopy analyses.

Keywords: plasma, nanoparticles, diagnostics

(Some figures may appear in colour only in the online journal)

1. Introduction

Dusty or complex plasmas are partially ionised gases which contain solid dust particles that acquire an electric charge due to their interactions with the surrounding ions and electrons. They can be either injected or grown directly inside the plasma. For example, nanoparticles (NPs) are produced as candidate analogue of dust in diffuse interstellar medium, in radio-frequency (RF) discharges using hydrocarbon gases [1]. In the context of dense plasmas, NPs were surprisingly found in dust samples collected in carbon-based wall tokamaks [2, 3]. The possibility of formation in the coldest regions, near the tokamak wall was therefore investigated [4–6].

Generally, NP formation [7–11], charging and transport [12–15] were extensively studied experimentally in silane-based RF discharges for semi-conductor applications such as the improvement of photovoltaic devices [16]. It was shown that their growth started by the formation of molecular precursors which were coming from trapped negative ions resulting from the dissociation of reactive gases in the plasma [17–19]. After nucleation, NP growth was attributed to successive agglomerations of the smallest NPs. This mechanism was found to inhibit further nucleations resulting in NPs with narrow size dispersions [20, 21]. Finally, the agglomeration stopped due to electrostatic repulsion and the growth continued at constant NP number concentration by surface deposition of molecular species.

[3] Present address: Center for Plasma-Materials Interactions, 216 Talbot Laboratory, 104 S Wright Street, University of Illinois at Urbana-Champaign, 61801 Illinois, USA.

 © 2016 IOP Publishing Ltd Printed in the UK

It was recently demonstrated that in direct-current (DC) sputtering discharges, in which the nucleation was initiated by sputtered metallic atoms, the growth mechanisms were more complex [22]: (i) small particles were always observed, indicating a constant nucleation and (ii) the growth by agglomeration did not seem to saturate. Moreover, a strong dispersion in the appearance time of the second NP generation was reported [23]. These experiments were performed using a tungsten cathode as source of metal atoms. The incident DC discharge power being rather low, the cathode surface oxide was sputtered away after few tens of seconds. During this time interval, the evolution of the discharge and plasma parameters was the result of a competition between the influence of the cathode surface state and the influence of the charging of growing NPs. The influence of the latter became dominant on the plasma and discharge parameters (loss of plasma electrons) only when the oxide layer was removed [22]. Scattering of a vertical laser sheet going through the plasma just above the anode revealed that the NP cloud was compressed and pushed towards the anode during the discharge. Scanning electron microscopy (SEM) images of substrates exposed to the plasma for given durations showed that NPs were continuously falling down on the anode during the discharge [24]. These observations were explained by the fact that the electrostatic force at the negative glow-anode sheath boundary could not balance the ion drag, gravity, and thermophoresis forces for NPs of more than a few tens of nanometres in diameter. From electron microscopy images, it was shown that up to ~ 500 s, only mono-modal or bi-modal populations of NPs were collected [22].

However, *in-situ* characterisation of the growing NP cloud at different heights between the cathode and the anode remained necessary to unveil completely the growth and transport processes of metallic NPs in a DC discharge. For this purpose, we decided to combine imaging of the NP cloud by the scattering of a laser-light sheet with light extinction spectrometry (LES) which permitted the direct measurement of the particle size distribution (PSD) and number concentration, N, of the NP cloud at different positions in the discharge. This diagnostic is based on the extinction of a collimated white light beam whose spectral range extends from ultra-violet to infra-red ranges. It has the capability to detect NPs smaller than 20 nm and is effectively used to measure PSDs and N in colloidal suspensions [25]. This optical diagnostic presents various advantages with respect to the Mie-scattering ellipsometry diagnostic, often used in dusty plasmas [15, 21, 26, 27]. In particular, in the latter case, it is experimentally more challenging as it requires accurate measurements of the ellipsometric angles and the iterative data procedure used to find the particle parameters (PSD, local density, refractive index) is not trivial and requires strong assumptions. Otherwise, a reduction of the number of parameters can be considered. For instance, the choice of a model providing the time evolution of the particle radius can help in this way [15, 21].

In the present paper, we report a complete study on the growth and transport of tungsten NPs in DC sputtering discharges, in similar conditions to our previous experiments [22–24]. Sections 2 and 3 are devoted to the description of the experimental set-up and different diagnostics (electron microscopy, Raman spectroscopy, laser-light scattering and LES). A special attention is given to the LES diagnostics whose resolution was numerically evaluated. Section 4 presents our experimental findings and finally, section 5 is an overall discussion with conclusions.

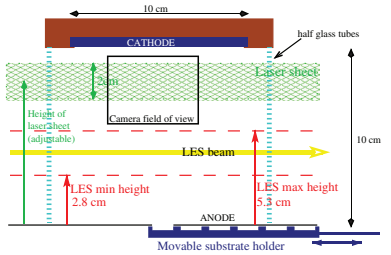

Figure 1. Schematic of the experimental set-up. The vertical position of the centre of the laser-light sheet can be adjust between 1 cm and 9 cm above the anode. The field of view of the camera is adjusted to the laser-light sheet position. Note that the LES diagnostics and the laser-light scattering imaging were not implemented simultaneously.

2. Plasma-discharge: experimental set-up

Tungsten NPs were grown in a DC argon glow discharge initiated between a $\sim$10 cm diameter tungsten cathode and a stainless-steal grounded anode (see figure 1). The inter-electrode distance was also 10 cm. Two glass half-cylinders were used to confine the plasma. A 1 cm gap was kept between them for optical diagnostics. A static argon pressure of 0.6 mbar (no gas flow) was set during the experiments. The electrode assembly was contained in a cylindrical vacuum chamber of 30 cm diameter and 40 cm length. An oil diffusion pump achieved a base pressure of $\leqslant 10^{-6}$ mbar. A manually operated gate valve was used to isolate the chamber from the oil diffusion pump during experiments.

A regulated power supply (Sefelec HT15A, 1 kV, 300 mA) was used to bias the cathode. The discharge current density was kept at a constant value (0.53 mA·cm^{-2} corresponding to a current of 40 mA). The current variations were less than 0.05%. The discharge parameters were such that the plasma mainly consisted of a negative glow. Under the chosen operating conditions, the cathode was sputtered and tungsten NPs were grown. More details about the experimental set-up and the evolution of discharge parameters during NP growth are given in [22].

3. Diagnostics

3.1. Electron microscopy

The anode disc had a 1.6 cm diameter hole at the centre through which the tungsten NPs produced during the

discharge were collected on stainless steel substrates. The substrate holder could be manipulated from one of the axial ports of the chamber, such that each substrate could be positioned under the hole in the anode. Two methods of collection were used:

(i) The substrate holder was moved under the anode so that successive substrates were exposed to the plasma during a given time interval.
(ii) The substrate saw the extinction of the discharge. Note that in this case, the substrate could, or not be exposed to the plasma during the whole discharge duration.

NPs were then analysed *ex-situ* using a scanning electron microscope. NPs have also been transferred from the stainless steal substrates to transmission electron microscopy (TEM) grid in order to perform high-angle annular dark-field imaging (HAADF) with a scanning transmission electron microscope (STEM). This technique, highly sensitive to atomic number variations in analysed samples, was used to check the tungsten content of the NPs.

3.2. Raman spectroscopy

Raman spectroscopy analyses were performed on collected NPs in order to determine if they were oxidised. The Raman spectrometer was a commercial Horiba-Jobin-Yvon HR LabRAM apparatus ($\times 50$ lens, $\lambda_R = 514.5$ nm, laser power at the surface ≈ 1 mW·μm^{-2}). This technique consists in measuring the wavelengths of photons produced by inelastic scattering of the incident light with the analysed sample. The energy difference between incident and scattered photons corresponds to a vibrational energy which can be used as a fingerprint of a given material. Tungsten oxides are known to display optical Raman active bending and stretching modes in the ranges 100–300 cm^{-1} and 700–800 cm^{-1}, respectively [28] whereas pure tungsten does not display any optical Raman active mode.

3.3. Laser-light-sheet scattering method

The NP cloud dynamics was studied using the laser-light-sheet scattering method [29, 30]. A vertical laser sheet of 2 cm height (40 mW, wavelength $\lambda_L = 532$ nm, linear polarisation at 45° with respect to the horizontal plane (i.e. scattering plane)) was passing through the electrode assembly in the gap between the half-cylinders (see figure 1). The light scattered by the dust particles was recorded at 90° by a 12 bits megapixel resolution digital CCD camera (BASLER ACE acA1300-60gm). A low frame rate of 1 frame per second and a long exposure time of 0.5 s were necessary to compensate for the low intensity of the scattered light. An interference filter centred on the laser wavelength was placed in front of the camera lens to reject most of the plasma emission. The position of the centre of the laser sheet was adjusted between 1 cm and 9 cm above the anode during the experiments.

3.4. Light extinction spectrometry (LES)

3.4.1. LES principle. N and the normalised PSD, n, were recovered in-line using the LES technique, which consists in analysing the spectral transmittance $T(\lambda)$ of a broadband and collimated light beam passing through the plasma containing the studied NP cloud. If I_0 and I_t are the spectral intensities of the incident and the exiting beam respectively, $T(\lambda)$ can be defined as follows:

$$T(\lambda) = \frac{I_t(\lambda) - I_{\text{plasma}}(\lambda) - I_b(\lambda)}{I_0(\lambda) - I_b(\lambda)} \quad (1)$$

where λ stands for the considered wavelength, I_{plasma} for the intensity of the plasma emission in the direction of propagation of the incident beam and I_b for the noise of the detection system (i.e. dark noise and residual background optical noise). If the detection of multiple scattered photons is negligible, the measured transmission is simply an exponentially decreasing function whose argument is the product of the probing length L (i.e. the cloud width), and the cloud turbidity τ. The latter is the product of N and the mean extinction cross section $\overline{C_{\text{ext}}}$ of the particles illuminated by the probing beam. $\overline{C_{\text{ext}}}$ is an integral quantity that depends on the extinction cross section of each particle (shape, size, refractive index, etc) and its statistical weight in the particulate medium. It is more convenient to write the LES transmission equation in its linearised and discretised form [25]:

$$\ln(T(\lambda_i)) = -NL \sum_{j=1}^{M_D} C_{ij} n_j \quad (2)$$

where C_{ij} is the statistical averaged extinction cross-section for the particle size class j (with $j = 1, 2, \ldots M_D$, where M_D is the maximum number of considered size classes) and for the wavelength λ_i (with $i = 1, 2, \ldots K_i$, where K_i is the maximum number of considered wavelengths); n_j is the probability density associated with the particle-size class centred on the diameter D_j.

The particle shape model used in the present study to describe tungsten NPs is a sphere (see section 4.1 for validation). Consequently, all the elements of C_{ij} can be calculated using the Lorenz–Mie theory [30]. Particle inhomogeneities, such as porosity or tungsten oxide spherical inclusions, can also be taken into account using the Maxwell–Garnett effective media approximation. More details and comparisons with other light scattering theories can be found in Refs. [25, 30]. To illustrate the effects of particle inhomogeneities, the evolution of C_{ext} is plotted in figure 2 for pure (tungsten mass fraction, $f_W = 100\%$), porous ($f_W = 74\%$, the remaining being empty) and oxidised ($f_W = 74\%$ and $f_{WO3} = 26\%$) tungsten NPs. The differences among the cases are mostly observed in the UV-range, where the size parameter ($\pi D/\lambda$) of these Rayleigh-like particles is maximum, as well as the imaginary part of their refractive index [31].

3.4.2. Inversion procedure of LES measurements. Solving equation (2) requires to solve a discrete ill-posed problem [25, 31] and thus, to implement in the inversion algorithm a

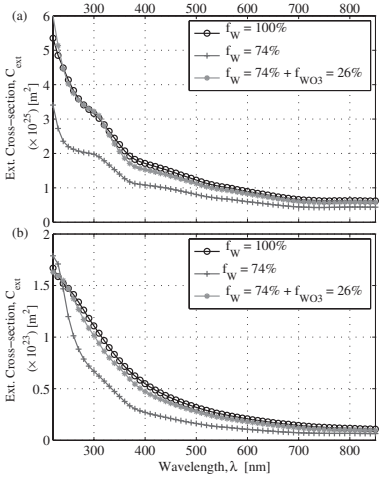

Figure 2. Spectral evolution of the extinction coefficient C_{ext} of spherical particles of (a) $D = 29$ nm, (b) $D = 65$ nm and of various compositions: pure tungsten, tungsten with spherical vacuum inclusions ($f_W = 74\%$), tungsten with tungsten oxide spherical inclusions ($f_W = 74\%$, $f_{WO3} = 26\%$).

specific regularisation scheme. The classical regularisation methods, such as the Philips–Twomey and Tikhonov methods or the truncated singular value decomposition, did not work properly when applied to the present experimental data. It mainly resulted from the weakness of the signal-to-noise ratio of experimental transmission spectra because of the relative low value of N in the discharge. In the present study, to get more robust inversions, additional physical inputs were required. In [22, 24], it was shown that up to 500 s, PSDs were mono-modal or bi-modal depending on the collection method. Based on these SEM analyses, PSDs were thus assumed to be of a particular type: unimodal or bimodal one. A mode $n(D)$ was simply described by a log-normal distribution depending of two parameters: a mean diameter $\overline{D}$ and a standard-deviation σ. The mode boundaries were deduced by truncating the PSD at 1/1000 of its global maximum [25]. It followed that, for a bimodal distribution (i.e. two distinct particle populations $n_1(D)$ and $n_2(D)$), five parameters needed to be estimated: two mean diameters $\overline{D_1}$ and $\overline{D_2}$, two standard deviations σ_1 and σ_2, and a constant α quantifying the relative weight in number of each distribution: $n(D) = \alpha n_1(D) + (1 - \alpha) n_2(D)$, with $0 \leqslant \alpha \leqslant 1$. All of these parameters could be deduced from a classical [25] iterative and weighted least squares algorithm that compares experimental and the theoretical extinction spectra (i.e. equation (2)).

Table 1. Parameters of synthetic PSDs associated with spectra of figure 3.

Dependent model: nominal parameters							
Cases	$\overline{D_1}$ [nm]	σ_1 [nm]	$\overline{D_2}$ [nm]	σ_2 [nm]	α [-]	$\overline{D_m}$ [nm]	σ_m [nm]
Unimodal cases							
Case (a)	29	5	0	0	1	29	5
Case (b)	65	5	0	0	1	65	5
Bimodal cases							
Case (c)	29	5	65	5	0.1	61.4	11.8
Case (d)	29	5	65	5	0.5	47.1	18.6
Case (e)	29	5	65	5	0.9	32.7	11.7

Note: $\overline{D_m}$ and σ_m are the statistical parameters of the unimodal populations equivalent to the bimodal populations (they are obviously unchanged for unimodal populations).

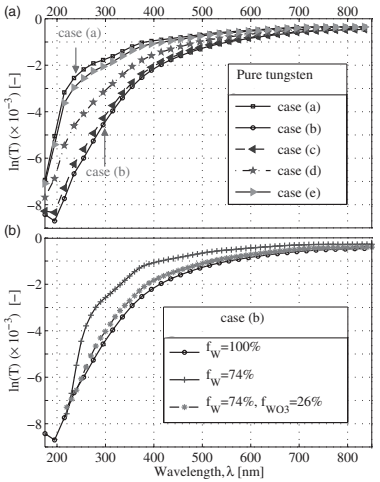

Figure 3. (a) Evolution of the logarithm of synthetic transmittance spectra calculated for tugnsten spherical particles. The associated PSD parameters are reported in table 1. (b) Evolution of synthetic ln(T) spectra calculated in the case of an unimodal population (case (b) in table 1) for pure, porous or oxidised tungsten NPs.

3.4.3. Sensitivity of the LES inversion procedure. In this section, numerical results providing physical insights and estimations of the LES technique resolution are reported. Five test cases, either unimodal or bimodal, are considered. Their statistical parameters and the associated logarithm of the synthetic transmittance spectra , ln(T), are reported in table 1 and figure 3(a) respectively. These spectra have been calculated for pure tungsten particles using the Lorenz–Mie theory. To focus on the effects of the particle size on the transmittance

Table 2. Error ('Err') between the recovered and nominal mean diameters and standard deviations of synthetic spectra of figure 3(a).

	Unimodal		Bimodal				
Cases	$Err(\overline{D})$ [nm]	$Err(\sigma)$ [nm]	$Err(\overline{D_1})$ [nm]	$Err(\sigma_1)$ [nm]	$Err(\overline{D_2})$ [nm]	$Err(\sigma_2)$ [nm]	$Err(\alpha)$ [-]
Case (a)	2.0	0.0	2.0	0.0	—	—	0.0
Case (b)	−1.0	−1.0	−1.0	−1.0	—	—	0.0
Case (c)	0.6	−4.8	2.0	0.0	−1.0	−1.0	0.0
Case (d)	1.9	−5.6	2.0	0.0	−1.0	−1.0	0.0
Case (e)	−0.7	1.3	2.0	0.0	−1.0	−1.0	0.0

Note: A negative error indicates an underestimation of the statistical parameter. In cases ((c)–(e)), for unimodal inversion method, the error between recovered and nominal parameters are calculated using the mean values: $\overline{D_m}$, and $\overline{\sigma_m}$.

spectra, they were all calculated for a constant particle number concentration.

For synthetic unimodal populations (see case (a) and case (b), table 1), an increase of the particle size leads to a decrease in transmistance, in particular at short wavelengths. In the case of a synthetic bimodal particle clouds, the shape of ln(T) spectra still depends on the size of the particles but also on the proportion α of a population with respect to the other one. A low proportion of small particles ($\alpha \leqslant 0.1$) changes only slightly transmission rate at short wavelengths, as show the spectra associated with the cases (b) and (c) (table 1). Larger proportion of small particles in the synthetic cloud ($\alpha \gtrsim 0.9$) leads to an increase of the transmission rate (see spectra associated with the cases (d) and (e)).

To further test the capability of LES inversion procedure to distinguish between one or two particle populations, a white noise with an amplitude corresponding to 4% (i.e. SNR $\approx 14dB$) of the minimum transmission was added to the transmittance spectra shown in figure 3(a). Note that this noise amplitude is representative of the experimental one. The error between the recovered (after inversion) and the nominal statistical parameters of these synthetic PSDs are reported on table 2. With an inversion of the first type (i.e. researching unimodal PSDs), the statistical parameters of cases (a) and (b) are perfectly recovered, while those of bimodal populations (cases (c) ... (e)) are naturally poorly recovered. Note that for low values of α, using a unimodal assumption leads to rather satisfactory estimation of $\overline{D_2}$ and σ_2, i.e. the particle population with the largest size and highest concentration. This is consistent with the previous observation regarding spectra of bimodal particle clouds containing only a low concentration of small particles. On the contrary, using a second type inversion (i.e. researching bimodal PSDs) allows a good reconstruction of all of these synthetic PSDs (see table 2).

LES measurements and inversions also depend on the particle composition (through the particle complex refractive index). As an illustration, table 3 reports the errors between the parameters of the recovered and the nominal PSDs in the case of an unimodal distribution (case (b), table 1): the tungsten particles were alternatively pure (tungsten mass fraction, $f_W = 100\%$), porous ($f_W = 74\%$) or partly oxidised ($f_W = 74\%$ and $f_{WO_3} = 26\%$). As mentioned above, for these calculations, the Maxwell-Garnett effective medium approximation was used to account for the effects of pores or WO_3 inclusions. As before, a white noise with a relative amplitude of 4% is added on the associated ln(T) spectra. It turns out that, globally, an overestimation of the particle density leads to an underestimation of the mean diameter and to a slight underestimation of the standard deviation. WO_3 inclusions do not have a large effect on the synthetic ln(T) spectra.

In figure 4, the recovered evolution of the mean diameter as a function of the relative noise amplitude of the synthetic transmission rate corresponding to the PSD of case (b) is plotted. When the relative amplitude is lower than 4%, the statistical parameters of case (b) are almost perfectly reconstructed, which is not the case for higher relative noise amplitude. In particular, an increase of the noise amplitude leads to an overestimation of the value of σ_1. However, the error on D_1 does not exceed 15% even for noise amplitude $\lesssim$12%. The absolute error on N also increases with the noise amplitude but the recovered values are within 30% of the real one for noise amplitude $\lesssim$12%.

Given all the numerical tests, it can be concluded that, on the conditions that one has a minimum knowledge on the NPs (shape, composition) and makes reasonable assumptions on the PSD shape, LES is an accurate diagnostic even in noisy environments.

3.4.4. LES Experimental setup. The LES set-up (see appendix) was composed of a highly-stabilised Halogen–Deuterium lamp (Ocean Optics, DH-2000-DUV), solarisation resistant optical fibres with a 100 μm core, an on-line intensity attenuator, achromatic coupling and collimating optics (50 nm focal length parabolic mirrors), a diaphragm and a CCD spectrometer (Oceans Optics, Maya Pro). This low noise and high dynamic range spectrometer has an enhanced response in the UV range and a global half-height resolution of 2–5 nm in the spectral range 220–1040 nm where LES measurements were performed. Full optical calculations have demonstrated that for the considered particle size and concentrations, and because of the small aperture angle of the LES detection system (less than 1°), multiple scattering is negligible. Optical choppers were used to chop the probing beam of 1 mm in diameter, in order to record periodically: the optical and electronic signals, the reference signal and the plasma light emissions. This allowed us to record one corrected transmission spectrum (see equation (2)) every 2 s.

4. Results

4.1. Electron microscopy

SEM results have been described in details in previous articles [22, 24]. Here is a quick outline of the main results obtained:

- NPs were pushed towards the anode located at the bottom of the discharge set-up and could get detrapped and fall on the anode. The later the substrate was exposed to the plasma, the bigger were the collected NPs. The biggest NPs could have diameter up to 150 nm for discharge duration of 500 s.

Table 3. Error between the recovered and nominal mean diameters and standard deviations of synthetic spectra of figure 3(b).

	Pure		Porous		Oxidised	
Assumed compositions	$Err(\overline{D})$ [nm]	$Err(\sigma)$ [nm]	$Err(\overline{D})$ [nm]	$Err(\sigma)$ [nm]	$Err(\overline{D})$ [nm]	$Err(\sigma)$ [nm]
Pure, $f_W = 100\%$	−1.0	−1.0	−2.0	20.0	5.0	0.0
Porous, $f_W = 74\%$	−9.0	−4.0	−1.0	−1.0	−20.0	0.0
Oxidised, $f_W = 74\%$	−8.0	−4.0	−1.0	13.1	−1.0	−1.0

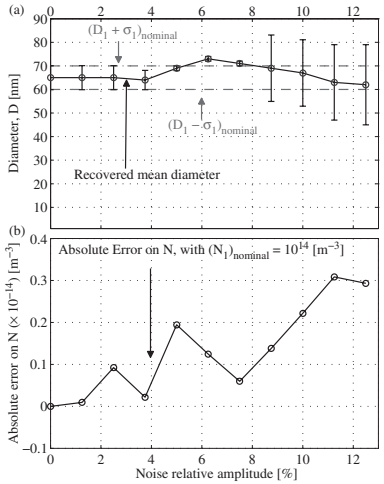

Figure 4. (a) Evolution of the recovered first two moments of the PSDs as a function of the relative noise amplitude. (b) Evolution of the absolute error on N as a function of the relative noise amplitude. Synthetic spectra are calculated using the PSD of case (b) (see table 1).

- Small particles (mean diameter ∼30 nm) were always observed on the substrate when the discharge was switched off (method (ii), see section 3.1). These results indicated constant nucleation and growth of NPs in the upper part of the discharge (cathode side).

Electron microscopy studies of particles collected after a 300 s plasma indicate that NPs are roughly spherical, and look mainly like a compact aggregate of tungsten crystallites ($d \simeq$ 2–4 nm) (see figure 5), justifying partially our hypotheses on the particle shape model for LES data inversion (see figure 7 in [25]).

4.2. Raman spectroscopy

Measurements were performed directly on the cathode and on stainless steel samples covered with NPs. Weak tungsten oxide signatures were observed by Raman spectroscopy. In order to check if NPs were weakly oxidised or not, they have been heated under an oxygen containing atmosphere. The growth of tungsten oxide bending and stretching modes was observed only for temperature higher than 700 °C. Final Raman scattering intensities were multiplied by a factor of ∼25 showing that the weak bands, observed at room temperature were due to surface oxide, probably formed during the venting of the chamber, after the experiments. It is worth reminding that we have shown in section 3.4.3 that a small amount of oxide in the NPs has a negligible impact on LES transmittance spectra. Therefore, for the rest of this study, it was assumed that the NPs in the plasma were composed of tungsten crystallites and, consequently, complex refractive index of pure tungsten [32] was used to inverse LES measurements.

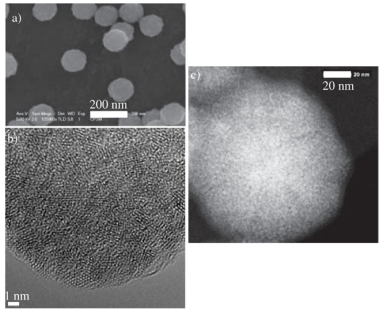

Figure 5. Images of a NP collected after a 300 s plasma. (a) SEM. (b) HR-TEM. (c)HAADF-STEM. The fringe patterns in (b) are the crystallites. The white dots in (c) are the tungsten crystallites.

4.3. laser-light-sheet scattering measurements

In an earlier study [24], laser-light-sheet scattering measurements just above the anode revealed that the dust particle cloud was compressed and pushed towards the anode during the discharge. For a better understanding of the dynamics of the growing process, further experiments with different positions of the laser-light sheet above the anode have been performed. In each experiment, no NPs could be detected by our laser-light scattering system during the first 30 s after plasma ignition.

In figure 6(a), a snapshot of the scattered laser-light 45 s after plasma ignition is shown. The centre of the laser-light-sheet was positioned at 2 cm of the cathode surface (i.e. 8 cm

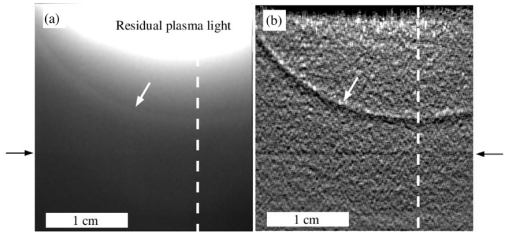

Figure 6. Typical snapshot of the scattered laser-light 45 s after plasma ignition : (a) raw image, (b) same as (a) with an edge detection filter applied to the image. The horizontal black arrow shows the position of the lower edge of the laser sheet which was positioned 2 cm below the cathode. The oblique white arrow shows the top edge of the NP cloud. The dashed vertical line indicates the position of the discharge axis.

from the anode). For a better visualisation of the boundary of the dust cloud, an edge detection was applied to the raw image (figure 6(b)). The top edge of the cloud had a very convex shape and an apparently dust-free hole centred on the discharge axis was visible (no NP detected by laser-light scattering). In figure 6(a), one can see that there was a strong plasma emission in this region. It corresponded to the expanding luminous 'blue glow' appearing at the centre of the tungsten cathode a few seconds after plasma ignition [22]. During the hemispherical expansion of this glow, the NP cloud was pushed toward the bottom and the side of the discharge gap explaining its convex shape.

In figure 7(a), three snapshots are shown for a laser-light sheet positioned 3.4 cm above the anode. The scattered light intensity increased with time until the dust cloud was pushed down and toward the side of the discharge and, as observed close to the cathode, an apparently 'dust-free' hole was expanding in the discharge. This behaviour was observed at all investigated heights between the electrodes and, as already stated, could be linked to the expanding luminous 'blue glow' observed on the cathode centre a few second after plasma ignition (see figure 6) [22]. This effect was clear at $t = 210$ s after plasma ignition: in figure 7(a) the top edge of the NP cloud is convex. Note that the intensity gradients observed in figure 7 are the result of a convolution between the vertical intensity profile of the laser-light sheet, with the NP size/number concentration gradients in the region illuminated by the laser-light sheet. Since the scattering regime for the considered NPs is in between the Rayleigh regime and the lower bound of the Mie scattering regime, the NP scattering efficiency is proportional to D^6 for the smallest and tends to (but does not reach) the limit of D^2 for the largest NPs. That is any detailed interpretation of the continuous changes in the intensity gradients (or 'inhomogeneities') observed in figure 7(a), has to be done with caution.

In figure 7(b), the distance of the upper edge of the NP cloud is plotted as a function of time. Note that even though every experiment was carried out with the same discharge parameters, there was a strong dispersion in the measured time (±50 s for the cloud top edge positioned at 3 cm above the anode). This is due to the high sensitivity of NP growth

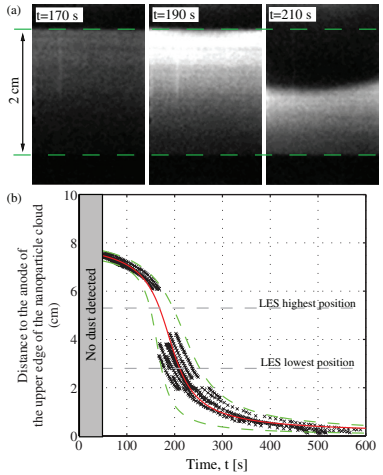

Figure 7. (a) Snapshots of the video of the scattered laser-light at different times after plasma ignition. The dashed green lines show the upper and lower edges of the vertical laser sheet. The centre of the laser sheet was 3.4 cm above the anode. (b) Distance of the upper edge of the NP cloud (1st generation) to the anode on the discharge axis as a function of time extracted from laser-light scattering data. The latter were accumulated over 21 experiments. The red line represents a fitted mean position of the upper edge of the NP cloud. The dashed green lines are the errorbars at 3 standard deviations.

to the initial conditions (base pressure, cathode surface state, etc). This effect was also observed in radio-frequency discharge in which NPs are grown by sputtering of a polymer layer on the electrode [33]. The general behaviour of the NP cloud was however always the same. The maximum height of the dust cloud edge was ∼7.5 cm above the anode at $t \simeq 30$ s

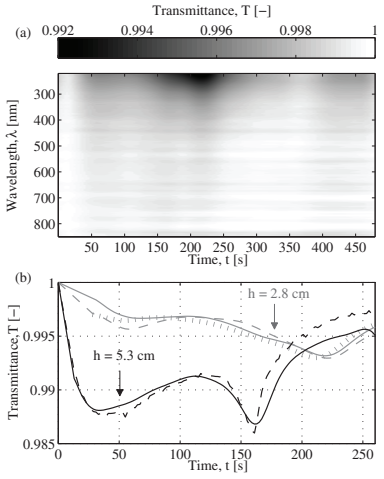

Figure 8. (a) Evolution of the transmitance at different wavelengths as a function of time, 2.8 cm above the anode for a 500 s discharge. (b) Transmittance at 250 nm at different heights above the anode: gray lines, $h = 2.8$ cm; black lines, $h = 5.3$ cm. Each plain, dashed, or dotted line corresponds to a separate experiment.

after plasma ignition. Soon after the NP cloud could be detected, it started to be pushed toward the anode and the edge of the discharge. For ∼100 s, the movement of the NP cloud was quite slow and the height variation of the upper edge was ∼1 cm. Then, in ∼200 s the upper edge position felt from ∼6.5 cm to less than 1 cm, meaning that a major part of the plasma seemed free of dust. However, our previous studies have shown that small NPs (hardly detectable by laser-light scattering) were growing in this region [24].

4.4. Light extinction spectrometry

In figure 8(a), the temporal evolution of the transmittance at different wavelengths is shown when the probing beam was positioned 2.8 cm above the anode. As expected for NPs, the transmittance at short wavelengths was more affected by the presence of the growing tungsten NPs than at long wavelengths (i.e. $T \simeq 1$). In figure 8(b), evolutions of the transmittance at $\lambda = 250$ nm for five experiments with the same discharge parameters (two measurements at $h = 5.3$ cm and three measurements at $h = 2.8$ cm) are shown. While not exactly the same, due to the high sensitivity of the experiments to the initial conditions, one can see that the measurements at the same height were similar.

The overall shape was comparable for both heights but the kinetics was faster in the measurements made at the highest positions. For instance, the minimum of transmittance occurred at $t \simeq 170$ s at $h = 5.3$ cm while it occurred at $t \simeq 220$ s

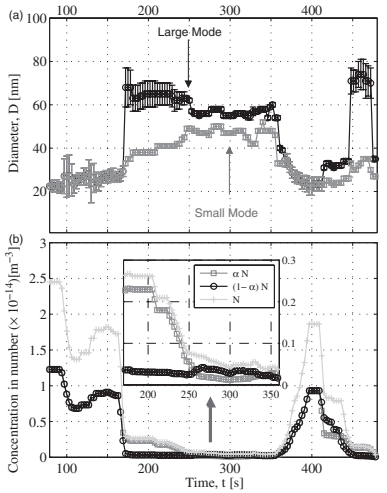

Figure 9. (a) Temporal evolution of mean diameters (represented by squares or by circles) and the associated standard-deviations (represented by bars) measured by LES at the height $h = 2.8$ cm from the anode. A bimodal PSD is detected, its large mode is represented by the circle line, while its small mode is represented by the square line. (b) Temporal evolution of N, as well as αN and $(1 - \alpha)N$ associated with the small and large modes of the PSD, respectively.

at $h = 2.8$ cm. These minima in transmittance could be linked to the opening of the apparently 'dust-free' hole at the investigated height. The times of the minima matched indeed within errorbars the position of the upper edge of the dust particle cloud on the discharge axis (see figure 7(b)). Before reaching a transmission minimum, the NP number concentration and/or NP size in the LES beam have increased which explained the transmittance decrease. From this time, the path length of the LES beam through the cloud visible by laser-light-sheet scattering started to decrease and the transmittance started to increase. Note that it was previously reported [24] that small NPs were present in this hole. Extinction being very sensitive to the NP size, the larger having the greatest effect, replacing large NPs by smaller one is almost similar in effect to a dust-free zone.

It may appear surprising that LES transmittances at higher probing positions in the plasma were smaller than at lower LES positions. However, as the cloud was pushed toward the side of the discharge, some particles were constantly lost through the vertical slits between the half glass tubes used for the optical diagnostics, explaining the higher transmittance at lower beam positions.

In figures 9(a) and (b), the recovered evolution of the PSD and N are presented. They correspond to the transmittance

spectrum shown in figure 8(a). Six different phases could be extracted in the measured NP growth and dynamics[4].

- Before ∼70 s, no information could be accurately extracted from the transmittance spectra. It indicates that NPs in the LES beam were very small and possibly in very low number concentration.
- From ∼70 s to ∼170 s, the PSD was found to be clearly unimodal, as the inversion procedure forcing a bimodal distribution gave two identical modes with the same weight. During this phase, the mean particle diameter increased from ∼20 nm to ∼30 nm. N was nearly constant ($\sim 2 \cdot 10^{14}$ m^{-3}) even if a smooth decrease (over ∼12 s) in N, coinciding with higher values of σ_{I}, was observed at $t \sim 80$ s. This increase in σ_{I} could be attributed to local higher values of the relative noise in LES measurements (see results of the synthetic study presented in section 3.4.3, more particularly in figure 4) that could be due to very intense and fluctuating plasma emissions occuring after ignition [22]. As a transmittance spectrum depends on a convolution between N and the PSD, large recovered values of σ_{I} (i.e. a large distribution) imply small recovered values of N. Moreover, the PSD remained mono-modal after 80s which favours the hypothesis of an inversion artefact.
- At t ∼170 s, an inflection point is observed on the transmittance rate at all wavelengths, while the PSD became abruptly bi-modal: each mode which were initially identical are suddenly well separated. Simultaneously, the total concentration in number decreased abruptly (in less than ∼6 s). The number concentration of the small (i.e. original) mode particles decreased also abruptly, while the concentration of the large mode particles, which just appeared, was very small. These observations suggest an agglomeration of the small particles at constant volume. Nevertheless as the agglomeration process was not instantaneous, small particles were not totally consumed and some remained in the LES beam. After this time, the mean diameter of the particles in the large mode stayed almost constant while the mean diameter of the particles of the small mode steadily increased.
  Two mechanisms could explain the apparent growth of the NPs of the small mode: surface growth by molecular sticking or agglomeration. If the NPs of the small mode were growing by surface deposition or by agglomeration with very small undetectable particles, their number concentration should be constant. It was not the case here, figure 9 clearly shows a decrease of their number concentration. In addition, it can be shown using the theory of [34], that tungsten vapour concentration is maximum around 1 cm below the cathode and is rapidly decreasing when going towards the anode. Consequently, surface growth on the anode side, where LES measurements were performed, was most probably negligible.
  A more likely explanation is that they were consummed by agglomeration to create the NPs of the large mode. Even if the agglomeration of the 35 nm particles should normally be suppressed because they are negatively charged, it may still exist due to a mechanism called the polarisation-induced ion flux asymmetry (PIFA) [35, 36]. In the PIFA mechanism, it is proposed that a NP becomes polarised due to the influence of the electric field created by the neighbouring grain which leads to an asymmetry of the ion flux onto the surface grain resulting in a force in the direction of the electric field. PIFA mechanism thus allows negatively charged large particle to agglomerate with smaller negatively charges one. It was verified experimentally in a RF discharge [36]. Furthermore, as NPs were getting deeper in the negative glow, i.e. closer to the anode, the electron temperature decreased and so did the NP charge (in absolute value) reducing the repulsive force.
  Finally, the agglomeration hypothesis is favoured by the sudden appearance of the large mode in concordance with a sudden decrease of the number concentration of the NPs of the small mode. One should also note that the two modes of the PSD are log-normal and only the mean sizes are given in figure 9. While the PIFA mechanism allows the agglomeration of negatively charged particles, it still favours the agglomeration of the smallest one with the largest one. Consequently, smallest NPs were consumed in priority and, in return, the mean diameter of the small mode increased. Experiments at different heights showed that this phase occurs quicker when closer to the cathode. A possible explanation for the triggering of the agglomeration phase is that when large particle pass through a cloud of smaller particle, agglomeration is enhanced [35–37].
- At ∼220 s, the transmittance reached a minima at all wavelengths and from this time N started to decrease rapidly. When looking at the two modes of the PSD, their mean size remained almost unchanged but the weight of the smaller particles decreased rapidly. As discussed previously, this corresponded to the opening of the 'dust-free' region in the LES beam. From this time, the path length of the LES beam through the cloud (visualised by laser-light-sheet scattering) started to decrease and the transmittance started to increase due to a decreasing number density. Note that in the region freed by the first generation of NPs, new NPs were starting to grow [24]. They however remained undetectable with the LES diagnostics as, extinction being very sensitive to NP size, large NPs had the greatest effect and the overall effects was almost similar to a 'dust-free' zone. It also explains why the weight of smaller mode of the PSD was more affected. As stated earlier, the evolution of the LES signal was similar for the different investigated positions of the probing beam. Only the dynamics was faster when closer to the cathode. After inversion of the LES spectra, another difference appeared. In figure 10, the size of the particle at the minimum of transmittance for different LES beam height are presented. The PSD was bimodal at all investigated heights. No trend is observable for the mean size of the NPs belonging to the small mode which remain around 40 nm while the mean size of the particle belonging to the large mode is increasing when getting closer to the anode. This is a clear indication for a continuous growth of NPs while getting transported towards the anode. Earlier measurements of the particle collected on the anode showed that the NPs can reach size up to 150 nm [24]. Such large size were not measured by LES, strongly suggesting that NP growth continued below the minimum investigated LES beam height. This is also compatible with the earlier hypothesis of an agglomeration phase enhanced by the penetration of large NPs into the cloud of smaller particles, the former growing further while transported towards the anode.
- From ∼250 s to ∼350 s (see figure 9), the two modes of the PSD were almost superimposed (∼50 nm and ∼60 nm). The number concentrations of both mode were equivalent ($\lesssim 0.1 \cdot 10^{14}$ m^{-3}) and the total number concentration was slowly decreasing. These observations were the consequence of two effects: the agglomeration process which consumed the smallest particle and the opening of the 'dust-free' zone in the LES beam. However, it has to be noted that the two modes of the PSD remain distinct from each other as the largest particles of the original small mode are probably too big to agglomerate, even considering the PIFA mechanism.
- From ∼350 s to ∼400 s, N increased rapidly while the mean NP diameter felt down to ∼35 nm (monomodal distribution). On the transmittance spectrum, it corresponded to a new decrease of the transmittance. This period of time corresponded to the expulsion of the last large NPs of the first generation and consequently, an easier detection of the second generation of NPs. It is in accordance with our earlier experiments [24]: large NPs were expelled from the plasma and new small ones were synthesised in the region freed from the first generation (mainly above as the NP cloud is pushed down) where nucleation could take place again from sputtered atoms. This behaviour is similar to the one observed in radio-frequency discharges where a 'void' usually appears in the plasma centre, in which new dust particles are grown [33, 38, 39].
- From ∼400 s, the PSD became again bi-modal with an associated decrease of N n in a very similar manner to what happened at $t \sim 170$ s. These were signs of an agglomeration process occurring in the second generation NP cloud.

[4] Note that these phases occurred independently of the LES scanning position, the kinetics at the highest position being only faster

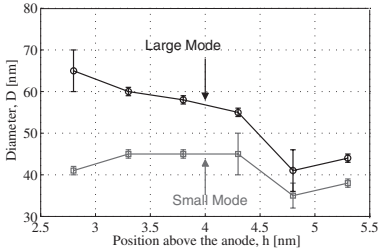

Figure 10. Evolution of the particle size reached at the minima in transmittance.

5. Conclusion and perspectives

In this article, a detailed characterisation of a growing NP cloud in a DC sputtering low pressure argon glow discharge with a tungsten cathode was performed. The shape and composition of NPs with *ex-situ* diagnostics (SEM,TEM. HAADF-TEM and Raman spectroscopy) was determined. The particles were found to be mainly compact spheroids of pure tungsten crystallites which allowed us to use the complex refractive index of pure tungsten for the LES diagnostics. Laser-light scattering of a vertical laser sheet positioned at different heights in the inter-electrode gap showed that the NP cloud was pushed towards the edge of the discharge and the anode leaving a zone in which nucleation of new NPs could take place. In addition, the evolution of the PSD and N were studied *in-situ* by LES. This diagnostic has revealed a phase of NP growth by agglomeration, followed by the appearance of a second NP generation. The agglomeration phase was identified by a sudden change of the PSD from monomodal to bi-modal followed by a gradual disappearance of the small NPs. Results have also confirmed that the second generation of NPs appeared in the space freed by the first NP generation. At the minimum of transmittance, while the PSD was bi-modal at all investigated positions between the electrode, the mean size of the NPs belonging to the large mode of the PSD increased when getting closer to the anode. On the contrary, the mean size of the NPs belonging to the small mode remained approximately constant. This results suggests that agglomeration was triggered when the biggest NPs passed through a cloud of smaller NPs. They thus grew until they reach the anode side of the discharge. It shows that the largest particles are agglomerates of smaller ∼35 nm particles and is consistent with our results reported in earlier studies using electron microscopy measurements to reconstruct PSDs of particle collected at the anode centre [22–24]. Furthermore, as the NP growth continued below the LES scanning positions, it explains the apparent dissimilarities observed between the *in-situ* optical and the *ex-situ* electron microscopy PSD measurements.

Future investigations will combine local measurements of plasma properties with the *in-situ* PSD diagnostics, to confirm some interpretations drawn in the present paper and to correlate NP growths and dynamics to the local evolution of the plasma parameters.

Acknowledgments

This work was supported by the INSIS of CNRS via PEPS (Projets Exploratoires Premier Soutien) grant. The authors would also like to thank S Khrapak and the A*MIDEX foundation for their financial support in the framework of

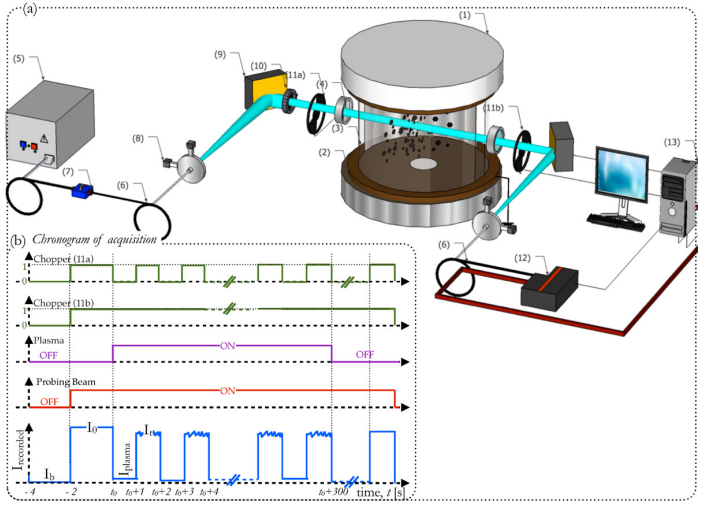

Figure A1. (a) Schematic of the LES acquisition system: (1) tungsten cathode, (2) stainless-steal grounded anode, (3) glass half cylinders, (4) UV fused silica windows, (5) highly-stabilised Halogen–Deuterium lamp, (6) optical fibers, (7) on-line intensity attenuator, (8) achromatic coupling and collimating optics, (9) parabolic mirrors, (10) diaphragm, (11a–11b) optical choppers, (12) UV-NIR spectrometer, (13) PC. (b) Acquisition chronogram of the intensities.

ANR-11-IDEX-0001-02 and ANR-11-LABX-0092 (Labex MEC). We are grateful to M Cabié for her technical support in electron microscopy.

Appendix. LES set-up

The LES set-up (see figure A1) was composed of a highly-stabilised Halogen-Deuterium lamp (Ocean Optics, DH-2000-DUV) (5), solarisation resistant optical fibres (6) with a 100 μm core, an on-line intensity attenuator (7), achromatic coupling and collimating optics (50 nm focal length parabolic mirrors) (8-9), a diaphragm (10) and a CCD spectrometer (Oceans Optics, Maya Pro) (12). Optical choppers (11a–11b) were used to chop the probing beam of 1 mm in diameter and a typical probing length of 10 cm, in order to record periodically: the optical and electronic signals, the reference signal and the plasma light emissions. This allowed us to record one corrected transmission spectrum (see equation (2)) every 2 s.

References

[1] Stefanovic I, Kovacevic E, Berndt J, Pendleton Y and Winter J 2005 *Plasma Phys. Control. Fusion* **47** A179
[2] Winter J and Gebauer G 1999 *J. Nucl. Mat.* **266–269** 228–33
[3] Arnas C, Pardanaud C, Martin C, Roubin P, Temmerman G D and Counsell G 2010 *J. Nucl. Mater.* **401** 130
[4] Winter J 2004 *Plasma Phys. Control. Fusion* **46** B583
[5] Smirnov R D, Pigarov A Y, Rosenberg M, Krasheninnikov S I and Mendis D A 2007 *Plasma Phys. Control. Fusion* **49** 347–71
[6] Arnas C, Martin C, Roubin P, Pégourié B, Temmerman G D, Hassouni K, Michau A, Lombardi G and Bonnin X 2010 *Plasma Phys. Control. Fusion* **52** 124007
[7] Boufendi L, Plain A, Blondeau J P, Bouchoule A, Laure C and Toogood M 1992 *Appl. Phys. Lett.* **60** 169
[8] Plain A 1998 *J. Appl. Phys.* **83** 4012
[9] Watanabe Y 2006 *J. Phys. D: Appl. Phys.* **39** R329
[10] Hollenstein C, Dorier J L, Dutta J, Sansonnens L and Howling A A 1994 *Plasma Sources Sci. Technol.* **3** 278
[11] Mikikian M, Couëdel L, Cavarroc M, Tessier Y and Boufendi L 2010 *Phys. Rev. Lett.* **105** 075002
[12] Graves D, Daugherty J, Kilgore M and Porteous R 1994 *Plasma Sources Sci. Technol.* **3** 433
[13] Stefanovic I, Berndt J, Maric D, Samara V, Radmilovic-Radjenovic M, Petrovic Z L, Kovacevic E and Winter J 2006 *Phys. Rev.* E **74** 026406
[14] Selwyn G S 1994 *Plasma Sources Sci. Technol.* **3** 340–7
[15] Hayashi Y and Tachibana K 1994 *Japan. J. Appl. Phys.* **33** L804–6
[16] Borowik L, Nuyen-Tran T, Cabarrocas P R I and Merlin T 2013 *J. Appl. Phys.* **114** 204305
[17] Fridman A A, Boufendi L, Hbid T, Potapkin B V and Bouchoule A 1996 *J. Appl. Phys.* **79** 1303
[18] Howling A A, Sansonnens L, Dorier J L and Hollenstein C 1994 *J. Appl. Phys.* **75** 1340–53

[19] Bhandarkar U, Swihart M, Girshick S and Kortshagen U 2000 *J. Phys. D: Appl. Phys.* **33** 2731
[20] Bouchoule A and Boufendi L 1993 *Plasma Sources Sci. Technol.* **2** 204–13
[21] Hong S K and Winter J 2006 *J. Appl. Phys.* **100** 064303
[22] Kumar K K, Couëdel L and Arnas C 2013 *Phys. Plasmas* **20** 043707
[23] Kumar K K, Couëdel L and Arnas C 2014 *J. Plasma Phys.* **80** 849
[24] Couëdel L, Kumar K K and Arnas C 2014 *Phys. Plasmas* **21** 123703
[25] Onofri F, Barbosa S, Touré O, Woźniak M and Grisolia C 2013 *J. Quant. Spectrosc. Radiat. Transfer* **126** 160
[26] Gebauer G and Winter J 2003 *New J. Phys.* **5** 38
[27] Greiner F, Carstensen J, Köhler N, Pilch I, Ketelsen H, Knist S and Piel A 2012 *Plasma Sources Sci. Technol.* **21** 065005
[28] Baserga A, Russo V, Fonzo F D, Bailini A, Cattaneo D, Casari C, Bassi A L and Bottani C 2007 *Thin Solid Films* **515** 6465–9
[29] Onofri F and Barbosa S 2012 *Chapter II: Optical Particle Characterization (Laser Metrology in Fluid Mechanics)* (London: Wiley)
[30] Onofri F, Wozniak M and Barbosa S 2011 *Contrib. Plasma Phys.* **51** 228–36
[31] Onofri F, Ren K and Grisolia C 2009 *J. Nucl. Mater.* **390–1** 1093–6
[32] Palik E D 1985 *Handbook of Optical Constants of Solid* (London: Academic)
[33] Mikikian M, Cavarroc M, Couëdel L and Boufendi L 2006 *Phys. Plasmas* **13** 092103
[34] Gras-Marti A and Valles-Abarca J A 1983 *J. Appl. Phys.* **54** 1071
[35] Mankelevich Y A, Olevanov M A and Rakhimova T V 2008 *Plasma Sources Sci. Technol.* **17** 015013
[36] Mankelevich Y, Olevanov M, Pal' A, Rakhimova T, Ryabinkin A, Serov A and Filippov A 2009 *Plasma Phys. Rep.* **35** 191–9
[37] Annaratone B M, Elskens Y, Arnas C, Antonova T, Thomas H M and Morfill G E 2009 *New J. Phys.* **11** 103013
[38] Cavarroc M, Mikikian M, Tessier Y and Boufendi L 2008 *Phys. Rev. Lett.* **100** 045001
[39] Couëdel L, Mikikian M, Samarian A A and Boufendi L 2010 *Phys. Plasmas* **17** 083705

Eur. Phys. J. D (2021)75:240
https://doi.org/10.1140/epjd/s10053-021-00239-9

THE EUROPEAN PHYSICAL JOURNAL D

Regular Article

Diagnostics of a high-pressure DC magnetron argon discharge with an aluminium cathode

S. Mitic[1,a], J. Moreno[2], C. Arnas[3], and L. Couëdel[2,3,b]

[1] Justus-Liebig-University, Giessen, Germany
[2] Department of Physics and Engineering Physics, University of Saskatchewan, Saskatoon, SK S7N 5E2, Canada
[3] CNRS, PIIM, Aix-Marseille Université, 13397 Marseille, France

Received 21 May 2021 / Accepted 3 August 2021
© The Author(s), under exclusive licence to EDP Sciences, SIF and Springer-Verlag GmbH Germany, part of Springer Nature 2021

Abstract. In this article, the plasma parameters of a direct current magnetron discharge in argon at moderate pressure (10 to 40 Pa) using an aluminium cathode are explored. The density of argon excited states, the sputtered aluminium atom density and the electron temperature are estimated using a collisional–radiative model. The electron temperature obtained using optical emission spectroscopic data agrees well with measurements taken using a Langmuir probe. The influence of the discharge parameters, namely the background argon pressure and the discharge current, are discussed.

1 Introduction

Magnetron discharges are widely used for thin-film deposition [1]. In planar magnetron discharges, magnetic fields created by permanent magnets positioned behind the cathode trap electrons near the cathode region allowing plasma production at relatively low pressures [2,3], thereby favouring cathode material sputtering by energetic ions [4]. For the deposition of metallic coating (copper, aluminium, tungsten, etc.), inert gases such as argon (Ar) or krypton (Kr) are usually used [1,5–8].

Nanoparticle (NP) formation in glow discharges has been the subject of many studies during the past decades. For example, NP growth and effects on discharge parameters have been studied in radio-frequency (RF) discharges using reactive gases such as silane [9] or acetylene [10], and by sputtering of the electrodes [11,12]. Studies have also been devoted to the study of the growth and the dynamics of the NP clouds in direct current (DC) sputtering glow discharges using different cathode materials [13–16]. It was shown that the growth process strongly depends on the type of cathode material and other discharge parameters, such as the neutral gas pressure and the discharge current. In the specific case of the formation of tungsten NPs, it was shown that the formation mechanisms and transport between electrodes exhibit complex dynamics [17]. Since the mid-1990s, RF and DC magnetron sputtering in gas aggregation sources (MS-GAS) is commonly used to produce metal NPs [18–26]. In most cases, MS-GAS consists of a high-pressure chamber in which the magnetron discharge is located connected to a low-pressure expansion chamber in which a beam of NP can be filtered and collected. NPs are formed in the high-pressure side of the MS-GAS from the atoms ejected by sputtering of the magnetron cathode. Even though MS-GAS are extensively used to produce NPs of many different materials, very few studies are devoted to the correlation of NP growth dynamics in the high-pressure chamber with the parameters of the magnetron discharges [24,27,28]. The formation of NPs in a DC planar magnetron discharge in argon at relatively high pressures (10s of Pa) is also possible [29,30]. In particular, experimental studies on the formation of tungsten NPs in high-pressure DC planar magnetron argon discharges and their influence on plasma parameters were recently done [31–33]. Nevertheless, DC magnetron plasmas in high-pressure regimes are still poorly understood.

In this article, the dependence of the plasma parameters on the discharge conditions in a conventional DC magnetron set-up was investigated. The cathode was made of aluminium (Al), and the background gas was Ar. The pressure (p_{Ar}) as well as the discharge current (I_d) was varied. The current–voltage relations of the magnetron plasma were established for different p_{Ar}. In addition, optical emission spectroscopy (OES) measurements on Ar I and Al I lines were taken. A collisional–radiative model including self-absorption corrections was used to find the argon metastable atom density, aluminium atom density, electron temperature T_e and the electron density n_e. Finally, the different plasma parameters (n_e, T_e and plasma potential V_p) were also measured at a fixed distance under the cathode on the symmetric axis of the magnetron discharge using a cylindrical Langmuir probe. Plasma parameters obtained with probe and OES measurements were compared and the different results are discussed.

[a] e-mail: slobodan.mitic@exp1.physik.uni-giessen.de
[b] e-mails: lenaic.couedel@usask.ca; lenaic.couedel@univ-amu.fr (corresponding author)

Published online: 09 September 2021

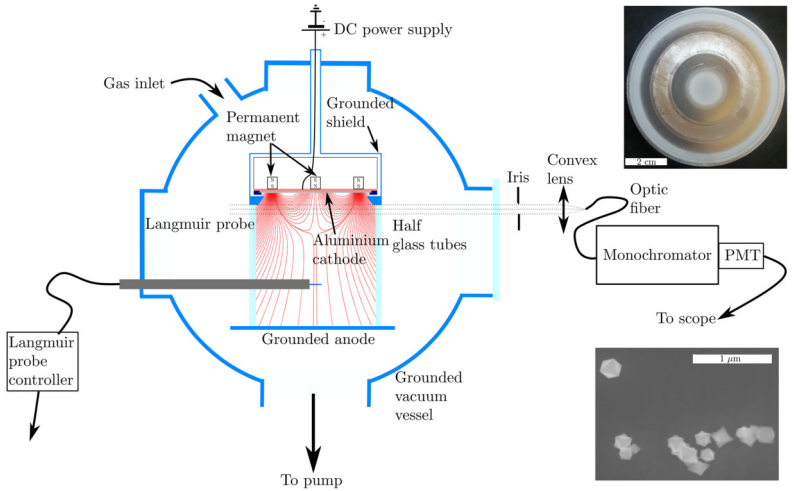

Fig. 1 Schematic of the experimental set-up. The red lines illustrate the magnetic field lines. The top right inset shows the state of aluminium cathode after the experiments. Note the circular sputtering track. The bottom right inset shows a scanning electron microscope image of aluminium nanoparticles grown in a plasma with $I_d = 300$ mA at $p_{Ar} = 30$ Pa for a plasma duration of 60 s

2 Experimental set-up

The experiments were performed using a planar unbalanced DC magnetron source (mcse-ROBEKO) in Ar. The aluminium cathode had a diameter of 3 inches and was facing a grounded anode 10 cm below its surface. A grounded guard ring of 2 cm width and 1 cm height and ∼7.4 cm inner diameter was positioned under and around the cathode assembly at a distance of 0.2 cm from the aluminium surface (see Fig.1). Two glass half cylinders were used to confine the plasma (and the produced nanoparticles). In order to perform optical emission spectroscopy and radial Langmuir probe measurements, a 1 cm gap was kept between them.

The discharge assembly was installed in a stainless steel cylinder device of 40 cm length and 30 cm diameter. The base vacuum was maintained at $\leq 10^{-6}$ mbar using a turbo molecular pump (Edwards TurboVac 400). An argon pressure between 10 Pa and 40 Pa at a flow of 5 sccm gas was set during the experiments. A current-regulated DC power supply (Glassman HV, 1 A–1 kV) was used to bias the cathode and maintain the discharge current at a constant value (from 100 to 500 mA). The cathode was actively cooled with a flow of ∼ 1 L/min of water at room temperature. Before each series of experiments, the cathode was cleaned by of low-pressure (∼ 10^{-1} Pa), high-current (>0.5 A) plasma pulses. Under the chosen operating conditions, the cathode was sputtered and aluminium nanoparticles could be grown (see bottom right inset of Fig.1). A precise description of these particles and their mechanisms of formation are out of the scope of this article. For each experiments, measurements were taken after the discharge had reached a steady state (constant V_c and optical emission intensities) in order to minimise the effect of changing cathode surface conditions and the effect of growing nanoparticles in the plasma [12,15,34,35].

3 Electrical characteristics of the DC magnetron discharge

The current–voltage relation in planar magnetrons can provide indirect information about the sputtering rate

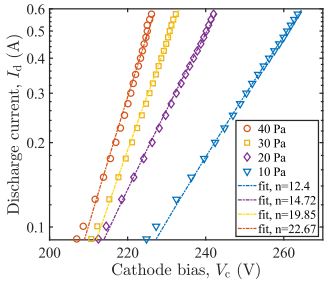

Fig. 2 Discharge current I_d as a function of the cathode voltage V_c for different argon pressures. Each $I_d - V_c$ curve is fitted by a power law curve of the form $I_d = k \cdot V_c^n$. The value of n obtained for each pressure is given in the inset

in the magnetron as it strongly depends on the background gas pressure and the dynamics of the sputtered cathode atoms [36]. Note that current–voltage relationships also depend on the gas–target combination, the secondary electron emission rate due to ion impact, the design of the magnetron, the magnetic field strength and other experimental parameters [37]. For this reason, the current–voltage relation was measured for four pressures, for currents varying between 100 and 600 mA. The results are shown in Fig. 2.

As can be seen, all measured $I_d - V_c$ characteristics follow a curve that obeys the relation:

$$I_d = k \cdot V_c^n \tag{1}$$

When increasing the pressure from 10 Pa to 40 Pa, the exponent n increases from $n \simeq 12$ to $n \simeq 23$. Ref. [2] indicates that the electron trapping in the plasma is more efficient at high pressures than at low pressures. Since collisions with the neutral background are more frequent at high pressures, the secondary electrons emitted by the cathode due to ion and fast neutral bombardment with a nonzero energy can be recaptured by the cathode due to gyration around the magnetic field lines [38,39]

4 Langmuir probe measurements

4.1 Experimental set-up

A cylindrical Langmuir probe (tungsten filament, 300 μm in diameter, 11.28 mm long) was used to measured plasma parameters ∼3 cm above the anode on the discharge axis (see Fig. 1). This corresponds to a region where the magnetic field is sufficiently low to consider the electrons unmagnetised. Moreover, the magnetic field lines are perpendicular to the probe axis, allowing us to use standard probe analysis to recover the plasma parameters. Finally being about 7 cm away from the cathode allowed us to take the measurements in a region where the number density of nanoparticles is low [28] and where the aluminium coating of the probe assembly develops slowly enough so the probe characteristics remain unaffected for the duration of the experiment.

The measurements were taken in a steady-state discharge (constant cathode bias and plasma emission intensity). Moreover, additional laser light scattering experiments seemed to indicate that there were indeed no trapped particles in the probed region. To obtain the current–voltage (IV) characteristics, the probe voltage V_p was ramped up from -35 V to $+10$ V by step of 0.33 V. Depending on the discharge parameters, the probe current I_p varied from ~ -100 μA to $\sim +35$ mA. Each measurement was repeated 3 times and averaged out to obtain the $I_\mathrm{p} - V_\mathrm{p}$ curves.

4.2 Results

Due to the high sputtering rate of aluminium, the probe was rapidly coated by an aluminium layer rendering a study over the range of parameters accessible to optical emission spectroscopy measurements very complicated. The Langmuir probe measurements were therefore limited to a smaller set of currents and pressures: $I_\mathrm{d} = 300$ mA and $I_\mathrm{d} = 500$ mA for pressures between 20 and 40 Pa.

In Fig. 3, raw Langmuir probe IV characteristics are shown for different conditions. Analysis showed that the electron energy distribution functions were quasi-Maxwellian (see Fig. 3c and inset of Fig. 4b). The analyses of the Langmuir probe IV characteristics were performed using both the Langmuir analysis [40] and Druyvesteyn analysis [41] which allowed us to recover the different n_e and T_e values. The two methods gave very close results, and the average values of n_e and T_e for the investigated discharge parameters are shown in Fig. 4. Note that the measurements being taken far away from the cathode where the electrons are confined by the magnetic field, the reported values of electron density are at least one to two orders of magnitude lower than that in the plasma ring confined by the magnetic arch near the cathode. Moreover, the electrons are colder by about ∼1 eV [24,33]. Consequently only the trends are of interest in this study.

As expected, a higher current results in a higher plasma density (Fig. 4a). With $n_e \sim 2.5 \cdot 10^{10}$ cm^{-3} at $I_\mathrm{d} = 300$ mA and $n_e \sim 5 \cdot 10^{10}$ cm^{-3} at $I_\mathrm{d} = 500$ mA, the values of electron density are in agreement with those observed in experiments using a tungsten cathode [33] or using a titanium cathode [24] with similar discharge currents and background gas pressures. The plasma density is only slightly dependent on the gas pressure and even show a small decrease when increasing the background gas pressure at constant discharge current.

Increasing the pressure results in a decrease in the electron temperature (from 0.65 eV down to 0.55 eV,

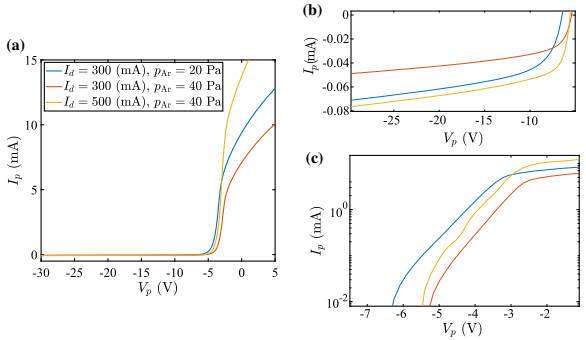

Fig. 3 **a** Raw IV curves for different discharge parameters. **b** Zoom on the ion part. **c** Zoom on the transition part in semi-log scale

see Fig. 4b). The electron temperature seems, however, almost insensitive to the discharge current. The measured electron temperatures are lower than the ones measured in the same experiment using a tungsten cathode [32,33] but close to the one measured under similar experimental conditions with a titanium cathode [24].

5 Optical emission spectroscopy

5.1 Experimental set-up

OES studies of the discharge plasma were carried out using a monochromator (Acton Spectra Pro 2500i, 500 mm focal length) coupled to a photomultiplier tube (Hamamatsu R3896). Convex lenses and an optic fibre were used to collect the emitted plasma radiation, ∼1.5 cm below the aluminium cathode where the line of sight crosses the high-density plasma ring below the cathode (see Fig. 1). A previous study with a tungsten cathode showed that nanoparticles could be trapped on the edge of the last magnetic arch (∼4 cm below the cathode) [33] and the line of sight used for the optical spectrum acquisition was considered free of large nanoparticles [1]. The spectra were then calibrated in intensity using a spectral radiance calibrated SphereOptics SR-3A integration sphere placed in front of the light collection system (glass window, convex lenses, optic fibre, monochromator and photomultiplier tube). After calibration, the relative intensities of each spectral line could be compared.

[1] The presence of small nanoparticle with diameter ≥10 nm can nevertheless not be ruled out

5.2 Collisional–radiative model of an argon discharge containing aluminium

Plasma parameters were evaluated based on the optical emission spectra recorded in the range from 300 to 830 nm consisting of a set of most prominent argon lines in the red and near-infrared range as well as a few strong Al transition lines close to the UV range, as visible in Fig. 5.

Emission spectra of an argon low-temperature plasma have been successfully analysed by modelling collisional and radiative processes responsible for the population of excited states [42,43]. In the complete model for argon [43,44], the populations of the first 14 excited states (Ar(1s) and Ar(2p) branches) were modelled including electron impact excitation from ground state, electron coupling between and within the Ar(1s) and Ar(2p) levels, and electron quenching and radiative processes including light trapping. It was shown that in the case of low-temperature plasmas with moderate electron densities and temperatures, the collisional–radiative model (CRM) can be simplified to an extended corona model including excitation from ground and 1s states and radiation transfer processes [43,45]. As an outcome of such a description, the population of Ar(2p) excited states linearly depends on the electron density making the analysis only dependent on the electron temperature.

In this case, the rate balance equation for excited Ar(2p$_\mathrm{i}$) state can be written as:

$$\frac{\mathrm{d}n_{2pi}}{\mathrm{d}t} = \frac{N \cdot K_{g-2pi}(T_e) + \sum_{j=2..5} n_{1sj} \cdot K_{1sj-2pi}(T_e)}{\sum_{j=2..5} A_{ij} \cdot \gamma(1s_j)} \tag{2}$$

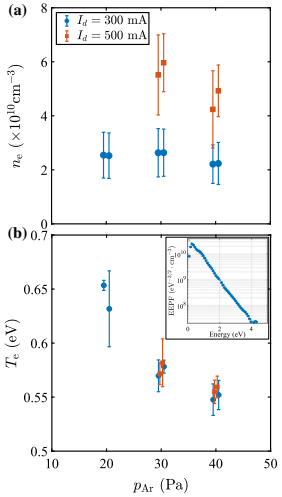

Fig. 4 **a** Electron density, n_e. **b** Electron temperature, T_e. The inset is the electron energy probability function (EEPF) obtained using Druyvesteyn analysis on the Langmuir probe IV characteristics measured at $p_{Ar} = 40$ Pa and $I_d = 300$ mA. In both (**a**) and (**b**), the presented values are the average of the Langmuir and Druyvesteyn analyses (T_e is obtained by a fit of the EEPF by a Maxwellian EEPF for the Druyvesteyn analysis). Note that the points have been artificially scattered around their true pressure value for clarity of the plot

where N is the argon ground-state density, n_{1sj} is the Ar(1s) state densities, K_{g-2pi} and $K_{1sj-2pi}$ are rate coefficients for electron impact excitation of $Ar(2p_i)$ from ground and Ar(1s) states, respectively. Radiative processes are described by Einstein coefficients for spontaneous emission A_{ij} corrected by radiation trapping (self-absorption) factor $\gamma(1sj)$ [46,47].

Similar to our previous works [43,45], the argon spectra was first analysed using the line branching method in order to estimate the argon 1s state densities that play an important role in the whole CRM and are non-trivial to model. The line branching model compares measured intensities of lines originating from the same excited level, to the theoretically estimated ratios (ratios of the Einstein coefficients for spontaneous emission), as in [43,48]. The difference can be further refined by a self-absorption mechanism [49] depending on the densities of the lower state of the considered transitions. In such a case, observing two sets of lines transitioning to the same two lower levels (e.g. Ar(1s4) and Ar(1s5))

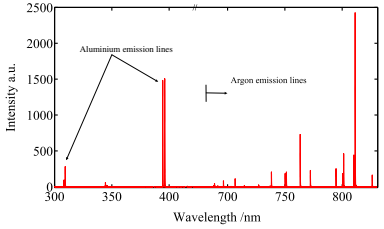

Fig. 5 Example of the measured emission spectra

would lead to the evaluation of the lower state densities. In the case of Ar emission spectra, the line branching analysis could be successfully used for evaluation of Ar 1s state densities, based on the pairs of the emission lines originating from different Ar(2p) excited states. Evaluated Ar(1s) states densities are further used as an input parameter in the rate balance equations describing populations of Ar(2p) states.

Steady-state solutions of the rate balance equations, for different Ar(2p) levels, were further used to describe emitted radiation including the radiation trapping effects (self-absorption). The resulting modelled spectra, depending on electron temperature, can be varied and compared with the measured spectra until the best fit is found.

The line branching method was also used for the characterisation of the aluminium-containing plasma by comparing the intensities of emission lines terminating on the ground states (Al(3p[1/2]) and Al(3p[3/2]) multiplets) providing an estimation of the Al atom density in the plasma. While the structure and the energy of the argon levels and the associated CR relations are well known, only partial information is available for the Al energy levels and the associated radiative coupling. A sketch of known Al levels based on NIST database [50] is given in Fig. 6.

Figures 5 and 6 show that the observed Al spectral lines are composed of two sets of transitions originating from the lower excited Al(4s) and Al(3d) states. Emission lines at 394 and 396 nm are clean single transitions originating from a single excited Al(4s) state. The second set of lines is actually composed of three lines: one line at 309.27 nm originating from the energetically higher multiplet Al(3d[5/2]), a second line at 309.28 line originating from the lower multiplet Al(3d[3/2]) and third line of this set being a pure single transition emitted from the lower Al(3d[3/2]) multiplet. The first two lines make a double line which cannot be resolved with the spectrometer used in the experiment.

In the case of aluminium, the rate balance equations describing the population of excited 4s and 3d states includes the electron impact excitation from ground states and the radiative decay from higher levels. However, in contrast to Ar plasmas where Ar atom density

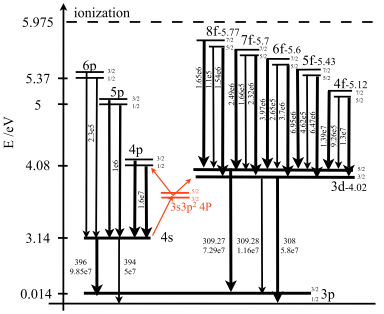

Fig. 6 Energy levels of Al atoms and radiative transitions

was known, the aluminium atom density in the plasma is an unknown variable used for the evaluation of the sputtering–deposition processes. The aluminium density is estimated by including Al line branching equations into the Ar/Al CRM.

5.3 Results

Measured optical emission spectra were first analysed using only Ar emission lines, ignoring possible interactions between Ar and Al. Ar spectra were first analysed by the line branching method considering three pairs of lines originating from different Ar(2p) levels in order to extract the densities of Ar(1s5,1s4) excited states. For this purpose the following ratios of line pairs were considered: 727/696, 738/706 and 800/763 originating from Ar(2p2), Ar(2p3) and Ar(2p6) excited levels, respectively.

Once these two values were known, similar line ratios could be recovered to evaluate the densities of other Ar(1s3) and Ar(1s2) excited states. Due to the limited observed spectral range, single line ratios were constructed for the evaluation of each of the two states: the 826/696 line ratio for the Ar(1s2) state and the 794/714 line ratio for the Ar(1s3) state. Evaluations of Ar(1s2) and Ar(1s3) states densities were prone to the error due to low intensity of the 714 nm line and the reduced spectral sensitivity of the spectrometer. (The 826 nm line is at the edge of the observable spectral range.) The reconstructed densities of all argon 1s states for the considered plasma conditions are shown in Fig. 7.

With known Ar(1s4,1s5) state densities, rate balance equations (Eq. (2)) were constructed for the excitation of 6 rmAr(2p) levels ($2p_1, 2p_3, 2p_5, 2p_6, 2p_7, 2p_8, 2p_9$) resulting in a steady-state solution depending only on electron temperature. Line ratios were then simulated for a wide range of electron temperatures and compared with the measured values in order to find the best

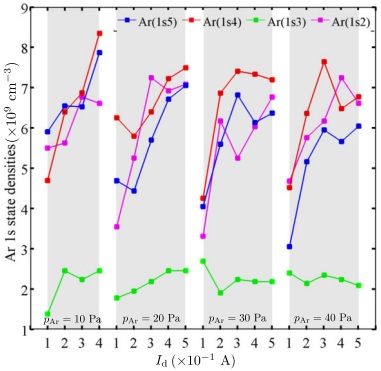

Fig. 7 Evaluated densities of Ar 1s states

match. Such a method was developed and discussed in details in Ref. [45] and compared with a complete CRM [43] for similar plasma conditions. Rate coefficients for electron impact excitation were calculated using the same set of excitation cross sections as in Refs. [42,43] and downloaded from the LXCAT database [51] and integrated over the desired electron energy distribution function. Rate coefficients calculated for Maxwell electron energy distribution function showed best agreements for most of line ratios. The resulting estimates of the average electron temperature based on argon CRM are presented in Fig. 8 in thick blue with solutions from individual line ratios shown in the background with thin green, cyan, magenta and black lines. Only the results with satisfactory confidence were shown in the figure, based on the analysis of a wide range of conditions discussed in Ref. [45]. Evaluated electron temperatures are relatively low ($\sim$ 1.5 eV) and show systematic dependence on pressure and power.

The electron temperature for each studied discharge condition was then used to reconstruct and compare the relative changes in the intensities of the lines and estimate the relative changes in the electron densities considering that the measurement conditions remained identical between each experiment. The estimated relative changes in electron densities are presented in Fig. 9 (blue lines).

Analysis of the Al spectra was done by building a simpler CRM due to the limited number of available cross sections and known interactions responsible for the population of Al levels. A set of cross sections for electron impact excitation from ground state, available for only a limited number of transitions, is taken from Ref. [52] and is used for calculations of rate coefficients. Einstein coefficients for spontaneous emission of Al levels were taken from the NIST database [50].

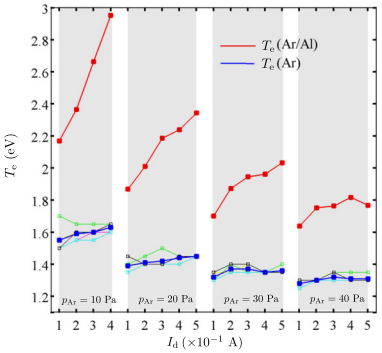

Fig. 8 Electron temperature estimation based on pure argon CRM—Te(Ar) and Ar/Al line ratio—Te(Ar/Al). The estimates of the average electron temperature based on argon CRM are the thick blue line. Solutions from individual line ratios are shown in the background with thin green, cyan, magenta and black lines. The hybrid Ar/Al model solution is the thick red line

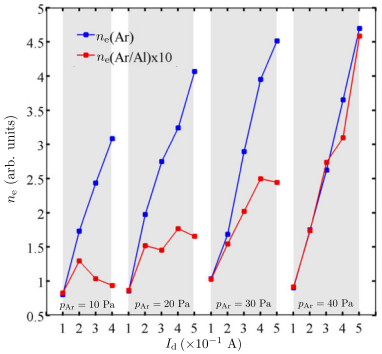

Fig. 9 Relative changes in the electron densities evaluated for the electron temperatures based on pure argon (Te(Ar) in blue) and argon/aluminium (Te(Ar/Al) in red) analysis

The population of the energetic levels shown in Fig. 6 are modelled by taking into account direct electron impact excitation from ground state (from both multiplets) while for lower energetic states Al($4s$) and Al($3d$), additional population by cascading radiation from upper levels was accounted for. In this description, no difference between the multiplets was considered in the collisional processes so that excitation from total ground-state density was taken in calculations. Considering that the CRM based on the line ratio method is only dependent on the electron temperature, the description of Al levels will additionally have two more unknowns which are the ground-state density multiplets. Observed emission spectra of Al consist of only a few strong emission lines originating from three different energetic levels. It limits the construction of a closed system of equations which would provide a unique solution. For this purpose, the Ar 750 nm line was also included in the description and used for comparison with Ar emission lines.

For this purpose, the ratio of Ar 750 nm and Al 308 nm lines was used to construct one equation while the other was built by comparing the intensities of Al 308 and Al 309 nm aluminium spectral lines. A third equation accounting for the radiation from the excited Al($4s$) state was also considered in the model as a ratio of the Al 394 nm and Ar 750 nm lines. The system of equations was additionally extended and improved by an additional line branching equation correlating the ratio of Al 394/396 nm lines with the ground-state multiplet densities. Therefore, the line branching equation was constructed to evaluate the ratio of 394/396 nm emission lines originating from the same Al($4s$) exited level decaying on different ground-state multiplets. With one more set of lines with the same properties (originating from the same level and decaying to the same ground-state multiplets), it would be possible to uniquely solve the system and determine the Al atom density in the plasma without additional modelling. However, in the presented measurements, a set of such lines was not observed. The best candidate would be the ratio of 265.24/266.03 nm lines originating from Al($5s$) excited state which is in a lower UV range usually not observable with standard (VIS–NIR) optics. However, the ratio of the Einstein coefficients of Al 394 nm and 396 nm lines is close to 0.5 while the measured ratio is close to unity, see Fig. 5. This difference can be used to describe the necessary density ratio of the ground-state multiplets based on self-absorption.

Hybrid Ar/Al model extended with the line branching relation consists of enough equations for finding a unique solution to the electron temperature and the density of aluminium in the ground state in the plasma. The evaluated electron temperature is presented in Fig. 8 (thick red line). Although the temperature shows similar systematic changes with controlled parameters, the absolute values are substantially higher than the one based on pure argon analysis. Based on this electron temperatures, reconstructed relative changes in electron densities appear lower, see Fig. 9.

The density of Al in the plasma, evaluated by hybrid Ar/Al analysis, is presented in Fig. 10 for each multiplet. The aluminium atom density is evaluated to be on the order of 10^{12} cm^{-3}, directly increasing with increasing plasma current and decreasing with pressure.

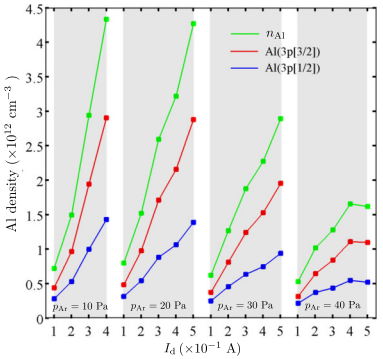

Fig. 10 Estimated number densities of aluminium ground-state multiplets

6 Discussion

Results obtained by different methods and techniques should be carefully analysed accounting for strong spatial inhomogeneity of the DC magnetron discharge and redistribution of the plasma glow due to changes of pressure and power. Therefore, the measurements further away from the cathode (electric probe) provide values characteristic of positive columns of DC magnetron discharges, while measurements closer to the cathode (OES) characterise the more energetic regions of the DC magnetron discharge (the high-density plasma ring confined by the magnetic arch). Nevertheless, both spectroscopy and Langmuir probe measurements show common trends of plasma parameters as a function of the working pressure, p_{Ar}, and the current discharge, I_d, but also present a few differences:

- At fixed I_d, an increase in the background gas pressure p_{Ar} results in a decrease in the electron temperature. The trend for the electron density is not so clear: Langmuir probe measurements indicate a small decrease in the electron density when increasing the pressure while spectroscopy measurements using argon lines tend to show a slight increase up to 30 Pa. Above 30 Pa, it depends on I_d. The hybrid Ar/Al CRM seem to favour a constant increase in the electron density. Langmuir probe measurement being taken relatively far away from the "active" plasma ring gave much lower values of T_e than spectroscopic measurements ($T_e \sim 0.60 \pm 0.05$ eV compared to $T_e \sim 1.5 \pm 0.2$ eV for the Ar CRM). Similar experiments performed with a tungsten cathode have shown that T_e is decreasing on the axis of the discharge when moving away from the cathode [33], explaining the difference in the reported values. However, the reported electron temperature is of the same order as the one found at the same position in the discharge when using a tungsten cathode ($T_e \sim 0.6$ eV for Al and $T_e \sim 1$ eV for W for $I_d = 300$ mA and $p_{Ar} = 30$ Pa [33]), and very close to the electron temperature reported for experiments in the plasma of the condensation chamber of a MS-GAS ($T_e \simeq 0.5$ eV for a titanium cathode, $I_d = 300$ mA and $p_{Ar} = 34.5$ Pa [24]). The measured plasma densities were in agreement with those reported in the literature [24,33] and with only a slight dependence to the gas pressure. Spectroscopic measurements taken just below the cathode and going through the high-density plasma ring unsurprisingly revealed a higher T_e but exhibited the same trend as the Langmuir probe measurements. Using Ar CRM, T_e decreased from $T_e \simeq 1.6$ eV at $p_{Ar} = 10$ Pa to $T_e \simeq 1.3$ eV at $p_{Ar} = 40$ Pa and showed little sensitivity to the intensity of the discharge current (i.e. a small increase of T_e is observed). This range of T_e is in agreement with the value reported in the literature for the electron temperature in the plasma ring of the condensation chamber of a MS-GAS [27]. The simultaneous use of aluminium and argon lines (hybrid A/Ar CRM) gave higher T_e. However, the trend in pressure remains the same: the higher the pressure, the lower the temperature. The main difference is that now the electron temperature reacts strongly to the discharge current, especially at the lowest investigated pressure. Both spectroscopic models have their drawbacks that could explain observed discrepancies in electron temperature. Due to the low density of Ar(1s) states, the excitation from ground-state Ar by energetic electrons is the dominant process and secondary excitation are negligible making the whole method impervious to low energetic electrons [45,48] and resulting in large uncertainties in electron temperature. The evaluated electron temperatures were used for an estimation of relative changes of electron density resulting in a different overall response of the system.
- At fixed background gas pressure p_{Ar}, an increase in the current results, as expected, in an increase in the plasma density and the electron temperature is marginally affected. Langmuir probe measurements on the axis of the discharge assembly and far below the plasma ring confined below the cathode showed density on the order of $n_e \sim 10^{10}$ cm^{-3}, which is comparable to what can be found in the literature [24,33]. The plasma density in the dense plasma ring below the cathode is one to two orders of magnitude higher [24,33]. Spectroscopy studies showed a linear increase in the relative plasma density with current when using the Ar CRM. The hybrid Ar/Al CRM did not show a linear increase of n_e at low pressure. The differences in T_e and n_e obtained from the Ar CRM and the hybrid Al/Ar CRM can be explained by the fact that low energetic electrons are directly included in the hybrid Ar/Al CRM since the excitation of Al states is possible at electron energies

as low as ~ 3 eV. However, the modelling of the excitation of Al states requires a good knowledge of Al collisional–radiative coupling constant and of the cross sections of excitation processes. Due to limited data on such processes, only a basic corona model was used for the modelling of Al excited state. Thus, in case of pure Ar CRM, changes of the discharge current is mostly reflected in electron density variations while in the hybrid analysis T_e is more sensitive to the current change. This discrepancy is most pronounced on lower pressure and slowly vanishes with pressure increase.

- In addition to T_e and n_e, spectroscopic studies provided the evolution of the densities of the argon resonant ($1s_2$, $1s_4$) and metastable ($1s_3$, $1s_5$) states. The density of the $1s_3$ state is revealed to be almost insensitive to both background gas pressure and discharge current even though it seems that at low pressure (10 Pa and 20 Pa) an increase in the current results in an increase in the $1s_3$ density. All other states show an increase in their densities with increasing current and tend to exhibit a slight decrease in density when increasing pressure at fixed current. This is particularly visible for the $1s_5$ metastable state. Overall Ar(1s) state densities are not very high compared with neutral Ar density making excitation from ground state the dominant process. As previously stated, under such conditions the evaluation of electron temperature based on the line ratio is less accurate and predominantly accounts for high energetic electrons in the electron energy distribution function, as discussed in [45]. As a result, evaluated electron temperature can be systematically over/under estimated due to the small errors in measurements, calibration procedure or data processing. The evaluation of T_e by the hybrid model is directly coupled to the aluminium atom density through excitation processes and self-absorption of Al emission lines which is quite strong in our experimental conditions. The resulting aluminium atom densities were thus estimated to be in the range $10^{11}-10^{12}$ cm^{-3}. This can be additionally justified considering that the line branching ratio of Al(394)/Al(396) lines imposes a lower limit of Al atom density of about 5×10^{16}m^{-3}. Al densities reported in this work are slightly higher than the ones reported in [53] which was operated on drastically lower pressures and close to the values reported for the sputtering of aluminium or titanium under similar conditions [54,55]. Note that the evaluation of Al densities could be improved and simplified by including one more pair of Al lines (preferably Al(265)/Al(266)) originating in deeper UV range.

In order to understand the influence of discharge conditions and the presence of aluminium atoms on plasma parameters, a simple global particle and power balance model for steady-state discharge is used. The model follows the methodology found in Refs. [41,53]. The plasma is reduced to a homogeneous half torus of mean radius $\bar{R}$ and of radius R_{tor} confined above the cathode racetrack [53]. In our experiment, $\bar{R}\simeq 2.2$ cm is the mean radius of the racetrack and $R_{tor}\simeq 0.5$ cm is the half width of the racetrack (see Fig. 1). The plasma volume is therefore $V_{plasma}=\pi^2\bar{R}R_{tor}^2$ and the bounding surface area $A_{plasma}=A_{planar}+A_{tor}$ is comprised of the planar contribution above the racetrack $A_{planar}=\pi\left[(\bar{R}+R_{tor})^2-(\bar{R}-R_{tor})^2\right]$ and the curved contribution $A_{tor}=2\pi\bar{R}R_{tor}$. The effect of the background gas pressure, the amplitude of the cathode voltage and the discharge current on the width and height of the "plasma ring" [38,39,56] is ignored. However, the fraction of ions f_t leaving the plasma towards the target is left as a free parameter in order to adjust the discharge current, voltage and power, $P=I_dV_c$ with the experimental ones. The model includes only the electron density n_e, the background neutral argon density n_{Ar} and the thermalised aluminium atom density n_{Al}. Direct impact ionisation of argon and aluminium as well as Penning ionisation of aluminium through collisions with argon metastable atoms is considered. It was indeed shown that ionisation of sputtered metal due to Penning ionisation through impact with metastable states of the argon is important in magnetron discharges and consistent with diffusive losses of argon meta- stables [57,58]. The particle balance equation, the power balance equation and the experimental adjustment of f_t equations are:

$$A_{planar}h_\ell u_B n_e = n_e V_{plasma} f_t\cdot\left[n_{Ar}K_{iz,Ar} + n_{Al}K_{iz,Al} + n_{Ar}K_{ex,Ar(4s)}\tau_{Ar^*}n_{Al}\sigma_p v_{T_{Al}}\right], \quad (3)$$

$$I_dV_c = P_{loss,e}+P_{loss,w}, \quad (4)$$

$$\frac{I_d}{e(1+\gamma)} = A_{planar}h_\ell u_B n_e, \quad (5)$$

where $h_\ell=0.80/\sqrt{4+R_{tor}/\lambda_{in}}$ is the effective area correction factor due to the variation of plasma density from the middle to the edge [41] in a plasma regime where transport is diffusive and ambipolar[2], $\lambda_{in}=1/(n_{Ar}\sigma_{in})$ is the ion-neutral mean free path where $\sigma_{in}=10^{-18}$ m^2 [41], $u_B=\sqrt{k_BT_e/m_e}\cdot(1+\pi\lambda_{De}/(2\lambda_{in}))^{-0.5}$ is the ion-collision corrected Bohm velocity [41] where λ_{De} is the electron Debye length at the cathode sheath edge, $K_{iz,Ar}$ is the argon electron impact direct ionisation rate, $K_{iz,Al}$ is the aluminium atom electron impact direct ionisation rate, $K_{ex,Ar(4s)}$ is the argon excitation rate towards metastable 4s levels, τ_{Ar^*} is the lifetime of argon metastable, $\sigma_p=7.15\cdot10^{-19}$ m^2 is the Penning ionisation cross section of aluminium [57], $v_{T_{Al}}$ is the thermal velocity of aluminium atoms, and $\gamma=0.1$ the effective ion-induced secondary electron emission coefficient which here is considered here. The argon metastable lifetime is given by $\tau_{Ar^*}^{-1}=\tau_D^{-1}+\tau_{m-e}^{-1}$ where the diffusion lifetime is $\tau_D^{-1}=K_2n_{Ar}+K_3n_{Ar}^2+\frac{D_0}{n_{Ar}}\Lambda^{-2}$ with $K_2=2.3\cdot10^{-15}$ cm^{3}s^{-1}, $K_3=1.4\cdot10^{-36}$ cm^{6}s^{-1}, and $D_0=2.4\cdot10^{18}$ cm^{-1}s^{-1} [59], and the electron metastable collision frequency is $\tau_{m-e}^{-1}=5\cdot10^{-8}n_eT_e$ with n_e in cm^{-3} and T_e in eV [57].

[2] The plasma is approximated by an infinite cylinder

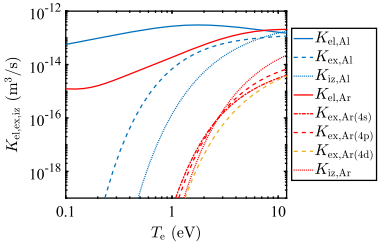

Fig. 11 Reaction rate constants as a function of T_e for argon (red curves) and aluminium (blue curves). The reaction rate for argon and aluminium were calculated assuming a Maxwellian EEDF and using the cross sections from Refs [52,60]

The power loss to the walls $P_{loss,w}$ carried by the particles lost at the plasma bounding surface is given by [41,53]:

$$P_{loss,w}=\frac{I_d}{e(1+\gamma)f_t}\left(\frac{5}{2}k_BT_e+0.75f_te|V_c| + (1-f_t)k_BT_e\ln\left(\sqrt{\frac{m_{Ar}}{2\pi m_e}}\right)\right). \quad (6)$$

The collisional power loss $P_{loss,e}$ are given by [41,53]:

$$P_{loss,e}=n_eV_{plasma}\left[n_{Ar}K_{iz,Ar}\epsilon_{c,Ar}+n_{Ar}K_{iz,Al}\epsilon_{c,Al}\right] \quad (7)$$

where the effective energy required per created electron–ion pair is given by [41,53]:

$$\epsilon_{c,s}=\left[\epsilon_{iz,s}+\sum_j\frac{K_{ex,s_j}}{K_{iz,s}}\epsilon_{ex,s_j}+\frac{K_{el,s}}{K_{iz,s}}\frac{3m_e}{m_s}k_BT_e\right]. \quad (8)$$

Species $s\in$ [Ar, Al] of atomic mass m_s interact with electron of mass m_e. $\epsilon_{iz,s}$ and ϵ_{ex,s_j} are the respective ionisation energies and excitation energies of the jth level with the corresponding reaction rate coefficient $K_{iz,s}$ and K_{ex,s_j}. $K_{el,s}$ is the elastic collision rate coefficients.

In Fig. 11, the reaction rate coefficients are calculated for argon and aluminium and were calculated assuming a Maxwellian electron energy distribution function (EEDF) and using the cross sections from Refs. [52,60].

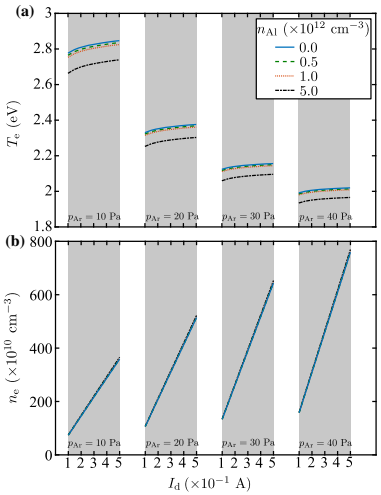

Fig. 12 Calculated plasma parameters as a function of p_{Ar} and I_d. **a** Electron temperature, T_e. **b** Electron density, n_e

The 4s, 4p and 4d levels of argon are considered and the excited levels of aluminium are grouped under one rate constant with an excitation energy $\epsilon_{ex,Al}=3.13$ eV. As can be seen, for electron temperatures around 1–2 eV, the reaction rate constants of aluminium are much higher than the ones for argon and one can expect moderate quantities of aluminium atoms in the plasma to have an impact on plasma parameters.

Equations (3–5) were solved numerically for different aluminium atom densities over the experimental range of I_d and p_{Ar}. The cathode voltage V_c is taken as the experimental one measured for a given set of I_d and p_{Ar} (see Fig. 2). The temperature of the background Ar gas and thermalised aluminium atoms is set at $T=400$ K which is close to the expected temperature [55]. The results of the calculation are shown in Fig. 12.

As expected, T_e decreases with increasing pressure. The calculated values are not far from the ones recovered using spectroscopic measurements but due to the numerous approximations of the model only qualitative comparison can be done. One can also see that the presence of a small density of aluminium atoms ($n_{Al}\simeq5\cdot10^{12}$ cm^{-3} corresponding to less than 0.3% of n_{Ar} at $p_{Ar}=10$ Pa) is enough to decrease the electron temperature by a few percent and might partially explain the relatively low measured electron temperatures. Increasing the discharge current results in a small increase in the electron temperature and a linear increase in

the plasma density. Note that the plasma density is almost unaffected by the presence of aluminium. The fraction of ions f_t leaving the plasma towards the target (not shown here) changed from around $f_t \sim 0.6$ at $p_{Ar} = 10$ Pa to $f_t \sim 0.9$ at $p_{Ar} = 40$ Pa.

However, our simple model cannot be used to obtained quantitative values since many relevant physical phenomena are not included. For instance, increasing pressure leads to lower sputtering rate due to lower energy of the ion hitting the cathode. Moreover, the influence of power and pressure on the width of the racetrack is not taken into account, nor is the thermalisation of sputtered atom and the heating of the background gas. Therefore, a high discharge current might not necessarily lead to more sputtering and a higher aluminium atom density in the plasma. For example, at the highest background gas pressure, collisions can result in a lower mean energy of the ion hitting the cathode and therefore a smaller sputtering rate and a reduced aluminium density (see Fig. 10)

7 Conclusion

In this article, the plasma parameters of an aluminium cathode direct current magnetron discharge in argon with operating pressures ranging from 10 to 40 Pa and discharge currents ranging from 100 to 500 mA were explored. The density of argon excited states, the sputtered aluminium atom density and the electron temperature were estimated using a collisional–radiative model and compared to plasma parameters obtained from Langmuir probe measurements. The trends of electron temperature and plasma density obtained using optical emission spectroscopic data agree well with probe measurements. The differences in reported values are explained by the different locations in the discharge that were studied using spectroscopy and Langmuir probes. However, the reported electron temperature were lower than the values found in the literature for similar discharge conditions and different cathode material [33]. By using a simple global model, the influence of the discharge parameters, namely the background argon pressure and the discharge current, as well as the density of sputtered aluminium atoms was investigated. It was shown that the presence of aluminium atoms in the plasma cools down the electrons and but has little effect on the plasma density. This is most probably due to the lower excitation and ionisation thresholds of aluminium with respect to argon.

Future studies will require the development of a more complete hybrid CRM. It will allow more precise derivation of plasma parameters. Direct measurement of the aluminium atom density through absorption spectroscopy will also be taken. A careful modelling of the magnetron discharge should also be done in order to study the influence of sputtering and transport of aluminium atoms on plasma parameters.

Acknowledgements LC acknowledges the support of the Natural Sciences and Engineering Research Council of Canada (NSERC), RGPIN201904333.

Author contributions

SM did the OES analysis and wrote the corresponding section. JM did Langmuir probe analysis and edited the manuscript. CA participated in the experimental measurement campaign and edited the manuscript. LC participated in the experimental measurement campaign and wrote Sects. 1, 2, 3, 6 and 7.

Data Availability Statement. This manuscript has no associated data or the data will not be deposited. [Authors' comment: Data will be made available upon request to the corresponding author.]

References

1. W.D. Gill, E. Kay, Efficient low pressure sputtering in a large inverted magnetron suitable for film synthesis. Rev. Sci. Instrum. **36**, 277 (1965). https://doi.org/10.1063/1.1719553
2. R.K. Waits, Planar magnetron sputtering. J. Vacuum Sci. Technol. **15**, 179 (1978). https://doi.org/10.1116/1.569451
3. T.E. Sheridan, M.J. Goeckner, J. Goree, Model of energetic electron transport in magnetron discharges. J. Vac. Sci. Technol. A Vac. Surf. Films **8**, 30 (1990)
4. D. Depla, W. Leroy, Magnetron sputter deposition as visualized by monte Carlo modeling. Thin Solid Films **520**, 6337 (2012). https://doi.org/10.1016/j.tsf.2012.06.032
5. M.L. Escrivão, A.M.C. Moutinho, M.J.P. Maneira, Planar magnetron glow discharge on copper: empirical and semiempirical relations. J. Vac. Sci. Technol. A **12**, 723 (1994). https://doi.org/10.1116/1.578813
6. S.M. Rossnagel, J. Hopwood, Metal ion deposition from ionized mangetron sputtering discharge. J. Vac. Sci. Technol. B Microelectron. Nanometer Struct. Process. Meas. Phenom. **12**, 449 (1994). https://doi.org/10.1116/1.587142
7. K. Matyash, M. Fröhlich, H. Kersten, G. Thieme, R. Schneider, M. Hannemann, R. Hippler, Rotating dust ring in an RF discharge coupled with a dc-magnetron sputter source. experiment and simulation. J. Phys. D Appl. Phys. **37**, 2703 (2004)
8. A.E. Farsy, J. Ledig, M. Desecures, J. Bougdira, L. de Poucques, Characterization of transport of titanium neutral atoms sputtered in Ar and Ar/N2 HIPIMS discharges. Plasma Sources Sci. Technol. **28**, 035005 (2019). https://doi.org/10.1088/1361-6595/ab022b
9. M. Cavarroc, M. Mikikian, Y. Tessier, L. Boufendi, Successive generations of dust in complex plasmas: a cyclic phenomenon in the void region. Phys. Rev. Lett. **100**, 045001 (2008). https://doi.org/10.1103/PhysRevLett.100.045001

10. I. Stefanović, N. Sadeghi, J. Winter, The influence of C_2H_2 and dust formation on the time dependence of metastable argon density in pulsed plasmas. J. Phys. D Appl. Phys. **43**, 152003 (2010)
11. D. Samsonov, J. Goree, Instabilities in a dusty plasma with ion drag and ionization. Phys. Rev. E **59**, 1047 (1999)
12. M. Mikikian, M. Cavarroc, L. Couëdel, L. Boufendi, Low frequency instabilities during dust particle growth in a radio-frequency plasma. Phys. Plasmas **13**, 092103 (2006)
13. G.M. Jellum, D.B. Graves, Particulates in aluminum sputtering discharges. J. Appl. Phys. **67**, 6490 (1990). https://doi.org/10.1063/1.346081
14. C. Arnas, A. Michau, G. Lombardi, L. Couëdel, K. Kishor Kumar, Effects of the growth and the charge of carbon nanoparticles on dc discharges. Phys. Plasmas **20**, 013705 (2013)
15. K. Kishor Kumar, L. Couëdel, C. Arnas, Growth of the growth and the charge of carbon nanoparticles on dc discharges. Phys. Plasmas **20**, 013705 (2013)
16. L. Couëdel, K. Kishor Kumar, C. Arnas, Detrapping of tungsten nanoparticles in a direct-current argon glow discharge. Phys. Plasmas **21**, 123703 (2014). https://doi.org/10.1063/1.4903465
17. S. Barbosa, L. Couëdel, C. Arnas, K. Kishor Kumar, C.Pardanaud, F. R. A. Onofri. In–situ characterisation of the dynamics of a growing dust particle cloud in a direct–current argon glow discharge. J. Phys. D. Appl. Phys **49**, 045203 (2016). https://stacks.iop.org/0022--3727/49/i=4/a=045203
18. H. Haberland, M. Mall, M. Moseler, Y. Qiang, T. Reiners, Y. Thurner, Filling of micron-sized contact holes with copper by energetic cluster impact. J. Vac. Sci. Technol., A **12**, 2925 (1994). https://doi.org/10.1116/1.578967
19. A. Majumdar, D. Köpp, M. Ganeva, D. Datta, S. Bhattacharyya, R. Hippler, Development of metal nanocluster ion source based on dc magnetron plasma sputtering at room temperature. Rev. Sci. Instrum. **80**, 095103 (2009). https://doi.org/10.1063/1.3213612
20. T. Momin, A. Bhowmick, A new magnetron based gas aggregation source of metal nanoclusters coupled to a double time-of-flight mass spectrometer system. Rev. Sci. Instrum. **81**, 075110 (2010). https://doi.org/10.1063/1.3465304
21. V. Bouchat, O. Feron, B. Gallez, B. Masereel, C. Michiels, T. V. Borght, S. Lucas, Carbon nanoparticles synthesized by sputtering and gas condensation inside a nanocluster source of fixed dimension, Surf. Coat. In: Technol. 205, Supplement 2, S577, pSE 2010 Special Issue: Proceedings of the 12th International Conference on Plasma Surface Engineering (2011) https://doi.org/10.1016/j.surfcoat.2011.03.055
22. N.K. Manninen, N.M. Figueiredo, S. Carvalho, A. Cavaleiro, Production and characterization of Ag nanoclusters produced by plasma gas condensation. Plasma Processes Polym. **11**, 629 (2014)
23. M.V. Dutka, A.A. Turkin, D.I. Vainchtein, J.T.M. De Hosson, On the formation of copper nanoparticles in nanocluster aggregation source. J. Vac. Sci. Technol. A **33**, 031509 (2015). https://doi.org/10.1116/1.4917002
24. J. Kousal, A. Kolpaková, A. Shelemin, P. Kudrna, M. Tichý, O. Kylián, J. Hanuš, A. Choukourov, H. Biederman, Monitoring of conditions inside gas aggregation cluster source during production of Ti/TiOx nanoparticles. Plasma Sources Sci. Technol. **26**, 105003 (2017)
25. T. Acsente, R. Negrea, L. Nistor, E. Matei, C. Grisolia, R. Birjega, G. Dinescu, Tungsten nanoparticles with controlled shape and crystallinity obtained by magnetron sputtering and gas aggregation. Mater. Lett. **200**, 121 (2017). https://doi.org/10.1016/j.matlet.2017.04.105
26. M. Vaidulych, J. Hanuš, J. Kousal, S. Kadlec, A. Marek, I. Khalakhan, A. Shelemin, P. Solař, A. Choukourov, O. Kylián, H. Biederman, Effect of magnetic field on the formation of Cu nanoparticles during magnetron sputtering in the gas aggregation cluster source. Plasma Processes Polym. **16**, 1900133 (2019). https://doi.org/10.1002/ppap.201900133
27. M. Koten, S. Voeller, M. Patterson, J. Shield, In situ measurements of plasma properties during gas-condensation of Cu nanoparticles. J. Appl. Phys. **119**, 114306 (2016)
28. J. Kousal, A. Shelemin, M. Schwartzkopf, O. Polonskyi, J. Hanuš, P. Solař, M. Vaidulych, D. Nikitin, P. Pleskunov, Z. Krtouš et al., Magnetron-sputtered copper nanoparticles: lost in gas aggregation and found by in situ x-ray scattering. Nanoscale **10**, 18275 (2018)
29. H. Hahn, R.S. Averback, The production of nanocrystalline powders by magnetron sputtering. J. Appl. Phys. **67**, 1113 (1990). https://doi.org/10.1063/1.345798
30. N. Nafarizal, K. Sasaki, Synthesis characteristics of cu particulates in high-pressure magnetron sputtering plasmas studied by in situ laser-light scattering. J. Phys. D Appl. Phys. **45**, 505202 (2012)
31. L. Couëdel, C. Arnas, T. Acsente, A. Chami, Characterisation of a high-pressure direct-current magnetron discharge used for tungsten nanoparticle production. AIP Conf. Proc. **1925**, 020020 (2018). https://doi.org/10.1063/1.5020408
32. C. Arnas, A. Chami, L. Couëdel, T. Acsente, M. Cabié, T. Neisius, Thermal balance of tungsten monocrystalline nanoparticles in high pressure magnetron discharges. Phys. Plasmas **26**, 053706 (2019). https://doi.org/10.1063/1.5095932
33. A. Chami, C. Arnas, Spatial distributions of plasma parameters in conventional magnetron discharges in presence of nanoparticles. J. Plasma Phys. **86**, 905860512 (2020). https://doi.org/10.1017/S0022377820001014
34. S. Mitic, M. Y. Pustylnik, G. E. Morfill, Spectroscopic evaluation of the effect of the microparticles on radiofrequency argon plasma. New J. Phys **11**, 083020. http://stacks.iop.org/1367-2630/11/i=8/a=083020 (2009)
35. S. Mitic, B. Klumov, M. Pustylnik, G. Morfill, Determination of electron temperature in low-pressure plasmas by means of optical emission spectroscopy. JETP Lett. **91**, 231 (2010)
36. S.M. Rossnagel, H.R. Kaufman, Current-voltage relations in magnetrons. J. Vac. Sci. Technol. A **6**, 223 (1988). https://doi.org/10.1116/1.574985
37. D. Depla, G. Buyle, J. Haemers, R. De Gryse, Discharge voltage measurements during magnetron sput-

tering. Surf. Coat. Technol. **200**, 4329 (2006). https://doi.org/10.1016/j.surfcoat.2005.02.166
38. G. Buyle, D. Depla, K. Eufinger, J. Haemers, R.D. Gryse, W.D. Bosscher, Simplified model for calculating the pressure dependence of a direct current planar magnetron discharge. J. Vac. Sci. Technol. A Vac. Surf. Films **21**, 1218 (2003). https://doi.org/10.1116/1.1572169
39. G. Buyle, D. Depla, K. Eufinger, J. Haemers, W. Bosscher, R. Gryse, Simplified model for the DC planar magnetron discharge, Vacuum **74**, 353, in *selected papers revised from the Proceedings of the Seventh International Symposium on Sputtering and Plasma Processes (ISSP 2003)*. https://doi.org/10.1016/j.vacuum.2004.01.014
40. R.L. Merlino, Understanding Langmuir probe current-voltage characteristics. Am. J. Phys. **75**, 1078 (2007)
41. M.A. Lieberman, A.J. Lichtenberg, *Principles of Plasma Discharges and Materials Processing*, 2nd edn. (Wiley, Hoboken, 2005)
42. X.-M. Zhu, Y.-K. Pu, A simple collisional-radiative model for low-temperature argon discharge with pressure ranging from 1 pa to atmospheric pressure: kinetics of paschen 1s and 2p levels. J. Phys. D Appl. Phys. **43**, 015204 (2010)
43. J. Kaupe, D. Coenen, S. Mitic, Phase-resolved optical emission spectroscopy of a transient plasma created by a low-pressure dielectric barrier discharge jet. Plasma Sources Sci. Technol. **27**, 105003 (2018)
44. J. Kaupe, P. Riedl, D. Coenen, S. Mitic, Temporal evolution of electron density and temperature in low pressure transient Ar/N2 plasmas estimated by optical emission spectroscopy. Plasma Sources Sci. Technol. **28**, 065012 (2019). https://doi.org/10.1088/1361-6595/ab252d
45. S. Mitic, J. Kaupe, P. Riedl, D. Coenen, Comparative studies of compact kHz and MHz driven low pressure plasmas by emission and laser spectroscopy. Phys. Plasmas **26**, 073507 (2019)
46. T. Holstein, Imprisonment of resonance radiation in gases. Phys. Rev. **72**, 12 (1947)
47. P.J. Walsh, Effect of simultaneous doppler and collisional broadening and a hyperfine structure on the imprisonment of resonance radiation. Phys. Rev. **116**, 3 (1959)
48. M. Schulze, A. von Yanguas-Gil, P. Awakowitz, Keudell, A robust method to measure metastable and resonant state densities from emission spectra in argon and argon-diluted low pressure plasmas. J. Phys. D: Appl. Phys. **41**, 065206 (2008)
49. R. Mewe, Relative intensity of helium spectral lines as a function of electron temperature and density. Br. J. Appl. Phys. **18**, 107 (1967). https://doi.org/10.1088/0508-3443/18/1/315
50. NIST database. https://www.nist.gov (2020)
51. NGFSRDW database, retrieved on June 17, 2020. and BSR database. www.lxcat.net. Retrieved on June 17, 2020 (2020)
52. V. Gedeon, S. Gedeon, V. Lazur, E. Nagy, O. Zatsarinny, K. Bartschat, *b*-spline *r*-matrix-with-pseudostates calculations for electron collisions with aluminum. Phys. Rev. A **92**, 052701 (2015). https://doi.org/10.1103/PhysRevA.92.052701
53. J. Trieschmann, S. Ries, N. Bibinov, P. Awakowicz, S. Mráz, J.M. Schneider, T. Mussenbrock, Combined experimental and theoretical description of direct current magnetron sputtering of Al by Ar and Ar/N2 plasma. Plasma Sources Sci. Technol. **27**, 054003 (2018). https://doi.org/10.1088/1361-6595/aac23e
54. K. Sasaki, N. Nafarizal, Enhancement of Ti + density in high-pressure magnetron sputtering plasmas. J. Phys. D Appl. Phys. **43**, 124012 (2010)
55. F.J. Jimenez, S.K. Dew, Comprehensive computer model for magnetron sputtering. I. Gas heating and rarefaction. J. Vac. Sci. Technol. A **30**, 041302 (2012). https://doi.org/10.1116/1.4712534
56. A.E. Wendt, M.A. Lieberman, Spatial structure of a planar magnetron discharge. J. Vac. Sci. Technol. A **8**, 902 (1990). https://doi.org/10.1116/1.576894
57. J. Hopwood, F. Qian, Mechanisms for highly ionized magnetron sputtering. J. Appl. Phys. **78**, 758 (1995). https://doi.org/10.1063/1.360334
58. C. Christou, Z.H. Barber, Ionization of sputtered material in a planar magnetron discharge. J. Vac. Sci. Technol. A Vac. Surf. Films **18**, 2897 (2000). https://doi.org/10.1116/1.1312370
59. I. Stefanović, T. Kuschel, S. Schröter, M. Böke, Argon metastable dynamics and lifetimes in a direct current microdischarge. J. Appl. Phys. 116, 113302 (2014). https://doi.org/10.1063/1.4895714
60. Cross sections extracted from program magboltz, version 7.1 june 2004, biagi-v7.1 database, www.lxcat.net, retrieved on April 20, 2021. https://www.lxcat.net/Biagi-v7.1 (2021)

Plasma Research Express

PAPER

Influence of magnetic field strength on nanoparticle growth in a capacitively-coupled radio-frequency Ar/C_2H_2 discharge

L Couëdel[1,2,3], D Artis[3], M P Khanal[3], C Pardanaud[2], S Coussan[2], S LeBlanc[3], T Hall[3], E Thomas Jr[3], U Konopka[3], M Park[3] and C Arnas[2]

[1] Department of Physics and Engineering Physics, University of Saskatchewan, Saskatoon, Saskatchewan S7N 5E2, Canada
[2] CNRS, Aix Marseille Univ., PIIM, UMR 7345, 13397 Marseille cedex 20, France
[3] Department of Physics, Auburn University, Auburn, Alabama 36849, United States of America

E-mail: lenaic.couedel@usask.ca **and** lenaic.couedel@univ-amu.fr

Keywords: plasma, nanoparticles, magnetic field

OPEN ACCESS

RECEIVED
12 October 2018

REVISED
21 January 2019

ACCEPTED FOR PUBLICATION
4 February 2019

PUBLISHED
12 February 2019

Original content from this work may be used under the terms of the Creative Commons Attribution 3.0 licence.

Any further distribution of this work must maintain attribution to the author(s) and the title of the work, journal citation and DOI.

Abstract

The growth of nanoparticles in a magnetised chemically active discharge (Ar/C_2H_2) is investigated. The influence of the strength of the magnetic field on dust particle growth dynamics is explored. The structure of the grown nanoparticles is studied *ex situ*. It is revealed that the strength of the magnetic field (up to 2.5 T) has a major impact on discharge parameters (such as the self-bias of the powered electrode) as well as on the growth and morphology of the nanoparticles. At high magnetic field, the dust cloud is confined in the sheath above the grounded electrode while without magnetic field the dust cloud occupies most of the interelectrode space. Moreover, at high magnetic field, large porous spherical agglomerates were grown. The modification of the self-bias is explained by the influence of the magnetic field on the diffusion of charged species resulting in a confinement of the plasma under the powered electrode. Complementary particle-in-cell simulations confirm that the electric field and plasma distributions are strongly affected by the magnetic field explaining the experimentally observed dust cloud localisation. The large porous spherical agglomerates are most probably due to an enhanced agglomeration caused by the modified confinement owing to the magnetic field.

1. Introduction

Dusty or complex plasmas are weakly ionised gases containing nanometre or micron size dust particles. In laboratory plasmas, due to their interactions with the background electrons and ions, these dust particles are electrically charged. This charge is usually negative due to the higher mobility of the electrons. Complex plasmas can thus be viewed as three charged component plasmas [1–3].

In nature, dusty plasmas can occur naturally in the mesosphere, interplanetary and interstellar clouds, planetary rings [4, 5], and cometary tails. In these systems the dust particles are formed from the agglomeration of complex molecules and ices that occur in the space environment [6]. Dust particle formation is also observed in the laboratory (see for example [7–9]) and industrial [10] chemically active discharges. Dust particle formation in an industrial reactor is an important issue: the occurrence of solid dust particles (nano- or micrometric) is unwanted (and even harmful) in some processes such as etching as it significantly changes the electrical properties of the discharge. As a result, the presence of growing dust particles can substantially alter the plasma etching processes and lead to substrate pollution. However, the dust particles can also be of value for technologies based on nanomaterials and nanocomposites, such as polymorphous silicon (amorphous silicon with embedded crystalline silicon nanoparticles created in silane-based discharges), a material of primary interest for the manufacture of solar cells [11]. Low-pressure radiofrequency plasmas have been thus extensively used in 'dusty-regime' as a tool to produce high quality nanocrystals and nanopowders of a broad range of materials [12]. The understanding of dust growth mechanisms in plasmas is consequently a crucial issue and is of interest to many subfields of plasma physics.

© 2019 IOP Publishing Ltd

In capacitively-coupled radio-frequency (cc-rf) discharges, dust growth mechanisms have been actively studied. Dust growth occurs following a well-defined pattern: formation of molecular precursors from sputtering products or by gas dissociation, formation and accumulation of nanocrystallites, aggregation and finally growth by molecular sticking [8, 11, 13, 14]. Particle growth depends on the discharge parameters [12] and the dust growth has a significant impact on the surrounding plasma [15, 16]. It is thus imperative to monitor the evolution of the discharge and plasma parameters carefully to have a full understanding of the growth process.

In the presence of a magnetic field, the transport of electrons and ions is altered and thus the properties of the plasma are affected. In a dusty plasma under low to moderate magnetic fields (or for large enough dust particles) the influence of the magnetic field is indirect and weak, due to the very small charge-to-mass ratio [17]. However, even at these low magnetic fields ($B < 1$ T) dust grain surface electron and ion fluxes will experience modifications. As a result, the dust particle charges and the forces acting on them are changed and the drag forces resulting from these ion and electron flows are of great importance for the dynamics of dust particles.

In moderately magnetised conventional discharges, dust particle growth is observed [18–20]. In such discharges, the magnetic field is used to trap electrons and thus enhance the plasma density through an increase in the number of ionising collisions. For example, in magnetron sputtering discharges, it is possible to grow and trap a dense cloud of metallic nanoparticles above the cathode [19]. In magnetron discharges, dust rotation arising from the ion $\mathbf{E} \times \mathbf{B}$ drift is sometimes observed and can be used to enhance particle coating [21]. In electron cyclotron resonance (ECR) discharges, the growth of nanoparticles occurs in the high magnetic field regions [20]. This means that the electrons trapped in this region (Lorenz force must be considered for electrons dynamics and transport) create plasma potential wells able to confine the negatively charged dust particles. Dust particle growth can be monitored by measuring the self-bias voltage of a probe immersed in the ECR plasma.

In this paper, we report on measurements of the plasma and characterisation of nanometre-sized particles that were formed in magnetised plasmas. Experiments were performed using the Magnetized Dusty Plasma Experiment (MDPX) device using a modified rf plasma source. Plasmas were generated in pure argon (Ar) or in a mixture of argon and acetylene (C_2H_2) gas. The magnetic field was varied from 0 T to 2.5 T. This paper reports on changes in discharge parameters such as the self-bias of the powered electrode due to the magnetic field in pristine argon discharge as well as the effect of dust particle growth in magnetised argon-acetylene discharges. It also reports on the characterisation of the grown particles using electron microscopy and Raman spectroscopy. The paper is presented as follows: section 2 describes the experimental set-up, section 3 describes the characterisation of the plasma discharge, section 4 describes the characterisation of the particles, section 5 presents a numerical model of the system and particle-in-cell simulations in order to qualitatively explain our results. Finally, section 6 will provide concluding remarks.

2. Experimental setup

The Magnetized Dusty Plasma Experiment (MDPX) device at Auburn University is a multi-user, high magnetic field experimental platform. It consists of two main components: the superconducting magnets and a plasma chamber which can be changed according to the type of experiments. The superconducting magnets of the MDPX device are described extensively in previous papers [17, 22, 23]. For the studies reported in this article, the MDPX device was operated in the vertical configuration (magnetic field aligned parallel to gravity). The four superconducting coils were energised at the same current to produce a uniform magnetic field (with $\Delta B/B < 1\%$) at the center of the experimental volume where the cc-rf discharge was placed.

The plasma source consisted of parallel aluminium electrodes installed at the center of a 6-way cross vacuum chamber with 100 mm ISO ports (see figure 1). A 13.56 MHz rf generator connected to the powered electrode through a matching network was used to produce the plasma. The rf power was set between $5 < P_{rf} < 30$ W. The top electrode with a diameter of 50.8 mm was powered and surrounded by a grounded guard ring. The powered electrode developed a self-bias, V_{bias} when the plasma was on, which was monitored using a National Instrument data acquisition card. The grounded bottom electrode had a diameter of 76.2 mm and a ~1 mm deep, 25 mm wide 75 mm long notch was cut in its center in order to install the microscopy glass slides used to collect the grown particles.

Before each plasma the vacuum chamber was evacuated to a base pressure of ~1 mTorr. Then a flow of argon $5 < Q_{Ar} < 10$ sccm and a flow of acetylene $0 < Q_{C_2H_2} < 2$ sccm were injected into the chamber and the opening of the pumping port was adjusted to stabilise the pressure p inside the chamber to a value 200 mTorr $< p <$ 600 mTorr before the plasma was switched on. The pressure was monitored using a MKS Baratron capacitance manometer. The grown particle cloud was then illuminated using a 532 nm, 100 mW green laser diode that was expanded into a thin, vertical laser light sheet (~3 cm height, ~200 μm width) using a cylindrical lens. The scattered light was recorded from the side port of the vacuum chamber at an angle of 90°

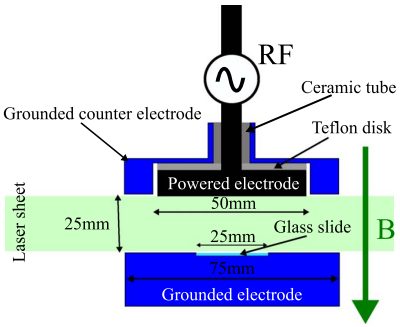

Figure 1. Schematic of the electrode assembly.

using a USB3-based, 2048 by 2048 pixel, Ximea model xiQ camera that could be operated up to 90 frames per second (fps). For the experiments described in this article, frame rates of 30 fps were usually used.

3. Discharge characterisation

3.1. Pristine argon plasma

The behaviour of the discharge as a function of the magnetic field strength was studied in pristine argon (experiments with no particle growth). The operating pressure was $p = 300$ mTorr ($Q_{Ar} = 7$ sccm) and the forward rf power $P_{rf} = 20$ W. A clean glass slide was installed in the notch of the bottom grounded electrode. The magnetic field was set at an initial high value of 2.5 T and was then slowly ramped down to 0.0 T. The plasma glow was recorded at 1 fps and the self-bias voltage of the powered electrode was measured. In figure 2, snapshots of the plasma glow for different magnetic field strengths are presented. As can be seen, the plasma light emission appears to increase with the magnetic field . Moreover, the glow is generally more localised under the powered electrode at high magnetic field, indicating a strong confinement of the charged species. Note that with magnetic fields $B > 0.25$ T, filamentation of the plasma occurred. Filaments were mostly localised at the edge of the powered electrode. The number of observed filaments was higher for the highest values of magnetic field. Note that the filaments were not fixed and could jump from one position to another. It is unclear what role these filaments could play in the subsequent growth experiments in which they were also observed.

In figure 3, the evolution of the self-bias voltage as a function of magnetic field strength is presented. As expected, at low magnetic field the self-bias is negative because the surface of the powered electrode is smaller than the surface of the grounded areas [24, 25]. When increasing the magnetic field, the self-bias of the powered electrode increased (or decreased in absolute value) and reached 0 V at B∼1 T. At magnetic field $B \gtrsim 1$ T, the self-bias started to decrease again. Note that the magnetic field did not noticeably affect the settings of the matching network and therefore the impedance of the whole circuit (plasma + external circuit) was almost constant. Consequently, the variations of rf peak to peak voltage at the powered electrode remained limited and could not explain the amplitude of the changes of the self-bias voltage. The physical mechanism of the self-bias evolution as a function of the magnetic field strength are discussed in section 5.1.

3.2. Ar/C_2H_2 discharge

When adding acetylene to the discharge, carbon nanoparticles could be grown. During our experiments, the pressure was set to $p = 300 \pm 2$ mTorr before plasma ignition using an Ar/C_2H_2 gas mixture ($Q_{Ar} = 7$ sccm and $Q_{C_2H_2} = 1$ sccm). The forward rf power was $P_{rf} = 20$ W. The discharge was pulsed manually with plasma duration $t_{on} = 60$ s followed by pauses of $t_{off} \simeq 60$ s. In figure 4(a) the evolution of the pressure normalised to the maximum pressure during the plasma pulse is presented. As can be seen, after the discharge was turned on, the pressure slightly increased to a maximum p_{max} due to heating of the gas. However, after 1 s, the total gas pressure started to decrease. The value at the end of the plasma pulse was 3%–4% lower than the pressure at ignition (well below the experimental pressure fluctuations due to our gas flow regulation system). This indicates that, while the acetylene flow was kept constant, it was partially dissociated. This behaviour was observed for all

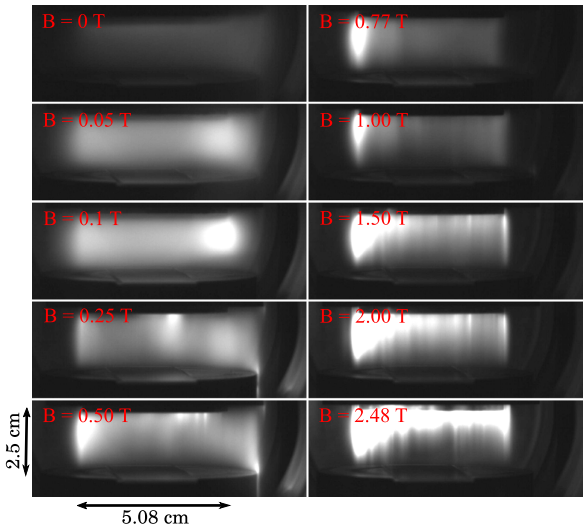

Figure 2. Snaphots of the plasma glow at different magnetic fields for pure argon plasmas. The argon flow was $Q_{Ar} = 7$ sccm, the pressure was $p = 300$ mTorr and the rf power was $P_w = 20$ W.

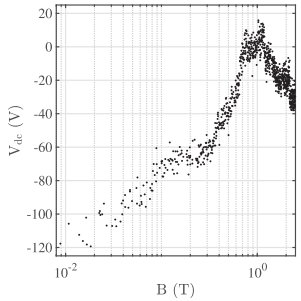

Figure 3. Self-bias as a function of magnetic field strength. Discharge parameters are the same as in figure 2.

magnetic fields. It should be nevertheless noted that increasing the magnetic field resulted in a faster and greater decrease of the pressure (the pressure decay rate is faster in the presence of a magnetic field and the minimum reached pressure is the smallest for the largest value of the magnetic field). In all cases at the end of each rf pulse, the pressure returned to its original value in ∼30 s.

The self-bias voltage of the powered electrode V_{bias} was also recorded during the different discharge pulses. The results are presented in figure 4(b) for different magnetic field strengths. The general behaviour observed in pure argon plasma was again observed, i.e. the stronger the magnetic field, the lower (in absolute value) the self-bias. However, contrary to pure argon plasma, the self-bias was not constant with time. It is known that the

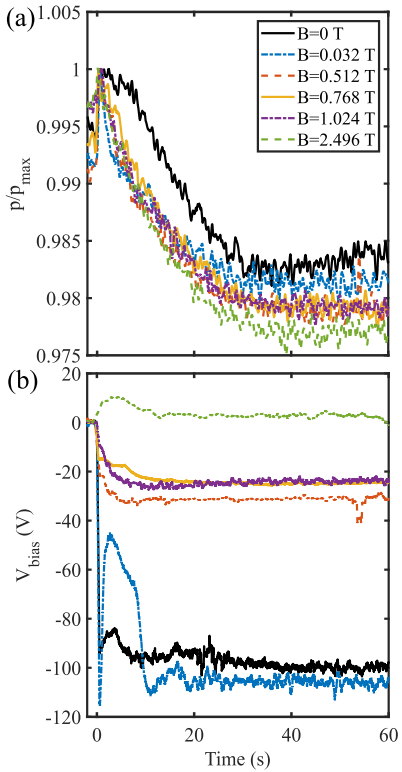

Figure 4. Evolution of (a) normalised chamber pressure and (b) self-bias voltage as a function of time for different magnetic field strengths in Ar/C_2H_2 discharges. The argon flow was $Q_{Ar} = 7$ sccm, the acetylene flow was $Q_{C_2H_2} = 1$ sccm, the pressure before ignition was $p = 300$ mTorr and the rf power was $P_w = 20$ W.

growing nanoparticles strongly affect the impedance of the plasma (see for examples [26]) and that working at fixed rf power therefore induces variations of the rf peak to peak voltage. These variations are correlated to the variations the self-bias voltage and directly associated to the growth dynamics of the nanoparticles. Large self-bias oscillations are linked to successive generation of nanoparticles as was already reported in cc-rf discharge in which particles are grown [7, 27–30]. However, at low or zero magnetic field, V_{bias} exhibited strong oscillations in the first 20 s after plasma ignition. The strongest oscillations were observed at $B = 0.032$ T (see figure 4(b)). Note that from one plasma to the other the shape of the V_{bias} signal was roughly the same (slight changes due the change in discharge conditions, i.e. coating of the electrode, gas purity, temperature of the electrode, etc). It should also be noted that at the highest investigated magnetic field ($B = 2.496$T), the self-bias of the powered electrode was, contrary to the pristine argon discharge, positive. In an electropositive plasma (such as a pristine argon plasma), the main reason for the appearance of self-bias on the powered electrode connected to the rf generator through a blocking capacitor (as in many rf matching network) is the irreversible escape of electrons into the electrodes, making the gap positively charged [24]. Since the discharge is asymmetric (the grounded area are much bigger than the area of the powered electrode), different amounts of charge are gained by the

electrodes. It causes a difference in the dc electrode potentials, the self-bias. In Ar/C_2H_2 discharges in which particles are growing, there are numerous kind of charged species (positive and negative ions such as Ar^+, $C_2H_2^+$, C_2H^-, $C_4H_2^+$, etc) due to the complicated chemistry [31–34]. Moreover, the growing dust particles are getting negatively charged which reduces the electron density [35].Consequently, the observed positive self bias is most probably caused by a very different balance of the charges collected at the electrodes due to the complicated chemistry of the Ar/C_2H_2 plasma and the presence of the growing particles.

In figure 5, snapshots of the laser light sheet scattered by the growing particle cloud at different magnetic fields are presented. At no magnetic field (figure 5(a)) the well-known cyclic growth behaviour was observed: ∼15 s after plasma ignition, the dust cloud started to be visible on the camera and occupied almost the entire interelectrode space. At $t \sim 20$ s, a 'void' (i.e. a region without visible dust particles) started to open in the discharge (see figure 5(a) at $t = 20$ s in the middle of the gap below the powered electrode edge) [36–47]. Note that in our experiment, the void did not have its typical eye shape as reported by other groups. The observed void was more bowl-shaped. This is most likely due to the geometry of our experiment which differs from the ones used in other studies (size of the electrodes and/or interelectrode spacing). Inside the void opening new particles are growing while the first cloud was pushed towards the edges(see figure 5(a)). With our experimental parameters, the duration of a growth cycle (appearance of a new generation of dust in the 'void') was ∼40–60 s, depending on how many plasma pulses had already occurred in the chamber. Density waves were visible near the lower electrode. Such density waves were observed in similar experiments [48, 49] and are known to favour the agglomeration of the nanoparticles [48, 50].

At low magnetic field ($B = 0.032$ T, figure 5(b)) the nanoparticle growth was faster which was demonstrated by direct imaging of the nanoparticle cloud. This correlates well with the faster decrease of the gas pressure during the plasma pulses and the stronger oscillations of the self-bias voltage previously described. The duration of a growth cycle was, in this case, ∼15–20 s. An interesting observation is the break of symmetry in the void opening (see figure 5(b) at $t = 20$ s). Moreover, a strong scattering intensity was observed close to the sheath of the top electrode indicating a very dense particle cloud and/or the presence of large particles.

At higher magnetic field ($B \gtrsim 0.1$ T), no growth cycles were observed. In figure 5(c), snapshots of the recorded laser light scattering at $B = 1.024$ T are presented but qualitatively similar observations were made at other values of magnetic field. In all high magnetic field cases, a cloud of nanoparticles above the grounded bottom electrode rapidly appeared (see figure 5(c)). This is in agreement with the fast decrease of the gas pressure after plasma ignition due to the dissociation/polymerisation of acetylene resulting in the formation of the dust particles. It is interesting to note that the dust cloud did not cover the entire area above the grounded electrode but was on the contrary confined near the interface between the glass slide used for dust collection and the rest of the electrode. Depending on the experiment, the dust cloud extended more or less above the glass slide. Laser light scattering also confirmed a quick agglomeration. Large individual particles levitating above the grounded electrode were indeed visible on camera only a few tens of seconds after plasma ignition (see figure 5(b) at $t = 40$ s and $t = 60$ s). The particles formed much closer to the electrode compared to the cases at no and low magnetic fields.

4. Dust characterisation

For the different magnetic fields, dust particles were collected for fifteen consecutive 60 s plasma pulses separated by an off period of 60 s during which the gas was renewed. After each series of fifteen plasmas, the electrodes were carefully cleaned and a new glass slide was installed in the grooved bottom electrode. An argon oxygen plasma was then run in the chamber for ∼15 min at 20 W in order to burn away all residual carbon coating. Finally the chamber was pumped down to its base pressure for a minimum of 30 min before the next series of plasmas was performed.

4.1. Electron microscopy

In figures 6 and 7, scanning electron microscopy (SEM) images and transmission electron microscocopy (TEM) images of dust particles grown at different magnetic fields are presented. As can be seen in figures 6(a) and 7(a), the nanoparticles grown at $B = 0$ T were almost spherical and looked quite compact as reported in similar experiments [51]. The observed particles had diameters ranging from ∼20 nm to ∼250 nm in agreement with the observation of a couple of growth cycles during a 60 s plasma pulses. In the zoom of figure 7(a), the surface roughness of the nanoparticles seems to indicate that the nanoparticles are agglomerate of smaller particles as reported in similar experiments [51, 52].

Increasing the magnetic field greatly affected the shape and size of the nanoparticles. At low magnetic field (see figure 6(b)), the size distribution seemed much broader than without magnetic field but the particles still looked quite compact. This observation coincides with the faster growth cycle reported in section 3.2. A further

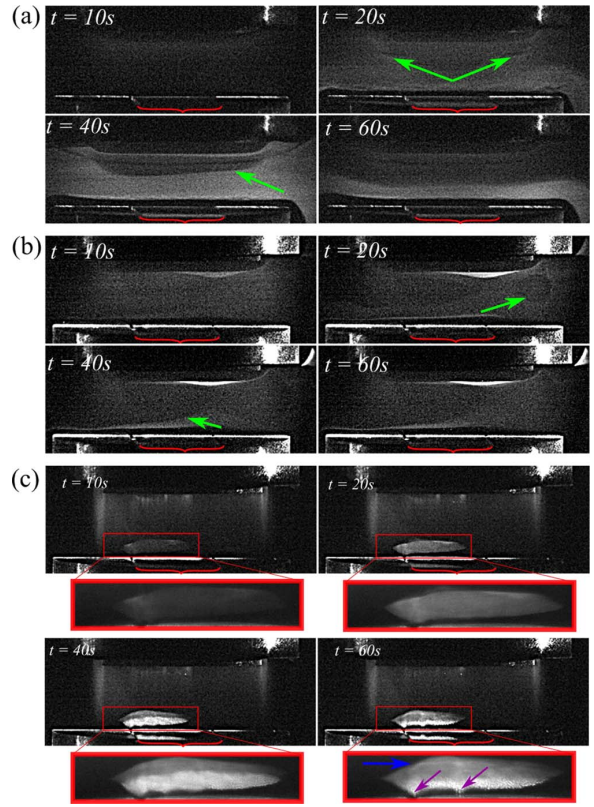

Figure 5. (a) Images of the scattered laser light at different instants after discharge ignition for: (a) B = 0.0 T, (b) B = 0.032 T and, (c) B = 1.024 T. The other discharge conditions are the same as in figure 4. The bright vertical and horizontal stripes visible on all images are reflections of the laser light on the electrode assembly. On all images, a red horizontal curly bracket indicates the position of the glass slide used to collect the dust particles. In (a) and (b), the oblique green arrows indicate the edge of the void in which a new generation of dust particles can grow. In (c), the horizontal blue arrow point to a dust density wave and the oblique purple arrows show dips in the dust cloud induced by plasma filamentation. On all images except the magnified ones, a sharpen filter has been applied to improve visibility of the different features.

increase of the magnetic field resulted in the sample being a mixture of very small (∼10 nm) nanoparticles with larger spherical 'fluffy' porous particles (with diameters up to a few hundreds of nanometres). These particles are clearly visible in figures 6(c)–(d). TEM images (figures 7(b)–(d)) clearly show that these porous particles are agglomerates of the smaller particles. Both SEM and TEM images indicate that higher magnetic field resulted in fluffier agglomerates. The agglomerates are probably the large particles levitating in the sheath above the grounded electrode observed by laser light scattering in figure 5(c) towards the end of the plasma pulse. The smaller particles correspond to the dim cloud levitating slightly above the larger dust particles.

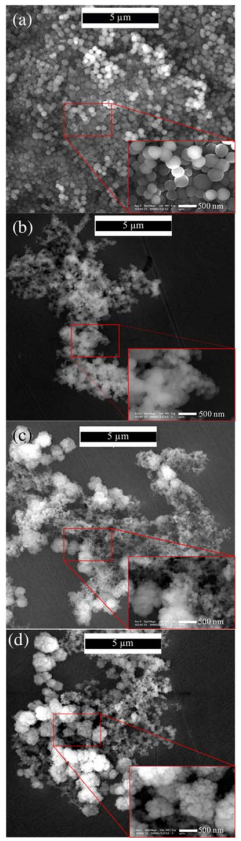

Figure 6. SEM images of dust particles grown for different magnetic fields. (a) 0 T, (b) 0.768 T, (c) 1.024 T and, (d) 2.496 T. The other discharge conditions are the same as in figure 4.

4.2. Raman microscopy

Carbon-based materials are routinely analysed using micro-Raman spectroscopy [53–61]. This technique consists in measuring the wavelengths of photons produced by inelastic scattering of the incident light with the analysed sample. The energy difference between incident and scattered photons correspond to vibrational energies which are fingerprints of a given material. Interpreting the spectral region between 1000 and 1800 cm^{-1} provides information on the chemical properties (hybridisation of the carbon atoms) and the structural order [53, 55, 60].

The Raman spectra were obtained using a commercial Horiba-Jobin-Yvon HR LabRAM apparatus (×100 lens, 514.5 nm, numerical aperture 0.9, laser power at the surface $\lesssim$1 mW · μm^{-2}). The resolution of our system is ∼0.2 cm^{-1}. Each final spectrum was an average of 9 spectra taken a few micrometers apart to avoid local inhomogeneity. The scanning time was ∼60 s averaged two times. Spectra have been acquired at the centre

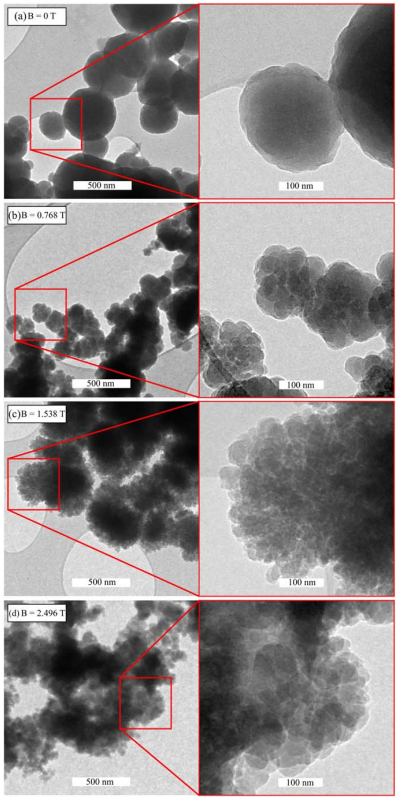

Figure 7. TEM images of dust particles grown for different magnetic fields. The other discharge conditions are the same as in figure 4.

of the substrate, where large amounts of dust particles were collected as well as on the edge of the substrate where a thinner coating was observed (especially at large magnetic fields).

In figure 8, Raman spectra of particles grown at $B = 0$ T, $B = 0.256$ T, $B = 1.024$ T, and $B = 2.496$ T are plotted. Figure 8(a) shows the raw spectra, displaying a huge photoluminescence background and weak vibrational bands. Figure 8(b) shows the vibrational bands after the photoluminescence background has been removed. Two broad peaks are visible in the spectra. The main one is located at 1570–1600 cm^{-1} (G band). In the low energy wing of the G band, the D-band at ~1350 cm^{-1} can be distinguished. These bands are assigned to the stretching modes of sp^2 hybridised carbon atoms and are a signature of aromaticity [53, 55, 58]. Peaks that might correspond to C−O and C=O bonds are also located at 1200 cm^{-1} and in the range 1800–1900 cm^{-1} (not shown) [62]. However, their attribution is unsure since the samples were stored in air prior to analysis and the bands can therefore be due to oxygen contamination. In addition, the pristine glass slides on which the dust particles have been collected also display weak bands located close to 1200 and 1800–2000 cm^{-1}.

Spectroscopic parameters of our samples are reported in table 1. As the bands are broad and overlapped, obtaining the exact values is in general difficult because several fitting models involving two main bands (the G

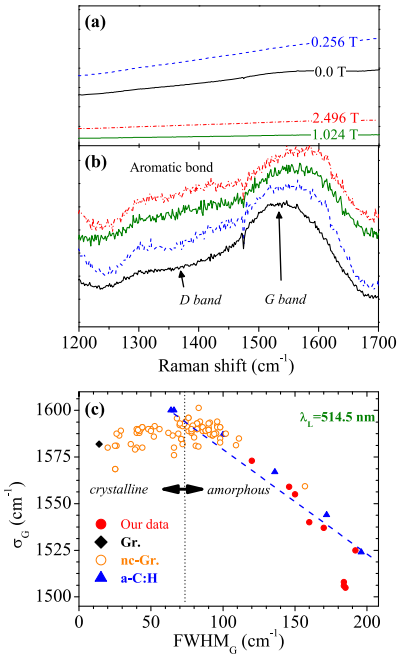

Figure 8. Raman spectra for dust particles grown at $B = 0$ T, $B = 0.256$ T, $B = 1.024$ T, and $B = 2.496$ T. The particles were located at the center of the substrate. (a) Raw spectra. (b) Spectra with linear background (baseline) removed a normalised to the height of the G-band. (c) σ_G as a function of $FWHM_G$ (edge and centre data points). See details in the text for the comparison of the samples.

Table 1. Position, width of the G-band and ratio of the slope of the baseline the spectrum over the intensity of the G-band for dust particles grown at different magnetic fields.

B (T)	σ_G (cm^{-1})		$FWHM_G$ (cm^{-1})		m/I_G (μm)	
	centre	edge	centre	edge	centre	edge
0.0	1540	1537	160	170	89.5	83.5
0.256	1559	1506	146	184	208	37.7
1.024	1555	1505	150	185	104	15.5
2.496	1573	1508	120	184	192	8.4

and D bands) plus additional subbands (up to three extra bands) can be found in the literature. More details on the subject can be found in [63]. In order to avoid any choice of models, we directly took the spectroscopic parameters of spectra of reference samples (graphite, nanocrystalline graphite, nc-Gr. [64], and hydrogenated amorphous carbon, a-C:H [60]) and applied the same procedure to our samples in order to compare them directly to well characterised materials. Figure 8(c) shows the position of the G-band σ_G as a function of its full width at half maximum $FWHM_G$ for all the samples. Reference samples are spread around a curve which

changes its slope around FWHMG = 80–100cm^{-1} which delimits the transition between crystalline and amorphous carbon. From that comparison, we can conclude that our samples are clearly amorphous.

In table 1, σ_G , $FWHM_G$ and, the ratio m/I_G, where m is the slope of the baseline, and I_G is the height of the G-band, are given for dust particles grown different magnetic fields. This ratio can be used to get a very rough estimate of the H-content of carbonaceous materials [65]. For instance, it has been used recently to investigate graphitisation of cabornaceous nanoparticles, and their hydrogen content [66]. A value of $m/I_G \sim 100$ is close to a H content of 50% whereas a value of $m/I_G \sim 10$ is close to a H content of 40 percent.Note that since the data point distribution obtained by Casiraghi *et al* is quite broad [65], m/I_G gives only an estimate. In our case, m/I_G ∼100 for the dust particles indicating a hydrogen content of ∼50% which is the expected value for particles grown in Ar/C_2H_2.

When $B = 0$ T, the Raman spectra recorded at the center and the edges of the sample coincide. It changes when the value of the applied magnetic field value increases. On the edges, m/I_G diminishes by a decade from ∼100 μm to ∼10 μm whereas it remains nearly constant in the centre, varying only from ∼100 μm to 200 μm. A qualitative interpretation is that, when the magnetic field increases, the hydrogen content does not change too much at the centre of the samples (i.e. in the dust particles) whereas it slightly decreases on the edges of the sample (in the coating). The value of $FWHM_G$ at the centre decreases from ∼160 cm^{-1} at $B = 0$ T to ∼120 cm^{-1} at B = 2.496 T, while being nearly constant at the edges (∼185 cm^{-1}). A possible interpretation is that the local order in the dust particles is slightly higher for particle growth at high magnetic fields.

The Raman microscopy results support the hypothesis of dust amorphous hydrogenated carbon particles consisting of large numbers of very small aromatic domains. Note that the G band position σ_G, $FWHM_G$, and the D/G band intensity ratio could be used to determine the degree of order of the carbonaceous dust materials [57, 60]. This is however beyond the scope of the present study.

5. Discussion

5.1. Evolution of the pristine argon discharge

To understand the process of particle growth in a magnetised plasma, it is necessary first to understand how a pristine argon discharge is affected by the magnetic field. For this purpose, a basic diffusion model of the plasma has been developed. We first assume a quasi-neutral transport (ambipolar diffusion). We also consider that the plasma is completely surrounded by conducting walls so that the ambipolar field is effectively short circuited at the end of the discharge plasma. The geometry of the system is reduced to a simple cylinder of radius R and length L. The powered electrode is at the top of the cylinder and has a radius $R_a < R$. To explain the behaviour of the discharge at different magnetic fields, a simple diffusion equation is used [25, 67]

$$\frac{\partial n(r,\,z)}{\partial t} = D_{a\perp}\nabla_\perp^2 n(r,\,z) + D_{a\parallel}\frac{\partial^2 n(r,\,z)}{\partial z^2} + \nu_{iz}(r,\,z)n(r,\,z), \tag{1}$$

where $D_{a\parallel}$ is the parallel diffusion coefficient defined as:

$$D_{a\parallel} = \frac{k(T_e + T_i)/e}{\mu_i^{-1} + \mu_e^{-1}}, \tag{2}$$

with $\nu_{iz}(r, z)$ the ionisation frequency, $\mu_{e(i)}$ the electron (ion) mobility coefficients, k the Boltzmann constant, e the elementary charge and, $T_{e(i)}$ the electron (ion) temperature. The perpendicular diffusion coefficient in the framework of the Simon's ambipolar diffusion joint model is [67]:

$$\begin{aligned} D_{a\perp} = {} & \frac{k/e}{(\mu_i^{-1} + \mu_e^{-1})}\left(\frac{(T_e + T_i)}{(1 + \mu_e\mu_i B^2)}\right) \\ & + \frac{k/e}{(\mu_i^{-1} + \mu_e^{-1})}\frac{\mu_e\mu_i B^2}{\frac{T_e/T_i - \mu_i/\mu_e}{1 - (\mu_i/\mu_e)(T_e/T_i)}} + \mu_e\mu_i B^2 \\ & \times\left(\frac{T_e}{1 + \mu_e^2 B^2} + \frac{T_i}{1 + \mu_i^2 B^2}\right). \end{aligned} \tag{3}$$

In cc-rf discharges, the ionisation rate is the highest at the sheath below the powered electrode and decreases as a function of the distance from the powered surfaces [68, 69]. However, in the plasma bulk in the interelectrode gap beneath the powered surfaces, the ionisation rate is still reasonably high (2-3 times lower than its maximum value) while it falls rapidly to zero in the region mostly surrounded by grounded surfaces. The electron temperature varies in contrast more slowly [68]. For this reason, the ionisation frequency is approximated as:

$$\nu_{iz}(r,\,z) = \nu_{iz}(r) = \begin{cases} \nu_{iz}, & R \leqslant R_a, \\ 0, & R > R_a. \end{cases} \tag{4}$$

Ionisation is due to inelastic collision between electron and atoms. For argon, the ionisation frequency can be approximated as [67, 70]:

$$\nu_{iz} = p \cdot 8.13 \cdot 10^8\left(\frac{kT_e}{e}\right)^{0.68}\exp\left(\frac{-\epsilon_1 e}{kT_e}\right), \tag{5}$$

where p is given in Torr and $\epsilon_1 = 15.76$ eV is the threshold ionisation energy of argon. The solution of the diffusion equation can be easily calculated:

$$n(r,\,z) = \begin{cases} n_0\cos\left(\pi\frac{z}{L}\right)J_0(\alpha_P r), & R \leqslant R_a, \\ n_0\cos\left(\pi\frac{z}{L}\right)J_0(\alpha_P R_a)\frac{K_0(\alpha_G R)I_0(\alpha_G r) - K_0(\alpha_G r)I_0(\alpha_G R))}{K_0(\alpha_G R)I_0(\alpha_G R_a) - K_0(\alpha_G R_a)I_0(\alpha_G R))}, & R > R_a, \end{cases} \tag{6}$$

where J_k, K_k and I_k are the Bessel function of the first kind and the modified Bessel functions of the first and second kind of order k, respectively. The coefficient α_P and α_G define the characteristic length of diffusion and are defined as follows:

$$\alpha_P^2 = \frac{\nu_{iz}}{D_{a\perp}} - \left(\frac{\pi}{L}\right)^2\frac{D_{a\parallel}}{D_{a\perp}}, \tag{7}$$

$$\alpha_G^2 = \left(\frac{\pi}{L}\right)^2\frac{D_{a\parallel}}{D_{a\perp}}. \tag{8}$$

At a given pressure and magnetic field, the $\alpha_{P,G}$ coefficients depend only on the electron temperature. The derivative of the plasma density being continuous, the electron temperature can then be found by solving:

$$\left.\frac{\partial n(r,\,z)}{\partial r}\right|_{r=R_a^-} = \left.\frac{\partial n(r,\,z)}{\partial r}\right|_{r=R_a^+} \tag{9}$$

or

$$\begin{aligned} 0 = {} & \alpha_P J_1(\alpha_P R_a) + \alpha_G J_0(\alpha_P R_a) \\ & \times\frac{K_0(\alpha_G R)I_1(\alpha_G R_a) + I_0(\alpha_G R)K_1(\alpha_G R_a))}{K_0(\alpha_G R)I_0(\alpha_G R_a) - K_0(\alpha_G R_a)I_0(\alpha_G R))}. \end{aligned} \tag{10}$$

equation (10) was solved numerically at $p = 300$ mTorr for different magnetic fields and the resulting density profiles are plotted in figure 9(a). It is shown that with increasing the magnetic field the plasma is increasingly confined under the powered electrode. This is in qualitative agreement with the experimental observation of the glow distribution presented in figure 2. It is also interesting to note that the increase of the magnetic field results in a slight decrease of the electron temperature (figure 9(b)). This is due to a better confinement of the electrons in the glow which leads to a more efficient ionisation of the gas. This can also explain the faster decrease of the gas pressure during the particle growth experiment with an applied magnetic field (figure 4(a)) caused by improved dissociation of acetylene which resulted from better electron confinement. Moreover, the forward RF power was kept constant during the experiment. In our model, by assuming that the effective rf power coupled to the plasma does not change and is totally used to ionise the gas and is then lost by recombination on the walls of the chamber, the relative density of the plasma, $n/\langle n\rangle$ where $\langle n\rangle$ is the plasma density averaged over the volume of the plasma chamber, compared to the case without magnetic field can be calculated[4]. Results are presented in figure 9(a). As can be seen, despite the fact the electron temperature decreases with increasing magnetic field, the relative plasma density increases with the magnetic field, qualitatively explaining the experimental observation of a more intense glow emission at high magnetic field. Note that since our model is not taking into account the spatial dependence of the ionisation rate and the electron temperature nor the surfaces covered by the dielectric glass slide, it is unable to explain the plasma filamentation observed experimentally.

Following the work of Lieberman and Savas [71], the self-bias voltage of the powered electrode can be estimated. In asymmetric cc-rf discharges, the powered and grounded electrode having different areas, the voltage drop in front of the powered (active) electrode V_a is different from the voltage drop V_g. The voltage ratio (V_a/V_g) can be obtained from the current fluxes at each electrode. In Lieberman and Savas model [71], the applied rf voltage is dropped across a thin sheath. It is also assumed that the glow region between the electrodes has a thickness much greater than those of the sheaths so that the discharge is maintained by ion generation in the glow and losses at the electrode. An approximate form of the dc voltage drop V_a and the rf voltage amplitude

[4] The plasma density cannot be properly estimated since it is not possible to know exactly how much power is effectively coupled to the plasma.

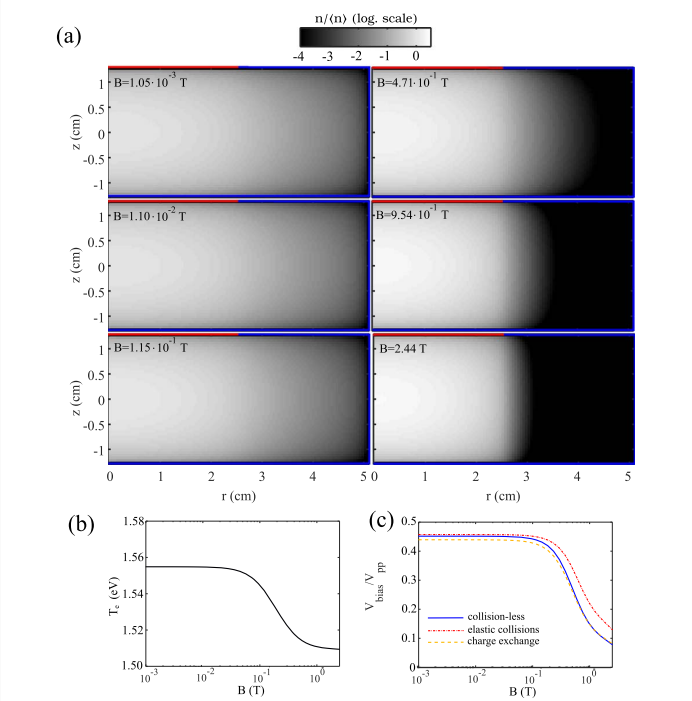

Figure 9. Results of the calculation: (a) plasma density distribution for different magnetic field strengths. The red lines represent the powered electrode and the blue lines represent the grounded surfaces. (b) Electron temperature as a function of the magnetic filed strength. (c) V_{bias}/V_{pp} as a function of magnetic field strength. The argon pressure is $p = 300$ mTorr and the peak-to-peak voltage is $V_{pp} = 300$ V.

$\tilde{V}_a$ is [71]:

$$V_a = (k_b T_e/e)\ln[I_0(\tilde{V}_a/T_e)] + (k_b T_e/e)\ln[m_i/(2\pi m_e)],$$
$$V_a \approx \tilde{V}_a + V_{fa}, \quad \text{if} \quad T_e \ll \tilde{V}_a, \tag{11}$$

where the floating potential V_{fa} is defined as:

$$V_{fa} = (k_b T_e/2e)\ln[m_i T_e/(4\pi^2 m_e \tilde{V}_a)] \tag{12}$$

In the case of high voltage capacitive sheath, $V_{fa} \ll V_a$ and $\tilde{V}_a \approx V_a$ so, by considering capacitive sheath, the rf current current density can be related to the dc sheath voltage:

$$J_a(\boldsymbol{x}) \propto V_a/s_a(\boldsymbol{x}) \tag{13}$$

Depending on the ion-neutral mean free path compared to the sheath thickness s, collisions can play a role and influence the plasma density at the sheath edge n_s [71]. For a collision-less sheath:

$$n_{sa} \propto V_a^{3/2}/s_a(\boldsymbol{x})^2 \tag{14}$$

For a collisional-resonant charge transfer- sheath:

$$n_{sa} \propto V_a^{3/2}/s_a(\boldsymbol{x})^{5/2} \tag{15}$$

For a collisional-elastic scattering- sheath:

$$n_{sa} \propto V_a^2/s_a(\boldsymbol{x})^3 \tag{16}$$

The rf current flowing through the rf electrode is:

$$I_a \propto \int_{S_a} J_a(\boldsymbol{x})\, d^2x \tag{17}$$

A similar expression can be obtained for the current flowing through the grounded surface I_g. By equating the two currents the following scaling formula can be obtained [71]:

$$\frac{V_a}{V_g} = \left\{\left(1 - \frac{V_{fg}}{V_g}\right)\left(1 - \frac{V_{fa}}{V_a}\right)^{-1} \times \left[\int_{S_g} n_{sg}^p(\boldsymbol{x})\, d^2x\right]\left[\int_{S_a} n_{sa}^p(\boldsymbol{x})\, d^2x\right]^{-1}\right\}^q \tag{18}$$

where p and q are exponents corresponding to the sheath scaling law (collision-less: $p = 1/2, q = 3$, elastic collisions: $p = 1/3, q = 4$, charge-exchange collisions: $p = 2/5, q = 5/2$) [71]. The dc voltage drops V_a and V_g can be linked to the peak-to-peak rf voltage V_{pp} applied to the discharge [71]:

$$V_a + V_g = V_{fa} + V_{fg} + V_{pp}/2. \tag{19}$$

In the experiment, the self-bias voltage is:

$$V_{bias} \approx V_a - V_g. \tag{20}$$

Using equations (18) and (19), the normalised bias voltage is [71]:

$$\frac{V_{bias}}{V_{pp}} \approx \frac{1}{2}\frac{V_a/V_g - 1}{V_a/V_g + 1 - V_{fa}/V_g - V_{fg}/V_g}. \tag{21}$$

The density at the sheath boundaries can be obtained by specifying that the ion flow velocity at the walls is perpendicular to the wall and has a velocity equal to the Bohm velocity $u_B = \sqrt{k_B T_e/m_i}$. Under these conditions the ion flux at the walls due to ambipolar diffusions is given by evaluating at the sheath edge:

$$n_s u_B = -\left(D_{a\perp}\nabla_\perp n(r, z) + D_{a\parallel}\frac{\partial n(r, z)}{\partial z}\right). \tag{22}$$

Using equation (6), the plasma-sheath edge density at the cylinder side is:

$$n_{s_1}(R, z) = \frac{n_0 J_0(\alpha_G R_a)}{u_B} D_{a\perp}\alpha_G \cos\left(\frac{\pi z}{L}\right) \times \frac{K_0(\alpha_G R)I_1(\alpha_G R) + I_0(\alpha_G R)K_1(\alpha_G R))}{K_0(\alpha_G R)I_0(\alpha_G R_a) - K_0(\alpha_G R_a)I_0(\alpha_G R))}, \tag{23}$$

and at the cylinder top and bottom:

$$n_{s_2}(r, \pm L/2) = \begin{cases} \frac{n_0 D_{a\parallel}\pi}{u_B L} J_0(\alpha_P r), & R \leqslant R_a, \\ \frac{n_0 D_{a\parallel}\pi}{u_B L} J_0(\alpha_P R_a)\frac{K_0(\alpha_G R)I_0(\alpha_G r) - K_0(\alpha_G r)I_0(\alpha_G R))}{K_0(\alpha_G R)I_0(\alpha_G R_a) - K_0(\alpha_G R_a)I_0(\alpha_G R))}, & R > R_a. \end{cases} \tag{24}$$

In the geometry of our experiment, the integrals of equation (18) are:

$$\int_{S_g} n_{sg}^p(\boldsymbol{x})\, d^2x = \int_{-L/2}^{+L/2} n_{s_1}^p \cdot 2\pi R\, dz + 2\int_{R_a}^{R} n_{s_2}^p \cdot 2\pi r\, dr + \int_0^{R_a} n_{s_2}^p \cdot 2\pi r\, dr, \tag{25}$$

and

$$\int_{S_a} n_{sa}^p(\boldsymbol{x})\, d^2x = \int_0^{R_a} n_{s_2}^p \cdot 2\pi r\, dr. \tag{26}$$

From equations (18), (25) and (26), it is obvious that the self-bias voltage does not depend on the maximum plasma density n_0 and u_B.

By solving numerically equations (1)–(26), the normalised self-bias voltage could be calculated. The evolution of the normalised self-bias voltage as a function the magnetic field strength is presented in figure 9(c)

for the different sheath models. As can be seen V_{bias}/V_{pp} exhibits a strong drop for magnetic field strength $B \gtrsim 0.1$ T. These results agree relatively well with the experimental observation of figure 3. The observed discrepancies are due to the simplicity of our model. The experimentally observed decrease of V_{bias} for $B \gtrsim 1$ T is however not explained by our basic ambipolar diffusion model. It might be due to a loss of ionisation when both electrons and ions are magnetised and/or to the influence of the dielectric glass slide on the bottom electrode.

5.2. Dust particle confinement and growth

In order to qualitatively explain the growth dynamics of the nanoparticles, it is necessary to understand how dust particle confinement is affected by the presence of the magnetic field. For this purpose, two-dimensional particle-in-cell (PIC) simulations of a simplified model of our discharge (similar to the one described in the previous section) have been performed using the VSIM software from TechX corporation [72]. The bottom and side walls were grounded. The powered electrode located at the top of the chamber is connected to a 13.56 MHz rf voltage source with a peak-to-peak amplitude $V_{pp} = 400$ V enough to maintain the plasma and a constant vertical magnetic field was imposed. In order to simulate the self-bias of the powered electrode, an additional DC bias was also applied to the powered electrode, the value of which was chosen to roughly correspond to the measured value of the self-bias at a given magnetic field for a pristine argon discharge (see figure 3). A small gap of 1 mm between the powered electrode and the grounded wall was included (to avoid diverging field and also match the gap between the grounded guard ring and the electrode in the experiment). A background Ar gas with a pressure of 95 mTorr was filled in the chamber[5]. An initial electron density at $1 \cdot 10^9$ cm^{-3} was seeded to start the simulation. The collisions involved were electron-neutral collisions that lead to ionisation and ohmic heating. The simulations were run for $\gtrsim$215 rf periods until the electron and ion densities have stabilised[6]. Then the plasma potential and ion density were averaged over 40 rf period. Radial and vertical electric fields were obtained from the gradient of the average potential. Note that only the cross sections for ionisation and one excited level of Argon were used in our simulation. Moreover since the simulations are performed at a constant peak-to-peak voltage instead of constant injected power (as in the experiment), the simulated plasma density cannot be directly compared to our experiments. Finally, the area covered by the dielectric glass slide on the grounded bottom electrode was not included in the simulation. Consequently, the simulation results are only qualitative information of the behaviour of the discharge at different magnetic fields.

In figure 10, the PIC results for $B = 0$ T, $B = 0.032$ T, $B = 0.25$ T and, $B = 0.50$ T are presented. As expected, when increasing the magnetic field, the plasma becomes more confined below the powered electrode (figures 10(a), (e), (i), (m)). These results are in qualitative agreement with the results obtained in the previous section from the simple diffusion model, our experimental observation of the plasma light emission (figure 2), and with measurements made in a similar experimental set-up [49]. However the ion density distribution has a slightly more complicated shape than the one inferred from the diffusion model. The potential and electric fields distributions are also greatly influenced by the presence of the magnetic field.

As can be seen, when there is no applied magnetic field (figures 10(b)–(d)), the potential is nearly constant and the vertical and radial electric fields are close to zero over a large volume of the discharge chamber. Only in the vicinity of the grounded walls and the powered electrode does the electric field reaches values of a few tens of V cm^{-1}, enough to confine negatively charged particles in the plasma. For this reason, the cloud of negatively charged nanoparticles extends in most of the interelectrode space as observed in figure 5(a).

At low magnetic field ($B = 0.032$ T, figures 10(e)–(h)), the gradient of the plasma potential is even weaker than without applied magnetic field. This is due to a decrease of the ambipolar field due to the magnetisation of the electrons which are confined in the discharge. This fact can partially explain the faster growth cycles observed experimentally since the dust particles are only very weakly confined in the plasma by the tiny radial electric field.

When further increasing the magnetic field (figures 10(i)–(p)), the radial confinement reappears but the maximum value of the confining electric field is shifted below the interface between the guard ring and the powered electrode. For radius larger than the powered electrode radius ($r > R_a$), the radial electric field rapidly falls to 0 and the plasma density decreases very quickly. This effect is enhanced by the strength of the magnetic field. For these reasons, at high magnetic field, nanoparticles are not confined at $r > R_a$ and are found only in the volume directly below the powered electrode (see figure 5(c)). The increase of the dust radial confinement when ramping up the magnetic field was also observed in experiments in which the dust particles were grown prior to the magnetic field application [49].

[5] A lower pressure than in the experiments was chosen to limit the number of collisions and reduce the computational time. The simulated values of densities, potential and fields are therefore not be directly comparable to the experiments. However the tendencies remain the same and are enough for a qualitative study.

[6] The higher the magnetic field, the longer the equilibration run.

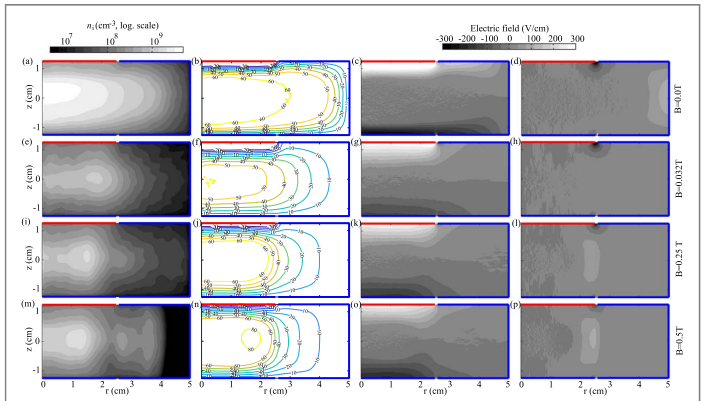

Figure 10. Ion density distribution (a), (e), (i), (m), Potential contour (b), (f), (j), (n), vertical electric field (c), (g), (k), (o), and radial electric field (d), (h), (l), (p) obtained from PIC simulation (pure argon, 1 excited argon neutral level) for $V_{pp} = 400$ V. (a), (b), (c), (d) $B = 0$ T, $V_{bias} = -90$ V, (e), (f), (g), (h) $B = 0.0.032$ T, $V_{bias} = -90$ V, (i), (j), (k), (l) $B = 0.25$ T, $V_{bias} = -50$ V and, (m), (n), (o), (p) $B = 0.50$ T, $V_{bias} = -30$ V The red lines represent the powered electrode and the blue lines represent the grounded surfaces.

From figure 10, it can also be seen that the vertical electric field in the sheath above the grounded electrode (as well as below the powered electrode) seems lower in magnetised discharges than in non-magnetised discharges (at constant power instead of constant V_{pp}, the effect might not be as strong). Moreover, the maximum ion density which is roughly at the centre of the discharge in the non-magnetised plasma (figure 10(a)), is shifted toward the side in the magnetised cases (figures 10(e), (i), (m)). Ion drag force is known to play an important role in the spatial organisation of growing nanoparticle clouds (such as dust 'voids' for instance [46, 73, 74]). The difference in ionisation and the weaker sheath electric fields might be the reason for the localisation of the dust particle cloud close to the bottom electrode for sufficiently high magnetic fields (see figure 5(c)). Note that the presence of the dielectric glass slide is not taken into account in our simulation which certainly influences the electric fields at high magnetic fields. It was indeed reported in section 3.2 that the dust cloud was confined near the glass-metal interface of the multi-part grounded electrode.

In the magnetised discharges, since the growing dust cloud is confined near or in the sheath above the grounded electrode, it can be subject to dust density waves (DDWs) which are spontaneously excited within the sheath when the dust particle density is high enough. DDWs are known to significantly enhance the agglomeration rate between particles by transferring significant kinetic energy to the particles thereby allowing them to overcome Coulomb repulsion [48, 50]. Moreover, the filamentation of the plasma when the magnetic field is high [49, 75] might also be a source of kinetic energy helping agglomeration. Thus the rapid agglomeration observed in the magnetised discharge could be due to the confinement of the growing cloud near the grounded electrode. It was also observed experimentally that the dust particle size distribution was much wider for growth occurring in strongly magnetised plasma ($B > 0.25$T) compared to dust grown in non or slightly magnetised plasma (via laser-light scattering, figure 5(c) and in SEM and TEM pictures, figures 6 and 7). Since in strongly coupled dusty plasmas, agglomeration is enhanced by a dispersed distribution in the sizes of the growing nanoparticles (due to charge fluctuation and the occupation of positively charged states of the smaller nanometre size particles) [76], the agglomeration can be further enhanced. One could argue that the presence of the magnetic field could also directly enhance the agglomeration due to stronger charge fluctuations induced by the reduction of the charging fluxes [77–80]. However, the magnetic field significantly affects the charging fluxes when $\beta_e = \sqrt{(\pi T_e m_e)/2e^2B^2} > 1$ [78]. Assuming $T_e \sim 1.5$eV, the charge of the particle will be strongly affected only when $r_d \gtrsim 3.66/B$ μm. In our experiments, the particles did not reach sizes large enough to have their charges significantly affected. However, the effect can be indirect through modifications of the discharge parameters [67, 81]. The magnetisation of the dust particles (i.e. the dust particle gyroradii become small enough to consider them magnetised [17]) might also play a role in the agglomeration process.

6. Conclusion

In this article, the influence of a constant magnetic field on discharge parameters and particle growth in a capacitively coupled rf discharge has been studied. Experiments were performed in pure argon and argon-acetylene plasmas at magnetic fields up to $B = 2.5$ T. It was found that high magnetic field strength has a major effect on the plasma glow distribution and the self-bias voltage of the powered electrode. To understand the plasma discharge characteristics, a basic ambipolar diffusion model taking into account the diffusion perpendicular and parallel to the magnetic field was developed. The model confirmed that a reduction of the perpendicular diffusion at high magnetic field would have a significant impact on the discharge and qualitatively good agreement was found between the model and the experimental observations of the reduction of the self-bias. Complementary PIC simulations have shown that the electric fields are also affected by the magnetic field.

The magnetic field also had a significant influence on the morphology of nanoparticle that are grown in the plasma. The addition of acetylene to the discharge led to the formation of carbon nanoparticles. At low magnetic fields, $B < 0.1$ T, the well-known cyclic growth behavior was observed with the opening of a void region in the plasma bulk in which the next generation of nanoparticles could grow. At higher magnetic fields, $B > 0.1$ T, no growth cycles were reported. However, a cloud of nanoparticles above the grounded bottom electrode appeared more rapidly than in the low magnetic field cases with larger agglomerates formed above the grounded, bottom electrode in just tens of seconds after plasma ignition. The enhanced agglomeration, which may be the reason of the observation of the big porous spherical agglomerates, could be explained by the presence of dust acoustic waves and plasma filamentation that appear in the plasma at the higher magnetic fields. Electron microscopy, both SEM and TEM, revealed that the big nanoparticles were porous spherical agglomerates of very small nanoparticles. Raman spectroscopy did not reveal any major differences of chemical properties and structural order between particles formed at lower versus higher magnetic fields. In all of the investigated synthesis conditions, the grown dust particles were composed of amorphous carbon.

In future studies, different magnetic field and electrode configurations will be investigated. Complementary diagnostics such as optical emission spectroscopy and light extinction spectrometry [82] will be added in order to obtain more insight on the influence of the magnetic field on dust growth kinetics. A particular interest will be on the influence of plasma filamentation on particle growth.

Acknowledgments

The authors would like to thank Prof M Bradley for his useful remarks and suggestions. This work is supported by funding from the US Dept. of Energy, Grant Number DE- SC0016330, and by the National Science Foundation, Grant Numbers PHY-1613087 and PHY-1126067. Additional support is provided by the NSF EPSCoR program (OIA- 1655280).

ORCID iDs

L Couëdel https://orcid.org/0000-0003-0749-9273
M P Khanal https://orcid.org/0000-0001-8265-4718

References

[1] Bouchoule A 1999 *Dusty Plasmas: Physics, Chemistry and Technological Impacts in Plasma Processing* (New York: Wiley)
[2] Morfill G E and Ivlev A V 2009 *Rev. Mod. Phys.* **81** 1353
[3] Shukla P K and Mamun A A 2002 *Introduction to Dusty Plasma* (Bristol: IOP Publishing)
[4] Morfill G E, Grun E, Goertz C K and Johnson T V 1983 *Icarus* **53** 230–5
[5] Mitchell C J, Horanyi M, Havnes O and Porco C C 2006 *Science* **311** 1587–9
[6] Mann I, Meyer-Vernet N and Czechowski A 2012 *Nanodust in the Solar System: Discoveries and Interpretations* vol 385 (Berlin: Springer)
[7] Cavarroc M, Jouanny M C, Radouane K, Mikikian M and Boufendi L 2006 *J. Appl. Phys.* **99** 064301
[8] Lopez T and Mangolini L 2014 *J. Vac. Sci. Technol.* B **32** 061802
[9] Mikikian M *et al* 2017 *Plasma Phys. Control. Fusion* **59** 014034
[10] Selwyn G S, Singh J and Bennett R S 1989 *J. Vac Sci. Technol.* A **7** 2758
[11] Cabarrocas P R I, Nguyen-Tran T, Djeridane Y, Abramov A, Johnson E and Patriarche G 2007 *J. Phys. D: Appl. Phys.* **40** 2258
[12] Kortshagen U R, Sankaran R M, Pereira R N, Girshick S L, Wu J J and Aydil E S 2016 *Chem. Rev.* **116** 11061
[13] Bouchoule A and Boufendi L 1993 *Plasma Sources Sci. Technol.* **2** 204
[14] Watanabe Y 2006 *J. Phys. D: Appl. Phys.* **39** R329
[15] Woodard A, Shojaei K, Nava G and Mangolini L 2018 *Plasma Sources Sci. Technol.* **27** 104003
[16] Bilik N, Anthony R, Merritt B, Aydil E and Kortshagen U 2015 *J. Phys. D: Appl. Phys.* **48** 105204
[17] Thomas E Jr, Merlino R L and Rosenberg M 2012 *Plasma Phys. Control. Fusion* **54** 124034
[18] Calafat M, Escaich D, Clergereaux R, Raynaud P and Segui Y 2007 *Appl. Phys. Lett.* **91** 181502

[19] Nafarizal N and Sasaki K 2012 *J. Phys. D: Appl. Phys.* **45** 505202
[20] Drenik A, Yuryev P, Vesel A, Margot J and Clergereaux R 2013 *Phys. Plasmas* **20** 100701
[21] Matyash K, Fröhlich M, Kersten H, Thieme G, Schneider R, Hannemann M and Hippler R 2004 *J. Phys. D: Appl. Phys.* **37** 2703
[22] Thomas E *et al* 2014 *J. Plasma Phys.* **80** 803–8
[23] Thomas E, Konopka U, Lynch B, Adams S, LeBlanc S, Merlino R L and Rosenberg M 2015 *Phys. Plasmas* **22** 113708
[24] Raizer Y P, Shneider M N and Yatsenko N A 1995 *Radio-Frequency Capacitive Discharges* ed C P LLC (Florida: CRC Press LLC)
[25] Lieberman M A and Lichtenberg A J 1994 *Principles of Plasma Discharges and Materials Processing* (New York: Wiley) Wiley
[26] Wattieaux G and Boufendi L 2012 *Phys. Plasmas* **19** 033701
[27] Massereau-Guilbaud V, Géraud-Grenier I and Plain A 2009 *J. Appl. Phys.* **106** 113305
[28] Wattieaux G, Carrasco N, Henault M, Boufendi L and Cernogora G 2015 *Plasma Sources Sci. Technol.* **24** 015028
[29] Wattieaux G, Mezeghrane A and Boufendi L 2011 *Phys. Plasmas* **18** 093701
[30] Hundt M, Sadler P, Levchenko I, Wolter M, Kersten H and Ostrikov K K 2011 *J. Appl. Phys.* **109** 123305
[31] Deschenaux C, Affolter A, Magni D, Hollenstein C and Fayet P 1999 *J. Phys. D: Appl. Phys.* **32** 1876
[32] Stoykov S, Eggs C and Kortshagen U 2001 *J. Phys. D: Appl. Phys.* **34** 2160
[33] Herrebout D, Bogaerts A, Gijbels R, Goedheer W J and Vanhulsel A 2003 *IEEE Trans. Plasma Sci.* **31** 659
[34] Baby A, Mahony C M O and Maguire P D 2011 *Plasma Sources Sci. Technol.* **20** 015003
[35] Winter J, Berndt J, Hong S H, Kovačević E, Stefanović I and Stepanović O 2009 *Plasma Sources Sci. Technol.* **18** 034010
[36] Cavarroc M, Mikikian M, Tessier Y and Boufendi L 2008 *Phys. Rev. Lett.* **100** 045001
[37] Couëdel L, Mikikian M, Samarian A A and Boufendi L 2010 *Phys. Plasmas* **17** 083705
[38] Heidemann R J *et al* 2011 *Phys. Plasmas* **18** 053701
[39] Killer C, Himpel M and Melzer A 2014 *Rev. Sci. Instrum.* **85** 103711
[40] Mikikian M, Boufendi L, Bouchoule A, Thomas H M, Morfill G E, Nefedov A P, Fortov V E and the PKE-Nefedov team 2003 *New J. Phys.* **5** 19.1
[41] Mikikian M, Cavarroc M, Couëdel L and Boufendi L 2006 *Phys. Plasmas* **13** 092103
[42] Mikikian M, Couëdel L, Cavarroc M, Tessier Y and Boufendi L 2007 *New J. Phys.* **9** 268
[43] Pilch I and Greiner F 2017 *J. Appl. Phys.* **121** 113302
[44] Praburam G and Goree J 1996 *Phys. Plasmas* **3** 1212
[45] Samsonov D and Goree J 1999 *J. Vac Sci. Technol.* A **17** 2835
[46] Samsonov D and Goree J 1999 *Phys. Rev.* E **59** 1047
[47] Greiner F, Carstensen J, Köhler N, Pilch I, Ketelsen H, Knist S and Piel A 2012 *Plasma Sources Sci. Technol.* **21** 065005
[48] Dap S, Hugon R, Lacroix D, de Poucques L, Briancon J-L and Bougdira J 2013 *Phys. Plasmas* **20** 033703
[49] Tadsen B, Greiner F and Piel A 2014 *Phys. Plasmas* **21** 103704
[50] Du C-R, Thomas H M, Ivlev A V, Konopka U and Morfill G E 2010 *Phys. Plasmas* **17** 113710
[51] Berndt J, Hong S, Kovačević E, Stefanović I and Winter J 2003 *Vacuum* **71** 377
[52] Stefanovic I, Kovacevic E, Berndt J, Pendleton Y and Winter J 2005 *Plasma Phys. Control. Fus.* **47** A179
[53] Tuinstra F and Koenig J L 1970 *J. Chem. Phys.* **53** 1126
[54] Mitura S, Mitura A, Niedzielski P and Chaos P C 1999 *Solitons & Fractals* **10** 2165
[55] Ferrari A C and Robertson J 2004 *Philos. Trans. Royal Soc.* A **362** 2477
[56] Géraud-Grenier I, Massereau-Guilbaud V and Plain A 2004 *Surf. Coat. Technol.* **187** 336
[57] Sadezky A, Muckenhuber H, Grothe H, Niessner R and Pöschl U 2005 *Carbon* **43** 1731
[58] Arnas C, Pardanaud C, Martin C, Roubin P, Temmerman G D and Counsell G 2010 *J. Nucl. Mater.* **401** 130
[59] Wang S M, Pei Y H, Wang X, Wang H, Meng Q N, Tian H W, Zheng X L, Zheng W T and Liu Y C 2010 *J. Phys. D: Appl. Phys.* **43** 455402
[60] Pardanaud C, Martin C, Roubin P, Giacometti G, Hopf C, Schwarz-Selinger T and Jacob W 2013 *Diam. Relat. Mater.* **34** 100
[61] Makdessi G A, Glad X, Dap S, Rojo M, Clergereaux R and Margot J 2017 *J. Phys. D: Appl. Phys.* **50** 155203
[62] Socrates G 2001 *Infrared and Raman Characteristic Group Frequencies: tables and Charts* ed T edition (New York: Wiley)
[63] Merlen A, Buijnsters J and Pardanaud C 2017 *Coatings* **7** 153
[64] Pardanaud C, Martin C and Roubin P 2014 *Vib. Spectrosc.* **70** 187
[65] Casiraghi C, Ferrari A C and Robertson J 2005 *Phys. Rev.* B **72** 085401
[66] Woodard A, Shojaei K, Nava G and Mangolini L 2018 *Plasma Chem. Plasma Process.* **38** 683
[67] Vidal F, Johnston T W, Margot J, Chaker M and Pauna O 1999 *IEEE Trans. Plasma Sci.* **27** 727
[68] Boeuf J P and Pitchford L C 1995 *Phys. Rev.* E **51** 1376
[69] Thomas H M *et al* 2008 *New J. Phys.* **10** 033036 (14pp)
[70] Ashida S, Lee C and Lieberman M A 1995 *J. Vac Sci. Technol.* A **13** 2498
[71] Lieberman M A and Savas S E 1990 *J. Vac Sci. Technol.* A **8** 1632
[72] Nieter C and Cary J R 2004 *J. Comput. Phys.* **196** 448
[73] Morfill G and Tsytovich V N 2000 *Plasma Physics Reports* **26** 682
[74] Akdim M R and Goedheer W J 2001 *Phys. Rev.* E **65** 015401
[75] Thomas E, Konopka U, Merlino R L and Rosenberg M 2016 *Phys. Plasmas* **23** 055701
[76] Annaratone B M, Elskens Y, Arnas C, Antonova T, Thomas H M and Morfill G E 2009 *New J. Phys.* **11** 103013
[77] Tsytovich V N, Sato N and Morfill G E 2003 *New J. Phys.* **5** 43
[78] Patacchini L, Hutchinson I H and Lapenta G 2007 *Phys. Plasmas* **14** 062111
[79] Hutchinson I H and Patacchini L 2010 *Plasma Phys. Control. Fusion* **52** 124005
[80] Lange D 2016 *J. Plasma Phys.* **82** 905820101
[81] Sternberg N, Godyak V and Hoffman D 2006 *Phys. Plasmas* **13** 063511
[82] Barbosa S, Couëdel L, Arnas C, Kumar K K, Pardanaud C and Onofri F R A 2016 *J. Phys. D: Appl. Phys.* **49** 045203

3.3 Two-dimensional plasma crystals

An important fraction of my research is dedicated to the study of two-dimensional complex plasma crystals (sometimes referred to as Yukawa crystals). This activity involves many collaborations (Dr. A. Ivlev and his graduate students (MPE, Garching, Germany); Dr. H. Thomas Dr. S. Zhdanov and Dr. V. Nosenko and their graduate students (DLR, Oberpfaffenhoffen, Germany); Dr. Y. Elskens (PIIM, Aix-Marseille University); Dr. L. Matthews and her graduate students (Baylor University, Waco, Texas, USA)).

In this section, I summarise the main results (experimental and theoretical) obtained on the investigations of waves and the mode coupling instability in 2D complex plasma crystals. The results are not presented in a chronological order but rather in a logical order. In Sec. 3.3.1, I present the experimental device used to perform experiments on 2D complex plasma crystals. In Sec. 3.3.2, I present the experimental method that allows the simultaneous measurement of the three wave modes in 2D complex plasma crystals. In Sec. 3.3.3, I present the experimental evidence of the existence of the hybrid mode due to ion wake mediated interactions and the resulting mode-coupling instability (MCI). In Sec. 3.3.4, I discuss the thresholds of the mode-coupling instability in 2D complex plasma crystals. In Sec. sec:earlystage, I present the early stage of MCI and, finally, in Sec. 3.3.6, I discuss the dynamics of MCI-induced 2D complex plasma crystal melting.

3.3.1 Experimental set-up

The experiments were performed in a capacitivelly-coupled rf glow discharge at 13.56 MHz (a modified GEC chamber). A sketch of the set-up is presented in Fig.3.27. The argon pressure $p_{\rm Ar}$ was typically set between 0.4 Pa and 2 Pa and the forward rf power $P_{\rm RF}$ was set between 5 W and 20 W. Langmuir probe measurments have shown that in the bulk discharge the electron temperature was $T_{\rm e} = 2.5$ eV and the electron density was $n_{\rm e} = 2 \times 10^9$ cm^{-3} at a pressure $p_{\rm Ar}$ =0.66 Pa and a rf power $P_{\rm RF}$=20 W [36].

A Miwitron Ka-band microwave interferometer MWI 2650 working at 26.5 GHz (resolution of $\sim 10^8$ cm^{-3}) could also be used to measure the electron density, $n_{\rm e}$, in pristine plasma condition (without microparticles) for different $p_{\rm Ar}$ and $P_{\rm W}$ [115].

To produce the microparticle monolayer, melamine-formaldehyde (MF) spherical microparticles with a diameter of 9.19 ± 0.09 μm were levitated in the plasma sheath above the lower rf electrode. The obtained horizontal monolayer was up to ∼60 mm in diameter depending on the number of injected microparticles. A horizontal laser sheet was used to illuminate the monolayer. The laser sheet had a had a Gaussian profile in the vertical direction with a standard deviation $\sigma \simeq 75$ μm (full width at half maximum of ~ 175 μm). The light scattered by the microparticles was recorded through a quartz window at the top of the chamber using a Photron FASTCAM camera (typcal recoding speed of 250 frames per second). It allowed the extraction of the particle horizontal coordinates, x and y, and velocities, v_x and v_y with sub-pixel resolution in each frame. An additional side-view camera (Basler Ace ACA640-100GM or Photron FASTCAM camera) was used to check that there was no extra particles above or below the monolayer.

An additional SpectraPhysics Millennia PRO 15sJ solid-state 532-nm laser with a continuous-wave (cw) output power of 0.30–2 W could also be focused on the crystal to manipulate the microparticles with the radiation pressure force. This could be used to melt locally the 2D complex plasma crystal [158].

More details can be found in the following publications [9–12, 114, 115, 135, 157, 158, 165].

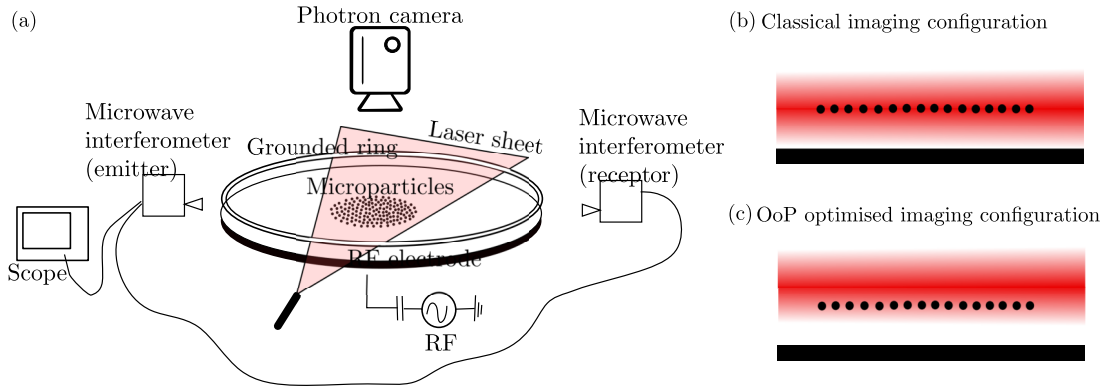

Figure 3.27 – (Colour online) (a) Schematic of the experimental set-up. (b) Classical position of the laser sheet for particle tracking, (c) out-of-plane motion optimised configurations for particle tracking (c) enables the study of the out-of-plane fluctuation spectra; see Fig. 3.28.

3.3.2 Measurement of in-plane and out-of-plane waves

From the fast camera images, the microparticles' position can be tracked frame after frame and their trajectories reconstructed [158]. These tracking data are then used to study wave propagation of the microparticle monolayer. For that purpose, the particle current fluctuation spectra need to be computed. First, the particle current components $V_{\mathbf{s}}(\mathbf{k}, t)$ are calculated as

$$V_s(\mathbf{k}, t) = \sum_{j=1}^{N} v_{s,j}(t) e^{-i\mathbf{k}\cdot\mathbf{s}_j(t)} \ . \tag{3.61}$$

The current components are calculated in a chosen s-direction at each time instant t, using a wave vector $\mathbf{k} = \{k_x, k_y\}$ located in the monolayer plane. In the above equation, i is the imaginary number, j is the particle index, $v_{s,j}(t)$ is the projection of the j-th particle velocity on the s-axis, $\mathbf{s}_j = \{x_j, y_j, z_j\}$ is its position, and N is the number of microparticles. The x, y-axes are chosen as shown in Fig. 3.9. The choice of the axis direction with respect to the lattice allows a detailed study of wave propagation in a chosen direction with respect to the lattice principal axis. The current fluctuation spectra are then obtained by performing a fast Fourier transform in the time domain.

The horizontal coordinates x and y can be extracted from the video frames using standard techniques [158, 259, 260]. Then, after an easy derivation of the corresponding velocities v_x and v_y, on can directly compute the in-plane current fluctuation spectra. In Fig. 3.29, the resulting fluctuation spectra are shown for two principal orientations of the wave vector, at $\theta = 0°$ and $30°$. The spectra show the distribution of the wave energy in the $(f, \mathbf{k})$ revealing the wave dispersion relation: ("ridge" of the distribution).

However,the measurement of the vertical position z (and the velocity v_z) of individual particles requires a very different technique described in [135] (a copy of which can be found at the end of this section). Unlike in small and compact dust clusters, where a combination of top view and side view imaging allows a direct measurement of the 3 components of the microparticles' positions, side view imaging cannot be used in large monolayers since not all individual particle can be imaged from the side. Therefore, one has to rely on top view imaging to resolve the the relative out-of-plane particle position and deduce the vertical displacement. This can be achieved by measuring the relative variation of the scattered light intensity [135].

In most experiments involving microparticles monolayer, the laser light sheet position is adjusted such that the peak of the Gaussian intensity profile practically coincides with the particle monolayer levitation height in order to maximize the scattered light intensity (see

Fig.3.27(b)). This "classical" method is well adapted to in-plane tracking (especially at high frame rates) but is not appropriate for the measurement of z and v_z. In this configuration, the variation in of the recorded scattered intensities between consecutive frames provides only the magnitude of the vertical displacement without any information on the direction. Indeed, the recorded scattered intensity by individual particles in each frame is proportional to the local laser sheet intensity:

$$I(z) \propto e^{-(z-z_{\max})^2/2\sigma^2}, \tag{3.62}$$

where $z_{\max}$ is the position of the laser sheet intensity maximum. When the mean levitation height $z_{\text{lev}} \sim z_{\max}$, the magnitude of the particle displacements $|\delta z| \gtrsim |z_{\text{lev}} - z_{\max}| \sim 0$. In addition, positive or negative displacement will produce the same scattered intensity variation [38]. The "classical" method has also sensitivity issue. Since $\delta z \gtrsim |z_{\text{lev}} - z_{\max}|$, the resulting i ntensity variations scale as $\delta I/I \approx \frac{1}{2}(\delta z/\sigma)^2$. Assuming that thermal fluctuations are the main source of vertical motion, its magnitude $|\delta z|$ is approximatively $|\delta z| \sim \sqrt{T_d/m_d\Omega_{\text{conf}}^2} \lesssim 10$ μm where T_{d} is the kinetic temperature of particles. $|\delta z|$ is thus much smaller than the laser sheet vertical profile standard deviation $\sigma \approx 75$ μm leading to hardly detectable relative intensity variations $\delta I/I \sim 1$ %.

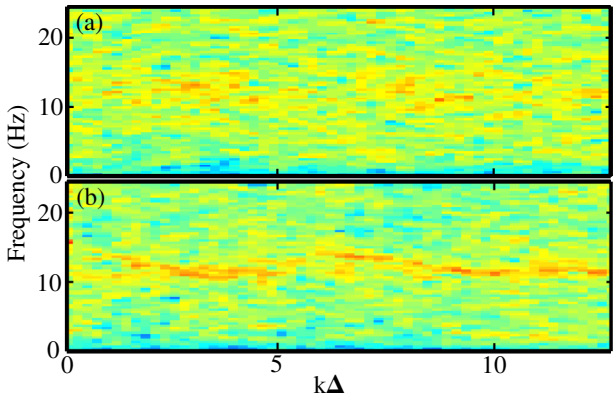

Figure 3.28 – (Reproduced from Ref. [166]) Example of out-of-plane current fluctuation spectra. (a) Using scattered light intensity from an unshifted laser sheet (conventional method). (b) using scattered light intensity from a shifted laser sheet (out-of-plane optimised method). In both cases, the analysed crystal area was a mixture of different crystal orientations.

In our experiments, we used an alternative visualization method adapted to the analysis of the microparticles' out-of-plane motion [135]. The laser light sheet was moved up so microparticles levitated $\sim$ 100 μm below maximum intensity. With this configuration, $|z_{\text{lev}} - z_{\max}|/|\delta z| \approx 10$ leading to two advantages compared to the "classical " method:

1. Relative intensity variations scale almost linearly with the displacement, $\delta I/I \approx |z_{\text{lev}} - z_{\max}|\delta z/\sigma^2$. Thus $(\delta I/I)_{\text{optimised}} \sim 15 \times (\delta I/I)_{\text{classical}}$.
2. The vertical intensity gradient is positive is the particles' motion range. Consequently, the direction of the displacement can be resolved.

Note that the quality of the tracking in the horizontal xy plane was not critically affected and remain of quality comparable to the "classical" imaging configuration. In addition, note that to the fundamental differences in tracking horizontal and vertical motion, different background noise intensities are obtained after the for the calculated in-plane and out-of-plane current fluctuation spectra.

Calculated out-of-plane particle current fluctuation spectra using the "classical" and "out-of-plane optimised" methods are shown in Fig. 3.28. As can be seen, the "classical" method (Fig. 3.28a) produces spectra containing very little to no information about the out-of-plane

wave modes . On the contrary, the out-of-plane dispersion relation is revealed by the "optimised" method (Fig. 3.28b) (ridges in the intensity distribution).

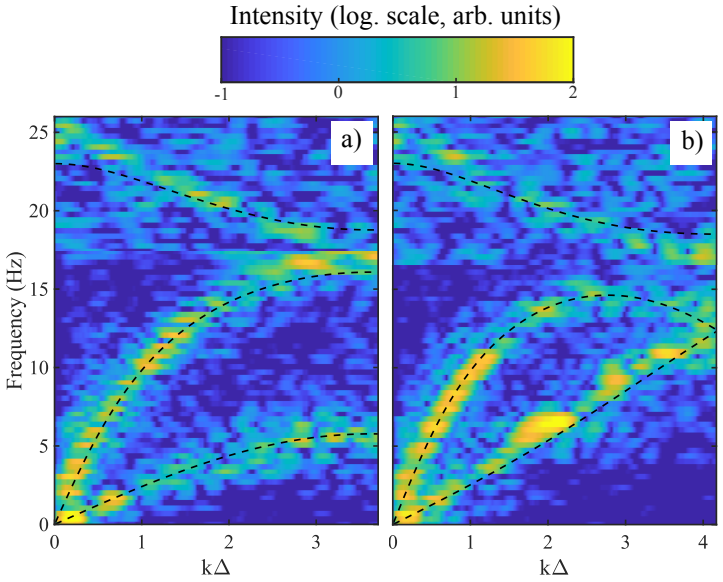

Figure 3.29 – (Reproduced from Ref. [166]) Experimentally measured dust-lattice dispersion relations vs theory. In-plane and out-of-plane current fluctuation spectra deduced from the experiments (see Table 3.1) and the theoretical curves are shown. The results are presented for two directions of the wave vector $\mathbf{k}$ (for a) $\theta = 0°$ and, b) $\theta = 30°$, see Fig. 3.27). The dashed lines are the theoretical dispersion relations for pure Yukawa interaction between particles [150]. The shown range of $\mathbf{k}$ is limited by the first Brillouin zone ($|\mathbf{k}|\Delta = \frac{2\pi}{\sqrt{3}}$ for $\theta = 0°$ and $|\mathbf{k}|\Delta = \frac{4\pi}{3}$ for $\theta = 30°$). Note the different background intensities for the in-plane and out-of-plane spectra induced by the different tracking method.

The out-of-plane optimised method allows the measurement of all three wave modes of a 2D plasma monolayer during a single experiment. In Fig. 3.29, the out-of-plane current fluctuation spectrum and the in plane spectra in the first Brillouin zone for two principal crystal orientations, $\theta = 0°$ and $30°$ are shown. In-plane and out-of-plane DL waves branches are clearly visible. The lines represent the theoretical dispersion relations plotted using Eq. 3.53. The crystal parameters (Z_d, λ_D, Δ, κ) were deduced from the in-plane fluctuation spectra using an method derived from Nunomura's work [162]. The values of Z_d and κ are obtained using the ratio of longitudinal and transversal sound speed extracted from the in-plane spectra shown in Fig. 3.29 combined with the interparticle Δ extracted from the position of the first peak of the pair correlation function $g(r)$. The values of the crystal parameters are listed in Table 3.1. Pure screened-Coulomb interactions (i.e. no ion wakes) were assumed for the theoretical dispersion curves. As can be seen, the experimental spectra and theoretical curves are in good qualitative agreement. The out-of-plane measurements confirms the optical character of the out-of-plane dispersion relation (the frequency of the long-wavelength waves is non zero). In addition, it showed that the long wavelengths dispersion is negative (the wave frequency is a decreasing function of $\mathbf{k}$ when $k \to 0$). As expected, the wave dispersion differs for $\theta = 0°$ and $30°$ at larger $|\mathbf{k}|$. The small differences between theory and experiments are due to the chosen interparticle potential for the calculation of the theoretical dispersion curves.

3.3.3 Hybrid modes in two-dimensional complex plasma crystals

The non-reciprocity of microparticle pair interactions induced by the ion wakes theoretically leads the appearance of an unstable hybrid mode when the in-plane longitudinal mode and the

Table 3.1 – (Reproduced from Ref. [166]) Parameters of the 2D crystal used for the spectra shown in Fig. 3.29. The lattice constant Δ is obtained from the position of the first peak of the pair correlation function. Parameters Z_d and κ are deduced from the in-plane phonon spectra.

P_{RF} (W)	p_{Ar} (Pa)	Z_d (e)	Δ (μm)	κ	f_v (Hz)
20	0.42	21000±3000	550±20	1±0.25	25±2

out-of-plane mode cross [149, 150, 157, 261] (see also Sec. 3.1.6). Under specific conditions, the crossing of the mode triggers the mode-coupling instability (MCI) which can lead to a rapid melting of the 2D complex plasma crystal [9, 10, 12, 114, 115, 157, 164–166, 262]. After the creation of a 2D complex plasma crystal, MCI induced melting of the crystalline monolayer can be triggered in (or a combination of) two different ways:

1. A progressive decrease of the forward rf power at a constant gas pressure (which naturally lowers f_{v} Ref. [263]),
2. a progressive decrease of the gas pressure at a constant rf power (which naturally lowers neutral gas friction, and modifies the radial and vertical confinements and therefore f_{v} and Δ).

More details about the pressure and rf power thresholds are given in Sec. 3.3.4 and Ref. [115].

In either case, MCI-induced melting developed in a specific manner [9, 12, 114, 164]: upon decrease of the control parameters (pressure and/or power) below threshold (pressure and power thresholds depend on the size of the monolayer and the sheath (confinement) parameters): MCI is triggered at the crystal's center where the particle number density is the highest. It then expands outwards gradually (but rapidly!) melting the 2D complex plasma crystal. MCI always is visible simultaneously in the horizontal and vertical directions (the hybrid mode as a mixed polarisation, see Sec. 3.1.6) [9, 114]. At the initial stage, due to the transfer of ion flow energy to the microparticles, the microparticle kinetic energy increases exponentially [9, 10, 164]. When the microparticles kinetic energy gets sufficiently high, a total disruption of the crystalline order is observed. It was shown theoretically that MCI always occurs in 2D complex plasma monolayer in the fluid state fluid [2]. Therefore, the system recrystallises only when increasing the control parameters well above certain pressure/power thresholds at which the MCI growth rate becomes lower than the damping rate due to neutral drag (strong hysteresis, see Refs. [115, 157, 264]. If the rf power is high enough and/or the monolayer particle number density is sufficiently low, the 2D complex crystal remain stable over a very large range of pressures.

The qualitative picture given by the MCI theory [150] (and originally predicted by the theory for a 1D string [148, 149, 261]) is in remarkable agreement with the reported experimental melting behaviour. Indeed, a distinctive fingerprint of MCI [148, 261] is the appearance of a *hybrid mode* due to ion wake-induced resonance coupling when longitudinal in-plane and transverse out-of-plane DL branches cross each other. This unstable hybrid mode consequently appears in the vicinity of the crossing in the (k, ω) space. This effect was experimentally observed by measuring the dispersion relations of all three principal DL modes [114, 157, 265, 266].

The first direct observation of the hybrid mode was reported in Ref. [114] (a copy of which is found at the end of this Section) and is evidenced on the current fluctuation spectra shown in Fig. 3.30. The theoretical curves (white lines) show the lattice modes fitting the shown frequency range. According to theory, the orientation $\theta = 0°$ (see Fig. 3.9) is the most unstable [150] (see Sec. 3.1.6) which is the direction chosen to calculate the experimental current fluctuation spectra. In the left column of Fig. 3.30, the current fluctuation spectra of a stable

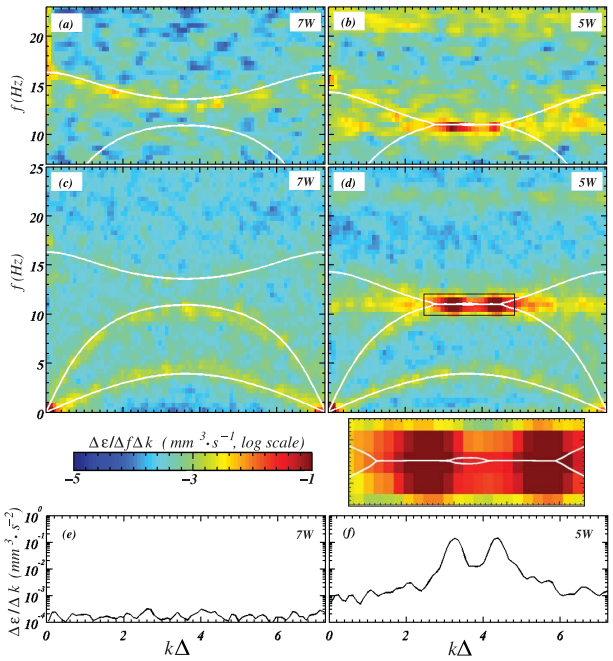

Figure 3.30 – (Reproduced from Ref. [114]) DL dispersion relations near the instability onset. The particle current fluctuation spectra were measured in an experiment performed at an argon pressure $p = 0.76$ Pa with particles 9.19 μm diameter, at a rf power of 7 W (left column, stable regime) and 5 W (right column, the instability onset). The logarithmic colour coding is used for the "fluctuation intensity" $\Delta\epsilon/\Delta k\Delta f$ (energy density, for unit mass, per unit wave number and frequency): Yellow ridges represent stable wave modes, the unstable hybrid mode are the dark-red "hot spots"; the upper panel shows the measured out-of-plane mode, the second-from-the-top panel depicts the pair of in-plane modes. The solid lines in both panels are theoretical results [150] (see text for details). The wave number k is normalised by the inverse interparticle distance Δ^{-1}. The shown range of k corresponds to the first two Brillouin zones at $\theta = 0°$ (branches are symmetric with respect to the border between the two zones). Below the fluctuation spectra the magnified hybrid mode in the unstable regime (marked by a rectangular box) is shown. The lower panel illustrates the distribution of the "fluctuation energy" $\Delta\epsilon/\Delta k$ at fixed frequency: In the stable case the frequency ($\simeq 12.5$ Hz) is chosen in the middle between the longitudinal in-plane branch and the out-of-plane branch (measured at the border between the Brillouin zones), for the instability onset the frequency ($\simeq 11$ Hz) corresponds to the hybrid mode.

regime (no MCI) are shown: all wave modes are well separated and the fluctuation intensity is equally distributed over all branches. In contrast, the right column of Fig. 3.30 shows current fluctuation spectra corresponding to the MCI regime: an intersection of the out-of-plane and the longitudinal in-plane branches in the vicinity of the first Brillouin zone boundary is clearly visible. The dark-red spots on the spectra around this region undoubtedly indicates the ion flow energy transfer to the microparticle crystal due to MCI.

The theoretical branches shown in Fig. 3.30 (solid white lines) were obtained using Zhdanov *et al.* results [150] and are used for comparison with the experimental data. A normalised wake dipole moment $\tilde{q}\tilde{\delta} = 0.1$ was used for the calculation. As can be seen, the theory is in excellent qualitative agreement with the experiment, both for the stable and unstable regimes. The agreement is qualitative only since the wake parameters were manually chosen to match the experimental observations, i.e so that the calculated unstable hybrid mode and the "hot spots" in the measured fluctuation spectra perfectly matches. Note that subtle effects, such as the splitting of "hot spots" at the border between the Brillouin zones is also experimentally

resolved (see the fluctuation energy distribution in the lower panel and the magnified hybrid mode). Traces of mixed polarisation are also seen in Fig. 3.30d (traces of out-of-plane mode are visible in the in-plane spectrum close to the location of the hybrid mode). These results are a clear proof of the existence of the unstable hybrid mode at the origin of MCI. Nevertheless, MCI is triggered only at defined thresholds in confinement strength and neutral damping rate [115, 157] linked to the forward rf power and the gas pressure. These thresholds depend directly on the ion wake properties and the ion wakes model used for calculation has an influence of the predicted MCI growth threshold and growth rate [151]. Obtaining good theoretical prediction remains an open issue. More details can be found in Refs. [115, 151, 157, 267, 268].

3.3.4 Threshold of the mode-coupling instability

In this subsection, the main results of Ref. [115] (a copy of which is found at the end of this Section) are summarised. In order to study the thresholds of the mode-coupling instability, a large monolayer of microparticles was suspended in the sheath of a rf discharge. The monolayer was used for the 2 different sets of experiments (referred to as Experiment I and Experiment II in Ref. [115]) performed ∼1 hour appart. Due to the etching of the MF microparticles by the argon plasma (~ 1.25 nm/min according to Ref.[269]), the MF microparticles of experiments II had diameter of ~ 9 μm.

The crystallisation and melting pressures of the monolayer, p_{cryst} and p_{MCI} respectively, were investigated for different forward rf powers. At a chosen fixed forward rf power, starting from a monolayer in the fluid state, the argon pressure was gradually increased until the full crystallisation of the monolayer was observed (pressure step of ~ 0.6 mTorr) and the crystallisation pressure p_{cryst} was recorded. During the pressure increase phase, the monolayer stayed in the fluid phase except when within a few 10^{-2} Pa below the crystallisation pressure where the outer part of the monolayer started crystallising. Then the gas pressure was very slowly decreased until MCI was triggered (minimum pressure: ∼0.06 mTorr) resulting in the rapid melting of the monolayer as reported in Refs. [9, 10, 12, 164, 165, 270] and the melting pressure p_{MCI} was recorded. The rf power was then decreased and the procedure was repeated.

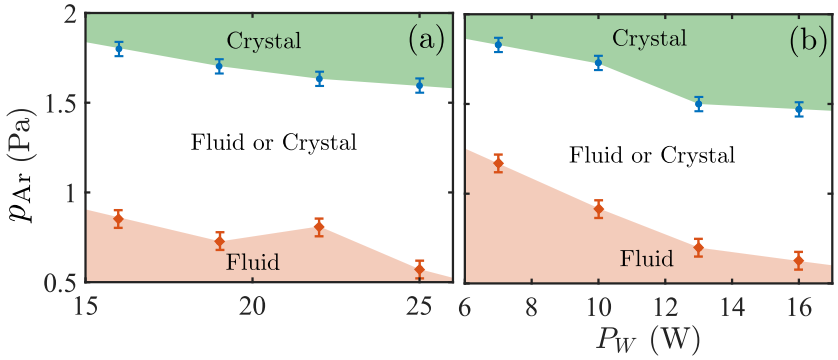

Figure 3.31 – (Reproduced from Ref. [115]) Crystallisation pressure, p_{cryst}, (blue dots) and MCI threshold pressure, p_{MCI}, (red diamonds) for different rf powers, P_{W}: (a) Experiment I; (b) Experiment II. Above the crystallisation pressure the monolayer is always in the crystalline state (green areas). Below the MCI threshold pressure, the monolayer is always in the fluid state (red areas). In-between, the monolayer remains in the crystalline phase when decreasing the pressure from above the crystallisation threshold and remains fluid when increasing the pressure from bellow the MCI threshold.

The results for both sets of experiments are shown in Fig. 3.31. As can be seen, in both cases, the higher the power the lower the crystallisation and melting pressures. In addition, the pressure range $\Delta p = p_{\mathrm{cryst}} - p_{\mathrm{MCI}}$, for which the monolayer remains a 2D crystal when decreasing

the pressure from above p_{cryst} and remains fluid when increasing the pressure from below p_{MCI} increases when increasing the RF power.

In Ref [115] the current fluctuation spectra of the monolayer in the crystal phase were extracted from imaging data and the compression and shear sound velocities were then measured. It was reported that decreasing the pressure at constant forward rf power leads to an increase of both sound speeds and a slight increase of the interparticle distance Δ. The microparticle kinetic temperature always remained quite low while the monolayer was in the crystal phase ($T_{cryst} \lesssim 0.2$ eV). Assuming pure screened Coulomb interactions, the sound speed increases correspond to an increase of the microparticle charges. From the maximum frequency of the longitudinal dispersion relation which increases when decreasing pressure, it could be deduced that a pressure decrease lead to the out-of-plane mode and the in-plane mode getting closer to each other as the MCI pressure threshold, p_{MCI}, was approached. No trend in the evolution of the coupling parameter $\kappa = \Delta/\lambda_{\mathrm{D}} \simeq 1.0$–$1.8$ was reported due to relatively large measurement errors on the sound speeds (especially the transverse sound speed) which propagated into κ. An evaluation the coupling parameter $\Gamma = (Z_d^2 e)/(T_{\mathrm{cryst}} 4\pi\epsilon_0 \Delta) \sim 2000$, showed that it remains far from the theoretical coupling parameters at the monolayer melting point ($\Gamma_m \sim 200$ at $\kappa \sim 1.2$ [271]).

The mode coupling instability in a 2D complex plasma crystal is know to be triggered when the in-plane longitudinal mode and the out-of-plane mode intersect [150, 157] (except in very special experimental conditions where ion wakes are really pronounced allowing coupling of the modes without direct crossing [272]). Thus, the simple rf sheath model detailed in Sec. 3.1.4 was first used to calculate the change of the rf sheath profile as a function of the forward rf power and the background argon pressure. These profile were further used to calculate a theoretical microparticle equilibrium charge, equilibrium levitation height and the vertical confinement frequency: (i) a power increase at constant pressure leads to increase of Z_{d}, z_{lev} and $f_{0_{\mathrm{v}}}$ and (ii) a pressure increase at constant rf power leads to decrease of Z_{d}, z_{lev} and an increase of $f_{0_{\mathrm{v}}}$ (see Sec.3.1.5).

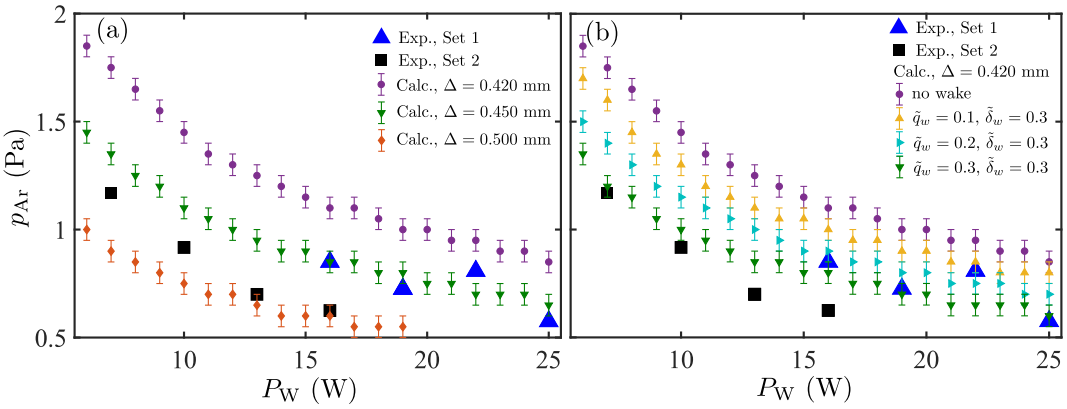

Figure 3.32 – (Reproduced from Ref. [115]) (a) Pressure at which the crossing of the in-plane longitudinal mode and the out-of-plane mode occurs as a function of rf power for different interparticle distances Δ and without ion wakes. The experimental MCI pressure thresholds are shown for comparison. (b) MCI pressure threshold as a function of rf power for an interparticle distance $\Delta = 420$ μm and different ion wake charges in the framework of the point-charge wake model [150]. The experimental MCI pressure thresholds are shown for comparison.

Then, the influence of the interparticle distance Δ on mode crossing was investigated while ignoring ion wakes [see Fig 3.32-(a)]: the minimum pressure for mode crossing decreases when increasing the rf power due to the competing effects of pressure decrease and rf power increase. In addition, at low pressure the microparticle charge is larger due to a higher electron tem-

perature, which for a given Δ, increases the maximum frequency of the longitudinal in-plane mode, facilitating mode crossing. Similarly, the pressure threshold is systematically lower for larger Δ due to weaker interparticle interaction which reduces the maximum frequency of the longitudinal in-plane mode and the minimum frequency of the out-of-plane mode. Experimental points follow roughly the same trend showing that the changes of the sheath profile (which depends on p_{Ar} and P_{W}) are of great importance to explain the crossing of the modes and the triggering of MCI in 2D complex plasma crystals.

Secondly, the effect of ion wakes was investigated (in the framework of the point wake model, see Sec.3.1.6). The interparticle distance was fixed to $\Delta = 420$ μm and only the value of the wake charge was varied ($0.1 \leq \tilde{q}_w \leq 0.3$), while the wake length was fixed ($\tilde{\delta}_w = \delta_w/\lambda = 0.3$). Then, the pressure threshold for mode crossing (and the triggering of MCI) were calculated again. The results are presented in Fig. 3.32-(b). As can be seen, the main experimental trends are again recovered: when increasing the rf power, the threshold pressure decreases. However, the ion wakes play an important role. Large ion wake charge significantly decreases the pressure threshold at fixed rf power. The experimental wake parameters are unknown and their overall effect on the measured pressure threshold are thus difficult to estimate. However, one can see in Fig. 3.32 that the calculated thresholds do not exactly match the experimental one. Note that, in Ref. [115] it is reported that the experimental particle charges are slightly smaller than the calculated ones and the Δ used in the thresholds calculation (with ion wakes) is slightly larger than the experimental one (which also slightly decreases with increasing pressure at fixed P_{W}). The calculation of the true MCI pressure threshold would therefore require the calculation of evolution of the horizontal confinement as a function of p_{Ar} and P_{W} as well as self-consistent wake parameters and more sophisticated (realistic) ion wake model such as those described in Refs. [142, 151, 267].

Note that the crystallisation pressure follows the same trend as the MCI threshold pressure: it decreases with increasing power. This can also be roughly explained with the evolution of the sheath profile. When P_{W} increases, the sheath electric field and therefore the vertical confinement become stronger. However, when in the fluid phase, MCI always exist unless the damping due to neutral drag is large enough to suppress it [2]. At fixed rf power, the microparticle charge decreases when increasing pressure (see Sec. 3.1.5). Therefore, the longitudinal sound speed decreases, the mode crossing is not as "deep" resulting in smaller MCI growth rate. Ref. [2] also demonstrate in the framework of the wake-layer model that when the vertical confinement frequency is increased above the MCI threshold in a 2D crystal with the same microparticle parameters as the fluid layer (same microparticle charges and same microparticle number density), the instability growth rate decreases as $\sim \exp(-\frac{1}{2}\omega_v^2\delta)$. The crystallisation threshold also depends on the wake parameters which are expected to have a non-negligible effects as for the MCI threshold pressure in 2D complex plasma crystals. Future studies will use self-consistent wake model such as in Ref. [142] or particle-in-cell results [146] to derive accurate MCI and crystallisation threshold pressures.

3.3.5 Early stage of the Mode-coupling instability: particle motion synchronisation

The formation of the hybrid mode often triggers MCI (for low enough gas pressure the MCI growth rates exceeds neutral damping). At the early stage of MCI, rhythmic patterns and synchronised oscillations of the microparticles around their equilibrium positions are observed [9, 10, 164]. The first dedicated experiments devoted to the study of the appearance of synchronised dust oscillations at the early stage of MCI were reported in Ref. [9] (a copy of which is found at the end of this Section). In this section, the results of investigation of the kinematics of microparticles during the early stage of MCI in a 2D complex plasma crystal are

summarized.

The instability was initiated by decreasing the argon pressure from $p_{\mathrm{Ar}} = 0.94$ Pa to 0.92 Pa at a fixed forward rf power $P_{\mathrm{RF}} = 12$ W. The longitudinal and transverse sound speeds, respectively $C_{\mathrm{L}} = (34.1 \pm 1.4)$ mm/s and $C_{\mathrm{T}} = (7.9 \pm 0.3)$ mm/s, were measured by using the long wavelength part ($k \to 0$) of the longitudinal and transverse in-plane current fluctuation spectra (see Fig. 2 of Ref. [9]). The interparticle distance in the centre of the crystal was $\Delta = 480 \pm 10$ μm and the microparticle charge number was estimated at $|Z_{\mathrm{d}}| \simeq 18600e$ and the coupling parameter was estimated at $\kappa = 1.26$ (the reported error on the charge was about 15% and the reported error on κ was about 30%). The frequency of the vertical confinement was measured from the out-of-plane fluctuation spectrum: $f_{\mathrm{v}} = 23 \pm 1$ Hz. The hybrid mode, showing as a hot spot at $f_{\mathrm{hyb}} = 16 \pm 1$ Hz was well pronounced in the longitudinal current fluctuation spectrum (Fig. 2a of Ref. [9]).

Shortly after MCI was triggered, synchronised microparticle oscillations around their equilibrium positions were observed. The degree of synchronisation was extracted from the microparticle trajectories as followed. The instantaneous phases of the particle oscillations as functions of time and position were recovered from the particle displacements $r_j(t) = \sqrt{x_j^2(t) + y_j^2(t)}$. The drift was removed to keep only the oscillatory parts. The "filtered" displacement $\tilde{r}_j(t)$ of the jth particle was defined as:

$$\tilde{r}_j(t) = r_j(t) - \frac{1}{\Delta t} \int_{t-\frac{\Delta t}{2}}^{t+\frac{\Delta t}{2}} r_j(t')dt'. \tag{3.63}$$

where the averaging time interval Δt was fixed at $\Delta t = 0.5$ s for all particles. A Hilbert transform was then performed to obtain the analytic displacement $r_{a_j}(t) = A_j(t) \exp\Big(i\phi_j(t)\Big)$, where $\phi_j(t)$ are instantaneous phases and $A_j(t)$ are the instantaneous amplitude [273].

The degree of synchronisation σ_j of particle j with its closest neighbours was then calculated as follows [274]:

$$\sigma_j = \frac{1}{n} \sum_{j'=1}^{n} \sigma_{jj'}, \tag{3.64}$$

$$\sigma_{jj'} = 1 - \frac{S_{jj'}}{S_{max}}, \tag{3.65}$$

where n is the number of the closest neighbours and $S_{jj'}$ is the Shannon entropy of the cycle phase distribution among neighbours,

$$S_{jj'} = -\sum_{l=1}^{M} p_{jj'l} \ln p_{jj'l}, \ \sum_{l=1}^{M} p_{jj'l} = 1. \tag{3.66}$$

Here, $p_{jj'l}$ is the fraction of the data in the l-th bin of the phase difference distribution $\phi_{jj'}(t) = \phi_j(t) - \phi_{j'}(t) \pmod{2\pi}$, $l = 1 \ldots M$ where $M = 20$ is the number of chosen bins, and $S_{max} = \ln M$ is the maximum entropy corresponding to a uniform distribution $p_{jj'l} = M^{-1}$. A moving window using the instantaneous phases $\phi_{jj'}(t)$ calculated over 101 consecutive frames centred on time t was used to compute the distribution. A completely synchronised state corresponds to $\sigma = 1$ while a fully desynchronised state corresponds to $\sigma = 0$.

Fig. 3.33a shows the trajectories of 2 neighbour particles during the early stage of MCI. As can be seen, both particles oscillated at the hybrid frequency in both the vertical and horizontal planes. This is a signature of the hybrid mode which has mixed polarisation and locks the particle motion in phase and frequency. As observed in Fig. 3.33b and c, the system

self-organises in a rhythmic pattern of alternating in-phase and anti-phase oscillating chains of particles. The interpenetrating antiphase oscillating 'sublattices" are shown in Fig. 3.33b. Rows of the in-phase (synchronised) oscillating particles can be seen in Fig. 3.33c. As MCI grows, more particles are involved in the MCI making the synchronisation pattern wider. Neighbouring rows of the synchronised particles are almost in anti-phase. In the experiment of Ref. [9], the motion of the synchronically moving particles was strongly "polarised" in the $\theta = 60°$ direction. This spatial orientation correlated well with the directions of the maximal increment of the (shear-free) hybrid mode. The quasi anti-phase oscillation of particles belonging to neighbouring rows can be explained the value hybrid mode wave number k_{hyb} which is close to $k_{hyb}\Delta \simeq \pi$. Indeed, since the jth particle oscillations are proportional to $\exp(i\mathrm{k_{hyb}} \cdot \mathrm{r_j})$, at $k = k_{hyb}$ the motion of neighbouring particles should obviously be almost anti-phase. Moreover, when MCI is triggered, only the hybrid mode oscillations have a growth rate larger than the damping rate, all other wave modes tending to equilibrate with the surrounding environment. Therefore, the hybrid mode accumulates energy resulting in an exponential growth of the amplitude of the hybrid mode oscillations (hiding all other wave modes). A second order Taylor expansion of the force between two neighbour particles easily shows that the phases of in-plane and out-of-plane motion of neighbour particle are coupled. It is known that oscillators with any phase-dependent interaction can evolve until their phases are (partially) synchronised [275]. Furthermore, since the shear in-plane component of the hybrid mode is very weak, rows of particles belonging to equivalent elementary cells must have synchronised motion. The crystalline order is destroyed when the oscillation amplitudes are too large, and the synchronisation naturally vanishes (see Fig. 3.33d). The melted zone then expands to the whole monolayer due to fluid MCI [2].

Note that the synchronisation pattern should normally occur in all equivalent directions of the maximal increment of the shear-free hybrid mode (i.e. every 60°). It is however rarely the case experimentally [9, 270]. The observed break of symmetry is due to crystal deformation (compression) due to small asymmetries in the horizontal confining potential [270, 276, 277]. Crystal compression leads to an asymmetric crystal elementary cells The triggering of MCI follows this anisotropy since the formation of the hybrid mode is favoured in the compressed direction.

3.3.6 Mode-coupling induced melting

As mentioned many times already, non-reciprocal wake-mediated interactions can trigger the MCI in 2D complex plasmas [150, 157, 261]. MCI also exists in complex plasma monolayer in the fluid state [2, 10, 264].

As discussed in Sec. 3.1.6 and Sec. 3.3.4, a necessary condition of MCI onset is a crossing of the longitudinal in-plane and out-of-plane wave modes, leading to the formation of the unstable hybrid mode and a rapid increase of the particles kinetic energy if the MCI growth rate surpasses the neutral damping rate. In 2D complex plasma crystals, for a given crystal density there is a vertical confinement threshold below which MCI is triggered (see Sec. 3.3.4 and Ref.[157]). This can be reformulated as follows: for a given strength of the vertical confinement, the 2D complex plasma crystal density must exceed a threshold to trigger MCI. Experimentally MCI always starts in the central (densest) region of the crystal where the crystal parameters favour for the crossing of the longitudinal in-plane mode and the out-of-plane mode. In contrast, wave modes always cross in fluid complex plasma monolayer[2]. Consequently there are no density nor confinement thresholds in a fluid monolayer and fluid MCI exist under conditions for which a crystalline monolayer is stable (no crossing of the modes, region between p_{MCI} and p_{cryst} described in Sec. 3.3.4). It is the reason why in many experiments the melting expands to the whole monolayer once MCI is triggered at (and only at) the centre of the monolayer. Hence heat activation of a stable monolayer complex plasma crystal can provide a direct analogy with

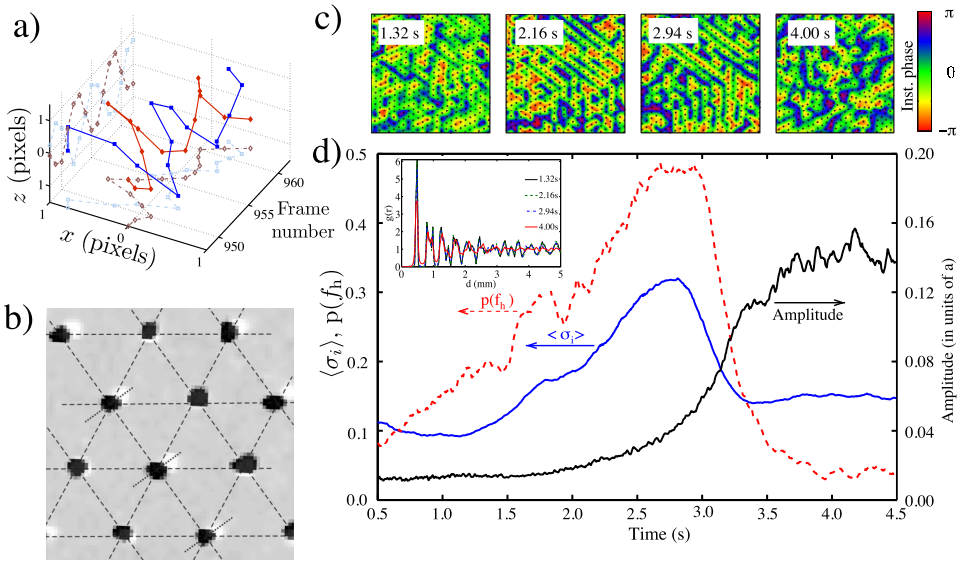

Figure 3.33 – (Reproduced from Ref. [9]) a) Trajectories of 2 neighbour particles [red (diamond) and blue (square) plain lines] showing vertical and horizontal periodic motion at the hybrid frequency $f_{\rm h} \simeq 16.5 \pm 0.8$ Hz. The dashed light-blue (open square) and light-red (open diamond) lines are the projection on the (x,t) and (z,t) planes. b) Two superposed images of the lattice layer separated in time by a half hybrid period ($\Delta t \simeq 0.032$ s) close to the maximum of the synchronisation index ($t \simeq 2.7$ s). The white and black dots show the particle positions. The mean interparticle distance in the studied region is $\Delta = 470 \pm 16$ μm. The parallel dashed lines are a guide to the eye. The stacked images were shifted along the main deformation direction to graphically demonstrate the character of the particle vibrations. The main deformation direction is indicated by the dotted lines (in this direction the lattice is about 7–9% more compact). Note that the distance between the in-phase oscillating rows of particles is nearly constant. c) Consecutive snapshots (300×300-pixel area of the original video) indicating the instantaneous phase distribution for desynchronised states (t=1.32 s and t=4.00 s), and during the synchronised state (t=2.16 s and t=2.94 s). The black dots show the position of the particles. d) Evolution of the cumulative probability $p(f_{hyb})$ (red dashed curve) to find a particle with an instantaneous frequency in the band 14 Hz$< f <$ 18 Hz around f_{hyb}, the mean value of the synchronisation index $\langle\sigma\rangle$ (averaged over particles, solid blue curve) and the averaged instantaneous amplitude of the particle oscillations (solid black curve). The average was done over ∼150 particle tracks at the centre of the crystal (145×145-pixel area of the original video). The inset shows the radial pair correlation functions at different times.

activation in ordinary reactive matter.

In this section, I will present the evolution of the MCI-induced melting in a 2D complex plasma crystals. I will first described the "natural" melting where MCI is triggered in the crystal phase by the crossing of the wave modes. Then, I will described "forced" melting for which fluid MCI is triggered by locally melting the monolayer crystal with the help of a laser beam.

Natural melting

The melting front propagation in a complex plasma monolayer in MCI induced melting has been the subject of a few articles [10, 12, 164].

Here, I will focus on the work reported in Ref. [164]. This work was done in collaboration with the group of Prof. S. Yurchenko at Bauman Moscow State. The experimental results reported here were obtained by the graduate students during my visit to Prof. Yurchenko's laboratory in 2015 and 2016.

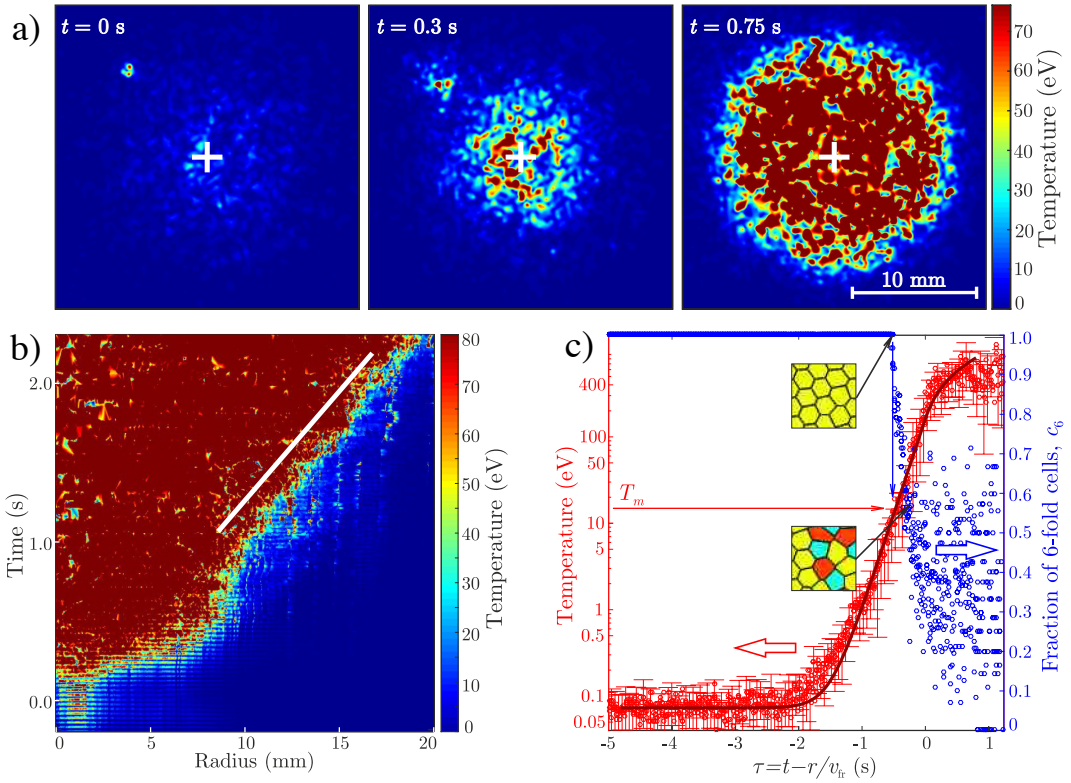

Figure 3.34 – (Reproduced from Ref. [164]. a) Typical evolution of the microparticle kinetic temperature during MCI-induced melting (top view). The crystalline MCI triggers melting of the central region, then the melting expands outward in the form of a sharp front, supported by intense heating behind the front due to fluid MCI. b) Radial expansion of the hot zone with time. At $t \sim 1$ s the ignition phase due to the crystalline MCI changes to a steady expansion sustained due to fluid MCI (indicated by the white solid line). c) Self-similar profiles of the particle kinetic temperature $T(\tau)$ (left axis) and of the fraction of sixfold cells $c_6(\tau)$ (right axis). The symbols are experimental results, and the solid line is a fit to Eq. 3.71. The insets are colour-coded snapshots of the Voronoi diagram near the flame front: sixfold cells are yellow, while five- and sevenfold cells are blue and red, respectively.

MCI was triggered in a monolayer crystal at a pressure of 1 Pa and a forward rf power 20 W. MCI rapidly melted the central region of the crystal leading to a melting front expanding outward and destroying the crystal order of the monolayer. In order to study the crystal melting evolution, Voronoi triangulation of the particles' position was performed and the bond orientational order parameter Ψ_6 was then calculated for each cell,

$$\Psi_6 = \frac{1}{N_{\rm nn}} \sum_{j=1}^{N_{\rm nn}} e^{6i\theta_j} \ , \tag{3.67}$$

where $N_{\rm nn}$ is the number of the nearest neighbours and θ_j is the bond angle for the jth neighbour. $|\Psi_6|$ quantifies the deformation of a hexagonal cell from a perfect hexagon ($|\Psi_6| = 1$). The particles' kinetic temperature (the thermal part of particles' kinetic energy) was also calculated. For that purpose, any collective motion due to acoustic fluctuations of the velocity field was subtracted from the particle velocities before the calculation of the kinetic energy:

$$T = \frac{m_{\rm d}}{2} \sum_i (\mathbf{v}_i - \langle \mathbf{v}_i \rangle)^2 \ , \tag{3.68}$$

where $\mathbf{v}_i$ is the instantaneous in-plane velocity of the ith particle, and $\langle \mathbf{v}_i \rangle$ is the instantaneous average velocity of all particles in a chosen radius of 2.4Δ around the ith particle The choice of such a small analysis area (with only a few particles) is preferable to reveal the details the spatial distribution of the studied parameters (velocity fields, density, thermal and hydrodynamic part of the kinetic energy). However, it also lead to large fluctuations due to the limited statistics. In contrast, the choice of a larger area would suppress fluctuations but leads to artificial and unphysical smoothing of the studied fields.

The evolution of the kinetic temperature can be seen in Fig. 3.34a. After a slight decrease of the rf discharge power needed to reduce the vertical confinement below MCI threshold, MCI was triggered in the 2D complex plasma crystal. At the center of the crystal, the kinetic energy rapidly increased and the crystalline order was rapidly destroyed. Then, as reported in earlier studies [10, 12], the melting expanded outward leading to a total destruction of the crystal. The observed melting front (or "flame" front) was very sharp and expended steadily thanks to the energy input provided by fluid MCI [2]. Behind the front (i.e. in the melted area), the kinetic temperature was $\sim$3 orders of magnitude larger than that of the crystalline region. Figs. 3.34a-b show the details of the flame front formation. First, at the initial (ignition) phase, oscillating lines of macroparticles were observed as described in Sec. 3.3.5 or Ref. [9]). In the crystal central region where MCI was triggered, the microparticles' kinetic energies rapidly grew. Then, as the microparticles' oscillations amplitudes became too large, the crystal locally melted. This initial melting rapidly evolved into a hot melted spot. The melted spot boundary were very sharp and expanded outward at a constant radial velocity. In Ref. [164], the front velocity was measured at $v_{\mathrm{fr}} = 7.0 \pm 0.2$ mm/s. Note that in the crystal periphery, the microparticle number density was noticeably lower than in the centre (up to $\sim$25%) preventing any crystalline MCI. However, it did prevent the hot spot to expand in this area, undoubtedly showing the activation of fluid MCI at the front edge. In the next subsection, I will also describe how crystal melting can be artificially triggered by external excitation. For example, local laser heating can be used (see Ref. [165] and the next subsection) or a rapidly moving particle under the monolayer (see Ref. [262]) or an external mechanical excitation (see Ref. [166]). Simulations report similar behaviour [166].

Let us discuss now the analogies between the propagation of a flame front in conventional reactive matter and the MCI induced melting front. As a matter of fact, the time-dependant spatial temperature distribution $T(r,t)$ in a continuous reactive medium can be described by the following heat equation [164, 278]:

$$\frac{\partial T}{\partial t} = \frac{Q(T)}{C n_{2\mathrm{D}}} + \chi\Big(\frac{\partial^2 T}{\partial r^2} + \frac{D-1}{r}\frac{\partial T}{\partial r}\Big), \tag{3.69}$$

where $Q(T)$ is the reaction heat rate of the medium (of spatial dimension D), χ is the thermal diffusivity, $n_{2\mathrm{D}}$ is the monolayer microparticle number density , and C is the isobaric heat capacity per particle. As the melting spot widen, the second term in the parentheses tends to 0, reducing the problem to one dimension.

The heat reaction heat rate is determined by the chemical kinetics in the given reactive medium. It is of the form $Q(T) \propto \exp(-T_{\mathrm{a}}/T)$ for an Arrhenius-like chemical activation where T_{a} is the activation energy. Additionally, fluid MCI essentially develops when the correlations between the microparticles are largely destroyed [2] which thus assume a significant overheating compared to the melting temperature T_{m} of a 2D complex plasma crystal. Consequently, the fluid MCI heat source term similarly requires the introduction of an activation temperature T_{a} well above T_{m} (pair correlations are destroyed when the monolayer temperature is well above the melting temperature [279, 280]). Critical heat phenomena (such as ignition or explosion) generally depends on the specific feature of $Q(T)$ which can be a complex function [281]. In the case described here (steady "flame" propagation), the temperature changes very quickly across

the front making the exact shape of $Q(T)$ of minor importance. The limit behaviours at low and high temperature have the dominant effects. It is thus common practice to approximate $Q(T)$ with a Heaviside step function in the theory of combustion and flames [281]. Here, the fluid MCI heat source can be written as [164]:

$$\frac{Q(T)}{Cn_{2D}} = \begin{cases} 0, & T \leq T_a, \\ \frac{\gamma_{MCI} T_\infty}{C}, & T > T_a, \end{cases} \tag{3.70}$$

where T_a is the activation temperature at which the unstable fluid hybrid mode forms, triggering the fluid MCI. The estimated maximum heating is $q_\infty = \gamma(T_\infty)T_\infty/C$, where $T_\infty \approx 1$ keV is the saturation temperature of the fluid monolayer due to fluid MCI and $\gamma(T)$ is the (temperature-dependent) MCI growth rate. The saturation temperature T_∞ arises from the thermal spreading of the monolayer which inhibits the mode crossing and consequently the fluid MCI growth rate [2]. Since the vertical confinement strength is finite, the heat capacity of the 2D fluid monolayer is in the range $C = 2 \ldots 3$ [282]. Solving Eqs. (3.69) and (3.70) leads to a self similar solution for the temperature profile across the front [164, 283]:

$$\frac{T(\tau) - T_0}{T_* - T_0} = \begin{cases} \exp(\tau v_{fr}^2/\chi), & \tau < 0;, \\ 1 + \tau v_{fr}^2/\chi, & \tau > 0, \end{cases} \tag{3.71}$$

where $\tau = t - r/v_{fr}$ is the self-similar time and v_{fr} is the melting front velocity. v_{fr} is linked to the activation temperature: $T_a - T_0 = q_\infty \chi / v_{fr}^2$. $\tau < 0$ represents the a non-activated crystalline regime in which the crystal is preheated by thermal diffusion ("inert zone") and $\tau > 0$ represents the activated fluid regime in which fluid MCI is transferring energy to the monolayer ("reactive" zone) [281]. Neutral gas damping should normally be added as an additional term $-2\gamma_d(T - T_0)/C$ on the right-hand side of Eq. (3.69), where T_0 is the equilibrium temperature in the absence of heating and γ_d is the Epstein damping rate (in our experimental conditions, $\gamma_d \simeq 1.2$ s^{-1}). Damping can be neglected if the growth rate v_{fr}^2/χ is much larger than $2\gamma_d/C$ [164].

In Fig. 3.34c, the experimental self-similar profile $T(\tau)$ was calculated by averaging the thermal energy at different radius from the centre of the hot spot. Fig. 3.34c also shows the calculated fraction of six-fold Voronoi cells, $c_6(\tau)$, which allows the detection of the onset of melting. The equilibrium temperature $T_0 = 0.07 \pm 0.04$ eV was obtained by averaging the thermal energies of the microparticles far from the melting front (corresponding to $\tau \leq -2.5$ s in Fig. 3.34c). The kinetic temperature in the crystal (i.e region where c_6 is close to unity) grows exponentially when approaching the "flame" front. When the melting starts, c_6 decreases sharply (see snapshots of the Voronoi diagram in Fig. 3.34c). Crystal melting occurs at $T \sim 14$ eV, which agrees with the predicted equilibrium melting temperature T_m for a 2D complex plasma crystal [271, 284] with the estimated experimental values of κ and Z_d. The self-similar profile $T(\tau)$ was then fitted with Eq. (3.71) (solid line) using the least-squares method with varying activation temperature T_*, growth rate v_{fr}^2/χ, and position of the activation point $\tau = 0$. As can be seen, the experimental curve could be fitted very accurately yielding $T_a = 160 \pm 15$ eV and $v_{fr}^2/\chi = 5.1 \pm 0.1$ s^{-1} ($> 2\gamma_d/C \sim 1.2$ s^{-1} justifying the neglect of neutral damping). The heat diffusivity was then derived: $\chi \simeq 9.6$ mm^2/s. This value is in good agreement with previously reported values of the thermal diffusivity in 2D complex plasma crystals [285].

To conclude this section, our experimental results have undoubtedly demonstrated that MCI in 2D complex plasmas exhibits all the essential features of combustion in ordinary reactive matter (activated heat release,self-similar temperature profile ("flame" front)). These results can be relevant for various fields ranging from combustion and thermochemistry, to chemical physics and synthesis of materials.

Forced melting

MCI in fluid complex plasma monolayer does not have any density nor confinement thresholds [2] and the instability exist under conditions for which a crystalline monolayer is stable (no crossing of the in-plan compression and out-of-plan modes, i.e between p_{MCI} and p_{cryst} as described in Sec. 3.3.4). It is the reason why in many experiments (as the one described in the previous subsection), the melted zone expands to the entire monolayer once MCI is triggered at (and only at) the centre of the monolayer. To artificially trigger MCI induced melting in a normally stable crystal, local laser heating [165], a rapidly moving particle under the monolayer [262], or an external mechanical excitation [166] can be used. In this subsection, I summarize the main results of Ref. [165] (a copy of which is found at the end of this Section) where laser pulses where used to locally melt the monolayer.

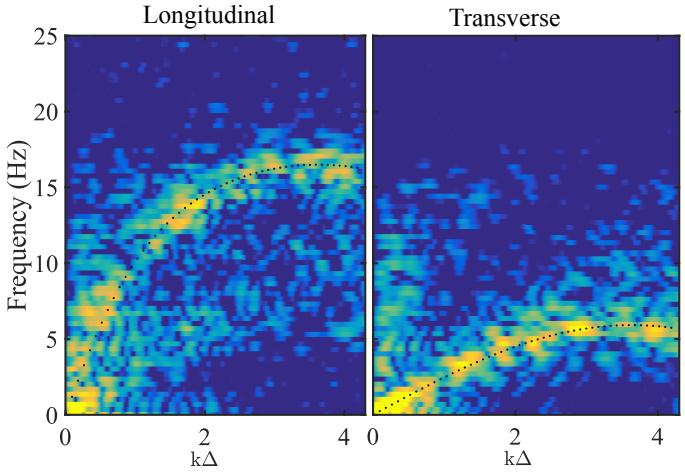

Figure 3.35 – (Reproduced from Ref. [165]) Longitudinal and transverse current fluctuation spectra at an angle $\theta = 0°$. The dotted black curves represent the fitted dispersion relations.

In the experiments of Ref. [165] [made in collaboration with V. Nosenko (DLR, Germany)], the microparticle monolayer was created under the following discharge conditions : $p_{\text{Ar}} = 1.04$ Pa and $P_{\text{RF}} = 12$ W. The mean interparticle distance was $\Delta = 415 \pm 10$ μm (microparticle number density $n_{\text{2D}} = 675 \pm 20$ cm^{-2}). By fitting simultaneously the theoretical waves mode in a 2D Yukawa crystal [150] over the in-plane compressional and shear microparticle current fluctuation spectra computed from the tracking data, the microparticle charge was estimated at $Q = -13800e \pm 500e$, the screening length at $\lambda_{\text{D}} = 408 \pm 47$ μm and the screening parameter at $\kappa = 1.0 \pm 0.15$. Fig. 3.35 shows the in-plane current spectra for a propagation angle $\theta = 0°$ (see Fig. 3.9a). No fingerprints of the unstable hybrid mode can be detected and only the normal eigenmodes are observed. The 2D complex plasma crystal was therefore stable with respect to MCI. The vertical confinement frequency was ~ 25 Hz which is in perfect agreement with no mode crossing (and therefore no MCI).

A SpectraPhysics Millennia PRO 15sJ solid-state 532-nm laser with a continuous-wave (cw) output power of 0.30–2 W was focused for a short period of time on the crystal. The microparticles in the laser spot were accelerated by the radiation pressure force and the crystal was melted locally. At the crystal surface, the laser spot had an elliptical shape with a major axis along the direction of propagation. The illuminated area had a surface $S_{\text{L}} \simeq 0.32$ mm^2. The duration of the laser pulse was changed from 0.05 s to 0.65 s. When the laser excitation resulted in a full melting of the 2D complex plasma crystal, the microparticle monolayer was recrystallized by increasing argon pressure and rf power above the crystallisation threshold and the discharge conditions were then restored to the initial values. The crystalline monolayer was allowed to further relax for a couple of minutes before the next laser pulse was applied to it.

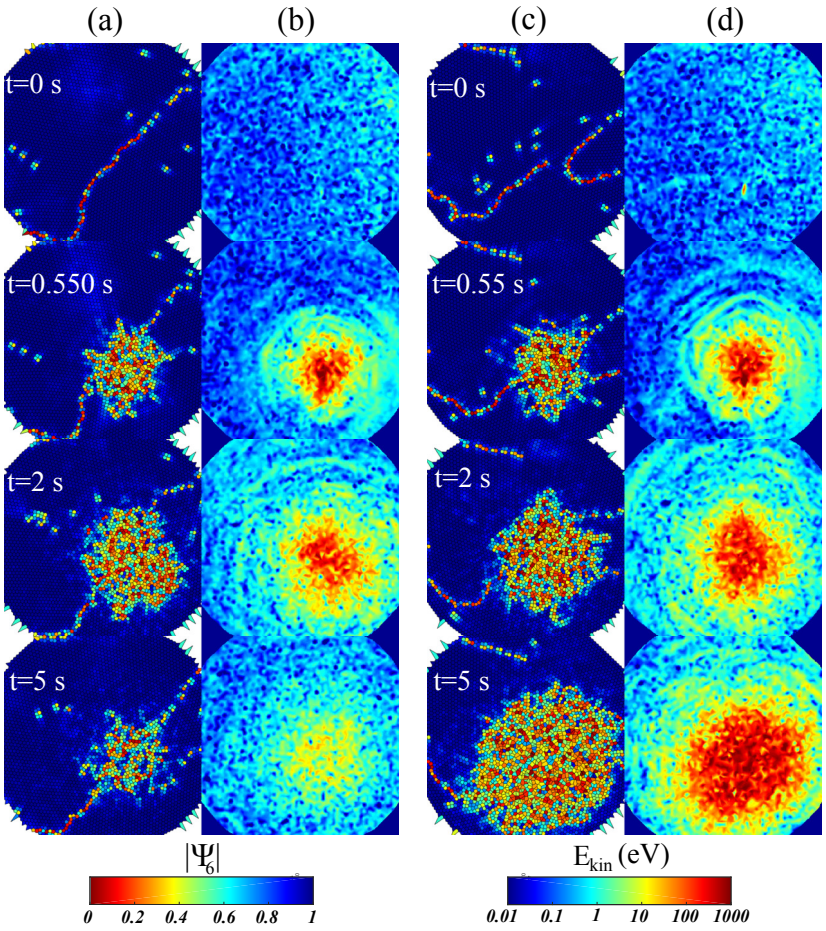

Figure 3.36 – (Reproduced from Ref. [165]) $|\Psi_6|$ maps (a,c) and kinetic energy maps (b,d) of the crystal during Exps. 19 (a,b) and 20 (c,d) (see Table 1 of Ref. [165]). Each map is a square of 24.6×24.6 mm^2.

Due to the small sized of the laser spot at the crystal surface, only a few particles were accelerated during the laser pulse (typically $N \leq 50$). As a result, a small melted spot was created a few Δ in front of the laser spot position in the direction of laser light propagation. The typical diameter of the melted spot at the end of the pulse was $1-4$ mm. The microparticles in the melted spot had high velocities. Depending on the pulse duration and the laser power, the melted area recrystallized or expanded over the whole crystalline monolayer. These two behaviour are illustrated in Fig. 3.36.

Particle tracking during and after the laser pulse allowed the measurement of the evolution of the particles' kinetic energies and the energy injected by the laser pulse into the crystal was estimated. At the end of the laser pulse, the total kinetic energy of the particles in the camera field of view (FoV) reached its maximum. Note that at the end of the pulse, the the melted spot particles had velocity vectors mainly directed along the direction of the laser beam but quickly thermalised (in the melted spot) due to collisions with other particles. From looking at the first and second moments of the microparticles velocity distribution function in x and y, the thermalisation was found complete after $t_{\rm th} \simeq 0.5$ s (similar Maxwellian velocity distribution centred on 0 in x and y). Table 1 of Ref.[165] lists the total kinetic energies $K_{\rm t} = \sum_i K_i(t)$ of the microparticles in the camera FoV at the end of the laser pulse ($K_{\rm t}(t_{\rm on})$) and after thermalisation ($K_{\rm t}(t_{\rm on}+t_{\rm th})$) for all investigated laser pulse durations. The main observation were as follows: for a given laser power, the total energy increased with the laser pulse duration and the energy after thermalisation was slightly smaller due to neutral damping and heat transport to the rest of the monolayer (outside of the FoV). Before a laser pulse, the average microparticle kinetic

temperature was $T_0 = 0.13 \pm 0.05$ eV corresponding to a total energy in the FoV $K_\mathrm{t} < 800$ eV. Thus, since the measured total energy at the end of the laser pulse was always much larger than a few keV, it corresponded roughly to energy injected by the laser.

Fig. 3.37 shows the state of the monolayer at the end of an experiment (recrystallized or fully melted) as a function of the total energy after thermalisation. As can be seen, when $K_\mathrm{t}(t_\mathrm{on} + t_\mathrm{th})$ reached $= 40 \pm 1$ keV (corresponding to $t_\mathrm{on} \geq 500$ ms at $P_\mathrm{l} = 0.85$ W), a full melting of the crystalline monolayer was triggered: this is a clear indication that the observed melting is a threshold phenomenon.

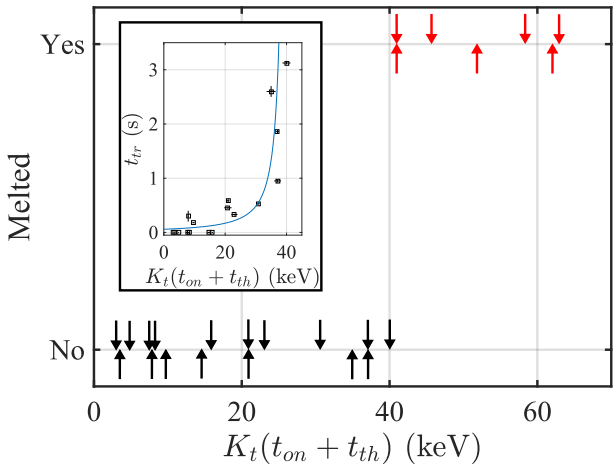

Figure 3.37 – (Reproduced from Ref. [165]) State of the monolayer (red, melted or black, unmelted) at the end of the experiment as a function of $K_\mathrm{t}(t_\mathrm{on} + t_\mathrm{th})$. Each experiment of Table 1 of Ref. [165] is indicated by an arrow of the appropriate color. A threshold at ∼40 keV is clearly identified. The inset shows the transition time before recrystallisation sets in for injected energies below the melting threshold. The blue line is a guide for the eye.

Fig. 3.36 shows Voronoi maps of the microparticle monolayer (coloured according to the value of $|\Psi_6|$) and the corresponding kinetic energy map. This figure clearly illustrate the difference between two experiments showing either recrystallization or melting (Exps. 19 and 20 in Ref.[165]). As can be seen, before the laser pulse ($t = 0$ s), the crystalline monolayer was cold in both cases with $T_0 \simeq 0.13$ eV. Both crystals were almost perfect with only a few dislocations and a few grain boundaries. At the end of the laser pulse ($t = 0.55$ s), a melted spot (identified as a region with high microparticles' kinetic energies and small values of $|\Psi_6|$) is clearly visible in the centre. In both cases, compression waves travelled preferentially in the direction of the laser beam (positive y direction) due to the non-thermalised motion of the laser-excited particles. At $t = 2$ s $> t_\mathrm{on} + t_\mathrm{th}$, the spot particles were thermalised and compressional waves emerged then isotropically from the hot spot. In both cases, the melted spot was slightly larger than at $t = 0.55$ s. However, the melted spot of experiment 20 (Figs. 3.36c–d) appeared slightly larger and the microparticles had slightly higher kinetic energies.

Experiments that did not lead to the full melting of the monolayer showed a transition period before the recrystallisation set in. The duration of this transition period depended on the amount of energy injected by the laser. The transition time t_tr (defined as the amount time before K_t exhibits a clear exponential decay after the end of the laser pulse) as a function of the injected energy is shown in the inset of Fig. 3.37. Experiment 19, used for the snaphot of Figs. 3.36a-b, had a transition time of 3.13 s. As can clearly be seen in the inset of Fig. 3.37, the transition time is an increasing function of the input energy that diverges at the energy threshold. For the experiments with injected energy above threshold, the reported kinetic energy growth after the pulse was nearly exponential with an average measured growth rate $\gamma_\mathrm{g}^{-1} = 1.1 \pm 0.2$ s.

The mechanism allowing crystal melting is linked to the the existence of the MCI in fluid microparticle monolayers. Ivlev *et al.* [2] showed that the wake-induced mode coupling always occurs in 2D fluid complex plasmas and, contrary to MCI in 2D complex plasma crystals, there is no confinement/density thresholds. Therefore for sufficiently low neutral gas pressure (small damping rates) the energy input from fluid MCI (i.e. the energy transferred by the ion flow to the crystal) prevent the crystallisation of the monolayer. In addition, if a large enough melted spot is created in the crystalline monolayer, the localised energy input due to MCI cannot be dissipated rapidly enough (through neutral damping and heat conduction in the crystal), leading to further increase of the microparticles' kinetic temperature triggering the expansion of the melted area in an uncontrolled positive feedback. This mechanism leads to the total destruction of the crystalline order in monolayer as observed for the regular (natural) MCI-induced melting discussed in the previous section and reported in Ref. [2, 10, 12, 157, 164].

As in the previous subsection, the time-dependant spatial temperature distribution $T(r,t)$ in a continuous reactive medium, now including neutral damping, can be described by a heat equation [164, 283]

$$\frac{\partial T}{\partial t} = \frac{Q(T)}{C n_{\mathrm{D}}} - \frac{2\gamma_{\mathrm{d}}}{C}(T - T_0) + \frac{\chi}{r}\frac{\partial}{\partial r}\Big(r\frac{\partial T}{\partial r}\Big) \tag{3.72}$$

with the initial condition (melted spot created by the laser)

$$T(r,0) = T_0 + \frac{E_{\mathrm{l}}}{2\pi w_{\mathrm{MZ}}^2 n_{\mathrm{D}} C}\exp\Big(-\frac{r^2}{2w_{\mathrm{MZ}}^2}\Big) \tag{3.73}$$

where E_{l} is the energy injected by the laser pulse, w_{MZ} is the width of the melted spot created by the laser pulse, γ_{d} is the Epstein damping rate (here $\gamma_{\mathrm{d}} \simeq 1.21 \pm 0.13$ s^{-1} [71]), As in the previous section and in Ref. [164], the fluid MCI heat source can roughly approximated by Eq. 3.70 with a saturation temperature in the range $T_\infty \sim 1 - 3$ keV. Note that this time the damping term was not omitted in Eq. 3.72.

Since $T_0 \ll T_{\mathrm{a}}$, T_0 can be ignored and Eq. (3.72) can be rewritten in a dimensionless manner:

$$\frac{\partial \Theta}{\partial \tau} = \lambda \mathrm{e}^{-1/\Theta} - \Gamma\Theta + \frac{1}{\tilde{r}}\frac{\partial}{\partial \tilde{r}}\Big(\tilde{r}\frac{\partial \Theta}{\partial \tilde{r}}\Big)\ , \tag{3.74}$$

where $\Theta = T/T_{\mathrm{a}}$, $\tilde{r} = r/r^*$ with $r^{*2} = E_{\mathrm{l}}/n_{\mathrm{2D}} C T_{\mathrm{a}}$, $\tau = t/t^*$ with $t^* = r^{*2}/\chi$. The initial condition becomes

$$\Theta(\tilde{r},0) = \frac{1}{2\pi\tilde{w}_{\mathrm{MZ}}^2}\exp\Big(-\frac{\tilde{r}^2}{2\tilde{w}_{\mathrm{MZ}}^2}\Big)\ , \tag{3.75}$$

with $\tilde{w}_{\mathrm{MZ}} = w_{\mathrm{MZ}}/r^*$. The normalisation $\int_0^{2\pi}\int_0^{\infty}\Theta(\tilde{r},0)\tilde{r}\mathrm{d}\tilde{r}\mathrm{d}\varphi = 1$ determines the characteristic length scale. Thus, in its dimensionless form, the problem is characterised by two numbers

$$\lambda = \frac{\gamma_{\text{MCI}} T_\infty E_{\mathrm{l}}}{C^2 \chi n_{\mathrm{D}} T_{\mathrm{a}}^2} \tag{3.76}$$

and

$$\Gamma = \frac{2\gamma_{\mathrm{d}} E_{\mathrm{l}}}{C^2 \chi n_{\mathrm{2D}} T_{\mathrm{a}}} = \frac{2\gamma_{\mathrm{d}}}{\gamma_{\text{MCI}}}\frac{T_{\mathrm{a}}}{T_\infty}\lambda\ . \tag{3.77}$$

Eq. (3.74) is similar to the one describing impulsive spot heating and thermal explosion in ordinary matter with the addition of a dimensionless damping coefficient Γ [164, 283]. Without damping and a sufficiently localized hot spot (so it can be accurately described with a Dirac distribution), the subsequent thermal evolution is characterized only by λ. A bifurcation between two distinct regimes can be identified. When exceeding a critical threshold, the solution of heat equation shows a rapid temperature growth. For 2D systems, the critical value is

$\lambda_{cr}(\Gamma = 0) = 9.94$ [283]. The damping term increases this critical value: numerical estimates lead to $\lambda_{cr}(\Gamma = 1.5) \sim 17$ and $\lambda_{cr}(\Gamma = 2.5) \sim 21$. In our experimental conditions, the thermal diffusivity of the crystal was estimated at $\chi \sim 10$ mm^2/s [285] and $\gamma_{MCI} \sim \gamma_g \sim 0.9$ s^{-1}. By fitting the temperature distribution after the laser pulse with a 2D Gaussian function, the width of the melted zone was $w_{MZ} \sim 1 - 2$ mm, which is noticeably smaller than the characteristic length $r^* \sim 4.5$ mm. These experimental parameters yield a value of $\Gamma \sim 2-4$ and, a threshold energy, $\lambda \sim 10 - 30$, in remarkable agreement with the theoretical estimate. Note that the width of the MZ has a significant effect on the energy threshold since for a given injected energy a wider spot results in a significant portion of the energy being distributed over particles with a kinetic temperature below the activation temperature. Therefore, for large melted spots ($w_{MZ} \geq r^*$), the threshold depends on the temperature of the melted spot and its size [283, 286].

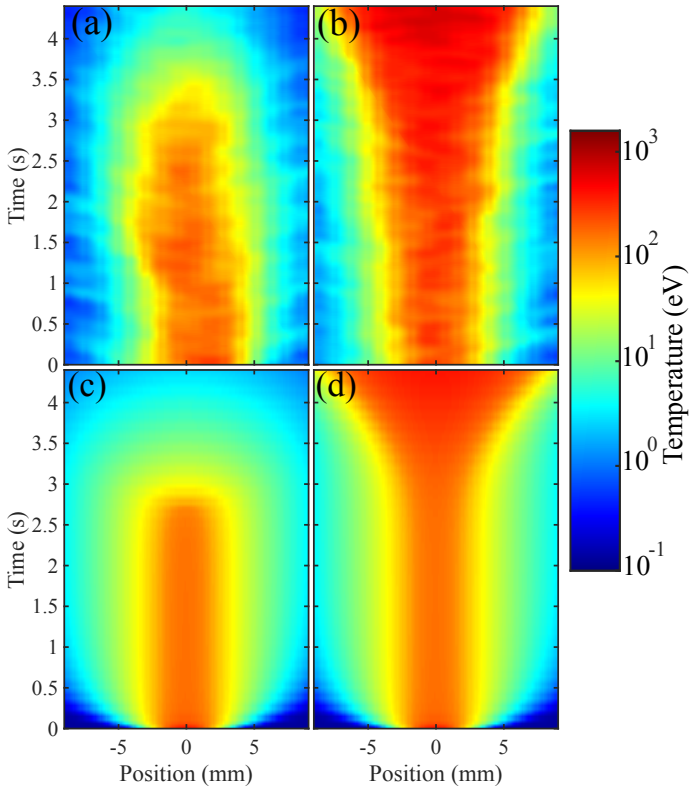

Figure 3.38 – (Reproduced from Ref. [165]) Evolution of the temperature profile. (a) Experiment 19: recrystallization, (b) Experiment 20: melting. Solution of Eqs. (3.72) using the reaction model (3.70): (c) slightly below threshold, (d) slightly above threshold. For the numerical profiles, the following parameters were used: $\chi = 9$ mm^2/s, γ_d=1.2 s^{-1}, $\gamma_{MCI} = 0.9$ s^{-1}, T_∞=1800 eV, T_a=105 eV, n_D=6.75 mm^{-2}, $C = 2$, w_{MZ}=1.15 mm and (c) E_l=40103 eV ($\lambda = 24.2497$, $\Gamma = 3.7722$) and (d) E_l=40103.7 eV ($\lambda = 24.2506$, $\Gamma = 3.7722$).

In Fig. 3.38, the time-dependant temperature profile of experiments 19 and 20 of Ref, [165] are shown along the numerical solution of Eqs. (3.70) and (3.72). The numerical input parameters were chosen to reproduce qualitatively the experimental behaviour. As can be seen in all cases, the energy is transported from the melted zone to the rest of the crystalline suspension. Fluid MCI provides the energy to the microparticle suspension inside the fluid region which is partially transported in the crystal through heat conduction and is partially dissipated through neutral damping. Therefore, the size of the melted area can slightly increase even if the total input energy is below the required melting threshold. The recrystallisation delay observed when increasing the amount of injected energy by the laser pulse while staying below threshold is also obtained numerically: it originates from the amount of energy pumped by fluid MCI into the melted spot which depends directly on its size. Indeed, recrystallization

occurs only after enough energy has been removed from the hot spot to suppress the fluid MCI heat flux (Fig. 3.38a and c). The transition period is obviously longer for larger spots since a significantly larger amount of energy has to be dissipated due to the large energy input due to fluid MCI. When the injected energy exceed a threshold, fluid MCI delivers more energy in the melted hot spot than the energy loss by neutral damping and heat conduction in the rest of the monolayer. This results in temperature growth over time (Fig. 3.38b and d) and a melting dynamics similar to the one reported in the regular (natural) MCI-induced melting of a 2D complex plasma crystal [2, 10, 150, 157, 164].

To summarize this section, the experimental demonstration of an externally induced wake-mediated resonant mode coupling (localised pulsed laser heating) in a 2D complex plasma crystal was described. Due to the co-existence of a stable crystalline state and a melted state experiencing fluid MCI, localised heating is able to trigger a full melting of the crystalline monolayer. In a stable crystal (with respect to crystalline MCI), the external energy input must exceed a threshold to trigger melting. Below threshold, recrystallisation preceded by a transition period is always observed. The transition period is longer when the input energy approaches threshold. In that case, the localized fluid MCI cannot pump enough energy to the microparticle suspension to maintain the fluid state and propagate a melting front through the entire crystal. Above threshold, a full melting of the crystal is observed due to the activated fluid MCI. This behaviour is remarkably similar to impulsive spot heating in ordinary reactive matter.

3.3.7 Main publications

The following publications corresponding to the main results described in this section are attached to the manuscript.

1. L. Couëdel, V. Nosenko, S. K. Zhdanov, A. V. Ivlev, et al., *First direct measurement of optical phonons in 2D plasma crystals*, Phys. Rev. Lett. **103**, 215001 (2009).

   Abstract: Spectra of phonons with out-of-plane polarization were studied experimentally in a 2D plasma crystal. The dispersion relation was directly measured for the first time using a novel method of particle imaging. The out-of-plane mode was proven to have negative optical dispersion at small wave numbers, comparison with theory showed good agreement. The effect of the plasma wakes on the dispersion relation is briefly discussed.

2. L. Couëdel, V. Nosenko, S. K. Zhdanov, A. V. Ivlev, et al., *Direct observation of mode-coupling instability in two- dimensional plasma crystals*, Phys. Rev. Lett. **104**, 195001 (2010).

   Abstract: Dedicated experiments on melting of two-dimensional plasma crystals were carried out. The melting was always accompanied by spontaneous growth of the particle kinetic energy, suggesting a universal plasma-driven mechanism underlying the process. By measuring three principal dust-lattice wave modes simultaneously, it is unambiguously demonstrated that the melting occurs due to the resonance coupling between two of the dust-lattice modes. The variation of the wave modes with the experimental conditions, including the emergence of the resonant (hybrid) branch, reveals exceptionally good agreement with the theory of mode-coupling instability.

3. L. Couëdel and V. Nosenko, *Stability of two-dimensional complex plasma monolayers in asymmetric capacitively-coupled radio-frequency discharges*, Phys. Rev. E **105**, 015210 (2022).

   Abstract: In this article, the stability of a complex plasma monolayer levitating in the sheath of the powered electrode of an asymmetric capacitively coupled radio-frequency argon discharge is studied. Compared to earlier studies, a better integration of the experimental results and theory is achieved by operating with actual experimental control parameters such as the gas pressure and the discharge power. It is shown that for a given microparticle monolayer at a fixed discharge power there exist two threshold pressures: (i) above a specific pressure p_{cryst}, the monolayer always crystallizes; (ii) below a specific pressure p_{MCI}, the crystalline monolayer undergoes the mode-coupling instability and the two-dimensional complex plasma crystal melts. In between p_{MCI} and p_{cryst}, the microparticle monolayer can be either in the fluid phase or the crystal phase: when increasing the pressure from below p_{MCI}, the monolayer remains in the fluid phase until it reaches p_{cryst} at which it recrystallizes; when decreasing the pressure from abovep_{cryst}, the monolayer remains in the crystalline phase until it reaches p_{MCI} at which the mode-coupling instability is triggered and the crystal melts. A simple self-consistent sheath model is used to calculate the rf sheath profile, the microparticle charges, and the microparticle resonance frequency as a function of power and background argon pressure. Combined with calculation of the lattice modes the main trends of p_{MCI} as a function of power and background argon pressure are recovered. The threshold of the mode-coupling instability in the crystalline phase is dominated by the crossing of the longitudinal in-plane lattice mode and the out-of plane lattice mode induced by the change of the sheath profile. Ion wakes are shown to have a significant effect too.

4. L. Couëdel, S. Zhdanov, V. Nosenko, A.V. Ivlev, at al., *Synchronization of particle motion induced by mode coupling in a two-dimensional plasma crystal*, Phys. Rev. E **89**, 053108 (2014).

   Abstract: The kinematics of dust particles during the early stage of mode-coupling induced melting of a two-dimensional plasma crystal is explored. It is found that the formation of the hybrid mode causes the particle vibrations to partially synchronize at the hybrid frequency. Phase- and frequency-locked hybrid particle motion in both vertical and horizontal directions (hybrid mode) is observed. The system self-organizes in a rhythmic pattern of alternating in-phase and antiphase oscillating chains of particles. The spatial orientation of the synchronization pattern correlates well with the directions of the maximal increment of the shear-free hybrid mode.

5. L. Couëdel, V. Nosenko, M. Rubin-Zuzic, et al., *Full melting of a two-dimensional complex plasma crystal triggered by localized pulsed laser heating*, Phys. Rev. E **97**, 043206 (2018).

   Abstract: The full melting of a two-dimensional plasma crystal was induced in a principally stable monolayer by localized laser stimulation. Two distinct behaviors of the crystal after laser stimulation were observed depending on the amount of injected energy: (i) below a well-defined threshold, the laser melted area recrystallized; (ii) above the threshold, it expanded outwards in a similar fashion to mode-coupling instability-induced melting, rapidly destroying the crystalline order of the whole complex plasma monolayer. The reported experimental observations are due to the fluid mode-coupling instability, which can pump energy into the particle monolayer at a rate surpassing the heat transport and damping rates in the energetic localized melted spot, resulting in its further growth. This behavior exhibits remarkable similarities with impulsive spot heating in ordinary reactive matter.

First Direct Measurement of Optical Phonons in 2D Plasma Crystals

L. Couëdel,* V. Nosenko, S. K. Zhdanov, A. V. Ivlev, H. M. Thomas, and G. E. Morfill

Max-Planck-Institut für extraterrestrische Physik, 85741 Garching, Germany

(Received 29 July 2009; published 17 November 2009)

Spectra of phonons with out-of-plane polarization were studied experimentally in a 2D plasma crystal. The dispersion relation was directly measured for the first time using a novel method of particle imaging. The out-of-plane mode was proven to have negative optical dispersion at small wave numbers, comparison with theory showed good agreement. The effect of the plasma wakes on the dispersion relation is briefly discussed.

DOI: 10.1103/PhysRevLett.103.215001 PACS numbers: 52.27.Lw, 52.27.Gr, 52.35.Fp, 82.70.Dd

Complex plasmas consist of particles immersed in a weakly ionized gas-discharge plasmas [1–3]. Because of the absorption of ambient electrons and ions, microparticles acquire significant (negative) charges and can form strongly coupled systems analogous to conventional soft matter (complex fluids). Two-dimensional (2D) complex plasmas are particularly convenient systems for the detailed experimental studies of strongly coupled phenomena at the atomistic level. The essential advantage of such systems is that one can gain complete information about the state of the entire particle ensemble in the phase space, which is an invaluable advantage for the investigation of collective processes occurring in strongly coupled media, such as transport, phase transitions, structural quenching, etc. [1,2].

2D complex plasmas are usually studied in ground-based experiments with rf discharges. Microparticles injected in such discharges levitate in the sheath region near the bottom electrode, where the electric field can balance gravity. Under certain conditions the particles can form a monolayer, and if the electrostatic coupling between them is strong enough, particles arrange themselves into ordered structures—2D plasma crystals [4]. In such crystals, numerous collective phenomena like melting and recrystallization, mass and heat diffusion, solitons and shocks [5–10], etc., have been reported. Propagation of dust-lattice (DL) waves in 2D lattices is often used as a diagnostic tool to determine parameters of the plasma crystal [9,11].

In 2D complex plasmas, as in any (strongly coupled) 2D system, two in-plane wave modes can be sustained (here we naturally leave aside polydisperse mixtures). In crystals, both modes have an acoustic dispersion, one of them is longitudinal, another is transverse. Since the strength of the vertical confinement in such systems is finite, there is a third fundamental wave mode associated with the out-of-plane oscillations [12–18]. Theory predicts that this mode has a negative (or inverse) optical dispersion and depends critically on the parameters of the plasma wakes (that are formed downstream from each particle levitating in the sheath) [14,18,19]. So far, the systematic experimental studies of the DL waves were limited to the in-plane modes, whereas direct measurements of the out-of-plane dispersion relation have never been carried out (see, however, Refs. [13,20]). To a large extent, this is due to the lack of reliable diagnostics of the vertical dynamics of individual particles.

In this Letter, we report on the first direct measurements of the out-of-plane DL wave mode in a 2D plasma crystal. The dispersion relation is recovered in a broad range of wave vectors, revealing remarkably good agreement with the existing theory. The measurements were performed by employing a new detection technique of the vertical (out-of-plane) particle displacement. The obtained results provide us with new insights into the mechanisms governing the individual particle dynamics in 2D complex plasmas (for example, role of the plasma wakes, influence of charge variation) and allow us to specify the conditions when such systems can be used to investigate generic properties of (classical) 2D solids and liquids.

A sketch of the experimental setup is shown in Fig. 1. We used a capacitively coupled rf glow discharge at 13.56 MHz. The argon pressure p was between 0.5 and 1 Pa and the rf peak-to-peak voltage V_{pp} was between 175 and 310 V (which corresponds to a forward rf power P between 5 and 20 W). The self-bias voltage V_{dc} was between -60 and -130 V. The plasma parameters in the bulk discharge were deduced from Langmuir probe measurements, yielding the electron temperature $T_e = 2.5$ eV and the electron density $n_e = 2 \times 10^9$ cm^{-3} at $p = 0.66$ Pa and $P = 20$ W [21]. A 2D particle suspension was formed by levitating melamine formaldehyde microspheres in the sheath above the rf electrode. The particles had a diameter of 8.77 ± 0.14 μm and a mass $m = 5.3 \times 10^{-13}$ kg. The diameter of the obtained crystalline structure was about 50–60 mm, depending on the number of injected particles. The microparticles were illuminated by a horizontal laser sheet which had a Gaussian profile in the vertical direction with a standard deviation $\sigma \simeq 75$ μm (corresponding to a full width at half maximum of 175 μm). The sheet thickness was approximatively constant across the whole crystal. The particles were imaged through a window at the top of the chamber by a Photron FASTCAM 1024 PCI camera at a speed of 250 frames per second. The horizontal coordinates x and y as well as velocity components v_x and v_y of individual particles were then extracted with subpixel resolution in each frame by using a standard particle tracking technique [22]. An additional side-view camera was used to verify that our experiments were carried out with a single layer of particles.

 © 2009 The American Physical Society

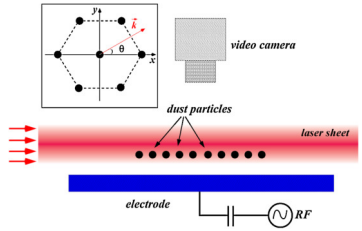

FIG. 1 (color online). Sketch of the experimental setup. Microparticles are confined above the rf electrode and are illuminated with a horizontal laser sheet having a Gaussian profile in the vertical direction. The monolayer is levitated well below the peak of the laser intensity, which results in strong intensity variations of the scattered light upon the vertical displacement of individual particles. The upward (downward) displacement corresponds to a positive (negative) intensity variation. Inset shows elementary cell of the hexagonal lattice and the frame of reference chosen in this Letter, the orientation of the wave vector $\mathbf{k}$ is measured in respect to the x axis.

In order to extract the vertical position z and velocity v_z of individual particles, we needed to employ a very different technique. Unlike relatively compact Coulomb clusters, where these values can be directly measured by using the side view, the particles forming large monolayers cannot be individually resolved from the side. Therefore, the out-of-plane tracking can be performed only by using the top view, and then z and v_z should be deduced from the relative variation of the scattered light intensity.

The ''conventional'' method of particle visualization, when the peak of the Gaussian intensity in the illuminating laser sheet practically coincides with the particle levitation height (this facilitates the in-plane tracking, especially at higher frame rates), is not appropriate to obtain z and v_z. The reason is twofold: The first problem of such configuration is that the variation in the (particle image) intensity between consecutive frames gives us only the magnitude of the vertical displacement (and hence velocity), whereas the direction remains undefined. Indeed, the intensity of the individual particle image at each frame is proportional to the local illumination intensity, which scales as

$$I(z) \propto e^{-(z-z_{\max})^2/2\sigma^2}, \qquad (1)$$

where $z_{\max}$ is the position of the intensity maximum. Therefore, if the mean levitation height z_{lev} is very close to $z_{\max}$, then the magnitude of the particle displacement $|\delta z|$ might be substantially larger than $|z_{\text{lev}} - z_{\max}|$. Obviously, a given variation of the image intensity in this case may equally imply either positive or negative displacement [13]. The second problem of the ''conventional'' method is associated with the sensitivity. Since $\delta z \gtrsim |z_{\text{lev}} - z_{\max}|$, the resulting intensity variations scale as $\delta I/I \approx \frac{1}{2}(\delta z/\sigma)^2$. The magnitude of vertical displacement (induced by thermal fluctuations) can be estimated as $|\delta z| \sim \sqrt{T_d/m_d\Omega_v^2} \lesssim 10$ μm (here T_d is the kinetic temperature of particles and $\Omega_v = 2\pi f_v$ is the resonance frequency in their vertical confinement), which is much smaller than the standard deviation $\sigma \approx 75$ μm. Thus, the relative intensity variations are at the level of $\sim 1\%$, which makes them very difficult to detect.

In our experiments we employed an alternative method of particle visualization. The position of the intensity maximum was set about 100 μm above the levitation height, so that $|z_{\text{lev}} - z_{\max}|/|\delta z| \sim 10$. This allowed us to overcome both drawbacks mentioned above: (i) particles moved in the region where the vertical gradient of the illumination intensity remained positive (which allowed us to avoid ambiguity in determining the direction of the displacement), and (ii) the relative intensity variations scaled almost linearly with the displacement, $\delta I/I \approx |z_{\text{lev}} - z_{\max}|\delta z/\sigma^2$, so that the resulting magnitude of $\delta I/I$ was about 15 times larger than that in the ''conventional'' tracking configuration. Note that this alternative visualization method does not critically affect the quality of the tracking in the horizontal xy plane compared to the ''conventional'' tracking configuration. A separate test has indeed shown that the pixel locking effect is roughly at the same level and that the in-plane fluctuation spectra are similar.

By performing the Fourier transform in time and space of the determined particle velocities, the dispersion relations $f(\mathbf{k})$ (both in-plane and out-of-plane) can then be obtained for a 2D crystal.

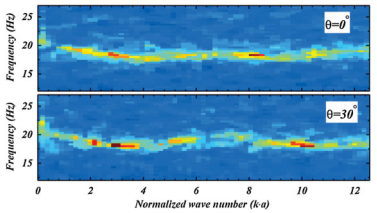

FIG. 2 (color). Fluctuation spectra of the naturally excited out-of-plane DL waves in a 2D crystal. The fluctuation amplitude is color coded linearly, from dark blue (10^{-3} a.u.) to dark red (1 a.u.), revealing the optical dispersion of the mode. The results are for a pressure of 0.8 Pa and rf power of 15 W. The upper and lower panels depict the fluctuation spectra with the wave vector $\mathbf{k}$ pointed along the principal lattice axes, $\theta = 0°$ and $\theta = 30°$, respectively (see Fig. 1). The wave number is normalized by the inverse lattice constant a^{-1}.

The resulting fluctuation spectra of the out-of-plane waves are shown in Fig. 2 for two principal orientations of the wave vector, at $\theta = 0°$ and 30°. The spectra represent the wave energy distribution in the $(f, \mathbf{k})$ space, so that the "ridge" of this distribution yields the wave dispersion relation. The most conspicuous feature of the measurements is the optical character of the dispersion relation—the frequency of the long-wavelength waves is finite. Moreover, the dispersion at long wavelengths is negative; i.e., the wave frequency falls off as the wave number increases. At larger $|\mathbf{k}|$, the wave dispersion is different for $\theta = 0°$ and 30°.

Experimental observation of the out-of-plane wave dispersion is the main result of our Letter. Figure 2 shows that the wave frequency as the function of the wave vector $\mathbf{k}$ changes in a narrow interval of 17 Hz $\lesssim f \lesssim$ 20 Hz, which makes resolving the wave dispersion a challenging task. Our method, however, allowed us to clearly identify the wave dispersion. Indeed, the frequency resolution of ≈1.5 Hz (defined as the standard deviation of a Gaussian fit) is smaller than the measured wave frequency range Δf (≈3 Hz).

Our method allowed us to measure all three wave modes of a 2D plasma crystal in a single experimental run. In Fig. 3 we show the fluctuation spectra of out-of-plane and in-plane wave modes obtained from the same experiment as in Fig. 2, for two principal lattice orientations, $\theta = 0°$ and 30°. Only the first Brillouin zone is shown here. Lines represent theoretical dispersion relations which depend on two parameters—particle charge number Z_d and the lattice screening parameter $\kappa = a/\lambda$, where a is the interparticle distance (lattice constant) and λ the effective screening length. The theoretical dispersion relations were calculated using the following procedure. First, the lattice parameters were deduced from the low-$|\mathbf{k}|$ part of in-plane fluctuation spectra using the method of Ref. [6]. The obtained values of Z_d and κ are shown in Table I for four different experiments. Second, these values were used in the theory of Ref. [18] to calculate the whole dispersion curves (the dashed and solid curves will be discussed later).

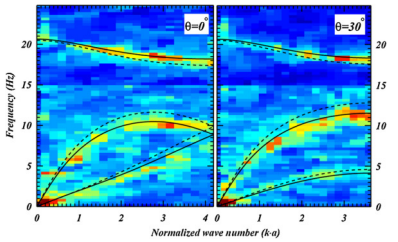

FIG. 3 (color online). Comparison of the experimentally measured DL dispersion relations with theory. Shown are the 2D in-plane and out-of-plane dispersion relations deduced from the experiments (at rf power of 15 W and pressure of 0.8 Pa) and the theoretical curves. The results are presented for two directions of the wave vector $\mathbf{k}$ (for $\theta = 0°$ and $\theta = 30°$, see Fig. 1). The dashed lines are theoretical dispersion relations for pure Yukawa interaction between particles (with the same parameters as in the experiment, see Table I), the solid lines represent the case when the interaction with plasma wakes is taken into account. The shown range of $|\mathbf{k}|$ is limited by the first Brillouin zone and therefore depends on the direction: $|\mathbf{k}|a = \frac{4}{3}\pi$ for $\theta = 0°$ and $|\mathbf{k}|a = \frac{2}{\sqrt{3}}\pi$ for $\theta = 30°$. The wave number is normalized by the inverse lattice constant a^{-1}.

As can be seen in Fig. 3, all three branches of the experimental wave spectra can be simultaneously fitted by theoretical curves calculated with the same set of parameters. This provides a useful consistency check for our experimental method and also for theory. Good overall agreement of our measurements and the theory of Ref. [18] serves as a verification that our method correctly measures the out-of-plane motion of particles and also as an indication that the theory of Ref. [18] correctly captures the essential physics of 2D plasma crystals.

The out-of-plane wave mode can also be useful for diagnostic purpose. The lattice parameters Z_d and κ are usually determined by fitting in-plane dispersion relations [6]. Another approach is to measure the propagation speed of externally excited pulses [11]. But under certain conditions (e.g., near the melting line) it is not practical and one must rely on natural waves; in this case, in-plane fluctuation spectra can be very noisy. Therefore, the additional fitting of the out-of-plane dispersion relation provides an important complementary tool to check consistency of the measurements. As an example, in Table I we compare the experimental frequency range for the out-of-plane mode Δf_{exp} to the theoretically calculated one Δf_{th} [18]. One can see that experimental and theoretical values agree well in most cases (except of experiment III that we discuss later), which is a strong indication that the crystal parameters were measured properly.

Next, we discuss how the out-of-plane waves are affected by the size of the plasma crystal. Theory [14,15,18,20] suggests that the frequency of the out-of-plane mode varies between f_v and $f_v - \Delta f$, in a narrow frequency range Δf. It scales with the lattice constant as $\Delta f_{\mathrm{th}} \propto \Omega_{\mathrm{DL}}^2 \propto a^{-3}$, where $\Omega_{\mathrm{DL}}^2 = e^2 Z_d^2/m_d a^3$ is the (squared) frequency scale of DL waves (it is assumed that $2\pi f_v \gg \Omega_{\mathrm{DL}}$). The exact factor that determines the magnitude of Δf_{th} has a relatively weak dependence on κ (which, in turn, only varies within 30% in our experiments) and can be obtained from the rigorous theory for a 2D crystal [18]. Thus, for bigger crystals where the lattice constant a is smaller (experiments I, II, and IV in Table I), the phonon frequency range Δf is larger, which makes it easier to resolve in an experiment. In addition, in big crystals the central part that is used for data analysis is fairly homogeneous. In contrast, for small crystals (experiment III in Table I) the situation is the opposite. The frequency range $\Delta f \propto a^{-3}$ is small and the fluctuation spectrum is broadened due to the significant variation of a within the analysis area. This clearly results in greater discrepancy between experiment III and theory, up to 50%. Thus, the out-of-plane wave mode can be better studied using bigger crystals.

TABLE I. Parameters of a 2D crystal extracted from different experiments (marked from I to IV). The lattice constant a is obtained from the position of the first peak of the pair correlation function. Parameters Z_d and $\kappa = a/\lambda$ are deduced from the in-plane phonon spectra with accuracy ≈15% and ≈30%, respectively. The accuracy for the measured vertical resonance frequency f_v is ≈8%. The frequency range Δf is the difference between f_v and the minimum frequency of the out-of-plane mode at $\theta = 0°$ (see Fig. 1). Subscripts "exp" and "th" stand for "experimental" and "theoretical," respectively, Δf_{th} is calculated using the theory of Ref. [18].

	P (W)	p (Pa)	a (μm)	$\lvert Z_d\rvert$ (e)	κ	f_v (Hz)	Δf_{exp} (Hz)	Δf_{th} (Hz)
I	20	0.8	525	14 000	1.3	23.3	2.7	1.9
II	15	0.8	514	14 200	1.0	20.5	2.9	3.1
III	5	0.8	1060	14 600	1.3	18.3	0.6	0.4
IV	5	0.9	600	18 000	1.0	16.3	3.7	3.9

It is worth mentioning that theory [14,18,20] predicts that both the out-of-plane and in-plane modes are affected by the presence of plasma wakes. If we introduce the effective positive charge q accumulated in the wake (normalized by the absolute value of particle charge), then the frequency of the in-plane modes is diminished by a factor $\sqrt{1-q}$, whereas the frequency range of the out-of-plane mode, Δf, is proportional to $(1-q)$. Figure 3 illustrates this effect: The dashed curves are calculated for a crystal with a pure Yukawa interaction between particles, whereas the solid curves are for the case when the additional particle-wake interactions are taken into account (with $q = 0.2$) [14,18,20]. This "wake correction" apparently improves agreement with the experiments. However, charge variation in the sheath field is also an important effect (opposite to the effect of wake) that can lead to a decrease of the characteristic frequency of optical phonons [23,24]. Because of the limited resolution of the experiments, this effect cannot be excluded.

Direct observations of the atomistic dynamics in "regular" 2D or quasi-2D systems (such as carbon nanotubes [25] and graphite [26]) are inhibited, and therefore experimental measurements of phonon spectra in such systems rely on indirect methods, e.g., Raman scattering technique [26,27]. Natural model systems, such as crystalline complex plasmas, provide us with a unique opportunity to study generic properties of wave modes sustained in classical strongly coupled ensembles, explore limits of small "nano"clusters, investigate peculiarities of the atomistic dynamics upon nonlinear mode coupling, etc. As compared to previously reported investigations of wave modes in 2D plasma crystals, the results presented in this Letter show a substantial improvement of the particle imaging technique. It allowed us for the first time to directly observe the optical phonon spectrum which has been predicted a long time ago. In the future, this development will enable much better discrimination of various subtle mechanisms affecting wave modes in 2D crystalline systems.

The authors thank U. Konopka, B. Klumov, and D. Samsonov for valuable discussions.

*lcouedel@mpe.mpg.de

[1] V. E. Fortov *et al.*, Phys. Rep. **421**, 1 (2005).
[2] V. E. Fortov *et al.*, Phys. Usp. **47**, 447 (2004).
[3] L. Couëdel *et al.*, Europhys. Lett. **84**, 35002 (2008).
[4] H. Thomas *et al.*, Phys. Rev. Lett. **73**, 652 (1994).
[5] S. I. Popel *et al.*, Phys. Rev. E **67**, 056402 (2003).
[6] S. Nunomura *et al.*, Phys. Rev. Lett. **89**, 035001 (2002).
[7] S. Nunomura, D. Samsonov, and J. Goree, Phys. Rev. Lett. **84**, 5141 (2000).
[8] S. Nunomura *et al.*, Phys. Rev. Lett. **94**, 045001 (2005).
[9] X. Wang, A. Bhattacharjee, and S. Hu, Phys. Rev. Lett. **86**, 2569 (2001).
[10] V. Nosenko *et al.*, Phys. Rev. Lett. **103**, 015001 (2009).
[11] V. Nosenko, S. Nunomura, and J. Goree, Phys. Rev. Lett. **88**, 215002 (2002).
[12] S. V. Vladimirov, V. V. Yaroshenko, and G. E. Morfill, Phys. Plasmas **13**, 030703 (2006).
[13] D. Samsonov, S. Zhdanov, and G. Morfill, Phys. Rev. E **71**, 026410 (2005).
[14] A. V. Ivlev and G. Morfill, Phys. Rev. E **63**, 016409 (2000).
[15] S. V. Vladimirov, P. V. Shevchenko, and N. F. Cramer, Phys. Rev. E **56**, R74 (1997).
[16] D. H. E. Dubin, Phys. Rev. Lett. **71**, 2753 (1993).
[17] K. Qiao and T. W. Hyde, Phys. Rev. E **68**, 046403 (2003).
[18] S. K. Zhdanov, A. V. Ivlev, and G. E. Morfill, Phys. Plasmas **16**, 083706 (2009).
[19] S. V. Vladimirov and M. Nambu, Phys. Rev. E **52**, R2172 (1995).
[20] A. V. Ivlev *et al.*, Phys. Rev. E **68**, 026405 (2003).
[21] V. Nosenko *et al.*, Phys. Plasmas **16**, 083708 (2009).
[22] S. S. Rogers *et al.*, Phys. Biol. **4**, 220 (2007).
[23] S. V. Vladimirov, N. F. Cramer, and P. V. Shevchenko, Phys. Rev. E **60**, 7369 (1999).
[24] S. V. Vladimirov and N. F. Cramer, Phys. Rev. E **62**, 2754 (2000).
[25] V. N. Popov and P. Lambin, Phys. Rev. B **73**, 085407 (2006).
[26] R. Saito *et al.*, Phys. Rev. Lett. **88**, 027401 (2001).
[27] Y. Kawashima and G. Katagiri, Phys. Rev. B **59**, 62 (1999).

Direct Observation of Mode-Coupling Instability in Two-Dimensional Plasma Crystals

L. Couëdel,* V. Nosenko, A. V. Ivlev, S. K. Zhdanov, H. M. Thomas, and G. E. Morfill
Max Planck Institute for Extraterrestrial Physics, 85741 Garching, Germany
(Received 8 February 2010; published 11 May 2010)

Dedicated experiments on melting of two-dimensional plasma crystals were carried out. The melting was always accompanied by spontaneous growth of the particle kinetic energy, suggesting a universal plasma-driven mechanism underlying the process. By measuring three principal dust-lattice wave modes simultaneously, it is unambiguously demonstrated that the melting occurs due to the resonance coupling between two of the dust-lattice modes. The variation of the wave modes with the experimental conditions, including the emergence of the resonant (hybrid) branch, reveals exceptionally good agreement with the theory of mode-coupling instability.

DOI: 10.1103/PhysRevLett.104.195001 PACS numbers: 52.27.Lw, 52.27.Gr

Strongly coupled complex (dusty) plasmas play an important role in the existing hierarchy of soft matter states [1]. Along with complex fluids and granular media as prominent examples of "regular" soft matter, complex plasmas represent natural model systems which enable remarkably broad interdisciplinary research. The characteristic length and time scales in such systems are dramatically stretched (e.g., in complex plasmas—to hundreds of microns and tens of milliseconds, respectively). Therefore, numerous generic processes occurring in classical fluids or solids can be studied in greatest detail, at the most fundamental "atomistic" level [1–3]. Especially important here are two-dimensional (2D) systems, where the complete information about all particles can be obtained at each moment of time. The current experimental capabilities make 2D complex plasmas ideal for comprehensive experimental studies of the atomistic dynamics [1,2,4,5].

The investigation of atomistic processes that trigger the melting and crystallization is of particular interest. It is well known that the mechanisms resulting in the destruction of the long-range crystalline order in 2D systems can be very different from those operating in 3D crystals: The classical Kosterlitz-Thouless-Halperin-Nelson-Young (KTHNY) theory of 2D melting [6] predicts two consecutive phase transitions (with an intermediate, so called hexatic phase in between). The alternative theory [7] relates 2D melting with the formation of dislocation chains ("grain boundaries") percolating the system. These are generic melting mechanisms which can operate in very different strongly coupled systems [8–12].

When studying generic classical phenomena occurring in regular liquids and solids, the relevance of a model system (be it colloidal suspensions, granular media, or complex plasmas) becomes crucial. Of course, careful analysis is required in the context of a given phenomenon (or, class of phenomena), but one can certainly identify essential common principles. In particular, the applicability of the Hamiltonian approach for the analysis of atomistic dynamics (for instance, to investigate kinetics of phase transitions) is one of these basic principles. This implies that non-Hamiltonian (nonconservative) behavior peculiar to model systems should play a minor role at the relevant time scales [13].

Non-Hamiltonian behavior of particle ensembles is often a manifestation of asymmetry, or nonreciprocity, in the interparticle interactions. Such asymmetry can be considered as a result of the system openness: In the presence of a strong flow of the ambient plasma, the screening cloud around each charged particle becomes highly asymmetric. These clouds, which are usually referred to as "plasma wakes" [14,15], play the role of an (external) "third body" in the interparticle interaction and hence make it nonreciprocal [16,17]. One should point out that such nonreciprocity is quite universal and can be very important for the hydrodynamic interactions of colloids [18] or droplets in conventional fluid flows [19].

The nonreciprocity of pair interaction in complex plasmas provides a very efficient mechanism of converting the energy of the flowing ions into the kinetic energy of microparticles [1,2,20]. In particular, dust-lattice (DL) wave modes [2,21,22] can contribute to that. The kinetic energy can grow due to resonant particle-wake interactions when different oscillation modes of interacting particles are properly synchronized: Ivlev and Morfill [23] suggested that the resonance between DL wave modes in a 2D plasma crystal can trigger the mode-coupling instability which, in turn, can cause the crystal melting. By comparing the melting experiments with the molecular dynamic simulations, this hypothesis has received strong confirmation [24]. However, the direct proof that the crystalline monolayers can indeed melt due to the mode-coupling instability (and even that the instability itself can be observed in experiments) was still outstanding. One should point out that the other known plasma-related scenarios of 2D crystal melting either require the presence of localized defects—single particles (or even sublayers) above or below the monolayer [25]—or are associated with the charge fluctuations and can only operate at very low pressures (well below 1 Pa) [26,27].

 © 2010 The American Physical Society

In this Letter we report on dedicated experimental investigation of 2D plasma crystal melting. We explored a fairly broad range of experimental parameters chosen well inside the crystalline regime predicted by the generic (KTHNY or grain-boundary) melting scenarios [12]. The melting was always accompanied by a spontaneous growth of the microparticle kinetic energy, which clearly suggests a universal plasma-driven mechanism underlying the process. By implementing simultaneous measurements of the dispersion relations for three principal DL wave modes, we unambiguously demonstrated that the melting occurred according to the mechanism predicted by Ivlev and Morfill [23]. The variation of the DL modes with the experimental conditions, including the emergence of the resonant (hybrid) mode, revealed exceptionally good agreement with the theoretical predictions of the mode-coupling instability.

The melting was systematically investigated in experiments performed with a (modified) Gaseous Electronics Conference (GEC) chamber, in a capacitively coupled rf glow discharge at 13.56 MHz (see Fig. 1). The argon pressure was between 0.4 Pa and 1 Pa and the forward rf power was between 5 W and 20 W (which corresponded to rf peak-to-peak voltage between 175 and 310 V). A horizontal monolayer was formed by levitating melamine-formaldehyde particles in the plasma sheath above the lower rf electrode. We used particles of two different sizes, 8.77 ± 0.14 μm and 9.19 ± 0.09 μm diameter. A high quality of the monolayer (with no detected particles above or below) was ensured by using a side-view camera. The diameter of the obtained crystalline structure was up to $\simeq$60 mm, depending on the number of injected particles (we explored a range from 1000 to 15 000).

One of two different discharge parameters was used as the control parameter for the melting: Either we gradually decreased the rf power at a constant gas pressure (which lowers the resonance frequency of the vertical confinement f_v, see Ref. [28]) or we decreased the pressure at a constant rf power (which naturally lowers neutral gas friction, but also makes the radial confinement stronger and hence the interparticle distance a smaller) [29]. In either case, the melting developed in the same way, as illustrated in Fig. 2 (see also supplemental movie S1 [30]): Upon decrease of the control parameter below a certain threshold the instability was triggered in the central part of the crystal (i.e., where the particle density was the highest) and then expanded outwards. The instability always set in simultaneously in the horizontal and vertical directions. At the initial stage it was accompanied by an exponential growth of the particle kinetic energy, eventually resulting in the total disruption of the crystal in the unstable zone. Upon

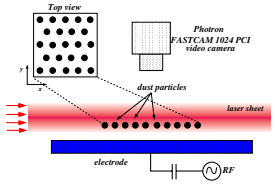

FIG. 1 (color online). Sketch of the experimental setup. Microparticles are confined above the rf electrode and are illuminated with a horizontal laser sheet having a Gaussian profile in the vertical direction (with a standard deviation $\sigma = 75$ μm). The monolayer is levitated well below the peak of the laser intensity, which results in strong intensity variations of the scattered light upon the vertical displacement of individual particles. The upward (downward) displacement corresponds to positive (negative) intensity variation. Microparticles are recorded from the top at a speed of 250 frames per second.

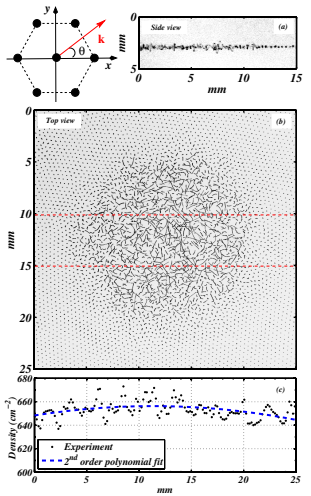

FIG. 2 (color online). Example of the instability onset in a 2D plasma crystal. The shown experiment is performed at a rf power of 20 W with particles of 8.77 μm diameter. The pressure of argon was ramped down in steps of 0.02 Pa (every $\simeq$300 s), and the instability was triggered at 0.90 Pa. The particle trajectories (superposition of consecutive video frames during 0.04 s) are plotted about 50 s after the critical pressure decrease: (a) side view; (b) top view. The profile of the particle density in the monolayer (c) was measured before the instability onset [averaged across the 5 mm stripe marked in (b) by two horizontal dashed lines]. In the upper left corner the elementary cell of the hexagonal lattice is depicted with the frame of reference chosen in this Letter; due to the lattice symmetry we consider the wave vector $\mathbf{k}$ at $0° \leq \theta \leq 30°$.

increase of the control parameter back above the threshold (usually, with a hysteresis), the system always recrystallized. It is noteworthy that if the rf power was sufficiently high and/or the particle density in the monolayer was low enough, the crystal remained stable at practically any pressure (e.g., at a rf power of 20 W, particle density of 160 cm^{-2}, and argon pressure down to $p \simeq 0.4$ Pa—the lowest pressure technically achievable with our setup).

The observed behavior fully agrees with the qualitative picture predicted by the theory of mode-coupling instability [23,24]: It can only set in when the out-of-plane and in-plane wave modes intersect, which is only possible when f_v is sufficiently low or/and the particle density in the monolayer ($\propto a^{-2}$) is high enough. The intersection should be accompanied by the simultaneous excitation of the vertical and horizontal oscillations. On the other hand, the instability should be suppressed by sufficiently high gas friction, i.e., by increasing the gas pressure.

The chief result of our Letter is the ultimate proof that the observed melting is indeed triggered by the mode-coupling instability. The unique fingerprint characterizing the instability [23,24] is the crossing of the longitudinal in-plane and transverse out-of-plane DL branches, which results in the (wake-induced) resonance coupling between them and the emergence of an unstable hybrid mode operating in a certain proximity of the crossing. This was directly proved by measuring the dispersion relations of all three principal DL modes. For this purpose, we used the technique by Nunomura *et al.* [31] of reconstructing the in-plane dispersion relations from thermal fluctuations of particle velocities in the horizontal plane. In addition, we implemented a novel method of particle imaging [22] which allowed us to measure simultaneously the vertical fluctuations and hence to retrieve also the out-of-plane mode. The essential advantage of this technique is that it does not involve any intermediate (model) assumptions about the interparticle interactions, and therefore yields "true" dispersion relations (or "fluctuation spectra") which can be obtained for arbitrary experimental conditions (that just allow the individual particle tracking).

We plotted the fluctuation spectra for the out-of-plane mode [Figs. 3(a) and 3(b)] separately from those for the in-plane modes [Figs. 3(c) and 3(d)], because the imaging method implemented for the simultaneous tracking of the vertical and horizontal fluctuations yields different background intensities [22]. As regards the theoretical curves, in each panel we plotted all principle modes that belong to the frequency range shown.

Figure 3 summarizes results of our analysis. In the stable regime (left column) the wave modes are well separated and the fluctuation intensity is evenly distributed over the branches. In contrast, the unstable regime (right column) is characterized by the apparent intersection between the out-of-plane and (one of the) in-plane branches. The intersection occurs in the vicinity of the first Brillouin zone boundary, resulting in the anomalous energy release (dark-red "hot spots").

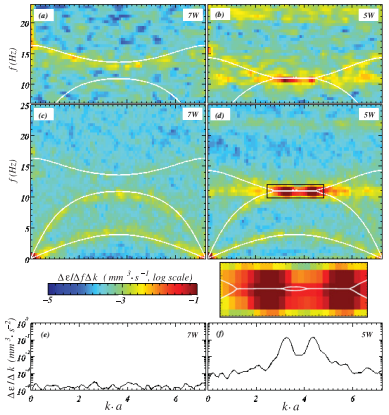

FIG. 3 (color). Evolution of the DL dispersion relations near the instability onset. The dispersion relations ("fluctuation spectra") were measured in the experiment performed at argon pressure of 0.76 Pa with particles of 9.19 μm diameter, at a rf power of 7 W (left column, stable regime) and 5 W (right column, the instability onset). The logarithmic color coding is used for the "fluctuation intensity" $\Delta\epsilon/\Delta k\Delta f$ (energy density, for unit mass, per unit wave number and frequency): Yellow ridges represent stable wave modes, and the dark-red "hot spots" are the unstable hybrid mode; (a) and (b) show the measured out-of-plane mode, and (c) and (d) depict the pair of in-plane modes. The solid lines in both panels are theoretical results [32] (see text for details). The wave number k is normalized by the inverse interparticle distance a^{-1} (determined from the first peak of the pair correlation function; the uncertainty of a was $\simeq 4\%$ due to density variations—see, e.g., Fig. 2(c)). The shown range of k corresponds to the first two Brillouin zones at $\theta = 30°$ (branches are symmetric with respect to the border between the two zones). Below the fluctuation spectra the magnified hybrid mode in the unstable regime (marked by a rectangular box) is shown. (e) and (f) illustrate the distribution of the "fluctuation energy" $\Delta\epsilon/\Delta k$ at fixed frequency: In the stable case the frequency ($\simeq$12.5 Hz) is chosen in the middle between the longitudinal in-plane branch and the out-of-plane branch (measured at the border between the Brillouin zones); for the instability onset the frequency ($\simeq$11 Hz) corresponds to the hybrid mode.

The qualitative effects and features of the mode-coupling instability mentioned above were originally predicted by the theory for a 1D string [23,24], and they all remain unaltered also in the 2D case. For rigorous quantitative comparison with the experiments we employed the theoretical results for 2D crystals obtained recently by Zhdanov *et al.* [32]. The theoretical branches are shown in Fig. 3 by solid lines: The upper curve represents the optical out-of-plane mode, and the middle and lower curves are for the pair of acoustic in-plane modes (longitudinal and transverse, respectively). These curves were calculated for the normalized dipole moment of the wake $\tilde{q}\,\tilde{\delta}$ (see Ref. [32]) equal to 0.1. We assumed the Yukawa interparticle interaction, with the parameters (viz., the particle charge and the effective screening length) deduced from the low-k part of in-plane fluctuation spectra (using the method of Ref. [31]).

Figure 3 shows that the theory yields excellent agreement with the experiment, both for the stable and unstable regimes. Especially important is that in the unstable regime (right column) the predicted unstable hybrid mode perfectly coincides with the locations of "hot spots" in the measured fluctuation spectra. Even subtle effects, such as the splitting of "hot spots" at the border between the Brillouin zones, are very well resolved [see distribution of the fluctuation energy in Figs. 3(e) and 3(f), and also the magnified hybrid mode] [33].

The fluctuation spectra shown in Fig. 3 were plotted for the wave vector $\mathbf{k}$ at $\theta = 30°$ (see Fig. 2), because the theory predicts this orientation to be the most unstable [see Fig. (4) of Ref. [32]]. In order to further highlight excellent comprehensive agreement between experiments and theory, we plotted additional spectra for different angles (see supplemental figure S2 [30]). They clearly show that at $\theta = 30°$ the fluctuation intensity of the "hot spots" is indeed the highest.

Note that rapid energy growth after the instability onset results in various nonlinear phenomena which can be easily identified in the right column of Fig. 3. The most prominent effects are the energy cascades from the "hot spots" along the k axis [bright red-yellow stripe in Figs. 3(b) and 3(d), see also the energy profile in Fig. 3(f)], and the generation of secondary harmonics at the double frequency of the hybrid mode [yellow bands at $\simeq$22 Hz in Figs. 3(b) and 3(d)].

In conclusion, one should point out that any instability operating in 2D plasma crystals and associated with collective processes [34] should be accompanied by anomalies in the fluctuation spectra. Therefore, the method of simultaneous measurement of all three principal DL modes promises to be very fruitful for further investigation of the melting scenarios. Especially important would be a systematic search for other possible resonant processes that can extend or alter the mechanism reported in this Letter.

*lcouedel@mpe.mpg.de

[1] G. E. Morfill and A. V. Ivlev, Rev. Mod. Phys. **81**, 1353 (2009).
[2] V. E. Fortov *et al.*, Phys. Usp. **47**, 447 (2004); Phys. Rep. **421**, 1 (2005); P. K. Shukla and B. Eliasson, Rev. Mod. Phys. **81**, 25 (2009).
[3] S. Vladimirov, K. Ostrikov, and A. Samarian, *Physics and Applications of Complex Plasmas* (Imperial Press, London, 2005).
[4] H. M. Thomas and G. E. Morfill, Nature (London) **379**, 806 (1996).
[5] C. H. Chiang and L. I, Phys. Rev. Lett. **77**, 647 (1996).
[6] J. M. Kosterlitz and D. J. Thouless, J. Phys. C **6**, 1181 (1973); B. I. Halperin and D. R. Nelson, Phys. Rev. Lett. **41**, 121 (1978); D. R. Nelson and B. I. Halperin, Phys. Rev. B **19**, 2457 (1979); A. P. Young, Phys. Rev. B **19**, 1855 (1979).
[7] S. T. Chui, Phys. Rev. Lett. **48**, 933 (1982); Phys. Rev. B **28**, 178 (1983).
[8] C. A. Murray and D. H. Van Winkle, Phys. Rev. Lett. **58**, 1200 (1987).
[9] K. Zahn and G. Maret, Phys. Rev. Lett. **85**, 3656 (2000).
[10] R. A. Quinn *et al.*, Phys. Rev. E **53**, R2049 (1996).
[11] T. E. Sheridan, Phys. Plasmas **15**, 103 702 (2008).
[12] V. Nosenko *et al.*, Phys. Rev. Lett. **103**, 015001 (2009).
[13] For 2D plasma crystals, the trivial origin of the non-Hamiltonian behavior associated with neutral gas friction can often be neglected, since the corresponding damping rate is typically 1-to-2 orders of magnitude smaller than the Einstein frequency [1].
[14] S. V. Vladimirov and M. Nambu, Phys. Rev. E **52**, R2172 (1995).
[15] S. V. Vladimirov and O. Ishihara, Phys. Plasmas **3**, 444 (1996).
[16] A. Melzer, V. A. Schweigert, and A. Piel, Phys. Rev. Lett. **83**, 3194 (1999).
[17] The *actio et reactio* principle is only violated for microparticles; for complete complex plasmas, with the ambient ions and electrons taken into account, this principle is of course satisfied.
[18] T. Araki and H. Tanaka, Europhys. Lett. **82**, 18 004 (2008).
[19] T. Beatus, T. Tlusty, and R. Bar-Ziv, Nature Phys. **2**, 743 (2006).
[20] A. Melzer *et al.*, Phys. Rev. E **54**, R46 (1996).
[21] S. V. Vladimirov, P. V. Shevchenko, and N. F. Cramer, Phys. Rev. E **56**, R74 (1997).
[22] L. Couëdel *et al.*, Phys. Rev. Lett. **103**, 215001 (2009).
[23] A. V. Ivlev and G. Morfill, Phys. Rev. E **63**, 016409 (2000).
[24] A. V. Ivlev *et al.*, Phys. Rev. E **68**, 026405 (2003).
[25] I. V. Schweigert *et al.*, Phys. Rev. E **62**, 1238 (2000).
[26] O. S. Vaulina *et al.*, Phys. Rev. E **60**, 5959 (1999).
[27] S. Nunomura *et al.*, Phys. Rev. Lett. **83**, 1970 (1999).
[28] V. Steinberg *et al.*, Phys. Rev. Lett. **86**, 4540 (2001).
[29] Changing either of these discharge parameters affects simultaneously all plasma characteristics (e.g., plasma density, particle charge, etc.). However, these parameters appear to be the most efficient in triggering the melting.
[30] See supplementary material at http://link.aps.org/supplemental/10.1103/PhysRevLett.104.195001 for movie S1 and figure S2.
[31] S. Nunomura *et al.*, Phys. Rev. Lett. **89**, 035001 (2002).
[32] S. K. Zhdanov, A. V. Ivlev, and G. E. Morfill, Phys. Plasmas **16**, 083 706 (2009).
[33] The structure of the hybrid mode is also shown in Fig. 3 of Ref. [32]; note the difference between the reference frames used in [32] and in our Letter.
[34] Here we leave aside the discussion of localized mechanisms of melting, e.g., due to defects.

Stability of two-dimensional complex plasma monolayers in asymmetric capacitively coupled radio-frequency discharges

L. Couëdel [1,2,*] and V. Nosenko [3]

[1] *Physics and Engineering Physics Department, University of Saskatchewan, Saskatoon, Saskatchewan S7N 5E2, Canada*
[2] *CNRS, Aix-Marseille Université, Laboratoire PIIM UMR 7345, 13397 Marseille cedex 20, France*
[3] *Institut für Materialphysik im Weltraum, Deutsches Zentrum für Luft- und Raumfahrt (DLR), D-82234 Weßling, Germany*

(Received 14 October 2021; accepted 11 January 2022; published 28 January 2022)

In this article, the stability of a complex plasma monolayer levitating in the sheath of the powered electrode of an asymmetric capacitively coupled radio-frequency argon discharge is studied. Compared to earlier studies, a better integration of the experimental results and theory is achieved by operating with actual experimental control parameters such as the gas pressure and the discharge power. It is shown that for a given microparticle monolayer at a fixed discharge power there exist two threshold pressures: (i) above a specific pressure p_{cryst}, the monolayer always crystallizes; (ii) below a specific pressure p_{MCI}, the crystalline monolayer undergoes the mode-coupling instability and the two-dimensional complex plasma crystal melts. In between p_{MCI} and p_{cryst}, the microparticle monolayer can be either in the fluid phase or the crystal phase: when increasing the pressure from below p_{MCI}, the monolayer remains in the fluid phase until it reaches p_{cryst} at which it recrystallizes; when decreasing the pressure from above p_{cryst}, the monolayer remains in the crystalline phase until it reaches p_{MCI} at which the mode-coupling instability is triggered and the crystal melts. A simple self-consistent sheath model is used to calculate the rf sheath profile, the microparticle charges, and the microparticle resonance frequency as a function of power and background argon pressure. Combined with calculation of the lattice modes the main trends of p_{MCI} as a function of power and background argon pressure are recovered. The threshold of the mode-coupling instability in the crystalline phase is dominated by the crossing of the longitudinal in-plane lattice mode and the out-of plane lattice mode induced by the change of the sheath profile. Ion wakes are shown to have a significant effect too.

DOI: 10.1103/PhysRevE.105.015210

I. INTRODUCTION

Two-dimensional (2D) complex plasma crystals are composed of negatively charged monosized spherical microparticles levitating in the sheath above a confining electrode [1]. Complex plasma crystals are generally studied in asymmetric capacitively coupled radio-frequency (cc-rf) argon discharges in which the injected monolayer of microparticles levitates in the sheath above the powered electrode and crystallizes under specific discharge conditions [2–9]. Since microparticles can easily be imaged thanks to laser light scattering and the use of fast cameras, microparticle trajectories can be recovered and one can obtain information about the crystal at the kinetic "particle" level. Thus, complex plasma crystals often serve as model systems to study generic phenomena such as wave propagation [5,10], shocks [11,12], and phase transitions [13–16].

However, due to the very nature of the complex plasma monolayer, complex plasma specific phenomena can occur. Because of the ion flow coming from the bulk plasma and directed toward the electrode, ion wakes are formed downstream of each microparticle [4,17–21]. The ion wakes exert attractive force on the neighboring particles making the microparticle-microparticle interactions nonreciprocal. Under specific conditions, these nonreciprocal interactions can trigger the mode-coupling instability (MCI) [9,22–26] in which energy from the flowing ions is transferred to the microparticles and can heat up the microparticle suspension. Indeed, in 2D complex plasma crystals, three wave modes can be sustained: longitudinal and transverse in-plane acoustic modes and, due to the finite strength of the vertical confinement, an out-of-plane optical mode (associated with vertical oscillations [7,22,24,27,28]). Due to wake attraction, when the longitudinal in-plane mode and the out-of-plane mode cross, an unstable hybrid mode is formed (the typical fingerprints being a hot spot in reciprocal space at the edge of the first Brillouin zone, angular dependence, and mixed polarization [24,25]), which can trigger MCI if the instability growth rate is larger than the damping rate due to friction with the neutral background [24]. MCI is observed in both crystalline [9,24,25] and fluid monolayers [26,29]. In the first case, MCI can result in rapid melting of the monolayer if its growth rate is high enough. In the latter case, MCI can prevent crystallization of the monolayer by pumping more kinetic energy into the microparticles than the energy dissipated through friction with the neutral gas background [29–31]. Since for given discharge parameters (rf power, neutral gas pressure, geometry) and fixed monolayer parameters (number density and size of the microparticles) the growth rate in a fluid monolayer is higher than in a crystalline monolayer [26], it allows external triggering of the MCI [32] and prevents recrystallization of a melted monolayer without strongly altering the discharge parameters [29,32].

It was shown experimentally that MCI is triggered at specific pressure and rf power thresholds [9,25]. MCI is very sensitive to the magnitude of the effective wake dipole moment since the shape of the dispersion relations critically depends on it [33]. MCI threshold and growth rate also strongly depend on the depth of the mode crossing [33], which is a function of the ion-wake parameters and vertical confinement frequency. Both the ion wake and the vertical confinement frequency depend on the parameters of the rf sheath in which the microparticles are levitating such as the strength of the confining sheath electric field and the local ion and electron densities. Therefore, in order to understand the dynamics of the microparticle monolayer, it is very important to be able to relate the discharge parameters (background argon pressure, rf power) to the sheath parameters (electric field profile, ion flux profile, ion and electron density profiles). Modeling the rf sheath in a cc-rf discharge is however not trivial and accurate calculation of the rf sheath profile has been a subject of active research for the past three decades; see for example Refs. [34–43].

In this article, the stability of 2D complex plasma monolayers levitating in the sheath above the powered electrode of a cc-rf discharge is experimentally studied. In Sec. II, the experimental setup is described. In Sec. III, the experimental characterization of the cc-rf discharge (electron density and powered electrode self-bias) as a function of the background argon pressure and the forward rf power is presented. In Sec. IV, a study of the stability (crystal or fluid) of specific microparticle monolayers as a function of rf power is performed. It allows us to measure the MCI pressure threshold and the crystallization pressure threshold over a wide range of rf powers. In Sec. V, a simple self-consistent sheath model is described and used to calculate the sheath profile and microparticle charge, and vertical resonance frequency as a function of discharge parameters. In Sec. VI, the results of Sec. V are used to calculate the lattice modes of 2D complex plasma crystal with and without ion wakes. The influence of the interparticle distance and wake parameters are investigated. The calculated results are compared to experimental results. In Sec. VII, the main results are summarized and future investigations are discussed.

II. EXPERIMENTAL SETUP

The experiments were performed in a modified gaseous electronic conference rf cell (GEC). It is an asymmetric cc-rf discharge at 13.56 MHz. A sketch of the setup is shown in Fig. 1. Experiments were performed with an argon pressure, p_{Ar}, between 0.5 and 2 Pa. The forward rf power, P_W, was set between 5 and 25 W. Langmuir probe studies using the same setup have shown that the electron temperature is $T_e \sim 2.5$ eV and that the electron density is $n_e \simeq 2 \times 10^9$ cm^{-3} at $p_{Ar} = 0.66$ Pa and $P_W = 20$ W [44]. A Miwitron Ka-band microwave interferometer MWI 2650 working at 26.5 GHz was used to measure the electron density, n_e, in pristine plasma

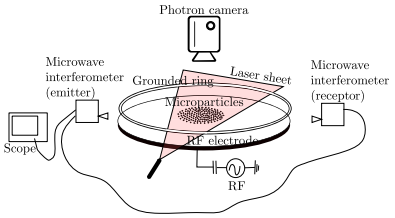

FIG. 1. Schematic of the experimental setup. Note that the microwave interferometer was used only for measurements in pristine plasmas (i.e., no microparticles).

condition (without injected microparticles) for different p_{Ar} and P_W. The interferometer had a resolution of $\sim 10^8$ cm^{-3}.

Melamine-formaldehyde (MF) spherical microparticles with a diameter of 9.19 ± 0.09 μm were injected in the plasma. They levitated in the sheath above the lower rf electrode where the electric force balanced their weight and formed a highly ordered horizontal monolayer. The microparticle monolayer was illuminated by a horizontal laser sheet and the microparticles were imaged through the top chamber window by using a 4 megapixel Photron FASTCAM Mini WX100 camera at a speed of 250 frames per second. Particle tracking allowed us to recover the particle horizontal coordinates, x and y, with subpixel resolution in each frame, and the velocities, v_x and v_y, were then calculated [8]. An additional side-view camera (Basler Ace ACA640-100GM) was used to check that no particles were levitating above or under the main monolayer. More details can be found in previous publications [9,44–46].

III. CHARACTERIZATION OF THE CC-RF DISCHARGE

Electron density measurements have been taken with the microwave interferometer for different pressure between 0.66 Pa and 6.0 Pa and for rf power between 1 W and 20 W. The results are are shown in Fig. 2. The density reported at $p_{Ar} = 0.66$ Pa and $P_W = 20$ W is $n_e \sim 2.5 \times 10^9$ cm^{-3} which is in agreement with previous Langmuir probe measurements [44]. As expected, n_e increases with forward rf power and pressure [41,47]. The measured values of bulk plasma density are used as input parameters for sheath profile calculations in Sec. V C.

The absolute value of self-bias voltage on the powered electrode, $|V_{dc}|$, has also been measured for a few relevant experimental discharge conditions. The results are shown in Fig. 3 (dots). As can be seen, $|V_{dc}|$ is not very sensitive to pressure. It has approximately a square-root dependence on the forward rf power.

It is known that the self-bias voltage is related to the ratio of the areas of the powered surface to the grounded surface interacting with the plasma A_{rf}/A_g [47,48]. The ratio of the self-bias voltage V_{dc} to the amplitude of the rf voltage

*lenaic.couedel@usask.ca; lenaic.couedel@univ-amu.fr

 ©2022 American Physical Society

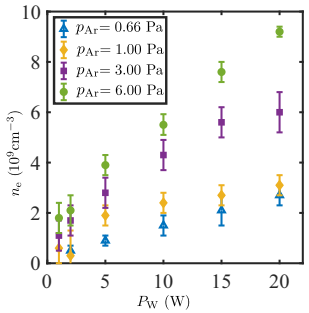

FIG. 2. Electron density, n_e, as a function of rf power, P_W, for different pressures.

$V_0 = V_{pp}/2$ is in first approximation given by [49,50]

$$\frac{V_{dc}}{V_0} = \sin\left[\frac{\pi}{2}\left(\frac{A_g - A_{rf}}{A_g + A_{rf}}\right)\right], \quad (1)$$

where V_{pp} is the peak-to-peak rf voltage. It was experimentally measured that in a modified GEC cell similar to the one that was used for the current set of experiments, $A_{rf}/A_g \sim 0.25$ [50]. Using the fit of V_{dc} as a function of P_W and Eq. (1), V_{pp} was calculated and the result is shown by the dotted red line in Fig. 3. The results match reasonably well with two measured values of V_{pp} at 15 W and 20 W for $p = 0.66$ Pa (blue squares). The calculated values of V_{dc} and V_{pp} are used as input parameters to calculate sheath profiles in Sec. V C.

IV. STABILITY OF COMPLEX PLASMA MONOLAYERS

A large monolayer suspension was created by injecting monosized melamine formaldehyde microparticles (diameter 9.19 ± 0.09 μm). The monolayer was kept for the 2 sets

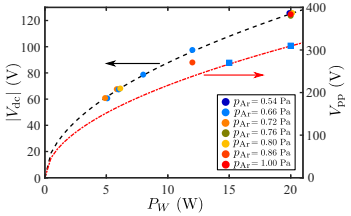

FIG. 3. (○) Self-bias voltage $|V_{dc}|$ as a function of rf power, P_W, for different working pressures (color coded). (□) Peak-to-peak rf voltage, V_{pp}, as a function of rf power, P_W, at $p_{Ar} = 0.66$ Pa. The dashed black line is the fit $|V_{dc}| = 27 \times P_W^{0.51}$. The dotted red line is V_{pp} calculated from Eq. (1).

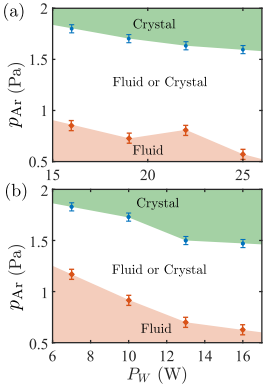

FIG. 4. Crystallization pressure, p_{cryst} (blue dots), and MCI threshold pressure, p_{MCI} (red diamonds), for different rf powers, P_W: (a) experiment I, (b) experiment II. Above the crystallization pressure the monolayer is always in the crystalline state (green areas). Below the MCI threshold pressure, the monolayer is always in the fluid state. In between, the monolayer remains in the crystalline phase when decreasing the pressure from above the crystallization threshold and remains fluid when increasing the pressure from below the MCI threshold.

of experiments (referred to as experiment I and experiment II) separated by ∼1 hour. According to Ref. [51], the MF microparticles are etched at a rate of ∼1.25 nm/min in an argon discharge meaning that the microparticle diameter for the second set of experiments was ∼9 μm.

The crystallization and melting pressures of the monolayer were explored for different rf powers. At a given rf power, starting from a fluid monolayer, the argon pressure was gradually increased until the monolayer was fully crystallized (pressure step of ∼0.6 mTorr) and the crystallization pressure was recorded. Note that during the pressure increase period, the monolayer remained in the *fluid phase* [52]. The dynamics of the microparticles at the crystallization threshold was not investigated in details and the crystallization event was identified with the naked eye (see Appendix A). Then the pressure was very slowly decreased until MCI was triggered in the crystal (pressure step of ∼0.6 mTorr when close to the crystallization threshold gradually reduced to ∼0.06 mTorr (at best) when getting closer to MCI threshold) resulting in the rapid melting of the monolayer in a pattern similar to the results reported in Refs. [29–32,53,54]. Note that during the pressure decrease period, the monolayer remained in the *crystalline phase* until MCI was triggered. The rf power was then decreased and the procedure was repeated.

The results for the two sets of experiments are shown in Fig. 4. As can be seen, in both cases, the higher the power the lower the crystallization and melting pressures. Moreover,

the gap $\Delta p = p_{cryst} - p_{MCI}$, in which the monolayer remains in the crystalline phase when decreasing the pressure from above the crystallization threshold and remains fluid when increasing the pressure from below the MCI melting threshold, increases when increasing the rf power.

During the decreasing pressure phase, the crystalline monolayer was imaged [55] with the high-speed Photron camera in order to track the particle trajectories, measure the crystalline monolayer kinetic temperature T_{cryst} by fitting the microparticle velocity distribution function by a Maxwellian distribution function, and recover the longitudinal and transverse current fluctuation spectra following the procedure described in Refs. [53,56,57]. To extract the longitudinal and transverse dispersion relations $\omega_{L,T}(k) = 2\pi f_{L,T}(k)$ where $f_{L,T}(k)$ is the frequency of the lattice modes with wave number k, the current fluctuation spectra $J_{L,T}(k, f)$ were fitted to a double-Lorentzian form [58,59]:

$$J_{L,T}(k,\omega) \propto \frac{A(k)}{(\omega - \omega_{L,T})^2 + A(k)} + \frac{A(k)}{(\omega + \omega_{L,T})^2 + A(k)}, \quad (2)$$

with $A(k)$ a constant proportional to the damping rate of the mode. The indices L and T are for longitudinal and transverse, respectively. In Fig. 5(a), the fit of the current spectrum for a normalized wave number $k\Delta = 1.3$, where Δ is the interparticle distance, is shown, and the entire experimental longitudinal dispersion relation is shown in Fig. 5(b) for a wave propagating at an angle of 0° with respect to the camera field of view. The interparticle distance Δ was obtained from the position of the first peak of the pair correlation function and error bars are the widths of the peaks at half maximum. Due to high noise level for $k\Delta < 0.25$, the frequencies of the mode at these long wavelengths were not measured. Then, longitudinal and transverse dispersion relations were fitted for $k\Delta < 1.5$ by the polynomial of the form $\omega_{L,T} = C_{L,T}|k| + b_{L,T}|k|^3$, where $C_{L,T}$ are the longitudinal and transverse sound speeds and $b_{L,T}$ are constants taking into account the nonlinearity of the dispersion relation for $|k\Delta| \gtrsim 1$.

By numerically rotating the frame with respect to the original camera field of view and repeating the procedure, wave propagation could be studied at different angles. $C_{L,T}$ were obtained every 5° [see Fig. 5(c)] and the average values of the sound speeds were calculated for different crystal conditions. Note that the camera field of view contained many crystallites with different orientations. This is not an issue since sound speeds are quasi-independent of the direction of propagation in the crystal [60,61]. Assuming screened Coulomb interactions and following the method of Ref. [6], these values were then used to extract the microparticle charge Z_d, the Debye (screening) length λ_d, and the coupling parameter $\kappa = \Delta/\lambda_d$. The results are summarized in Table I. As can be seen, decreasing the pressure at constant rf power resulted in an increase of both sound speeds and a slight increase of the interparticle distance. The microparticle kinetic temperature showed no clear trends and remained quite low while the monolayer was in the crystal phase ($T_{cryst} \lesssim 0.2$ eV). Assuming pure screened Coulomb interactions, it corresponded to an increase of the microparticle charges. Accordingly, the maximum frequency of the longitudinal dispersion relation (not shown here) increased when decreasing pressure making the out-of-plane mode and the in-plane mode closer to each other as the MCI pressure threshold, p_{MCI}, was approached. No trend in the evolution of the coupling parameter $\kappa = \Delta/\lambda_D \simeq$ 1.0–1.8 could be extracted due to the large error on the sound

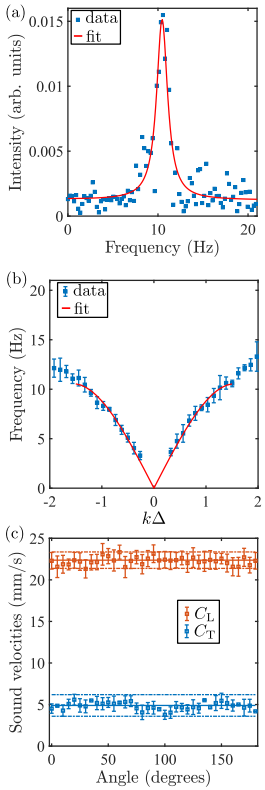

FIG. 5. (a) Fit of the longitudinal current fluctuation spectrum for $k\Delta = 1.3$. Only the "positive" frequency side of the Fourier transform is shown. (b) Fit of the reconstructed longitudinal dispersion relation for wave propagating at an angle of 0° with respect to the camera field of view. (c) Longitudinal sound speed, C_L, and transverse sound speed, C_T, measured for different wave propagation angles with respect to the camera field of view. All plots correspond to measurements at $P_W = 16$ W and $p = 1.80$ Pa.

TABLE I. Two-dimensional crystal parameters for different discharge conditions between the crystallization pressure, $p_{\rm cryst}$, and the MCI threshold pressure, $p_{\rm MCI}$. The microparticle charge Z_d and the Debye (screening) length λ_d were calculated assuming screened Coulomb interactions [6]. The crystalline monolayer kinetic temperature $T_{\rm cryst}$ was measured by fitting the microparticle velocity distribution function by a Maxwellian distribution function.

$P_{\rm W}$ (W)	$p_{\rm cryst}$ (Pa)	$p_{\rm MCI}$ (Pa)	$p_{\rm Ar}$ (Pa)	Δ (mm)	$C_{\rm L}$ (mm/s)	$C_{\rm T}$ (mm/s)	Z_d (e)	$T_{\rm cryst}$ (eV)	$\lambda_{\rm D}$ (μm)
					Experiment I				
25	1.595 ± 0.05	0.575 ± 0.033	1.583	0.361 ± 0.020	21.53 ± 1.66	4.94 ± 3.24	10500 ± 2900	0.061 ± 0.003	330 ± 180
	$\Delta p = 1.020 \pm 0.083$		1.167	0.372 ± 0.014	22.23 ± 1.79	4.82 ± 2.88	10100 ± 2400	0.095 ± 0.002	370 ± 170
			0.750	0.391 ± 0.027	25.60 ± 2.16	6.51 ± 2.91	14600 ± 3000	0.104 ± 0.003	270 ± 90
22	1.633 ± 0.05	0.808 ± 0.033	1.633	0.352 ± 0.021	22.44 ± 2.35	5.31 ± 3.25	11100 ± 3000	0.080 ± 0.002	300 ± 150
	$\Delta p = 0.825 \pm 0.083$		1.167	0.362 ± 0.013	23.04 ± 2.53	6.23 ± 3.90	14300 ± 5100	0.124 ± 0.003	240 ± 120
			0.833	0.376 ± 0.015	26.50 ± 2.58	6.29 ± 5.37	14100 ± 6000	0.128 ± 0.006	470 ± 390
19	1.703 ± 0.05	0.725 ± 0.017	1.703	0.348 ± 0.015	21.41 ± 1.47	4.89 ± 2.44	10000 ± 2100	0.096 ± 0.001	300 ± 110
	$\Delta p = 0.978 \pm 0.067$		1.167	0.363 ± 0.016	25.42 ± 1.05	5.63 ± 2.76	11700 ± 2300	0.072 ± 0.001	330 ± 120
			1.000	0.371 ± 0.014	26.00 ± 1.25	5.89 ± 2.01	12300 ± 1700	0.112 ± 0.002	310 ± 70
			0.833	0.378 ± 0.024	27.61 ± 5.31	5.77 ± 3.43	12100 ± 2800	0.132 ± 0.015	400 ± 190
16	1.800 ± 0.05	0.850 ± 0.017	1.800	0.349 ± 0.013	22.37 ± 0.99	4.89 ± 1.30	9800 ± 1000	0.080 ± 0.002	310 ± 50
	$\Delta p = 0.950 \pm 0.067$		1.250	0.363 ± 0.017	25.06 ± 3.95	5.24 ± 2.13	10700 ± 1700	0.185 ± 0.014	360 ± 110
			1.000	0.369 ± 0.015	26.33 ± 0.95	6.31 ± 2.37	13400 ± 2100	0.101 ± 0.004	280 ± 70
					Experiment II				
16	1.470 ± 0.05	0.625 ± 0.017	1.47	0.374 ± 0.013	21.71 ± 1.31	5.16 ± 1.26	10900 ± 1100	0.112 ± 0.004	280 ± 50
	$\Delta p = 0.845 \pm 0.067$		1.167	0.382 ± 0.015	22.88 ± 1.06	5.54 ± 2.77	12100 ± 2100	0.129 ± 0.005	300 ± 110
			0.750	0.392 ± 0.013	25.93 ± 2.18	5.97 ± 3.52	13100 ± 3200	0.128 ± 0.003	350 ± 160
13	1.500 ± 0.05	0.700 ± 0.017	1.500	0.385 ± 0.015	21.56 ± 1.80	4.88 ± 2.18	10400 ± 1900	0.113 ± 0.003	340 ± 110
	$\Delta p = 0.800 \pm 0.067$		1.167	0.387 ± 0.015	23.98 ± 1.10	4.97 ± 1.53	10400 ± 1200	0.079 ± 0.003	380 ± 80
			0.750	0.393 ± 0.011	28.18 ± 1.49	6.49 ± 3.96	14200 ± 3700	0.105 ± 0.004	350 ± 170
10	1.730 ± 0.05	0.917 ± 0.008	1.730	0.369 ± 0.015	23.58 ± 4.32	5.12 ± 2.30	10600 ± 1900	0.174 ± 0.003	350 ± 120
	$\Delta p = 0.813 \pm 0.058$		1.167	0.381 ± 0.017	26.46 ± 1.23	5.44 ± 2.1	11300 ± 1700	0.095 ± 0.003	390 ± 100
			0.967	0.373 ± 0.011	27.69 ± 2.62	6.16 ± 4.23	13100 ± 3700	0.161 ± 0.004	370 ± 220
7	1.830 ± 0.083	1.167 ± 0.008	1.830	0.377 ± 0.012	25.76 ± 1.77	5.46 ± 2.45	11400 ± 2000	0.129 ± 0.009	370 ± 110
	$\Delta p = 0.663 \pm 0.091$		1.250	0.383 ± 0.010	28.17 ± 1.40	5.60 ± 1.51	11600 ± 1200	0.136 ± 0.015	410 ± 70

speeds, especially the transverse sound speed. Note that the coupling parameter $\Gamma = (Z_d^2 e)/(T_{\rm cryst} 4\pi\epsilon_0 \Delta) \sim 2000$, where e is the elementary charge and ϵ_0 the vacuum permittivity, remains far from the coupling parameters at the melting point, $\Gamma_m \sim 200$ at $\kappa \sim 1.2$ [62].

V. SHEATH PROFILE ABOVE THE POWERED ELECTRODE OF A CAPACITIVELY COUPLED RADIO-FREQUENCY DISCHARGE

Any modification of the discharge parameters ($p_{\rm Ar}$ and/or $P_{\rm W}$) has an impact on the plasma and therefore on the sheath properties. It is then evident that since the microparticle monolayer levitates in the rf sheath above the powered electrode, any changes of the discharge parameters also affect the monolayer properties. In this section, a simple model allowing calculation of the sheath profile above the powered electrode in an asymmetric cc-rf discharge as a function of the discharge parameters is described. The model is then validated against available experimental data and then used to obtain the dependence of sheath parameters (sheath length, ion and electron densities, electric field) as a function of the discharge parameters ($p_{\rm Ar}$ and $P_{\rm W}$).

A. Description of the model

In a cc-rf discharge, the rf frequency is generally much higher than the ion plasma frequency and much lower than the electron plasma frequency, i.e., $\omega_{\rm pi} \ll \omega_{\rm rf} \ll \omega_{\rm pe}$, where $\omega_{\rm pi}$, $\omega_{\rm pe}$, $\omega_{\rm rf}$ are the ion, electron, and rf angular frequency, respectively. In that respect, the ions respond to the time-averaged sheath electric field. Moreover, in most of 2D complex plasma crystal experiments, the working pressure is around 1 Pa. In this situation, ion collisions cannot be neglected [35]. The main assumptions of the following model are based on earlier work by Lieberman [35]:

(i) collisional ion motion with a constant ion mean free path λ_i in the sheath,

(ii) cold ions (ion temperature $T_i \simeq 0$),

(iii) inertia-less electrons that respond instantaneously to the electric field,

(iv) no secondary electrons emitted from the electrode,

(v) no ionization in the sheath.

In most experiments, asymmetric cc-rf discharges with grounded area much larger than the powered electrode area are used. Moreover, since the matching circuit very often contains a blocking capacitor, no direct current can flow in the external circuit. Since the area of each electrode is different, the amount of collected ions and electrons during each

rf cycle is also different and results in the appearance of a self-bias voltage on the powered electrode [37,48]. Ideally, it would be necessary to consider both sheaths in front of both electrodes simultaneously [37]. However, in order to simplify the problem, the following assumptions are made:

(i) The voltage on the rf electrode is of the form

$$V_{\rm rf}(t) = -V_0 \cos(\omega_{\rm rf} t) - |V_{\rm dc}|. \tag{3}$$

The input values of V_0 and $V_{\rm dc}$ were discussed in Sec. III.

(ii) At all time instants, the plasma must remain quasineutral and therefore the current going through the powered electrode sheath and the anode sheath must be equal in intensity and of opposite signs. Following the method described by Song *et al.* [49], the time dependence of the plasma potential with respect to the grounded wall is approximated by

$$V_p(t) = T_e \ln\left\{\left[1 + \frac{A_{\rm rf}}{A_g} \exp\left(\frac{V_{\rm rf}(t)}{T_e}\right)\right] \times \left(1 + \frac{A_{\rm rf}}{A_g}\right)^{-1}\right\} + \frac{T_e}{2} \ln\left(\frac{M}{2.3 m_e}\right), \tag{4}$$

where T_e is the electron temperature in eV, m_e is the electron mass, and M is the ion mass.

In the following, the plasma potential is taken as the reference potential ($V_p = 0$). At any given instant of time, the potential of the rf electrode V_c with respect to the plasma is

$$V_c(t) = V_{\rm rf}(t) - V_p(t). \tag{5}$$

The time-dependant potential profile $V(z,t)$ in the sheath follows the Poisson equation:

$$\nabla^2 V(z,t) = -\frac{e}{\epsilon_0}[n_{\rm i}(z) - n_e(z,t)], \tag{6}$$

where $n_{\rm i(e)}(z)$ is the ion (electron) density. The boundary conditions are $V(0,t) = 0$ and $V(\ell_s, t) = V_c(t)$, where ℓ_s is the length of the ion sheath.

Since $\omega_{\rm pi} \ll \omega_{\rm rf}$, ions react only to the time-averaged electric field $\bar{E} = -d\bar{V}/dz$ where $\bar{V}$ is the time-averaged electric potential across the sheath of the powered electrode. Therefore, in the sheath, the ion particle conservation and momentum conservation equations are [36,63]

$$n_0 v_s = n_i v_i, \tag{7}$$

$$M v_i \frac{dv_i}{dz} + e\frac{d\bar{V}}{dz} + \frac{\pi M v_i^2}{2\lambda_i} = 0, \tag{8}$$

where n_0 is the plasma density at the plasma sheath boundary, v_i is the ion velocity at a given position z in the sheath, and v_s is the velocity of the ions at the ion sheath boundary ($z = 0$). When taking into account collisions, v_s is the modified Bohm velocity [36,63]:

$$v_s = \left(\frac{eT_e}{M}\right)^{1/2} \left(1 + \frac{\pi\lambda_{\rm D_s}}{2\lambda_i}\right)^{-1/2}, \tag{9}$$

where $\lambda_{\rm D_s} = (\epsilon_0 T_e / n_0 e)^{1/2}$ is the electron Debye length.

In order to calculate the sheath profile, one needs to make a few approximations. First of all, in order to solve Eq. (6), one needs to know the exact position of the time-varying sheath boundary. Indeed, depending on the voltage across the sheath,

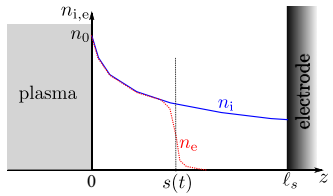

FIG. 6. Schematic of a capacitive rf sheath at a time $0 < t < \pi/\omega_{\rm rf}$. The dotted vertical line shows the position of the electron sheath boundary $s(t)$. For $z < s(t)$, $n_e \sim n_i$ and for $z > s(t)$, $n_e \sim 0$.

the electron sheath boundary $s(t)$ will change and oscillate between the position of the ion sheath boundary to a minimum distance to the electrode (see Fig. 6). Generally, in cc-rf discharges, the amplitude of the rf voltage is much higher than the electron temperature, i.e., $V_0 \gg T_e$, and the electron Debye length is much smaller than the sheath width ℓ_s. It is thus clear that on the plasma side [$z < s(t)$], the quasineutrality holds ($n_e \sim n_i$), while on the sheath side [$z > s(t)$], the electron density falls very rapidly ($n_e \sim 0$). Many studies dealing with the structure of cc-rf sheath therefore use this approximation known as the step model which has been extensively used in different models of the cc-rf sheath [34–40,42]. In many of these models, the solution of the rf sheath relies on calculating the rf current through the sheaths (powered and grounded) and assuming a zero net current [34–37,40]. It allows one to calculate the position of the electron sheath at all times and from there the other quantities such as the average potential drop and average electric field in the sheath can be derived. Calculations of these kind have been performed for both symmetric [34–36] and asymmetric discharges [37,40]. It was nevertheless shown that, in the case of symmetric cc-rf discharges, these models were able to accurately describe the current-voltage characteristics but showed discrepancies in the potential and electric field profiles with respect to the exact solution [38]. More recent models allow for very accurate descriptions of the cc-rf sheath but require input such as the maximum sheath extension, the ion mean free path, and the electron Debye length [42]. The ion mean free path and the electron Debye length can be easily obtained from discharge pressure, interferometry measurements, and literature data. However, the maximum sheath extension is not a parameter which is very often measured. Moreover, the current and voltage wave forms on the powered electrode are usually not monitored. However, in our experiments, the self-bias voltage and the electron density were measured as a function of the forward rf power and argon pressure over a wide range of parameters which can be used to recover the rf voltage amplitude V_0 using Eq. (1). The electron temperature can be estimated using the uniform density discharge model [47]:

$$\frac{K_{iz}(T_e)}{u_{\rm B}(T_e)} = \frac{1}{n_g d_{\rm eff}}, \tag{10}$$

where $K_{iz}(T_e) = 2.34 \times 10^{-14} \times T_e^{0.59} \times \exp(-17.44/T_e)$ is the ionization rate [47], $u_{\rm B}(T_e) = \sqrt{eT_e/M}$ is the Bohm

velocity, n_g is the neutral gas number density, and $d_{\text{eff}} = 0.5 \times Rl/(Rh_l + lh_r)$ is the effective plasma size for particle loss with l the height of the discharge chamber, R its radius, $h_r = 0.80(4 + R/\lambda_{in})^{-1/2}$ and $h_l = 0.86[3 + l/(2\lambda_{in})]^{-1/2}$ [47], and λ_{in} the ion mean free path in the plasma bulk.

The sheath profile can then be calculated using the following approximation for the time-dependent Poisson equation:

$$\nabla^2 V(z,t) \simeq -\frac{en_i(z)}{\epsilon_0}\left(1 - \exp\frac{V(z,t)}{T_e}\right). \tag{11}$$

As can be seen, this approximation lies between the ion matrix sheath approximation [$n_i(z) = n_0$] and the step model. It however allows us to solve the Poisson equation at anytime knowing the voltage drop in the sheath. The mean electric field and ion density profiles are then obtained in a recursive approach. Starting from the collision-less dc sheath profile with a potential drop equal to the maximum of $V_c(t)$, a maximum sheath length and an initial ion density profile are calculated [47,64]:

$$\ell_s = \frac{\sqrt{2}}{3}\lambda_{D_e}\left(\frac{2\max[|V_c(t)|]}{T_e}\right)^{3/4}, \tag{12}$$

$$\bar{V}(z) = -\max[|V_c(t)|]\left(\frac{z}{\ell_s}\right)^{4/3}, \tag{13}$$

$$n_i(z) = n_0\left(1 - \frac{2\bar{V}(z)}{T_e}\right)^{-1/2}. \tag{14}$$

Then the time-dependant potential profile over one rf period is calculated by solving Eq. (11) with MATLAB and using the following boundary conditions:

$$V(0,t) = 0, \tag{15}$$

$$V(\ell_s,t) = V_c(t), \tag{16}$$

and a new time-averaged potential and electric field are calculated. If the time-averaged electric field on the plasma side ($z = 0$) is lower than $E_{\min} = (\pi/2)(T_e/\lambda_i)$, a value necessary to ensure monotonically decreasing ion density and increasing ion velocity in the sheath region, then the sheath boundary on the plasma side is moved toward the wall until the average electric field reaches $E_{\min}$ and a new sheath length ℓ_s is obtained. Using Eqs. (7) and (8) with the boundary conditions

$$n_i(0) = n_0, \tag{17}$$

$$v_i(0) = v_s, \tag{18}$$

a new ion density profile is obtained and the time-dependant potential profile is calculated again. The procedure is repeated until it converges, which typically occurs in 10 to 15 iterations.

B. Comparison to experimental data, validation of the model

Schulze *et al.* have measured experimentally the time-dependant electric field of a cc-rf capacitive discharge in krypton at different pressures [65]. Czarnetzki used this set of measurements to validate with success his advanced model of the cc-rf sheath [42].

Two sets of discharge parameters were used to validate our model:

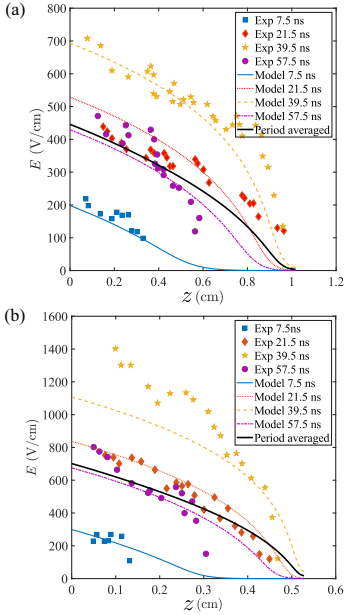

FIG. 7. Experimental time-resolved electric field in krypton cc-rf discharge compared to the calculated electric field using the model described in this article. The experimental data are extracted from Ref. [65]. (a) $p_{\text{Kr}} = 1$ Pa and $P_{\text{rf}} = 8$ W, (b) $p_{\text{Kr}} = 10$ Pa and $P_{\text{rf}} = 8$ W. The time instants are given in the inset and in both plots the plain black line corresponds to the time-averaged electric field.

(i) $p_{\text{Kr}} = 1$ Pa and $P_{\text{rf}} = 8$ W, corresponding to $V_0 \simeq 250$ V and $V_{\text{dc}} \simeq -250$ V (see Fig. 12 of Ref. [65]). As in Ref. [42], the electron temperature is fixed to $T_e = 2.6$ eV and the plasma density at the sheath edge to $n_0 = 2.0 \times 10^{15}$ m^{-3}. The grounded surface is assumed to be 100 times larger than the powered surface. The charge exchange cross section is $\sigma_{CX} = 40 \times 10^{-20}$ m^2 [66].

(ii) $p_{\text{Kr}} = 10$ Pa and $P_{\text{rf}} = 8$ W, corresponding to $V_0 \simeq 225$ V and $V_{\text{dc}} \simeq -225$ V (see Fig. 5 of Ref. [65]). As in Ref. [42], the electron temperature is fixed to $T_e = 1.1$ eV and the plasma density at the sheath edge to $n_0 = 7.3 \times 10^{15}$ m^{-3}. The grounded surface is assumed to be 100 times larger than the powered surface. The charge exchange cross section is $\sigma_{CX} = 40 \times 10^{-20}$ m^2 [66].

In Fig. 7, the model results are compared to the experimental data of Schulze *et al.* [65]. As can be seen, the agreement is not perfect and the model tends to slightly underestimate the electric field, especially at large pressure. However, one

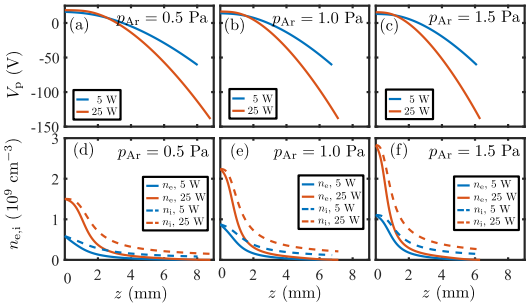

FIG. 8. (a)–(c) Potential and (d)–(f) density profiles for different pressures and powers. Note that potentials are plotted with respect to ground [i.e., $V_p(0) \neq 0$].

should note that the length of the sheath is recovered within a few percent and that the electric field values are in respectable agreement with the measured ones.

We can therefore conclude that our simple model is able to catch the main features of the collisional cc-rf sheath and can reasonably estimate the main sheath parameters as a function of position for an adequate range of discharge parameters.

C. Calculated sheath profile

The model was then used for conditions relevant to our experimental conditions. The argon pressure was varied between 0.5 Pa and 2 Pa by steps of 0.05 Pa and the rf power was varied between 5 W and 25 W by steps of 1 W. In Fig. 8 the sheath potential [Figs. 8(a)–8(c)] and the electron and ion densities [Figs. 8(d)–8(f)] are shown as a function of position for different pressures and rf powers.

As can be seen in the top row of Fig. 8, increasing pressure at constant rf power results in shorter sheath length for a similar potential drop (the sheath length is ∼8–9 mm at $p = 0.5$ Pa and drops down to ∼6–6.5 mm at $p = 1.5$ Pa). Therefore, the vertical electric field is weaker at lower pressures. One can therefore expect a weaker vertical confinement for microparticles levitating in the rf sheath at low pressure for a given rf power. Increasing the rf power at constant pressure results in a slight increase of the sheath length but larger plasma potential drops due to increasing self-bias voltage (the potential drop is ∼50 V at $P_{\text{W}} = 5$ W and ∼140 V at $P_{\text{W}} = 25$ W). Therefore, a stronger vertical electric field and a stiffer vertical confinement for microparticles levitating in the rf sheath at high rf power are expected.

Both P_{W} and p_{Ar} have an impact on plasma density. We know that at a given pressure, the plasma density is increasing almost linearly with rf power (see Fig. 2). Since the sheath length is weakly dependant on rf power (see previous paragraph), the gradients of ion and electron densities in the sheath increase with rf power as can be seen in the bottom row of Fig. 8. At high pressure, the plasma density is higher (due to collisions) and the sheath length is short, resulting in steep density gradients.

Using the calculated sheath profiles, the dependence of dust particle charge number, Z_d, levitation height, z_{lev}, and vertical resonance frequency, f_v, on discharge parameters is explored in the next section.

VI. MICROPARTICLE PROPERTIES AND MODE-COUPLING INSTABILITY

In this section, the influence of discharge parameters on Z_d, z_{lev}, and f_v is investigated. Then, the threshold of MCI in 2D complex plasma crystal as a function of discharge parameters is studied.

A. Dust particle charge, levitation height, and vertical resonance frequency

With the calculated sheath profile as a function of rf power and pressure, the equilibrium dust particle charge and levitation height can be calculated. At any point in the sheath, the ion and electron densities are known allowing the calculation of ion and electron currents, I_i and I_e, respectively, onto the microparticle surface in a collisional plasma [67,68]:

$$I_e = (-e)\sqrt{8\pi}r_d^2 n_e v_{T_e}\exp(-\tilde{\varphi}), \tag{19}$$

$$I_i = (e)\sqrt{8\pi}r_d^2 n_e v_{T_i}\left(1+\tilde{\varphi}\right)\left[1 + \frac{\tilde{\varphi}\left(\frac{T_e}{T_i}\frac{r_d}{\lambda_i}\right)}{0.07 + 2\left(\frac{r_d}{\lambda}\right) + 2.5\left(\frac{r_d}{\lambda_i}\right) + \left[0.27\left(\frac{r_d}{\lambda}\right)^{1.5} + 0.8\left(\frac{r_d^2}{\lambda_i\lambda}\right)\right]\frac{T_e}{T_i}\tilde{\varphi} + \frac{0.4\left(\frac{r_d}{\lambda_i}\right)^2\left(\frac{T_e}{T_i}\right)\tilde{\varphi}}{1-0.4\left(\frac{r_d}{\lambda_i}\right)^2}}\right], \tag{20}$$

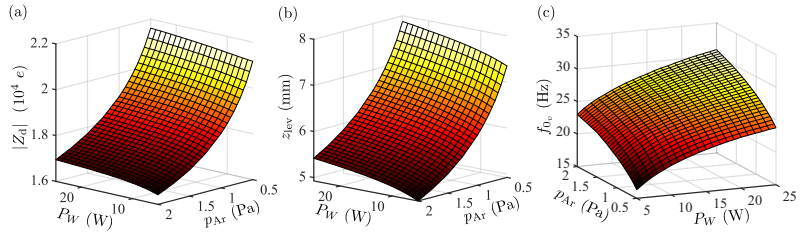

FIG. 9. (a) Equilibrium particle charge. (b) Equilibrium levitation height. (c) Vertical resonance frequency. The microparticle has a diameter $d = 9.16$ μm and its mass density is $\rho_m = 1510$ kg m^{-3} (MF density).

where r_d is the radius of the microparticle, $\tilde{\varphi}$ is the normalized microparticle floating potential, and $\lambda = \lambda_{D_i}/\sqrt{1+(\lambda_{D_i}/\lambda_{D_e})^2}$ is the linearized Debye length at the considered position in the sheath with $\lambda_{D_{i,e}} = (\epsilon_0 T_{i,e}/n_{i,e}e)^{1/2}$. At equilibrium $I_i + I_e = 0$ and the normalized floating potential $\tilde{\varphi}$ can be obtained for any position in the sheath (ions are assumed to be in thermal equilibrium with the background gas, $T_i = 0.03$ eV). The microparticle charge number $Z_d = Q_d/e$, where Q_d is the microparticle charge, is then obtained:

$$Z_d = -4\pi\epsilon_0 r_d T_e \tilde{\varphi}/e. \tag{21}$$

Since r_d and therefore the mass m_d of the microparticle are known and since the sheath electric field profile has been calculated, the equilibrium levitation height z_{lev} and the vertical resonance (confinement) frequency $f_v = \omega_v/(2\pi)$ can be obtained using the following equations [69–72]:

$$Q_d E(z_{lev}) = -m_d g, \tag{22}$$

$$\omega_v = \sqrt{\frac{|Q_d|}{m_d}\frac{\partial E(z)}{\partial z}}_{|z=z_{lev}}. \tag{23}$$

In Fig. 9, the results of the calculation of levitation height, particle charge at equilibrium position, and vertical resonance frequency as a function of rf power and background argon pressure are shown. The obtained equilibrium particle charges are between $-2.2\times10^4 e$ and $-1.6\times10^4 e$ [see Fig. 9(a)], which is of the order of the experimental ones (see Table I).

One can see that at a given argon background pressure, Z_d and z_{lev} are only slightly increasing with rf power. Moreover, the microparticles levitate quite high in the sheath near the sheath edge (for example at 1 Pa, the sheath length is around ∼7 mm (see Fig. 8) and the levitation height is around ∼6.5 mm [see Fig. 9(b)]). This is due to the fact that even though the ion and electron densities are increasing with rf power, the electron temperature is mostly set by the background gas pressure. Since T_e has a greater influence than n_e on the magnitude of the electron current onto a microparticle and therefore the microparticle charge, the microparticle equilibrium charge depends only weekly on rf power. Since at equilibrium levitation height, the gravity force is compensated by the electric force and, as seen previously, the sheath length is only weakly dependant on rf power, the particle levitation height will only slightly change.

The calculated vertical resonance frequency varies in the range 15–30 Hz depending on discharge parameters and is very close to the vertical resonance frequency reported in similar setups [9,10,28,73–75]. The vertical resonance frequency is increasing significantly with both rf power and argon background pressure [see Fig. 9(c)]. In both cases, this is due to steeper electric field when increasing rf power (resulting in larger self-bias) and when increasing the background argon pressure (resulting in shorter sheath). Therefore, decreasing pressure or rf power results in weaker vertical confinement and favors MCI for 2D complex plasma crystals. On the contrary, high pressure and high rf power favor crystallization of the complex plasma monolayer by providing stiffer vertical confinement. More details are given in the next subsection.

B. Mode-coupling instability

It is well known that MCI can occur in 2D complex plasma crystals [9,24,25] and in fluid complex plasma monolayers [26,29,32]. In Sec. IV, it was demonstrated experimentally that decreasing pressure and/or rf power leads to MCI in 2D complex plasma crystals and that the MCI threshold and crystallization threshold have defined trends.

One of the simplest ways to simulate MCI is to use the point-charge wake model [22,24,25,76–78]. In this model, the ion wake is approximated by a positive point charge q_w downstream of each microparticle at a distance δ_w below the microparticle. Then each microparticle interacts with the other microparticles and their respective ion wakes through screened-Coulomb (Yukawa) interactions. The interparticle distance in the 2D crystal is set at a fixed value Δ. In the calculation, the screening length is taken as the electron Debye length, λ_{D_e} at the equilibrium leviation height. To compute the different lattice modes in the 2D complex plasma crystals, one can calculate the dynamical matrix which has the form [24,25,78]

$$\mathbf{D} = \begin{pmatrix} \alpha_h - \beta & 2\gamma & \imath\sigma_x \\ 2\gamma & \alpha_h + \beta & \imath\sigma_y \\ \imath\sigma_x & \imath\sigma_y & \omega_v^2 - 2\alpha_v \end{pmatrix}, \tag{24}$$

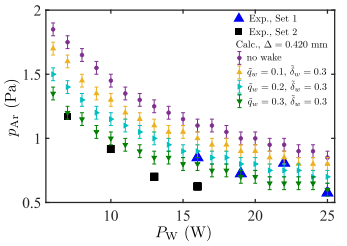

FIG. 10. MCI pressure threshold as a function of rf power for an interparticle distance $\Delta = 420$ μm and different ion wake charges in the framework of the point-charge wake model [24]. The experimental MCI pressure thresholds are shown for comparison.

where $\alpha_{h,v}$, β, and γ are the dispersion elements, and $\sigma_{x,y}$ are the coupling terms between the in-plane and out-of-plane modes due to the particle-wake interaction. Detailed expressions of these different terms as functions of Q_d, λ_{D_e}, q_w, δ_w, Δ, and $\mathbf{k}$, where $\mathbf{k}$ is the wave vector of the considered lattice mode, can be found in Refs. [24,25,78]. The dispersion relation of the microparticle lattice modes are obtained for any $\mathbf{k}$ by solving $\det[\mathbf{D} - \omega(\omega + \imath\nu)\mathbf{I}] = 0$, where $\mathbf{I}$ is the unit matrix, so that $\omega(\omega + \imath\nu)$ are the eigenvalues of the dynamical matrix, where ν is the damping rate due to neutral gas friction.

It is known that the mode-coupling instability in a 2D complex plasma crystal is triggered when the out-of-plane mode and the in-plane longitudinal mode cross [24,25] except in very specific experimental conditions where the ion wake charges are really strong allowing coupling of the modes without direct crossing [79]. First, the influence of the interparticle distance Δ on mode crossing is investigated in the case where ion wakes are ignored (see Appendix B for details). It is found that the out-of-plane and in-plane longitudinal mode crossing minimum pressure decreases when increasing the rf power due to the competing effects of the pressure decrease and the rf power increase. Moreover, at low pressure the microparticle charge is larger due to a higher electron temperature, which for a fixed Δ increases the maximum frequency of the longitudinal in-plane mode and makes mode crossing easier. Similarly, the pressure threshold is systematically lower for larger Δ to the weaker interparticle interaction which reduces the maximum frequency of the longitudinal in-plane mode and the minimum frequency of the out-of-plane mode. Experimental points follow roughly the same trend showing that the sheath profile (which depends on p_{Ar} and P_W) plays a major role in the crossing of the modes and the triggering of MCI in 2D complex plasma crystals.

In a second step, the interparticle distance was fixed to $\Delta = 420$ μm and point-charge wakes were considered. Only the value of the wake charge was varied ($0.1 \leqslant \tilde{q}_w = q_w/Q_d \leqslant 0.3$), while the distance to the microparticle is fixed ($\tilde{\delta}_w = \delta_w/\lambda = 0.3$). Then, the pressure threshold for the crossing of the modes (and the triggering of MCI) were calculated again. The results are presented in Fig. 10. As can be seen, the main trends are still there: when increasing the rf power, the threshold pressure decreases. However, the ion wakes have a significant effect. Increasing the ion wake charge significantly decreases the pressure threshold at a given rf power. The wake charges are unknown in the experiment and their overall effect on the measured pressure threshold are difficult to estimate. However, one can see in Fig. 10 (and Fig. 12 in Appendix B) that the experimental threshold values are not exactly aligned with the calculated one. Note again that the experimental particle charges are slightly smaller than the calculated ones and Δ used in the calculation is slightly larger than the experimental one (which is in addition not a constant for a given P_W but slightly decreases with p_{Ar}). In order to calculate the true MCI pressure threshold, it would be necessary to take into account the evolution of the horizontal confinement as a function of p_{Ar} and P_W as well as self-consistent wake parameters for the calculation of the lattice modes. A more sophisticated model for the ion wake such as those described in Refs. [78,80,81] is also needed as the wake model has a strong influence on the shape of the lattice modes [78].

To conclude, let us discuss the trend for the crystallization pressure observed in Fig. 4. As was shown in Sec. IV, the crystallization pressure follows the same trend as the MCI threshold pressure: it decreases with increasing power. This can be roughly explained through the modification of the sheath profile. When the P_W increases, the sheath electric field and therefore the vertical confinement become stronger. However, when in the fluid phase, the crossing of the out-of-plane mode with the longitudinal in-plane mode always occurs and MCI will exist unless damping due to neutral friction is high enough to suppress it [26]. At constant rf power, the microparticle charges decrease when increasing pressure (see Fig. 9 and Table I). Therefore, the longitudinal in-plane mode is not as steep (the longitudinal sound speed decreases; see Table I) and it will result in smaller instability growth rate. It was also shown in Ref. [26], in the framework of the wake-layer model, that when the vertical confinement frequency is increased above the threshold for mode crossing for MCI in a 2D crystal with the same microparticle parameters as in the fluid layer (same microparticle charges and same microparticle number density), the instability growth rate decreases as $\sim\exp(-\frac{1}{2}\omega_v^2\delta)$. The crystallization threshold is therefore also influenced by the wake parameters. Since these parameters are unknown, the crystallization pressures were not calculated but ion wakes are expected to have a non-negligible effect as for the MCI threshold pressure in 2D complex plasma crystals. A sweep of wake parameter space could be performed to find values that match the best the experimental observations but it is out of scope of the current article. In future studies, the use of a self-consistent wake model such as in Ref. [81] in addition to proper modeling of the horizontal confinement as a function of discharge parameters should enable us to derive self-consistently the MCI threshold and crystallization pressures.

VII. SUMMARY AND CONCLUSION

In this article, the MCI threshold pressure and crystallization pressure of monolayer complex plasma levitating in the sheath of an argon cc-rf discharge were investigated. It was

found that the stability of a crystalline microparticle monolayer increases with pressure and with the rf power: at constant rf power, the higher the rf power the lower the crystallization and MCI threshold pressures; at constant background argon pressure, the higher the pressure the lower the rf power for crystallization of the monolayer and for the triggering of MCI. It was also found by measuring the longitudinal and transverse sound speeds in two-dimensional complex plasma crystal that at constant rf power, lower pressure resulted in larger sound speeds and therefore larger microparticle charges. These results are in agreement with previous observations of the MCI [9,25].

A simple rf sheath model was developed to calculate the evolution of the rf sheath profile as a function of the input rf power and the background argon pressure. Using experimental measurements of the electron density in the plasma bulk and the powered electrode self-bias as input parameters, the model was able to show that the argon pressure and the rf power have significant influence on sheath profiles. Using the calculated sheath parameters, the microparticle equilibrium charge, the equilibrium levitation height, and the vertical confinement frequency were also calculated. It was found that (i) a power increase at constant pressure leads to increase of Z_d, z_{lev} and f_{0_z} and (ii) a pressure increase at constant rf power leads to decrease of Z_d, z_{lev} and an increase of f_{0_z}. Combined with the point-charge wake model [24], the trends for MCI threshold pressure could be reproduced (i.e., decreasing the pressure at constant power would lead to the crossing of the longitudinal in-plane mode and the out-of-plane mode and trigger MCI, lower rf power results in higher MCI threshold pressure). However, it was also shown that the MCI threshold is sensitive to interparticle distance and wake parameters.

Compared to earlier studies, a better integration of the experimental results and theory was achieved by operating with actual experimental control parameters such as the gas pressure and the discharge power. A sweep of wake parameters space could be performed to find values that match the best experimental observations. However, future studies will concentrate on the use of a self-consistent wake model [81] to study the influence of ion wakes on dust equilibrium position and vertical resonance frequency. The influence of the plasma parameters on horizontal confinement should also be taken into account in order to model self-consistently the interparticle distance in monolayer complex plasma enabling more detailed investigations of fluid MCI and the crystallization threshold pressure.

ACKNOWLEDGMENTS

The authors would like to thank S. Zhdanov for fruitful comments and discussions. The authors would also like to thank H. Thomas for his careful reading of our manuscript. L.C. acknowledges the support of the Natural Sciences and Engineering Research Council of Canada (NSERC), Grant No. RGPIN-2019-04333.

APPENDIX A: CRYSTALLIZATION OF THE MONOLAYER

The crystallization process was similar to the one happening during a below MCI threshold localized laser induced melting reported in Ref. [32]. Until the crystallization pressure threshold p_{cryst} was overcome, the microparticle kinetic energy remained quite large (a few eV). When p_{cryst} was finally reached, a rapid cooling of the monolayer was induced (in a matter of a few seconds) due to the neutral drag damping rate being higher than the fluid MCI growth rate, and the crystallization occurred (average bond orientational order $\langle \Psi_6 \rangle$ increased to a value close to 1 and the numbers of 5-fold and 7-fold defects decreased tremendously). In this article, the particle kinetics at crystallization threshold was not investigated in detail and was only detected with the naked eye. As illustrated in Fig. 11 for a similar experiment (i.e., different monolayer), the recrystallization event is unmissable.

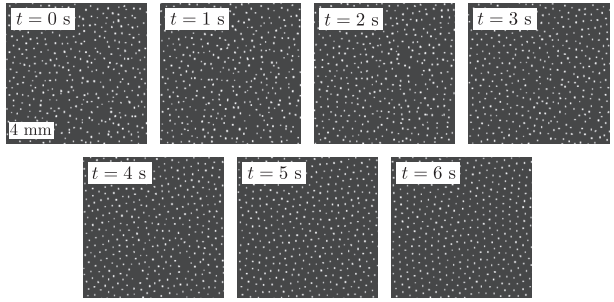

FIG. 11. Snapshots of a microparticle monolayer during recrystallization at $p_{\mathrm{Ar}} = 0.90$ Pa and $P_{\mathrm{W}} = 5$ W. Note that this is a different smaller monolayer than the one used for the results reported in the main text. Therefore the MCI and crystallization thresholds are also different and the above images should only be used as an illustration.

APPENDIX B: MODE-CROSSING WITHOUT ION WAKE

The influence of the interparticle distance on mode crossing is investigated in the case where ion wakes are ignored ($\sigma_{x,y} = 0$). Using the results of Sec. V C and Sec. VI A, the minimum pressure for out-of-plane and in-plane longitudinal mode crossing as a function of power was calculated for different Δ (420 μm, 450 μm, and 500 μm). The results are presented in Fig. 12. As can be seen, the out-of-plane and in-plane longitudinal mode crossing minimum pressure decreases when increasing the rf power. This can be understood due to the competing effects of the pressure decrease, which makes the sheath longer and therefore weakens the confining electric field, and the rf power increase, which increases the self-bias of the powered electrode and makes the vertical confinement stiffer. Moreover, at low pressure the microparticle charge is larger due to a higher electron temperature, which for a fixed interparticle distance renders the interaction force greater and therefore increases the maximum frequency of the longitudinal in-plane mode and makes mode crossing easier. In addition, one can see that the pressure threshold is systematically lower for larger Δ. This is due to the weaker interparticle interaction which reduces the maximum frequency of the longitudinal in-plane mode and the minimum frequency of the out-of-plane mode. Finally, we can see that experimental points follow roughly the same trend. This shows that the sheath profile (which depends on p_{Ar} and P_{W}) plays a major role in the crossing of the modes and the triggering of MCI in 2D complex plasma crystals.

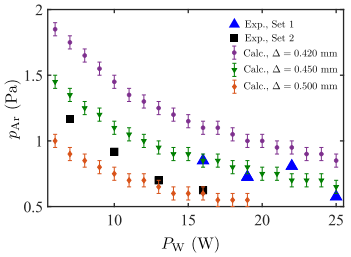

FIG. 12. Pressure at which the crossing of the in-plane longitudinal mode and the out-of-plane mode occurs as a function of rf power for different interparticle distances Δ and without ion wakes. The experimental MCI pressure thresholds are shown for comparison.

[1] G. E. Morfill and H. Thomas, Plasma crystal, J. Vac. Sci. Technol. A **14**, 490 (1996).

[2] A. Melzer, S. Nunomura, D. Samsonov, Z. W. Ma, and J. Goree, Laser-excited Mach cones in a dusty plasma crystal, Phys. Rev. E **62**, 4162 (2000).

[3] S. Nunomura, D. Samsonov, and J. Goree, Transverse Waves in a Two-Dimensional Screened-Coulomb Crystal (Dusty Plasma), Phys. Rev. Lett. **84**, 5141 (2000).

[4] V. A. Schweigert, I. V. Schweigert, V. Nosenko, and J. Goree, Acceleration and orbits of charged particles beneath a monolayer plasma crystal, Phys. Plasmas **9**, 4465 (2002).

[5] V. Nosenko, J. Goree, Z. Ma, D. Dubin, and A. Piel, Compressional and shear wakes in a two-dimensional dusty plasma crystal, Phys. Rev. E **68**, 056409 (2003).

[6] S. Nunomura, J. Goree, S. Hu, X. Wang, A. Bhattacharjee, and K. Avinash, Phonon Spectrum in a Plasma Crystal, Phys. Rev. Lett. **89**, 035001 (2002).

[7] K. Qiao and T. W. Hyde, Dispersion properties of the out-of-plane transverse wave in a two-dimensional Coulomb crystal, Phys. Rev. E **68**, 046403 (2003).

[8] L. Couëdel and V. Nosenko, Tracking and linking of microparticle trajectories during mode-coupling induced melting in a two-dimensional complex plasma crystal, J. Imaging **5**, 41 (2019).

[9] L. Couëdel, V. Nosenko, A. V. Ivlev, S. K. Zhdanov, H. M. Thomas, and G. E. Morfill, Direct Observation of Mode-Coupling Instability in Two-Dimensional Plasma Crystals, Phys. Rev. Lett. **104**, 195001 (2010).

[10] D. Samsonov, S. Zhdanov, and G. Morfill, Vertical wave packets observed in a crystallized hexagonal monolayer complex plasma, Phys. Rev. E **71**, 026410 (2005).

[11] P. Qiu, T. Sun, and Y. Feng, Observation of the solid and liquid separation after the shock propagation in a two-dimensional Yukawa solid, Phys. Plasmas **28**, 113702 (2021).

[12] A. Kananovich and J. Goree, Shock width measured under liquid and solid conditions in a two-dimensional dusty plasma, Phys. Rev. E **104**, 055201 (2021).

[13] H. M. Thomas and G. E. Morfill, Melting dynamics of a plasma crystal, Nature (London) **379**, 806 (1996).

[14] J. Berumen and J. Goree, Experiment and model for a Stokes layer in a strongly coupled dusty plasma, Phys. Rev. E **104**, 035208 (2021).

[15] B. Liu, J. Goree, M. Y. Pustylnik, H. M. Thomas, V. E. Fortov, A. M. Lipaev, A. D. Usachev, O. F. Petrov, A. V. Zobnin, and M. H. Thoma, Time-dependent shear motion in a strongly coupled dusty plasma in PK-4 on the International Space Station (ISS), IEEE Trans. Plasma Sci. **49**, 2972 (2021).

[16] E. V. Vasilieva, O. F. Petrov, and M. M. Vasiliev, Laser-induced melting of two-dimensional dusty plasma system in RF discharge, Sci. Rep. **11**, 523 (2021).

[17] O. Ishihara and S. V. Vladimirov, Wake potential of a dust grain in a plasma with ion flow, Phys. Plasmas **4**, 69 (1997).

[18] A. Melzer, V. A. Schweigert, and A. Piel, Measurement of the Wakefield attraction for "dust plasma molecules", Phys. Scr. **61**, 494 (2000).

[19] S. V. Vladimirov, S. A. Maiorov, and O. Ishihara, Molecular dynamics simulation of plasma flow around two stationary dust grains, Phys. Plasmas **10**, 3867 (2003).

[20] I. V. Schweigert, V. A. Schweigert, and F. M. Peeters, Perturbation of collisional plasma flow around a charged dust particle: Kinetic analysis, Phys. Plasmas **12**, 113501 (2005).

[21] L. S. Matthews, D. L. Sanford, E. G. Kostadinova, K. S. Ashrafi, E. Guay, and T. W. Hyde, Dust charging in dynamic ion wakes, Phys. Plasmas **27**, 023703 (2020).

[22] A. V. Ivlev and G. Morfill, Anisotropic dust lattice modes, Phys. Rev. E **63**, 016409 (2000).

[23] A. V. Ivlev, U. Konopka, G. Morfill, and G. Joyce, Melting of monolayer plasma crystals, Phys. Rev. E **68**, 026405 (2003).

[24] S. K. Zhdanov, A. V. Ivlev, and G. E. Morfill, Mode-coupling instability of 2D plasma crystals, Phys. Plasmas **16**, 083706 (2009).

[25] L. Couëdel, S. K. Zhdanov, A. V. Ivlev, V. Nosenko, H. M. Thomas, and G. E. Morfill, Wave mode coupling due to plasma wakes in two-dimensional plasma crystals: In-depth view, Phys. Plasmas **18**, 083707 (2011).

[26] A. V. Ivlev, S. K. Zhdanov, M. Lampe, and G. E. Morfill, Mode-Coupling Instability in a Fluid Two-Dimensional Complex Plasma, Phys. Rev. Lett. **113**, 135002 (2014).

[27] S. V. Vladimirov, P. V. Shevchenko, and N. F. Cramer, Vibrational modes in the dust-plasma crystal, Phys. Rev. E **56**, R74 (1997).

[28] L. Couëdel, V. Nosenko, S. K. Zhdanov, A. V. Ivlev, H. M. Thomas, and G. E. Morfill, First Direct Measurement of Optical Phonons in 2D Plasma Crystals, Phys. Rev. Lett. **103**, 215001 (2009).

[29] S. O. Yurchenko, E. V. Yakovlev, L. Couëdel, N. P. Kryuchkov, A. M. Lipaev, V. N. Naumkin, A. Y. Kislov, P. V. Ovcharov, K. I. Zaytsev, E. V. Vorob'ev, G. E. Morfill, and A. V. Ivlev, Flame propagation in two-dimensional solids: Particle-resolved studies with complex plasmas, Phys. Rev. E **96**, 043201 (2017).

[30] J. D. Williams, E. Thomas, L. Couëdel, A. V. Ivlev, S. K. Zhdanov, V. Nosenko, H. M. Thomas, and G. E. Morfill, Kinetics of the melting front in two-dimensional plasma crystals: Complementary analysis with the particle image and particle tracking velocimetries, Phys. Rev. E **86**, 046401 (2012).

[31] T. B. Röcker, L. Couëdel, S. K. Zhdanov, V. Nosenko, A. V. Ivlev, H. M. Thomas, and G. E. Morfill, Nonlinear regime of the mode-coupling instability in 2D plasma crystals, Europhys. Lett. **106**, 45001 (2014).

[32] L. Couëdel, V. Nosenko, M. Rubin-Zuzic, S. Zhdanov, Y. Elskens, T. Hall, and A. V. Ivlev, Full melting of a two-dimensional complex plasma crystal triggered by localized pulsed laser heating, Phys. Rev. E **97**, 043206 (2018).

[33] T. B. Röcker, A. V. Ivlev, S. K. Zhdanov, and G. E. Morfill, Effect of strong wakes on waves in two-dimensional plasma crystals, Phys. Rev. E **89**, 013104 (2014).

[34] M. A. Lieberman, Analytical solution for capacitive rf sheath, IEEE Trans. Plasma Sci. **16**, 638 (1988).

[35] M. A. Lieberman, Dynamics of a collisional, capacitive rf sheath, IEEE Trans. Plasma Sci. **17**, 338 (1989).

[36] V. A. Godyak and N. Sternberg, Dynamic model of the electrode sheath in a symmetrically driven plasma, Phys. Rev. A **42**, 2299 (1990).

[37] M. Chandhok and J. W. Grizzle, Modeling the pressure dependence of dc bias voltage in asymmetric, capacitive rf sheaths, IEEE Trans. Plasma Sci. **26**, 181 (1998).

[38] J. Gierling and K.-U. Riemann, Comparison of a consistent theory of radio frequency sheaths with step models, J. Appl. Phys. **83**, 3521 (1998).

[39] M. A. Sobolewski, Sheath model for radio-frequency-biased, high-density plasmas valid for all ω/ω_i, Phys. Rev. E **62**, 8540 (2000).

[40] M. N. A. Dewan, P. J. McNally, and P. A. F. Herbert, Plasma modeling for a nonsymmetric capacitive discharge driven by a nonsinusoidal radio frequency current, J. Appl. Phys. **91**, 5604 (2002).

[41] P. Chabert and N. Braithwaite, *Physics of Radio-Frequency Plasmas* (Cambridge University Press, Cambridge, 2011).

[42] U. Czarnetzki, Analytical model for the radio-frequency sheath, Phys. Rev. E **88**, 063101 (2013).

[43] P. Chabert, T. V. Tsankov, and U. Czarnetzki, Foundations of capacitive and inductive radio-frequency discharges, Plasma Sources Sci. Technol. **30**, 024001 (2021).

[44] V. Nosenko, A. V. Ivlev, S. K. Zhdanov, M. Fink, and G. E. Morfill, Rotating electric fields in complex (dusty) plasmas, Phys. Plasmas **16**, 083708 (2009).

[45] V. Nosenko, J. Goree, and A. Piel, Laser method of heating monolayer dusty plasmas, Phys. Plasmas **13**, 032106 (2006).

[46] V. Nosenko, S. Zhdanov, and G. Morfill, Supersonic Dislocations Observed in a Plasma Crystal, Phys. Rev. Lett. **99**, 025002 (2007).

[47] M. A. Lieberman and A. J. Lichtenberg, *Principles of Plasma Discharges and Materials Processing* (Wiley, New York, 1994).

[48] Y. P. Raizer, M. N. Shneider, and N. A. Yatsenko, *Radio-Frequency Capacitive Discharges* (CRC Press, Boca Raton, FL, 1995).

[49] Y. P. Song, D. Field, and D. F. Klemperer, Electrical potentials in RF discharges, J. Phys. D **23**, 673 (1990).

[50] V. Land, E. Shen, B. Smith, L. Matthews, and T. Hyde, Experimental and computational characterization of a modified GEC cell for dusty plasma experiments, New J. Phys. **11**, 063024 (2009).

[51] N. Kohlmann, F. Wieben, O. H. Asnaz, D. Block, and F. Greiner, High-precision *in situ* size measurements of single microparticles in an rf plasma, Phys. Plasmas **26**, 053701 (2019).

[52] Except when within a few 10^{-2} Pa of the crystallization pressure where the outer part of the monolayer has started crystallizing while the center remained melted.

[53] L. Couëdel, S. Zhdanov, V. Nosenko, A. V. Ivlev, H. M. Thomas, and G. E. Morfill, Synchronization of particle motion induced by mode coupling in a two-dimensional plasma crystal, Phys. Rev. E **89**, 053108 (2014).

[54] I. Laut, C. Räth, S. Zhdanov, V. Nosenko, L. Couëdel, and H. M. Thomas, Synchronization of particle motion in compressed two-dimensional plasma crystals, Europhys. Lett. **110**, 65001 (2015).

[55] The pressure was kept constant during imaging.

[56] J.-P. Hansen and I. R. McDonald, *Theory of Simple Liquids*, 3rd ed. (Elsevier/Academic Press, Cambridge, 2006).

[57] B. Liu, J. Goree, V. E. Fortov, A. M. Lipaev, V. I. Molotkov, O. F. Petrov, G. E. Morfill, H. M. Thomas, H. Rothermel, and A. V. Ivlev, Transverse oscillations in a single-layer dusty plasma under microgravity, Phys. Plasmas **16**, 083703 (2009).

[58] N. P. Kryuchkov, L. A. Mistryukova, V. V. Brazhkin, and S. O. Yurchenko, Excitation spectra in fluids: How to analyze them properly, Sci. Rep. **9**, 10483 (2019).

[59] S. Khrapak and L. Couëdel, Dispersion relations of Yukawa fluids at weak and moderate coupling, Phys. Rev. E **102**, 033207 (2020).

[60] D. H. E. Dubin, The phonon wake behind a charge moving relative to a two-dimensional plasma crystal, Phys. Plasmas **7**, 3895 (2000).

[61] S. Nunomura, J. Goree, S. Hu, X. Wang, and A. Bhattacharjee, Dispersion relations of longitudinal and transverse waves in two-dimensional screened Coulomb crystals, Phys. Rev. E **65**, 066402 (2002).

[62] P. Hartmann, G. J. Kalman, Z. Donkó, and K. Kutasi, Equilibrium properties and phase diagram of two-dimensional Yukawa systems, Phys. Rev. E **72**, 026409 (2005).

[63] V. A. Godyak and N. Sternberg, Smooth plasma-sheath transition in a hydrodynamic model, IEEE Trans. Plasma Sci. **18**, 159 (1990).

[64] M. Moisan and J. Pelletier, *Physique des Plasmas Collisionnels: Application aux Décharges Haute Fréquence* (Grenoble Sciences, Bonchamp-Lès-Laval, 2006).

[65] J. Schulze, B. G. Heil, D. Luggenhölscher, R. P. Brinkmann, and U. Czarnetzki, Stochastic heating in asymmetric capacitively coupled RF discharges, J. Phys. D **41**, 195212 (2008).

[66] M. L. Hause, B. D. Prince, and R. J. Bemish, Krypton charge exchange cross sections for Hall effect thruster models, J. Appl. Phys. **113**, 163301 (2013).

[67] A. V. Zobnin, A. D. Usachev, O. F. Petrov, and V. E. Fortov, Ion current on a small spherical attractive probe in a weakly ionized plasma with ion-neutral collisions (kinetic approach), Phys. Plasmas **15**, 043705 (2008).

[68] S. Khrapak and G. Morfill, Basic processes in complex (dusty) plasmas: Charging, interactions, and ion drag force, Contrib. Plasma Phys. **49**, 148 (2009).

[69] T. Trottenberg, A. Melzer, and A. Piel, Measurement of the electric charge on particulates forming Coulomb crystals in the sheath of a radiofrequency plasma, Plasma Sources Sci. Technol. **4**, 450 (1995).

[70] A. Homann, A. Melzer, and A. Piel, Measuring the charge on single particles by laser-excited resonances in plasma crystals, Phys. Rev. E **59**, R3835 (1999).

[71] E. B. Tomme, D. A. Law, B. M. Annaratone, and J. E. Allen, Parabolic Plasma Sheath Potentials and Their Implications for the Charge on Levitated Dust Particles, Phys. Rev. Lett. **85**, 2518 (2000).

[72] A. Melzer, Laser manipulation of particles in dusty plasmas, Plasma Sources Sci. Technol. **10**, 303 (2001).

[73] B. J. Harris, L. S. Matthews, and T. W. Hyde, Vertical-probe-induced asymmetric dust oscillation in complex plasma, Phys. Rev. E **87**, 053109 (2013).

[74] S. K. Zhdanov, L. Couëdel, V. Nosenko, H. M. Thomas, and G. E. Morfill, Spontaneous pairing and cooperative movements of micro-particles in a two dimensional plasma crystal, Phys. Plasmas **22**, 053703 (2015).

[75] M. Jambor, V. Nosenko, S. K. Zhdanov, and H. M. Thomas, Plasma crystal dynamics measured with a three-dimensional plenoptic camera, Rev. Sci. Instrum. **87**, 033505 (2016).

[76] V. A. Schweigert, I. V. Schweigert, A. Melzer, A. Homann, and A. Piel, Alignment and instability of dust crystals in plasmas, Phys. Rev. E **54**, 4155 (1996).

[77] A. Melzer, V. A. Schweigert, I. V. Schweigert, A. Homann, S. Peters, and A. Piel, Structure and stability of the plasma crystal, Phys. Rev. E **54**, R46 (1996).

[78] T. B. Röcker, A. V. Ivlev, R. Kompaneets, and G. E. Morfill, Mode coupling in two-dimensional plasma crystals: Role of the wake model, Phys. Plasmas **19**, 033708 (2012).

[79] J. K. Meyer, I. Laut, S. K. Zhdanov, V. Nosenko, and H. M. Thomas, Coupling of Noncrossing Wave Modes in a Two-Dimensional Plasma Crystal, Phys. Rev. Lett. **119**, 255001 (2017).

[80] T. B. Röcker, S. K. Zhdanov, A. V. Ivlev, M. Lampe, G. Joyce, and G. E. Morfill, Effective dipole moment for the mode coupling instability: Mapping of self-consistent wake models, Phys. Plasmas **19**, 073708 (2012).

[81] R. Kompaneets, G. E. Morfill, and A. V. Ivlev, Wakes in complex plasmas: A self-consistent kinetic theory, Phys. Rev. E **93**, 063201 (2016).

Synchronization of particle motion induced by mode coupling in a two-dimensional plasma crystal

L. Couëdel,[1,*] S. Zhdanov,[2] V. Nosenko,[2,3] A. V. Ivlev,[2] H. M. Thomas,[2,3] and G. E. Morfill[2]

[1]*CNRS, Aix-Marseille Université, Laboratoire de Physique des Interactions Ioniques et Moléculaires, 13397 Marseille cedex 20, France*

[2]*Max Planck Institute for Extraterrestrial Physics, D-85741 Garching, Germany*

[3]*Forschungsgruppe Komplexe Plasmen, Deutsches Zentrum für Luft-und-Raumfahrt, Oberpfaffenhofen, Germany*

(Received 25 February 2014; published 30 May 2014)

The kinematics of dust particles during the early stage of mode-coupling induced melting of a two-dimensional plasma crystal is explored. It is found that the formation of the hybrid mode causes the particle vibrations to partially synchronize at the hybrid frequency. Phase- and frequency-locked hybrid particle motion in both vertical and horizontal directions (hybrid mode) is observed. The system self-organizes in a rhythmic pattern of alternating in-phase and antiphase oscillating chains of particles. The spatial orientation of the synchronization pattern correlates well with the directions of the maximal increment of the shear-free hybrid mode.

DOI: 10.1103/PhysRevE.89.053108 PACS number(s): 52.27.Lw

I. INTRODUCTION

An odd "kind of sympathy" in pendulum clocks discovered about 350 years ago by C. Huygens was later rigorously explained as a specific synchronization process between the weakly coupled close-frequency oscillators [1,2]. Since then synchronization phenomena have become an important topic in explorations of biological, physical, chemical, cybernetical, and many other dynamical systems. Their diversity and complexity required a principally new approach to develop a network analysis, allowing to systematically study intercorrelations in large populations of interacting units [3–8]. Spontaneous emergence of synchronized signals and spontaneous symmetry breaking are typical behaviors in such nonlinear systems, e.g., in spatially distributed mutually coupled lasers [9–11]. A large system of weakly coupled nearly identical oscillators with a phase-dependent interaction is normally considered as a model to explore collective synchronization in detail. Analytical studies [12], computational simulations [13], as well as model systems, e.g., the dynamics of disordered Josephson arrays [14], predict a nonlinear dynamical phase transition in such systems. In this sense, complex plasmas are ideal systems to observe the synchronization process generically in all its complexity and diversity at an "atomistic" scale and in real time.

Complex or dusty plasmas are weakly ionized gases containing micron-size particles called dust particles or microparticles. In a laboratory radio-frequency (rf) plasma these particles are negatively charged. Due to their strong interactions with the plasma and with each other, they can form strongly coupled systems, analogous to colloids [15]. Microparticles are often confined in the sheath region of electrical discharges, where the electrostatic force is strong enough to balance the gravity force. They can form monolayers or (quasi-)two-dimensional (2D) crystals [16–20] extended vertically to a finite width, which strongly depends on the strength of the vertical confinement [19]. In such systems, two in-plane wave modes with an acoustic dispersion can be sustained: a longitudinal mode and a transverse mode. Since the strength of the vertical confinement is finite, there is a third fundamental wave mode associated with the out-of-plane oscillations which has an optical dispersion [19–25].

Due to the strong electric field in the sheath region of the discharge, every particle is influenced by a strong ion flow exerting an additional force on it. Moreover, the screening cloud around each particle in such conditions is strongly distorted, being more extended in the direction of the flow. The ions tend to focus downstream of the particle making the system highly polarized. This mechanism is often referred to as "plasma wake" [26–33]. One of the easiest ways to represent the plasma wake is to add a pointlike positive wake charge downstream of the particle [23,25], or consider the polarization self-consistently in the framework of the linear response models [26,33–35].

The existing theories predict that all three wave modes depend critically on the parameters of the plasma wake. Moreover, the wake-mediated interactions between the particles result in the coupling of the "usual" crystal modes into a new "hybrid" mode of the lattice layer. This mode can be evidenced as localized "hot spots" in the lattice phonon's spectra [36]. The theory of mode-coupling instability [23,25,37] provides a detailed picture of a *plasma-specific* melting scenario operating in 2D plasma crystals. The melting associated with the wake-mediated coupling between the longitudinal in-plane and out-of-plane modes can only be triggered if (i) the modes intersect, and (ii) the neutral gas damping is sufficiently low. In the vicinity of the hybrid mode, one can observe traces of mixed polarization for the two intersecting wave branches [37]. These features can be considered as distinct fingerprints to identify the onset of the wake-induced mode coupling. In theoretical investigations [25,37] the hybrid mode was found to preferentially emerge with a wave vector parallel to the rows of the minimal packing density in the lattice. For instance, it is valid for the waves propagating at an angle $\theta = 0^\circ$ or along any other direction equivalent by hexagonal symmetry, e.g., at an angle $\theta = 60^\circ$ or 120°, etc. The propagation angle θ is as introduced in Fig. 1.

It is well known that in a system of coupled limit-cycle oscillators, a macroscopic fraction of them can synchronize to a common frequency when the coupling among oscillators is strong enough [38]. A two-dimensional plasma crystal can be seen as an ensemble of coupled nonlinear oscillators. During the mode-coupling induced melting, dust particles interact strongly with each other, and, as has been shown previously, the hybrid mode can be a source of anomalous heating [36,37]. First experimental observations showed that at the nonlinear stage of the mode-coupling instability the crystal melts and spreads out vertically [36,39,40].

In this paper, we demonstrate experimentally that during the melting process mediated by the mode-coupling instability, the microparticle oscillations are synchronized dominantly in the direction along which the instability increment is maximal. The side-view imaging revealed that the particles exhibit both vertical and horizontal oscillatory motions at the hybrid mode frequency. The synchronization is explained by the fact that only the wave modes at the hybrid frequency have a positive growth rate while the other waves are damped. Moreover, the hybrid mode with a maximal increment is dominantly compressional.

*lenaic.couedel@univ-amu.fr

 ©2014 American Physical Society

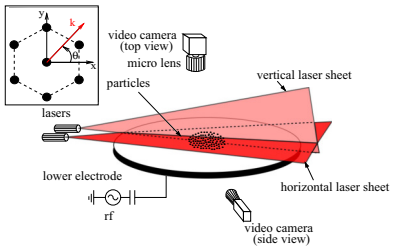

FIG. 1. (Color online) Sketch of the experimental setup. Microparticles are confined above the rf electrode and are illuminated with a horizontal laser sheet. Microparticles are recorded from top at a speed of 250 frames per second. A second vertical laser sheet illuminates the microparticle cloud allowing us to record a slice of it using a side-view camera at 103.56 fps. In the inset the elementary cell of the hexagonal lattice is depicted with the frame of reference chosen in this article.

II. EXPERIMENTAL SETUP

Mode coupling and plasma crystal melting were systematically investigated in experiments performed with a (modified) gaseous electronics conference (GEC) chamber, in a capacitively coupled rf glow discharge at 13.56 MHz (see Fig. 1). The argon pressure was between 0.4 and 1 Pa and the forward rf power was between 5 and 20 W (which corresponded to rf peak-to-peak voltage between 175 and 310 V). The plasma parameters in the bulk discharge were deduced from Langmuir probe measurements, yielding the electron temperature $T_e = 2.5$ eV and the electron density $n_e = 2 \times 10^9$ cm^{-3} at $p = 0.66$ Pa and $P = 20$ W [41]. A horizontal monolayer was formed by levitating melamine-formaldehyde particles in the plasma sheath above the lower rf electrode. Particles with a diameter of 9.19 ± 0.14 μm were used. The dust particle cloud was illuminated by two laser sheets: a vertical one and a horizontal one. The particles were imaged through a window at the top of the chamber by a Photron FASTCAM 1024 PCI camera at a speed of 250 frames per second. The horizontal coordinates x and y as well as velocity components v_x and v_y of individual particles were then extracted with subpixel resolution in each frame by using a standard particle tracking technique [42]. An additional side-view camera (Basler Ace ACA640-100GM at 103.56 fps) was used to verify that our experiments were carried out with a single layer of particles. This side-view camera was also used to study the in-plane and out-of-plane motion of the microparticles in a slice of the crystal. The diameter of the obtained crystalline structure, depending on the number of injected particles [43], was up to ~60 mm.

III. DATA PROCESSING

A. Dynamical characteristics

To explore the wave properties of the microparticle monolayer, the in-plane and out-of-plane tracking data obtained are used to compute the particle velocity fluctuation spectra. First the particle current components $V_s(\mathbf{k},t)$ introduced as

$$V_s(\mathbf{k},t) = \sum_{j=1}^{N} v_{s,j}(t) e^{-i\mathbf{k}\mathbf{s}_j(t)} \tag{1}$$

are calculated in the s direction at the time moment t, using a wave vector $\mathbf{k} = \{k_x, k_y\}$ located in the horizontal plane. Here, i is the imaginary unit, j is the particle index, $v_{s,j}(t)$ is the s projection of the jth particle velocity, $\mathbf{s}_j = \{x_j, y_j, z_j\}$ is its position, and N is the number of microparticles. Note that the x, y axes are chosen as shown in Fig. 1. Fixing the axes directions allows us to easily choose the direction of the wave propagation with respect to the lattice principal axis. A fast Fourier transform in time domain is then implemented to obtain the current fluctuation spectra. The structure factor of the crystal was also calculated from the particle positions:

$$S(\mathbf{k},t) = \frac{1}{N} \left| \sum_{j=1}^{N} e^{-i\mathbf{k}\cdot\mathbf{s}_j(t)} \right|^2 . \tag{2}$$

B. Instantaneous phase and frequency of particle oscillations

From the tracks of each traced particle, it is possible to obtain the instantaneous phases of the particle trajectories as a function of time and position. The displacements $r_j(t) = \sqrt{x_j^2(t) + y_j^2(t)}$ at hand were first filtered to remove the drift and to keep only the oscillatory parts, i.e., the "filtered" displacement $\tilde{r}_j(t)$ of the jth particle is defined as

$$\tilde{r}_j(t) = x_j(t) - \frac{1}{\Delta t} \int_{t-\Delta t/2}^{t+\Delta t/2} r_j(t')dt' \tag{3}$$

where Δt, the interval of averaging, was chosen to be the same, $\Delta t = 0.5$ s, at all $j = 1 \ldots N$. Finally the Hilbert transform was implemented to obtain the analytic signals $r_{a_j}(t)$, their instantaneous phases $\phi_j(t) = \arg[r_{a_j}(t)]$, and amplitudes $A_j(t) = |r_{a_j}|$ [44]. Maps of particle instantaneous phases were then constructed for each frame and stacked together to assemble a video [45].

The instantaneous phase computed for each particle j was used to calculate the degree of synchronization σ_j between the particle j with its closest neighbors [46],

$$\sigma_j = \frac{1}{n}\sum_{j'=1}^{n}\sigma_{jj'}, \tag{4}$$

$$\sigma_{jj'} = 1 - \frac{S_{jj'}}{S_{\max}}, \tag{5}$$

where n is the number of the closest neighbors, $S_{jj'}$ is the Shannon entropy of the cycle phase distribution between neighbors,

$$S_{jj'} = -\sum_{l=1}^{M} p_{jj'l}\ln p_{jj'l}, \quad \sum_{l=1}^{M} p_{jj'l} = 1. \tag{6}$$

Here, $p_{jj'l}$ is the fraction of the data in the lth bin in the distribution of phase differences $\phi_{jj'}(t) = \phi_j(t) - \phi_{j'}(t) (\mathrm{mod}\, 2\pi)$, $l = 1 \ldots M$, $M = 20$ is the number of bins, and $S_{\max} = \ln M$ is the maximum entropy corresponding to a uniform distribution $p_{jj'l} = M^{-1}$. The distribution of phase differences was computed with the help of a moving window procedure using the instantaneous phases $\phi_{jj'}(t)$ calculated for the 101 consecutive frames centered on the time moment t.

The synchronization index σ_j introduced by relationship (4) scales between 0 and 1. The completely synchronized (desynchronized) state corresponds to $\sigma = 1(0)$.

The time derivative of the instantaneous phase yields the instantaneous frequency $2\pi f_{\mathrm{inst}} = |\partial\phi(t)/\partial t|$.

IV. EXPERIMENTAL RESULTS

In this section, the early stage of the mode-coupling instability of a 2D complex plasma crystal triggering the frequency and phase synchronization and followed by the melting is discussed. The instability was initiated by decreasing the argon pressure from $p = 0.94$ Pa to 0.92 Pa at a fixed forward rf power $P = 12$ W.

A. Fluctuation spectra of the monolayer

The longitudinal and transverse sound speeds, respectively $C_L = (34.1 \pm 1.4)$ mm/s and $C_T = (7.9 \pm 0.3)$ mm/s, were obtained by using the low-k part of the longitudinal and transverse in-plane spectra; see Fig. 2. The interparticle separation in the center of the crystal was found to be $a = 480 \pm 10$ μm. Given the measured values of a, C_L, and C_T, and following the method proposed in Ref. [47], the charge of the dust particles $Q \simeq -18\,600e$, where e is the elementary charge, the coupling parameter $\kappa \equiv a/\lambda_D = 1.26$ and the Debye length $\lambda_D = 380$ μm were calculated. The error on the charge is about 15% and the error on κ is about 30%.

The frequency of the vertical particle oscillations (the "vertical confinement parameter") $f_v = 23 \pm 1$ Hz was extracted from the out-of-plane fluctuation spectrum (not shown here).

The hot spot at the frequency $f_{\mathrm{hyb}} = 16 \pm 1$ Hz, indicating emergence of the hybrid mode, is well pronounced in the longitudinal velocity fluctuation spectrum; see Fig. 2(a). To obtain the wave energy distribution in the $\mathbf{k}$ plane around the hybrid mode resonance frequency $f = f_{\mathrm{hyb}}$ the spectrum

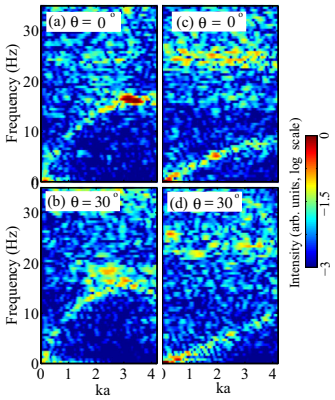

FIG. 2. (Color online) Fluctuation spectra of the in-plane particle velocity at $\theta = 0^\circ$ and $\theta = 30^\circ$: (a),(b) longitudinal, (c),(d) transverse velocity fluctuations. A bright "hot spot" at the frequency of $f_{\mathrm{hyb}} = 16 \pm 1$ Hz well seen in the spectrum (a) is worth noting.

of the in-plane velocity fluctuations was integrated over the narrow frequency band 14–18 Hz. Performing computations, the interrogation window was chosen to be a square of 400 × 400 pixels. It was thus ~35 × 35 interparticle distances giving a resolution of $\sim 0.18ka$. The resultant spectral map is shown in Fig. 3. The upper (lower) panel of Figs. 3(a) and 3(b) shows the compressional (shear) component of the velocity fluctuation.

Note that the $k_x > 0$ semiaxis corresponds to the $\theta = 0^\circ$ direction in the frame of reference introduced in Fig. 1. As predicted by the linear isotropic theory [25,37], it is the "most unstable" direction in which the instability develops. Therefore, in what follows, the $\theta = 0^\circ$ direction (as well as any other, e.g., at $\theta = \pm 60^\circ$, $\pm 120^\circ$, and 180° which are equivalent by symmetry) is referred to as the "most unstable direction."

The synchronized nonlinear state of the crystal layer oscillations happened to be highly anisotropic; see Fig. 3. For instance, inside the first Brillouin zone, the hot spot located at $\theta = 60^\circ$ is about nine times brighter than its "counterpart" located at $\theta = -120^\circ$ [Fig. 3(a)]. The hot spots expected to be at $\theta = -60^\circ$ and 120° by symmetry have astonishingly disappeared. Therefore the energy spectrum of the synchronized hybrid mode oscillations is strongly intensity and angle modulated. In this sense, the hexagonal symmetry of the crystal state is broken.

Note that "spontaneous" symmetry breaking phenomenon is a typical behavior for, e.g., driven colloids [48]. This phenomenon explains rigorously the asymmetry of the escape directions and the chirality of the defect configurations revealed by the newly nucleated dislocations in 2D complex plasma experiments [49,50].

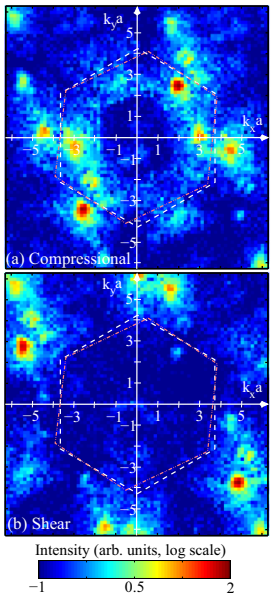

FIG. 3. (Color online) Spectrum of the particle velocity fluctuations in the $\{k_x, k_y\}$ plane integrated over the frequency in the range 14 Hz $< f <$ 18 Hz. (a) Compressional component. (b) Shear component. The white dashed lines show the border of an ideal (theoretical) first Brillouin zone. The dotted-dashed pink lines show the border of the real first Brillouin zone obtained from the time averaged structure factor $S(\mathbf{k})$. The bright hot spots located inside this zone are well recognizable in the compressional spectrum by the higher energy concentration. Their positions in the first half of the Brillouin zone are $k_1 a = 3.0 \pm 0.2$, $\theta_1 = (3 \pm 5)^\circ$, and $k_2 a = 3.2 \pm 0.3$, $\theta_2 = (60 \pm 7)^\circ$. Note an asymmetry effect: the 60° hot spot is certainly brighter and no hot spot is observed at -60°. A large-scale inhomogeneity of the monolayer is most probably responsible for all of the observed anisotropy.

As can be seen in Fig. 3(a), the hot spot positioned, for instance, along a $k_x > 0$ semiaxis is located in the $\mathbf{k}$ map at $k_x = k_{\mathrm{hyb}}$, which is close to the very right border of the first Brillouin zone k_{Br}, still distinguishably well separated from it:

$$k_{Br}a = 2\pi/\sqrt{3} > k_{\mathrm{hyb}}a \simeq \pi, \ (k_{Br} - k_{\mathrm{hyb}})/k_{\mathrm{hyb}} \simeq 15\%.$$

The accuracy of given measurements, around 5–10%, allows us to certainly state this.

It should also be noted that in Fig. 3(b), one can see a slight excitation of shear waves in the direction of main instability (especially at 60°). Since the theory predicts that the hybrid mode does not have a shear component, this is quite surprising. However, the intensity of the shear component is around two orders of magnitude less than the compressional component. This probably originates in the nonlinearity of the coupled waves.

B. Partial synchronization

The evolution of the cumulative probability $p(f_{\mathrm{hyb}})$ to find the instantaneous frequency inside the frequency band 14–18 Hz around the hybrid resonance $f_{\mathrm{inst}} \sim f_{\mathrm{hyb}}$ is presented in Fig. 4. At start ($t < 0.5$ s), the frequency synchronization probability is low. Then, as the mode-coupling instability sets in, the probability gradually increases as more and more particles get locked at the hybrid frequency. Between $t = 2.5$ s and $t = 3$ s, there appears a significant fraction of the particles that oscillate at the hybrid frequency, indicating emergence of the partial frequency synchronization state. When the crystalline suspension melts (at $t > 3$ s), the cumulative probability drops down stepwise to the lowest level ~0.05 indicating no frequency synchronization, and, hence, no mode coupling. Only the central parts of the monolayer were involved in calculations, half in size compared to those used to assemble the phase distribution maps shown on top in Fig. 4.

Note that sharp change in the phase locking probability is typical for the dynamical phase transitions, e.g., for Josephson junction arrays [14].

The pair correlation functions shown in the inset in the bottom panel of Fig. 4 demonstrate partial degradation of the crystalline order during the transitions between the synchronized and desynchronized states.

The snapshots of the instantaneous phase variation during the mode-coupling instability are presented in the top panels of Fig. 4. The phase locking proceeds as follows:

(i) At the beginning at $t < 1$ s, no recognizable synchronization pattern can be extracted and the instantaneous phases appear to be randomly distributed over the crystal layer.

(ii) Starting from $t \simeq 1.3$ s (first map shown on top in Fig. 4), short rows of in-phase oscillating particles can be detected in the central part of the crystal, indicating that partial synchronization of the particle motions takes place.

(iii) With time passed, at $t = 2.16$ s, rows of the in-phase oscillating particles elongate as more particles become involved in synchronization (second map shown on top in Fig. 4). It is worth mentioning that neighboring rows of the synchronically oscillating particles are moving almost in antiphase (i.e., having a phase difference $\Delta\phi \simeq \pi$). Note also that the motion of the synchronically moving particles is strongly "polarised" in the $\theta = 60^\circ$ direction.

(iv) Later on, at $t = 2.94$ s (third map shown on top in Fig. 4), two types of the phase alignment, one oblique (corresponding to the wave propagation angle $\theta \simeq 60^\circ$) and another almost vertical (corresponding to the wave propagation angle $\theta \simeq 0^\circ$), are clearly seen. Apparently, they correspond to two equivalent directions, by symmetry, in the crystal. The synchronization effect can also be well identified through increase in the mean value of the synchronization index $\langle\sigma\rangle$ (averaged over particles). The averaged Shannon entropy of the cental part of the crystal (blue line in bottom panel of

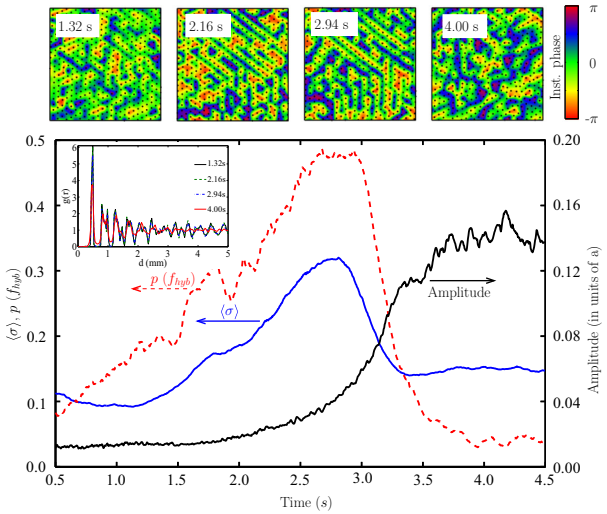

FIG. 4. (Color online) (top) Consecutive snapshots (a 300×300-pixel area of the original video) indicating the instantaneous phase distribution for desynchronized phase states (the very left and right images, $t = 1.32$ s and $t = 4.00$ s), and during the synchronization state (two middle images, $t = 2.16$ s and $t = 2.94$ s). Black dots show the position of the particles. (bottom) Evolution of the cumulative probability $p(f_{\rm hyb})$ (red dashed curve) to find a particle with an instantaneous frequency in the band 14 Hz $< f <$ 18 Hz around $f_{\rm hyb}$, the mean value of the synchronization index $\langle\sigma\rangle$ (averaged over particles, solid blue curve) and the averaged instantaneous amplitude of the particle oscillations (solid black curve). Performing the averaging, about 150 particle tracks at the center of the crystal (a 145×145-pixel area of the original video) were taken into account. The inset shows the radial pair correlation functions taken at the indicated time moments.

Fig. 4) grows almost linearly during the first 1.5 s, and shows a maximum at the most synchronized state.

(v) The lifetime of the synchronized state is about $\Delta t = 1$ s in our conditions. It is important to emphasize that the synchronization pattern self-assembles (and then disappears after a while) almost simultaneously in the phase-locking and frequency-locking processes. It is also worth noting that the degree of phase synchronization is maximal when the probability to find the frequency locked in the vicinity of the hybrid resonance is also maximal; see blue and red curves in Fig. 4. Notice that phase and frequency synchronization starts at small but finite amplitude of particle oscillations. It can be clearly seen in Fig. 4 that the amplitude of the particle oscillations (solid black line) is nearly exponentially growing during the synchronization period. It corresponds fairly well to the theoretical expectations [37].

(vi) The pair correlation function $g(r)$ (see the inset in Fig. 4) shows that the crystalline structure is preserved for a surprisingly long time. Nonetheless, at $t > 3$ s, when the oscillations become too intense, the synchronization degree goes down indicating that the phase locking no longer takes place and the particle oscillations desynchronize (see fourth map shown on top of Fig. 4). The crystal melts and the partial synchronization state is lost.

C. Tracks of synchronically oscillating particles

To study in detail the out-of-plane particle vibrations, the mode-coupling induced crystal melting process was recorded from the side of the monolayer at a frame rate of 103.56 fps (see Fig. 1). The trajectories of two neighboring particles were traced and extracted from the recorded sequence of the side-view images. These trajectories are presented in Fig. 5. The time averaged values were subtracted from the actual particle positions in order to emphasize the oscillatory part of the particle movements. Both particles exhibit an oscillatory motion at the hybrid frequency $f_{\rm hyb} \simeq 16.5 \pm 0.8$ Hz. Their motion consists of the vertical ("out-of-plane") and horizontal ("in-plane") approximately equally energized components. This fact is in a fairly good agreement with that theoretically expected [23,25,37,51]. It is also worth noting that the trajectories shown in Fig. 5, belonging to the neighboring

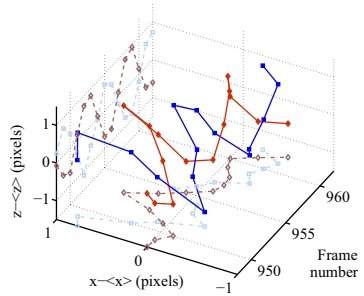

FIG. 5. (Color online) Trajectories of two neighbor particles [red (plain diamond symbols) and blue (plain square symbols) plain lines] exhibiting a periodic motion at the hybrid frequency $\simeq 16.5 \pm 0.8$ Hz in both the vertical and horizontal directions. The dashed light-blue (opened square symbols) and light-red (opened diamond symbols) lines are the projection on the (x,t) and (z,t) planes.

chains of particles, present antiphase oscillations in pretty good agreement with that shown in Fig. 4. (The measured phase difference is in the z direction, $\langle\Delta\phi_z\rangle = (1.03 \pm 0.10)\pi$, and in the x direction, $\langle\Delta\phi_x\rangle = (1.49 \pm 0.70)\pi$. The large error in the last case can be explained by the fact that the laser sheet was not properly aligned along the crystal main axis.)

The interpenetrating antiphase oscillating "sublattices" is the general pattern most closely explaining synchronization in a 2D plasma crystal; see Fig. 6. In this sense, the synchronized state of a 2D complex plasma obeys the common well-established rule stated in Ref. [1]: "symmetry breaking governs the ways that coupled oscillators can behave."

V. DISCUSSION AND CONCLUSION

The equation of motion of each particle in an infinite quasi-2D crystal can be written as

$$m\frac{d^2\mathbf{r}_j}{dt^2} = -m\nu\frac{d\mathbf{r}_j}{dt} - m\Omega_{\rm conf}^2(z_j - z_{eq})\mathbf{e}_z + \sum_{j'\neq j}\mathbf{F}_{jj'} + \mathbf{L}_j, \tag{7}$$

where m is the mass of the microparticles, $\mathbf{r}_j = \{x_j, y_j, z_j\}$ is the coordinate of the jth particle, z_{eq} is the vertical equilibrium coordinate same for all particles (the particles are assumed to be monodisperse), $\mathbf{e}_z$ is the unit vector in the vertical z direction, ν is the neutral gas drag coefficient, $\Omega_{\rm conf} = 2\pi f_v$ is the confinement parameter of the vertical confinement potential well (here assumed to be parabolic). The Langevin force is defined as

$$\langle\mathbf{L}_j(t)\rangle = \mathbf{0}, \quad \langle\mathbf{L}_j(t+\tau)\mathbf{L}_k(t)\rangle = 2\nu m T\delta_{jk}\delta(\tau),$$

where T is the temperature of the background gas (thermostat) in energy units [here, δ_{jk} is the Kronecker δ and $\delta(\tau)$ is the Dirac δ function]. $\mathbf{F}_{jj'} = \mathbf{F}_{jj'}^{(Y)} + \mathbf{F}_{jj'}^{(w)}$ is the interaction force

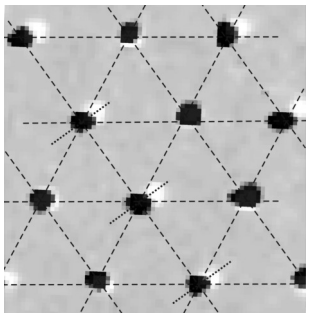

FIG. 6. Two superposed images of the lattice layer separated in time by a half period ($\Delta t \simeq 0.032$ s). The absolute time moment, $t \simeq 2.7$ s, was taken close to the maximum of the synchronization index; see Fig. 4. The white and black dots represent the particle positions. The mean interparticle separation in the chosen region is $\langle a\rangle = 470 \pm 16$ μm. Three sets of parallel dashed lines are shown to guide the eye. The stacked images were shifted along the main deformation direction to graphically demonstrate the character of the particle vibrations. The main deformation direction is as the dotted lines indicate. Note that in this direction the lattice is about 7–9% more compact. Importantly, the distance between the in-phase oscillating rows of particles is kept nearly constant.

between the two particles. This force consists of the screened Coulomb interaction

$$\mathbf{F}_{jj'}^{(Y)} = Q^2\frac{\mathbf{r}_{jj'}}{r_{jj'}^3}\left(1 + \frac{r_{jj'}}{\lambda_D}\right)\exp\left(-\frac{r_{jj'}}{\lambda_D}\right)$$

and the ion-wake-mediated interaction force $\mathbf{F}_{jj'}^{(w)}$, introduced, e.g., in Ref. [23]. In [23], by using a simple model, in which the ion wake was modelled by a pointlike positive charge located at a fixed distance below the particle, it was shown that the longitudinal in-plane and transverse out-of-plane wave modes $\omega(\mathbf{k})$ merge at a certain critical value of $\Omega_{\rm conf}$. Strongly coupled vertical and horizontal particle movements result in the formation of the hybrid mode. The hybrid mode emergence is characterized by a positive growth rate, which can trigger the mode-coupling instability (see Refs. [23,25,37] for details). Calculations done for a more refined wake potential model (performed in Refs. [34,35]) do not change the main characteristics of the mode coupling. According to [23,25,37,51], the hybrid mode has both in-plane longitudinal and out-of-plane transverse components, which are equally strong. In Ref. [25], it is also shown that the coupling occurs close to the boundary of the first Brillouin zone. All these predictions are well in line with our observation results.

As can be seen in Figs. 2 and 3, most of the spectral energy of fluctuations is concentrated in the hybrid modes excited in the most unstable direction (i.e., for $\theta = 0^\circ$ in our adopted frame of reference). Consequently, the particle motion surveyed from the top view should be mainly seen as

oscillations around the equilibrium positions, occurring in this direction at the hybrid frequency. Figure 5 confirms that the hybrid mode has both the vertical and horizontal components. In Fig. 4, it can be seen that the entire rows comprising 10–20 particles have the same instantaneous phase, especially at the latest stage of the instability (before the crystal melts). This effective "one-dimensionalization" by phase and frequency locking deeply affects the synchronization pattern. As already mentioned in the previous section, it can also be seen in Fig. 4 that every two consecutive rows containing "in-phase" moving particles oscillate almost in antiphase with each other. The latter can be explained by the fact that the hybrid mode with synchronized particle motion has a wave number $k \simeq k_{\mathrm{hyb}}$ closely obeying the relationship $ka \simeq k_{\mathrm{hyb}}a \simeq \pi$. Since the wave oscillations of the particle j are proportional to $e^{i\mathbf{k}\cdot\mathbf{r}_j}$, we immediately conclude that for such k the motion of neighboring particles should indeed be almost antiphase; see also Ref. [23].

When the instability is triggered, only the oscillations associated with the hybrid mode can surpass the damping, while all other wave modes tend to equilibrium with the surrounding plasma. Consequently, the kinetic energy is accumulated in the hybrid mode and the amplitude of the corresponding oscillations grows exponentially, hiding any motion related to other modes sustained in the crystal. This effect explains why the particle motion gets synchronized with time in the direction of the main instability, and the amplitude exhibits an exponential growth (see Fig. 4). Moreover, it is easy to show that, by making a second order Taylor expansion of the force between two neighbor particles, a coupling between the particle phases of both the in-plane motions and out-of-plane motions exists (i.e., terms in $x_j z_{j+1}$, $z_j x_{j+1}$, $x_j x_{j+1}$, and $z_j z_{j+1}$, which make a dependence of the force exerted on the jth particle on the horizontal and vertical phases of the $(j+1)$th particle automatically appear). It is well known that oscillators with any phase-dependent interaction can evolve until their phases are (partially) synchronized [12].

Since the hybrid mode with maximal increment has only a very weak shear in-plane component (Fig. 3), it naturally occurs that rows of particles which belong to equivalent elementary cells must have synchronized motion (two cells are equivalent when the translation necessary to pass from one to the other results in a phase shift such that $\Delta\Phi \mod 2\pi = 0$).

When the amplitude of motion is too large, the monolayer becomes disordered and the synchronization power naturally vanishes.

In Fig. 4, it can be seen that only two of three possible equivalent by symmetry directions were excited. We believe that the third direction has a higher excitation level due to inhomogeneity of the horizontal confinement, leading to inhomogeneities in the density of the crystal, breaking the symmetry of synchronization pattern.

It is worth noting that despite synchronization in plasma crystals was so far never systematically studied, traces of the synchronized particle motion could be also detected in Ref. [36] (especially at a low discharge power and low gas pressure). Interestingly, when the crystal layer is not circular but elliptical, the synchronization pattern seems to be preferentially observed in the direction of the minor axis of the ellipse.

Thus, we have shown that during the mode-coupling induced melting, the formation of the unstable hybrid mode leads to the partial synchronization of the particle motion in the direction of the main instability. It was evidenced by analysis of the instantaneous phase, instantaneous frequency, and synchronization index (Shannon entropy). The frequency and the phase synchronization processes could be explained by the fact that only wave modes at the hybrid frequency have a positive growth rate while the other modes are well attenuated by the damping.

ACKNOWLEDGMENTS

This work was supported by the European Research Council under the European Union's Seventh Framework Programme (FP7/2007-2013), ERC Grant Agreement No. 267499, and by the French-German PHC PROCOPE program (Project No. 28444XH/55926142). The authors would like to thank Dr. O. Agullo, Dr. D. Escande for fruitful discussions, and Dipl. Ing. M. Zhdanova for help.

[1] S. H. Strogatz and I. Stewart, Sci. Am. **269**(6), 102 (1993).
[2] M. Bennett, M. F. Schatz, H. Rockwood, and K. Wiesenfeld, Proc. R. Soc. London Ser. A **458**, 563 (2002).
[3] N. Wiener, *Cybernetics; or Control and Communication in the Animal and the Machine* (Wiley, New York, 1948).
[4] A. T. Winfree, J. Theor. Biol. **16**, 15 (1967).
[5] S. H. Strogatz, Nature (London) **410**, 268 (2001).
[6] S. H. Strogatz, *Sync: The Emerging Science of Spontaneous Order* (Hyperion, New York, 2003).
[7] J. A. Freund, L. Schimansky-Geier, and P. Hänggi, Chaos **13**, 225 (2003).
[8] A. Arenas, A. Díaz-Guilera, J. Kurths, Y. Moreno, and C. Zhou, Phys. Rep. **469**, 93 (2008).
[9] H. G. Winful and L. Rahman, Phys. Rev. Lett. **65**, 1575 (1990).
[10] T. Heil, I. Fischer, W. Elsässer, J. Mulet, and C. R. Mirasso, Phys. Rev. Lett. **86**, 795 (2001).
[11] E. A. Rogers-Dakin, J. García-Ojalvo, D. J. DeShazer, and R. Roy, Phys. Rev. E **73**, 045201 (2006).
[12] Y. Kuramoto, *Chemical Oscillations, Waves, and Turbulence* (Springer-Verlag, New York, 1984).
[13] R. Mirollo and S. Strogatz, SIAM J. Appl. Math. **50**, 1645 (1990).
[14] K. Wiesenfeld, Physica B: Condens. Matter **222**, 315 (1996).
[15] G. E. Morfill and A. V. Ivlev, Rev. Mod. Phys. **81**, 1353 (2009).
[16] D. Samsonov, A. V. Ivlev, G. E. Morfill, and J. Goree, Phys. Rev. E **63**, 025401 (2001).
[17] S. Nunomura, D. Samsonov, and J. Goree, Phys. Rev. Lett. **84**, 5141 (2000).
[18] V. A. Schweigert, I. V. Schweigert, V. Nosenko, and J. Goree, Phys. Plasmas **9**, 4465 (2002).
[19] D. Samsonov, S. Zhdanov, and G. Morfill, Phys. Rev. E **71**, 026410 (2005).

[20] L. Couëdel, D. Samsonov, C. Durniak, S. Zhdanov, H. M. Thomas, G. E. Morfill, and C. Arnas, Phys. Rev. Lett. **109**, 175001 (2012).
[21] S. V. Vladimirov, P. V. Shevchenko, and N. F. Cramer, Phys. Rev. E **56**, R74 (1997).
[22] D. H. E. Dubin, Phys. Plasmas **7**, 3895 (2000).
[23] A. V. Ivlev and G. Morfill, Phys. Rev. E **63**, 016409 (2000).
[24] K. Qiao and T. W. Hyde, Phys. Rev. E **68**, 046403 (2003).
[25] S. K. Zhdanov, A. V. Ivlev, and G. E. Morfill, Phys. Plasmas **16**, 083706 (2009).
[26] O. Ishihara and S. V. Vladimirov, Phys. Plasmas **4**, 69 (1997).
[27] M. Lampe, G. Joyce, G. Ganguli, and V. Gavrishchaka, Phys. Plasmas **7**, 3851 (2000).
[28] A. Melzer, V. A. Schweigert, and A. Piel, Phys. Scr. **61**, 494 (2000).
[29] L.-J. Hou, Y.-N. Wang, and Z. L. Mišković, Phys. Rev. E **64**, 046406 (2001).
[30] S. V. Vladimirov, S. A. Maiorov, and O. Ishihara, Phys. Plasmas **10**, 3867 (2003).
[31] A. Samarian, S. Vladimirov, and B. James, JETP Lett. **82**, 758 (2005).
[32] W. J. Miloch, Plasma Phys. Controlled Fusion **52**, 124004 (2010).
[33] R. Kompaneets, U. Konopka, A. V. Ivlev, V. Tsytovich, and G. Morfill, Phys. Plasmas **14**, 052108 (2007).
[34] T. B. Röcker, A. V. Ivlev, R. Kompaneets, and G. E. Morfill, Phys. Plasmas **19**, 033708 (2012).
[35] T. B. Röcker, S. K. Zhdanov, A. V. Ivlev, M. Lampe, G. Joyce, and G. E. Morfill, Phys. Plasmas **19**, 073708 (2012).
[36] L. Couëdel, V. Nosenko, A. V. Ivlev, S. K. Zhdanov, H. M. Thomas, and G. E. Morfill, Phys. Rev. Lett. **104**, 195001 (2010).
[37] L. Couëdel, S. K. Zhdanov, A. V. Ivlev, V. Nosenko, H. M. Thomas, and G. E. Morfill, Phys. Plasmas **18**, 083707 (2011).
[38] J. A. Acebrón, L. L. Bonilla, C. J. Pérez Vicente, F. Ritort, and R. Spigler, Rev. Mod. Phys. **77**, 137 (2005).
[39] A. V. Ivlev, U. Konopka, G. Morfill, and G. Joyce, Phys. Rev. E **68**, 026405 (2003).
[40] J. D. Williams, E. Thomas, L. Couëdel, A. V. Ivlev, S. K. Zhdanov, V. Nosenko, H. M. Thomas, and G. E. Morfill, Phys. Rev. E **86**, 046401 (2012).
[41] V. Nosenko, A. V. Ivlev, S. K. Zhdanov, M. Fink, and G. E. Morfill, Phys. Plasmas **16**, 083708 (2009).
[42] S. S. Rogers, T. A. Waigh, X. Zhao, and J. R. Lu, Phys. Biol. **4**, 220 (2007).
[43] We explored a range of the particle numbers from 1000 to 20 000.
[44] K. O. Menzel, O. Arp, and A. Piel, Phys. Rev. E **83**, 016402 (2011).
[45] See Supplemental Material at http://link.aps.org/supplemental/10.1103/PhysRevE.89.053108 for a video showing the evolution of the instantaneous phase distribution.
[46] R. Toth and A. F. Taylor, J. Chem. Phys. **125**, 224708 (2006).
[47] S. Nunomura, J. Goree, S. Hu, X. Wang, A. Bhattacharjee, and K. Avinash, Phys. Rev. Lett. **89**, 035001 (2002).
[48] C. Reichhardt and C. J. O. Reichhardt, Europhys. Lett. **68**, 303 (2004).
[49] V. Nosenko, S. Zhdanov, and G. Morfill, Philos. Mag. **88**, 3747 (2008).
[50] S. K. Zhdanov, M. H. Thoma, C. A. Knapek, and G. E. Morfill, New J. Phys. **14**, 023030 (2012).
[51] T. B. Röcker, A. V. Ivlev, S. K. Zhdanov, and G. E. Morfill, Phys. Rev. E **89**, 013104 (2014).

Full melting of a two-dimensional complex plasma crystal triggered by localized pulsed laser heating

L. Couëdel,[1,2,3,*] V. Nosenko,[4] M. Rubin-Zuzic,[4] S. Zhdanov,[4] Y. Elskens,[2] T. Hall,[3] and A. V. Ivlev[5]

[1]*Department of Physics and Engineering Physics, University of Saskatchewan, Saskatoon, SK S7N 5E2, Canada*
[2]*Aix-Marseille Université, CNRS, PIIM, UMR 7345, 13397 Marseille cedex 20, France*
[3]*Department of Physics, Auburn University, Auburn, Alabama 36849, USA*
[4]*Institut für Materialphysik im Weltraum, Deutsches Zentrum für Luft und Raumfahrt, D-82234 Weßling, Germany*
[5]*Max Planck Institute for Extraterrestrial Physics, D-85741 Garching, Germany*

(Received 9 October 2017; published 18 April 2018)

The full melting of a two-dimensional plasma crystal was induced in a principally stable monolayer by localized laser stimulation. Two distinct behaviors of the crystal after laser stimulation were observed depending on the amount of injected energy: (i) below a well-defined threshold, the laser melted area recrystallized; (ii) above the threshold, it expanded outwards in a similar fashion to mode-coupling instability-induced melting, rapidly destroying the crystalline order of the whole complex plasma monolayer. The reported experimental observations are due to the fluid mode-coupling instability, which can pump energy into the particle monolayer at a rate surpassing the heat transport and damping rates in the energetic localized melted spot, resulting in its further growth. This behavior exhibits remarkable similarities with impulsive spot heating in ordinary reactive matter.

DOI: 10.1103/PhysRevE.97.043206

I. INTRODUCTION

Complex (or dusty) plasmas are weakly ionized gases containing solid micro- or nanoparticles (often referred to as dust particles). Due to interactions with electrons and ions in the ambient plasma, dust accumulates a net electric charge [1–3]. In laboratory low-pressure gas discharges, this charge is negative due to the high mobility of the electrons. By injecting monosized spherical microparticles in the sheath of a capacitively coupled radio-frequency (cc-rf) discharge, it is possible for particles to form a monolayer. This is a result of all the microparticles levitating at the same height in the sheath region above the lower electrode where the electric field is strong enough to balance gravity and ensure stiff confinement [4,5]. Under specific conditions, they form strongly coupled ordered structures known as two-dimensional (2D) complex plasma crystals [6–11].

2D complex plasmas are often used as model systems for studies of generic phenomena occurring in liquids and crystals at the kinetic (particle) level [3]. In such systems, it is indeed possible to obtain complete information about the state of the whole system of particles in the kinetic $(\mathbf{x},\mathbf{v})$-space. This offers an important advantage for the investigation of collective processes occurring in strongly coupled media including melting and recrystallization [12–15], mass and heat diffusion [16], solitons and shocks [17].

In 2D complex plasmas, as in any strongly coupled 2D system, two in-plane wave modes can be sustained. In crystals, one of these modes is longitudinal, while the other is transverse, with both having an acoustic dispersion [18]. Since the strength of the vertical confinement due to the sheath electric field is finite, there is a third fundamental wave mode with negative optical dispersion associated with the out-of-plane oscillations [19,20]. The propagation of dust-lattice (DL) waves in these 2D lattices is often used as a diagnostic tool to determine parameters of the plasma crystal since the wave dispersion depends directly on them [8,21–23].

In the sheath of a cc-rf discharge, the ion stream coming from the bulk plasma and directed toward the electrode is focused downstream of each negatively charged particle of the monolayer and creates a perturbed region called the "ion (or plasma) wake." Ion wakes exert an attractive force on the neighboring particles. They can thus be considered as an (external) "third body" in the interparticle interaction resulting in non-reciprocal particle pair interactions [24–27]. Under certain conditions, this can lead to the formation of an unstable hybrid mode and the melting of the crystalline monolayer when the out-of-plane mode crosses the in-plane compressional mode: the mode coupling instability (MCI) [28–32]. The hybrid mode has clear fingerprints: critical angular dependence, a mixed polarization [33], distinct thresholds [30], and synchronization of the particle motion [34].

Wake-induced mode coupling is also possible in liquid complex plasma monolayers [31]. Remarkably, in such cases, the confinement and dust particle density thresholds, which are important features of the MCI in 2D complex plasma crystals, disappear and the instability has a higher growth rate. Consequently, conditions exist for which both the crystalline and the fluid states are viable, meaning no crossing of the modes in the crystal state and MCI growth rate high enough in the fluid state to prevent crystallization. This explains why, in many experiments, the crystallization of a monolayer is achieved only by increasing the gas pressure and/or the rf power (confinement strength is an increasing function of the discharge power [35]). In addition, it is in principle possible to trigger sporadic melting of a stable crystal which is not too far from the crystalline MCI threshold by applying a sufficiently strong mechanical perturbation.

*lenaic.couedel@usask.ca

 ©2018 American Physical Society

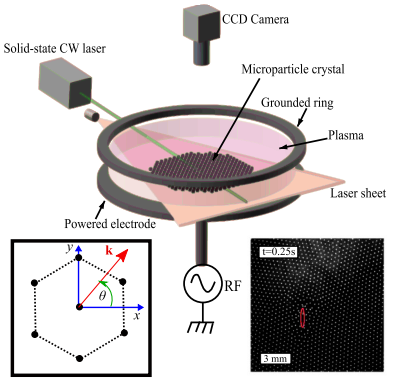

FIG. 1. Sketch of the experimental setup. The left inset shows an elementary cell of the hexagonal lattice and the frame of reference chosen in this article. The orientation of the wave vector **k** is measured in respect to the x axis. The right inset is a snapshot of the crystal after 0.25 s of laser heating. The red ellipse shows where the laser light beam interacts with the monolayer.

In this article, we demonstrate experimentally that wake-mediated resonant mode coupling can be induced in a principally stable 2D plasma crystal (no crossing of the modes) levitating in the sheath of a cc-rf discharge through an external excitation mechanism. Localized laser stimulation of the monolayer can trigger MCI-induced melting of the stable crystal if the injected energy is sufficient to create a melted spot in which the excess energy due to the fluid MCI is high enough to overcome neutral damping and heat conduction in the rest of the crystal. This causes a further increase in temperature leading to the extension of the melted area over the whole monolayer in a kind of uncontrolled positive feedback. This uncontrollable melting exhibits similarities with impulsive spot heating in ordinary matter.

II. EXPERIMENTAL SETUP

The experiments were carried out in a cc-rf glow discharge at 13.56 MHz (modified GEC chamber). A sketch of the setup is presented in Fig. 1. The argon pressure p_{Ar} was between 0.6 and 1 Pa, and the forward rf power P_{RF} was between 10 and 20 W. In the bulk discharge, the electron temperature was $T_e = 2.5$ eV and the electron density was $n_e = 2 \times 10^9$ cm^{-3} at $p_{\mathrm{Ar}} = 0.66$ Pa and $P_{\mathrm{RF}} = 20$ W [36]. Melamine-formaldehyde spherical particles with a diameter of $9.19 \pm 0.09\mu$m were levitated in the plasma sheath above the lower rf electrode and formed a horizontal monolayer, up to 60 mm in diameter. The dust particle suspension was illuminated by a horizontal laser sheet. The particles were imaged through a window at the top of the chamber by a 4 Megapixel Photron FASTCAM Mini WX100 camera at a speed of 250 frames per second.

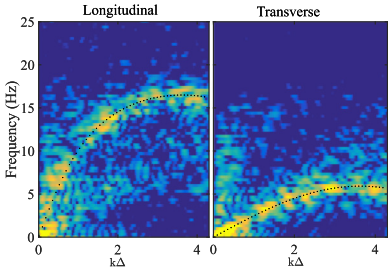

FIG. 2. Longitudinal and transverse current fluctuation spectra at an angle $\theta = 0°$. The dotted black curves represent the fitted dispersion relations.

The particle horizontal coordinates, x and y, and velocities, v_x and v_y, were then extracted with subpixel resolution in each frame. An additional side-view camera (Basler Ace ACA640-100GM) was used to confirm that we were indeed working with a single layer of particles. More details can be found in previous publications [30,32,37].

A SpectraPhysics Millennia PRO 15sJ solid-state 532-nm laser with a continuous-wave (cw) output power of 0.30–2 W was focused for a short period of time on the crystal. Particles in the laser spot were accelerated and the crystal was melted locally. At the crystal surface, the laser spot had an elliptical shape with its major axis in the direction of propagation and the illuminated area was $S_{\mathrm{L}} \simeq 0.32$ mm^2. The duration of the laser pulse was varied from 0.05 s to 0.65 s.

III. RESULTS

A. Characterization of the stable crystal

Prior to laser excitation, a stable 2D crystal with respect to the mode coupling instability (no crossing of the eigenmodes [30]) was levitated above the rf electrode. In the set of experiments presented in this article, the following discharge conditions were chosen: $p_{\mathrm{Ar}} = 1.04$ Pa and $P_{\mathrm{RF}} = 12$ W. For each run, the same microparticles were used and, in case of melting induced by the laser excitation, the monolayer was recrystallized by increasing argon pressure and rf power. The discharge conditions were then restored to the chosen values and the crystalline monolayer was allowed to relax a few minutes before the next laser pulse.

From the particle positions, the mean interparticle distance $\Delta = 415 \pm 10$ μm (number density $n_{2\mathrm{D}} = 675 \pm 20$ cm^{-2}) was obtained by calculating the pair correlation function and measuring the position of the first peak. Using particle velocities, the in-plane compressional and shear particle current fluctuation spectra of the crystalline monolayer were computed. In Fig. 2, the spectra are shown for a propagation angle $\theta = 0°$ (see inset of Fig. 1). No fingerprints of the unstable hybrid mode could be detected and only the eigenmodes were present. By fitting simultaneously the in-plane compressional and shear current fluctuation spectra

by the theoretical curves of a 2D Yukawa crystal [29], the microparticle charge $Q = -13800e \pm 500e$, where e is the elementary charge, the screening length $\lambda_D = 408 \pm 47$ μm and the screening parameter $\kappa = 1.0 \pm 0.15$ were obtained. The vertical confinement frequency was ∼25 Hz, which is in perfect agreement with a crystal far from the MCI threshold.

B. Propagation of the melting front: A threshold behavior

The laser beam was focused on the crystal so that only a few particles were accelerated during the pulse ($N \leqslant 50$). It created, at a few Δ in front of the laser spot position in the direction of laser light propagation, a small melted spot (1–4 mm in diameter) containing particles having high velocities. Depending on the pulse duration and the laser power, the melted area recrystallized or expanded over the whole crystalline monolayer. By tracking the particles during and after the laser pulse, the evolution of the particle kinetic energies was measured, and the energy injected by the laser into the crystal was estimated. At the end of the laser pulse, the total kinetic energy of the particles in the camera field of view (FoV) was at its maximum. However, the particles in the melted spot had trajectories directed along the direction of the laser beam. By looking at the first and second moments of the velocity distribution function in x and y, thermalization due to collisions with other particles was completed after $t_{th} = 0.5$ s (similar Maxwellian velocity distribution centered on 0 in x and y [38]).

In Table I, the sum of the kinetic energies of the particles $K_t = \sum_i K_i(t)$ (total energy) in the camera FoV at the end of the laser pulse $[K_t(t_{on})]$ and after thermalization ($[K_t(t_{on} + t_{th})]$ are listed for the different runs. As expected, at a given laser power, the total energy increased with the pulse duration. The energy after thermalization was slightly smaller due to damping by the neutral background and heat transport in the whole crystalline suspension (which was not entirely comprised in the FoV). Before the laser pulse, the average kinetic temperature of the particles was estimated at $T_0 = 0.13 \pm 0.05$ eV, giving a total energy in the field of view $K_t < 800$ eV. Thus, the measured total energy just after the laser pulse corresponds roughly to the energy injected by the pulse into the crystal since it was always much higher than a few keV.

In Fig. 3, the state of the monolayer at the end of the experiment (recrystallized or fully melted) is plotted as a function of the total energy after thermalization. As can be seen, when $K_t(t_{on} + t_{th})$ reached $= 40 \pm 1$ keV (corresponding to $t_{on} \geqslant 500$ ms at $P_l = 0.85$ W), the crystalline monolayer fully melted. The observed step function is a clear sign of a threshold phenomenon.

In Figs. 4 and 5, we illustrate the difference between two experiments showing either recrystallization or melting (experiments 19 and 20, respectively; see Table I). In Fig. 4, the monolayer Voronoi map (colored according to $|\Psi_6|$) and the kinetic energy map are presented for two experiments using the same laser pulse setting. Here, $\Psi_6(j) = (1/N)\sum_{l=1}^{N} e^{i\theta_{jl}}$, where N is the number of closest neighbors and θ_{jl} is the angle of vector linking the jth to the lth particle with respect to the x axis. This order parameter $|\Psi_6|$ represents the deformation of a hexagonal cell from a perfect hexagon ($|\Psi_6| = 1$). As can be seen, before the laser pulse ($t = 0$ s), the crystalline monolayer was cold in both cases with $T_0 \simeq 0.13$ eV and the crystals were almost perfect with only a few dislocations and a few grain boundaries. At the end of the laser pulse ($t = 0.55$ s), a melted spot (high kinetic energy and low values of $|\Psi_6|$) could be seen in the center of the frame. In both cases, compressional waves traveled preferentially in the direction of the laser beam (positive y direction) due to the nonthermalized motion of the excited particles. At $t = 2$ s $> t_{on} + t_{th}$, the particles were thermalized and compressional waves emerged from the hot spot isotropically. It was observed that, in both cases, the melted spot became slightly larger than at $t = 0.55$ s due to heat transport in the crystalline monolayer. However, the spot in experiment 20 showed a slightly larger melted spot and the particle kinetic energies were slightly higher.

This observation is confirmed in Fig. 5, in which the time evolution (after the laser pulse) of the radius of the melted zone (MZ) and the evolution of the total kinetic energy in the MZ and the camera FoV are plotted. In this article, the MZ is defined as the area in which the mean kinetic energy is greater than 30 eV [39]. As can be seen in both experiments, most of the kinetic energy in the FoV is carried by the particles in the MZ, though in experiment 19, the injected energy and the radius of the MZ were slightly smaller. In both cases the kinetic energy and MZ radius initially increased, but in experiment 19

TABLE I. Laser power P_l, pulse duration t_{on}, the sum K_t of the kinetic energy of the particles in the camera FoV, and, depending on whether the crystal recrystallized at the end of the laser pulse or melted, the transition time t_{tr} before recrystallization or the inverse of energy growth rate γ_g^{-1}, respectively. The boldface entries are the experiments for which a full melting of the monolayer was induced by the laser pulse.

Expt.	P_l (W)	t_{on} (s)	$K_t(t_{on})$ (keV)	$K_t(t_{on}+t_{th})$ (keV)	t_{tr}, γ_g^{-1} (s)
1	0.3	0.50	6.22 ± 0.5	3.1 ± 0.1	—
2	0.35	0.50	7.65 ± 0.5	3.6 ± 0.1	—
3	0.40	0.50	11.3 ± 1.0	4.8 ± 0.2	—
4	0.45	0.50	13.0 ± 1.4	7.7 ± 0.5	—
5	0.50	0.50	18.2 ± 2.0	8.3 ± 0.2	—
6	0.55	0.50	23.0 ± 2.1	14.6 ± 0.5	—
7	0.60	0.50	21.9 ± 3.0	15.8 ± 0.2	—
8	0.65	0.50	25.5 ± 1.5	21.0 ± 0.4	0.59 ± 0.03
9	0.70	0.50	28.5 ± 2.4	20.9 ± 1.2	—
10	0.75	0.50	33.1 ± 3.5	23.0 ± 1.0	—
11	0.80	0.50	40.1 ± 1.3	37.1 ± 1.1	0.95 ± 0.03
12	0.85	0.30	14.4 ± 1.3	9.7 ± 0.4	—
13	0.85	0.40	42.8 ± 3.5	30.7 ± 0.6	0.53 ± 0.02
14	**0.85**	**0.50**	**48.1 ± 4.1**	**45.7 ± 0.7**	**0.92 ± 0.02**
15	0.85	0.50	34.3 ± 1.1	37.1 ± 0.5	1.86 ± 0.03
16	0.85	0.50	43.4 ± 3.2	35.0 ± 1.5	2.60 ± 0.10
17	**0.85**	**0.55**	**43.3 ± 2.7**	**40.9 ± 1.1**	**0.87 ± 0.04**
18	**0.85**	**0.55**	**52.4 ± 2.1**	**63.0 ± 1.8**	**1.26 ± 0.01**
19	0.85	0.55	42.6 ± 3.9	40.0 ± 1.3	3.13 ± 0.03
20	**0.85**	**0.55**	**49.9 ± 1.9**	**51.9 ± 1.2**	**0.97 ± 0.01**
21	**0.85**	**0.60**	**60.6 ± 1.3**	**62.2 ± 1.2**	**1.21 ± 0.01**
22	**0.85**	**0.65**	**64.1 ± 14.3**	**58.3 ± 10.2**	**1.21 ± 0.01**
23	2.00	0.05	12.0 ± 7.4	8.0 ± 0.2	—
24	**2.00**	**0.20**	**40.9 ± 3.6**	**41.0 ± 2.0**	**1.23 ± 0.01**

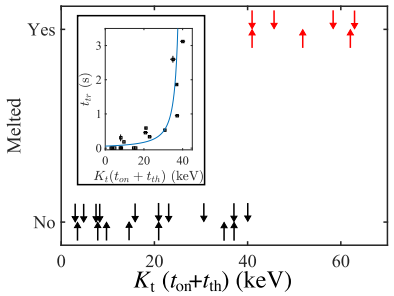

FIG. 3. State of the monolayer (red, melted or black, unmelted) at the end of the experiment as a function of $K_t(t_{on} + t_{th})$. Each experiment of Table I is indicated by an arrow of the appropriate color. A threshold at ∼40 keV is clearly identified. The inset shows the transition time before recrystallization sets in for injected energies below the melting threshold. The blue line is a guide for the eye.

the total energy inside the MZ became stable, meaning that the kinetic energy began to decrease. On the contrary, K_{MZ} continued to grow in the case of experiment 20. After ∼2.25 s, the MZ started to shrink in experiment 19 and the total energy started to decrease while both parameters kept growing in the case of experiment 20 (the energy growth seemed exponential).

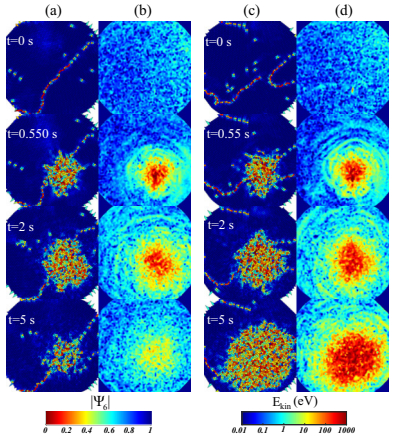

FIG. 4. $|\Psi_6|$ maps (a, c) and energy maps (b, d) of the crystal during Expts. 19 (a, b) and 20 (c, d) (see Table I). Each map is a square of 24.6 × 24.6 mm^2.

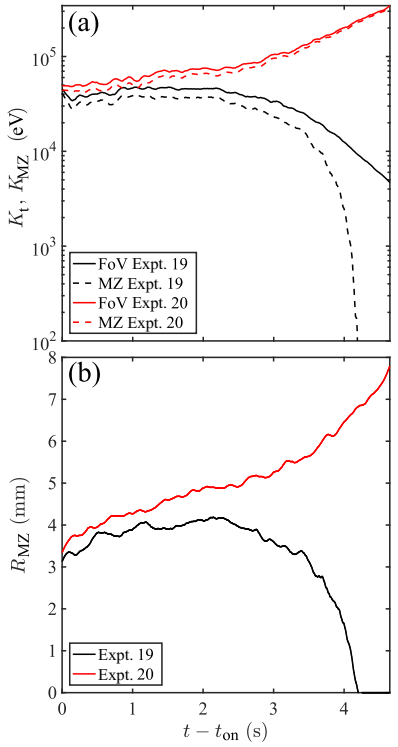

FIG. 5. (a) Evolution of the sum the kinetic energies of the particles in the field of view and in the melted zone as a function of time for Expts. 19 and 20 (see Table I). (b) Evolution of the radius of the melted zone as a function of time.

Finally, in the case of experiment 19, after ∼3.1 s, the total energy exhibited an exponential decay while the MZ was rapidly shrinking, denoting recrystallization. In experiment 20, the energy kept growing and the MZ eventually extended to the whole monolayer. After 3.5 s, the radius of the MZ grew quasi linearly with a velocity $v_{MZ} \sim 2$ mm/s. A snapshot of the monolayer during the final stage of both experiments can be seen in Fig. 4 ($t = 5$ s).

Another interesting observation is the existence of a transition period before the recrystallization sets in for injected energy below the melting threshold. For the purpose of analysis, the transition time t_{tr} is defined as the time before K_t exhibits

a clear exponential decay after the end of the laser pulse [40]. In experiment 19, the transition time was 3.13 s [see Fig. 5(a)]. As can be seen in the inset of Fig. 3, the transition time gets longer as the input energy gets closer to the induced-melting energy threshold (experimental values are listed in Table I). For the experiments with injected energy above the threshold the energy growth looked nearly exponential. In Table I, the measured growth times γ_g^{-1} are listed [41]. The average measured value was $\gamma_g^{-1} = 1.1 \pm 0.2$ s.

IV. DISCUSSION

As reported in the previous section, the laser-induced melting of the crystal exhibited a clear energy threshold: above a well-defined amount of energy injected by the laser, the full melting of the crystalline monolayer was triggered. The mechanism by which the monolayer melted can be understood when taking into account the existence of the MCI in fluid monolayers. It was indeed shown by Ivlev *et al.* [31] that the wake-induced coupling of wave modes always occurs in 2D fluid complex plasmas and, contrary to MCI onset in 2D complex plasma crystals, there is no confinement-density threshold. This means that for sufficiently low damping rates the energy input from the fluid MCI (i.e., energy transferred by the ion flow to the crystal) can prevent crystallisation of the monolayer. Moreover, if a large enough melted spot is induced in the crystalline monolayer, the energy input from the localized fluid MCI will not be dissipated rapidly enough (through neutral damping and heat conduction in the crystal), causing a further increase in temperature triggering the expansion of the melted area in an uncontrolled positive feedback. This mechanism will lead to the total destruction of the crystalline monolayer as observed for regular MCI-induced melting of 2D complex plasma crystals [30–32,42,43]. Such an "explosive melting" of a 2D complex plasma crystal has been recently studied in detail by Yurchenko *et al.* [43] and was found to be similar to impulsive spot heating and thermal explosion in ordinary matter [44].

In the presented experiments, the laser pulse created a localized melted spot in the crystal where the fluid MCI exists. The spatial temperature distribution $T(r,t)$ in a continuous reactive medium, including damping, can be described by the following heat equation [43,44]:

$$\frac{\partial T}{\partial t} = \frac{Q(T)}{Cn_{2D}} - \frac{2\gamma_d}{C}(T - T_0) + \frac{\chi}{r}\frac{\partial}{\partial r}\left(r\frac{\partial T}{\partial r}\right), \quad (1)$$

with the initial condition

$$T(r,0) = T_0 + \frac{E_l}{2\pi w_{MZ}^2 n_{2D} C}\exp\left(-\frac{r^2}{2w_{MZ}^2}\right), \quad (2)$$

where E_l is the energy injected by the laser pulse, w_{MZ} is the width of the melted zone, $C \simeq 2$–3 is the heat capacity per particle, γ_d is the Epstein damping rate (for our experimental conditions, $\gamma_d \simeq 1.21 \pm 0.13$ s^{-1} [45]), and χ is the thermal diffusivity.

In Eq. (1), the first term in the right-hand side is the heat input due to the fluid MCI. Since fluid MCI essentially develops when the correlations between the particles are largely destroyed (so that a horizontal layer, uniform and of infinite extent, can be considered [31]), it supposes a significant overheating compared to the melting temperature T_m of a 2D complex plasma crystal ($T_m \sim 10$–20 eV in our condition [46,47]). Consequently, the MCI heat source term requires the introduction of an activation temperature T_a well above T_m. It was indeed demonstrated that pair correlations are destroyed when the monolayer temperature is well above the melting temperature [48,49]. Accordingly, the fluid MCI heat source can be roughly modeled as a reaction rate governed by the Arrhenius law

$$\frac{Q(T)}{Cn_{2D}} = \frac{\gamma_{MCI}T_\infty}{C}e^{-T_a/T}, \quad (3)$$

which can be approximated by [43]

$$\frac{Q(T)}{Cn_{2D}} = \begin{cases} 0, & T < T_a, \\ \frac{\gamma_{MCI}T_\infty}{C}, & T \geqslant T_a, \end{cases} \quad (4)$$

where $\gamma_{MCI}T_\infty$ is the saturated fluid MCI heat source with the fluid MCI growth rate γ_{MCI} and the saturation temperature $T_\infty \sim 1$–3 keV. In a recent study on the melting front propagation in MCI-induced 2D crystal melting, the activation temperature was found to be $T_a \sim 150$ eV [43]. The saturation temperature T_∞ arises from the thermal spreading of the monolayer which inhibits the mode crossing and consequently the fluid MCI growth rate [31].

Since $T_0 \ll T_a$, we can neglect T_0. Equation (1) can be then written in a dimensionless manner,

$$\frac{\partial\Theta}{\partial\tau} = \lambda e^{-1/\Theta} - \Gamma\Theta + \frac{1}{\tilde{r}}\frac{\partial}{\partial\tilde{r}}\left(\tilde{r}\frac{\partial\Theta}{\partial\tilde{r}}\right), \quad (5)$$

where $\Theta = T/T_a$, $\tilde{r} = r/r^*$ with $r^{*2} = E_l/n_{2D}CT_a$, $\tau = t/t^*$ with $t^* = r^{*2}/\chi$. The initial condition becomes

$$\Theta(\tilde{r},0) = \frac{1}{2\pi\tilde{w}_{MZ}^2}\exp\left(-\frac{\tilde{r}^2}{2\tilde{w}_{MZ}^2}\right), \quad (6)$$

with $\tilde{w}_{MZ} = w_{MZ}/r^*$. The normalization $\int_0^{2\pi}\int_0^\infty \Theta(\tilde{r},0)\tilde{r}d\tilde{r}d\varphi = 1$ determines the characteristic length scale. Thus, in its dimensionless form, the problem is characterized by two numbers:

$$\lambda = \frac{\gamma_{MCI}T_\infty E_l}{C^2\chi n_{2D}T_a^2} \quad (7)$$

and

$$\Gamma = \frac{2\gamma_d E_l}{C^2\chi n_{2D}T_a} = \frac{2\gamma_d}{\gamma_{MCI}}\frac{T_a}{T_\infty}\lambda. \quad (8)$$

Equation (5) is similar to the one describing impulsive spot heating and thermal explosion in ordinary matter with the addition of a dimensionless damping coefficient Γ [43,44]. When there is no damping and the heating of a reactive medium occurs within a sufficiently localized spot (so it can be accurately described with a Dirac distribution), the subsequent thermal evolution is characterized only by λ which identifies a bifurcation between two distinct regimes. When exceeding a critical threshold, the heat equation exhibits rapid temperature growth. For a 2D system, the critical value is $\lambda_{cr}(\Gamma = 0) = 9.94$ [44]. The damping term increases the critical value: numerical estimates are, for example, $\lambda_{cr}(\Gamma = 1.5) \sim 17$ and $\lambda_{cr}(\Gamma = 2.5) \sim 21$. In our experimental conditions, we assume that the thermal diffusivity of the crystal was $\chi \sim 10$ mm^2/s [16]

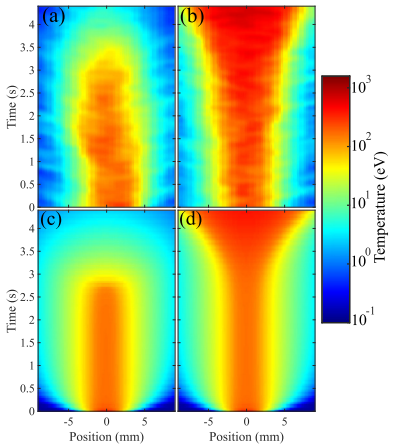

FIG. 6. Evolution of the temperature profile. (a) Experiment 19: recrystallization, (b) Experiment 20: melting. Solution of Eqs. (1) using the reaction model (4): (c) slightly below threshold, (d) slightly above threshold. For the numerical profiles, the following parameters were used: $\chi = 9$ mm^2/s, $\gamma_d = 1.2$ s^{-1}, $\gamma_{MCI} = 0.9$ s^{-1}, $T_\infty = 1800$ eV, $T_a = 105$ eV, $n_{2D} = 6.75$ mm^{-2}, $C = 2$, $w_{MZ} = 1.15$ mm and (c) $E_l = 40103$ eV ($\lambda = 24.2497$, $\Gamma = 3.7722$) and (d) $E_l = 40103.7$ eV ($\lambda = 24.2506$, $\Gamma = 3.7722$).

and $\gamma_{MCI} \sim \gamma_g \sim 0.9$ s^{-1}. By fitting the temperature distribution after laser excitation with a 2D Gaussian for experiments near threshold, the width of the melted zone was $w_{MZ} \sim 1$–2 mm [50], which is noticeably smaller than the characteristic length $r^* \sim 4.5$ mm. These experimental parameters yield the value of $\Gamma \sim 2$–4 and, at threshold energy, $\lambda \sim 10$–30, in remarkable agreement with the theoretical estimate. Note that the width of the MZ has a significant effect on the energy threshold since at a given injected energy a wider spot results in a significant portion of the energy being distributed over particles with a kinetic temperature below the activation temperature. Moreover, for large melted spots ($w_{MZ} \geqslant r^*$), the problem is no longer characterized by a single dimensionless number and the threshold depends on the temperature of the melted spot and its size [44,51].

In Fig. 6, the evolution of the temperature profile is presented for experiments 19 and 20 and the numerical solution of Eqs. (1) and (4). The input parameters have been chosen to reproduce qualitatively the experimental observations. As can be seen in all cases, the energy is transported from the MZ to the rest of the crystalline suspension. The instability provided energy to the microparticle suspension inside the fluid region, which is partially transported in the crystal through heat conduction and partially dissipated through neutral damping. For these reasons, the size of the melted area can slightly increase even if the total input energy is below the required melting threshold. As reported in the previous section, when increasing the amount of injected energy while staying below threshold (for example, increasing the duration of the laser pulse), the crystallization is delayed. This behavior was also observed in the numerical solutions and can be explained by the amount of energy pumped by the fluid MCI into the melted spot which depends directly on its size. Indeed, crystallization can occur only after enough energy has been removed from the MZ. Consequently, this suppresses the fluid MCI heat flux [Figs. 6(a) and 6(c)]. This transition period is longer for larger spots since a significantly larger amount of energy has to be removed due to the fluid MCI energy input. When the injected energy is slightly above the threshold, fluid MCI delivers more energy to the monolayer than what can be extracted away from the MZ which grows as a result [Figs. 6(b) and 6(d)]. The melting pattern is then similar to the one observed in the regular (crystal) MCI induced melting of a crystal [29–32,43].

In all experiments in which the melting was successfully induced, the MZ radius grew at a constant velocity. For $\tilde{r}$ large enough in Eq. (5), the last term on the right-hand side tends asymptotically toward $\partial^2\Theta/\partial\tilde{r}^2$, reducing the problem to one dimension. The reaction model Eq. (3) or (4) in the evolution Eq. (1) defines a bistable system, with two uniform stationary solutions [in the reduced version with $T_0 = 0$ and the rate Eq. (4), these states are 0 and $\Theta_{max} = \lambda/\Gamma$]. With inhomogeneous boundary conditions, the front profile is a heteroclinic connection between these two states, propagating at constant velocity v_{MZ}. As the MZ radius grows linearly, a self-similar solution $\Theta(\tilde{r},\tau) = \Theta(X)$, with $X = \tilde{r} - \tilde{v}_{MZ}\tau$, where $\tilde{v}_{MZ}$ is the dimensionless velocity of the melting front, can be obtained analytically using the approximation Eq. (4) [43],

$$\Theta(X) = \begin{cases} \exp(-\sigma_1 X), & X > 0, \\ \Theta_{max} + (1 - \Theta_{max})\exp(-\sigma_2 X), & X \leqslant 0, \end{cases} \quad (9)$$

with $\sigma_1 = (\tilde{v}_{MZ}/2) + \sqrt{4\Gamma + \tilde{v}_{MZ}^2}/2 > 0$ and $\sigma_2 = (\tilde{v}_{MZ}/2) - \sqrt{4\Gamma + \tilde{v}_{MZ}^2}/2 < 0$. The boundary conditions are $\Theta(+\infty) = 0$ and $\Theta(-\infty) = \Theta_{max}$. The position of the melting front is given by $\Theta(0) = 1$ and its velocity is $\tilde{v}_{MZ} = -\partial_\tau\Theta/\partial_X\Theta$. It exists only if the two partial derivatives are continuous, giving the condition

$$(1 - \Theta_{max})\sigma_2 = \sigma_1. \quad (10)$$

The velocity of the melting front is then straightforwardly obtained

$$\tilde{v}_{MZ} = \frac{\lambda - 2\Gamma}{\sqrt{\lambda - \Gamma}}. \quad (11)$$

For $\lambda > 2\Gamma$ (viz. $\Theta_{max} > 2$), the front velocity is positive, which corresponds to the melting of the monolayer, due to the fact that the final temperature is further away from the threshold T_a than the cold crystal is ($T_\infty - T_a > T_a - T_0 = T_a$). For $\Gamma < \lambda < 2\Gamma$ (viz. $1 < \Theta_{max} < 2$), the front velocity is negative, corresponding to recrystallization due to the fact that the melted state equilibrium temperature is closer to the activation threshold than the cold crystal is. The case $\lambda = 2\Gamma$ is the bifurcation case, for which the front would be stationary. It would be interesting to further investigate

this range, recalling that model Eq. (4) is very crude and does not yield accurate values for the actual front velocity, though being qualitatively relevant. Under our experimental conditions, $\tilde{v}_{MZ} \sim 0.5-5$ or $v_{MZ} \sim 1-10$ mm/s, which is in agreement with our measured value. This velocity yields the spatial decay exponents for the front, $\sigma_1 = (\lambda-\Gamma)/\sqrt{\lambda-\Gamma}$ and $\sigma_2 = \tilde{v}_{MZ} - \sigma_1 = -\Gamma/\sqrt{\lambda-\Gamma}$. The slope of the front and the temperature difference Θ_{max} yield an estimate $\Theta_{max}/\sigma_1 = \lambda/(\Gamma\sqrt{\lambda-\Gamma})$ for its width. Given the experimental ranges of λ and Γ, the front width is $\Theta_{max}/\sigma_1 \sim 1-3$ or in physical units 4.5–13.5 mm. This value is close to the one observed in Figs. 4 and 6.

Finally, in the framework of our model, the evolution of the total kinetic energy in the monolayer K_{tot} can be obtained

$$K_{tot}(t) = 2\pi n_{2D}\int_0^\infty T(r,t) r dr. \tag{12}$$

Multiplying Eq. (1) by n_{2D} and integrating over space, one obtains

$$\dot{K}_{tot} + \frac{2\gamma_d}{C}K_{tot} = S, \tag{13}$$

where the heat source S due to the fluid mode-coupling instability is [using the reaction model Eq. (4)]

$$S = 2\pi\int_0^\infty \frac{Q(T)}{C} r dr \simeq 2\pi n_{2D}\frac{\gamma_{MCI}T_\infty}{C}\int_0^{r_a(t)} r dr$$
$$\simeq \pi n_{2D}\frac{\gamma_{MCI}T_\infty}{C} r_a^2(t) = \pi n_{2D}\frac{\gamma_{MCI}T_\infty}{C} v_{MZ}^2 t^2, \tag{14}$$

where $r_a(t)$ is the front radius, such that $T(r_a,t) = T_a$. The solution of Eq. (13) is trivial and one immediately sees that, in the limit $t \to \infty$, $K_{tot} \propto t^2$. This result cannot be confirmed at the present time by experimental observations since the video recordings of the laser-induced melting were not long enough. In addition, using the reaction model Eq. (4), the stage of exponential growth reported in the experiments is lost. It has indeed been reported that, during MCI-induced melting in crystals, the microparticles kinetic temperature in the MZ grows exponentially until it saturates [32]. Moreover, in the present study, the total kinetic energy growth in the FoV seems to be nearly exponential (even though the videos were not long enough to recover the kinetic energy evolution over a significant energy interval to draw a firm conclusion). However, using the reaction model Eq. (3), the stage of exponential growth can be recovered. Indeed, the "source term" in Eq. (5) is

$$\Sigma(\Theta) = \lambda\exp(-1/\Theta) - \Gamma\Theta. \tag{15}$$

For $\lambda > \Gamma\exp(1)$ (which is always the case for $\lambda > \lambda_{cr}$), the source term Σ has two nonzero real roots: the unstable one $\Theta_1 = -1/W_{-1}(-\Gamma/\lambda) < 1$ and the stable one $\Theta_2 = -1/W_0(-\Gamma/\lambda) > 1$ where W_k is the kth branch of the Lambert W function. The maximum of Σ occurs at $\Theta_{gm} = -1/[2W_0(-0.5\sqrt{\Gamma/\lambda})]$, such that $\Theta_1 < \Theta_{gm} < \Theta_2$. Since $\Sigma'(\Theta_1) > 0$, the stage of exponential growth can be explained by the lower, unstable root. In the early stage of the instability, the dimensionless heat equation can be approximated by

$$\frac{\partial\Theta}{\partial\tau} - \frac{1}{\tilde{r}}\frac{\partial}{\partial\tilde{r}}\left(\tilde{r}\frac{\partial\Theta}{\partial\tilde{r}}\right) \simeq \Sigma'(\Theta_1)(\Theta-\Theta_1). \tag{16}$$

Given the experimental ranges of λ and Γ, the unstable root is $0.28 < \Theta_1 < 0.34$ and the instability growth rate is $5 < \Sigma'(\Theta_1) < 8$. Using our experimental parameters, the timescale is $t^* = 2-3$ s, giving a growth rate $1.7\ s^{-1} < \gamma_g < 4\ s^{-1}$. This range slightly overestimates the reported experimental value but, given the simplicity of our reaction rate model, it is in remarkable agreement. It nevertheless calls for more investigations and better modeling of the fluid MCI heat source in order to obtain the full physical picture of the energy input due to the fluid MCI.

V. CONCLUSION

To conclude, we have experimentally demonstrated that wake-mediated resonant mode coupling can be induced in a 2D plasma crystal through a localized pulsed laser heating. Due to the coexistence of a stable crystalline state and a melted state experiencing fluid MCI, this heating can trigger a rapid full melting of the crystalline monolayer. In a stable crystal (with respect to crystalline MCI), an energy threshold was observed. Below the threshold, recrystallization was always observed with a transition period which grew longer when approaching the threshold. The localized fluid MCI could not pump enough energy to the microparticle suspension to maintain the fluid state and propagate through the crystal. Above the threshold, the full melting of the crystal was observed due to the activated fluid MCI (i.e., the crystalline order of the whole complex plasma monolayer was rapidly destroyed). Remarkable similarities with impulsive spot heating in ordinary reactive matter were reported.

In future investigations, detailed studies of the threshold for various crystal parameters and laser spot sizes will be performed. The influence of the temperature of the fluid state on the MCI growth rate will be of particular interest.

ACKNOWLEDGMENTS

This work was partially supported by the French-German PHC PROCOPE Program (Project No. 35325NA/57211784). The authors thank Prof. E. Thomas Jr. and Dr I. Laut for fruitful discussions and suggestions. The authors also thank the anonymous referees who have helped to improve the article.

[1] A. Bouchoule, *Dusty Plasmas: Physics, Chemistry and Technological Impacts in Plasma Processing* (Wiley, New York, 1999).
[2] P. K. Shukla and A. A. Mamun, *Introduction to Dusty Plasma* (IOP Publishing, Bristol, 2002).
[3] G. E. Morfill and A. V. Ivlev, Rev. Mod. Phys. **81**, 1353 (2009).
[4] A. Brattli and O. Havnes, J. Vac. Sci. Technol. A **14**, 644 (1996).
[5] A. A. Samarian and B. W. James, Phys. Lett. A **287**, 125 (2001).
[6] D. H. E. Dubin, Phys. Plasmas **7**, 3895 (2000).
[7] A. Melzer, S. Nunomura, D. Samsonov, Z. W. Ma, and J. Goree, Phys. Rev. E **62**, 4162 (2000).

[8] S. Nunomura, D. Samsonov, and J. Goree, Phys. Rev. Lett. **84**, 5141 (2000).
[9] D. Samsonov, J. Goree, H. M. Thomas, and G. E. Morfill, Phys. Rev. E **61**, 5557 (2000).
[10] J. H. Chu and Lin I, Phys. Rev. Lett. **72**, 4009 (1994).
[11] H. Thomas, G. E. Morfill, V. Demmel, J. Goree, B. Feuerbacher, and D. Möhlmann, Phys. Rev. Lett. **73**, 652 (1994).
[12] V. A. Schweigert, I. V. Schweigert, A. Melzer, A. Homann, and A. Piel, Phys. Rev. Lett. **80**, 5345 (1998).
[13] A. Melzer, A. Homann, and A. Piel, Phys. Rev. E **53**, 2757 (1996).
[14] A. Melzer, V. A. Schweigert, I. V. Schweigert, A. Homann, S. Peters, and A. Piel, Phys. Rev. E **54**, R46 (1996).
[15] H. M. Thomas and G. E. Morfill, Nature **379**, 806 (1996).
[16] V. Nosenko, S. Zhdanov, A. V. Ivlev, G. Morfill, J. Goree, and A. Piel, Phys. Rev. Lett. **100**, 025003 (2008).
[17] D. Samsonov, S. Zhdanov, and G. Morfill, Phys. Rev. E **71**, 026410 (2005).
[18] K. Qiao and T. W. Hyde, Phys. Rev. E **68**, 046403 (2003).
[19] B. Liu, K. Avinash, and J. Goree, Phys. Rev. Lett. **91**, 255003 (2003).
[20] L. Couëdel, V. Nosenko, S. K. Zhdanov, A. V. Ivlev, H. M. Thomas, and G. E. Morfill, Phys. Rev. Lett. **103**, 215001 (2009).
[21] S. Nunomura, J. Goree, S. Hu, X. Wang, A. Bhattacharjee, and K. Avinash, Phys. Rev. Lett. **89**, 035001 (2002).
[22] S. Nunomura, S. Zhdanov, G. E. Morfill, and J. Goree, Phys. Rev. E **68**, 026407 (2003).
[23] S. Nunomura, S. Zhdanov, D. Samsonov, and G. Morfill, Phys. Rev. Lett. **94**, 045001 (2005).
[24] O. Ishihara and S. V. Vladimirov, Phys. Plasmas **4**, 69 (1997).
[25] S. Nunomura, T. Misawa, N. Ohno, and S. Takamura, Phys. Rev. Lett. **83**, 1970 (1999).
[26] A. Melzer, V. A. Schweigert, and A. Piel, Physica Scripta **61**, 494 (2000).
[27] G. A. Hebner and M. E. Riley, Phys. Rev. E **69**, 026405 (2004).
[28] A. V. Ivlev and G. Morfill, Phys. Rev. E **63**, 016409 (2000).
[29] S. K. Zhdanov, A. V. Ivlev, and G. E. Morfill, Phys. Plasmas **16**, 083706 (2009).
[30] L. Couëdel, S. K. Zhdanov, A. V. Ivlev, V. Nosenko, H. M. Thomas, and G. E. Morfill, Phys. Plasmas **18**, 083707 (2011).
[31] A. V. Ivlev, S. K. Zhdanov, M. Lampe, and G. E. Morfill, Phys. Rev. Lett. **113**, 135002 (2014).
[32] T. B. Röcker, L. Couëdel, S. K. Zhdanov, V. Nosenko, A. V. Ivlev, H. M. Thomas, and G. E. Morfill, Europhys. Lett. **106**, 45001 (2014).
[33] J. K. Meyer, I. Laut, S. K. Zhdanov, V. Nosenko, and H. M. Thomas, Phys. Rev. Lett. **119**, 255001 (2017).
[34] L. Couëdel, S. Zhdanov, V. Nosenko, A. V. Ivlev, H. M. Thomas, and G. E. Morfill, Phys. Rev. E **89**, 053108 (2014).
[35] V. Steinberg, R. Sütterlin, A. V. Ivlev, and G. Morfill, Phys. Rev. Lett. **86**, 4540 (2001).
[36] V. Nosenko, A. V. Ivlev, S. K. Zhdanov, M. Fink, and G. E. Morfill, Phys. Plasmas **16**, 083708 (2009).
[37] L. Couëdel, D. Samsonov, C. Durniak, S. Zhdanov, H. M. Thomas, G. E. Morfill, and C. Arnas, Phys. Rev. Lett. **109**, 175001 (2012).
[38] t_{th} slightly depends on the laser pulse duration and the laser power; the chosen t_{th} corresponds to the value at which the microparticles are thermalized in all experiments.
[39] For the measured crystal parameters, the melting occurs when the microparticle mean kinetic energy is around 10–20 eV [46,47]. It slightly underestimates the size of the MZ but catches the main features of its evolution without including particles in the crystalline state.
[40] In logarithmic scale, t_{tr} is the time at which the straight line with a negative slope fitting the exponential decay of the energy at large t crossed the line defined by $K_t = K_t(t_{on}+t_{th})$.
[41] γ_g is obtained by fitting the following function to the total energy: $K_t(t+t_{on}+t_{th}) = K_t(t_{on}+t_{th}) + A\exp(\gamma_g t)$, where A is a positive constant.
[42] J. D. Williams, E. Thomas, L. Couëdel, A. V. Ivlev, S. K. Zhdanov, V. Nosenko, H. M. Thomas, and G. E. Morfill, Phys. Rev. E **86**, 046401 (2012).
[43] S. O. Yurchenko, E. V. Yakovlev, L. Couëdel, N. P. Kryuchkov, A. M. Lipaev, V. N. Naumkin, A. Y. Kislov, P. V. Ovcharov, K. I. Zaytsev, E. V. Vorob'ev, G. E. Morfill, and A. V. Ivlev, Phys. Rev. E **96**, 043201 (2017).
[44] A. Ivlev, T. Röcker, A. Vasyunin, and P. Caselli, Astrophys. J. **805**, 59 (2015).
[45] B. Liu, J. Goree, V. Nosenko, and L. Boufendi, Phys. Plasmas **10**, 9 (2003).
[46] P. Hartmann, G. J. Kalman, Z. Donkó, and K. Kutasi, Phys. Rev. E **72**, 026409 (2005).
[47] N. P. Kryuchkov, S. A. Khrapak, and S. O. Yurchenko, J. Chem. Phys. **146**, 134702 (2017).
[48] V. E. Fortov, O. S. Vaulina, and O. F. Petrov, Plasma Phys. Control. Fusion **47**, B551 (2005).
[49] T. E. Sheridan, Phys. Plasmas **16**, 083705 (2009).
[50] According to Fig. 5, the area defined by R_{MZ} includes ~90% of the energy, giving $R_{MZ} \sim 2w_{MZ}$ which is in agreement with the measured values.
[51] A. Merzhanov, Combust. Flame **10**, 341 (1966).

Chapter 4

Current and future research projects

4.1 Context

In plasma devices used for laboratory experiments or industrial applications, plasmas are confined and bound by the walls of the vessel. Plasma-surface or plasma-wall interactions are thus common to all laboratory plasma systems. The interface between the quasi-neutral bulk plasma and the confining wall plays a major role in determining the plasma discharge parameters. The plasma-wall interface (referred to as the plasma sheath) is a narrow region in which the quasi-neutrality condition applicable to bulk plasmas does not hold. Hence non-zero electric fields exist in the sheath region, in contrast with the quasi-neutral bulk plasma. The flux of energetic particles to the wall and the concomitant heating of the plasma-facing surface are determined by the properties of the sheath. Therefore, it is of fundamental importance to many branches of plasma science and engineering to have detailed knowledge of the sheath parameters in order to design properly plasma-facing surfaces.

In complex (dusty) plasmas, dust particles have a net electric charge due to their interactions with the plasma ions and electrons (The charge is usually negative in low temperature, low pressure laboratory plasmas, see Sec. 3.1). Sheaths are form in the vicinity of dust particles affecting the flux of charge particle on dust surfaces and the transport of dust particles. A good understanding of the dust-plasma interactions requires a good knowledge of the sheath around these small objects as well as the local plasma parameters (electric field, ion and electron temperatures, ion and electron velocity distribution functions, etc.). Dust-plasma interactions are therefore part of the more general studies on plasma-surface interactions (PSI). While sheath formation in front of conducting surface (polarised or floating) interacting with a non-magnetised collision-less Maxwellian low-temperature plasma is very well known, sheath formation in front of surfaces emitting particles (secondary electrons, atoms, or negative ions) or in magnetised plasma (such as magnetron) is still poorly understood.

4.2 Main research themes

The long term objectives of my research program are to gain deep understanding of sheath formation (at different scales) in front of different surfaces as well as to obtain clear insights on the transport and dynamics of dust particles in plasmas. Both problems are obviously tied together and can be formulated under three major themes:

1. Structure of plasma sheaths
2. Dynamics and transport of dust particles in plasmas
3. Formation of nanoparticle in plasmas

My research project spans over the next few years and can be divided in four principal themes. It is funded until the end of 2024 by the NSERC Discovery program of the Canadian Federal government (C$170 000 ($\sim$ 110 000€)) and by the University of Saskatchewan (starting funds C$110 000 ($\sim$ 90 000€))

4.2.1 Theme 1: Sheath studies, plasma-surface surface interactions

Specific experiments are currently in progress to study the perturbations of the bulk plasma and the sheath in front of different biased surfaces immersed in a radio-frequency gas discharges. Conducting surfaces (tungsten, Aluminium, stainless steal) and dielectric surfaces (SiO_2, Al_2O_3) are of interest. The dynamics of the plasma sheath in front of target biased with high negative voltage pulses in the context of plasma immersion ion implantation is of particular interest. This study already lead to a publication by PhD Student J. Moreno [see Publication 6 in App. B.1]. This is one of the main subject of his PhD thesis (defence in early 2023). A master thesis was also written on the subject (Ayub Khodaee MSc thesis, defended in December 2019 [287]). Similar studies are also underway for the magnetised sheaths of magnetron targets (pulsed or DC, MSc thesis of Mr Alex Chang, defended in October 2020 [288], currently looking for a new student to continue this project).

The detailed study of the sheath structure also requires the implementation of non-intrusive and sensitive diagnostics with high temporal and spatial resolution diagnostics. Indeed, the spatial extent of a plasma sheath is about a few Debye lengths ($\sim$500 μm–$\sim$ 1 cm) and the perturbation of the electric potential is of the order of the electron temperature (a few volts). The diagnostics must therefore have a spatial resolution $\sim$10 μm and a high sensitivity ($\sim$5 V/cm for electric fields, $\sim$1-100 m/s for velocities, $\sim 10^{8-9}$ cm^{-3} for densities). This cannot be achieved using classical plasma diagnostic techniques such as Langmuir probes, microwave interferometry (MWI) or optical emission spectroscopy (OES): intrusive diagnostics (Langmuir probes) have a $\sim$1-5 mm spatial resolution due to the size of the probes and induce sheath perturbations (due to the formation of a sheath around the probe itself). Integrated line-of-sight measurements (OES, MWI) cannot achieve the desired spatial resolution. Therefore, a laser-induced fluorescence (LIF) diagnostic to measure the argon ion velocity distribution function (IVDF) on the University of Saskatchewan's ion implantation system has been installed. LIF is a diagnostic based on resonant laser excitation between a lower electronic state of a selected system and an excited electronic state [289, 290]. It has the ability to measure low densities of laser-excited species ($\sim 10^8$ cm^{-3}) [290] and to resolve IVDFs of excited species using the Doppler shift of the excitation frequency [289]. Spatial resolutions of $\sim$50 μm can theoretically be obtained by imaging the fluorescence signal. This is part of the PhD project of Mr Joel Moreno who is currently finalising measurements on a PIII system. I am looking for a new student to continue the LIF study after the defence of Mr Moreno.

4.2.2 Theme 2: Dynamics and transport of micro- and nano-particles in laboratory plasmas

This research theme is a direct continuation of my work at CNRS prior to my secondment to the University of Saskatchewan. The aim is to explore two limits for dusty plasmas: (i) very dense 3D clouds of nanoparticles produced directly in the plasma using reactive gases or sputtering, and (ii) strongly coupled systems of calibrated microparticles injected directly into the plasma whose motion can be resolved individually using conventional imaging methods:

— Very dense clouds of nanoparticles will be produced in a rf glow discharge at the University of Saskatchewan. The dynamics of the dust clouds will then be studied by laser light scattering and by light extinction spectrometry [56, 57]. The grown nanoparticles will

also be analysed ex-situ by electron microscopy. The evolution of the plasma parameters will be studied using OES, Langmuir probes, microwave interferometry, and LIF. For the growth of dust in magnetised plasmas, studies are carried out in collaboration with the PIIM laboratory (particle growth in magnetron discharges [22, 213]), the MDPX team at Auburn University (particle growth in highly magnetised cc-rf discharges [19, 258]) and the LAPLACE laboratory at Université Paul sabatier (collaboration with Dr. R. Clergereaux on the growth of nanoparticles in magnetised low pressure microwave plasmas).

— Thanks to my active collaboration with DLR (German space agency), I have access to experimental data on the transport and dynamics of injected microparticles that form 2D and 3D strongly coupled systems. The DLR group runs the PK-4 laboratory on board the international space station [47], an experiment dedicated to the study of complex plasmas under microgravity conditions in order to eliminate the effects of gravity which tends to confine the microparticles in the sheath regions where electrical forces can compensate the weight of the microparticles. As a member of the scientific team of the PK-4 experiment, I can propose experiments dedicated to the study of interactions between microparticles in dense clouds trapped in plasma (last experiments performed in March 2021, analysis in progress). In addition, the research group at DLR also has a device dedicated to the study of monolayer complex plasma on which I regularly experiment to study waves and plasma-specific instabilities (the mode-coupling instability induced by ion wake mediated interactions [114, 115, 157, 158, 165]). This activity is essential for a better understanding of the physics of plasma sheaths containing microparticles. A Master's student (Navy Smith, thesis defense at the end of 2023) is building at the University of Saskatchewan a similar reactor dedicated to the experimental study of complex monolayer plasmas.

4.2.3 Theme 3: Dynamics, transport and lifetime of dusts in tokamaks

Dust dynamics and lifetime are crucial information for the transport of impurities and other related problems in tokamaks. The different forces acting on the dust such as the ion drag force, magnetised particle flow effects, heat fluxes and ablation rates are important parameters that need to be extracted (directly or indirectly) from experimental data. However, to obtain accurate information, it is necessary to know the size and composition of the dust as well as its geometry, which is often not the case for dust particles produced directly by plasma-surface interactions.

The study of the relationship between the dynamics of calibrated spherical injected dust particles [291] of different materials (high Z (tungsten) and low Z (boron, carbon), sizes 1-100 μm) and the ablation rate in the STOR-M tokamak at the University of Saskatchewan (STOR-M parameters: $B_t = 0.5 - 0.7$ T, $I_{pl} = 15 - 20$ kA, $n_e \sim 10^{13}\text{cm}^{-3}$, discharge duration $\sim$60 ms [292]) is currently in progress. It is the project of the Master's thesis (defended in December 2020) and PhD thesis of Mr Nathan Nelson. The trajectories of the particles are studied using fast cameras combined with particle tracking velocimetry (PTV) and/or particle image velocimetry (PIV) [12, 293]. The analysis of the dust trajectory is also complemented by careful measurements of the scrape-off layer parameters (electrical probes, interferometry, etc.). We also plan to perform emission spectroscopy to estimate the amount of impurities injected by the dust into the plasma. By comparing the experimental measurements with the simulation results of the dust transport models and codes [32, 294–296], we expect to extract accurate values of the ablation rate and lifetime of dust particles. This would allow us to assess the validity of existing dust transport models [294, 295]. This work will be carried out in collaboration with Dr. E. Barnat and Dr C. Grisolia (IRFM, CEA, Cadarache) and Prof.

C. Martin and Dr C. Arnas (PIIM, Aix-Marseille Université) and complemented by analyses of plasma facing components of the WEST tokamak after plasma exposure. Note that PhD student, Mr Nelson, has already done a 6 months internship at PIIM/CEA-IRFM in 2022 in order to work on the analyses of plasma facing components exposed to WEST tokamak plasmas.

4.2.4 Theme 4: Theoretical and numerical studies

The aim of this research theme is to develop a relevant kinetic model to interpret part of the experimental results of Theme 1. A 1D3V kinetic model (based on the Boltzmann equation) of sheath formation taking into account the emission of charged particles (such as secondary electrons) from surfaces interacting with plasmas is currently under development. An undergraduate student (Minh Duong Au) is currently working on this project. The improvement of the current kinetic models (see for example Refs [297–299]), in order to describe accurately the formation of the sheath in the presence of secondary electrons and taking into account the essential parameters of the discharge (power, temperature and density of the gas, temperature of the walls, velocity distribution function of the ions and electrons, electron density, ion density, collisions, etc.), is in progress. Special attention is given to collision operators and ionisation sources.

In the framework of a collaboration with Prof. A. Smolyakov at the University of Saskatchewan, numerical studies are performed to study instabilities in unmagnetised and magnetised plasmas. Numerical solutions from different codes are compared with each other (e.g. particle-in-cell softwares such as VSim from TechX corp (https://www.txcorp.com/vsim), EDPIC, etc). This collaboration has already lead to two publications on the subject [see Publications 7 and 12 in App. B.1].

In the particular case of magnetron discharges, a PhD student (Mr Mun Jong Hern) has been recruited (under a cotutelle agreement with Aix-Marseille University, co-supervised by Dr O. Agullo, Dr M. Muraglia and Dr C. Arnas at the PIIM laboratory, defence planned for the end of 2023) in order to develop a fluid model allowing the simulation of the magnetron plasmas under the conditions used for the growth of nanoparticles by cathode sputtering

4.3 Collaboration with industry

The startup company Fuse Energy Technologies Inc. (Fuse) in Napierville (QC) and the Plasma Physics Laboratory (PPL) at the University of Saskatchewan are currently collaborating to work on experimental and theoretical characterisation of flow-through Z-pinch (FZP) to develop new methods to form and sustain FZP and possibly demonstrate increased neutron production, net power gain and potential use for commercial applications (propulsion, neutron source, green energy). PPL has signed a non disclosure agreement with Fuse and I am therefore not allowed to elaborate more on the scientific details behind this collaborative research work.

The collaboration is currently funded by MITACS Globalink grant (Mitacs is a nonprofit Canadian research organization that operates research and training programs in fields related to industrial and social innovation in partnership with academia, industry and government agencies). I currently supervised one MITACS-funded MSc student (J. Vaneigas), who is currently finishing his thesis on the characterisation of the FZP plasma sources (defence in December 2022), and one MITACS-funded PhD student (M. Jimenez) working on spectroscopy measurements of FZP plasma (defence mid 2024).

Appendix A
Curriculum Vitae

Lénaïc Couëdel

PhD

309-2233 St Henry Avenue,
Saskatoon, SK S7M 5K6,
Canada.
+1 (306) 280 - 1789
+33 (0)6 99 07 86 94
lenaic.couedel@usask.ca

Current professional situation

2022/07–present **Professor**, *Department of Physics and Engineering Physics*, University of Saskatchewan, Saskatoon, SK, Canada

2018/03–present **Chargé de Recherche classe normale**, *en détachement à l'Université de la Saskatchewan*, CNRS, France

Professional address

- Department of Physics and Engineering Physics, College of Arts and Science, University of Saskatchewan, 116 Science place, Saskatoon, SK S7N 5E2, Canada.

Education

2005/10–2008/09 **Ph.D. in Plasma Physics**, *graduated with highest honours*, Cotutelle, Université d'Orléans (France) and the University of Sydney (Australia)

Ph.D. Thesis: "*Nanoparticles formation and dynamics in a complex (dusty) plasma: from the plasma ignition to the afterglow.*," under the supervision of **Prof. L. Boufendi** and **Dr. A. Samarian**

Past professional experiences

2018/03–2022/06 **Associate Professor**, *Department of Physics and Engineering Physics*, University of Saskatchewan, Saskatoon, SK, Canada

2011/02–2018/02 **Chargé de Recherche classe normale**, *Laboratoire PIIM, UMR 7345*, CNRS/Aix-Marseille Université, Marseille, France

2008/10–2011/01 **Postoctoral fellow**, *Max-Planck Institute for Extraterrestrial Physics*, Garching bei München, Allemagne

Research Interests

- **Complex and dusty plasmas**
  Nanoparticle growth, complex plasma crystals, waves and instabilities
- **Plasma diagnostics**
  Electrical probes, spectroscopy, laser-induced fluorescence
- **Plasma sources**
  rf discharges (ICP and CCP), magnetron discharges, DC glow discharges, magnetised plasmas
- **Plasma surface interactions**
  Ion implantation, thin films, dusts in tokamaks
- **Plasma simulations**
  Particle-in-cell simulations

Honors & Awards

- 2020 Mourou-Strickland Mobility Program Award, Ambassade de France au Canada. Project title: "Influence of hydrogen content on dust particle growth in moderately magnetised plasmas"
  Partner Institution: Laboratoire LAPLACE, Université Paul Sabatier, Toulouse (France)
- 2019 Physics and Engineering Physics Research award, University of Saskatchewan, Canada
- 2018 Asia-Pacific Conference on Plasma and Terahertz Science best paper award, IEEE Nuclear and Plasma Sciences Society, August 2018
- 8th International Conference on the Physics of Dusty Plasmas (ICPDP) Young Investigator Award, Charles University, May 2017
- Young scientist best oral presentation winner, 6th International Conference on the Physics of Dusty Plasmas, 15-20 May 2011, Garmisch-Partenkirchen, Germany.
- School of Physics (University of Sydney) Postgraduate Alumni Prize for the most outstanding PhD thesis, Sydney, 2009.
- French Foreign Affairs Ministry Lavoisier Scholarship recipient, 2007/01–2008/07
- Young scientist best oral presentation winner, 5e Conf. de la Sté Française d'Electrostatique, 30-31 August 2006, Grenoble, France.

Research funding history

2021/08–2024/07 **Mitacs Accelerate Internship Program**, *Production of Flow-Through Z-Pinches Using Advanced Methods*, Partner company: Fuse Energy Inc, C$ 533,333.33

2021/01–2021/12 **New Faculty Graduate Student Support Program**, *Supported student: Nathan Nelson*, University of Saskatchewan (Canada), C$ 20,000.00

2019/04–2024/03 **Discovery Grant**, *Sheath and dust particle transport in plasmas*, Natural Sciences and Engineering Research Council of Canada, C$ 170,000.00

2018/05–2020/04 **President's NSERC Fund**, *Sheath, electric fields and dust particle transport in plasmas*, Office of the Vice-President Research, University of Saskatchewan, C$ 7,200.00

2018/03–2023/03 **Starting funds**, Faculty Recruitment and Retention Program, University of Saskatchewan, C$ 135,000.00

2013/01–2014/12 **PHC PROCOPE**, *Project 28444XH, "2D complex plasmas: Mode coupling and interparticle interactions"*, Ministère de l'Europe et des Affaires étrangères/Ministère de l'Enseignement supérieur, de la Recherche et de l'Innovation (MESRI)/Deutscher Akademischer Austausch Dienst, € 5,400.00
Co-applicant: Dr. A. Ivlev, Max Planck Institute for extraterrestrial Physics, Garching b. München (Allemagne).

Student supervision

PhD student supervision

2021/01–present **Marilyn Jimenez**, *Spectro-tomography of flow-through Z-Pinches*, PhD, Physics, University of Saskatchewan (Canada), Principal supervisor
Collaboration with Fuse Energy Inc., Napierville, Quebec, Canada

2020/01–present **Nathan Nelson**, *Dust transport in the STOR-M tokamak*, PhD, Physics, University of Saskatchewan (Canada), Principal supervisor

2019/09–present **Jung Hern Mun**, *Impurity transport modelling in a magnetron discharge*, PhD, Physics, Cotutelle, Aix-Marseille Université (France) and University of Saskatchewan (Canada), co-supervisor

2019/06–2021/04 **Dominique Vu**, *Effects of ion bombardment on polycrystalline tungsten surfaces*, PhD, Physics, Cotutelle, Aix-Marseille Université (France) and University of Saskatchewan (Canada), Co-supervisor
WITHDRAW

2018/09–present **Joel Moreno**, *Diagnostics and modelling of plasma sheath*, PhD, Physics, University of Saskatchewan (Canada), Principal supervisor

Master student supervision

2021/09–present **Navy Smith**, *Experimental studies of two-dimensional complex plasma crystals*, MSc, Physics, University of Saskatchewan (Canada), Principal supervisor

2021/01–present **Jeisson Vanegas**, *Probe diagnostics of the plasma source of a flow-through Z-Pinch*, MSc, Physics, University of Saskatchewan (Canada), Principal supervisor
Collaboration with Fuse Energy Inc., Napierville, Quebec, Canada

2018/09–2020/12 **Nathan Nelson**, *Design and Characterization of a Dust Injector for Future Studies of Tungsten Dust in the STOR-M Plasma*, MSc, Physics, University of Saskatchewan (Canada), Co-supervisor

2018/03–2020/09 **Alex Chang**, *ICP Enhanced HIPIMS System Design and Characterization*, MSc, Physics, University of Saskatchewan (Canada), Co-supervisor

2018/03–2019/12 **Ayub Khodaee**, *RF-compensated Langmuir Probe Diagnostics of Pulsed Plasma Ion Implantation System*, MSc, Physics, University of Saskatchewan (Canada), Co-supervisor

2017/03–2017/08 **Alebia Chami**, *Characterisation of a magnetron discharge used for nanoparticle growth*, MSc, Fusion Sciences, Aix-Marseille Université (France), Co-supervisor

2016/03–2016/08 **Loan Terraz**, *Simulation Monte-Carlo de la thermalisation d'atomes éjectés par pulvérisation cathodique*, MSc, Fusion Sciences, Aix-Marseille Université (France), Principal supervisor

2015/03–2015/08 **Amin Ghaith**, *Formation of Nanoparticles in Magnetron discharge*, MSc, Fusion Sciences, Aix-Marseille Université (France), Co-supervisor

2013/03–2013/08 **Chunxuan Hu**, *Agglomération de nanoparticules dans un plasma*, MSc, Fusion Sciences, Aix-Marseille Université (France), Principal supervisor

Undergraduate student supervision

2020/01–present **Minh Duong Au**, *Vlassov-Boltzmann simulation of plasma-enhanced ion implantation system*, B. Eng., Engineering Physics, University of Saskatchewan (Canada), Principal Supervisor
4h/week

2020/09–2022/05 **Daniel Okerstrom**, *Construction of the light acquisition system of a laser induced fluorescence diagnostics*, B. Eng., Engineering Physics, University of Saskatchewan (Canada), Principal Supervisor
4h/week

2020/01–2021/05 **William Kozicki**, *Design and construction of a Langmuir probe controller*, B. Eng., Engineering Physics, University of Saskatchewan (Canada), Principal Supervisor
4h/week

2020/01–2020/03 **Graham Elder**, *PIC Simulation of $E \times B$ instabilities*, B. Eng., Engineering Physics, University of Saskatchewan (Canada), Principal Supervisor
3h/week

2019/06–2019/08 **Jeremy Pascal**, *Langmuir probe measurements in an ICP discharge*, B.Sc., Université Paul Sabatier, Toulouse (France), Principal Supervisor
Summer internship,full-time

2018/05–2018/08 **William Kozicki**, *Langmuir probe measurements in an ICP discharge*, B. Eng., Engineering Physics, University of Saskatchewan (Canada), Co-supervisor
full-time

2016/04–2016/06 **Zineb Samahna**, *Caractérisation expérimentale d'une décharge magnétron à courant continu et haute pression pour la production de nanoparticules métalliques*, IUT Mesure Physique, Aix-Marseille Université (France), Principal advisor
full-time

Teaching Activities

2021/01–2021/03 **Lectures**, *Phys 156: Electromagnetism and waves for engineering*, Undergraduate Course, University of Saskatchewan (Canada)
Course coordinator, 24h

2021/091–2012/04 **Reading course**, *Phys 898: Plasma wall interactions in fusion reactors*, Graduate Course, University of Saskatchewan (Canada)

2021/091–2012/04 **Seminar series**, *Phys 490: Physics seminars*, Undergraduate course, University of Saskatchewan (Canada)

2021/01–2021/04 **Lectures**, *Phys 155: Introduction to electricity and magnetism*, Undergraduate Course, University of Saskatchewan (Canada)
Course coordinator, 36h

2021/01–2021/04 **Reading course**, *Phys 865: Plasma transport and plasma diagnostics*, Graduate Course, University of Saskatchewan (Canada)

2020/09–2020/12 **Lectures**, *Phys 873: Statistical physics*, Graduate Course, University of Saskatchewan (Canada)
36h

2020/01–2020/04 **Lectures**, *Phys 155: Introduction to electricity and magnetism*, Undergraduate Course, University of Saskatchewan (Canada)
Course coordinator, 36h

2019/01–2019/04 **Lectures**, *Phys 155: Introduction to electricity and magnetism*, Undergraduate Course, University of Saskatchewan (Canada)
36h

2015/01–2016/11 **Tutorials and Laboratories**, *Experimental complex plasma physics*, Master classes, Bauman Moscow State Technical University (Russia)
∼40h over two years, classes given in the framework of the international research project "Complex plasma : interdisciplinary research" leaded by Prof. Gregor Morfill (MPE, Germany) and Prof. Stanislav Yurchenko (Bauman Moscow State Technical University, Moscow, Russia) in which I was a partner investigator.

2013/01–2016/03 **Lectures** , *Introductory lecture to dusty plasmas and plasma diagnostics*, Master 2 course, Aix-Marseille Université (France)
9h/year

2008/02–2008/05 **Teaching Assistant**, *1st year Regular Physics laboratories*, University of Sydney (Australia)

2008/02–2008/05 **Teaching Assistant**, *1st year Regular Physics Workshop*, University of Sydney (Australia)

2008/02–2008/05 **Teaching Assistant**, *2nd year Computational Physics laboratories*, University of Sydney (Australia)

2007/07–2001/11 **Teaching Assistant**, *1st year Advanced Physics laboratories*, University of Sydney (Australia)

2007/07–2001/11 **Teaching Assistant**, *2nd year Computational Physics laboratories*, University of Sydney (Australia)

2007/07–2001/11 **Teaching Assistant**, *1st year electronic laboratories*, Polytech' Orléans (France)

Research Facilitation

2021 **Chair**, *Annual Symposium day of the Division of Plasma Physics*, Annual Congress of the Canadian Association of Physicists, June 2021
On-line symposium

2020/11–present **Member of the Science Definition Team**, *COMPACT project (COMplex PlAsma faCiliTy)*, DLR, NASA, ESA, NSF, ROSCOSMOS
International Space Station experiment

2020 **Chair**, *Annual Symposium day of the Division of Plasma Physics*, Annual Congress of the Canadian Association of Physicists, June 2020
On-line symposium

2019/07–2021/06 **Chair**, *Division of Plasma Physics*, Canadian Association of Physicists

2018 **Committee Member**, *International Scientific Committee*, International Congress on Plasma Physics, June 2018, International Union of Pure and Applied Physics

2015 **Co-Chair**, *local organising committee*, Frontier in Low Temperature Plasma Diagnostics workshop, May 2015, Aix-Marseille Université (France)

Practice of professional skills

2018 **External examiner**, *PhD thesis*, University of Alberta (Canada)
1 PhD thesis

2022 **Academic Reviewer**, *Research tools and Instruments grant*, Natural Sciences and Engineering Research Council of Canada

2020, 2021 **Academic Reviewer**, *Discovery grant*, Natural Sciences and Engineering Research Council of Canada

2020, 2021, 2022 **Academic Reviewer**, Fonds de Recherche du Québec – Nature et technologies

2020 **Academic Reviewer**, German Research Foundation

2019 **Academic Reviewer**, Agence Nationale de la Recherche (France)

2018 **External examiner**, *PhD thesis*, University of Montreal (Canada)
2 PhD theses

Since 2018 **Committee member**, *Graduate student advisory committee(s)*, Physics and Engineering Physics department, University of Saskatchewan (Canada)
Numerous MSc and PhD advisory committees

2016,2019 **Examiner**, *Master thesis*, Master 2: Fusion sciences, Aix-Marseille Université

2014-2019 **External examiner**, *PhD thesis*, University of Sydney (Australia)
5 PhD theses

Since 2009 **Reviewer**, Many scientific journals including Physical Review Letters, Physical Review E, Physics of Plasmas, Plasma Sources, Science and Technology, Journal of Physics D: Applied Physics, IEEE Transactions on Plasma Science, etc

Administrative services

2021/07–present **Chair**, *Graduate Affairs Committee*, Department of Physics and Engineering Physics, University of Saskatchewan

2021/07–present **Treasurer**, University of Saskatchewan Faculty Association (Canada)
Faculty union

2020/07–present **Chair**, *External relation committee*, University of Saskatchewan Faculty Association (Canada)
Faculty union

2020/07–present **Member**, *Joint Committee on the Management of the Collective Agreement*, University of Saskatchewan Faculty Association (Canada)
Faculty union

2020/07–present **Member**, *Equity & Internationalisation Committee*, College of Graduate and Postdoctoral Studies, University of Saskatchewan (Canada)

2019/07–present **Chair**, *Committee on committees*, University of Saskatchewan Faculty Association (Canada)
Faculty union

2019/07–2020/06 **Member**, *Committee on Administrative practices*, University of Saskatchewan Faculty Association (Canada)
Faculty union

2019/07–present **Member**, *Executive committee*, University of Saskatchewan Faculty Association (Canada)
Faculty union

2019/07–2020/07 **Chair**, *Equity & Internationalisation Committee*, College of Graduate and Postdoctoral Studies, University of Saskatchewan (Canada)

2019/06–2020/05 **Member**, *Indigenous Recruitment Committee*, College of Arts and Science, University of Saskatchewan (Canada)

2019/01–2019/06 **Member**, *Nomination Committee*, College of Arts and Science, University of Saskatchewan (Canada)

2018/03–present **Member**, *Graduate Affairs Committee*, Department of Physics and Engineering Physics, College of Arts and Science, University of Saskatchewan (Canada), Chair since July 2021

Academic collaboration activities

- Since 2020, collaboration with Dr Richard Clergereaux at Laboratoire LAPLACE (UMR 5213) CNRS/Université Paul Sabatier, Toulouse (France) on dust particle growth in moderately magnetised plasmas.
  2020 Mourou-Strickland Mobility Program Award
- Since 2019, collaboration with Prof. Andrei Smolyakov at the University of Saskatchewan (Canada) on numerical studies of magnetised plasmas
- Since 2018, collaboration with the PIIM laboratory (UMR 7345) at CNRS/Aix-Marseille Université (France) on impurities and dust transport in magnetised plasmas (Dr Cecile Arnas, Associate Prof. Olivier Agulo, Associate Prof. Magali Muraglia) and plasma surface interaction (Prof. Gilles Cartry, Associate Prof. Céline Martin) .
  1 Cotutelle PhD student
- Since 2017, collaboration with Prof. Edward Thomas Jr. at Auburn University, Alabama, USA on nanoparticle growth in highly magnetised plasma using the Magnetized Dusty Plasma eXperiment (MDPX).
  2017/07–2017/12: Invited research scholar at Auburn University, Alabama, USA
- Since 2014, collaboration with Associate Prof. Stanislav Yurchenko at Bauman Moscow State Technical University, Moscow, Russia on experimental studies of complex plasmas
- Since 2014, collaboration with German Aerospace Agency (DLR), Research group on the physics of complex plasmas, leaded by Dr Hubertus Thomas on experimental studies of complex plasmas
- Since 2013, collaboration with Dr. Fabrice Onofri and Associate Prof. Séverine Barbosa at IUSTI (UMR 7343) CNRS/Aix-Marseille Université (France) on diagnostics of nanoparticle growth in plasmas using light extinction spectrometry
- Since 2012, collaboration with Prof. E. Thomas Jr. at Auburn University, Alabama, USA and Prof Jeremiah Williams at Wittenberg University, Springfield, Ohio, USA on dust kinetics in two-dimensional plasma crystals.
- Since 2011, collaboration with Dr Alexei Ivlev at the Max Planck Institute for Extraterrestrial Physics (Germany) on waves and instabilities in complex plasma crystals
- Since 2011, collaboration with Dr Christian Grisolia at CEA, IRFM (France) on dusts in tokamaks

Publications

73 publications in peer-reviewed journals since 2006 including 6 articles in Physical Review Letters (3 as lead author), h-index: 20, 940+ citations excluding auto-citations.

10 Most significant publications

1. L. Couëdel, V. Nosenko, S. K. Zhdanov, A. V. Ivlev, H. M. Thomas, and G. E. Morfill, *Direct observation of mode-coupling instability in two- dimensional plasma crystals*, Phys. Rev. Lett. 104, 195001 (2010).
   doi.org/10.1103/PhysRevLett.104.195001
2. L. Couedel and V. Nosenko, *Stability of two-dimensional complex plasma monolayers in asymmetric capacitively-coupled radio-frequency discharges*, Physical Review E 105, 015210 (2022).

doi.org/10.1103/PhysRevE.105.015210

3. L. Couëdel, D. Artis, M. P. Khanal, et al., *Influence of magnetic field strength on nanoparticle growth in a capacitively-coupled radio-frequency Ar/C_2H_2 discharge*, Plasma Research Express 1(1), 015012 (2019).
doi.org/10.1088/2516-1067/ab045e
4. S. Barbosa, L. Couëdel, C. Arnas, et al., *In-situ characterisation of the dynamics of a growing dust particle cloud in a direct-current argon glow discharge*, J.Phys. D : Appl. Phys. 49, 045203 (2016).
doi.org/10.1088/0022-3727/49/4/045203
5. S. Mitic, S. Coussan, C. Martin,and L. Couëdel, *Hydro-carbon material design in a capacitively coupled radio-frequency discharge*, Plasma Processes and Polymers 15 1700152 (2018).
doi.org/10.1002/ppap.201700152
6. S. Khrapak and L. Couëdel, *Dispersion relations of Yukawa fluids at weak and moderate coupling*, Physical Review E 102, 033207 (2020).
doi.org/10.1103/PhysRevE.102.033207
7. L. Couëdel, V. Nosenko, M. Rubin-Zuzic, et al., *Full melting of a two-dimensional complex plasma crystal triggered by localized pulsed laser heating*, Physical Review E 97(4), 043206 (2018).
doi.org/10.1103/PhysRevE.97.043206
8. J. Moreno, A. Khodaee, D. Okerstrom, M. P. Bradley, and L. Couëdel, *Time-resolved evolution of plasma parameters in a plasma immersion ion implantation source*, Phys. Plasmas 28, 123523 (2021).
doi.org/10.1063/5.0063610
9. S. Mitic, J. Moreno, C. Arnas and. L. Couëdel, *Diagnostics of a high-pressure DC magnetron argon discharge with an aluminium cathode*, Eur Phys. J. D 75, 240 (2021).
doi.org/10.1140/epjd/s10053-021-00239-9
10. L. Couëdel, V. Nosenko, S. K. Zhdanov, A. V. Ivlev, H. M. Thomas, and G. E. Morfill, *First direct measurement of optical phonons in 2D plasma crystals*, Phys. Rev. Lett. 103, 215001 (2009).
doi.org/10.1103/PhysRevLett.103.215001

Languages

- French (mother tongue)
- English (fluent)
- German (European B1 level)

Hobbies

Theater	Actor in the Programme d'Improvisation Francophone, Saskatoon, Canada
Sports	Rugby (Gophers Rugby Football Club, Saskatoon, Canada), Hiking, Rock climbing

Appendix B

Complete list of publications and presentations

73 publications in peer-reviewed journals since 2006 including 6 articles in Physical Review Letters (3 as lead author), h-index: 20, 940+ citations excluding auto-citations.

B.1 Articles in refereed journals

1. C. A. Knapek, L. Couëdel, A. Dove, J. Goree, U. Konopka, A. Melzer, S. Ratynskaia, M. Thoma,H. M. Thomas,"COMPACT - A new complex plasma facility for the ISS", Plasma Phys. Control. Fus., In press (2022)
2. L. Couëdel,"Temporal dusty plasma afterglow: A review", Frontiers in Physics **10**, Special Issue: *Particle Interaction With Afterglow Plasma and Non-Quasi-Neutral Plasma* (Editor: John Goree), 1015603 (2022)
3. C. Arnas,T. Guidez,A. Chami, J. H. Mun, and L. Couedel, "Forces applied to nanoparticles in magnetron discharges and the resulting size segregation", Physics of Plasmas**29**, 073703 (2022)
4. N. Nelson, L. Couëdel, and C. Xiao, "Design and Characterization of a Dust Dispenser for Tungsten Dust Injection Experiments in the STOR-M Tokamak", Radiation Effects and Defects in Solids **177**, 181 (2022)
5. L. Couëdel and V. Nosenko, "Stability of two-dimensional complex plasma monolayers in asymmetric capacitively-coupled radio-frequency discharges", Review E **105**, 015210 (2022)
6. J. Moreno, A. Khodaee, D. Okerstrom, M. P. Bradley, and L. Couëdel, "Time-resolved evolution of plasma parameters in a plasma immersion ion implantation source" Phys. Plasmas 28, 123523 (2021)
7. A. Tavassoli1, O. Chapurin, M. Jimenez, M. Papahn Zadeh, T. Zintel, M. Sengupta, L. Couëdel, et al. "The role of noise in PIC and Vlasov simulations of the Buneman instability", Phys. Plasmas 28, 122105 (2021)
8. S. Mitic, J. Moreno, C. Arnas and. L. Couëdel "Diagnostics of a high-pressure DC magnetron argon discharge with an aluminium cathode" Eur Phys. J. D **75**, 240 (2021)
9. X. Yang, D. Kogut, L. Couëdel, et al. "TALIF measurements of hydrogen and deuterium surface loss probabilities on quartz in low pressure high density plasmas", Plasma Sources Sci. Technol. **30**, 015013 (2020)
10. S. Khrapak and L. Couëdel. "Dispersion relations of Yukawa fluids at weak and moderate coupling", Physical Review E **102**, 033207 (2020)

11. M. Menati, T. Hall, B. Rasoolian, L. Couëdel et al. "Experimental observation and numerical investigation of imposed pattern formation in magnetized plasmas by a wide wire mesh", Plasma Sources Sci. Technol. **29**, 085015 (2020)

12. A. Smolyakov, T. Zintel, L. Couëdel, et al. "Anomalous electron transport in one-dimensional Electron Cyclotron Drift Turbulence", Plasma Physics Reports **46**, 496 (2020)

13. C. Pardanaud, D. Dellasega, M. Passoni, C. Martin, P. Roubin, Y. Addab, C. Arnas, L. Couëdel et al. "Post-mortem analysis of tungsten plasma facing components in tokamaks: Raman microscopy measurements on compact, porous oxide and nitride films and nanoparticles", Nucl. Fusion **60**, 086004 (2020)

14. V Pigeon, M. Muraglia, C. Arnas, N. Claire and L. Couëdel. "Evaluating the uncertainty for a complex experiment:the case of the plasma potential measurement", European Journal of Physics, **41**, 035806 (2020)

15. S. Jaiswal, M. Menati, L. Couëdel, et al. "Effect of growing nanoparticle on the magnetic field induced filaments in a radio-frequency Ar/C2H2 discharge plasma", Japanese Journal of Applied Physics, **59** SHHC07 (2020)

16. C. Arnas, A. Chami, L. Couëdel, et al. "Thermal balance of tungsten monocrystalline nanoparticles in high pressure magnetron discharges", Phys. Plasmas **26**, 053706 (2019)

17. L. Couëdel and V. Nosenko. "Tracking and Linking of Microparticle Trajectories During Mode- Coupling Induced Melting in a Two-Dimensional Complex Plasma Crystal", Journal of Imaging, **5**(3), 41 (2019)

18. K. Ouaras, G. Lombardi, L. Couëdel, et al. "Microarcing-enhanced tungsten nano and micro-particles formation in low pressure high-density plasma", Phys. Plasmas **26**, 023705 (2019)

19. L. Couëdel, D. Artis, M. P. Khanal, et al. "Influence of magnetic field strength on nanoparticle growth in a capacitively-coupled radio-frequency Ar/C2H2 discharge. Plasma Research Express, **1**(1), 015012 (2019)

20. L. Couëdel, V.M. Nosenko, S. Zhdanov et al. "Experimental studies of two-dimensional complex plasma crystals: waves and instabilities" Physics-Uspekhi, **62**(10), 1000 (2019)

21. N. P. Kryuchkov, E. V. Yakovlev, E. A. Gorbunov, L. Couëdel, et al. (2018). "Thermoacoustic Instability in Two-Dimensional Fluid Complex Plasmas", Physical Review Letters **121**, 075003 (2018)

22. A. Autricque, S. A. Khrapak, L. Couëdel, et al. "Electron collection and thermionic emission from a spherical dust grain in the space-charge limited regime", Phys. Plasmas **25**, 063701 (2018)

23. L. Couëdel, V. Nosenko, M. Rubin-Zuzic, et al. "Full melting of a two-dimensional complex plasma crystal triggered by localized pulsed laser heating" Physical Review E **97**(4), 043206 (2018)

24. S.Khrapak, B. Klumov, L. Couëdel "Self-diffusion in single-component Yukawa fluids", J. Phys. Commun. **2**, 045013 (2018)

25. S. Mitic, S. Coussan, C. Martin,and L. Couëdel "Hydro-carbon material design in a capacitively coupled radio-frequency discharge", Plasma Processes and Polymers **15** 1700152 (2018)

26. A. Autricque, N. Fedorczak, S. A. Khrapak, L. Couëdel, et al. "Magnetized electron emission from a small spherical dust grain in fusion related plasmas", Phys. Plasmas **24**, 124502 (2017)

27. N. Ning, L. Couëdel, C, Arnas, and S. Khrapak. "Computational Prediction of Rate Constant for Reactions Involved in Al Clustering", Journal of Physical Chemistry A, **121** (2017)

28. S. O. Yurchenko, E. V. Yakovlev, and L. Couëdel, "Flame propagation in two-dimensional solids: Particle- resolved studies with complex plasmas", Physics Review E **96**, 043201 (2017)

29. S. Khrapak, B. Klumov, and L. Couëdel, "Collective modes in simple melts: Transition from soft spheres to the hard sphere limit", Scientific Reports **7**, 7985 (2017)

30. C. Arnas, J. Irby, S. Celli, G. D. Temmerman, Y. Addab, L. Couëdel, et, al. "Characterization and origin of large size dust particles produced in the Alcator C-Mod tokamak", Nuclear Materials and Energy, **11**, 12-19 (2017)

31. L. Couëdel, T. B. Röcker, S. K. Zhdanov, et al. "Forced mode coupling in 2D complex plasmas", EPL **115**, 45002 (2016)

32. S. Barbosa, F. R. A. Onofri, L. Couëdel, et al. "An introduction to light extinction spectrometry as a diagnostic for dust particle characterisation in dusty plasmas", J Plasma Phys. **82**, 615820403 (2016)

33. S. A. Khrapak, B. Klumov, L. Couëdel and, H. M. Thomas, "On the long-waves dispersion in Yukawa systems", Phys. Plasmas **23**, 023702 (2016)

34. W. Horton, H. Miura, O. Onishchenko, L. Couëdel, et al. "Dust devil dynamics", J. Geophys. Res. **121**, 7197-7214 (2016)

35. S. Barbosa, L. Couëdel, C. Arnas, et al. "In-situ characterisation of the dynamics of a growing dust particle cloud in a direct-current argon glow discharge", J.Phys. D.: Appl. Phys. **49**, 045203 (2016)

36. S. A. Khrapak, I. L. Semenov, L. Couëdel, et al., "Thermodynamics of Yukawa fluids near the one-component-plasma limit", Phys. Plasmas **22**, 083706 (2015)

37. A. V. Ivlev, T. B. Roecker, L. Couëdel, et al., "Wave modes in shear-deformed two-dimensional plasma crystals", Phys. Rev. E **91**, 063108 (2015)

38. I. Laut, C. Raeth, S. Zhdanov, V. Nosenko, L. Couëdel, et al., "Synchronization of particle motion in compressed two-dimensional plasma crystals", Eur. Phys. Lett. **110**, 65001 (2015)

39. S. K. Zhdanov, L. Couëdel, V. Nosenko, et al., "Spontaneous pairing and cooperative movements of micro-particles in a two dimensional plasma crystal", Phys. Plasmas **22**, 053703 (2015)

40. L. Couëdel, Kishor Kumar K., and C. Arnas, "Detrapping of tungsten nanoparticles in a direct-current argon glow discharge", Phys. Plasmas **21**, 123703 (2014)

41. Kishor Kumar, K.;, L. Couëdel, and C. Arnas, "Nanoparticles in direct-current discharges: Growth and electrostatic coupling", J. Plasma Phys. **80**, 849-854 (2014)

42. T. B. Röcker, A. V. Ivlev, S. K. Zhdanov, L. Couëdel and, G. E.Morfill, "Wake-induced bending of two-dimensional plasma crystals", Phys. Plasmas **21** , 073711 (2014).

43. L. Couëdel, S. Zhdanov, V. Nosenko, A.V. Ivlev, H.M. Thomas and, G. E. Morfill, "Synchronization of particle motion induced by mode coupling in a two-dimensional plasma crystal", Phys. Rev. E **89**, 053108 (2014).

44. T. B. Röcker, L. Couëdel, S. K. Zhdanov, V. Nosenko„ A. V. Ivlev, H. M. Thomas and, G. E. Morfill, "Nonlinear regime of the mode-coupling instability in 2D plasma crystals", Eur. Phys. Lett. **106**, 45001 (2014).

45. S. K. Zhdanov, V. Nosenko, H. M. Thomas, G. E. Morfill, and L. Couëdel, "Observation of particle pairing in a two-dimensional plasma crystal ", Phys. Rev. E **89**, 023103 (2014)
46. L. Wörner, A. V. Ivlev, L. Couëdel, P. Huber, et al. "The effect of a direct current field on the microparticle charge in the plasma afterglow", Phys. Plasmas **20**, 123702 (2013).
47. M. Pustylnik, L. Hou, A. Ivlev, L. Vasilyak, L. Couëdel, H. Thomas, G. Morfill, V. Fortov, "High-voltage nanosecond pulses in a low-pressure radiofrequency discharge", Phys. Rev. E **87**, 063105 (2013).
48. Kishor Kumar K., L. Couëdel, and C. Arnas, "Growth of tungsten nanoparticles in direct-current argon glow discharges" Phys. Plasmas **20**, 043707 (2013).
49. C. Arnas, A. Michau, G. Lombardi, L. Couëdel, L. and, Kishor Kumar K., "Effects of the growth and the charge of carbon nanoparticles on DC discharges", Phys. Plasmas **20**, 013705 (2013).
50. L. Couëdel, D. Samsomov, C. Durniak et al., "Three-dimensional structure of Mach cones in monolayer complex plasma crystal", Phys. Rev. Lett. **109**, 175001 (2012).
51. J. D. Williams, E. Thomas Jr., L. Couëdel, et al., "Kinetics of the melting front in twodimensionalplasma crystals: Complementary analysis with the particle image and particle tracking velocimetries", Phys. Rev. E **86**, 046401(2012).
52. Mikikian Maxime, Couëdel Lenaic, Tessier Yves, et al., "Carousel Instability in a Capacitively Coupled RF Dusty Plasma", IEEE Trans. Plasma Sci. **39**, 2748 (2011)
53. Layden, Brett and Couëdel, Lenaic and Samarian, Alexander A. and Boufendi, Laifa, "Residual Dust Charges in a Complex Plasma Afterglow", IEEE Trans. Plasma Sci. **39**, 2764 (2011).
54. Tawidian, H. and Mikikian, M. and Couëdel, L. and Lecas, T., "Plasma inhomogeneities near the electrodes of a capacitively-coupled radio-frequency discharge containing dust particles", Eur. Phys. J. Appl. Phys. **56**, 24018 (2011).
55. L. Couëdel, S.K. Zhdanov, A.V. Ivlev, V. Nosenko, H.M. Thomas, and G.E. Morfill, "Wave mode coupling due to plasma wakes in two-dimensional plasma crystals: In depth view", Phys. Plasmas **18**, 083707 (2011).
56. R.J. Heidemann, L. Couëdel, S. Zhdanov, et al., "Comprehensive experiemntal study of heartbeat oscillations observed under microgravity conditions in the PK-3 Plus laboratory on board the International Space Station", Phys. Plasmas **18**, 053701 (2011).
57. L. Couëdel, M. Mikikian, A.A. Samarian, and L. Boufendi, "Self-excited void instability during dust particle growth in a dusty plasma", Phys. Plasmas **17**, 083705 (2010).
58. M. Mikikian, L. Couëdel, M. Cavarroc, Y. Tessier, and L. Boufendi, "Threshold phenomena in a throbbing complex plasma", Phys. Rev. Lett. **105**, 075002 (2010).
59. L. Couëdel, V. Nosenko, S. K. Zhdanov, A. V. Ivlev, H. M. Thomas, and G. E. Morfill, "Direct observation of mode-coupling instability in two-dimensional plasma crystals", Phys. Rev. Lett. **104**, 195001 (2010).
60. M. Mikikian, L. Couëdel, M. Cavarroc, Y. Tessier, and L. Boufendi, "Dusty plasmas: synthesis, structure and dynamics of a dust cloud in a plasma", Eur. Phys. J. Appl. Phys. **49**, 13106 (2010).
61. M. Mikikian, M. Cavarroc, L. Couëdel, Y.Tessier, and L. Boufendi, "Dust particles in low pressure plasmas: formation and induced phenomena", Pure Appl. Chem. **82**, 1273 (2010).
62. L. Couëdel, V. Nosenko, S. K. Zhdanov, A. V. Ivlev, H. M. Thomas, and G. E. Morfill, "First direct measurement of optical phonons in 2D plasma crystals", Phys. Rev. Lett. **103**, 215001 (2009).

63. L. Couëdel, A. Mezeghrane, A.A. Samarian, M. Mikikian, Y. Tessier, M. Cavarroc and L. Boufendi, "Complex plasma afterglow", Contrib. Plasma Phys. **49**, 235 (2009).
64. L. Couëdel, A. Mezeghrane, M. Mikikian, A.A. Samarian, C. Cuthbert and L. Boufendi, "Charge électrique résiduelle sur des poudres à l'extinction d'un plasma poussiéreux", J. Electrostatics **67**, 625 (2009).
65. L. Couëdel, A.A. Samarian, M. Mikikian and L. Boufendi, "Dust density effect on complex plasma decay", Phys. Lett. A **372**, 5339 (2008).
66. L. Couëdel, A.A. Samarian, M. Mikikian and L. Boufendi, "Dust charge distribution in complex plasma afterglow", Eur. Phys. Lett. **84**, 35002 (2008).
67. M. Mikikian, M. Cavarroc, L. Couëdel, Y. Tessier and L. Boufendi, "Evidence of mixed-mode oscillations in complex plasma instabilities ", Phys . Rev. Lett **100**, 225005 (2008).
68. L. Couëdel, A.A. Samarian, M. Mikikian and L. Boufendi, "Influecnce of the ambiploar-to-free diffusion transition on dust particle charge in a complex plasma afterglow", Phys. Plasmas **15**, 063705 (2008).
69. L. Couëdel, A.A. Samarian, M. Mikikian and L. Boufendi, "Dust cloud dynamics in complex plasma afterglow", IEEE Trans. Plasma Sci. **36**(4), 1014 (2008).
70. M. Mikikian, L. Couëdel, M. Cavarroc, Y. Tessier and L. Boufendi, "Plasma Emission Modifications and Instabilities Induced by the Presence of Dust Particles", IEEE Trans. Plasma Sci. **36**(4), 1012 (2008).
71. M. Mikikian, L. Couëdel, M. Cavarroc, Y. Tessier and L. Boufendi, "Self-excited void instability in dusty plasmas: plasma and dust cloud dynamics during the heartbeat instability", New J. Phys. **9**, 268, (2007).
72. L. Couëdel, M. Mikikian, L. Boufendi, and A. A. Samarian, "Residual dust charges in discharge afterglow", Phys. Rev. E **74**, 026403 (2006).
73. M. Mikikian, M. Cavarroc, L. Couëdel and L. Boufendi, "Low frequency instabilities during dust particle growth in a radio-frequency plasma", Phys. Plasmas **13**, 092103 (2006).

B.1.1 Submitted articles

1. R. Banka, K. Vermillion, L. Matthews, T. Hyde, and L. Couëdel , "Evolution of Ion Wake Characteristics with Experimental Conditions", submitted to Plasma Physics and Controlled Fusion (2022)

B.2 Invited Presentations

1. L. Couëdel. Nanopaprticle growth in highly magnetized chemically active plasmas. MagNetUS 2022, Williamsburg, June 7–10, 2022.
2. L. Couëdel. Influence of discharge parameters on the mode-coupling instability in two-dimensional complex plasma crystals. Canadian Association of Physicists Division of Plasma Physics Symposium 2022, Hamilton, June 7, 2022.
3. L. Couëdel. Influence of discharge parameters on the mode-coupling instability in two-dimensional complex plasma crystals. 48th European Conference on Plasma Physics, Online, June 27–July 1 2022.
4. L., Couëdel, V. Nosenko, M. Rubin-Zuzic, S. Zhdanov, Y. Elskens. T. Hall, and A. V. Ivlev. Explosive Melting of A 2D Complex Plasma Crystal Triggered by Localized Laser

Heating. 2018 Asia-Pacific Conference on Plasma and Terahertz Science, Xi'an, August 1, 2018 to August 1, 2018.

5. L. Couëdel, V. Nosenko, S. Zhdanov, I. Laut, A. V. Ivlev, E. V. Yakovlev, A. Y. Kislov, S. O. Yurchenko, and A. M. Lipaev. Two-dimensional plasma crystals: waves and instabilities. International Conference on Phenomena in Ionized Gases (ICPIG), Estoril, January 1, 2017 to January 1, 2017.
6. L. Couëdel et al. "Melting induced by the mode-coupling instability in a two-dimensional complex plasma crystal",Communication orale invitée, ICPP 2016, Kaoshiung, Taiwan.
7. L. Couëdel et al. "Synchronization in two-dimensional plasma crystals", Mini Symposium on Self Organizing effects in complex (dusty) plasmas, Communication orale invitée, Dynamics Days Europe 2015, Exeter, UK.
8. L. Couëdel, V. Nosenko, Z. Zhdanov and A. Ivlev, H. Thomas, and G. Morfill, "Mode coupling due to ion wakes in 2D complex plasma crystals", Invited oral communication, 6th International Conference on the Physics of Dusty Plasmas, 15-20 May 2011, Garmisch-Partenkirchen, Germany.

B.3 Peer-reviewed conference proceedings

1. Rubin-Zuzic, M.; Nosenko, V.; Zhdanov, S.; Ivlev, A.; Thomas, H.; Khrapak, S. & Couëdel, L. "Single particle dynamics in a radio-frequency produced plasma sheath" AIP Conference Proceedings **1925**, 020023 (2018)
2. Couëdel, L.; Nosenko, V.; Rubin-Zuzic, M.; Zhdanov, S. & Ivlev, A. "Laser-stimulated melting of a two-dimensional complex plasma crystal", AIP Conference Proceedings **1925**, 020016 (2018)
3. Couëdel, L.; Arnas, C.; Acsente, T. & Chami, A. "Characterisation of a high-pressure direct-current magnetron discharge used for tungsten nanoparticle production", AIP Conference Proceedings, **1925**, 020020 (2018)
4. L. Couëdel, M. Cavarroc, Y. Tessier, M. Mikikian, L. Boufendi, A.A. Samarian, "Formation, Growth, and Behavior of Dust Particles in a Sputtering Discharge", f-2, pp. 42–47 in WDS'06 Proceedings of Contributed Papers: Part II : Physics of Plasmas and Ionized Media
5. L. Couëdel, A. Samarian, M. Mikikian, L. Boufendi and Cameron Cuthbert, "Dust charge in complex plasma afertglow", Australian Institute of Physics 17th National Congress 2006 – Brisbane, 3-8 December 2006 , Paper No. 0080

B.4 Contributed Oral Presentations

* Presentation by graduate students I supervised

1. J. Moreno, L. Couëdel and M. Bradley. Experimental Characterization of a Plasma Immersion Ion Implantation System. 1^{rmst} SoPlasma workshop, Marseille, Marseille, June 14–16, 2022.
2. *J.H., Mun., M., Muraglia., O., Agulo., C., Arnas. and L., Couedel. (June 2022). Impurity transport modelling in a magnetron discharge. 1st SoPlasma workshop, Marseille, Marseille, June 14, 2022 to June 16, 2022.

3. *J. Vanegas, E. Dewit, C. Chamberlain, A. Choudhury, R. Golingo and L. Couëdel. Preliminary characterization of a plasma source at FUSE using a triple Langmuir probe.. Gaseous Electronics Meeting 2022, Sydney, February 14–16, 2022.
4. *N. Nelson, L. Couëdel and C. Xiao. Design and Characterization of a Dust Dispenser for Tungsten Dust Studies in the STOR-M tokamak. Gaseous Electronics Meeting 2022, Sydney, February 14–16, 2022.
5. L. Couëdel, V. Nosenko and Sergey, Zhdanov, Mode-coupling instability of two- dimensional complex plasma crystals in asymmetric capacitively-coupled radio-frequency discharges, 2021 Canadian Association of Physicists (CAP) Congress (virtual), June 7, 2021 to June 11, 2021.
6. * J. Moreno, L. Couëdel, M. Bradley, and A. Khodaee, Time Resolved Characterization of a Plasma Immersion Ion Implantation System, 2021 Canadian Association of Physicists (CAP) Congress (virtual), June 7, 2021 to June 11, 2021.
7. * N. Nelson, C. Xiao, and L. Couëdel, Design and Characterization of a Dust Injector for STOR-M, 2021 Canadian Association of Physicists (CAP) Congress (virtual), June 7, 2021 to June 11, 2021.
8. L. Couëdel, S. Barbosa, C. Arnas, F. Onofri,In-situ characterisation of the dynamics of a growing dust particle cloud in a direct-current argon glow discharge. 43rd IOP Plasma Physics conference, 23-26 May 2016, Sabhal Mòr Ostaig, Isle of Skye, UK
9. L. Couëdel, S. Barbosa, C. Arnas, F. Onofri, S. Khrapak, In-situ characterization of the dynamics of a growing dust particle cloud in a direct-current argon glow discharge, GEM 2016: Gaseous Electronics Meeting, 14-17 February 2016, Geelong, Victoria, Australia
10. L. Couëdel, S. Barbosa, C. Arnas, F. Onofri, C. Pardanaud, "Dynamics of a growing dust particle cloud in a direct-current argon sputtering glow discharge", CIP 2015, Communication orale, Saint Etienne, France
11. L. Couëdel, C.-R. Du, S. Zhdanov, V. Nosenko, A. Ivlev, H. Thomas, and G.E. Morfill, "Synchronisation of particle motion induced by mode coupling in a two-dimensional plasma crystal", Oral communication O3.307, 41^{st} EPS Conference on Plasma Physics, Berlin, Germany, 23-27 June 2014.
12. L. Couëdel, V. Nosenko, Z. Zhdanov and A. Ivlev, H. Thomas, and G. Morfill, "Mode coupling'due to ion wakes in 2D complex plasma crystals", Oral communication, 17th Gaseous Electronics Meeting, Murramarang NSW, Australia, February 5-8 2012
13. L. Couëdel, V. Nosenko, Z. Zhdanov and A. Ivlev, H. Thomas, and G. Morfill, "Out-of-plane modes in 2D complex plasma crystals", Oral communication, 37th EPS Conference on Plasma Physics, 21-25 June 2010, Dublin, Ireland.
14. L. Couëdel, V. Nosenko, Z. Zhdanov and A. Ivlev, "Out-of-plane modes in 2D complex plasma crystals", Oral communication, 16th Gaseous Electronics Meeting, Murramarang NSW (Australia), January 31- February 3 2010
15. L. Couëdel, A.A. Samarian, M. Mikikian, and L. Boufendi, "Diffusion in complex (dusty) plasma afterglow", Oral communication , 15th Gaseous Electronics Meeting, Murramarang NSW (Australia), 3-7 February 2008
16. L. Couëdel, A.A. Samarian, M. Mikikian, L. Boufendi, "Dependance of residual charge on dusty plasma parameters", Oral communication, 34th EPS Conference on Plasma Physics, 2-6 July 2007, Warsaw, Poland.
17. L. Couëdel, M. Mikikian, Y. Tessier, L. Boufendi, A.A. Samarian, "Charge électrique résiduelle sur des poudres à l'extinction d'un plasma poussiéreux", 5e Conf. de la Sté Française d'Electrostatique, 30-31 August 2006, Grenoble, France.

B.5 Posters presentations

* Presentation by graduate students I supervised

1. * J. Hern MUN., L. Couedel, O. Agullo, M. Muraglia and C. Arnas, Impurity transport modelling in a magnetron discharge, 2021 Canadian Association of Physicists (CAP) Congress (virtual), June 7, 2021 to June 11, 2021
2. * A. Chang, A. Khodaee, J. Moreno, L. Couëdel, and M. Bradley. "Pulsed-Target Magnetron- Enhanced ICP Plasma System", Canadian Association of Physicists annual congress, Burnaby, June 2, 2019 to July 12, 2019.
3. * N. Nelson, C Xiao, and L. Couëdel. "Effect of CT Injection on Dusty Plasma in the STOR-M Tokamak", Canadian Association of Physicists annual congress, Burnaby, June 2, 2019 to July 12, 2019.
4. L. Couëdel, A. Chami, and C. Arnas. DC magnetron discharge used for nanoparticle growth: comparison of particle- in-cell simulations with experimental measurements. Canadian Association of Physicists annual congress, Burnaby, June 2, 2019 to July 12, 2019.
5. * J, Moreno, L, Couëdel., M., Bradley. Laser-Induced Fluorescence Measurements of Ion Implantation in Inductively Coupled Plasma PIII Device. 13th Frontiers in Low-Temperature Plasma Diagnostics, Bad Honnef, May 13, 2019 to May 16, 2019.
6. L. Couëdel, A. Chami, C. Arnas. DC magnetron discharge used for nanoparticle growth: comparison of particle- in-cell simulations with experimental measurements. 13th Frontiers in Low-Temperature Plasma Diagnostics, Bad Honnef, May 13, 2019 to May 16, 2019.
7. Couëdel, L., D., Artis., M., P. Khanal., et al. Particle growth in highly magnetized Ar/C2H2 cc-rf discharge. International Congress on Plasma Physics (ICPP), Vancouver, BC, June 1, 2018 to June 1, 2018.
8. L. Couëdel, S. LeBlanc, T. Hall, U. Konopka, E. Thomas, Growth of nanoparticles in a strongly magnetized plasma, 59th Annual Meeting of the APS Division of Plasma Physics, October 23–27, 2017; Milwaukee, Wisconsin, USA
9. L. Couëdel, S. Barbosa, C. Arnas, F. Onofri, C. Pardanaud, "Dynamics of a growing dust particle cloud in a direct-current argon sputtering glow discharge", FLTPD XI, 2015, Poster, Porquerolles, France
10. L. Couëdel, S. Barbosa, C. Arnas, F. Onofri, C. Pardanaud, "Dynamics of a growing dust particle cloud in a direct-current argon sputtering glow discharge", ICPIG 2015, Poster, Iasi, Roumanie
11. L. Couëdel, S. Barbosa, Kishor Kumar K., C. Arnas and, F. Onofri, "Optical investigations of tungsten dust particles in a DC glow discharge", P5.122, 41^{st} EPS Conference on Plasma Physics, Berlin, Germany, 23-27 June 2014.
12. L. Couëdel, Kishor Kumar K., and C. Arnas, "Growth of tungsten nanoparticles in direct-current argon glow discharges", P2.308, 40^{th} EPS Conference on Plasma Physics, Espoo, Finland, 1—5 July 2013.
13. L. Couëdel, C. Arnas, K. Kishor Kumar and B. Pégourié, "Tungsten erosion and dust formation in plasmas", Poster A174, 14th International Conference on Plasma-Facing Materials and Components for Fusion Applications, 13-17 May 2013, Jülich, Germany
14. L. Couëdel, Kishor Kumar K., and C. Arnas, "Formation and growth of tungsten nanoparticles in a low pressure argon discharge", P5.139, 39^{th} EPS Conference & 16^{th} Int. Congress on Plasma Physics, Stockholm, Sweden, 2 - 6 July 2012.

15. Samarian, AA; Boufendi, L; Couëdel, L, et al., "Afterglow complex plasma", 5th Interantional Conference on Physics of Dusty Plasmas, MAY 18-23, 2008 Ponta Delgada PORTUGAL, MULTIFACETS OF DUSTY PLASMA Volume: 1041 Pages: 37-40 (2008)

16. Couëdel, L; Samarian, AA; Mikikian, M, et al., "Influence of plasma diffusion losses on dust charge relaxation in discharge afterglow", 5th Interantional Conference on Physics of Dusty Plasmas, MAY 18-23, 2008 Ponta Delgada PORTUGAL, MULTIFACETS OF DUSTY PLASMA Volume: 1041 Pages: 183-184 (2008)

17. Couëdel, L; Samarian, AA; Mikikian, M, et al., "Dust density influence on complex plasma decay", 5th Interantional Conference on Physics of Dusty Plasmas, MAY 18-23, 2008 Ponta Delgada PORTUGAL, MULTIFACETS OF DUSTY PLASMA Volume: 1041 Pages: 185-186 (2008)

18. Churton, B; Couëdel, L; Samarian, AA, et al., "Dust growth by RF sputtering", 5th Interantional Conference on Physics of Dusty Plasmas, MAY 18-23, 2008 Ponta Delgada PORTUGAL, MULTIFACETS OF DUSTY PLASMA Volume: 1041 Pages: 187-188 (2008)

19. Layden, B; Couëdel, L; Samarian, AA, et al., "Dust cloud dynamics in complex plasma afterglow", 5th Interantional Conference on Physics of Dusty Plasmas, MAY 18-23, 2008 Ponta Delgada PORTUGAL,MULTIFACETS OF DUSTY PLASMA Volume: 1041 Pages: 189-190 (2008)

20. L. Couëdel, A. Mezeghrane, B. W. James, M. Mikikian, A. A. Samarian, M. Cavarroc, Y. Tessier and L. Boufendi, "Plasma decays in dusty afterglow", 34th EPS Conference on Plasma Phys. Warsaw, 2 - 6 July 2007 ECA Vol.31F, P-2.068 (2007) ISBN: 978-83-926290-0-9

21. L. Couëdel, A. Mezeghrane, M. Mikikian, A. A. Samarian, M. Cavarroc, Y. Tessier and L. Boufendi, "Complex plasma afterglow", 34th EPS Conference on Plasma Phys. Warsaw, 2 - 6 July 2007 ECA Vol.31F, P-2.122 (2007) ISBN: 978-83-926290-0-9

22. A. Mezeghrane, L. Couëdel, G. Wattieaux, M. Mikikian, O. Lamrous, Y. Tessier, L. Boufendi, "Dust particle synthesis in N2 – CH4 gas mixture capacitively coupled radiofrequency discharge", 34th EPS Conference on Plasma Phys. Warsaw, 2 - 6 July 2007 ECA Vol.31F, O-3.006 (2007) ISBN: 978-83-926290-0-9

23. L. Couëdel, M. Mikikian, A. A. Samarian, L. Boufendi, "Dependance of dust residual charge on plasma parameters", 34th EPS Conference on Plasma Phys. Warsaw, 2 - 6 July 2007 ECA Vol.31F, O-5.008 (2007) ISBN: 978-83-926290-0-9

24. A. Mezeghrane, L. Couëdel, G. Wattieaux, M. Mikikian, O. Lamrous, Y. Tessier, L. Boufendi, "Study of hydrocarbon dust particle formation in Ar-CH4 radiofrequency low pressure discharge", 34th EPS Conference on Plasma Phys. Warsaw, 2 - 6 July 2007 ECA Vol.31F, P-5.047 (2007) ISBN: 978-83-926290-0-9

25. M. Mikikian, L. Couëdel, M. Cavarroc, Y. Tessier, L. Boufendi, "Dusty Plasma Dynamics During a Void Instability: Heartbeat Instability", 34th EPS Conference on Plasma Phys. Warsaw, 2 - 6 July 2007 ECA Vol.31F, P-5.053 (2007) ISBN: 978-83-926290-0-9

26. L. Couëdel, M. Mikikian, Y. Tessier, L. Boufendi, A. A. Samarian , "Residual electric charges on dust grains at plasma extinction", 33rd EPS Conference on Plasma Phys. Rome, 19 - 23 June 2006 ECA Vol.30I, P-4.042 (2006) ISBN: 2-914771-40-1

27. M. Cavarroc, M. Mikikian, L. Couëdel, L. Boufendi, "Formation of single-crystal silicon nanoparticles at very low gas temperature in a rf silane-based discharge", 33rd EPS Conference on Plasma Phys. Rome, 19 - 23 June 2006 ECA Vol.30I, P-4.043 (2006) ISBN: 2-914771-40-1

28. L. Couëdel, M. Mikikian, L. Boufendi and A.A. Samarian, “Residual dust charges in an afterglow plasma”, 13th International Congress on Plasma Physics, Kiev (Ukraine), May 22-26, 2006
29. L. Couëdel, M. Mikikian, Y. Tessier, L. Boufendi, A. A. Samarian, “Charges résiduelles sur des poudres à l’extinction d’un plasma”, IX congrès de la division plasmas de la société française de physique, 2-5 mai 2006, Pont-à-Mousson (France)
30. M. Mikikian, M. Cavarroc, L. Couëdel, Y. Tessier, L. Boufendi, “Instabilités dans les plasmas: formation de poussières”, IX congrès de la division plasmas de la société française de physique, 2-5 mai 2006, Pont-à-Mousson (France)
31. A. A. Samarian, S. V. Vladimirov, T. Olshansky, L. Couëdel, and B. W. James, “Wake Pairing of Dust Particles” , AIP Conf. Proc. 799, 557 (2005) ISBN: 0-7354-0287-6
32. L. Couëdel and A. A. Samarian, “Particle charges determination for two vertically aligned dust particles in a complex plasma”, AIP Conf. Proc. 799, 549 (2005) ISBN: 0-7354-0287-6
33. B. W. James, A. A. Samarian, W. Tsang, and L. Couëdel, “Measurements of Electric Field And Dust Charge in A Plasma Sheath”, AIP Conf. Proc. 799, 545 (2005) ISBN: 0-7354-0287-6

B.6 Seminars and workshops

1. L. Couëdel, “Two-dimensional plasma crystals: waves and instabilities", Invited seminar. University of Illinois, September 2020
2. L. Couëdel, “Études expérimentales des cristaux coulombiens: ondes et instabilités”, Invited seminar, Université de Montreal, January 2020
3. L. Couëdel, “Experimental studies of two-dimensional complex plasma crystals: waves and instabilities”, Invited seminar, University of Manitoba, September 2019
4. L. Couëdel, Experimental studies of two-dimensional complex plasma crystals: waves and instabilities. Invited seminar,University of Winnipeg, September 2019
5. L. Couëdel, “Two-dimensional plasma crystals: waves and instabilities", Invited seminar. University of Alberta, June 2019
6. L. Couëdel and C. Arnas, “Growth of tungsten nanoparticles in direct-current argon glow discharges”, Workshop : Turbulence, Transport and Structures in Magnetized Plasmas, IMERA, Marseille, 3-6 june 2013
7. L. Couëdel, “Direct Measurement of Optical Phonons in Plasma Crystals”, Workshop on Current Topics in Plasma Physics and Space Science of Societal Importance, IMERA, Marseille, 24-25 january 2013
8. L. Couëdel, M. Mikikian, R. Heidemann et al., “Void instabilities and void oscillations in complex plasmas”, Oral communication, 11h Workshop on Fine Particle Plasmas, NIFS, Toki, Japan, 19-20 November 2010
9. L. Couëdel, V. Nosenko, Z. Zhdanov and A. Ivlev, “First Direct measurement of optical phonons in 2D plasma crystals”, Oral communication, 10th Workshop on Fine Particle Plasmas, NIFS, Toki, Japan, 26-27 November 2009
10. L. Couëdel, B. Layden, B.W. James and A.A. Samarian, “Electron temperature measurement in a complex plasma”, Oral communication, 8th Australia-Japan plasma diagnostics workshop, Australia, 2-5 February 2009

11. L. Couëdel, A. Mezeghrane, B. W. James, M. Mikikian, A. A. Samarian, M. Cavarroc, Y. Tessier and L. Boufendi, “Plasma decays in dusty afterglow”, Poster, 9th International Workshop on the Interrelationship between Plasma Experiments in Laboratory and Space, 5th-10th August 2007 - Palm Cove Resort, Cairns (Australia)
12. L. Couëdel, M. Mikikian, Y. Tessier, L. Boufendi, A.A. Samarian, “Charge électrique résiduelle sur des poudres à l’extinction d’un plasma poussiéreux”, GDR Microgravity, 4-6 December 2006, Frejus, France.

B.7 Science outreach

1. L. Couëdel, "Physique des plasmas: recherches fondamentales et applications", Public lecture, Association Francophone pour le Savoir, March 2019

Bibliography

[1] A. Melzer *et al.*, 2019, *Physics of Dusty Plasmas*, Springer-Verlag GmbH, ISBN 9783030202606.

[2] A. V. Ivlev, S. K. Zhdanov, M. Lampe, *et al.*, 2014, "Mode-coupling instability in a fluid two-dimensional complex plasma", *Phys. Rev. Lett.*, vol. 113, p. 135002.

[3] C. J. Mitchell, M. Horanyi, O. Havnes, *et al.*, 2006, "Saturn's Spokes: Lost and Found", *Science*, vol. 311, no. 5767, pp. 1587–1589.

[4] G. S. Selwyn, C. A. Weiss, F. Sequeda, *et al.*, 1997, "Particle contamination formation in magnetron sputtering processes", *Journal of Vacuum Science & Technology A*, vol. 15, no. 4, pp. 2023–2028.

[5] G. S. Selwyn, J. Singh, and R. S. Bennett, 1989, "In situ laser diagnostic studies of plasma-generated particulate contamination", *J. Vac. Sci. Technol. A*, vol. 7, no. 4, pp. 2758–2765.

[6] C. Arnas, J. Irby, S. Celli, *et al.*, 2017, "Characterization and origin of large size dust particles produced in the Alcator C-Mod tokamak", *Nuclear Materials and Energy*, vol. 11, pp. 12–19, ISSN 2352-1791.

[7] M. Balden, N. Endstrasser, P. Humrickhouse, *et al.*, 2014, "Collection strategy, inner morphology, and size distribution of dust particles in asdex upgrade", *Nucl. Fusion*, vol. 54, no. 7, p. 073010.

[8] E. Fortuna-Zalesna, J. Grzonka, M. Rasinski, *et al.*, 2014, "Characterization of dust collected after plasma operation of all-tungsten asdex upgrade", *Phys. Scr.*, vol. 2014, no. T159, p. 014066.

[9] L. Couëdel, S. Zhdanov, V. Nosenko, *et al.*, 2014, "Synchronization of particle motion induced by mode coupling in a two-dimensional plasma crystal", *Phys. Rev. E*, vol. 89, p. 053108.

[10] T. B. Röcker, L. Couëdel, S. K. Zhdanov, *et al.*, 2014, "Nonlinear regime of the mode-coupling instability in 2d plasma crystals", *EPL (Europhysics Letters)*, vol. 106, no. 4, p. 45001.

[11] L. Couëdel, D. Samsonov, C. Durniak, *et al.*, 2012, "Three-dimensional structure of mach cones in monolayer complex plasma crystals", *Phys. Rev. Lett.*, vol. 109, p. 175001.

[12] J. D. Williams, E. Thomas, L. Couëdel, *et al.*, 2012, "Kinetics of the melting front in two-dimensional plasma crystals: Complementary analysis with the particle image and particle tracking velocimetries", *Phys. Rev. E*, vol. 86, p. 046401.

[13] G. E. Morfill and A. V. Ivlev, 2009, "Complex plasmas: An interdisciplinary research field", *Rev. Mod. Phys.*, vol. 81, no. 4, pp. 1353–1404.

[14] Y. Watanabe, 2006, "Formation and behaviour of nano/micro-particles in low pressure plasmas", *J. Phys. D: Appl. Phys.*, vol. 39, no. 19, p. R329.

[15] M. Cavarroc, M. Mikikian, Y. Tessier, *et al.*, 2008, "Instabilities during the growth of dust successive generations in silane-based plasmas", *Phys. Plasmas*, vol. 15, no. 10, p. 103704.

[16] Y. Qin, U. R. Kortshagen, and E. S. Aydil, 2016, "Laser light scattering from silicon particles generated in an argon diluted silane plasma", *J. Phys. D: Appl. Phys.*, vol. 49, no. 8, p. 085203.

[17] S. Groth, F. Greiner, B. Tadsen, *et al.*, 2015, "Kinetic mie ellipsometry to determine the time-resolved particle growth in nanodusty plasmas", *J. Phys. D: Appl. Phys.*, vol. 48, no. 46, p. 465203.

[18] S. Mitic, S. Coussan, C. Martin, *et al.*, 2018, "Hydro-carbon material design in a capacitively coupled radio-frequency discharge", *Plasma Processes Polym.*, vol. 15, no. 3, p. 1700152.

[19] L. Couëdel, D. Artis, M. P. Khanal, *et al.*, 2019, "Influence of magnetic field strength on nanoparticle growth in a capacitively-coupled radio-frequency ar/c2h2 discharge", *Plasma Research Express*, vol. 1, no. 1, p. 015012.

[20] D. Samsonov and J. Goree, 1999, "Particle growth in a sputerring discharge", *J. Vac. Sci. Technol. A*, vol. 17, no. 5, p. 2835.

[21] M. Mikikian and L. Boufendi, 2004, "Experimental investigations of void dynamics in a dusty discharge", *Phys. Plasmas*, vol. 11, no. 8, p. 3733.

[22] C. Arnas, A. Chami, L. Couëdel, *et al.*, 2019, "Thermal balance of tungsten monocrystalline nanoparticles in high pressure magnetron discharges", *Phys. Plasmas*, vol. 26, no. 5, p. 053706.

[23] A. Bouchoule, 1999, *Dusty Plasmas: Physics, Chemistry and Technological impacts in Plasma Processing*, John Wiley & Sons, New York, ISBN 0471973866.

[24] P. K. Shukla and A. A. Mamun, 2002, *Introduction to dusty plasma*, IOP Publishing, Bristol.

[25] G. E. Morfill, V. N. Tsytovich, and H. Thomas, 2003, "Complex plasmas: Ii. elementary processes in complex plasmas", *Plasma Phys. Rep.*, vol. 29, p. 1.

[26] V. Fortov, A. Ivlev, S. Khrapak, *et al.*, 2005, "Complex (dusty) plasmas: Current status, open issues, perspectives", *Phys. Rep.*, vol. 421, no. 1-2, pp. 1 – 103.

[27] V. Fortov, A. Nefedov, O. Vaulina, *et al.*, 1998, "Dusty plasma induced by solar radiation under microgravitational conditions: An experiment on board the mir orbiting space station", *J. Exp. Theor. Phys.*, vol. 87, no. 6, pp. 1087–1097.

[28] A. A. Samarian and O. S. Vaulina, 2000, "Uv-induced coulomb structure in discharge plasma", *Phys. Lett. A*, vol. 278, no. 3, pp. 146–151.

[29] X. Wang, M. Horányi, and S. Robertson, 2009, "Experiments on dust transport in plasma to investigate the origin of the lunar horizon glow", *Journal of Geophysical Research: Space Physics*, vol. 114, no. A5, pp. n/a–n/a.

[30] R. D. Smirnov, A. Y. Pigarov, M. Rosenberg, *et al.*, 2007, "Modelling of dynamics and transport of carbon dust particles in tokamaks", *Plasma Physics and Controlled Fusion*, vol. 49, no. 4, pp. 347–371.

[31] L. Vignitchouk, G. L. Delzanno, P. Tolias, *et al.*, 2018, "Electron reflection effects on particle and heat fluxes to positively charged dust subject to strong electron emission", *Phys. Plasmas*, vol. 25, no. 6, p. 063702.

[32] A. Autricque, S. A. Khrapak, L. Couëdel, *et al.*, 2018, "Electron collection and thermionic emission from a spherical dust grain in the space-charge limited regime", *Phys. Plasmas*, vol. 25, no. 6, p. 063701.

[33] S. Khrapak and G. Morfill, 2009, "Basic processes in complex (dusty) plasmas: Charging, interactions, and ion drag force", *Contrib Plasm Phys*, vol. 49, no. 3, pp. 148–168.

[34] I. H. Hutchinson, 2011, "Forces on a small grain in the nonlinear plasma wake of another", *Phys. Rev. Lett.*, vol. 107, no. 9, p. 095001.

[35] S. A. Khrapak, A. V. Ivlev, and G. E. Morfill, 2010, "Shielding of a test charge: Role of plasma production and loss balance", *Physics of Plasmas*, vol. 17, no. 4, p. 042107.

[36] V. Nosenko, A. V. Ivlev, S. K. Zhdanov, *et al.*, 2009, "Rotating electric fields in complex (dusty) plasmas", *Phys. Plasmas*, vol. 16, no. 8, p. 083708.

[37] V. Nosenko, J. Goree, Z. Ma, *et al.*, 2003, "Compressional and shear wakes in a two-dimensional dusty plasma crystal", *Physical Review E*, vol. 68, no. 5, p. 056409.

[38] D. Samsonov, S. Zhdanov, and G. Morfill, 2005, "Vertical wave packets observed in a crystallized hexagonal monolayer complex plasma", *Phys. Rev. E*, vol. 71, no. 2, p. 026410.

[39] P. Qiu, T. Sun, and Y. Feng, 2021, "Observation of the solid and liquid separation after the shock propagation in a two-dimensional yukawa solid", *Physics of Plasmas*, vol. 28, no. 11, p. 113702.

[40] A. Kananovich and J. Goree, 2021, "Shock width measured under liquid and solid conditions in a two-dimensional dusty plasma", *Physical Review E*, vol. 104, no. 5, p. 055201.

[41] H. M. Thomas and G. E. Morfill, 1996, "Melting dynamics of a plasma crystal", *Nature*, vol. 379, pp. 806–809.

[42] J. Berumen and J. Goree, 2021, "Experiment and model for a stokes layer in a strongly coupled dusty plasma", *Physical Review E*, vol. 104, no. 3, p. 035208.

[43] B. Liu, J. Goree, M. Y. Pustylnik, *et al.*, 2021, "Time-dependent shear motion in a strongly coupled dusty plasma in PK-4 on the international space station (ISS)", *IEEE Transactions on Plasma Science*, vol. 49, no. 9, pp. 2972–2978.

[44] E. V. Vasilieva, O. F. Petrov, and M. M. Vasiliev, 2021, "Laser-induced melting of two-dimensional dusty plasma system in RF discharge", *Scientific Reports*, vol. 11, no. 1.

[45] A. P. Nefedov, G. E. Morfill, V. E. Fortov, *et al.*, 2003, "Pke-nefedov: plasma crystal experiments on the international space station", *New J. Phys.*, vol. 5, pp. 33.1–33.10.

[46] H. M. Thomas, G. E. Morfill, V. E. Fortov, *et al.*, 2008, "Complex plasma laboratory pk-3 plus on the international space station", *New J. Phys.*, vol. 10, no. 3, p. 033036 (14pp).

[47] M. Y. Pustylnik, M. A. Fink, V. Nosenko, *et al.*, 2016, "Plasmakristall-4: New complex (dusty) plasma laboratory on board the international space station", *Rev. Sci. Instrum.*, vol. 87, no. 9, p. 093505.

[48] H. Rothermel, T. Hagl, G. E. Morfill, *et al.*, 2002, "Gravity compensation in complex plasmas by application of a temperature gradient", *Phys. Rev. Lett.*, vol. 89, p. 175001.

[49] M. Schwabe, M. Rubin-Zuzic, S. Zhdanov, *et al.*, 2007, "Highly resolved self-excited density waves in a complex plasma", *Phys. Rev. Lett.*, vol. 99, no. 9, p. 095002.

[50] B. M. Annaratone, Y. Elskens, C. Arnas, *et al.*, 2009, "Agglomeration of mesoscopic particles in plasma", *New J. Phys.*, vol. 11, no. 10, p. 103013.

[51] S. Dap, D. Lacroix, F. Patisson, *et al.*, 2010, "Agglomeration processes in carbonaceous dusty plasmas, experiments and numerical simulations", *New J. Phys.*, vol. 12, no. 9, p. 093014.

[52] C. Arnas, A. Michau, G. Lombardi, *et al.*, 2013, "Effects of the growth and the charge of carbon nanoparticles on dc discharges", *Phys. Plasmas*, vol. 20, p. 013705.

[53] K. K. K., L. Couëdel, and C. Arnas, 2013, "Growth of tungsten nanoparticles in direct-current argon glow discharges", *Phys. Plasmas*, vol. 20, no. 4, p. 043707.

[54] L. Couëdel, K. Kumar K., and C. Arnas, 2014, "Detrapping of tungsten nanoparticles in a direct-current argon glow discharge", *Physics of Plasmas*, vol. 21, no. 12, p. 123703.

[55] K. K. K., L. Couëdel, and C. Arnas, 2014, "Nanoparticles in direct-current discharges: Growth and electrostatic coupling.", *J. Plasma Phys.*, vol. 80, p. 849.

[56] S. Barbosa, L. Couëdel, C. Arnas, *et al.*, 2016, "In-situ characterisation of the dynamics of a growing dust particle cloud in a direct-current argon glow discharge", *J. Phys. D: Appl. Phys.*, vol. 49, no. 4, p. 045203.

[57] S. Barbosa, F. R. A. Onofri, L. Couëdel, *et al.*, 2016, "An introduction to light extinction spectrometry as a diagnostic for dust particle characterisation in dusty plasmas", *J. Plasma Phys.*, vol. 82, no. 4, p. 615820403.

[58] M. Mikikian, L. Couëdel, M. Cavarroc, *et al.*, 2007, "Self-excited void instability in dusty plasmas: plasma and dust cloud dynamics during the heartbeat instability", *New J. Phys.*, vol. 9, no. 8, p. 268.

[59] R. J. Heidemann, L. Couëdel, S. K. Zhdanov, *et al.*, 2011, "Comprehensive experimental study of heartbeat oscillations observed under microgravity conditions in the pk-3 plus laboratory on board the international space station", *Phys. Plasmas*, vol. 18, no. 5, p. 053701.

[60] M. Mikikian, L. Couëdel, M. Cavarroc, *et al.*, 2010, "Threshold phenomena in a throbbing complex plasma", *Phys. Rev. Lett.*, vol. 105, p. 075002.

[61] M. Y. Pustylnik, A. V. Ivlev, N. Sadeghi, *et al.*, 2012, "On the heterogeneous character of the heartbeat instability in complex (dusty) plasmas", *Phys. Plasmas*, vol. 19, no. 10, p. 103701.

[62] H. M. Mott-Smith and I. Langmuir, 1926, "The theory of collectors in gaseous discharges", *Phys. Rev.*, vol. 28, no. 4, pp. 727–763.

[63] J. E. Allen, 1992, "Probe theory - the orbital motion approach", *Phys. Scr.*, vol. 45, no. 5, p. 497.

[64] J. E. Allen, B. M. Annaratone, and U. de Angelis, 2000, "On the orbital motion limited theory for a small body at floating potential in a Maxwellian plasma", *J. Plasma Phys.*, vol. 63, pp. 299–309.

[65] A. Piel, 2017, "Plasma crystals: experiments and simulation", *Plasma Phys. Controlled Fusion*, vol. 59, no. 1, p. 014001.

[66] A. Piel, 2017, *Plasma physics: an introduction to laboratory, space, and fusion plasmas*, Springer, ISBN 978-3-319-87553-8.

[67] I. Goertz, F. Greiner, and A. Piel, 2011, "Effects of charge depletion in dusty plasmas", *Physics of Plasmas*, vol. 18, no. 1, p. 013703.

[68] O. Havnes, T. K. Aanesen, and F. Melandsø, 1990, "On dust charges and plasma potentials in a dusty plasma with dust size distribution", *J. Geophys. Res.*, vol. 95, no. A5, pp. 6581–6585.

[69] A. V. Zobnin, A. D. Usachev, O. F. Petrov, *et al.*, 2008, "Ion current on a small spherical attractive probe in a weakly ionized plasma with ion-neutral collisions (kinetic approach)", *Phys. Plasmas*, vol. 15, no. 4, p. 043705.

[70] E. C. Whipple, 1981, "Potentials of surfaces in space", *Rep. Prog. Phys.*, vol. 44, no. 11, pp. 1197–1250.

[71] B. Liu, J. Goree, V. Nosenko, *et al.*, 2003, "Radiation pressure and gas drag forces on a melamine-formaldehyde microsphere in a dusty plasma", *Phys. Plasmas*, vol. 10, no. 1, pp. 9–20.

[72] F. Zheng, 2002, "Thermophoresis of spherical and non-spherical particles: a review of theories and experiments", *Adv. Colloid & Interface Sci.*, vol. 97, pp. 255–278.

[73] C. Arnas, T. Guidez, A. Chami, *et al.*, 2022, "Forces applied to nanoparticles in magnetron discharges and the resulting size segregation", *Physics of Plasmas*, vol. 29, no. 7, p. 073703.

[74] L. Couëdel, M. Mikikian, L. Boufendi, *et al.*, 2006, "Residual dust charges in discharge afterglow", *Phys. Rev. E*, vol. 74, no. 2, p. 026403.

[75] M. S. Barnes, J. H. Keller, J. C. Forster, *et al.*, 1992, "Transport of dust particles in glow-discharge plasmas", *Phys. Rev. Lett.*, vol. 68, no. 3, pp. 313–316.

[76] C. Zafiu, A. Melzer, and A. Piel, 2002, "Ion drag and thermophoretic forces acting on free falling charged particles in an rf-driven complex plasma", *Phys. Plasmas*, vol. 9, p. 4794.

[77] C. Zafiu, A. Melzer, and A. Piel, 2003, "Measurement of the ion drag force on falling dust particles and its relation to the void formation in complex (dusty) plasmas", *Physics of Plasmas*, vol. 10, no. 5, pp. 1278–1282.

[78] S. A. Khrapak, A. V. Ivlev, S. K. Zhdanov, *et al.*, 2005, "Hybrid approach to the ion drag force", *Phys. Plasmas*, vol. 12, p. 042308.

[79] I. H. Hutchinson, 2006, "Collisionless ion drag force on a spherical grain", *Plasma Physics and Controlled Fusion*, vol. 48, no. 2, pp. 185–202.

[80] L. Patacchini and I. H. Hutchinson, 2008, "Fully self-consistent ion-drag-force calculations for dust in collisional plasmas with an external electric field", *Physical Review Letters*, vol. 101, no. 2, p. 025001.

[81] A. Ashkin, 1970, "Acceleration and trapping of particles by radiation pressure", *Physical Review Letters*, vol. 24, no. 4, pp. 156–159.

[82] M. Rosen and C. Orr, 1964, "The photophoretic force", *Journal of Colloid Science*, vol. 19, no. 1, pp. 50–60.

[83] G. M. Hidy and J. R. Brock, 1967, "Photophoresis and the descent of particles into the lower stratosphere", *Journal of Geophysical Research*, vol. 72, no. 2, pp. 455–460.

[84] H. Rohatschek, 1985, "Direction, magnitude and causes of photophoretic forces", *Journal of Aerosol Science*, vol. 16, no. 1, pp. 29–42.

[85] K. G. Spears, T. J. Robinson, and R. M. Roth, 1986, "Particle distributions and laser-particle interactions in an rf discharge of silane", *Plasma Science, IEEE Transactions on*, vol. 14, no. 2, pp. 179–187, ISSN 0093-3813.

[86] G. S. Selwyn, J. E. Heidenreich, and K. L. Haller, 1990, "Particle trapping phenomena in radio frequency plasmas", *Appl. Phys. Lett.*, vol. 57, no. 18, pp. 1876–1878.

[87] A. Bouchoule, A. Plain, L. Boufendi, *et al.*, 1991, "Particle generation and behavior in a silane-argon low-pressure discharge under continuous or pulsed radio-frequency excitation", *J. Appl. Phys.*, vol. 70, p. 1991.

[88] A. A. Howling, C. Hollenstein, and P. Paris, 1991, "Direct visual observation of powder dynamics in rf plasma-assisted deposition", *Appl. Phys. Lett.*, vol. 59, no. 12, pp. 1409–1411.

[89] L. Boufendi, A. Plain, J. P. Blondeau, *et al.*, 1992, "Measurements of particle size kinetics from nanometer to micrometer scale in a low-pressure argon-silane radio-frequency discharge", *Appl. Phys. Lett*, vol. 60, p. 169.

[90] A. Bouchoule and L. Boufendi, 1993, "Particule formation and dusty plasma behaviour in argon-silane rf discharge", *Plasma Sources Sci. Technol.*, vol. 2, pp. 204–213.

[91] L. Boufendi, A. Bouchoule, R. K. Porteous, *et al.*, 1993, "Particle-particle interactions in dusty plasmas", *J. Appl. Phys.*, vol. 73, p. 2160.

[92] A. Bouchoule and L. Boufendi, 1994, "High concentration effects in dusty plasmas", *Plasma Sources Sci. Technol.*, vol. 3, pp. 292–301.

[93] C. Hollenstein, J. L. Dorier, J. Dutta, *et al.*, 1994, "Diagnostics of particle genesis and growth in rf silane plasmas by ion mass spectrometry and light scattering", *Plasma Sources Sci. Technol.*, vol. 3, no. 3, p. 278.

[94] P. R. i Cabarrocas, P. Gay, and A. Hadjadj, 1996, "Experimental evidence for nanoparticle deposition in continuous argon–silane plasmas: Effects of silicon nanoparticles on film properties", *J. Vac. Sci. Technol. A*, vol. 14, no. 2, pp. 655–659.

[95] E. Stoffels, W. W. Stoffels, G. M. W. Kroesen, *et al.*, 1996, "Dust formation and charging in an ar/sih[sub 4] radio-frequency discharge", *J. Vac. Sci. Technol.*, vol. 14, no. 2, pp. 556–561.

[96] F. Vivet, A. Bouchoule, and L. Boufendi, 1998, "Synthesis and characterization of sic:h ultrafine powder generated in an argon/silane/methane low-pressure radio-frequency discharge", *J. Appl. Phys.*, vol. 83, p. 7474.

[97] G. Viera, S. Huet, E. Bertran, *et al.*, 2001, "Polymorphous si thin films from radio frequency plasmas of sih4 diluted in ar: A study by transmission electron microscopy and raman spectroscopy", *J. Appl. Phys.*, vol. 90, p. 4272.

[98] M. Cavarroc, M. C. Jouanny, K. Radouane, *et al.*, 2006, "Self-excited instability occurring during the nanoparticle formation in an ar/sih_4 low pressure radio frequency plasma", *J. Appl. Phys.*, vol. 99, p. 064301.

[99] K. B. Chai, C. R. Seon, S. Park, *et al.*, 2009, "Dust particle growth in rf silane plasmas using two-dimensional multi-pass laser light scattering", *New J. Phys.*, vol. 11, no. 10, p. 103006 (8pp).

[100] C. Deschenaux, A. Affolter, D. Magni, *et al.*, 1999, "Investigations of ch 4 , c 2 h 2 and c 2 h 4 dusty rf plasmas by means of ftir absorption spectroscopy and mass spectrometry", *J. Phys. D: Appl. Phys.*, vol. 32, no. 15, p. 1876.

[101] S. Stoykov, C. Eggs, and U. Kortshagen, 2001, "Plasma chemistry and growth of nanosized particles in a c 2 h 2 rf discharge", *J. Phys. D: Appl. Phys.*, vol. 34, no. 14, p. 2160.

[102] J. Berndt, S. Hong, E. Kovacevic, *et al.*, 2003, "Dust particle formation in low pressure ar/ch4 and ar/c2h2 discharges used for thin film deposition", *Vacuum*, vol. 71, no. 3, pp. 377 – 390, ISSN 0042-207X.

[103] S. Mitic, M. Y. Pustylnik, G. E. Morfill, *et al.*, 2011, "In situ characterization of nanoparticles during growth by means of white light scattering", *Opt. Lett.*, vol. 36, no. 18, pp. 3699–3701.

[104] M. Cavarroc, 2007, *Nucleation, growth and behavior of dust particles in reactive low pressure radiofrequency plasmas: From nanocrystals to submicron polycrystalline grains.*, Theses, Université d'Orléans.

[105] U. R. Kortshagen, R. M. Sankaran, R. N. Pereira, *et al.*, 2016, "Nonthermal plasma synthesis of nanocrystals: fundamental principles, materials, and applications", *Chem. Rev.*, vol. 116, no. 18, pp. 11061–11127.

[106] A. Michau, C. Arnas, G. Lombardi, *et al.*, 2016, "Nanoparticle formation and dusty plasma effects in dc sputtering discharge with graphite cathode", *Plasma Sources Sci. Technol.*, vol. 25, no. 1, p. 015019.

[107] L. Boufendi and A. Bouchoule, 1994, "Particle nucleation and growth in a low-pressure argon-silane discharge", *Plasma Sources Sci. Technol.*, vol. 3, p. 262.

[108] P. R. i Cabarrocas, T. Nguyen-Tran, Y. Djeridane, *et al.*, 2007, "Synthesis of silicon nanocrystals in silane plasmas for nanoelectronics and large area electronic devices", *J. Phys. D: Appl. Phys.*, vol. 40, no. 8, pp. 2258–2266.

[109] M. Mikikian, L. Boufendi, A. Bouchoule, *et al.*, 2003, "Formation and behaviour of dust particle clouds in a radio-frequency discharge: results in the laboratory and under microgravity conditions", *New J. Phys.*, vol. 5, p. 19.1.

[110] M. Cavarroc, M. Mikikian, Y. Tessier, *et al.*, 2008, "Successive generations of dust in complex plasmas: A cyclic phenomenon in the void region", *Phys. Rev. Lett.*, vol. 100, no. 4, p. 045001.

[111] L. Couëdel, M. Mikikian, A. A. Samarian, *et al.*, 2010, "Self-excited void instability during dust particle growth in a dusty plasma", *Phys. Plasmas*, vol. 17, no. 8, p. 083705.

[112] M. Mikikian, M. Cavarroc, L. Couëdel, *et al.*, 2010, "Dust particles in low-pressure plasmas: Formation and induced phenomena", *Pure Appl. Chem.*, vol. 82, p. 1273.

[113] L. Couëdel, A. Mezeghrane, M. Mikikian, *et al.*, 2009, "Charge électrique résiduelle sur des poudres à l'extinction d'un plasma poussiéreux", *J. Electrostat.*, vol. 67, p. 625.

[114] L. Couëdel, V. Nosenko, A. V. Ivlev, *et al.*, 2010, "Direct observation of mode-coupling instability in two-dimensional plasma crystals", *Phys. Rev. Lett.*, vol. 104, no. 19, p. 195001.

[115] L. Couëdel and V. Nosenko, 2022, "Stability of two-dimensional complex plasma monolayers in asymmetric capacitively-coupled radio-frequency discharges", *Phys. Rev. E*, vol. 105, no. 1, p. 015210.

[116] M. A. Lieberman, 1989, "Model of plasma immersion ion implantation", *J. Appl. Phys.*, vol. 66, no. 7, pp. 2926–2929.

[117] Y. P. Raizer, M. N. Shneider, and N. A. Yatsenko, 1995, *Radio-Frequency Capacitive discharges*, CRC Press LLC, Florida.

[118] M. Chandhok and J. W. Grizzle, 1998, "Modeling the pressure dependence of dc bias voltage in asymmetric, capacitive rf sheaths", *IEEE Transactions on Plasma Science*, vol. 26, no. 2, pp. 181–189.

[119] Y. P. Song, D. Field, and D. F. Klemperer, 1990, "Electrical potentials in RF discharges", *Journal of Physics D: Applied Physics*, vol. 23, no. 6, pp. 673–681.

[120] V. A. Godyak and N. Sternberg, 1990, "Smooth plasma-sheath transition in a hydrodynamic model", *IEEE transactions on plasma science*, vol. 18, no. 1, pp. 159–168.

[121] V. A. Godyak and N. Sternberg, 1990, "Dynamic model of the electrode sheaths in a symmetricaly driven plasma", *Phys. Rev. A*, vol. 42, no. 4, p. 2299.

[122] M. A. Lieberman and A. J. Lichtenberg, 1994, *Principles of plasma discharges and materials processing*, Wiley, New York, ISBN 94-28954.

[123] M. A. Lieberman, 1988, "Analytical solution for capacitive rf sheath", *IEEE Trans. Plasma Sci*, vol. 16, p. 638.

[124] M. A. Sobolewski, 2000, "Sheath model for radio-frequency-biased, high-density plasmas valid for all ω/ω_i", *Phys. Rev. E*, vol. 62, pp. 8540–8553.

[125] M. N. A. Dewan, P. J. McNally, and P. A. F. Herbert, 2002, "Plasma modeling for a nonsymmetric capacitive discharge driven by a nonsinusoidal radio frequency current", *Journal of Applied Physics*, vol. 91, no. 9, pp. 5604–5613.

[126] J. Gierling and K.-U. Riemann, 1998, "Comparison of a consistent theory of radio frequency sheaths with step models", *Journal of Applied Physics*, vol. 83, no. 7, pp. 3521–3528.

[127] U. Czarnetzki, 2013, "Analytical model for the radio-frequency sheath", *Phys. Rev. E*, vol. 88, p. 063101.

[128] M. Moisan and J. Pelletier, 2006, *Physique des plasmas collisionnels: Application aux décharges haute fréquence*, Grenoble Sciences, Bonchamp-Lès-Laval, ISBN 978-2-7598-1129-8.

[129] J. Schulze, B. G. Heil, D. Luggenhölscher, *et al.*, 2008, "Stochastic heating in asymmetric capacitively coupled RF discharges", *Journal of Physics D: Applied Physics*, vol. 41, no. 19, p. 195212.

[130] M. L. Hause, B. D. Prince, and R. J. Bemish, 2013, "Krypton charge exchange cross sections for hall effect thruster models", *Journal of Applied Physics*, vol. 113, no. 16, p. 163301.

[131] T. Trottenberg, A. Melzer, and A. Piel, 1995, "Measurement of the electric charge on particulates forming coulomb crystals in the sheath of a radiofrequency plasma", *Plasma Sources Science and Technology*, vol. 4, no. 3, pp. 450–458.

[132] A. Homann, A. Melzer, and A. Piel, 1999, "Measuring the charge on single particles by laser-excited resonances in plasma crystals", *Physical Review E*, vol. 59, no. 4, pp. R3835–R3838.

[133] E. B. Tomme, D. A. Law, B. M. Annaratone, *et al.*, 2000, "Parabolic plasma sheath potentials and their implications for the charge on levitated dust particles", *Phys. Rev. Lett.*, vol. 85, p. 2518.

[134] A. Melzer, 2001, "Laser manipulation of particles in dusty plasmas", *Plasma Sources Science and Technology*, vol. 10, no. 2, pp. 303–310.

[135] L. Couëdel, V. Nosenko, S. K. Zhdanov, *et al.*, 2009, "First direct measurement of optical phonons in 2d plasma crystals", *Phys. Rev. Lett.*, vol. 103, no. 21, p. 215001.

[136] B. J. Harris, L. S. Matthews, and T. W. Hyde, 2013, "Vertical-probe-induced asymmetric dust oscillation in complex plasma", *Physical Review E*, vol. 87, no. 5, p. 053109.

[137] S. K. Zhdanov, L. Couëdel, V. Nosenko, *et al.*, 2015, "Spontaneous pairing and cooperative movements of micro-particles in a two dimensional plasma crystal", *Physics of Plasmas*, vol. 22, no. 5, p. 053703.

[138] M. Jambor, V. Nosenko, S. K. Zhdanov, *et al.*, 2016, "Plasma crystal dynamics measured with a three-dimensional plenoptic camera", *Review of Scientific Instruments*, vol. 87, no. 3, p. 033505.

[139] S. V. Vladimirov and M. Nambu, 1995, "Attraction of charged particulates in plasmas with finite flows", *Phys. Rev. E*, vol. 52, pp. R2172–R2174.

[140] S. V. Vladimirov and O. Ishihara, 1996, "On plasma crystal formation", *Phys. Plasmas*, vol. 3, no. 2, pp. 444–446.

[141] O. Ishihara and S. V. Vladimirov, 1997, "Wake potential of a dust grain in a plasma with ion flow", *Phys. Plasmas*, vol. 4, no. 1, pp. 69–74.

[142] R. Kompaneets, G. E. Morfill, and A. V. Ivlev, 2016, "Wakes in complex plasmas: A self-consistent kinetic theory", *Phys. Rev. E*, vol. 93, p. 063201.

[143] W. J. Miloch, 2010, "Wake effects and mach cones behind objects", *Plasma Phys. Controlled Fusion*, vol. 52, no. 12, p. 124004.

[144] L. S. Matthews, D. L. Sanford, E. G. Kostadinova, *et al.*, 2020, "Dust charging in dynamic ion wakes", *Physics of Plasmas*, vol. 27, no. 2, p. 023703.

[145] K. Vermillion, D. Sanford, L. Matthews, *et al.*, 2022, "Influence of temporal variations in plasma conditions on the electric potential near self-organized dust chains", *Physics of Plasmas*, vol. 29, no. 2, p. 023701.

[146] R. Banka, K. Vermillion, L. Matthews, *et al.*, 2022, "Evolution of ion wake characteristics with experimental conditions", *Plasma Physics and Controled Fusion*, , no. submitted.

[147] M. Lampe, G. Joyce, G. Ganguli, *et al.*, 2000, "Interactions between dust grains in a dusty plasma", *Phys. Plasmas*, vol. 7, no. 10, pp. 3851–3861.

[148] A. V. Ivlev, U. Konopka, G. Morfill, *et al.*, 2003, "Melting of monolayer plasma crystals", *Phys. Rev. E*, vol. 68, no. 2, p. 026405.

[149] V. V. Yaroshenko, A. V. Ivlev, and G. E. Morfill, 2005, "Coupled dust-lattice modes in complex plasmas", *Phys. Rev. E*, vol. 71, no. 4, p. 046405.

[150] S. K. Zhdanov, A. V. Ivlev, and G. E. Morfill, 2009, "Mode-coupling instability of 2d plasma crystals", *Phys. Plasmas*, vol. 16, p. 083706.

[151] T. B. Röcker, A. V. Ivlev, R. Kompaneets, *et al.*, 2012, "Mode coupling in two-dimensional plasma crystals: Role of the wake model", *Phys. Plasmas*, vol. 19, no. 3, p. 033708.

[152] R. Kompaneets, G. E. Morfill, and A. V. Ivlev, 2016, "Interparticle attraction in 2d complex plasmas", *Phys. Rev. Lett.*, vol. 116, p. 125001.

[153] A. Melzer, 2014, "Connecting the wakefield instabilities in dusty plasmas", *Phys. Rev. E*, vol. 90, p. 053103.

[154] V. A. Schweigert, I. V. Schweigert, A. Melzer, *et al.*, 1996, "Alignment and instability of dust crystals in plasmas", *Physical Review E*, vol. 54, no. 4, pp. 4155–4166.

[155] V. A. Schweigert, I. V. Schweigert, A. Melzer, *et al.*, 1998, "Plasma crystal melting: A nonequilibrium phase transition", *Phys. Rev. Lett.*, vol. 80, no. 24, pp. 5345–5348.

[156] A. Melzer, A. Homann, and A. Piel, 1996, "Experimental investigation of the melting transition of the plasma crystal", *Phys. Rev. E*, vol. 53, no. 3, pp. 2757–2766.

[157] L. Couëdel, S. K. Zhdanov, A. V. Ivlev, *et al.*, 2011, "Wave mode coupling due to plasma wakes in two-dimensional plasma crystals: In-depth view", *Phys. Plasmas*, vol. 18, no. 8, p. 083707, ISSN 1070-664X.

[158] L. Couëdel and V. Nosenko, 2019, "Tracking and linking of microparticle trajectories during mode-coupling induced melting in a two-dimensional complex plasma crystal", *Journal of Imaging*, vol. 5, no. 3, ISSN 2313-433X.

[159] A. Melzer, S. Nunomura, D. Samsonov, *et al.*, 2000, "Laser-excited mach cones in a dusty plasma crystal", *Phys. Rev. E*, vol. 62, pp. 4162–4176.

[160] S. Nunomura, D. Samsonov, and J. Goree, 2000, "Transverse waves in a two-dimensional screened-coulomb crystal (dusty plasma)", *Phys. Rev. Lett.*, vol. 84, no. 22, pp. 5141–5144.

[161] V. A. Schweigert, I. V. Schweigert, V. Nosenko, *et al.*, 2002, "Acceleration and orbits of charged particles beneath a monolayer plasma crystal", *Phys. Plasmas*, vol. 9, no. 11, pp. 4465–4472, ISSN 1070-664X.

[162] S. Nunomura, J. Goree, S. Hu, *et al.*, 2002, "Phonon spectrum in a plasma crystal", *Phys. Rev. Lett.*, vol. 89, no. 3, p. 035001.

[163] K. Qiao and T. W. Hyde, 2003, "Dispersion properties of the out-of-plane transverse wave in a two-dimensional coulomb crystal", *Phys. Rev. E*, vol. 68, no. 4, p. 046403.

[164] S. O. Yurchenko, E. V. Yakovlev, L. Couëdel, *et al.*, 2017, "Flame propagation in two-dimensional solids: Particle-resolved studies with complex plasmas", *Phys. Rev. E*, vol. 96, p. 043201.

[165] L. Couëdel, V. Nosenko, M. Rubin-Zuzic, *et al.*, 2018, "Full melting of a two-dimensional complex plasma crystal triggered by localized pulsed laser heating", *Phys. Rev. E*, vol. 97, p. 043206.

[166] L. Couëdel, V. Nosenko, S. Zhdanov, *et al.*, 2019, "Experimental studies of two-dimensional complex plasma crystals: waves and instabilities", *Physics-Uspekhi*, vol. 62, no. 10, pp. 1000–1011.

[167] G. S. Selwyn, 1994, "Optical characterization of particle traps", *Plasma Sources Sci. Technol.*, vol. 3, no. 3, pp. 340–347.

[168] Y. Watanabe, M. Shiratani, Y. Kubo, *et al.*, 1988, "Effects of low-frequency modulation on rf discharge chemical vapor deposition", *Appl. Phys. Lett.*, vol. 53, no. 14, pp. 1263–1265.

[169] C. Arnas, C. Dominique, P. Roubin, *et al.*, 2006, "Characterisation of carbon dust produced in sputtering discharges and in the tore supra tokamak", *J. Nucl. Mater.*, vol. 353, no. 1-2, pp. 80 – 88, ISSN 0022-3115.

[170] C. Arnas, C. Martin, P. Roubin, *et al.*, 2010, "Similarities and differences between dust produced in laboratory plasmas and in the mast and tore supra tokamaks", *Plasma Phys. Controlled Fusion*, vol. 52, no. 12, p. 124007.

[171] C. Arnas, C. Pardanaud, C. Martin, *et al.*, 2010, "Analyses of dust samples collected in the mast tokamak", *J. Nucl. Mater.*, vol. 401, no. 1-3, pp. 130 – 137, ISSN 0022-3115.

[172] M. Bacharis, M. Coppins, and J. E. Allen, 2010, "Critical issues for modeling dust transport in tokamaks", *Phys. Rev. E*, vol. 82, p. 026403.

[173] F. Brochard, A. Shalpegin, S. Bardin, *et al.*, 2017, "Video analysis of dust events in full-tungsten asdex upgrade", *Nucl. Fusion*, vol. 57, no. 3, p. 036002.

[174] W. Carmack, G. Smolik, R. Anderl, *et al.*, 1998, "Tokamak dust particle size and surface area measurement", *Fusion Technol.*, vol. 34, p. 604.

[175] P. Chappuis, E. Tsitrone, M. Mayne, *et al.*, 2001, "Dust characterization and analysis in tore-supra", *J. Nucl. Mater.*, vol. 290-293, pp. 245 – 249, ISSN 0022-3115, 14th Int. Conf. on Plasma-Surface Interactions in Controlled Fusion D evices.

[176] C. Grisolia, S. Rosanvallon, A. Loarte, *et al.*, 2009, "From eroded material to dust: An experimental evaluation of the mobilised dust production in tore supra", *J. Nucl. Mater.*, vol. 390-391, no. 0, pp. 53 – 56, ISSN 0022-3115, <ce:title>Proceedings of the 18th International Conference on Plasma-Surface Interactions in Controlled Fusion Device</ce:title> <xocs:full-name>Proceedings of the 18th International Conference on Plasma-Surface Interactions in Controlled Fusion Device</xocs:full-name>.

[177] S. Ratynskaia, H. Bergsåker, B. Emmoth, *et al.*, 2009, "Capture by aerogel—characterization of mobile dust in tokamak scrape-off layer plasmas", *Nucl. Fusion*, vol. 49, no. 12, p. 122001.

[178] J. Winter, 2004, "Dust in fusion devices—a multi-faceted problem connecting high- and low-temperature plasma physics", *Plasma Phys. Controlled Fusion*, vol. 46, p. B583.

[179] J. Sharpe, V. Rohde, T. A.-U. E. Team, *et al.*, 2003, "Characterization of dust collected from ASDEX-upgrade and LHD", *Journal of Nuclear Materials*, vol. 313-316, pp. 455–459.

[180] M. Richou, C. Martin, P. Delhaès, *et al.*, 2007, "Physico-chemical characteristics of carbon deposits collected in TEXTOR and tore supra tokamaks", *Carbon*, vol. 45, no. 14, pp. 2723–2731.

[181] S. Rosanvallon, C. Grisolia, P. Andrew, *et al.*, 2009, "Dust limit management strategy in tokamaks", *J. Nucl. Mater.*, vol. 390-391, pp. 57 – 60, ISSN 0022-3115, proceedings of the 18th International Conference on Plasma-Surface Interactions in Controlled Fusion Device, Proceedings of the 18th International Conference on Plasma-Surface Interactions in Controlled Fusion Device.

[182] J. Roth, E. Tsitrone, A. Loarte, *et al.*, 2009, "Recent analysis of key plasma wall interactions issues for iter", *J. Nucl. Mater.*, vol. 390-391, no. 0, pp. 1 – 9, ISSN 0022-3115, <ce:title>Proceedings of the 18th International Conference on Plasma-Surface Interactions in Controlled Fusion Device</ce:title> <xocs:full-name>Proceedings of the 18th International Conference on Plasma-Surface Interactions in Controlled Fusion Device</xocs:full-name>.

[183] T. Tanabe, 2021, *Plasma-Material Interactions in a Controlled Fusion Reactor*, Springer Nature Singapore, ISBN 978-981-16-0328-0.

[184] A. V. Phelps and Z. L. Petrovic, 1999, "Cold-cathode discharges and breakdown in argon: surface and gas phase production of secondary electrons", *Plasma Sources Sci. Technol.*, vol. 8, pp. R21–R44.

[185] G. Vida, V. Josepovits, M. Gyor, *et al.*, 2003, "Characterization of tungsten surfaces by simultaneous work function and secondary electron emission measurements", *Microsc. Microanal.*, vol. 9, no. 04, pp. 337–342.

[186] R. Boulmani, M. Bendahan, C. Lambert-Mauriat, *et al.*, 2007, "Correlation between rf-sputtering parameters and wo3 sensor response towards ozone", *Sens. Actuators, B*, vol. 125, no. 2, pp. 622 – 627, ISSN 0925-4005.

[187] J. Heller, 1973, "Reactive sputtering of metals in oxidizing atmospheres", *Thin Solid Films*, vol. 17, no. 2, pp. 163 – 176, ISSN 0040-6090.

[188] A. Michau, G. Lombardi, L. Colina Delacqua, *et al.*, 2012, "Field reversal and particle growth in dc discharge", *Plasma Chem. Plasma Process.*, vol. 32, pp. 451–470, ISSN 0272-4324.

[189] Z. Donkó, P. Hartmann, and K. Kutasi, 2006, "On the reliability of low-pressure dc glow discharge modelling", *Plasma Sources Sci. Technol.*, vol. 15, no. 2, p. 178.

[190] W. D. Gill and E. Kay, 1965, "Efficient low pressure sputtering in a large inverted magnetron suitable for film synthesis", *Review of Scientific Instruments*, vol. 36, no. 3, pp. 277–282.

[191] R. K. Waits, 1978, "Planar magnetron sputtering", *Journal of Vacuum Science and Technology*, vol. 15, no. 2, pp. 179–187.

[192] T. E. Sheridan, M. J. Goeckner, and J. Goree, 1990, "Model of energetic electron transport in magnetron discharges", *Journal of Vacuum Science & Technology A: Vacuum, Surfaces, and Films*, vol. 8, no. 1, pp. 30–37.

[193] D. Depla and W. Leroy, 2012, "Magnetron sputter deposition as visualized by monte carlo modeling", *Thin Solid Films*, vol. 520, no. 20, pp. 6337–6354, ISSN 0040-6090.

[194] M. L. Escrivão, A. M. C. Moutinho, and M. J. P. Maneira, 1994, "Planar magnetron glow discharge on copper: Empirical and semiempirical relations", *Journal of Vacuum Science & Technology A*, vol. 12, no. 3, pp. 723–726.

[195] S. M. Rossnagel and J. Hopwood, 1994, "Metal ion deposition from ionized mangetron sputtering discharge", *Journal of Vacuum Science & Technology B: Microelectronics and Nanometer Structures Processing, Measurement, and Phenomena*, vol. 12, no. 1, pp. 449–453.

[196] K. Matyash, M. Fröhlich, H. Kersten, *et al.*, 2004, "Rotating dust ring in an rf discharge coupled with a dc-magnetron sputter source. experiment and simulation", *J. Phys. D: Appl. Phys.*, vol. 37, no. 19, p. 2703.

[197] A. E. Farsy, J. Ledig, M. Desecures, *et al.*, 2019, "Characterization of transport of titanium neutral atoms sputtered in ar and ar/n2 HIPIMS discharges", *Plasma Sources Sci. Technol.*, vol. 28, no. 3, p. 035005.

[198] H. Haberland, M. Mall, M. Moseler, *et al.*, 1994, "Filling of micron-sized contact holes with copper by energetic cluster impact", *J. Vac. Sci.Technol. A*, vol. 12, no. 5, pp. 2925–2930.

[199] A. Majumdar, D. Köpp, M. Ganeva, *et al.*, 2009, "Development of metal nanocluster ion source based on dc magnetron plasma sputtering at room temperature", *Rev. Sci. Instrum.*, vol. 80, no. 9, pp. –.

[200] T. Momin and A. Bhowmick, 2010, "A new magnetron based gas aggregation source of metal nanoclusters coupled to a double time-of-flight mass spectrometer system", *Rev. Sci. Instrum.*, vol. 81, no. 7, pp. –.

[201] V. Bouchat, O. Feron, B. Gallez, *et al.*, 2011, "Carbon nanoparticles synthesized by sputtering and gas condensation inside a nanocluster source of fixed dimension", *Surf. Coat. Technol.*, vol. 205, Supplement 2, no. 0, pp. S577 – S581, ISSN 0257-8972, pSE 2010 Special Issue: Proceedings of the 12th International Conference on Plasma Surface Engineering.

[202] N. K. Manninen, N. M. Figueiredo, S. Carvalho, *et al.*, 2014, "Production and characterization of ag nanoclusters produced by plasma gas condensation", *Plasma Processes Polym.*, vol. 11, no. 7, pp. 629–638.

[203] M. V. Dutka, A. A. Turkin, D. I. Vainchtein, *et al.*, 2015, "On the formation of copper nanoparticles in nanocluster aggregation source", *Journal of Vacuum Science & Technology A*, vol. 33, no. 3, pp. –.

[204] J. Kousal, A. Kolpaková, A. Shelemin, *et al.*, 2017, "Monitoring of conditions inside gas aggregation cluster source during production of ti/tio x nanoparticles", *Plasma Sources Sci. Technol.*, vol. 26, no. 10, p. 105003.

[205] T. Acsente, R. Negrea, L. Nistor, *et al.*, 2017, "Tungsten nanoparticles with controlled shape and crystallinity obtained by magnetron sputtering and gas aggregation", *Mater. Lett.*, vol. 200, pp. 121 – 124, ISSN 0167-577X.

[206] M. Vaidulych, J. Hanuš, J. Kousal, *et al.*, 2019, "Effect of magnetic field on the formation of cu nanoparticles during magnetron sputtering in the gas aggregation cluster source", *Plasma Processes and Polymers*, vol. 16, no. 11, p. 1900133.

[207] M. Koten, S. Voeller, M. Patterson, *et al.*, 2016, "In situ measurements of plasma properties during gas-condensation of cu nanoparticles", *J. Appl. Phys.*, vol. 119, no. 11, p. 114306.

[208] J. Kousal, A. Shelemin, M. Schwartzkopf, *et al.*, 2018, "Magnetron-sputtered copper nanoparticles: lost in gas aggregation and found by in situ x-ray scattering", *Nanoscale*, vol. 10, no. 38, pp. 18275–18281.

[209] H. Hahn and R. S. Averback, 1990, "The production of nanocrystalline powders by magnetron sputtering", *J. Appl. Phys.*, vol. 67, no. 2, pp. 1113–1115, ISSN 0021-8979.

[210] N. Nafarizal and K. Sasaki, 2012, "Synthesis characteristics of cu particulates in high-pressure magnetron sputtering plasmas studied by in situ laser-light scattering", *J. Phys. D: Appl. Phys.*, vol. 45, no. 50, p. 505202.

[211] L. Couëdel, C. Arnas, T. Acsente, *et al.*, 2018, "Characterisation of a high-pressure direct-current magnetron discharge used for tungsten nanoparticle production", *AIP Conference Proceedings*, vol. 1925, no. 1, p. 020020.

[212] A. Chami and C. Arnas, 2020, "Spatial distributions of plasma parameters in conventional magnetron discharges in presence of nanoparticles", *Journal of Plasma Physics*, vol. 86, no. 5, p. 905860512.

[213] S. Mitic, J. Moreno, C. Arnas, *et al.*, 2021, "Diagnostics of a high-pressure dc magnetron argon discharge with an aluminium cathode", *The European Physical Journal D*, vol. 75, no. 9, p. 240, ISSN 1434-6079.

[214] M. Mikikian, M. Cavarroc, L. Couëdel, *et al.*, 2006, "Low frequency instabilities during dust particle growth in a radio-frequency plasma", *Phys. Plasmas*, vol. 13, p. 092103.

[215] S. Mitic, M. Y. Pustylnik, and G. E. Morfill, 2009, "Spectroscopic evaluation of the effect of the microparticles on radiofrequency argon plasma", *New J. Phys.*, vol. 11, no. 8, p. 083020.

[216] S. Mitic, B. Klumov, M. Pustylnik, *et al.*, 2010, "Determination of electron temperature in low-pressure plasmas by means of optical emission spectroscopy", *JETP Lett.*, vol. 91, no. 5, pp. 231–235.

[217] S. M. Rossnagel and H. R. Kaufman, 1988, "Current–voltage relations in magnetrons", *Journal of Vacuum Science & Technology A*, vol. 6, no. 2, pp. 223–229.

[218] D. Depla, G. Buyle, J. Haemers, *et al.*, 2006, "Discharge voltage measurements during magnetron sputtering", *Surface and Coatings Technology*, vol. 200, no. 14, pp. 4329–4338, ISSN 0257-8972.

[219] G. Buyle, D. Depla, K. Eufinger, *et al.*, 2003, "Simplified model for calculating the pressure dependence of a direct current planar magnetron discharge", *Journal of Vacuum Science & Technology A: Vacuum, Surfaces, and Films*, vol. 21, no. 4, pp. 1218–1224.

[220] G. Buyle, D. Depla, K. Eufinger, *et al.*, 2004, "Simplified model for the {DC} planar magnetron discharge", *Vacuum*, vol. 74, no. 3–4, pp. 353 – 358, ISSN 0042-207X, selected papers revised from the Proceedings of the Seventh International Symposium on Sputtering and Plasma Processes (ISSP 2003).

[221] R. L. Merlino, 2007, "Understanding langmuir probe current-voltage characteristics", *Am. J. Phys*, vol. 75, no. 12, pp. 1078–1085.

[222] M. A. Lieberman and A. J. Lichtenberg, 2005, *Principles of Plasma Discharges and Materials Processing*, John Wiley & Sons, Inc., ISBN 9780471720010.

[223] J. Kaupe, D. Coenen, and S. Mitic, 2018, "Phase-resolved optical emission spectroscopy of a transient plasma created by a low-pressure dielectric barrier discharge jet", *Plasma Sources Sci. Technol.*, vol. 27, no. 10, p. 105003.

[224] S. Mitic, J. Kaupe, P. Riedl, *et al.*, 2019, "Comparative studies of compact khz and mhz driven low pressure plasmas by emission and laser spectroscopy", *Physics of Plasmas*, vol. 26, no. 7, p. 073507.

[225] R. Mewe, 1967, "Relative intensity of helium spectral lines as a function of electron temperature and density", *British Journal of Applied Physics*, vol. 18, no. 1, pp. 107–118.

[226] M. Schulze, A. Yanguas-Gil, A. von Keudell, *et al.*, 2008, "A robust method to measure metastable and resonant state densities from emission spectra in argon and argon-diluted low pressure plasmas", *J. Phys. D: Appl. Phys.*, vol. 41, no. 6, p. 065206.

[227] J. Trieschmann, S. Ries, N. Bibinov, *et al.*, 2018, "Combined experimental and theoretical description of direct current magnetron sputtering of al by ar and ar/n2 plasma", *Plasma Sources Sci. Technol.*, vol. 27, no. 5, p. 054003.

[228] K. Sasaki and N. Nafarizal, 2010, "Enhancement of ti + density in high-pressure magnetron sputtering plasmas", *J. Phys. D: Appl. Phys.*, vol. 43, no. 12, p. 124012.

[229] F. J. Jimenez and S. K. Dew, 2012, "Comprehensive computer model for magnetron sputtering. i. gas heating and rarefaction", *Journal of Vacuum Science & Technology A*, vol. 30, no. 4, p. 041302.

[230] J. Hopwood and F. Qian, 1995, "Mechanisms for highly ionized magnetron sputtering", *J. Appl. Phys.*, vol. 78, no. 2, pp. 758–765.

[231] C. Christou and Z. H. Barber, 2000, "Ionization of sputtered material in a planar magnetron discharge", *Journal of Vacuum Science & Technology A: Vacuum, Surfaces, and Films*, vol. 18, no. 6, pp. 2897–2907.

[232] W. P. West, B. D. Bray, and J. Burkart, 2006, "Measurement of number density and size distribution of dust in diii-d during normal plasma operation", *Plasma Phys. Controlled Fusion*, vol. 48, no. 11, p. 1661.

[233] V. Rohde, M. Balden, T. Lunt, *et al.*, 2009, "Dust investigations at asdex upgrade", *Phys. Scr.*, vol. T138, no. T138, p. 014024.

[234] D. Rudakov, A. Litnovsky, W. West, *et al.*, 2009, "Dust studies in diii-d and textor", *Nucl. Fusion*, vol. 49, no. 8, p. 085022.

[235] M. Calafat, D. Escaich, R. Clergereaux, *et al.*, 2007, "Particle formation in acetylene very low-pressure high density magnetized plasmas", *Appl. Phys. Lett.*, vol. 91, no. 18, p. 181502.

[236] A. Drenik, P. Yuryev, A. Vesel, *et al.*, 2013, "Observation of plasma instabilities related to dust particle growth mechanisms in electron cyclotron resonance plasmas", *Phys. Plasmas*, vol. 20, no. 10, pp. –.

[237] M. Rojo, X. Glad, J. Margot, *et al.*, 2019, "Charging and heating processes of dust particles in an electron cyclotron resonance plasma", *Plasma Sources Sci. Technol.*, vol. 28, no. 8, p. 085004.

[238] E. T. Jr., R. L. Merlino, and M. Rosenberg, 2012, "Magnetized dusty plasmas: the next frontier for complex plasma research", *Plasma Phys. Controlled Fusion*, vol. 54, no. 12, p. 124034.

[239] E. Thomas, A. M. DuBois, B. Lynch, *et al.*, 2014, "Preliminary characteristics of magnetic field and plasma performance in the magnetized dusty plasma experiment (mdpx)", *J. Plasma Phys.*, vol. 80, no. 6, p. 803–808.

[240] E. Thomas, U. Konopka, B. Lynch, *et al.*, 2015, "Quasi-discrete particle motion in an externally imposed, ordered structure in a dusty plasma at high magnetic field", *Phys. Plasmas*, vol. 22, no. 11, p. 113708.

[241] G. Wattieaux and L. Boufendi, 2012, "Discharge impedance evolution, stray capacitance effect, and correlation with the particles size in a dusty plasma", *Phys. Plasmas*, vol. 19, no. 3, p. 033701.

[242] V. Massereau-Guilbaud, I. Géraud-Grenier, and A. Plain, 2009, "Determination of the electron temperature by optical emission spectroscopy in a 13.56 mhz dusty methane plasma: Influence of the power", *J. Appl. Phys.*, vol. 106, no. 11, p. 113305.

[243] G. Wattieaux, N. Carrasco, M. Henault, *et al.*, 2015, "Transient phenomena during dust formation in a n 2 –ch 4 capacitively coupled plasma", *Plasma Sources Sci. Technol.*, vol. 24, no. 1, p. 015028.

[244] G. Wattieaux, A. Mezeghrane, and L. Boufendi, 2011, "Electrical time resolved metrology of dust particles growing in low pressure cold plasmas", *Phys. Plasmas*, vol. 18, no. 9, p. 093701.

[245] M. Hundt, P. Sadler, I. Levchenko, *et al.*, 2011, "Real-time monitoring of nucleation-growth cycle of carbon nanoparticles in acetylene plasmas", *J. Appl. Phys.*, vol. 109, no. 12, p. 123305.

[246] D. Herrebout, A. Bogaerts, R. Gijbels, *et al.*, 2003, "A one-dimensional fluid model for an acetylene RF discharge: a study of the plasma chemistry", *IEEE Transactions on Plasma Science*, vol. 31, no. 4, pp. 659–664.

[247] A. Baby, C. Mahony, and P. Maguire, 2011, "Acetylene–argon plasmas measured at a biased substrate electrode for diamond-like carbon deposition: I. mass spectrometry", *Plasma Sources Sci. Technol.*, vol. 20, no. 1, p. 015003.

[248] J. Winter, J. Berndt, S. H. Hong, *et al.*, 2009, "Dust formation in ar/ch4 and ar/c2h2 plasmas", *Plasma Sources Sci. Technol.*, vol. 18, no. 3, p. 034010.

[249] C. Killer, M. Himpel, and A. Melzer, 2014, "Computer tomography of large dust clouds in complex plasmas", *Rev. Sci. Instrum.*, vol. 85, no. 10, pp. –.

[250] I. Pilch and F. Greiner, 2017, "Diagnostics of void expansion during cyclic growth and formation of layered nanoparticle clouds", *J. Appl. Phys.*, vol. 121, no. 11, p. 113302.

[251] G. Praburam and J. Goree, 1996, "Experimental observation of very low-frequency macroscopic modes in a dusty plasma", *Phys. Plasmas*, vol. 3, no. 4, pp. 1212–1219.

[252] D. Samsonov and J. Goree, 1999, "Instabilities in a dusty plasma with ion drag and ionization", *Phys. Rev. E*, vol. 59, p. 1047.

[253] F. Greiner, J. Carstensen, N. Köhler, *et al.*, 2012, "Imaging mie ellipsometry: dynamics of nanodust clouds in an argon–acetylene plasma", *Plasma Sources Sci. Technol.*, vol. 21, no. 6, p. 065005.

[254] S. Dap, R. Hugon, D. Lacroix, *et al.*, 2013, "Agglomeration processes sustained by dust density waves in ar/c2h2 plasma: From c2h2 injection to the formation of an organized structure", *Phys. Plasmas*, vol. 20, no. 3, pp. –.

[255] B. Tadsen, F. Greiner, and A. Piel, 2014, "Preparation of magnetized nanodusty plasmas in a radio frequency-driven parallel-plate reactor", *Phys. Plasmas*, vol. 21, no. 10, p. 103704.

[256] C.-R. Du, H. M. Thomas, A. V. Ivlev, *et al.*, 2010, "Agglomeration of microparticles in complex plasmas", *Phys. Plasmas*, vol. 17, no. 11, p. 113710.

[257] I. Stefanovic, E. Kovacevic, J. Berndt, *et al.*, 2005, "Hydrocarbon nanoparticles as a diffuse ism analogue: morphology and infrared absorption in the 2000–500 cm-1 region", *Plasma Phys. Control. Fus.*, vol. 47, p. A179.

[258] S. Jaiswal, M. Menati, L. Couëdel, *et al.*, 2020, "Effect of growing nanoparticle on the magnetic field induced filaments in a radio-frequency ar/c 2 h 2 discharge plasma", *Jpn. J. Appl. Phys.*, vol. 59, no. SH, p. SHHC07.

[259] S. S. Rogers, T. A. Waigh, X. Zhao, *et al.*, 2007, "Precise particle tracking against a complicated background: polynomial fitting with gaussian weight", *Phys. Biol.*, vol. 4, no. 3, pp. 220–227.

[260] Y. Feng, J. Goree, and B. Liu, 2007, "Accurate particle position measurement from images", *Rev. Sci. Instrum.*, vol. 78, no. 5, p. 053704.

[261] A. V. Ivlev and G. Morfill, 2000, "Anisotropic dust lattice modes", *Phys. Rev. E*, vol. 63, p. 016409.

[262] Couëdel, L., Röcker, T. B., Zhdanov, S. K., *et al.*, 2016, "Forced mode coupling in 2d complex plasmas", *EPL*, vol. 115, no. 4, p. 45002.

[263] V. Steinberg, R. Sütterlin, A. V. Ivlev, *et al.*, 2001, "Vertical pairing of identical particles suspended in the plasma sheath", *Phys. Rev. Lett.*, vol. 86, no. 20, pp. 4540–4543.

[264] N. P. Kryuchkov, E. V. Yakovlev, E. A. Gorbunov, *et al.*, 2018, "Thermoacoustic instability in two-dimensional fluid complex plasmas", *Phys. Rev. Lett.*, vol. 121, p. 075003.

[265] B. Liu, J. Goree, and Y. Feng, 2010, "Mode coupling for phonons in a single-layer dusty plasma crystal", *Phys. Rev. Lett.*, vol. 105, no. 8, p. 085004.

[266] B. Liu, J. Goree, and Y. Feng, 2010, "Erratum: Mode coupling for phonons in a single-layer dusty plasma crystal [phys. rev. lett. 105, 085004 (2010)]", *Phys. Rev. Lett.*, vol. 105, no. 26, p. 269901.

[267] T. B. Röcker, S. K. Zhdanov, A. V. Ivlev, *et al.*, 2012, "Effective dipole moment for the mode coupling instability: Mapping of self-consistent wake models", *Phys. Plasmas*, vol. 19, no. 7, p. 073708.

[268] T. B. Röcker, A. V. Ivlev, S. K. Zhdanov, *et al.*, 2014, "Effect of strong wakes on waves in two-dimensional plasma crystals", *Phys. Rev. E*, vol. 89, p. 013104.

[269] N. Kohlmann, F. Wieben, O. H. Asnaz, *et al.*, 2019, "High-precision in-situ size measurements of single microparticles in an rf plasma", *Physics of Plasmas*, vol. 26, no. 5, p. 053701.

[270] I. Laut, C. Räth, S. Zhdanov, *et al.*, 2015, "Synchronization of particle motion in compressed two-dimensional plasma crystals", *EPL (Europhysics Letters)*, vol. 110, no. 6, p. 65001.

[271] P. Hartmann, G. J. Kalman, Z. Donkó, *et al.*, 2005, "Equilibrium properties and phase diagram of two-dimensional yukawa systems", *Phys. Rev. E*, vol. 72, p. 026409.

[272] J. K. Meyer, I. Laut, S. K. Zhdanov, *et al.*, 2017, "Coupling of noncrossing wave modes in a two-dimensional plasma crystal", *Phys. Rev. Lett.*, vol. 119, p. 255001.

[273] K. O. Menzel, O. Arp, and A. Piel, 2011, "Frequency clusters and defect structures in nonlinear dust-density waves under microgravity conditions", *Phys. Rev. E*, vol. 83, p. 016402.

[274] R. Toth and A. F. Taylor, 2006, "Loss of coherence in a population of diffusively coupled oscillators", *The Journal of Chemical Physics*, vol. 125, no. 22, p. 224708.

[275] Y. Kuramoto, 1984, *Chemical oscillations, waves, and turbulence*, Springer-Verlag, New York, NY, USA.

[276] I. Laut, S. K. Zhdanov, C. Räth, *et al.*, 2016, "Anisotropic confinement effects in a two-dimensional plasma crystal", *Phys. Rev. E*, vol. 93, p. 013204.

[277] A. V. Ivlev, T. B. Röcker, L. Couëdel, *et al.*, 2015, "Wave modes in shear-deformed two-dimensional plasma crystals", *Phys. Rev. E*, vol. 91, p. 063108.

[278] L. D. Landau and E. M. Lifshitz, 1987, *Fluid Mechanics*, Oxford, 2nd ed.

[279] V. E. Fortov, O. S. Vaulina, and O. F. Petrov, 2005, "Dusty plasma liquid: structure and transfer phenomena", *Plasma Phys. Controlled Fusion*, vol. 47, no. 12B, p. B551.

[280] T. E. Sheridan, 2009, "Monte carlo study of melting in a finite two-dimensional dusty plasma", *Phys. Plasmas*, vol. 16, no. 8, p. 083705.

[281] I. Zeldovich, G. I. Barenblatt, V. Librovich, *et al.*, 1985, "Mathematical theory of combustion and explosions", .

[282] M. T. Dove, 1993, *Introduction to lattice dynamics*, vol. 4, Cambridge university press.

[283] A. Ivlev, T. Röcker, A. Vasyunin, *et al.*, 2015, "Impulsive spot heating and thermal explosion of interstellar grains revisited", *Astrophys. J.*, vol. 805, no. 1, p. 59.

[284] N. P. Kryuchkov, S. A. Khrapak, and S. O. Yurchenko, 2017, "Thermodynamics of two-dimensional yukawa systems across coupling regimes", *J. Chem. Phys.*, vol. 146, no. 13, p. 134702.

[285] V. Nosenko, S. Zhdanov, A. V. Ivlev, *et al.*, 2008, "Heat transport in a two-dimensional complex (dusty) plasma at melting conditions", *Phys. Rev. Lett.*, vol. 100, no. 2, p. 025003.

[286] A. Merzhanov, 1966, "On critical conditions for thermal explosion of a hot spot", *Combust. Flame*, vol. 10, no. 4, pp. 341–348, ISSN 0010-2180.

[287] A. Khodaee, 2020, *RF-compensated Langmuir Probe Diagnostics of Pulsed Plasma Ion Implantation System*, Master's thesis, College of Graduate and Postdoctoral Studies, University of Saskatchewan.

[288] A. Chang, 2020, *ICP Enhanced HIPIMS System Design and Characterisation*, Master's thesis, College of Graduate and Postdoctoral Studies, University of Saskatchewan.

[289] N. Claire, S. Mazouffre, C. Rebont, *et al.*, 2012, "Examination of argon metastable atom velocity distribution function close to a conducting wall", *Phys. Plasmas*, vol. 19, no. 3, p. 032108.

[290] E. V. Barnat, 2011, "Multi-dimensional optical and laser-based diagnostics of low-temperature ionized plasma discharges", *Plasma Sources Sci. Technol.*, vol. 20, no. 5, p. 053001.

[291] N. Nelson, L. Couëdel, and C. Xiao, 2022, "Design and characterization of a dust dispenser for tungsten dust injection experiments in the STOR-m tokamak", *Radiation Effects and Defects in Solids*, vol. 177, no. 1-2, pp. 181–197.

[292] M. Dreval, C. Xiao, D. Trembach, *et al.*, 2008, "Simultaneous evolution of plasma rotation, radial electric field, mhd activity and plasma confinement in the stor-m tokamak", *Plasma Phys. Controlled Fusion*, vol. 50, no. 9, p. 095014.

[293] E. Thomas and J. Williams, 2006, "Applications of stereoscopic particle image velocimetry: Dust acoustic waves and velocity space distribution functions", *Phys. Plasmas*, vol. 13, no. 5, p. 055702.

[294] R. Smirnov, S. Krasheninnikov, A. Pigarov, *et al.*, 2011, "Modeling of dust impact on tokamak edge plasmas", *J. Nucl. Mater.*, vol. 415, no. 1, Supplement, pp. S1067 – S1072, ISSN 0022-3115, proceedings of the 19th International Conference on Plasma-Surface Interactions in Controlled Fusion.

[295] R. D. Smirnov and S. I. Krasheninnikov, 2017, "Impact of cross-field motion on ablation of high-z dust in fusion edge plasmas", *Phys. Plasmas*, vol. 24, no. 7, p. 072505.

[296] L. Vignitchouk, S. Ratynskaia, P. Tolias, *et al.*, 2018, "Survival and in-vessel redistribution of beryllium droplets after iter disruptions", *Nucl. Fusion*.

[297] P. Cagas, A. Hakim, J. Juno, *et al.*, 2017, "Continuum kinetic and multi-fluid simulations of classical sheaths", *Phys. Plasmas*, vol. 24, no. 2, p. 022118.

[298] M. D. Campanell and M. V. Umansky, 2017, "Are two plasma equilibrium states possible when the emission coefficient exceeds unity?", *Phys. Plasmas*, vol. 24, no. 5, p. 057101.

[299] M. D. Campanell and M. V. Umansky, 2016, "Strongly emitting surfaces unable to float below plasma potential", *Phys. Rev. Lett.*, vol. 116, p. 085003.